MONASH University

Stability, Transition and Turbulence in

Quasi-Two-Dimensional MHD Duct Flows

Christopher John Camobreco

Bachelor of Aerospace Engineering (Honours)

A Thesis submitted for the degree of

Doctor of Philosophy at

Monash University in 2021

Department of Mechanical and Aerospace Engineering

Copyright notice

Abstract

Quasi-two-dimensional (Q2D) flows exhibit three-dimensionality which is either contained to asymptotically small regions, or is asymptotically small in amplitude. In spite of this, the oft-investigated route to large scale Q2D turbulence, from a Q2D laminar state, is through the generation of small scale three-dimensional (3D) turbulence, which two-dimensionalizes. The overarching aim of this thesis is to determine whether a Q2D laminar state can directly transition to Q2D turbulence. However, the gold standard for generating turbulence is with 3D perturbations, which cannot be present in purely Q2D routes to turbulence.

This thesis shows that purely Q2D routes to turbulence are not only possible, but exhibit distinct differences to the presumed optimal (maximized nonlinear growth) routes to turbulence in 3D systems. Understanding a purely Q2D route to turbulence may aid predictions of 3D magnetohydrodynamic (MHD) flows in Q2D regimes. Predicting the properties of an MHD flow of an electrically conducting fluid through the coolant ducts of a magnetic confinement fusion reactor forms the practical motivation of this research.

The purely Q2D transitions are initiated by laminar perturbations, to permit observation of the inception of turbulence. First, perturbations maximizing transient growth are considered. However, at subcritical Reynolds numbers, these trigger only single turbulent episodes. In spite of this, further analysis provides key insights into how nonlinearity manifests and turbulence develops. Nonlinear analogues of the Orr mechanism, and the formation of thin, arched jets of vorticity, which form the backbones underlying the large Q2D structures, are particularly important.

Supercritical Reynolds numbers, and the dependence on the level of imposed friction (magnetic field strength) are then considered. Interestingly, even when bifurcation analysis implies that subcritical transitions are possible, they are rarely observed; in such cases, even supercriticality is not sufficient to guarantee transition. This result depends strongly on the imposed level of friction.

By focusing on a friction parameter capable of subcritical transition, purely Q2D routes to the first sustained subcritical Q2D turbulence are observed. To initiate the transition, it will ultimately prove best to forgo transient growth, and to instead optimally energize the leading eigenmode, via its adjoint. This laminar nonmodal perturbation provides access to the lower edge state on the laminar-turbulent basin, through

a weakly nonlinear route. However, the direct numerical simulations slightly deviate from the classical predictions of a subcritical bifurcation upon departing the edge. Rather than a slow, modulated growth to turbulence, departure from the edge state is rapid, which may indicate that the modulated base flow briefly experiences supercritical conditions. Overall, transitions to sustained turbulence are only observed at weakly subcritical Reynolds numbers.

Thus, to tackle the practical application of this research, in reducing the Reynolds number required to sustain turbulence in MHD cooling conduits under strong magnetic fields, modifications are made to the base flow. Base flow inflection points are introduced via a time-varying pressure gradient, which greatly reduces the critical Reynolds number. However, inciting and sustaining turbulence with these modified base flows is still problematic when at low Reynolds numbers.

Publications during enrolment

Camobreco, C. J., Pothérat, A. & Sheard, G. J. 2020 Subcritical route to turbulence via the Orr mechanism in a quasi-two-dimensional boundary layer. *Phys. Rev. Fluids* **5** (11), 113902. © 2020 American Physical Society

Camobreco, C. J., Pothérat, A. & Sheard, G. J. 2021a Stability of pulsatile quasi-two-dimensional duct flows under a transverse magnetic field. *Phys. Rev. Fluids* **6** (5), 053903. © 2021 American Physical Society

Camobreco, C. J., Pothérat, A. & Sheard, G. J. 2021b Transition to turbulence in quasi-two-dimensional MHD flow driven by lateral walls. *Phys. Rev. Fluids* **6** (1), 013901. © 2021 American Physical Society

Camobreco, C. J., Pothérat, A. & Sheard, G. J. 2020 Linear stability analysis of pulsatile quasi-two-dimensional duct flows under a transverse magnetic field. In *Proceedings of the 22nd Australasian Fluid Mechanics Conference AFMC2020* (Eds: H. Chanson and R. Brown, Pub: The University of Queensland, ISBN: 978-1-74272-341-9), Paper 173. Conference: 22nd Australasian Fluid Mechanics Conference, Brisbane, Queensland, Australia, 7-10 December 2020.

Thesis including published works declaration

I hereby declare that this thesis contains no material which has been accepted for the award of any other degree or diploma at any university or equivalent institution and that, to the best of my knowledge and belief, this thesis contains no material previously published or written by another person, except where due reference is made in the text of the thesis.

This thesis includes 3 original papers published in peer reviewed journals. The core theme of the thesis is purely quasi-two-dimensional routes to turbulence in duct flows. The ideas, development and writing up of all the papers in the thesis were the principal responsibility of myself, the student, working within the department of Mechanical and Aerospace Engineering under the supervision of Gregory J. Sheard (G.J.S.; Monash University) and Alban Pothérat (A.P.; Coventry University). The inclusion of co-authors reflects the fact that the work came from active collaboration between researchers and acknowledges input into team-based research.

I have not renumbered sections of published papers in order to generate a consistent presentation within the thesis; as stated in the copyright notice, all three papers have been included in published (unmodified) form.

In the case of Chapters 5, 6 and 8 my contribution to the work involved the following:

Thesis Chapter	Publication Title	Status	Nature and percentage of student contribution	Co-author(s), nature and percentage contributions	Co-author(s) Monash student (Y/N)
5	*Subcritical route to turbulence via the Orr mechanism in a quasi-two-dimensional boundary layer*	Published	90%; Concept, simulations, analysis, interpretation, visualization, write up	5% G.J.S; in-house solver modifications, revision; 5% A.P; concept, revision	N
6	*Transition to turbulence in quasi-two-dimensional MHD flow driven by lateral walls*	Published	90%; as above	5% G.J.S; revision; 5% A.P; concept, recommended weakly nonlinear analysis, revision, rewrote introduction	N
8	*Stability of pulsatile quasi-two-dimensional duct flows under a transverse magnetic field*	Published	90%; as above	5% G.J.S; concept, revision; 5% A.P; timescale analysis for SM82, revision	N

Student signature: (Signature removed from final thesis)

Candidate: Christopher J. Camobreco
21/02/2021

I hereby certify that the above declaration correctly reflects the nature and extent of the student's and co-author's contributions to this work. In instances where I am not the responsible author, I have consulted with the responsible author to agree on the respective contributions of the authors.

Main supervisor signature: (Signature removed from final thesis)

Main supervisor: Gregory J. Sheard
21/02/2021

Acknowledgments

First, it would be improper not to acknowledge the breadth of research which already exists in the realm of subcritical turbulence, which provided such a solid foundation for this research. In particular, I am grateful to the benevolence of certain authors, Trefethen (2000) and Schmid & Henningson (2001) in particular, whose work greatly reduced the barrier of entry to the field. The time saved in having access to the basic numerical means to solve problems in fluid mechanics was much appreciated, as are the many useful, but often unattributed, solutions to numerical problems found on file (D'Errico 2019) or stack exchange websites. In addition, I am grateful to the organisers and speakers of the AFMS (*Australasian Fluid Mechanics Society*) and SFITT (*Shear Flow Instability, Transition and Turbulence*) seminar series, and particularly, their move online during COVID19. These not only greatly broadened my research horizon, but also motivated many side investigations, and in many cases, were just plain interesting. Particular mention should be made of Ashley Willis, one of its presenters, who assisted with ironing out difficulties with the nonlinear optimization scheme employed in this work. Similar praises can be sung of the community at Monash University, with many useful discussions, particularly during team meetings. Special mention to Zhi Ng, for assistance with many of the computational issues associated with the setup of simulations and use of high performance computing clusters, to Tony Vo, for getting me started with MATLAB linear stability analysis, and to Stephen Terrington, for some particularly useful points regarding boundary conditions. Most importantly, acknowledgement goes to my supervisors, Alban Pothérat and Gregory Sheard. I am grateful (for the most part) for their continued efforts to improve the rigorousness of my research and the clarity of my writing. However, I make no apology for my consistent speculation, 'trust' that conclusions will hold in similar systems (that with finite time, other things are worth investigating), and peculiar choices when it comes to certain plotting options. I am also grateful for the freedom they afforded me in my research endeavours, which has hopefully allowed this thesis to include some interesting new conclusions. Some specific thanks to Alban, for his introduction to weakly nonlinear analysis, which proved very useful, as well as for the assistance of his colleague, Jānis Priede, with coding up the weakly nonlinear solver, and to Greg, for maintaining such a useful open access computational fluid dynamics solver, and particularly one with so many inbuilt packages. Finally, mention should be made of the direct financial support of Monash

University and the Australian government, with this research supported by an Australian Government Research Training Program (RTP) Scholarship. The provision of computational resources supported by the Australian Government via the Australian Research Council (Discovery Grants DP150102920 and DP180102647), the National Computational Infrastructure (NCI) and Pawsey Supercomputing Centre (PSC), and Monash University via the MonARCH cluster, are also gratefully acknowledged.

Contents

Chapter 1

Introduction

1.1 Motivations

Broadly, fluid flows are either laminar or turbulent. A laminar flow is ordered, with flow structures predominantly characterized by large length scales. Such flows exhibit poor momentum transfer, as so few length scales are present. On the one hand, this leads to smaller frictional forces transferred to the laminar flow, from a no-slip boundary. But equally, other transfers from the wall, such as heat, are poor, and inefficiently mixed through the fluid. In contrast, a turbulent flow is disordered, with flow structures exhibiting a wide range of scales, from large, to very small. With so many scales present, momentum is efficiently transferred. While this leads to increased frictional forces, so too is mixing improved. In theory, the question the engineer then asks themselves, is do I want a laminar flow, or a turbulent one? In reality, the question is more often can the flow be kept laminar, given the ubiquity of turbulence in nature. However, in this thesis, the question considered is instead, when *can* turbulence be triggered and sustained? Thus, this work has two motivations, one practical, and the other theoretical.

The practical motivation for this research focuses on the efficient excitement of turbulence. Typically, turbulent duct flows are undesirable, due to increased pumping costs (Hof *et al.* 2010; Kühnen *et al.* 2018). However, in certain situations, the benefits of greatly enhanced turbulent mixing outweigh the drawbacks in pumping costs. One such situation, toward which this thesis is directed, is the magnetohydrodynamic flow through a dual coolant/reebreeder duct of a magnetic confinement fusion reactor (Barleon *et al.* 2000a,b). The coolant ducts blanket the plasma chamber and are thereby subjected to strong pervading magnetic fields, which tend to two-dimensionalize and relaminarize the flow. The possibility of these coolant ducts being self-cooled, and thereby self-sufficient, is of practical interest due to their relative simplicity compared to other designs. However, the predicted heat transfer rates are insufficient, if the duct flows remain laminar. Thus, sustained turbulent flows, and their accompanying boost to heat transfer rates, are sought.

The theoretical motivation regards the unexplored dynamics of the equations governing quasi-two-dimensional (Q2D) flows, which may be present in fusion relevant regimes, and can also approximate large scale geophysical and astrophysical flows. Clear subcritical transitions to sustained turbulence are yet to be numerically observed in Q2D flows, and are not well understood. Furthermore, it is unknown whether Q2D turbulence can be generated solely by Q2D mechanisms, or if Q2D turbulence is the saturated state of initially three-dimensional (3D) turbulence. The complications quasi-two-dimensionality introduces also necessitate new avenues of investigation, for what is ultimately an old problem (Reynolds 1883). This new outlook may also aid in formulating universal explanations of subcritical transitions to turbulence, as much still remains unanswered in the field.

1.2 Foundations

The dimensional velocity vector $\check{\boldsymbol{u}} = (\check{u}, \check{v}, \check{w})$ and pressure scalar $\check{p}$, for an incompressible, Newtonian fluid with density ρ and kinematic viscosity ν, are solutions to the Navier–Stokes equations:

$$\frac{\partial \check{\boldsymbol{u}}}{\partial \check{t}} = -(\check{\boldsymbol{u}} \cdot \check{\boldsymbol{\nabla}})\check{\boldsymbol{u}} - \frac{1}{\rho}\check{\boldsymbol{\nabla}}\check{p} + \nu \check{\boldsymbol{\nabla}}^2 \check{\boldsymbol{u}} + \check{\boldsymbol{f}}, \tag{1.1}$$

$$\check{\boldsymbol{\nabla}} \cdot \check{\boldsymbol{u}} = 0, \tag{1.2}$$

subject an initial condition, where $\check{t}$ is the dimensional time, and forcing and boundary conditions, where $\check{\boldsymbol{f}}$ represents a dimensional force. The dimensional gradient operator is $\check{\boldsymbol{\nabla}} = (\check{\partial}_x, \check{\partial}_y, \check{\partial}_z)$, where $\check{\boldsymbol{\nabla}}\cdot$ represents taking the divergence, while $\check{\boldsymbol{\nabla}}^2$ denotes the vectorial Laplacian. Magnetohydrodynamic (MHD) phenomena will not be considered until Chapter 2.

The selection or design of an initial condition on the velocity $\check{\boldsymbol{u}}_0 = \check{\boldsymbol{u}}(\check{t} = 0)$ is a key part of this thesis, and will be discussed in detail in later sections. For now, it is only noted that the selection of $\check{\boldsymbol{u}}_0$ requires the choice of the structure (e.g. random noise, a leading eigenmode from stability analysis, an analytic solution under fully developed flow assumptions) and magnitude of the initial velocity field. Magnitudes are quantified

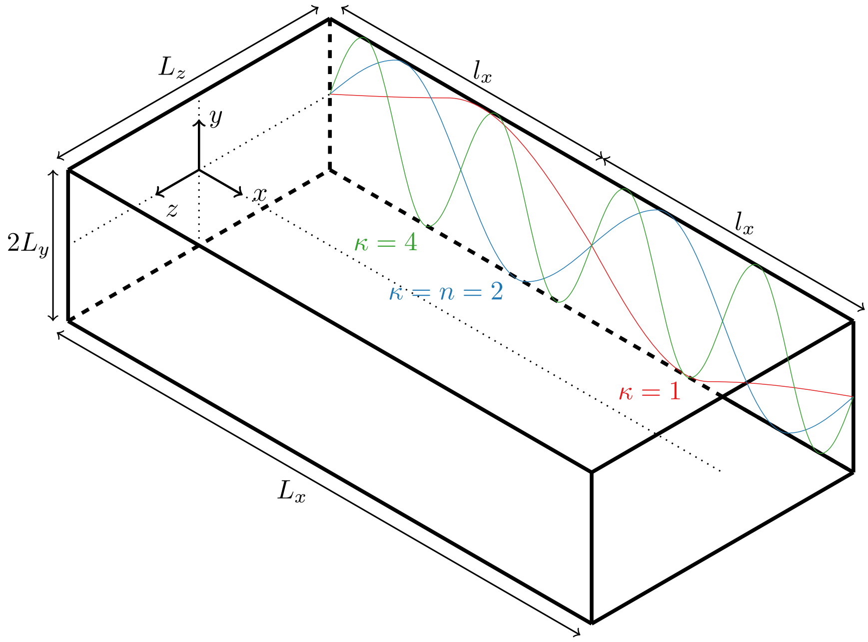

FIGURE 1.1: Sketch of the duct geometry, indicating the relevant characteristic lengths. The streamwise direction is periodic, with $\check{\boldsymbol{u}}(0) = \check{\boldsymbol{u}}(L_x)$ for all κ. For a specified n ($n = 2$ as drawn), periodicity is also valid over $\check{\boldsymbol{u}}(0) = \check{\boldsymbol{u}}(l_x)$ when assuming linearity. A mode with $\kappa = n = 2$ (blue) can, through nonlinear interaction, generate a mode with $\kappa = 1$ ($< n$; red) which breaks periodicity over l_x. This point is highlighted here as the orthodox choice ($\kappa = n = 1$) is not always made in this thesis, to test domain length effects. The linear mode is defined as the lowest mode periodic over l_x, $\check{\boldsymbol{u}}(0) = \check{\boldsymbol{u}}(l_x)$.

by the energy norm

$$||\check{\boldsymbol{u}}||_{\mathrm{E}} = \left(\int \check{\boldsymbol{u}} \cdot \check{\boldsymbol{u}} \, \mathrm{d}\Omega\right)^{1/2}, \tag{1.3}$$

where Ω represents the computational domain, and where the use of the notation $||\ldots||$ should be taken to mean the energy norm squared, e.g. $||\check{\boldsymbol{u}}|| = ||\check{\boldsymbol{u}}||_{\mathrm{E}}^2$. Note from the form of the Navier–Stokes equations, Eqs. (1.1) and (1.2), that an initial condition on the pressure is not required.

The forcing condition $\check{\boldsymbol{f}}$ may include body forces (e.g. gravity), driving forces (e.g. a constant or time varying pressure gradient) or externally imposed frictional forces, which may be a function of the velocity vector. Of these, body forces will be neglected, driving forces will sometimes be included, and an externally imposed frictional force will always be present.

Before moving to boundary conditions, the domain of interest is defined. With a right-handed coordinate system, the position vector $\check{\boldsymbol{x}} = (\check{x}, \check{y}, \check{z})$ fully describes each point in the spatial domain. As this thesis is solely focused on duct flows, the x direction shall henceforth be known as the *streamwise* wall-parallel direction, the y direction the in-plane *wall-normal*, and the z direction the *out-of-plane* wall-normal (the italicised terms for short). By virtue of the duct walls, characteristic lengths at the duct scale in the y and z directions will be based on the duct (half) height L_y and width L_z. These characteristic lengths are sketched in Fig. 1.1. However, the streamwise direction yields no natural characteristic length, as mathematically, the walls are perfectly smooth and of infinite streamwise extent. Thus, the x direction is considered periodic, so $\check{\boldsymbol{u}}(\check{x}) = \check{\boldsymbol{u}}(\check{x} + 2\pi n/\check{\alpha})$ and $\check{p}(\check{x}) = \check{p}(\check{x} + 2\pi n/\check{\alpha})$, where $\check{\alpha}$ is the (dimensional) wave number, and n an integer. The wave number $\check{\alpha}$ then defines a characteristic wavelength $l_x = 2\pi/\check{\alpha}$ and characteristic duct length $L_x = nl_x$. Sinusoidal modes with wavelength $2\pi n/\kappa\check{\alpha}$ exactly fit within the domain, for $\kappa = 0,\ 1,\ 2,\ \ldots,\ \infty$. However, for any $\kappa < n$, excluding the streamwise independent $\kappa = 0$, periodicity can be broken over l_x, $\check{\boldsymbol{u}}(\check{x}) \neq \check{\boldsymbol{u}}(\check{x} + l_x)$, as is shown in Fig. 1.1. Thus, nonlinearly, periodicity must be enforced over L_x, $\check{\boldsymbol{u}}(\check{x}) = \check{\boldsymbol{u}}(\check{x} + L_x)$. Linearly, the $\kappa = n$ mode cannot interact with modes of any other wave number, and periodicity is maintained over $\check{\boldsymbol{u}}(\check{x}) = \check{\boldsymbol{u}}(\check{x} + l_x)$. If a driving pressure gradient is applied, it is included in the forcing condition $\check{\boldsymbol{f}}$, so the fluctuating part of the pressure $\check{p}$, remains periodic.

To fully define the boundary conditions, and thereby the problem, requires constraints on $\check{\boldsymbol{u}}$ and $\check{p}$ at the duct walls, and the selection of n and $\check{\alpha}$. The selection of n and $\check{\alpha}$ is not trivial, and is also the focus of a large part of this thesis. At all duct walls, impermeable $\check{\boldsymbol{u}} \cdot \check{\boldsymbol{n}} = 0$ and no-slip $\check{\boldsymbol{u}} = \check{\boldsymbol{u}}_{\text{wall}}$ boundary conditions are applied, where $\check{\boldsymbol{n}}$ is a wall-normal unit vector and $\check{\boldsymbol{u}}_{\text{wall}}$ is the prescribed wall velocity. The no-slip condition is a Dirichlet boundary condition on the velocity, where $\check{\boldsymbol{u}}_{\text{wall}}$ may be zero, constant or time varying, by design, to enable analysis of various flows. If non-zero, it may be the characteristic velocity for the flow. In this work, the out-of-plane duct walls will always have zero velocity Dirichlet boundary conditions.

When considering boundary conditions on the pressure, there are two things to note. First, as $\check{\boldsymbol{\nabla}}\check{p}$, rather than $\check{p}$, appears in Eq. (1.1), the pressure is only uniquely defined up to an arbitrary constant. Second, the pressure does not directly have an evolution equation (there are no $\partial\check{p}/\partial\check{t}$ terms). Thus at each time $\check{t}$, the pressure $\check{p}$ only acts to enforce the divergence free condition, Eq. (1.2).

Quasi-two-dimensional flows are now introduced. To do so, the flow components and flow dimensions are defined. The total number of velocity components which are non-zero somewhere within the domain represents the total number of flow components. For example, a two-component flow has two of the three velocity components non-zero (e.g. $\check{u}$ and $\check{v}$ non-zero at some or all $\check{\boldsymbol{x}}$, and $\check{w}$ zero at all $\check{\boldsymbol{x}}$). The total number of non-zero derivatives (of any flow component) somewhere within the domain represents the total number of flow dimensions. For example, a two-dimensional flow has at least two non-zero derivatives of any velocity components (of which there can still be three), e.g. $\check{\partial}_x$ and $\check{\partial}_y$ of any flow quantity are non-zero, somewhere within the spatial domain, and $\check{\partial}_z$ of all flow quantities zero everywhere within the domain.

Quasi-two-dimensional flows are a *class* of three dimensional flows, with any number of flow components. For a 3D flow to be classed as Q2D, it must exhibit:

- Three-dimensionality, of any amplitude, only in regions of asymptotically small thickness (typically boundary layers), and/or
- Three-dimensionality, in any region, that is asymptotically small in amplitude.

In the duct setup introduced earlier, Fig. 1.1, a flow will be classed as Q2D if $\check{\partial}_z$ (of any flow quantity) is large, but finite, only in asymptotically small regions of the flow, and satisfies $\check{\partial}_z \ll \check{\partial}_x$, $\check{\partial}_y$ everywhere else. The asymptotic qualification on these conditions will be discussed shortly. However, it is important to note that no approximations have yet been made about the flow. A three-dimensional flow is merely classified as quasi-two-dimensional flow if it exhibits the aforementioned properties.

Three schematics follow in Fig. 1.2, one for a 3D flow that cannot be classed as Q2D, another a 3D flow that may be classed as Q2D, and last, a 2D flow. To do so, the domain is first subdivided, into regions of asymptotically small thickness near the duct walls (shaded) and the remaining core flow. Thus, if $\check{\partial}_z$ is only large within the shaded regions, and if at all other points in the domain $\check{\partial}_z$ is small (relatively speaking), the flow can be classed as Q2D. Note that $\check{\partial}_x$ and $\check{\partial}_y$ can be of any magnitude in any region of the domain, so long as they are not so large that they invalidate the timescale analysis introduced in Chapter 2, § 2.1. To facilitate this comparison, structures in Fig. 1.2 have been visualized with two isolines of an in-plane velocity component. For example, the black solid curves represent $\check{v} = 0$, and the black dotted curves $\check{v} = 0.5\check{v}_{\max}$. Thus, the difference in velocity between any two points from the dotted to the solid curve is $\Delta\check{v} = 0.5\check{v}_{\max}$ always, and some approximations of $\Delta\check{v}/\Delta\check{x}$, $\Delta\check{v}/\Delta\check{y}$ and $\Delta\check{v}/\Delta\check{z}$ can be constructed over finite *distances*, where e.g. $\Delta\check{x}$ represents a finite distance in $\check{x}$ between two points. However, note that the constraint of $\check{\partial}_z$ of zero applies at all *points* outside shaded regions.

Let us first consider the 3D flow that cannot be classed as Q2D: the characteristic lengths of each of the flow structures in all three directions are of similar order of magnitude. Furthermore, the complexity of the flow structure yields large $\Delta\check{v}/\Delta\check{z}$ at many locations within the domain, see out-of-plane Slice A (left column), and importantly outside the regions of asymptotically small thickness. Thus, this 3D flow cannot be classed as Q2D. Next, consider the 3D flow which can be classed as Q2D. Note first, that the structure is elongated in the z direction, such that the out-of-plane characteristic length of the flow structure is much larger than any in-plane characteristic length. This leads to small $\Delta\check{v}/\Delta\check{z}$ in the bulk of the flow, which if asymptotically small may permit this 3D flow as being classed as Q2D. In addition, although the impermeable, no-slip walls still induce large $\Delta\check{v}/\Delta\check{z}$ near the walls, this then occurs within the asymptotically small (shaded) regions. Note that the accompanying in-plane Slice B (right column) exhibits large $\Delta\check{v}/\Delta\check{x}$, $\Delta\check{v}/\Delta\check{y}$ outside the asymptotically thin regions. This is not an issue for the Q2D assumption, although is of interest in ensuring that $\check{\partial}_z \ll \check{\partial}_x$, $\check{\partial}_y$ everywhere else. Finally, the 2D flow is now considered. This flow is not possible in a duct configuration, as the out-of-plane boundary conditions would either have to be periodic, or free-slip surfaces. However, it does provide context, as it is only when $\check{\partial}_z$ is everywhere zero that a 2D flow is produced.

Note that the 2D flow is *not* the limiting case of the Q2D flow (at finite ν), as the limiting case represents finite gradients maintained in asymptotically thinner and thinner regions near the walls. This, in itself, presents quite a challenge. Numerical analysis would be far simpler if the limiting case were the two-dimensional flow. Instead, the direct numerical simulation (DNS) of a full 3D domain is required to evolve a flow classed as Q2D without approximation, and with (computationally expensive) high resolution necessary to resolve the asymptotically thin regions. This issue would be further exacerbated by the parameter regimes at which Q2D flows are observed. To circumvent these challenges, 2D models have been developed (hereafter referred to as Q2D models, rather than 2D models, to indicate that a modified version of the Navier–Stokes equations are solved in a 2D domain). These models are based upon equations that govern the velocity field averaged along the z direction, rigorously derived by

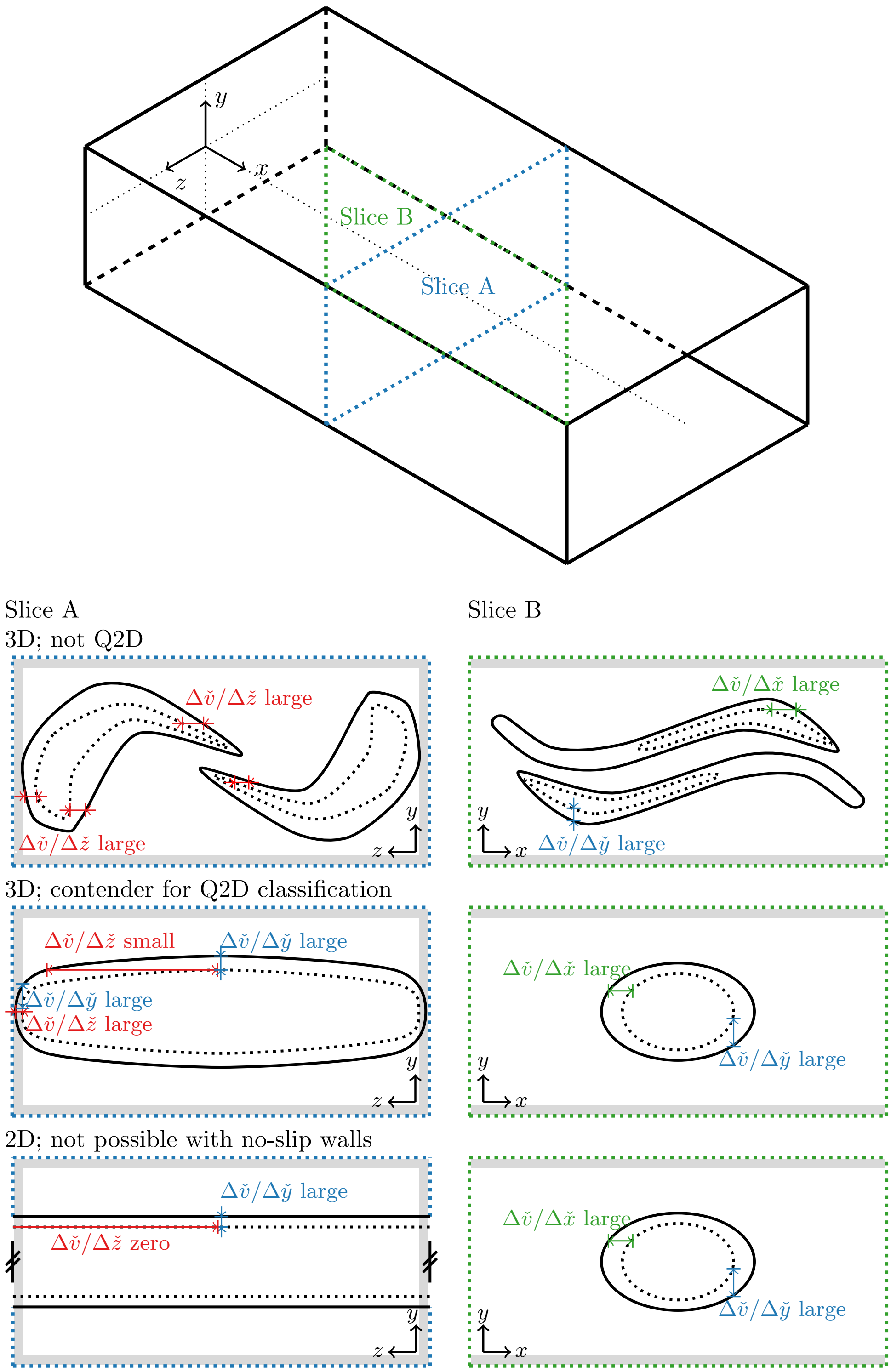

FIGURE 1.2: Sketches of three-dimensional, quasi-two-dimensional and two-dimensional flows on slices, A and B, of the full three-dimensional domain. Shaded regions represent subdivisions of the domain with (asymptotically) small thickness. Approximations of derivatives can be large over $\Delta\check{x}$ or $\Delta\check{y}$. However, derivatives with respect to $\check{z}$ can only be large within the asymptotically small (shaded) regions, and must be asymptotically small elsewhere. For flow structures, solid black lines represent $\check{v} = 0$, and dotted black lines $\check{v} = 0.5\check{v}_{\max}$.

Sommeria & Moreau (1982) and Pothérat *et al.* (2000), which can then be evolved in a two-dimensional domain (the modelling aspect comes from the approximation of some of the three-dimensional effects in the 2D domain).

There are two common averaging procedures upon which Q2D models are based. Both are mentioned here, although only the latter is applied in Chapter 2, § 2.2. Although the same (low order) three-dimensional effects are modelled, they are introduced differently.

The first approach is to consider the limits of certain key parameters (e.g. the Reynolds number $Re \gg 1$, among others), to justify the decomposition of the velocity field as (Bühler 1996)

$$\check{u}(\check{x},\check{y},\check{z}) = -\frac{\partial\check{\psi}(\check{x},\check{y})}{\partial\check{y}}\check{h}(\check{z}),\ \ \check{v}(\check{x},\check{y},\check{z}) = -\frac{\partial\check{\psi}(\check{x},\check{y})}{\partial\check{x}}\check{h}(\check{z}),\ \ \check{w}=0, \tag{1.4}$$

where $\check{\psi}$, the streamfunction, represents the Q2D solution of the averaged equations. The limits under which such a decomposition is justified yield the asymptotic qualifications mentioned earlier. The term $\check{h}(\check{z})$, which retains the three-dimensional effects, requires modelling.

The second approach is to integrate each term in the governing equations, as (Pothérat *et al.* 2000)

$$\check{g}_\perp(\check{x},\check{y}) = \int_{-L_z/2}^{L_z/2} \check{g}(\check{x},\check{y},\check{z})\,\mathrm{d}\check{z}, \tag{1.5}$$

where $\check{g}_\perp$ represent the integrated (often referred to as averaged) term. Terms of the form $\partial\check{\boldsymbol{u}}/\partial\check{z}$ yield conditions on $\check{\boldsymbol{u}}$ at the walls after integration, which vanish after applying the zero boundary conditions on velocities at the out-of-plane walls. However, terms of the form $\partial^2\check{\boldsymbol{u}}/\partial\check{z}^2$ yield conditions on the shear stress $\partial\check{\boldsymbol{u}}/\partial\check{z}$ after integration. These remaining constraints on the shear stresses at the walls retain the three-dimensional effects, and require modelling. Part of this modelling involves series expansions of each flow quantity, in terms of key flow parameters. The choice of when to truncate the series yields the asymptotic qualifications introduced earlier (the work described in this thesis takes only the zeroth order expansion, omitting higher order terms).

This section concludes with an introduction of the natural and industrial conditions under which 3D flows may be classed as Q2D. Four examples of physical phenomena capable of reducing $\partial/\partial\check{z}$ in the bulk flow are (Davidson 2013):

- The interaction of a strong uniform magnetic field oriented in the z direction with an electrically conducting fluid (the focus of this thesis),
- Domains with a small aspect ratio $A = L_y/L_z$ (Hele–Shaw/shallow water flows),
- Rapid rotation about the z-axis (the Taylor–Proudman theorem),
- Stratification induced by density differences (due to temperature or salinity gradients perpendicular to the z direction).

Thus, quasi-two-dimensionality is naturally observed in geophysical and astrophysical flows, which typically have small aspect ratios, as for oceanic and atmospheric flows, or large rotation rates, as for protostellar or cold accretion disks (Lindborg 1999; Davidson 2013). By comparison, Q2D flows due to the interaction of a strong magnetic field with an electrically conducting fluid are most commonly observed industrially (Smolentsev *et al.* 2008). Magnetic fields may be intentionally applied to control flows in the continuous casting of metals (Davidson 2001; Thomas *et al.* 2015a). Alternately, magnetic fields may be unavoidable, as is in the design of magnetic confinement fusion reactors (Abdou *et al.* 2015). As the dual purpose coolant/fuel rebreeder ducts require the flow of an electrically conducting fluid, the ensuing interaction between the rebreeder fluid and plasma confining magnetic field leads to quasi-two-dimensionalization of the coolant duct flow.

Regardless of the phenomena responsible for inducing quasi-two-dimensionality, the z-averaged Navier–Stokes equations, including only zeroth order three-dimensional effects, are identical (under the appropriate conversion of non-dimensional parameters, and assuming axisymmetry and the inclusion of the Coriolis force for rotating flows). Thus, flow solutions in any one system may be applicable to the other three. Note that the lowest order three-dimensional effect is *always* a friction exerted on the bulk by the out-of-plane boundary layers (in plane channels). However, some additional higher order (recirculation) effects are also analogous (Pothérat *et al.* 2000). Thus, understanding the Q2D dynamics exhibited by any one of these flows may lead to a much broader understanding of fluid dynamics as a whole.

Chapter 2

Review of magnetohydrodynamics and its approximation in duct flows

The results presented in this thesis are the exact solutions of a model for quasi-two-dimensional flows (numerical error aside). However, the Q2D solutions are only an approximation of 3D magnetohydrodynamic duct flows. From a practical perspective, the derivation and applicability of the Q2D model are quite important, as these factors directly impact the translation of results to real world decisions. Thus, this chapter introduces the various approximations made to MHD flows, while deriving the Q2D model. To further gauge the relative importance of the approximations made, the MHD literature is reviewed, with specific focus on the accuracy of Q2D predictions of 3D flows. As the issue of approximation predominantly pertains to practical application, a benchmark of Q2D and 3D studies aimed at self-cooled fusion are reviewed. Finally, error trends for the Q2D approximation are provided for the underlying steady flow.

Before proceeding with this chapter, it is worth noting the following. First, the theoretical motivation of this thesis takes precedence over any possible practical applications. Thus, this chapter predominantly exists to provide providence for the Q2D model, and to establish its validity and applicability. Second, this chapter *does not* aim to educate the reader on the workings of nuclear fusion reactors, nor understand much past the basics of magnetohydrodynamics, as for the most part, neither is required to process the results chapters in this thesis. So long as the reader is satisfied with the foundations of the Q2D model, then this chapter will have served its purpose. Where possible, a broader context (beyond the scope of this research) is provided, particularly throughout the literature review.

2.1 Approximations made to MHD duct flows

Focus is now directed to the incompressible flow of a Newtonian, electrically conducting fluid, having electrical conductivity σ and magnetic permeability μ, through a duct of rectangular cross-section. The duct walls are electrically insulating, and the entire duct is subject to an imposed uniform magnetic flux density B_0 (henceforth magnetic field) in the z-direction. The dimensional fluid velocity $\check{\boldsymbol{u}}$, magnetic field $\check{\boldsymbol{B}}$, current density $\check{\boldsymbol{j}}$, electric field $\check{\boldsymbol{E}}$ and pressure $\check{p}$ are solutions to the full MHD equations:

$$\frac{\partial \check{\boldsymbol{u}}}{\partial \check{t}} = -(\check{\boldsymbol{u}} \cdot \check{\boldsymbol{\nabla}})\check{\boldsymbol{u}} - \frac{1}{\rho}\check{\boldsymbol{\nabla}}\check{p} + \nu \check{\boldsymbol{\nabla}}^2 \check{\boldsymbol{u}} + \check{\boldsymbol{f}} + \frac{1}{\rho}\check{\boldsymbol{j}} \times \check{\boldsymbol{B}}, \tag{2.1}$$

$$\check{\boldsymbol{\nabla}} \cdot \check{\boldsymbol{u}} = 0, \tag{2.2}$$

$$\frac{\partial \check{\boldsymbol{B}}}{\partial \check{t}} = \check{\boldsymbol{\nabla}} \times (\check{\boldsymbol{u}} \times \check{\boldsymbol{B}}) - \frac{1}{\sigma\mu}\check{\boldsymbol{\nabla}}^2 \check{\boldsymbol{B}}, \tag{2.3}$$

$$\check{\boldsymbol{j}} = \sigma(\check{\boldsymbol{E}} + \check{\boldsymbol{u}} \times \check{\boldsymbol{B}}), \tag{2.4}$$

$$\check{\boldsymbol{\nabla}} \times \check{\boldsymbol{E}} = -\frac{\partial \check{\boldsymbol{B}}}{\partial \check{t}} \tag{2.5}$$

$$\check{\boldsymbol{\nabla}} \cdot (\check{\boldsymbol{\nabla}} \times \check{\boldsymbol{B}}) = \mu \check{\boldsymbol{\nabla}} \cdot \check{\boldsymbol{j}}, \tag{2.6}$$

subject to initial, forcing and boundary conditions. Eqs. (2.1) through (2.6) are, respectively, the momentum equation, incompressibility constraint, induction equation, Ohm's law, the Maxwell–Faraday equation, and the divergence of the differential form of Ampère's law (Davidson 2001). Note that the solenoidal condition on the magnetic field $\check{\boldsymbol{\nabla}} \cdot \check{\boldsymbol{B}} = 0$, has been built into Eq. (2.3). Note also that simplifications made in deriving the full MHD equations (e.g. non-relativistic velocities) are not of interest in this work, being thoroughly discussed in Moreau (1990), Müller & Bühler (2001) and Davidson (2001), although this lends a less conventional form to Eq. (2.6). The key difference between the full MHD equations, and the Navier–Stokes equations introduced earlier, Eqs. (1.1) and (1.2), is the final term on the right hand side of Eq. (2.1). This term represents the Lorentz force, through which the (induced and/or imposed) magnetic field interacts with the (induced and/or applied) current, resulting in a body force on the fluid.

The first simplification made to the full MHD equations is the quasi-static approximation. This approximates the induced magnetic field, specifically one governed by a linearized version of Eq. (2.3), as time steady. In addition, an inductionless approximation of the flow will be considered, given the relatively low magnetic Reynolds numbers expected in liquid metal cooling conduits (discussed in further detail shortly). Under the inductionless approximation, the magnetic field $\check{\boldsymbol{B}}$ is composed entirely of the imposed field (the induced field being negligible), i.e. $\check{\boldsymbol{B}} = B_0\boldsymbol{e}_z$ in this setup, where $\boldsymbol{e}_z$ is a unit vector in the z-direction. These approximations then allow Eqs. (2.1) and (2.3) to be decoupled, such that the magnetic field influences the velocity field, but ensures that the velocity field cannot influence the magnetic field.

The quasi-static approximation is now derived. First, the magnetic field is decomposed into an imposed component $\check{\boldsymbol{B}}_0$ and an induced component $\check{\boldsymbol{b}}$, so $\check{\boldsymbol{B}} = \check{\boldsymbol{B}}_0 + \check{\boldsymbol{b}}$. This decomposition is substituted into Eq. (2.3), and simplified based on the known properties of the imposed field (which is uniform and time steady),

$$\frac{\partial \check{\boldsymbol{b}}}{\partial \check{t}} - B_0\check{\boldsymbol{\nabla}} \times (\check{\boldsymbol{u}} \times \boldsymbol{e}_z) - \check{\boldsymbol{\nabla}} \times (\check{\boldsymbol{u}} \times \check{\boldsymbol{b}}) + \frac{1}{\sigma\mu}\check{\boldsymbol{\nabla}}^2\check{\boldsymbol{b}} = 0. \tag{2.7}$$

The order of magnitude of each term, taking characteristic scales for gradients, velocity, the induced magnetic field and time as $1/L_y$, U_0, b and L_z/v_A, respectively, are

$$\frac{\partial \check{\boldsymbol{b}}}{\partial \check{t}} \to \frac{bv_\mathrm{A}}{L_z}, \tag{2.8}$$

$$B_0\check{\boldsymbol{\nabla}} \times (\check{\boldsymbol{u}} \times \boldsymbol{e}_z) \to \frac{B_0U_0}{L_y}, \tag{2.9}$$

$$\check{\boldsymbol{\nabla}} \times (\check{\boldsymbol{u}} \times \check{\boldsymbol{b}}) \to \frac{U_0 b}{L_y}, \tag{2.10}$$

$$(\sigma\mu)^{-1}\check{\boldsymbol{\nabla}}^2\check{\boldsymbol{b}} \to \frac{b}{\sigma\mu L_y^2}, \tag{2.11}$$

where $v_\mathrm{A} = B_0(\mu_0\rho)^{-1/2}$ is the Alfvén velocity (Alfvén 1942) and μ_0 is the permeability of free space. First, the convection and diffusion terms for the induced field are compared,

$$\frac{\|\check{\boldsymbol{\nabla}} \times (\check{\boldsymbol{u}} \times \check{\boldsymbol{b}})\|}{\|(\sigma\mu)^{-1}\check{\boldsymbol{\nabla}}^2\check{\boldsymbol{b}}\|} \to \frac{U_0 b\sigma\mu L_y^2}{L_y b} = \sigma\mu U_0 L_y = R_\mathrm{m}. \tag{2.12}$$

The ratio of the convection and diffusion terms yields the magnetic Reynolds number (the ratio of induction to diffusion of the magnetic field at the duct scale). For most liquid metals involved in laboratory and industrial applications $R_\mathrm{m} \lesssim 10^{-2}$ (Moreau 1990; Knaepen *et al.* 2004) when at moderate $Re \lesssim 10^4$. Whether industry operates at $Re \lesssim 10^4$ depends on the specifics of the application (some examples are considered in § 2.3, with Re varying from order 10^2 to order 10^6); in the following $Re \lesssim 10^4$ and thereby $R_\mathrm{m} \lesssim 10^{-2}$ are assumed. Thus, the convection term involving the induced magnetic field is neglected, i.e. $\check{\boldsymbol{\nabla}} \times (\check{\boldsymbol{u}} \times \check{\boldsymbol{b}}) \to 0$, as the magnetic Reynolds number is small. Second, the temporal and diffusion terms for the induced field are compared,

$$\frac{\|\partial\check{\boldsymbol{b}}/\partial\check{t}\|}{\|(\sigma\mu)^{-1}\check{\nabla}^2\check{\boldsymbol{b}}\|} \rightarrow \frac{B_0\sigma\mu L_y^2}{(\mu\rho)^{1/2}L_z} = \frac{B_0 L_z\sigma^{1/2}}{(\rho U_0 L_y)^{1/2}}\frac{L_y^2}{L_z^2}(\sigma\mu U_0 L_y)^{1/2} = (N\,R_\mathrm{m})^{1/2}A^2, \quad (2.13)$$

recalling the definition of the Alfvén velocity $v_\mathrm{A} = B_0(\mu\rho)^{-1/2}$, which forms the characteristic timescale for the induced magnetic field. Note that $\mu \approx \mu_0$ can be assumed without issue for non-ferritic materials (Müller & Bühler 2001). The interaction parameter $N = B_0^2 L_z^2\sigma(\rho U_0 L_y)^{-1}$ represents the ratio of electromagnetic to inertial forces at the duct scale, while the aspect ratio $A = L_y/L_z$. Eq. (2.13) can also be rewritten, taking $1/L_z$ as the characteristic scale for gradients to avoid the aspect ratio term,

$$\frac{\|\partial\check{\boldsymbol{b}}/\partial\check{t}\|}{\|(\sigma\mu)^{-1}\check{\boldsymbol{\nabla}}^2\check{\boldsymbol{b}}\|} \rightarrow \frac{B_0\sigma\mu L_z^2}{(\mu\rho)^{1/2}L_z} = (N\,R_\mathrm{m})^{1/2} = \left(\frac{Ha^2}{Re}Pr_\mathrm{m}Re\right)^{1/2} = Ha\,{Pr_\mathrm{m}}^{1/2} = S, \quad (2.14)$$

to yield the Lundquist number S, where the Hartmann number $Ha = (N Re)^{1/2} = L_z B_0(\sigma/\rho\nu)^{1/2}$ (the square root of the ratio of electromagnetic to viscous forces at the duct scale) and the magnetic Prandtl number $Pr_\mathrm{m} = R_\mathrm{m}/Re = \nu\mu\sigma$. Thus, for liquid metals at room temperature, with Pr_m of 10^{-5} to 10^{-6} (Pothérat & Kornet 2015), a $Ha \lesssim 10^3$ ensures Alfvén waves dissipate faster than they propagate. Equally, for $R_\mathrm{m} \lesssim 10^{-2}$ (Moreau 1990; Knaepen *et al.* 2004), and so for $Re \lesssim 10^4$, the same condition is ensured if $N \lesssim 100$. Problematically, in magnetic confinement fusion reactors, Ha can be of the order 10^4 to 10^5, N of the order 10^3 to 10^4 and Re of the order 10^2 to 10^6 (Abdou *et al.* 2015; Smolentsev *et al.* 2008, 2010b; Mistrangelo *et al.* 2014). At these parameters, Alfvén waves may exist for significant periods of time. To maintain freedom in the magnitude of Re, $N \lesssim 100$ and $Ha \lesssim 1000$ would need to be maintained to ensure Alfvén waves are not present.

Even when Alfvén waves are absent, electromagnetic diffusion can still be rapid. This permits the quasi-static approximation, under which the temporal term in Eq. (2.3) can be neglected, so long as electromagnetic forces act far more rapidly than viscous or inertial forces (in each of the in-plane directions). To show this, two timescale comparisons at the duct scale are considered. The first is between in-plane inertial and electromagnetic forces, and the second viscous and electromagnetic forces. The remaining comparisons differ only by factors of the aspect ratio. By noting that the imposed magnetic field is time steady, the ratio of the characteristic inertial timescale

$\tau_{\mathrm{I,L}} = L_y/U_0$ to the characteristic Alfvén wave timescale $\tau_{\mathrm{A}} = L_z/v_{\mathrm{A}}$, is

$$\frac{\tau_{\mathrm{I,L}}}{\tau_{\mathrm{A}}} = \frac{L_y B_0}{U_0 L_z (\mu\rho)^{1/2}} = \frac{B_0 L_z \sigma^{1/2}}{(\rho U_0 L_y)^{1/2}} \frac{1}{(\mu\sigma L_y U_0)^{1/2}} \frac{L_y^2}{L_z^2} = \left(\frac{N}{R_{\mathrm{m}}}\right)^{1/2} A^2$$
$$= \frac{1}{{Pr_{\mathrm{m}}}^{1/2}} \frac{Ha}{Re} A^2. \quad (2.15)$$

Thus, even with $1 < N \ll 100$, the ratio of the inertial velocity timescale to the Alfvén timescale is large, as $R_{\mathrm{m}} \ll 1$, or equally if $10^3 Ha \gg Re$ for Pr_{m} of order 10^{-6}. Hence, any temporal variations in the in-plane velocity, due to inertia, occur far more slowly than any temporal variations in the induced magnetic field (at $N \gg 1$ as expected in fusion conditions the timescale ratio would be even larger). By further establishing the ratio of the characteristic viscous timescale $\tau_{\nu,\mathrm{L}} = L_y^2/\nu$ to the characteristic Alfvén wave timescale $\tau_{\mathrm{A}} = L_z/v_{\mathrm{A}}$,

$$\frac{\tau_{\nu,\mathrm{L}}}{\tau_{\mathrm{A}}} = \frac{L_y^2 B_0}{\nu L_z (\mu\rho)^{1/2}} = \frac{B_0 L_z \sigma^{1/2}}{(\rho U_0 L_y)^{1/2}} \frac{1}{(\mu\sigma L_y U_0)^{1/2}} \frac{L_y U_0}{\nu} \frac{L_y^2}{L_z^2} = \left(\frac{N}{R_{\mathrm{m}}}\right)^{1/2} Re\, A^2$$
$$= \frac{Ha}{{Pr_{\mathrm{m}}}^{1/2}} A^2, \quad (2.16)$$

it is again shown that the induced magnetic field varies far more rapidly than the velocity field (viscous forces acting a further Re times slower than inertial forces, and $Re \gg 1$ in the applications of interest). Although the induced magnetic field varies rapidly, $\partial\check{\boldsymbol{b}}/\partial\check{t} \to 0$ can still be assumed while $\check{\boldsymbol{u}}$ varies slowly, recalling that B_0 is steady. This statement may appear contradictory. However, any departure from the steady magnetic field (i.e. the distribution of field lines which satisfies the steady magnetic boundary conditions, completely independent of the presence of the fluid) diffuses so rapidly back to the steady result, that the velocity field never sees a magnetic topology different to the steady, imposed one (Knaepen *et al.* 2004). Thus, under the quasi-static approximation, Eq. (2.3) becomes

$$-B_0 \check{\boldsymbol{\nabla}} \times (\check{\boldsymbol{u}} \times \boldsymbol{e}_z) + (\sigma\mu)^{-1} \check{\boldsymbol{\nabla}}^2 \check{\boldsymbol{b}} = 0. \quad (2.17)$$

Before moving on to the inductionless approximation it is worth noting that the characteristic velocity scale U_0 is yet to be defined. Depending how the velocity field is driven, e.g. by $\check{\boldsymbol{f}}$ in Eq. (2.1), the most rapid changes to the velocity field should be encapsulated in U_0, for these approximations to be most useful.

The inductionless approximation is now considered, which aims to establish a ratio of the size of $\check{\boldsymbol{B}}_0 = B_0 \boldsymbol{e}_z$ to $\check{\boldsymbol{b}}$. Under the quasi-static approximation, only two terms from Eq. (2.3) remain in Eq. (2.17). Thus, to balance, they must be of similar order of magnitude,

$$\frac{\|B_0\check{\boldsymbol{\nabla}}\times(\check{\boldsymbol{u}}\times\boldsymbol{e}_z)\|}{\|(\sigma\mu)^{-1}\check{\boldsymbol{\nabla}}^2\check{\boldsymbol{b}}\|}\to\frac{B_0U_0\sigma\mu L_y^2}{L_y b}=\frac{B_0R_\mathrm{m}}{b}\to 1$$
$$\therefore\frac{B_0}{b}\to\frac{1}{R_\mathrm{m}}. \tag{2.18}$$

Thus, the characteristic scale for the induced field is R_m times smaller than the characteristic scale for the imposed field. As the induced magnetic field is R_m times smaller than the imposed field, if $R_\mathrm{m}\ll 1$ (which it may or may not be in the industrial applications of interest), the magnetic field can be approximated as being composed only of the imposed field, i.e. $\check{\boldsymbol{B}}=\check{\boldsymbol{B}}_0$. Thus, under the inductionless approximation, Eq. (2.3) is not required, so long as the substitution of $\check{\boldsymbol{B}}=B_0\boldsymbol{e}_z$ is made in Eqs. (2.1), (2.4) and (2.6). As the induced magnetic field is neglected, and thus, the overall magnetic field steady, the electric field is irrotational $\check{\boldsymbol{\nabla}}\times\check{\boldsymbol{E}}=0$ from Eq. (2.5). Thus, an electric potential $\check{\phi}$ can be introduced by the definition $\check{\boldsymbol{E}}=-\check{\boldsymbol{\nabla}}\check{\phi}$, and substituted into Eq. (2.4). This leaves:

$$\frac{\partial\check{\boldsymbol{u}}}{\partial\check{t}}=-(\check{\boldsymbol{u}}\cdot\check{\boldsymbol{\nabla}})\check{\boldsymbol{u}}-\rho^{-1}\check{\boldsymbol{\nabla}}\check{p}+\nu\check{\boldsymbol{\nabla}}^2\check{\boldsymbol{u}}+\check{\boldsymbol{f}}+B_0\rho^{-1}\check{\boldsymbol{j}}\times\boldsymbol{e}_z, \tag{2.19}$$

$$\check{\boldsymbol{\nabla}}\cdot\check{\boldsymbol{u}}=0, \tag{2.20}$$

$$\check{\boldsymbol{j}}=\sigma(-\check{\boldsymbol{\nabla}}\check{\phi}+B_0\check{\boldsymbol{u}}\times\boldsymbol{e}_z), \tag{2.21}$$

$$\check{\boldsymbol{\nabla}}\cdot\check{\boldsymbol{j}}=0. \tag{2.22}$$

This work simplifies Eqs. (2.19) through (2.22) following the slightly different approach of Pothérat *et al.* (2000). However, there is still much to be gained by showing the common approach to simplify Eq. (2.19) by eliminating the current $\check{\boldsymbol{j}}$. Although it will not allow as explicit a treatment of the matching conditions at the boundary layers, it forms a key part of the SM82 model (Sommeria & Moreau 1982), which is the quasi-two-dimensional model used and referenced throughout all the results chapters (if derived slightly differently). First, the vector calculus identity,

$$\boldsymbol{\nabla}\times(\boldsymbol{\nabla}\times\boldsymbol{A})=\boldsymbol{\nabla}(\boldsymbol{\nabla}\cdot\boldsymbol{A})-\boldsymbol{\nabla}^2\boldsymbol{A}, \tag{2.23}$$

for an arbitrary vector field $\boldsymbol{A}$ is introduced. To simplify the final term of Eq. (2.19), this identity, with $\boldsymbol{A}=\check{\boldsymbol{j}}\times\boldsymbol{e}_z$, is rearranged as

$$\check{\boldsymbol{j}}\times\boldsymbol{e}_z=-\check{\boldsymbol{\nabla}}^{-2}\big(\check{\boldsymbol{\nabla}}\times[\check{\boldsymbol{\nabla}}\times(\check{\boldsymbol{j}}\times\boldsymbol{e}_z)]-\check{\boldsymbol{\nabla}}[\check{\boldsymbol{\nabla}}\cdot(\check{\boldsymbol{j}}\times\boldsymbol{e}_z)]\big). \tag{2.24}$$

The latter term is a gradient which can be absorbed in the forcing term $\check{\boldsymbol{f}}$ as a constant pressure gradient contribution (Pothérat *et al.* 2000; Sommeria & Moreau 1982); recall that the absolute value of the pressure is arbitrary. Thus, in a Cartesian coordinate system,

$$\check{\boldsymbol{j}} \times \boldsymbol{e}_z = \left[-\frac{\partial \check{\phi}}{\partial \check{y}} - B_0 \check{u} \right] \boldsymbol{e}_x + \left[\frac{\partial \check{\phi}}{\partial \check{x}} - B_0 \check{v} \right] \boldsymbol{e}_y, \tag{2.25}$$

so

$$\begin{aligned} \check{\boldsymbol{\nabla}} \times [\check{\boldsymbol{\nabla}} \times (\check{\boldsymbol{j}} \times \boldsymbol{e}_z)] = B_0 \Bigg(& \left[\frac{1}{B_0} \frac{\partial}{\partial \check{y}} \check{\nabla}^2 \check{\phi} - \frac{\partial^2 \check{v}}{\partial \check{x} \partial \check{y}} + \frac{\partial^2 \check{u}}{\partial \check{y}^2} + \frac{\partial^2 \check{u}}{\partial \check{z}^2} \right] \boldsymbol{e}_x + \\ & \left[\frac{1}{B_0} \frac{\partial}{\partial \check{x}} \check{\nabla}^2 \check{\phi} + \frac{\partial^2 \check{v}}{\partial \check{x}^2} - \frac{\partial^2 \check{u}}{\partial \check{x} \partial \check{y}} + \frac{\partial^2 \check{v}}{\partial \check{z}^2} \right] \boldsymbol{e}_y + \left[-\frac{\partial^2 \check{u}}{\partial \check{x} \partial \check{z}} - \frac{\partial^2 \check{v}}{\partial \check{y} \partial \check{z}} \right] \boldsymbol{e}_z \Bigg). \end{aligned} \tag{2.26}$$

Taking the divergence of Eq. (2.21),

$$\sigma^{-1} \check{\boldsymbol{\nabla}} \boldsymbol{\cdot} \check{\boldsymbol{j}} = -\check{\boldsymbol{\nabla}} \boldsymbol{\cdot} \check{\boldsymbol{\nabla}} \check{\phi} + B_0 \check{\boldsymbol{\nabla}} \boldsymbol{\cdot} (v \boldsymbol{e}_x - u \boldsymbol{e}_y), \tag{2.27}$$

which is then zero from Eq. (2.22), yields,

$$\frac{1}{B_0} \check{\nabla}^2 \check{\phi} = \frac{\partial v}{\partial x} - \frac{\partial u}{\partial y}. \tag{2.28}$$

Substituting Eq. (2.28) into Eq. (2.26), and rewriting the last term

$$\begin{aligned} \check{\boldsymbol{\nabla}} \times [\check{\boldsymbol{\nabla}} \times (\check{\boldsymbol{j}} \times \boldsymbol{e}_z)] = B_0 \Bigg(& \left[\frac{\partial^2 \check{u}}{\partial \check{z}^2} \right] \boldsymbol{e}_x + \left[\frac{\partial^2 \check{v}}{\partial \check{z}^2} \right] \boldsymbol{e}_y \\ & + \left[\frac{\partial}{\partial \check{z}} \left(-\frac{\partial \check{u}}{\partial \check{x}} - \frac{\partial \check{v}}{\partial \check{y}} - \frac{\partial \check{w}}{\partial \check{z}} \right) + \frac{\partial^2 \check{w}}{\partial \check{z}^2} \right] \boldsymbol{e}_z \Bigg), \end{aligned} \tag{2.29}$$

which, with continuity, Eq. (2.20), simplifies to $\check{\boldsymbol{\nabla}} \times [\check{\boldsymbol{\nabla}} \times (\check{\boldsymbol{j}} \times \boldsymbol{e}_z)] = B_0 \partial^2 \check{\boldsymbol{u}} / \partial \check{z}^2$. Thus,

$$\check{\boldsymbol{j}} \times \boldsymbol{e}_z = -B_0 \check{\boldsymbol{\nabla}}^{-2} \frac{\partial^2 \check{\boldsymbol{u}}}{\partial \check{z}^2} + \check{\boldsymbol{\nabla}} \check{p}_{\mathrm{f}}, \tag{2.30}$$

assuming the operator $\check{\boldsymbol{\nabla}}^2$ has appropriately defined boundary conditions to be invertible, and where $\check{p}_{\mathrm{f}}$ is absorbed into any constant pressure gradient present. Substituting Eq. (2.30) into Eq. (2.19)

$$\frac{\partial \check{\boldsymbol{u}}}{\partial \check{t}} = -(\check{\boldsymbol{u}} \boldsymbol{\cdot} \check{\boldsymbol{\nabla}}) \check{\boldsymbol{u}} - \rho^{-1} \check{\boldsymbol{\nabla}} \check{p}_{\mathrm{t}} + \nu \check{\nabla}^2 \check{\boldsymbol{u}} + \check{\boldsymbol{f}} - B_0^2 \rho^{-1} \check{\boldsymbol{\nabla}}^{-2} \frac{\partial^2 \check{\boldsymbol{u}}}{\partial \check{z}^2}, \tag{2.31}$$

where $\check{p}_{\mathrm{t}}$ accounts for the pressure contribution from the irrotational component of the Lorentz force. By assuming that $\check{\partial}_z \ll \check{\partial}_x, \check{\partial}_y$ and that $\check{w} \ll \check{u}, \check{v}$ (Sommeria & Moreau 1982), i.e. that the flow can be classed as quasi-two-dimensional, the velocity $\check{\boldsymbol{u}}$ and gradient operator $\check{\boldsymbol{\nabla}}$ can be substituted for their two-dimensional counterparts, $\check{\boldsymbol{u}}_\perp = (\check{u}, \check{v})$ and $\check{\boldsymbol{\nabla}}_\perp = (\check{\partial}_x, \check{\partial}_y)$, respectively,

$$\frac{\partial \check{\boldsymbol{u}}_\perp}{\partial \check{t}} = -(\check{\boldsymbol{u}}_\perp \boldsymbol{\cdot} \check{\boldsymbol{\nabla}}_\perp) \check{\boldsymbol{u}}_\perp - \rho^{-1} \check{\boldsymbol{\nabla}}_\perp \check{p}_{\perp,\mathrm{t}} + \nu \check{\boldsymbol{\nabla}}_\perp^2 \check{\boldsymbol{u}}_\perp + \check{\boldsymbol{f}}_\perp - B_0^2 \rho^{-1} \check{\boldsymbol{\nabla}}_\perp^{-2} \frac{\partial^2 \check{\boldsymbol{u}}_\perp}{\partial \check{z}^2}, \tag{2.32}$$

$$\check{\boldsymbol{\nabla}}_\perp \cdot \check{\boldsymbol{u}}_\perp = 0. \tag{2.33}$$

Eq. (2.32) shows that the predominant action of the Lorentz force is a diffusion of momentum along magnetic field lines, when (for a given eddy) the action of the operator $\check{\boldsymbol{\nabla}}_\perp^{-2}$ simplifies to multiplication by $-L_y^2$ (Sommeria & Moreau 1982). The timescale for diffusion of momentum along magnetic field lines is $\tau_{2\mathrm{D}} = (\rho/\sigma B_0^2)(L_z^2/L_y^2) = (1/N)(L_z^4/U_0 L_y^3)$ (Pothérat 2007). Here, $\rho/\sigma B_0^2$ is the Joule damping time, the timescale for energy dissipation via the flow of electric current through the resistive fluid; heat generated by both Ohmic and viscous dissipation are neglected, given their magnitude relative to any wall or neutron heating (Hossain 1992). In a similar manner to the quasi-static assumption, this momentum diffusion timescale $\tau_{2\mathrm{D}}$ can be compared to those of inertia $\tau_{\mathrm{I,L}} = L_y/U_0$ and viscosity $\tau_{\nu,\mathrm{L}} = L_y^2/\nu$, to provide a stronger constraint on the bounds of validity of the quasi-two-dimensional approximation. Respectively, these are $\tau_{2\mathrm{D}}/\tau_{\mathrm{I,L}} = 1/NA^4$ and $\tau_{2\mathrm{D}}/\tau_{\nu,\mathrm{L}} = 1/Ha^2A^4$ (again, the remaining timescale ratios which can be constructed differ only in the factors of the aspect ratio). Thus, at fusion-relevant conditions, for a duct of order unity aspect ratio, large N and Ha should ensure rapid diffusion of momentum via the Lorentz force, and yield flows which can be classed as quasi-two-dimensional. The validity of the Q2D model is discussed further in § 2.3. However, at its heart, so long as $\tau_{2\mathrm{D}}/\tau_{\nu,\mathrm{L}}$ and $\tau_{2\mathrm{D}}/\tau_{\mathrm{I,L}}$ are sufficiently small, there should be little issue with the use of the Q2D model. Note that the Q2D model is *not* Eqs. (2.32) and Eqs. (2.33); a different derivation of the Q2D model will be followed to completion in § 2.2, after first returning to Eqs. (2.19) through (2.22).

2.2 Derivation of the Q2D model

With the last of the timescales compared, Eqs. (2.19) through (2.22) are nondimensionalized, before being averaged to obtain the quasi-two-dimensional model. Taking the characteristic scales for length, velocity, time, pressure, current and electric potential as L_y, U_0, L_y/U_0, ρU_0^2, $\sigma B_0 U_0$ and $L_y U_0 B_0$, respectively, the nondimensional governing equations become (dropping the forcing term for now):

$$\frac{\partial \boldsymbol{u}}{\partial t} = -(\boldsymbol{u} \cdot \boldsymbol{\nabla})\boldsymbol{u} - \boldsymbol{\nabla} p + \frac{1}{Re}\boldsymbol{\nabla}^2 \boldsymbol{u} + NA^2 \boldsymbol{j} \times \boldsymbol{e}_z, \tag{2.34}$$

$$\boldsymbol{\nabla} \cdot \boldsymbol{u} = 0, \tag{2.35}$$

$$\boldsymbol{j} = -\boldsymbol{\nabla}\phi + \boldsymbol{u} \times \boldsymbol{e}_z, \tag{2.36}$$

$$\boldsymbol{\nabla}\cdot\boldsymbol{j} = 0. \tag{2.37}$$

To facilitate averaging, following Pothérat *et al.* (2000), Eqs. (2.34), (2.35) and (2.37) are expanded into terms perpendicular and parallel to magnetic field lines, $\boldsymbol{u} = (\boldsymbol{u}_\perp, w)$, $\boldsymbol{j} = (\boldsymbol{j}_\perp, j_z)$, $\boldsymbol{\nabla} = (\boldsymbol{\nabla}_\perp, \partial_z)$:

$$\frac{\partial \boldsymbol{u}_\perp}{\partial t} = -(\boldsymbol{u}_\perp\cdot\boldsymbol{\nabla}_\perp)\boldsymbol{u}_\perp - w\frac{\partial \boldsymbol{u}_\perp}{\partial z} - \boldsymbol{\nabla}_\perp p + \frac{1}{Re}\boldsymbol{\nabla}_\perp^2\boldsymbol{u}_\perp + \frac{1}{Re}\frac{\partial^2\boldsymbol{u}_\perp}{\partial z^2} + NA^2\boldsymbol{j}_\perp\times\boldsymbol{e}_z, \tag{2.38}$$

$$\frac{\partial w}{\partial t} = -(\boldsymbol{u}_\perp\cdot\boldsymbol{\nabla}_\perp)w - w\frac{\partial w}{\partial z} - \frac{\partial p}{\partial z} + \frac{1}{Re}\nabla_\perp^2 w + \frac{1}{Re}\frac{\partial^2 w}{\partial z^2}, \tag{2.39}$$

$$\boldsymbol{\nabla}_\perp\cdot\boldsymbol{u}_\perp + \frac{\partial w}{\partial z} = 0, \tag{2.40}$$

$$\boldsymbol{j} = -\boldsymbol{\nabla}\phi + \boldsymbol{u}\times\boldsymbol{e}_z, \tag{2.41}$$

$$\boldsymbol{\nabla}_\perp\cdot\boldsymbol{j}_\perp + \frac{\partial j_z}{\partial z} = 0. \tag{2.42}$$

As introduced earlier, the z-average of a quantity g is

$$\bar{g}(x,y) = \int_{-L_z/2}^{L_z/2} g(x,y,z)\mathrm{d}z. \tag{2.43}$$

Applying this average to Eq. (2.38), and neglecting the average of products of fluctuations about the mean, leads to

$$\frac{\partial \bar{\boldsymbol{u}}_\perp}{\partial t} = -(\bar{\boldsymbol{u}}_\perp\cdot\boldsymbol{\nabla}_\perp)\bar{\boldsymbol{u}}_\perp - \boldsymbol{\nabla}_\perp\bar{p} + \frac{1}{Re}\boldsymbol{\nabla}_\perp^2\bar{\boldsymbol{u}}_\perp + \frac{1}{Re}\left(\left.\frac{\partial \boldsymbol{u}_\perp}{\partial z}\right|_{L_z/2} - \left.\frac{\partial \boldsymbol{u}_\perp}{\partial z}\right|_{-L_z/2}\right) + NA^2\bar{\boldsymbol{j}}_\perp\times\boldsymbol{e}_z, \tag{2.44}$$

with zero Dirichlet boundary conditions eliminating the $w\partial\boldsymbol{u}_\perp/\partial z$ term in Eq. (2.38). The same occurs for $\partial w/\partial z$ in Eq. (2.40), while $\partial j_z/\partial z$ in Eq. (2.42) vanishes as this work always assumes walls are perfectly electrically insulating, leaving

$$\boldsymbol{\nabla}_\perp\cdot\bar{\boldsymbol{u}}_\perp = 0, \tag{2.45}$$

$$\boldsymbol{\nabla}_\perp\cdot\bar{\boldsymbol{j}}_\perp = 0. \tag{2.46}$$

Given the identity $\boldsymbol{\nabla}\times(\boldsymbol{\nabla}\phi) = 0$, the curl of Eq. (2.41) yields

$$\boldsymbol{\nabla}\times\boldsymbol{j} = \boldsymbol{\nabla}\times(\boldsymbol{u}\times\boldsymbol{e}_z) = \frac{\partial u}{\partial z}\boldsymbol{e}_x + \frac{\partial v}{\partial z}\boldsymbol{e}_y - (\boldsymbol{\nabla}_\perp\cdot\boldsymbol{u}_\perp)\boldsymbol{e}_z. \tag{2.47}$$

Averaging Eq. (2.47), applying no-slip boundary conditions at the out-of-plane walls, and substituting Eq. (2.45) yields $\boldsymbol{\nabla}_\perp\times\bar{\boldsymbol{j}}_\perp = 0$. As $\bar{\boldsymbol{j}}_\perp$ is both irrotational and incompressible, it can be written as the gradient of a potential field $\bar{\boldsymbol{j}}_\perp = \nabla_\perp\psi_0/Ha$ (Pothérat *et al.* 2000). This defines the two-dimensional forcing velocity

$$u_0 = Ha\,\bar{\boldsymbol{j}}_\perp\times\boldsymbol{e}_z, \tag{2.48}$$

as forced by the streamfunction ψ_0. With electrically insulating walls this forcing term can be absorbed into an adjusted pressure gradient, in the same manner as the irrotational component of the Lorentz force, leaving only the shear stress terms to deal with.

The shear stress terms require modelling. In the limits of large Ha and large N, which permit the flow to be classed as quasi-two-dimensional, an approximate solution can be built, by matching the profiles for isolated exponential boundary layers at each wall perpendicular to the magnetic field with the core flow. Recall that $\boldsymbol{j}_\perp \times \boldsymbol{e}_z$ can be written as proportional to a velocity, either as shown after Eq. (2.47), or in Eq. (2.32). Thus, with a boundary layer approximation, $(\partial^2/\partial z^2 - Ha^2)u = 0$, such that the analytic solution for an isolated Hartmann boundary layer is an exponential profile (Roberts 1967).

To aid this discussion, numerical solutions of the steady, streamwise invariant velocity profile and induced current magnitude are shown in Fig. 2.1 at $Ha = 300$ (see § 2.3 for more). Overlaying the figure are various key features. Hartmann boundary layers, forming on walls perpendicular to the magnetic field, each have thickness δ_H, which scales as Ha^{-1} while laminar. Shercliff boundary layers, forming on walls parallel to the magnetic field, each have thickness δ_S, which scales as $Ha^{-1/2}$ while laminar. Laminar (passive) Hartmann boundary layers are required for the validity of the Q2D model. At $Re = 10^5$, $Ha \geq 200$ is required for laminar Hartmann layers, and $Ha \geq 400$ for laminar Shercliff layers (Krasnov *et al.* 2012). Thin sheets of current form in the Hartmann boundary layers, as the walls are perfectly electrically insulating, and all current loops must close within the duct. These current loops, which are highly dense within the Hartmann boundary layers, spread almost equally through the core. Thus, the Lorentz force applies a strong acceleration to flow within the Hartmann boundary layers, and applies a corresponding (fairly uniform) damping, to the core flow. This lends the Hartmann boundary layers their exponential profile. Note that even at this large Ha, small induced currents are present within the Shercliff layers, lending them some three-dimensionality (Pothérat *et al.* 2000).

Formally, at the edge of thin (L_z/Ha) Hartmann boundary layers, which contain the majority of the induced current, in the scaled coordinate $\xi = A^2 Ha z$, the limit of $\boldsymbol{u}$ is

$$\lim_{\xi\to\infty} \boldsymbol{u}_\mathrm{H} = \boldsymbol{u}(-L_z/2) \equiv \boldsymbol{u}^-, \tag{2.49}$$

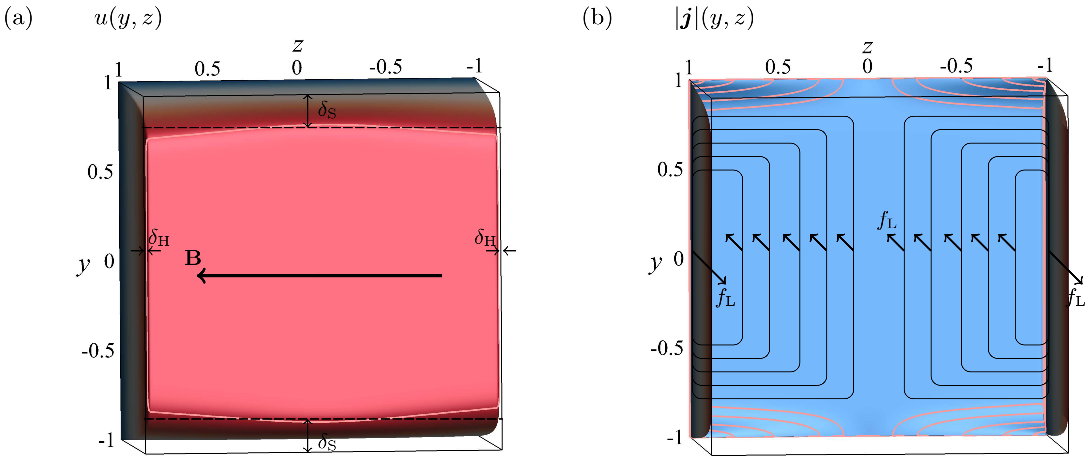

FIGURE 2.1: Time steady, streamwise invariant duct flow at $Ha = 300$, with sketched features following Müller & Bühler (2001). (a) Streamwise velocity profile, with a single contour line at $u = 0.99$ to help define the boundary layer thicknesses (for the Shercliff layers, a rough average width has been shown with dashed lines). (b) Induced current magnitude, with (light red) contour lines at magnitudes of 0.005, 0.01, 0.02, 0.03 and 0.04 $|\boldsymbol{j}|$. The remaining current within the core has $|\boldsymbol{j}| < 0.005$. Example current loops (black lines) are just for reference (they are not a computed part of the solution; the 'squared' profile is to help indicate that the Lorentz force f_L is roughly equal everywhere within the core flow, and differs only in the boundary layers).

where $\boldsymbol{u}_H$ is the velocity profile of the Hartmann boundary layer, and $\boldsymbol{u}$ the velocity profile in the bulk of the duct. An isolated exponential boundary layer, with zero wall velocity, has the profile $1 - \exp(-\xi)$ in the scaled wall coordinate. To satisfy the matching condition at $\xi \to \infty$, the Hartmann layer takes the form

$$\boldsymbol{u}_\perp = \boldsymbol{u}^-[1 - \exp(-\xi)]. \tag{2.50}$$

Considering the wall at $z = L_z/2$, $\xi = -A^2 Ha z$, and from the chain rule

$$\left.\frac{\partial \boldsymbol{u}_\perp}{\partial z}\right|_{L_z/2} = -A^2 Ha \left.\frac{\partial \boldsymbol{u}_\perp}{\partial \xi}\right|_{\xi=0} = -A^2 Ha \boldsymbol{u}^-. \tag{2.51}$$

Similarly at $z = -L_z/2$, $\xi = A^2 Ha z$ and

$$\left.\frac{\partial \boldsymbol{u}_\perp}{\partial z}\right|_{-L_z/2} = A^2 Ha \left.\frac{\partial \boldsymbol{u}_\perp}{\partial \xi}\right|_{\xi=0} = A^2 Ha \boldsymbol{u}^-. \tag{2.52}$$

Assuming (for the first time) the flow is two-dimensional in the core, so $\boldsymbol{u}^- \approxeq \bar{\boldsymbol{u}}_\perp$ (neglecting contributions of order Ha^{-1}, N^{-1} or higher), and substituting Eq. (2.48) for the forced velocity, and Eqs. (2.51) and (2.52) for the wall shear stresses, into

Eq. (2.44), the governing equations for the quasi-two-dimensional SM82 model

$$\frac{\partial \bar{\boldsymbol{u}}_\perp}{\partial t} = -(\bar{\boldsymbol{u}}_\perp \cdot \boldsymbol{\nabla}_\perp)\bar{\boldsymbol{u}}_\perp - \boldsymbol{\nabla}_\perp \bar{p}_\perp + \frac{1}{Re}\boldsymbol{\nabla}_\perp^2 \bar{\boldsymbol{u}}_\perp + A^2\frac{Ha}{Re}(u_0 - 2\bar{\boldsymbol{u}}_\perp), \tag{2.53}$$

$$\boldsymbol{\nabla}_\perp \cdot \bar{\boldsymbol{u}}_\perp = 0, \tag{2.54}$$

are attained (with $w = 0$ and $\bar{p}_\perp$ in the place of $\bar{p}$). The final term of Eq. (2.53) can be rewritten, by introducing the Hartmann friction coefficient $H = 2A^2 Ha$ (Pothérat 2007). This affords freedom in the selection of H, in spite of the $Ha \gg 1$ constraint, as A is only required when translating back to the full 3D problem (Ha alone not being a true parameter of the Q2D problem). In addition, the forcing u_0 can be absorbed into the pressure, or included in $\boldsymbol{f}$. Thus, henceforth, the following form of the SM82 model will be considered (although overbars will be dropped):

$$\frac{\partial \bar{\boldsymbol{u}}_\perp}{\partial t} = -(\bar{\boldsymbol{u}}_\perp \cdot \boldsymbol{\nabla}_\perp)\bar{\boldsymbol{u}}_\perp - \boldsymbol{\nabla}_\perp \bar{p}_\perp + \frac{1}{Re}\boldsymbol{\nabla}_\perp^2 \bar{\boldsymbol{u}}_\perp - \frac{H}{Re}\bar{\boldsymbol{u}}_\perp, \tag{2.55}$$

$$\boldsymbol{\nabla}_\perp \cdot \bar{\boldsymbol{u}}_\perp = 0. \tag{2.56}$$

A final note for this section. All MHD aspects of the flow are encapsulated in the friction term, directly related to the shear stresses at the out of plane walls, or are absorbed into the pressure gradient (as for the irrotational part of the Lorentz force). Thus, so long as *any* physical phenomena can be simplified in such a manner (as *only* an irrotational contribution to pressure, and a contribution from shear stresses at the walls), the governing equations, Eqs. (2.55) and (2.56), would remain identical for the analogous system. Such simplifications are indeed possible for shallow water flows, where thin channels induce Rayleigh friction, rather than Hartmann friction, and axisymmetric flows under strong rotation (Pedlosky 1987; Vo *et al.* 2015), in which Ekman friction is present. Thus, solutions for such flows can be solved in a Q2D framework, assuming in the latter case that the Coriolis force is also modelled, making Eqs. (2.55) and (2.56) much broader reaching than the field of magnetohydrodynamics. Of course, the definition of the friction term would differ, see Vo *et al.* (2017) for conversions, as would the bounds of validity of the model.

2.3 Applicability and accuracy of the Q2D model; a literature review

A complete numerical reproduction of a liquid metal duct flow in a fusion relevant setting would require modelling a wide variety of physical phenomena. Such features include: a realistic geometry (duct corners/inlets/outlets), wall roughness or slip, thermodynamic heating (directly at the plasma facing wall, volumetrically via a neutron flux, radiatively, and dissipatively, viscous or Ohmic), interactions with pumps or heat exchangers, imperfect electrical conductivity of the walls, etc. (Smolentsev *et al.* 2010a; Abdou *et al.* 2015). The exclusion of these complexities may impact both the efficacy of the numerical solutions in making real-world predictions, and the validity of the assumption of quasi-two-dimensionality. The latter is considered shortly. As for the former, it is prudent to analyse an idealized, streamwise invariant duct first. The driving reason is that a great deal remains unknown about Q2D transitions and turbulence, and particularly whether purely Q2D transitions are possible. Thus, the simplest geometry forms a natural starting point. This avoids any complexities which may obscure the underlying dynamics; dynamics which, hopefully, may underlie many of the more physically realistic flows.

First, the applicability of the Q2D model to fusion relevant regimes is considered. Table 2.1 provides some of the key parameters for anticipated liquid metal coolant/reebreeder duct flows in magnetic confinement fusion reactors. For the most part, based on this simple quantitative comparison, it is not unreasonable to expect that solutions of the Q2D model should be good predictors of z-averaged fully 3D solutions at comparable parameters (in a straight geometry). The main exception is that the quasi-static assumption appears questionable. Although supported by the rapid timescales of the induced field (e.g. $\tau_{\nu,\mathrm{L}}/\tau_{\mathrm{A}}$ and $\tau_{\mathrm{I,L}}/\tau_{\mathrm{A}}$ are often much greater than unity), the accompanying requirement of rapid dissipation of Alvén waves is never satisfied (S is never less than unity). However, the evolution of a time varying induced magnetic field is rarely performed in either Q2D or 3D MHD problems in the field of fluid mechanics, in laboratory and industrial contexts. This is primarily due to the computational expense associated with introducing (and timestepping over) the Alfvén timescale, see Choi *et al.* (1997) and Lee & Choi (2001) for more. Even if inappropriate, a quasi-static induced field is almost always assumed, in both Q2D and full 3D solvers. Thus, the issue is not further considered. Importantly, the timescale analysis does otherwise support the classification of 3D flows as Q2D (Smolentsev *et al.* 2008), based on fusion relevant parameters, as momentum diffusion along field lines is rapid. Lastly, note that this work is motivated by self-cooled duct designs, which would most resemble the design proposed in the rightmost column of Table 2.1, with $U_0 \geq 1$ ms^{-1}.

Conduit Reactor Location Refs.	DCLL ITER Outboard S10, A15	DCLL DEMO Outboard S10, A15	DCLL DEMO Inboard S10, A15	HCLL ITER Inboard M14, A15	DRM DEMO Outboard M11
U_0 (ms^{-1})	0.04	0.07	0.15	10^{-3}	0.1 - 1
B_0 (T)	4	4	10	4	7
$2L_y$ (m)	0.2	0.2	0.2	0.059	0.355
L_z (m)	0.2	0.2	0.2	0.265	0.610
$A_z = 2L_y/L_z$	1	1	1	0.223	0.582
$Re \gg 1$	$3{\times}10^4$	$6{\times}10^4$	$1.2{\times}10^5$	670	$3.3{\times}10^5$ - 3.3×10^6
$Ha \gg 1$	$6.5{\times}10^3$	$1.2{\times}10^4$	$3{\times}10^4$	$1.1{\times}10^4$	$5.139{\times}10^4$
$R = Re/2Ha \lesssim 380$	2.3	2.5	2	0.03	3.2 - 32
$N \gg 1$	$1.4{\times}10^3$	$2.4{\times}10^3$	$7.5{\times}10^3$	1.806×10^5	$8.0{\times}10^2$ - 8.0×10^3
$S \ll 1$	2.9	5.4	13.4	4.9	23.0
$R_{\mathrm{m}} \ll 1$	$6{\times}10^{-3}$	$1.2{\times}10^{-2}$	$2.4{\times}10^{-2}$	$1.34{\times}10^{-4}$	$6.6{\times}10^{-2}$ - 0.66
$\tau_{\mathrm{I,L}}/\tau_{\mathrm{A}} \gg 1$	$4.8{\times}10^2$	$4.5{\times}10^2$	$5.6{\times}10^2$	$1.8{\times}10^3$	1.2 - 11.8
$\tau_{\nu,\mathrm{L}}/\tau_{\mathrm{A}} \gg 1$	$1.5{\times}10^7$	$2.7{\times}10^7$	$6.7{\times}10^7$	$1.2{\times}10^6$	$3.9{\times}10^7$
$\tau_{\mathrm{2D}}/\tau_{\mathrm{I,L}} \ll 1$	$7.1{\times}10^{-4}$	$4.2{\times}10^{-4}$	$1.3{\times}10^{-4}$	$2.3{\times}10^{-3}$	$1.1{\times}10^{-3}$ - $1.1{\times}10^{-2}$
$\tau_{\mathrm{2D}}/\tau_{\nu,\mathrm{L}} \ll 1$	$2.4{\times}10^{-8}$	$6.9{\times}10^{-9}$	$1.1{\times}10^{-9}$	$3.4{\times}10^{-6}$	$3.3{\times}10^{-9}$
$Ri \ll 1$	7.8	$5.6{\times}10^2$	$1.1{\times}10^2$	$2.2{\times}10^3$	2.6×10^{-4} - 2.6×10^{-2}

TABLE 2.1: Validity assessment of the Q2D assumption, particularly through timescale analysis of key flow parameters in proposed liquid metal coolant ducts of magnetic confinement fusion reactors. A modified aspect ratio is temporarily considered (switching $A = L_y/L_z$ for $A_z = 2L_y/L_z$), as many of the references for this table take the characteristic duct dimensions as $2L_y$ and $2L_z$ (when defining *Re* or *Ha*), rather than $2L_y$ and L_z as in this work. Note that where multiple references were required for the full spread of flow parameters, the characteristic length implicit in *Ha* or *Re* may not exactly match with a characteristic L_y or L_z stated elsewhere. As discussed later, laminar Hartmann layers are assumed in the Q2D model, which requires $R \lesssim 380$ (Krasnov *et al.* 2004; Moresco & Alboussiére 2004; Zienicke & Krasnov 2005). Furthermore, when calculating $R_{\mathrm{m}} = RePr_{\mathrm{m}}$ the value of Pr_{m} was determined at fusion relevant conditions, rather than taking order 10^{-6} as at room temperature (Pothérat & Kornet 2015). A representative value of $Pr_{\mathrm{m}} = 2 \times 10^{-7}$ for PbLi[17] was considered (based on Pr_{m} of 2.19 - 1.39×10^{-7} at the bounding temperatures of 600-800 K over which correlations were valid (Martelli *et al.* 2019), which was slightly more pessimistic than $Pr_{\mathrm{m}} = 1.08865 \times 10^{-7}$ at 773.15 K (Bühler & Mistrangelo 2013). As a final note for the curious reader, the Richardson number (the ratio of buoyant to inertial forces) has been included in the final row, even though heat transfer is not directly considered (excepting in Appendix B). $Ri \ll 1$ represents negligible natural convection (assumed in this work), while natural convection dominates for $Ri \gg 1$. Acronyms and shorthand are as follows: dual-coolant lead-lithium (DCLL), helium-cooled lead-lithium (HCLL), Spanish acronym of modular dual-coolant (DRM), international thermonuclear experimental reactor (ITER), demonstration power plant (DEMO). References are as follows: S10 - Smolentsev *et al.* (2010b), A15 - Abdou *et al.* (2015), M14 - Mistrangelo *et al.* (2014) and M11 - de les Valls *et al.* (2011).

Since the seminal works of Kolesnikov & Tsinober (1974) and Alemany *et al.* (1979), and the development of the SM82 model by Sommeria & Moreau (1982), both experimental and numerical focus on Q2D flows has greatly increased. Various works of particular importance follow, roughly in chronological order, although are by no means exhaustive. These works are sufficiently broad to consider quasi-two-dimensionality of everything from the underlying basic flows, to large scale eddies and finally, to fully turbulent flows. Hopefully, the consistent observations of quasi-two-dimensionality, the widespread use of Q2D modelling (e.g. for buoyant flows, cylinder wakes, electrically driven vortices, etc.) and the accuracy of the Q2D model (when at the appropriate parameters) will be made apparent by this literature review.

Kolesnikov & Tsinober (1974) experimentally investigated decaying grid generated turbulence. A coefficient quantifying the degree of three-dimensionality of the turbulence (0: 2D, to 1: 3D) was measured at near unity at a field strength of 0.08 T, and decreased to order 10^{-3} at field strength 0.8 T. Furthermore, by introducing a passive tracer, the momentum transfer parallel and perpendicular to the field, due to turbulent perturbations, could be inferred. At higher field strengths, almost no transfer was observed along field lines, with the turbulence inferred to be quasi-two-dimensional.

Alemany *et al.* (1979) also investigated decaying turbulence (behind a moving grid). The observation of a power law scaling exponent of -3, for wave numbers parallel to the magnetic field, indicated an equilibrium had been established between nonlinear transfers and Joule dissipation. This balance represented the degree of anisotropy maintained for a given magnetic field strength, as a function of the turbulent scales. For a sufficiently high degree of anisotropy, or a sufficiently large magnetic field strength, a quasi-two-dimensional phase could be attained.

Sommeria (1986) experimentally studied forced turbulence in a square box. The validity of the Q2D equations were well supported as properties of the turbulent spectra were consistently obtained under different experimental setups (differing field strength and/or free/rigid upper surface), so long as the Reynolds number based on the friction time Re/H was matched. Q2D dynamics were observed at lower field strengths than Kolesnikov & Tsinober (1974), as low as 0.25 T, due to a smaller aspect ratio (of unity, compared to 6/5 and 3). Sommeria (1986) also introduced conversion relations between Q2D models of MHD flows and Q2D quasi-geostrophic models of atmospheric flows. Although an analogous friction term could be derived, the Coriolis force contribution could not be translated to an equivalent term in the SM82 model (as energy would be propagated by Rossby waves but dissipated in an MHD context). This would limit Q2D modelling of atmospheric flows to either axisymmetric or very small aspect ratio configurations.

Sommeria (1988) experimentally examined electrically driven vortices in a circular tank, subjected to strong magnetic fields. Measurements of the electrical resistance (electric potential/injected current) agreed well with asymptotic Q2D theory as the magnetic field was increased, with excellent agreement at higher Ha. This was further supported by observing that current was contained within thin layers of thickness L_z/Ha, except in vortex cores of thickness $L_z/Ha^{1/2}$. The main differences between the experimental and asymptotic results were expected due to recirculating flows not accounted for in the Q2D model.

Davidson (1995) analytically assessed the the magnetic damping of jets and vortices. Although these flows are not wall bounded, many of the conclusions are still relevant to this work. Davidson (1995) showed that the predominantly diffusive action of the Lorentz force, in elongating vortices along field lines, reduced the Joule dissipation (relative to the kinetic energy). This ensured that linear momentum is conserved, and is of relevance to duct flows with electrically insulating walls, as current loops are required to close within the duct. As noted by Sommeria & Moreau (1982), this allows the Lorentz force to act as a local source of momentum, so long as there is a corresponding sink of momentum acting elsewhere on the same current loop. The angular momentum parallel to the magnetic field was also shown to be conserved, explaining why Q2D vortices are observed to have long lifetimes (many turnover times), in spite of Joule dissipation induced by the Lorentz force.

Zikanov & Thess (1998) numerically simulated MHD flows in a periodic box, obtaining clear alignment of columnar vortical structures along the magnetic field direction. However, the periodic boundary conditions meant these flows could be truly two-dimensional. This was shown by Zikanov & Thess (1998) when the same final two-dimensional state was obtained by both an isotropic 3D initial condition evolved with the 3D Navier–Stokes equations, and from a 2D initial condition evolved with the 2D Navier–Stokes equations (not a Q2D model), so long as the initial interaction parameter was large ($N = 10$). With a large interaction parameter, any angular momentum transferred to the perpendicular directions was rapidly dissipated by Joule damping.

At lower interaction parameters, only when velocity variations in the field direction were large could Joule damping reinstate a two-dimensional structure for a short time, before nonlinear energy transfers between modes destabilized the columnar vortex.

Bühler (1996) numerically investigated, with a Q2D model, a variation in the electrically conductivity of the wall perpendicular to the magnetic field. Vortex streets were shed from the conducting region. However, the instability mechanism appeared to be hydrodynamic in origin, as the smooth variation of the electrical conductivity avoided the generation of three-dimensional instabilities. Overall, the critical Reynolds number increased with an increasing magnetic field strength over the range of parameters for which the Q2D model was valid.

Mück *et al.* (2000) numerically simulated the flow past a square cylinder, performing full 3D DNS in a rectangular duct with electrically insulating walls. Q2D dynamics were observed at $0.2 < N < 1$ (based on velocity fluctations in the field direction tending to zero), as further support of works such as Kolesnikov & Tsinober (1974) and Bühler (1996) which also suggest that $N \gg 1$ is not a necessary constraint for quasi-two-dimensionality. A cigar or barrel shape was observed in the otherwise columnar vortices, which were broadest at the midplane, but still remained perpendicular very near to the Hartmann walls to a fairly good approximation, as predicted by Sommeria & Moreau (1982).

Pothérat *et al.* (2000) analytically and numerically investigated the Q2D model proposed by Sommeria & Moreau (1982). Analytic solutions (local and averaged) for the three dimensional flow in a laminar Shercliff boundary layer and an isolated electrically driven vortex were compared to the Q2D model solutions. The agreement in the former case was very good (within 10% error). In the latter case, the Q2D solution overpredicted the velocity close to the vortex core, and was excellent thereafter. Higher order effects (recall the SM82 model is zeroth order in Ha and N) were also considered. These included recirculating flows in the Hartmann layers, of order N^{-1}, generating current of order $(HaN)^{-1}$ outside the Hartmann layers. A three-dimensional 'barrel' effect, of order Ha^{-1}, was also predicted for vortices, as was observed by Mück *et al.* (2000). The 'barrel' effect was induced by a two-dimensional force generated by the perpendicular current density.

Burr *et al.* (2000) experimentally assessed turbulent flows in rectangular ducts with electrically conducting walls. The degree of two-dimensionality (anisotropy of the turbulent flow) was quantified by deviations in fluctuations of the electric potential relative to the field angle (fluctuations are purely perpendicular in a two-dimensional flow). Clear anisotropy was present at $Ha = 600, N = 3.6$, and was particularly stark for $Ha = 1200, N = 14.4$ and above. Some slight reductions in anisotropy were observed at $Ha > 1200$, expected due to nonlinearity and the greatly increased shear generated by electrically conducting walls at higher Ha (the shear does not increase as rapidly with increasing Ha when the walls are insulating). Although the degree of isotropy increased at the turbulent scale size reduced, measurements still indicated the small scales were strongly anisotropic, and thereby possibly Q2D.

Barleon *et al.* (2000a) experimentally measured the critical Reynolds numbers for a circular cylinder wake in a channel flow (magnetic field along the cylinder axis). Overall, the theoretical prediction, of a linear dependence of the critical Reynolds number on Ha, was well matched by the Q2D model for $250 < Ha < 1250$. A linear dependence of the critical parameter on the (length scale defined by the) damping term was considered to be general to all Q2D flows.

Burr & Müller (2002) experimentally investigated Rayleigh–Bénard convection in a rectangular box, and compared to predictions of a Q2D model including natural convection. There was some agreement in the critical Rayleigh numbers for Ha of 400 and 800 (approximately 20% error), with quite erroneous Q2D predictions at lower $Ha \lesssim 200$. The Q2D model included significantly more Joule dissipation that the experimental setup, as in the latter the side layers impinged upon the Hartmann layers. The critical conditions at large H were further validated by Vo *et al.* (2017) using a Q2D model of a duct flow with a heated bottom wall, at $Re = 0$.

Authié *et al.* (2003) numerically compared Q2D and 3D natural convection flows in finite length ducts. Qualitative comparisons of the flow fields indicated the laminarization and clear quasi-two-dimensionality at $Ha > 100$ for Grashof numbers $Gr = Ri Re^2$ (ratio of buoyant to viscous forces at the duct scale) of order 10^6, and $Ha > 200$ for Gr of order 10^7. Passive Hartmann layers (Hartmann layers that predominantly act to damp the core flow) were required for quasi-two-dimensionality. A modified interaction parameter $N_{\mathrm{G}} = Ha^2/Gr^{1/2} \gtrsim 4$ was required for Q2D dynamics to be observed.

Krasnov *et al.* (2004), Zienicke & Krasnov (2005) and Moresco & Alboussiére (2004) analysed the transition to turbulence in Hartmann layers. Although the transition behavior is further discussed in Chapter 3, § 3.6, there is a direct relevance to Q2D modelling, which assumes passive, laminar Hartmann layers. The Hartmann layers were observed to remain laminar when $R = Re/2Ha < 380$ (R is the Reynolds number based on the Hartmann layer thickness). Recalling Table 2.1, the Hartmann layers are thus expected to remain laminar at fusion relevant conditions.

Pothérat (2007) provided a detailed numerical analysis of the stability and transient growth of Q2D pressure-driven flows. Although not a comparison between Q2D and 3D flows, Pothérat (2007) forms the basis of much of the present work. Furthermore, the timescale analysis of the preceeding section was based on Pothérat (2007), as only when $\tau_{\rm 2D} \ll \tau_{\rm I,L}$ and $\tau_{\rm 2D} \ll \tau_{\nu,\rm L}$ does momentum diffuse rapidly enough to quasi-two-dimensionalize the entire core flow. It was also noted that the thickness of the Shercliff layer is determined by the equality of the $\tau_{\rm 2D}$ and $\tau_{\nu,\rm L}$ timescales. Thus, viscous friction will always have acted within the Shercliff layer, and momentum diffusing from outside the Hartmann layers will by unable to quasi-two-dimensionalize parallel layers (which always retain some intrinsic three-dimensionality). Pothérat (2007) also showed that the thickness of the Q2D Shercliff layer scales as $H^{-1/2}$, similar to the full 3D Shercliff layer thickness scaling with $Ha^{-1/2}$.

Krasnov *et al.* (2008) numerically investigated the optimal growth and transition to turbulence in channel flows with a spanwise magnetic field. Although not directly comparable to a Q2D flow, as the out-of-plane (magnetic field) direction was periodic, it was still observed that Ha of 50 and 100 resulted in the optimal out-of-plane wave number falling to zero (structures invariant along the magnetic field), for Re of 3000 and 5000, respectively. The energy amplification and optimal wave number in the field direction were also found to vary as Ha^{-1} for large Ha.

Kanaris *et al.* (2013) and Dousset & Pothérat (2008) simulated the MHD flow around a confined circular cylinder, in 3D and Q2D, respectively. The percentage error in the critical Reynolds number was 20-30% (comparisons were hampered by the different means of computation), although the error still reduced with increasing Ha. In all other measures (drag coefficient, recirculation length, base pressure coefficient), excellent agreement was obtained between the Q2D and 3D results, with maximum errors of 10% and 6% at $Ha = 320$ and $Ha = 1120$, respectively. 3D effects were predominantly contained in thin viscous layers, and in the smallest scales when vortices were shed from the cylinder. The alignment of the vortex cores along the magnetic field was also excellent, with minimal deviation, at $Ha = 1120$.

Young *et al.* (2014) experimentally investigated underlying base flow profiles with inflection points, by electrically driving the flow, while still otherwise maintaining electrically insulating walls. A Q2D flow was observed at magnetic field strengths above 0.25 T. The velocity measured at the Hartmann wall then closely matched that in the core flow.

Pothérat & Klein (2014) experimentally forced turbulence in an electrically insulating cube. Electrical stimulation of the flow at the bottom wall generated structures that could be qualitatively matched at the unforced top wall for $N_t' \geq 65$. Note that the true interaction parameter $N_t'(L_i) = (\sigma B^2 L_i/\rho U_b')(2L/a)^{-2}$ is a function of the injection length scale L_i, where U_b' is the fluctuating velocity just outside the bottom Hartmann layer. Even N_t' as low as 4.5 was still sufficient for quantitative correlation of flow structures across the entire box. As Q2D flows and 3D flows driven by viscous friction are inertialess, they obey a scaling in the measured bottom wall Reynolds number of $Re_b \sim Re_0$, where Re_0 is the forcing Reynolds number, as predicted by Sommeria (1988). By comparison, inertial and 3D turbulent flows scale as $Re_b \sim Re_0^{2/3}$. By observing the switch in Re_0 scaling coefficient, Pothérat & Klein (2014) were able to find a clear $Re_b' \simeq 1.27 \times 10^3$ above which the flow switched from an inertial to an intertialess regime. Pothérat & Klein (2014) also found that although three-dimensionality asymptotically reduces with an increasing true interaction parameter, there is no sharp limit at which the flow becomes Q2D at all scales. However, for any N_t a cutoff scale will still exist, sharply dividing those scales which are 3D and those which are Q2D.

Pothérat & Kornet (2015) numerically simulated 3D decaying turbulence in a Hartmann channel flow (two periodic directions). In flows governed by Q2D dynamics (once most of the turbulent scales became Q2D), dissipation predominantly occurred in the Hartmann layers. In the presence of Hartmann walls, anisotropy was observed to increase more rapidly in the larger scales, and the energy in the velocity component aligned with the field decayed much faster, with increasing field strength. The two-dimensionality of the turbulence was measured by the skewness, which for sufficiently long evolution times tended to zero for $Ha < 224$ (the final result of higher Ha simulations remained unknown). Further support of the barrel effect (Pothérat *et al.* 2000), induced due to currents of order Ha^{-1}, was also consistently observed, regardless of the degree of three-dimensionality in the initial condition. The barrel effect was less observable at higher Ha, and with the barrel structures only slowly varying in time.

Baker *et al.* (2018) experimentally validated the numerical observation of a cutoff length, based only on the true interaction parameter, between scales exhibiting Q2D and 3D dynamics (Pothérat & Klein 2014). The cutoff length scale was shown to vary as $N_t^{-1/3}$, until the injection scale is reached (below which an inverse energy cascade cannot transfer energy and three dimensionality is maintained). However, an inverse cascade was still observed at scales well below the cutoff scale (possibly attributed to the forcing not acting at a single precise injection scale), in addition to the direct energy cascade expected to be present. Joule dissipation damped all scales of energy in 3D turbulence, while Q2D turbulence was only appreciably damped if the turnover time exceeded the friction time.

Cassels *et al.* (2019) compared numerical solutions of Q2D and 3D linear transient growth optimals. For a given Reynolds number, a sufficiently large Hartmann number could induce Q2D dynamics (in a 3D simulation), such that Q2D predictions of modal growth and structure became excellent; see also Chapter 6 (Camobreco *et al.* 2021b), Table II therein. Even in increasingly Q2D regimes, inertial effects were still the predominant driver of non-normality (and thereby transient growth). The level of Joule dissipation in the bulk flow dropping below that in the Hartmann layers was the clearest means of identifying the Q2D regime. Q2D transient growth scaled with a Reynolds number based on the thickness of the Shercliff layer ($Ha^{-1/2}$, i.e. the ratio of 2D inertia to the Lorentz force). This translated to $R_H = Re/Ha < 33.3$ for Q2D dynamics to be observed, well below the $Re/2Ha < 380$ requirement for laminar Hartmann layers (Zienicke & Krasnov 2005).

This concludes the literature review of Q2D modelling studies. Hopefully, the usefulness of the Q2D model is now apparent, given the various flow configurations which can exhibit Q2D dynamics, and given that parameter ranges exist in which Q2D solutions should be excellent predictions of the fully 3D solutions.

2.4 Practical application and baseline comparisons from the literature

The motivation for this work stems from improving the performance of dual purpose tritium breeder/coolant blanket module designs in magnetic confinement fusion reactors, and specifically, their efficient cooling. If the blanket ducts were solely for cooling, non-electrically conducting fluids would be the simplest design solution, as they would avoid the action of the Lorentz force, regardless of their proximity to the plasma-confining magnetic field. However, a lithium alloy (likely lead lithium) is necessary to rebreed the tritium required to sustain the plasma reactions. Thus, an electrically conducting fluid cannot be simply avoided. Many of the MHD phenomena resulting from the action of the Lorentz force were discussed in the preceding sections; some of the engineering aspects are discussed here. The two key efficiency aspects are:

- The rate of heat transfer (per unit length) at the plasma facing wall.
- The pressure drop (per unit length) necessary to drive the lead lithium fluid.

Given the complexity of nuclear fusion reactors, there remain many other design issues to consider, besides the rate of heat transfer and pressure drop. However, due to the reactor's complexity, many studies (this thesis included) isolate only one or two design issues to analyse. There is undeniable danger in such a method, as not only could the solution to one problem impact possible solutions to another, but many issues are intertwined, and cannot always be easily isolated (e.g. buoyant forces, due to temperature differences, can influence the velocity field, but are neglected on the grounds of a small Richardson number in the self-cooled conduit design investigated in this work). Even so, computational limits exist, which prevent modelling all real-world details. Thus, a solution to an isolated problem, which minimally impacts the ability for other researchers or engineers to solve their own problems is preferred, and this thesis strives to find such a (minimally impactful) solution. Although the engineering problems which are beyond the scope of this work need not be understood, neither can they be completely ignored, and so the following list acknowledges the existence of reactor blanket engineering problems:

- A flow rate that ensures the maximum pressure drop does not exceed structural limitations of $\approx$ 2 MPa (Smolentsev *et al.* 2010a,b). The total pressure drop for a 3D blanket flow was estimated to be 1.17 MPa (Smolentsev *et al.* 2010b), predominantly from 3D effects, for a flow velocity of 0.015 m/s (35 kg/s flow rate) at $Re = 1.2 \times 10^5$. This implies a limit on the maximum operating Reynolds number, or equally on the maximum increase in the pressure gradient.
- An acceptable first wall temperature, which must have outlet flow temperatures below 550 °C with Eurofer steel (de les Valls *et al.* 2011), or below 700 °C with the

addition of Silicon Carbide flow channel inserts (the latter primarily electrically insulate the duct to reduce the driving pressure required but also allow for higher wall temperatures). Extended operation at these high temperatures could cause thermal creep to be of concern.

- Imperfections in the electrically insulating wall coating (Bühler 1995, 1996) can drastically impact the required pressure gradient. An ideal wall insulation should provide a uniform wall conductivity $\sigma_{\mathrm{w}} < 0.1$ S/m (Smolentsev *et al.* 2008).

- Mechanical and thermal stresses introduced by strong temperature or velocity fluctuations; the former are due predominantly to uneven volumetric heating from the plasma neutron flux (Zikanov *et al.* 2013). These fluctuations can generate low frequency convective rolls, although buoyant temperature fluctuations appear relevant only at $Ri > 0.5$ for $Ha < 500$ (Belyaev *et al.* 2018).

- Non-uniform volumetric heating, which occurs when energy is released by the neutron-lithium reactions during fuel rebreed events. This is not localized at the plasma facing wall, but must still be efficiently transported through the coolant ducts. The estimated neutron load is 0.78 MW/m^2 (Smolentsev *et al.* 2008).

- Interfacial slip, which may be sizeable at the conditions expected within DCLL blankets (Smolentsev *et al.* 2010a). Slip can quite drastically change the base flow profile, particularly as the slip length can be comparable to the thickness of the Hartman layer. However, this increases the thickness of the parallel boundary layers, which is likely to be beneficial at reducing the critical Reynolds number, and also increases the Hartmann braking time (Smolentsev 2009). Overall, interfacial slip could be beneficial, although would warrant further investigation of the actual base flow profiles.

- Corrosion, which is a significant structural issue for all blanket concepts, as the rate of corrosion is much higher in the presence of a magnetic field for high temperature lead lithium alloys (Bucenieks *et al.* 2006); as observed in experiments conducted on Eurofer steel at 550 °C up to 1.7 T, at velocities up to 0.05 m/s. Higher duct velocities, and turbulence, can further exacerbate the issue (Smolentsev *et al.* 2013; Abdou *et al.* 2015).

- Recirculating flows are an issue both for impeding the extraction of tritium from the rebreeder ducts, and due to high temperature fluid remaining in contact with the wall for damaging periods of time (Klüber *et al.* 2019).

- Fluid interactions in complex duct geometries (including pumps, heat exchangers and sharp corners) could drastically alter the mean flow (Sapardi *et al.* 2017). Note that duct lengths are approximately 20 (DEMO) to 50 (ITER) times longer than characteristic in plane dimensions, helping the flow settle (Smolentsev *et al.* 2008).
- Electromagnetic coupling between inboard and outboard ducts (Smolentsev *et al.* 2008, 2010a,b) by virtue of current distributions which loop through multiple channels. However, in a self-cooled design, all walls are electrically insulated.

Focus is now placed on the efficiency considerations. Sadly, a benchmark for the enhancement of heat transfer for a time-averaged turbulent flow, relative to the commonly used laminar baseline, is lacking (for a duct with perfectly electrically insulating walls, with either wall or volumetric heating). Thus, it is not possible to comment as to whether inciting turbulence to enhance heat transfer will be more effective than previous attempts to enhance heat transfer in MHD flows, e.g. via vortex promoters (Kolesnikov & Andreev 1997; Barleon *et al.* 2000a; Hussam & Sheard 2013; Cassels *et al.* 2016; Hamid *et al.* 2016a,b; Hussam *et al.* 2018; Murali *et al.* 2021). This thesis attempts to rectify this issue by computing a baseline for the heat transfer enhancement ratio (of a passive scalar) in a sustained subcritical Q2D turbulent flow, detailed in Appendix B. While these computations may serve as a useful benchmark for future works which aim to assess heat transfer enhancement, it is also worth determining the minimum necessary conditions required to trigger and sustain turbulence. If these conditions (e.g. very large Reynolds numbers, very small duct aspect ratios) are by themselves impractical, this may rule out a simple self-cooled blanket design. However, if these conditions are accessible, they can then form the focus of any (future) heat transfer computations.

2.5 The accuracy of Q2D modelling in the current context

The preceding sections have elucidated the breadth of the background for MHD flows in cooling conduits. However, this work specifically focuses on streamwise invariant, electrically insulating duct flows, in Q2D regimes. Thus, this section considers time steady fully developed solutions for 3D MHD duct flows and compares them to their Q2D equivalents. These fully developed profiles are the underlying laminar base flows upon which turbulence may develop. When all walls are perfectly electrically insulating, these base flows yield the lowest driving pressure gradient for a given flow rate and Ha (Müller & Bühler 2001), and are thereby the most efficient pressure driven flows.

First, a brief introduction of how these base flows are computed. Interestingly, the most computationally efficient method, when interested in solutions over a wide range of Ha, is to independently solve both the momentum and induction equations, Eqs. (2.1) and (2.3), prior to the invocation of the quasi-static and inductionless approximations. Eqs. (2.1) and (2.3) are simplified by seeking streamwise invariant ($\partial_x \to 0$), time steady solutions for $\boldsymbol{u}$ and $\boldsymbol{b}$. Once non-dimensionalized in the same manner as before, Eqs. (2.1) and (2.3) become (Müller & Bühler 2001):

$$Re\frac{\partial p}{\partial x} = \frac{\partial^2 u}{\partial y^2} + \frac{\partial^2 u}{\partial z^2} + Ha\frac{\partial b_x}{\partial z}, \tag{2.57}$$

$$0 = \frac{\partial^2 b_x}{\partial y^2} + \frac{\partial^2 b_x}{\partial z^2} + Ha\frac{\partial u}{\partial z}, \tag{2.58}$$

where b_x is the x-component of the induced magnetic field, and Eq. (2.6) was used to simplify the Lorentz force term. Continuity, in concert with zero velocity wall boundary conditions on v and w and zero far field boundary conditions on b_y and b_z, ensures that $v = w = b_y = b_z = 0$ everywhere within the domain. Furthermore, as the Hartmann number can be adjusted by varying either the fluid's electrical conductivity or the magnetic field strength, B_0 is constrained to unity by appropriate choice of reference variables (as required to permit the preceding simplifications). Eqs. (2.57) and (2.58) are also subject to zero Dirichlet boundary conditions on the induced magnetic field, $b_x(y = \pm 1, z = \pm 1) = 0$, as all walls are perfectly electrically insulating.

The first setup investigated, shown in Fig. 2.2(a), has zero Dirichlet velocity boundary conditions applied at all walls, $u(y = \pm 1, z = \pm 1) = 0$, with the driving pressure gradient set to $\partial p/\partial x = -1/Re$ (the pressure gradient can be arbitrarily set to attain the desired flow rate). The second setup investigated, shown in Fig. 2.2(b), has zero driving pressure gradient, $\partial p/\partial x = 0$, with the flow driven by constant velocity Shercliff walls $u(y = 1, z) = U_{S1}$, $u(y = -1, z) = U_{S0}$; the Hartmann walls remain stationary, $u(y, z \pm 1) = 0$. Q2D equivalents to both setups are investigated in Chapter 6 (Camobreco *et al.* 2021b); in the latter case, at the top Shercliff wall $U_{S1} = 1$ and at the bottom Shercliff wall, the wall velocity is varied through $-1 < U_{S0} < 1$.

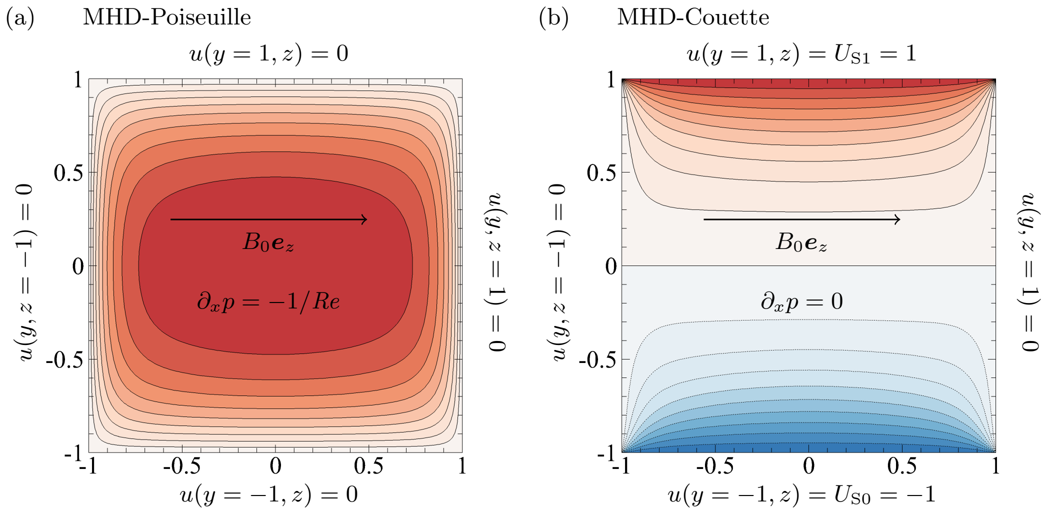

FIGURE 2.2: Two setups for which the Q2D equivalent is investigated in this work, and for which the accuracy of the Q2D model is directly calculated (relative to the z-averaged 3D solutions). (a) Pressure driven MHD-Poiseuille flow, with stationary Hartmann and Shercliff walls, and a driving pressure gradient. (b) MHD-Couette flow, with stationary Hartmann walls and moving Shercliff walls, and with no driving pressure gradient. In all setups, $b_x = 0$ on all walls. Two example streamwise invariant velocity profiles are overlayed (positive streamwise velocity is into the page), each at $Ha = 10$. In the MHD-Poiseuille case, the pressure gradient is chosen to ensure unit maximum velocity. In the MHD-Couette case, the same is achieved by taking a top Shercliff wall velocity $U_{\mathrm{S}1} = 1$ always. $U_{\mathrm{S}0} = -1$ is only for MHD-Couette flow; other base flow velocity profiles are obtained as $U_{\mathrm{S}0}$ is varied between -1 and 1. Red flooding (solid lines) denote positive streamwise velocity, blue flooding (dotted lines) negative.

Eqs. (2.57) and (2.58) are decoupled via the introduction of the Elsasser variables $A = u + b$ and $A' = u - b$ (Dragoş 1975; Müller & Bühler 2001), and become:

$$Re\frac{\partial p}{\partial x} = \frac{\partial^2 A}{\partial y^2} + \frac{\partial^2 A}{\partial z^2} + Ha\frac{\partial A}{\partial z}, \tag{2.59}$$

$$Re\frac{\partial p}{\partial x} = \frac{\partial^2 A'}{\partial y^2} + \frac{\partial^2 A'}{\partial z^2} - Ha\frac{\partial A'}{\partial z}. \tag{2.60}$$

For a non-zero pressure gradient, boundary conditions become $A(y = \pm1, z = \pm1) = A'(y = \pm1, z = \pm1) = 0$. For a zero pressure gradient, boundary conditions become $A(y, z = \pm1) = A'(y, z = \pm1) = 0$, $A(y = 1, z) = A'(y = 1, z) = U_{\mathrm{S}1}$, $A(y = -1, z) = A'(y = -1, z) = U_{\mathrm{S}0}$. Thus, Eqs. (2.59) and (2.60) can be solved independently, and the velocity and induced magnetic fields reconstructed via $u = (A + A')/2$ and $b = (A - A')/2$. The magnitude of the induced current

$$|\boldsymbol{j}| = \frac{1}{R_{\mathrm{m}}}\left[\left(\frac{\partial b_x}{\partial y}\right)^2 + \left(\frac{\partial b_x}{\partial z}\right)^2\right]^{1/2}, \tag{2.61}$$

is also computed, from Eq. (2.6), where R_m is taken as unity without loss of generality.

Müller & Bühler (2001) provide solutions to Eqs. (2.59) and (2.60) that are either approximations for large Ha, or series solutions for small Ha. Although the latter were used for numerical validation, it was simpler to numerically solve Eqs. (2.59) and (2.60) when interested in a wide range of Ha. The numerical method used to solve Eqs. (2.59) and (2.60) is similar to that discussed in Chapter 6 (Camobreco *et al.* 2021b). A Chebyshev discretization was applied to both the y and z directions, and derivative matrices incorporating boundary conditions constructed, following Weideman & Reddy (2001) and Trefethen (2000). $N_\mathrm{c} = 120$ Chebyshev points was found to be sufficient to both provide clean solutions, and to match series solutions well at low Ha (not shown). As the numerical solution of elliptic equations in two dimensions is thoroughly covered in Trefethen (2000), as is the application of various boundary conditions, the interested reader is directed there.

The motionless wall, pressure driven solutions are depicted first, in Fig. 2.3, with comparisons to Q2D profiles following after comparison to wall-driven flows. A Poiseuille-like profile is observed for $Ha \leq 1$ (the $Ha = 0.01$ and $Ha = 1$ cases are virtually coincident, indicating a hydrodynamic equivalent solution has been reached). At higher Ha, the velocity profiles rapidly flatten over an increasing extent of the duct, with very thin Hartmann layers forming on walls perpendicular to the magnetic field, as shown by the $u = 0.99$ contour lines plotted in Fig. 2.3(a). These contour lines are nearly parallel to z at large Ha, indicating quasi-two-dimensionalization at large magnetic field strengths. Accompanying the thinner Hartmann layers are increasingly thinner sheets of induced current (Fig. 2.3(b) has been rotated almost 90 degrees to help show this). Note that the current magnitude also increases, to account for the increased shear in the thinner Hartmann layers, but this is normalized out as plotted in Fig. 2.3(b). Only at lower Ha does appreciable induced current leak into the core.

The zero pressure gradient, moving wall solutions are shown in Fig. 2.4, taking $U_{\mathrm{S}1} = 1$, $U_{\mathrm{S}0} = -1$, to compare to a Couette like flow. At small Ha, as in the pressure driven case, the hydrodynamic Couette flow solution (of a linear velocity profile) is well attained. With increasing Ha, the profile flattens through a broader region of the core, approaching a step velocity profile. Unlike the pressure driven solution, current sheets do not form along the entirety of the Hartmann walls (note the Hartmann walls are stationary). Instead, spikes of current from both the Hartmann and Shercliff layers

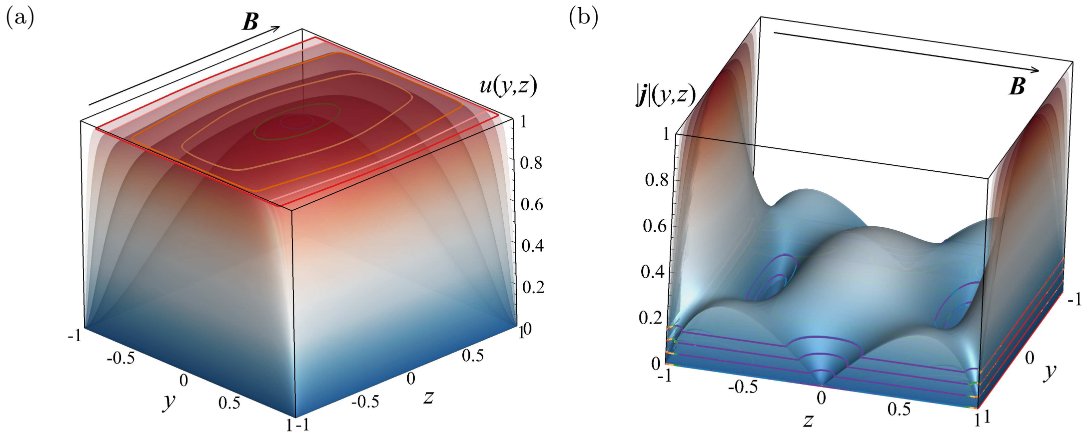

FIGURE 2.3: Streamwise invariant, time steady velocity and induced current profiles with a finite pressure gradient. The maximum velocity and current magnitude were normalized to unity. The colored contour lines represent Ha of: — 1000, — 300, — 100, — 30, — 10, — 1, — 0.01. (a) Velocity profiles, with a single contour line at $u = 0.99$ to help define the boundary layer thicknesses (the most transparent case is the *largest* Ha). (b) Induced current magnitudes, with contour lines at magnitudes of 0.001, 0.04, 0.1 and 0.15 $|\boldsymbol{j}|$.

merge at the corners. Again, with reducing Ha, these spikes of current increasingly encroach on the core flow.

Additional solutions for the zero pressure gradient, moving wall case are provided in Fig. 2.5, taking $U_{\mathrm{S1}} = 1$ and varying U_{S0}. The Q2D equivalent of Poiseuille flow will appear to be similar to the 3D solution when $U_{\mathrm{S0}} = 1$, while the Q2D equivalent of Couette flow is similar to the 3D solution when $U_{\mathrm{S0}} = -1$. Figure 2.5 also provides two cases at different Ha in separate figures, to help show the flattening of the core region, and thinning of boundary layers, at larger Ha.

With the 3D streamwise invariant, time steady profiles qualitatively considered, formal comparisons are made to the equivalent Q2D solutions. The normalized Q2D motionless wall, pressure driven velocity profile is (Pothérat 2007)

$$u_{\perp}(y) = \frac{\cosh(H^{1/2})}{\cosh(H^{1/2}) - 1}\left(1 - \frac{\cosh(H^{1/2}y)}{\cosh(H^{1/2})}\right), \tag{2.62}$$

while the Q2D moving wall, zero pressure gradient family of solutions (a new result investigated in this thesis) is

$$u_{\perp}(y) = C_1 \exp(-H^{1/2}y) + C_2 \exp(H^{1/2}y), \tag{2.63}$$

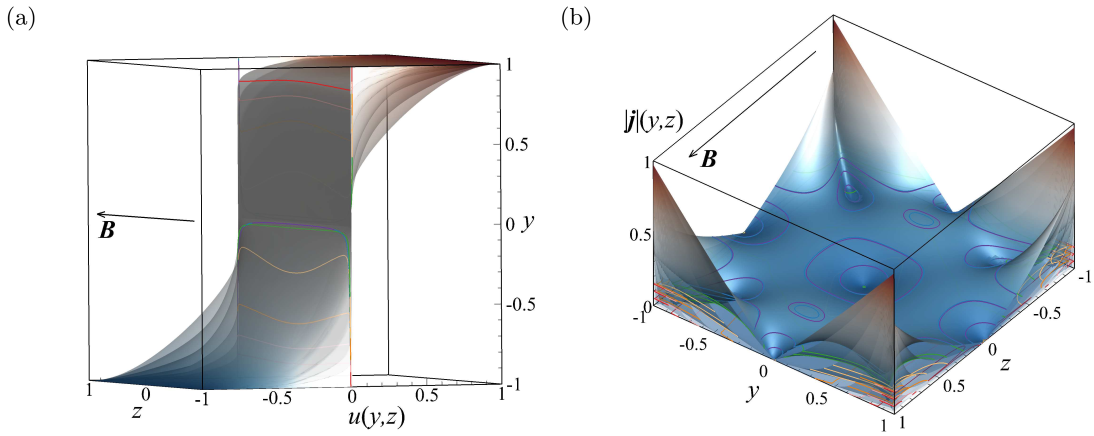

FIGURE 2.4: Streamwise invariant, time steady velocity and induced current profiles with zero pressure gradient, and Shercliff walls moving at $U_{S1} = 1$, $U_{S0} = -1$. The maximum velocity and current magnitude were normalized to unity. The colored contour lines represent Ha of: — 1000, — 300, — 100, — 30, — 10, — 1, — 0.01. (a) Velocity profiles, with a single contour line at $u = 0.01$ (the most transparent case is the *smallest* Ha). (b) Induced current magnitudes, with contour lines at magnitudes of 0.001, 0.04, 0.1, 0.15 and 0.4 $|\boldsymbol{j}|$.

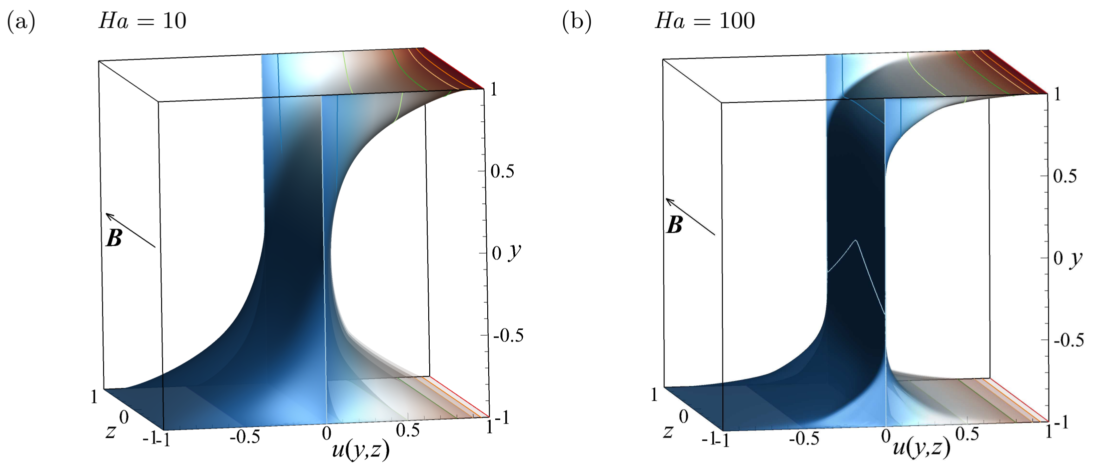

FIGURE 2.5: Streamwise invariant, time steady velocity profiles with zero pressure gradient, and Shercliff walls moving at $U_{S1} = 1$ and varied U_{S0}. (a) $Ha = 10$. (b) $Ha = 100$. The colored contour lines represent U_{S0} of: — 1, — 0.95, — 0.9, — 0.8, — 0.5, — 0.1, — 0, — -0.5, — -1; the contour lines are at these velocity levels. The most transparent case is the *largest* U_{S0}.

as given in Chapter 6 (Camobreco *et al.* 2021b), where

$$C_1 = \frac{U_\mathrm{R}\exp(H^{1/2}) - \exp(-H^{1/2})}{\exp(2H^{1/2}) - \exp(-2H^{1/2})},\ C_2 = \frac{\exp(H^{1/2}) - U_\mathrm{R}\exp(-H^{1/2})}{\exp(2H^{1/2}) - \exp(-2H^{1/2})}. \tag{2.64}$$

U_R is the velocity of the Shercliff wall at $y = -1$, as the $y = 1$ wall is at unit velocity, and H is as introduced earlier. The Q2D velocity profiles of Eqs. (2.62) and (2.63) are compared to various $z = cons.$ slices of the full 3D solutions, and in particular are compared to the z-average of the 3D solution, based on the average introduced in Eq. (2.43). Integration of the numerical solution over z is performed with Clenshaw–Curtis quadrature for each y_n, following Trefethen (2000), where y_n are the y locations of the $N_\mathrm{c} - 1$ internal Chebyshev nodes. The sum squared error

$$\epsilon_\mathrm{SS} = \sum_{n=1}^{n=N_\mathrm{c}-1} [u_\perp(y_n) - u_\mathrm{p}(y_n)]^2 \tag{2.65}$$

is used to quantify comparisons, where u_p is from the 3D solution, either the z-averaged profile, or a profile at $z = cons.$ (in either case normalized to unit maximum).

The pressure driven velocity profiles (Q2D, 3D slices and 3D averaged) are displayed in Figs. 2.6(a-c) at $Ha = 10$, 100 and 1000, with the sum squared error over a wide range of Ha depicted in Fig. 2.6(d). There is very good agreement between the various 3D profiles, and the Q2D profile, for all Ha, although with a slight overprediction of the Shercliff boundary layer thickness in the Q2D profile. Interestingly, as shown in Fig. 2.6(d), the agreement at small Ha is actually quite good for the pressure driven profiles (recalling Fig. 2.3(a), a Poiseuille-like profile is well achieved), with the smallest errors around $Ha = 10$. At higher Ha the error for the centreline profile ($z = 0$) becomes largest, although the overall error between the Q2D and averaged profile remains quite small. More importantly, the error decreases proportional to $Ha^{-1/4}$ at larger Ha.

The zero pressure gradient, moving wall profiles are depicted in Figs. 2.7(a-c) at the same Ha as the pressure driven case, with the sum squared error shown in Fig. 2.7(d). In particular, note that these results are a new contribution provided by this thesis, to further validate the use of the Q2D model in the moving wall setups investigated in this work. Unlike the pressure driven case, there are appreciable differences between the Q2D profile and 3D $z = cons.$ slices, particularly for $Ha \leq 10$. In spite of this, there is still good agreement between the Q2D and 3D z-averaged profiles, as highlighted particularly well in Fig. 2.7(a). Differences between the $z = cons.$ slices of the 3D profile noticeable reduce by $Ha = 100$, although again the Q2D profile is overpredicting

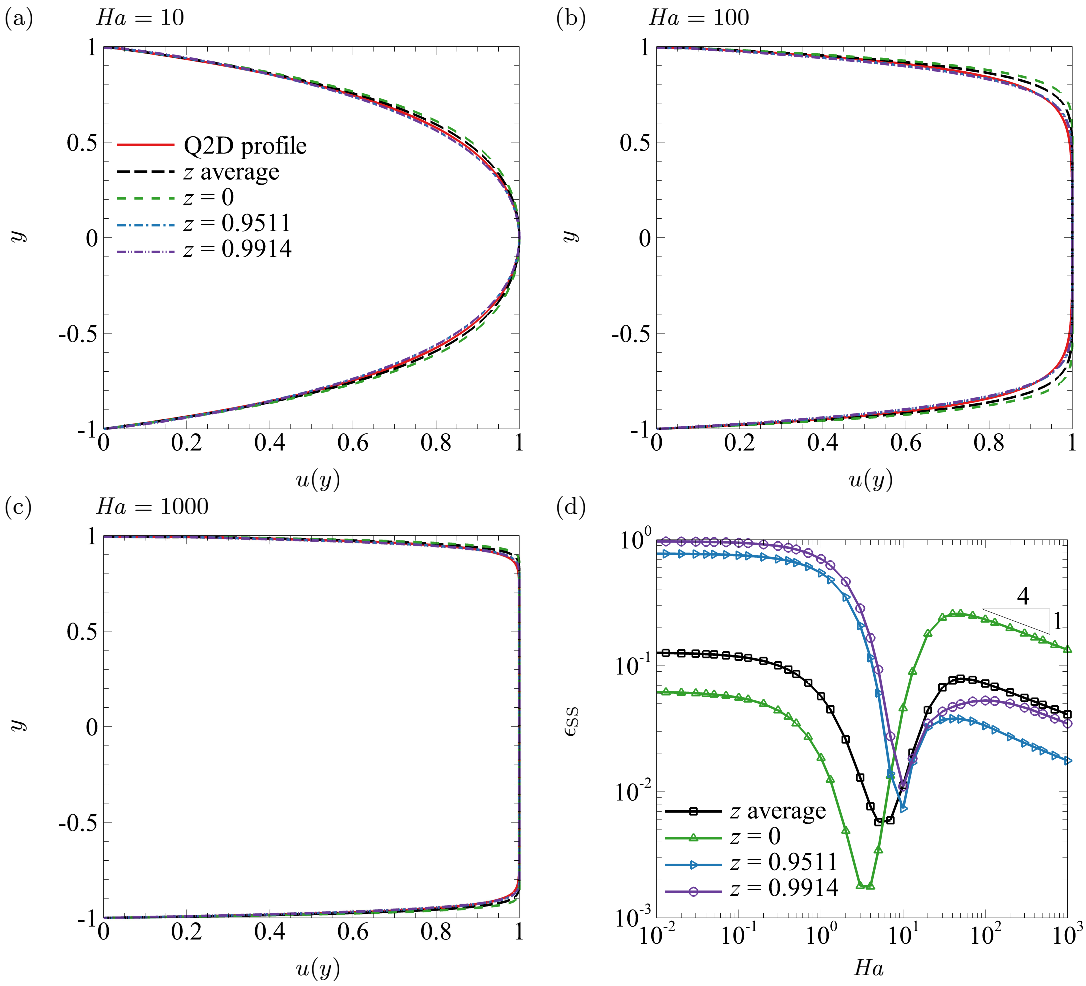

FIGURE 2.6: (a-c) Constant z and z-averaged velocity profiles for the pressure driven, motionless wall flow for various Hartmann numbers, compared to the Q2D profile. (d) Sum squared error (relative to the Q2D profile) for a range of Ha. All velocity profiles were normalized to unit maximum. The Q2D profiles were computed with $H = Ha$.

the height of the Shercliff layers, particularly so near the Hartmann walls. However, the sum squared errors are still reducing for the slices near the Hartmann walls, but remain much larger than the error between the Q2D and 3D z-averaged profile (which again exhibits a local minimum near $Ha = 10$). Again, the errors reduce as $Ha^{-1/4}$ for large Ha. However, as this is a global error measure, and as the Hartmann layers will become increasingly thin but never vanish, this error is unlikely to drop to zero in the $Ha \to \infty$ limit.

Last, comparisons between the Q2D and z-averaged profiles are shown for various lower Shercliff wall velocities U_{S0} at $Ha = 10$ and $Ha = 100$ in Figs. 2.8(a-b). The

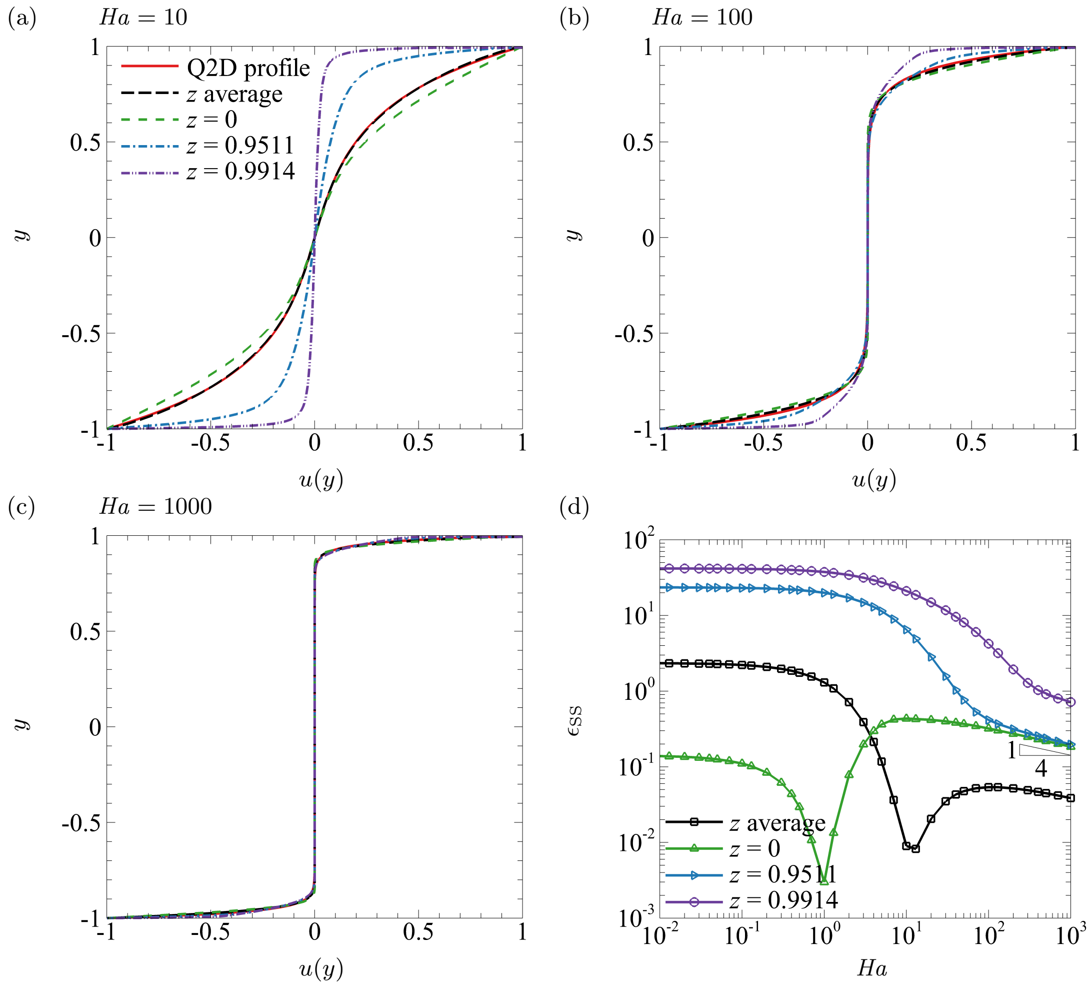

FIGURE 2.7: (a-c) Constant z and z-averaged velocity profiles for moving wall, zero pressure gradient flow at various Hartmann numbers, compared to the Q2D profile. (d) Sum squared error (relative to the Q2D profile) for a range of Ha. The Q2D profiles were computed with $H = Ha$.

sum squared errors between the Q2D and z-averaged profiles are shown in Fig. 2.8(c), and between the Q2D and $z = 0.9511$ slice in Fig. 2.8(d). Qualitatively, the results at $Ha = 10$ and $Ha = 100$ appear relatively similar regardless of U_{S0}. At small Ha, the errors (considering either the z-averaged or $z = 0.9511$ results) steadily increase with increasing lower wall velocity ($U_{S0} = 1$ yields the largest errors), even though the velocity difference through the profile is smallest in these cases (the velocity difference through the profile is largest, and yet the error smallest, when $U_{S0} = -1$). However, once $Ha \geq 10$, the error is smallest the closer the velocity of the bottom wall is to zero (with a zero bottom wall velocity all error is then concentrated in the top wall Shercliff layer). The motionless wall, pressure driven case is also provided for comparison in Figs.

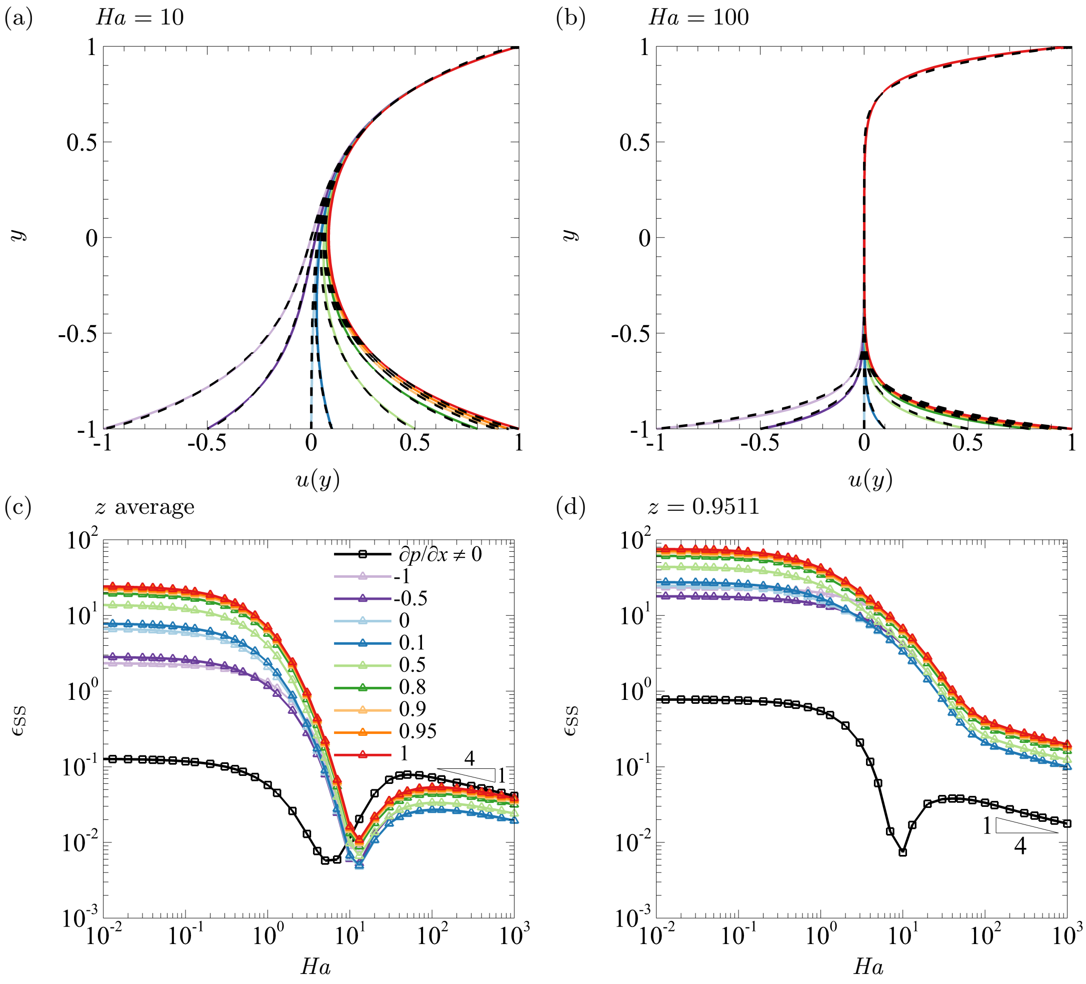

FIGURE 2.8: (a-b) Comparison between the z-averaged (dashed) and Q2D (solid) velocity profiles for various lower Shercliff wall velocities at $Ha = 10$ and $Ha = 100$, respectively. (c-d) Sum squared error (relative to the Q2D profile) for a range of Ha for the z-averaged and $z = 0.9511$ slice, respectively. The Q2D profiles were computed with $H = Ha$.

2.8(c-d). The pressure driven case yields the smallest error in the near wall $z = 0.9511$ slice for all Ha, although the error in the averaged profile is larger than any U_{S0} case for $Ha \gtrsim 10$ (and has a smaller error than any U_{S0} case for $Ha \lesssim 7$). Again at larger Ha, regardless of U_{S0} or the presence of a driving pressure gradient, the sum squared error reduces as $Ha^{-1/4}$.

In summary, this chapter has introduced the information pertinent to the practical motivation of this work, the design of cooling conduits for magnetic confinement fusion reactors. First, the quasi-two-dimensional model was derived, with particular focus on the realm of validity of key approximations (such as the quasi-static, inductionless and quasi-two-dimensional approximations). Second, fusion relevant parameters were tabulated, with most shown to fit well within the bounds for which Q2D models should reasonably match their full 3D equivalents. Third, to further support the use of Q2D models, literature providing both numerical and experimental evidence of good agreement between Q2D and 3D solutions was provided. Some key findings of these MHD studies were also discussed, as well as a baseline for currently proposed cooling conduit strategies provided. Finally, quantitative error bounds were computed for the underlying base flows in pressure- and wall-driven conduit flows, by comparing averaged 3D solutions to their Q2D counterparts (error bounds on the transitional or fully turbulent flows being beyond the scope of the investigation).

Having covered the key aspects of the practical motivation, focus turns in the next chapter to introducing the concepts and literature relevant to the theoretical motivation of this work: understanding how Q2D flows might undergo subcritical transitions to turbulence.

Chapter 3

The means by which perturbation energy grows and flows transition to turbulence

This chapter introduces the concepts necessary to explain how flows may transition to turbulence. This work is theoretically motivated by understanding whether Q2D flows are able to transition to turbulence at subcritical Reynolds numbers (Reynolds numbers at which linear eigenmodes exponentially decay) via purely Q2D mechanisms, and explaining how this may occur. Much like the breakdown of the transition process into various stages, so too is this chapter subdivided. First, concepts such as perturbations and criticality are defined. Second, the various linear and nonlinear mechanisms by which a perturbation (with small initial amplitude) can experience energy growth are described, and contextualized within the Q2D duct setup investigated. Before detailing the transitional stages, the scene is set by introducing the dynamical systems viewpoint and providing a clearer definition of turbulence. Third, as the underlying processes behind subcritical transitions are not well understood, some of the lasting theories (minimal defect, weakly nonlinear/Stuart–Landau) are presented. Fourth, in light of these theories, two case studies are considered, in which numerical and experimental transition thresholds matched well. Although useful, these case studies both required three-dimensionality to observe turbulent transitions, and thus, cannot be replicated in a purely Q2D environment. Finally, the ability to indefinitely sustain turbulence is considered, as are means of identifying turbulence.

3.1 The perturbation decomposition of an instantaneous flow field

Attention is now directed to the topic of transitions to turbulence. To analyse the transition process, the Q2D velocity and pressure (with overbars dropped) are decomposed into base ($\boldsymbol{U}_\perp$, $P_\perp$) and perturbation components ($\hat{\boldsymbol{u}}_\perp$, $\hat{p}_\perp$), as

$$\boldsymbol{u}_\perp = \boldsymbol{U}_\perp + \hat{\boldsymbol{u}}_\perp, \;\; p_\perp = P_\perp + \hat{p}_\perp. \tag{3.1}$$

The base flow velocity and pressure ($\boldsymbol{U}_\perp$, $P_\perp$) are laminar solutions of the Q2D equations, Eqs. (2.55) and (2.56), subject to the appropriate boundary conditions. These laminar base flow solutions are in equilibrium. If in stable equilibrium, there exists a bounding energy, for which any perturbation to the equilibrium, with energy less than this bounding energy, will eventually decay, with the equilibrium base flow solution reinstated. If in unstable equilibrium, even a perturbation with infinitesimally small energy will force the solution away from the laminar base flow indefinitely. Some examples of said laminar solutions were provided in Chapter 2, § 2.3. Note that this work only investigates streamwise-invariant base flow solutions, which may be either time steady, or time periodic. No constraints are placed on the form of the velocity and pressure perturbations ($\hat{\boldsymbol{u}}_\perp$, $\hat{p}_\perp$), except that the perturbation velocity field must be divergence free

$$\boldsymbol{\nabla}_\perp \cdot \hat{\boldsymbol{u}}_\perp = 0, \tag{3.2}$$

as enforced by $\hat{p}_\perp$, and subject to zero Dirichlet velocity boundary conditions on all duct walls. As the instantaneous flow ($\boldsymbol{u}_\perp$, $p_\perp$) must satisfy the Q2D equivalent of the Navier–Stokes equations, if the perturbation ($\hat{\boldsymbol{u}}_\perp$, $\hat{p}_\perp$) remains laminar, then so too does the instantaneous flow. Whereas, if the perturbation becomes turbulent, then the instantaneous flow has transitioned to turbulence; see § 3.4 for the criteria employed to identify turbulence.

Two reasons why the decomposition introduced in Eq. (3.1) was chosen are discussed here; another is discussed in § 3.7. First, such a decomposition provides a very simple means of measuring the difference between the full Q2D flow ($\boldsymbol{u}_\perp$, $p_\perp$) and the laminar base flow ($\boldsymbol{U}_\perp$, $P_\perp$), the equilibrium point, at any given time. This greatly aids in identifying transitions to turbulence. Perturbation energy is measured by computation of either an energy norm or a 2-norm of a perturbation:

$$||\hat{\boldsymbol{u}}_\perp|| = \int \hat{\boldsymbol{u}}_\perp \cdot \hat{\boldsymbol{u}}_\perp \, \mathrm{d}\Omega = \int \hat{u}_\perp^2 + \hat{v}_\perp^2 \, \mathrm{d}\Omega, \tag{3.3}$$

$$||\hat{\boldsymbol{u}}_\perp||_2 = \left(\sum \hat{\boldsymbol{u}}_\perp^2\right)^{1/2} = \left(\sum \hat{u}_\perp^2 + \hat{v}_\perp^2\right)^{1/2}, \tag{3.4}$$

respectively, the former introduced earlier in Eq. (1.3), and where in the latter the sum is taken over all points within the domain. Moreover, as only streamwise invariant base flows $\boldsymbol{U}_\perp = (U_\perp,\ V_\perp) = (U_\perp(y),\ 0)$ are considered in this work, any non-zero wall-normal velocity $\hat{v}_\perp$ immediately identifies a perturbation. Thus, a common norm used in this work will be (for a complex valued perturbation)

$$||\hat{v}_\perp||_2 = \left(\sum |\hat{v}_\perp|^2\right)^{1/2}. \tag{3.5}$$

The second reason for a perturbation decomposition, rather than a Reynolds decomposition of fluctuations about a time mean, stems from the necessity of linear growth mechanisms (Joseph 1976; Henningson 1996; Schmid & Henningson 2001). As the model system considered in this work is two-dimensional, which greatly eases the identification of the various modal and nonmodal growth mechanisms, it is worth briefly reviewing this necessity. First, an equation governing the full nonlinear evolution of a perturbation is derived. Eq. (3.1) is substituted into Eqs. (2.55) and (2.56), and all terms which involve only the laminar base flow cancelled, as the laminar base flow satisfies Eqs. (2.55) and (2.56) by definition. The remaining terms are a nonlinear evolution equation for the perturbation velocity

$$\frac{\partial \hat{\boldsymbol{u}}_\perp}{\partial t} = -(\hat{\boldsymbol{u}}_\perp\cdot\boldsymbol{\nabla}_\perp)\boldsymbol{U}_\perp - (\boldsymbol{U}_\perp\cdot\boldsymbol{\nabla}_\perp)\hat{\boldsymbol{u}}_\perp - (\hat{\boldsymbol{u}}_\perp\cdot\boldsymbol{\nabla}_\perp)\hat{\boldsymbol{u}}_\perp - \boldsymbol{\nabla}_\perp\hat{p}_\perp + \frac{1}{Re}\boldsymbol{\nabla}_\perp^2\hat{\boldsymbol{u}}_\perp - \frac{H}{Re}\hat{\boldsymbol{u}}_\perp, \tag{3.6}$$

$$\boldsymbol{\nabla}_\perp \cdot \hat{\boldsymbol{u}}_\perp = 0. \tag{3.7}$$

Taking the dot product of Eq. (3.6) with $\hat{\boldsymbol{u}}_\perp$ and integrating over the streamwise periodic domain Ω gives (summing over repeated indices)

$$\frac{\partial}{\partial t}\int \hat{u}_{\perp i}\hat{u}_{\perp i}\,\mathrm{d}\Omega = \int -2\hat{u}_\perp\hat{v}_\perp\frac{\partial U_\perp}{\partial y} - \frac{1}{Re}\left(\frac{\partial \hat{u}_{\perp i}}{\partial x_j}\frac{\partial \hat{u}_{\perp i}}{\partial x_j}\right) - 2\frac{H}{Re}\hat{u}_{\perp i}\hat{u}_{\perp i}\,\mathrm{d}\Omega, \tag{3.8}$$

after the use of Eq. (3.7), the divergence theorem, and zero Dirichlet boundary conditions for the perturbation velocity on all walls. The first term on the right hand side of Eq. (3.8) has also been simplified based on a Q2D streamwise invariant base flow, to show that the laminar base flow can only transfer energy to the perturbation through $\hat{u}_\perp\hat{v}_\perp$ (when their product is of opposite sign to $\partial U_\perp/\partial y$). The remaining terms on the right hand side represent perturbation energy decay due to viscous dissipation and Hartmann friction. Note that the nonlinear terms have vanished in determining Eq. (3.8), highlighting their energy conserving nature, acting only to redistribute energy. Thus, Eq. (3.8) is independent of the perturbation amplitude, and although the evolution of the perturbation $\hat{\boldsymbol{u}}_\perp$ is not linear, any instantaneous growth of perturbation energy remains governed by linear equations. As mentioned in Henningson (1996), a decomposition about a time mean, as proposed by Waleffe (1995), rather than about the laminar base flow, would render Eq. (3.8) nonlinear, as the time mean flow (which would appear in the first term in the right hand side of Eq. (3.8) in the place of $U_\perp$) would depend on the perturbation amplitude ϵ. This lends a great deal of credence to linear analysis even when attempting to understand nonlinear processes, as instantaneous energy growth remains linear, even when perturbations have finite (not infinitesimally small) amplitudes, when viewed relative to the laminar base flow.

3.2 Modal stability and criticality; exponential perturbation energy growth

Analysis now turns to modal instabilities. In this thesis, modal instabilities are considered to be linear instabilities (perturbations governed by linear evolution equations), which contain all perturbation energy in a single eigenmode of the linear operator (introduced shortly), at a single specified streamwise wave number α (due to the streamwise invariance of $U_\perp$). No perturbation energy will be present in any other eigenmode at that, or any other, streamwise wave number (at any time). Such perturbations are useful to analyse as they allow a precise injection of energy into the system, through a well-defined perturbation structure with calculable linear growth properties, unlike, say, spatially distributed random noise.

An equation governing the linear evolution of a perturbation is obtained by neglecting the nonlinear term in Eq. (3.6),

$$\frac{\partial \hat{\boldsymbol{u}}_{\perp,L}}{\partial t} = -(\hat{\boldsymbol{u}}_{\perp,L} \cdot \boldsymbol{\nabla}_\perp)\boldsymbol{U}_\perp - (\boldsymbol{U}_\perp \cdot \boldsymbol{\nabla}_\perp)\hat{\boldsymbol{u}}_{\perp,L} - \boldsymbol{\nabla}_\perp \hat{p}_{\perp,L} + \frac{1}{Re}\boldsymbol{\nabla}_\perp^2 \hat{\boldsymbol{u}}_{\perp,L} - \frac{H}{Re}\hat{\boldsymbol{u}}_{\perp,L}. \quad (3.9)$$

While the amplitude ϵ of a nonlinear perturbation $\hat{\boldsymbol{u}}_\perp$ remains small, $\epsilon \ll 1$, the linear predictions of the growth of $\hat{\boldsymbol{u}}_{\perp,L}$, from Eq. (3.6), may reasonably predict the nonlinear perturbation growth of $\hat{\boldsymbol{u}}_\perp$ from a full direct numerical simulation. Taking twice the curl of Eq. (3.9), and substituting Eq. (3.7) to eliminate $\hat{u}_{\perp,L}$, yields a 4th-order equation for $\hat{v}_{\perp,L}$,

$$\frac{\partial \hat{v}_{\perp,L}}{\partial t} = \left[\nabla_\perp^{-2}\left(\frac{\partial^2 U_\perp}{\partial y^2}\frac{\partial}{\partial x} - U_\perp \frac{\partial}{\partial x}\nabla_\perp^2 + \frac{1}{Re}\nabla_\perp^4 - \frac{H}{Re}\nabla_\perp^2\right)\right]\hat{v}_{\perp,L}, \quad (3.10)$$

subject to $\hat{v}_{\perp,L}(y = \pm 1) = \partial \hat{v}_{\perp,L}/\partial y|_{y=\pm 1} = 0$. Henceforth, the linear operator refers to all terms within the square brackets of Eq. (3.10).

In this section, the search for solutions of Eq. 3.10 is restrained to all perturbations which exhibit exponential growth (or decay), and for which all energy is contained within a single eigenmode. In § 3.3, the search criteria for solutions will be broadened to admit any perturbation composed of a weighted sum of eigenvectors, by virtue of the linearity of Eq. (3.10). Not only do such styles of perturbation have calculable growth properties, but the linear growth can be maximized or optimized over setup parameters (such as wavelength, eigenmode to energize, etc.). Such predictability is desirable to assess which features of an initial condition are the key to inciting transitions to turbulence, and sustaining said turbulence.

Due to the streamwise invariance of $U_\perp$, modal instabilities take the form

$$\hat{v}_{\perp,\mathrm{m}} = \tilde{v}_\perp e^{\mathrm{i}\alpha x} e^{-\mathrm{i}\lambda t}, \tag{3.11}$$

where the imaginary unit $\mathrm{i} = (-1)^{1/2}$, α is the streamwise wave number and $\tilde{v}_\perp$ represents any one eigenvector of the linear operator with a corresponding complex eigenvalue λ. The eigenmode has a growth rate of $\mathrm{Im}(\lambda)$, and advects with a wave speed of $\mathrm{Re}(\lambda)/\alpha$. Note that $\hat{v}_{\perp,\mathrm{m}}$ specifically represents a modal perturbation of the form introduced in Eq. (3.11), while $\hat{v}_{\perp,L}$ represents an otherwise arbitrary linear ($\epsilon \ll 1$) perturbation, composed of the sum of any number of eigenvectors of the linear operator.

Substituting Eq. (3.11) into Eq. (3.10) yields the eigenvalue problem

$$-\mathrm{i}\lambda\tilde{v}_\perp = \left[\mathscr{L}^{-1}\left(\mathrm{i}\alpha\frac{\partial^2 U_\perp}{\partial y^2} - \mathrm{i}\alpha U_\perp \mathscr{L} + \frac{1}{Re}\mathscr{L}^2\right) - \frac{H}{Re}\right]\tilde{v}_\perp, \tag{3.12}$$

where $\mathscr{L} = \partial^2/\partial y^2 - \alpha^2$. As all base flow solutions investigated in this work are Q2D and streamwise invariant, analytic expressions for $U_\perp$ (and thereby $\partial U_\perp/\partial y$ and $\partial^2 U_\perp/\partial y^2$) were determined. For reference, the expressions for all base flows investigated in this work are listed here. Examples of the MHD-Couette-Shercliff profiles were provided earlier, in Figs. 2.6 through 2.8, while examples of the pulsatile profiles can be found in Chapter 8 (Camobreco *et al.* 2021a). The base flows investigated in this work are:

- An isolated exponential boundary layer (a function of zero parameters, as it represents the limit of $H \to \infty$):

$$U_\perp(y) = 1 - \exp(-y). \tag{3.13}$$

- The family of MHD-Couette-Shercliff profiles (a function of two parameters, the friction parameter H and the ratio of the Shercliff wall velocities U_{R}):

$$U_{\perp}(y) = C_1 \exp(-H^{1/2}y) + C_2 \exp(H^{1/2}y), \tag{3.14}$$

  where

$$C_1 = \frac{U_{\mathrm{R}} \exp(H^{1/2}) - \exp(-H^{1/2})}{\exp(2H^{1/2}) - \exp(-2H^{1/2})},\ C_2 = \frac{\exp(H^{1/2}) - U_{\mathrm{R}} \exp(-H^{1/2})}{\exp(2H^{1/2}) - \exp(-2H^{1/2})}. \tag{3.15}$$

  Note that the Q2D Shercliff boundary layer thickness (also denoted by δ_{S}, as for the 3D case) for these velocity profiles scales as $H^{-1/2}$ for large H.

- The pulsatile velocity profiles composed of the sum of a steady pressure driven and oscillatory wall driven flow (a function of four parameters, the Reynolds number Re, Strouhal number Sr, friction parameter H and amplitude ratio Γ):

$$\begin{aligned} U_{\perp}(y,t) = \frac{\Gamma}{\Gamma+1}\frac{\cosh(H^{1/2})}{\cosh(H^{1/2})-1}\left(1 - \frac{\cosh(H^{1/2}y)}{\cosh(H^{1/2})}\right) \\ + \frac{1}{\Gamma+1}\mathrm{Re}\left(\frac{\cosh((r+s\mathrm{i})y)}{\cosh(r+s\mathrm{i})}e^{\mathrm{i}t}\right), \end{aligned} \tag{3.16}$$

  where

$$r = H^{1/2}[(Sr Re/H)^2 + 1]^{1/4}\cos([\tan^{-1}(Sr Re/H)]/2), \tag{3.17}$$

$$s = H^{1/2}[(Sr Re/H)^2 + 1]^{1/4}\sin([\tan^{-1}(Sr Re/H)]/2). \tag{3.18}$$

Note that Eq. (3.12) was non-dimensionalized based on the characteristic scales relevant to the family of MHD-Couette-Poiseuille base flows, Eq. (3.14), which are most often investigated in this work. Eq. (3.12) is still valid for the isolated exponential boundary layer by performing a change of variables, and redefining the Reynolds number based on the Shercliff layer thickness, via $\delta_{\mathrm{S}} = L/H^{1/2}$ (with the boundary condition pertaining to $y \to \infty$ also adjusted). For time-periodic base flows, see Chapter 8 (Camobreco *et al.* 2021a) for the appropriate modifications to permit solution of the eigenproblem. Considering a base flow from Eq. (3.14) for the remainder of this section, a choice of H, Re and α allow Eq. (3.12) to be numerically solved. The linear evolution operator is discretized with N_{c} Chebyshev nodes (Trefethen 2000; Weideman & Reddy 2001)

$$y = \cos(\pi j/N_{\mathrm{c}}) = \sin(\pi[N_{\mathrm{c}} - 2j]/2N_{\mathrm{c}}),\ \ j = 0, 1, 2, \ldots, N_{\mathrm{c}}, \tag{3.19}$$

over the domain $y \in [-1, 1]$. Derivative operators, to represent partial derivatives with respect to y, with boundary conditions built in, are constructed following Trefethen (2000). Once the linear operator has been discretized, Eq. (3.12) is solved for a subset of the eigenvalues λ_j and eigenvectors $\tilde{v}_{\perp,j}$ of the discretized linear evolution operator. Note that the eigenvalues could also be computed via Eq. (3.10), after assuming a streamwise dependence of $e^{\mathrm{i}\alpha x}$ (so $\partial/\partial x \to \mathrm{i}\alpha$). However, different eigenvalue routines would be required. Regardless of the computational approach, if operators are constructed with sufficient discretization, the eigenvalues and eigenvectors of the discretized operator have been shown to be sufficiently good approximations of the eigenvalues and eigenvectors of the (continuous) linear evolution operator (Reddy *et al.* 1993). Some discussion of the various means of computing eigenvalues and eigenvectors is provided in Chapter 8 (Camobreco *et al.* 2021a). Further details, relevant to either Eq. (3.10) or Eq. (3.12), can be found in Lehoucq *et al.* (1998), Anderson *et al.* (1999) or Barkley *et al.* (2008). For the most part, a call to the MATLAB routine `eig` (or `eigs`) is the simplest, when considering Eq. (3.12), which yields $N_\mathrm{c} - 1$ eigenvalues, for a domain discretized with $N_\mathrm{c} - 1$ internal points. Eigenvalues are provided to a tolerance $||\boldsymbol{A}\tilde{\boldsymbol{v}}_{\perp,j} - \tilde{\boldsymbol{v}}_{\perp,j}\boldsymbol{\Lambda}||_2/||\boldsymbol{A}||_2 < 10^{-14}$, where $\boldsymbol{A}$ represents the linear operator once multiplied by i (noting that, in Eq. (3.12), the $-\mathrm{i}$ coefficient is not usually absorbed into the definition of λ), $\tilde{\boldsymbol{v}}_{\perp,j}$ are the right eigenvectors (in columns), and $\boldsymbol{\Lambda}$ a diagonalized matrix of the corresponding eigenvalues.

There are two key parameters when performing modal stability analysis. The first is the wave number α_max, which for a given Re and H, provides the largest growth rate $\mathrm{Im}(\lambda_j)$ over all wave numbers, where the j'th eigenmode is of interest. Note that α_max is sometimes defined based on the largest growth rate over all eigenvalues $\mathrm{Im}(\lambda)$ and over all wave numbers, a definition which is not applied here. α_max is of particular importance given the setup introduced in Fig. 1.1. By setting the domain length based on α_max, a specific perturbation (eigenvector) can be given the greatest chance of becoming dominant in DNS. Equally, the domain length could be set with a wave number far from α_max, to attempt to avoid a modal instability, allowing nonlinear analysis of an optimally growing nonmodal instability. The second key parameter is the critical Reynolds number Re_c, the smallest Reynolds number at which a non-negative growth rate is attained at wave number α_max, for the eigenvalue with the largest imaginary component (i.e. the slowest decaying/fastest growing). Interest in the critical Reynolds number stems from the fact that an eigenmode with positive growth rate, can, with sufficient time, grow from near zero amplitude (e.g. 10^{-16}), to an amplitude of similar order to the base flow (i.e. where $\epsilon \ll 1$ will no longer be satisfied). While the amplitude of the perturbation is not relevant in a linear analysis, a modal instability targeted in nonlinear DNS could trigger a transition to turbulence once at sufficiently large amplitudes (those amplitudes approaching the characteristic magnitude of the base flow). This would arguably be the most efficient route to turbulence, if a transition indeed occurs at a supercritical Reynolds number, and if efficiency is measured solely by the magnitude of the initiating perturbation. However, in this work, efficiency is measured both by the magnitude of the initiating perturbation and by the size of the Reynolds number necessary to transition to and sustain turbulence. Note that the latter clause does not render modal analysis irrelevant (fusion relevant conditions are expected to be at, often severely, subcritical Reynolds numbers), as modal stability behavior increasingly dictates nonmodal stability behavior at large evolution times. In particular, in Q2D systems, the initial nonmodal growth stages will be of less interest when optimizing transitions to turbulence, than the large time modal stability behavior.

Some examples of the determination of $\alpha_{\max}$ and Re_{c} follow shortly, as there are some slight complications introduced as H is varied. However, first some definitions are provided, regarding modal instabilities analysed with respect to a given base flow:

- Stable: No eigenvalues have positive imaginary components; the Reynolds number may be greater or less than Re_{c}, as $\alpha_{\max}$ may not have been selected. If simulating $\alpha_{\max}$ stability can only be assumed to imply $Re < Re_{\mathrm{c}}$ if the base flow is independent of Re, which is not always the case, recalling Eqs. (3.16) and (3.17).

- Unstable: At least one eigenvalue has a positive imaginary component; it is only safe to assume this implies $Re > Re_{\mathrm{c}}$ if the base flow does not depend on Re.

- Stabilization: An increase in Re_{c} for a given change in another parameter (e.g. H, U_{R}, Sr or Γ, where said other parameter is modifying the base flow profile).

- Destabilization: A decrease in Re_{c} for a given change in another parameter.

For each wave number, the discretized eigenvalues λ_j are ordered by imaginary component, such that λ_1 has the largest imaginary component. Examples of the growth

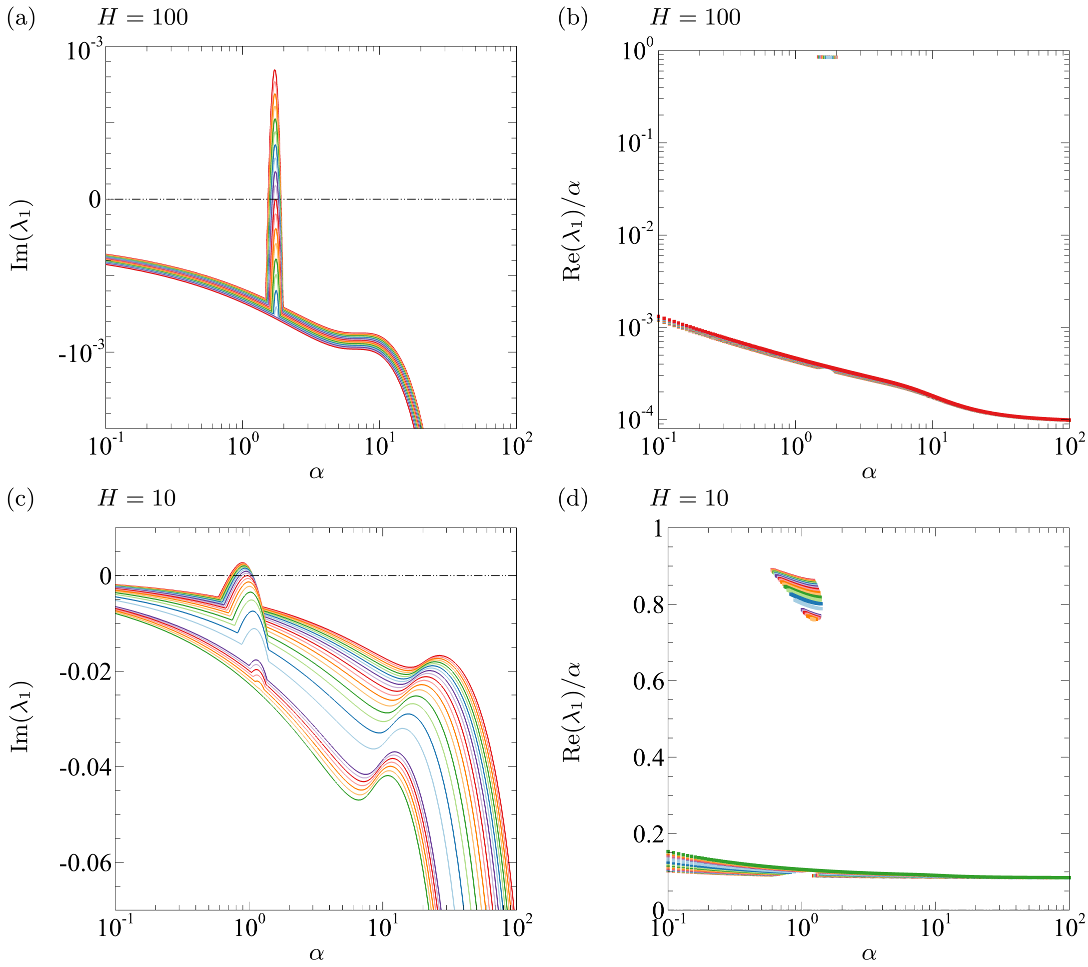

FIGURE 3.1: Eigenvalues with the largest growth rate for each wave number, over $\alpha \in [0.1, 100]$, comparing $H = 100$ and $H = 10$, with a Shercliff velocity profile at $U_\mathrm{R} = 1$, recalling Eq. (3.14). (a & c) Growth rates. (b & d) Wave speeds. At $H = 100$, $Re_\mathrm{c} = 4.40263 \times 10^5$ and 21 curves are plotted, at $Re = r_\mathrm{c} Re_\mathrm{c}$, where $r_\mathrm{c} = 1.1, 1.09, 1.08, \ldots, 0.91, 0.9$. At $H = 10$, $Re_\mathrm{c} = 7.91232 \times 10^4$ and 25 curves are plotted at $Re = r_\mathrm{c} Re_\mathrm{c}$, where $r_\mathrm{c} = 2$, 1.9, 1.8 $\ldots$ 0.3, 0.2, 0.19, 0.18, $\ldots$, 0.15, 0.14.

rate and wave speed for λ_1 over a wide range of wave numbers are plotted in Fig. 3.1 at $H = 100$ and $H = 10$. The curve pertaining to the critical Reynolds number ($r_\mathrm{c} = 1$) just touches the zero growth line in Figs. 3.1 (a & c). However, the present work is often more interested in the determination of α_max. At $H = 100$, the set of narrow peaks which pierce the positive imaginary half plane rapidly diminish with reducing Re; for $r_\mathrm{c} = Re/Re_\mathrm{c} \leq 0.92$ this local peak cannot be observed in Fig. 3.1(a). This is also shown by plotting the corresponding wave speeds in Fig. 3.1(b), where, for example, there is no break in the set of symbols representing $r_\mathrm{c} = 0.9$. The wave speed

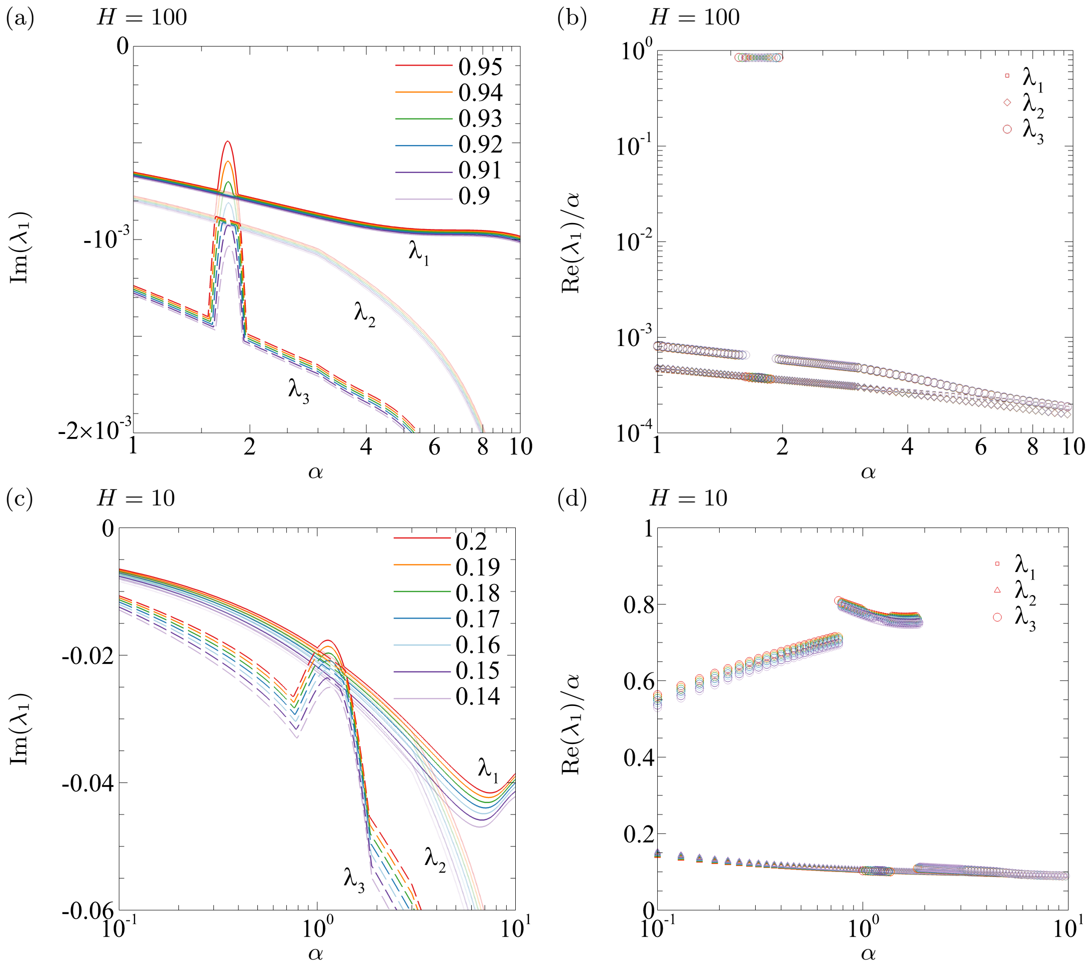

FIGURE 3.2: $r_c = Re/Re_c$ curves (see legends) for each of the first three eigenmodes with the largest growth rates for a range of wave numbers, comparing $H = 100$ and $H = 10$, with a Shercliff velocity profile at $U_R = 1$. (a & c) Growth rates. (b & d) Wave speeds (every third symbol plotted).

often forms a simple means of assessing which eigenvector to target (i.e. the eigenmode which will eventually attain positive growth rates), as identified by a wave speed in the vicinity of 0.8 for wall-driven flows, for the parameters investigated in this work. By comparison, at $H = 10$, a local maximum can still be observed until $r_c \leq 0.14$, with a similar corresponding wave speed. Note that when determining α_{max}, it is only the *local* maximum yielding the least negative growth rate that is searched for when $Re < Re_c$, as the lower streamwise wave numbers do not correspond to the eigenmode of interest.

To further highlight the importance of finding a local maximum, rather than merely the largest growth rate, Fig. 3.2 depicts the leading three eigenvalues over a range of wave numbers near α_{max}. It is particularly clear at $H = 100$ that the local maximum

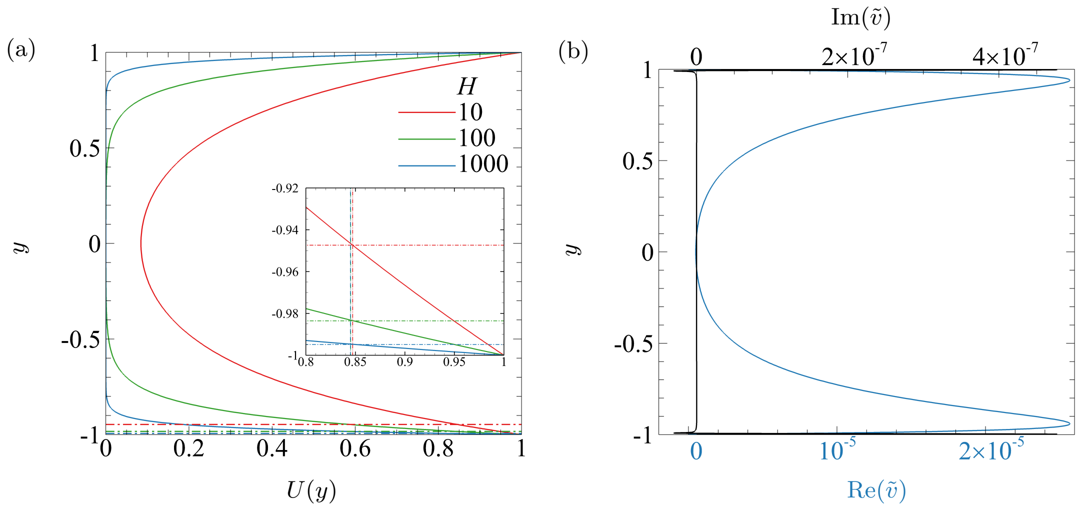

FIGURE 3.3: (a) Shercliff base flow velocity profiles, with dot-dashed lines indicating the critical layer heights at various H (as highlighted in inset; dot-dot-dashed lines in inset indicate the wave speed of the TS wave for each of these H). (b) The real and imaginary components of the eigenvector corresponding to the TS wave at $H = 1000$, at $r_c = 1$.

follows through to the subdominant eigenvalues, such that these subdominant eigenmodes should also be considered when attempting to determine $\alpha_{\max}$ at more strongly subcritical r_c. The wave speeds depicted in Fig. 3.2(b) again indicate that the local maxima for these subdominant eigenvalues correspond to the eigenmode of interest (wave speed around 0.8).

The eigenmode of interest, subcritically or supercritically, and with wave speed around 0.8, has an eigenvector corresponding to the Q2D equivalent of the Tollmien–Schlichting (TS) wave (when the base flow is steady). In hydrodynamic duct flows ($H \to 0$), the TS wave is a wall-bounded mode, with a wave speed of 0.736000 at the critical Reynolds number; or 0.264000 in the $H \to 0$ pressure driven duct flow variant (Drazin & Reid 2004). As an example, Fig. 3.3(a) depicts the Shercliff base flow at $H = 1000$, and Fig. 3.3(b) depicts the corresponding (real and imaginary components of the) Q2D equivalent TS wave. Henceforth, this one eigenmode will be referred to as two TS wave modes (one at each wall). Note that this symmetry in the TS wave is present only because the $U_R = 1$ base flow is symmetric, so the Shercliff walls both move at unit velocity. Thus, the two TS wave modes can advect along the walls at the same wave speed, and grow in amplitude at the same rate; that of the overall eigenmode. For any other U_R (combination of Shercliff wall velocities), the TS waves will advect at different velocities along each wall. In such cases, the TS waves at each wall will be observed in different eigenmodes. The corresponding eigenvalues will only have identical growth rates if the local shear in each boundary layer is also identical, e.g. only $U_{\mathrm{R}} = -1$ and $U_{\mathrm{R}} = 1$. However, these TS waves will still be similar in all other respects.

At lower H, the wall-boundedness of the TS wave modes can be difficult to observe, particularly when depicting just the wall-normal perturbation for symmetric base flows. Thus, both $\hat{v}_{\perp,\mathrm{m}}$ and $\hat{u}_{\perp,\mathrm{m}}$ are depicted in Fig. 3.4, for all three Shercliff profiles considered in Fig. 3.3(a). At lower H, the perturbation structures are conjoined, as indicated by $\hat{v}_{\perp,\mathrm{m}}$, and become isolated at higher H. However, for all H, two TS waves running along each wall are still observable in $\hat{u}_{\perp,\mathrm{m}}$. Once at high H, the TS waves running along each wall are isolated, and cannot appreciably interact. At high H, each TS wave behaves as if evolving in an isolated exponential boundary layer (Takashima 1996, 1998; Pothérat 2007), identifiable by an eigenmode wave speed of 0.844996 at $r_{\mathrm{c}} = 1$, or 0.155004 in the pressure driven equivalent.

The existence and dynamics of the TS wave are now briefly discussed, with the reader referred to Baines & Mitsudera (1994) and Baines *et al.* (1996) for further details. The key dynamics of the TS wave are related to the action of viscosity, as by Rayleigh and Fjørtoft's inflection point criteria (Schmid & Henningson 2001), the steady base flows investigated in this work are stable to inviscidly evolving perturbations. Viscosity acts in two locations in duct shear flows (per half height), at the wall, as necessary to satisfy the no-slip criterion, and at the critical layer. The critical layer, for a given j'th eigenmode, forms at the y location where the base flow velocity equals the wave speed of that eigenmode, $U_{\perp}(y_{\mathrm{c}}) = \mathrm{Re}(\lambda_j)/\alpha$. Viscosity must act in the vicinity of the critical layer (Schmid & Henningson 2001) to ensure non-trivial solutions to Eq. (3.12) exist. This is shown by rearranging Eq. (3.12),

$$\mathrm{i}\alpha\left(U_{\perp} - \frac{\lambda_j}{\alpha}\right)\mathscr{L}\tilde{v}_{\perp,j} = \left(\mathrm{i}\alpha\frac{\partial^2 U_{\perp}}{\partial y^2} + \frac{1}{Re}\mathscr{L}^2 - \frac{H}{Re}\mathscr{L}\right)\tilde{v}_{\perp,j}, \tag{3.20}$$

which has a left hand side of zero at the critical layer, and no non-trivial solutions if $Re \to \infty$; $\partial^2 U_{\perp}/\partial y^2$ is non-zero at the critical layer for base flows investigated in this work.

The action of viscosity at the wall and at the critical layer differs. At the wall, viscosity forces a response to what is denoted an inviscid partial mode of the TS wave (Baines *et al.* 1996), where the latter satisfies a free slip boundary condition. The

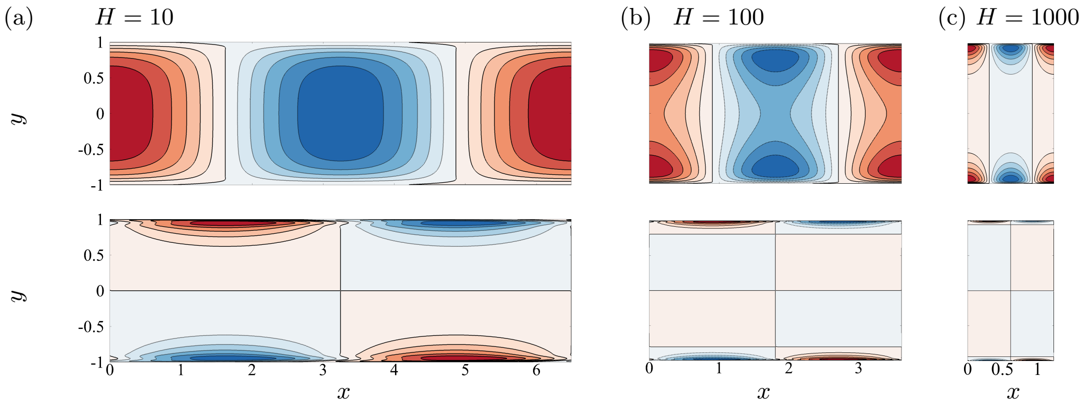

FIGURE 3.4: Eigenvectors expanded in the streamwise direction at $r_{\mathrm{c}} = 1$. (a) $H = 10$. (b) $H = 100$. (c) $H = 1000$. Top row: wall-normal perturbation $\hat{v}_{\perp,\mathrm{m}} = \tilde{v}_{\perp} e^{\mathrm{i}\alpha x}$. Bottom row: streamwise perturbation $\hat{u}_{\perp,\mathrm{m}} = \tilde{u}_{\perp} e^{\mathrm{i}\alpha x}$, where $\tilde{u}_{\perp} = \mathrm{i}(\partial \tilde{v}_{\perp}/\partial y)/\alpha$. Solid lines (red flooding) denote positive velocities, dotted lines (blue flooding) negative.

viscous partial mode applies a restoring force to ensure the no-slip condition is satisfied. If the least damped viscous mode has the appropriate phase relative to the inviscid mode, the amplitude of the viscous mode can be increased by advection (the partial modes constructively interfere when in phase, thereby increasing in amplitude).

Viscosity at the critical layer is then relevant as it introduces an additional length scale into the system. This additional length scale is shown in the inset of Fig. 3.3(a). The dot-dashed lines represent the critical layers corresponding to the TS wave mode, where the critical layers form at the intersections between the base flow velocity and perturbation advection speed (the wave speeds for each H indicated with dot-dot-dashed lines). Resonant effects, generated by the viscous response at the wall, can then occur, further amplifying the TS wave eigenmode, allowing for positive growth rates at sufficiently large Re. Resonance occurs when the perturbation advection speed yields a critical layer height in appropriate ratio to the key base flow length scale, i.e. a ratio of length scales that is roughly an integer multiple. Advection speeds yielding larger integer multiples then yield other discrete modes of the linear operator. However, as weaker resonances, they are rarely sufficiently amplified to attain positive growth rates at the Re of interest. Note that the ratio of key base flow length scale to critical layer height is not always well defined, being either $L/(1 - y_{\mathrm{c}})$ or $\delta_{\mathrm{S}}/(1 - y_{\mathrm{c}})$, depending whether H is sufficient to ensure $\delta_{\mathrm{S}} < L$. Note also that $1 - y_{\mathrm{c}}$ is the distance from the wall to the critical layer, or the critical layer height for short, which differs from the

H	Re_c	$\alpha_{\max}$	$\mathrm{Re}(\lambda_1)/\alpha_{\max}$	$1-y_c$	δ_S	$\delta_S/(1-y_c)$
10	7.91232×10^4	0.968327	0.84728883566370	0.0526	0.3162277660	6.01
100	4.40263×10^5	1.738971	0.84525720091868	0.0168	0.1	5.95
1000	1.52869×10^6	5.10755	0.84499623551127	0.0053	0.0316227766	5.97

TABLE 3.1: Critical layer and boundary layer heights for the three H cases considered in Fig. 3.3, where y_c represents the y location of the critical layer, and $\delta_S = H^{-1/2}$.

Re-dependent width of the layer (Schmid & Henningson 2001).

The wave speeds, critical layer heights and boundary layer heights are tabulated in Table 3.1 for the Shercliff flows considered in Fig. 3.3(a). These further highlight that the TS wave mode remains wall bounded for all H, as the critical layer heights remain small, regardless of whether the mode appears conjoined or isolated. It is also interesting that the ratios of the boundary layer to the critical layer heights remains roughly constant over a wide range of H, highlighting the similarity in the TS wave modes over this range of H. Note that for Shercliff flow ($U_R = 1$), isolated boundary layer dynamics hold only for $H \geq 1000$, see Chapter 6 (Camobreco *et al.* 2021b), yet $\delta_S/(1-y_c)$ remains similar for $H \gtrsim 10$, further indicating the importance of the critical layer in generating the TS wave disturbance. For reference, the hydrodynamic flow has $1 - y_c = 0.142$ and an $L/y_c = 7.04$. The difference (an approximate integer ratio of 7 rather than 6) may be due to L not being as meaningful a choice of length scale as a boundary layer height in the hydrodynamic problem, as at low H, the boundary layer height cannot be defined to any greater accuracy than L. Alternately, it may be due to the critical layer height being much larger in the hydrodynamic problem (with an integer multiple of 6 no longer being feasible).

3.3 Nonmodal initial value problems; algebraic perturbation energy growth

3.3.1 Methods to compute and optimize nonmodal transient growth

Having previously discussed the means of analysing the modal stability of the linear operator, focus now turns to nonmodal perturbations. Investigating nonmodal perturbations, which are capable of transient and exponential growth, allows further diagnosis of which initial conditions may be beneficial (or detrimental) to triggering transitions to turbulence. Importantly, nonmodal initial conditions are not too complicated that their linear growth cannot be efficiently calculated, permitting the broad investigation of the parameter space necessary to determine which features (of either the setup, or initial condition) are desirable for triggering turbulent transitions.

Nonmodal perturbations consist of the weighted sum of any number of modal perturbations,

$$\hat{v}_{\perp,L}(t,x,y) = \hat{v}_{\perp,\mathrm{nm}}(t,y)e^{\mathrm{i}\alpha x} = \sum_{j=1}^{M} \gamma_j(t)\tilde{v}_{\perp,j}(y)e^{\mathrm{i}\alpha x}, \tag{3.21}$$

where $\gamma(t)$ is a time dependent set of weighting coefficients (amplitudes) for each eigenmode, and $\tilde{v}_{\perp,j}(y)$ are the eigenvectors of the linear evolution operator. Note that, at least for unbounded flows, the eigenmodes of the linear operator have been shown to be a complete set. Thus, any smooth perturbation can be represented to an arbitrarily high accuracy if a sufficient number of eigenmodes are included (Gustavsson 1979; Schmid & Henningson 2001). As an initial value problem, interest is then in the initial amplitude spectrum $\gamma(t=0)$, assigned to the eigenmodes of the linear operator. Such an initial condition presumes the eigenvalues and eigenvectors of the discretized linear evolution operator are known, from Eq. (3.12).

Nonmodal stability considers linear superposition of modal solutions, so the governing linear evolution equation takes the form

$$\begin{aligned}\frac{\partial\gamma_1}{\partial t}\tilde{v}_{\perp,1} + \frac{\partial\gamma_2}{\partial t}\tilde{v}_{\perp,2} + \ldots + \frac{\partial\gamma_M}{\partial t}\tilde{v}_{\perp,M} = \Bigg[\mathscr{L}^{-1}\Bigg(&\mathrm{i}\alpha\frac{\partial^2 U_\perp}{\partial y^2} \\ - \mathrm{i}\alpha U_\perp \mathscr{L} + \frac{1}{Re}\mathscr{L}^2\Bigg) - \frac{H}{Re}\Bigg]&\Bigg(\gamma_1\tilde{v}_{\perp,1} + \gamma_2\tilde{v}_{\perp,2} + \ldots + \gamma_M\tilde{v}_{\perp,M}\Bigg).\end{aligned} \tag{3.22}$$

By virtue of linearity, each term in Eq. (3.22) can be considered separately, and defining everything inside the set of square brackets as the operator $\boldsymbol{L}$, the j'th term of Eq. (3.22) satisfies

$$\frac{\partial\gamma_j}{\partial t}\tilde{v}_{\perp,j} = \boldsymbol{L}\gamma_j\tilde{v}_{\perp,j}. \tag{3.23}$$

As the eigenmodes form the basis of nonmodal perturbations, and as the linear evolution behavior of the former is known from Eq. (3.12), then, for the j'th eigenmode

$$-\mathrm{i}\lambda_j\tilde{v}_{\perp,j} = \boldsymbol{L}\tilde{v}_{\perp,j}. \tag{3.24}$$

Substituting, Eq. (3.24) into Eq. (3.23) yields

$$\frac{\partial\gamma_j}{\partial t} = -\mathrm{i}\lambda_j\gamma_j. \tag{3.25}$$

Note that as only the amplitude of each eigenvector varies with time, recalling Eq. (3.21), each amplitude in the spectrum is constrained to grow or decay exponentially at the rate of the corresponding j'th eigenvalue (for a steady base flow). The solution of Eq. (3.25) yields an initial value problem

$$\gamma_j(t) = \gamma_j(t=0)e^{-\mathrm{i}\lambda_j t}, \tag{3.26}$$

subject to a choice of $\gamma_j(t=0)$. Or, considering all terms simultaneously,

$$\gamma(t) = \gamma(t=0)e^{-\mathrm{i}\boldsymbol{\Lambda} t}, \tag{3.27}$$

where $\boldsymbol{\Lambda}$ is a diagonalized matrix of the eigenvalues of the discretized linear stability operator.

The question becomes how to choose $\gamma_j(t=0)$, which is usually computed via the optimization of a chosen functional. Common goals informing design of the functional are (Farrell 1988):

- Optimal excitation: what is the smallest total initial energy, distributed over a subset of eigenmodes, that will yield a unit initial energy in a chosen eigenmode?
- Optimal linear growth: for a unit total initial energy, distributed over a subset of eigenmodes, what is the largest ratio of final to initial perturbation energy at a chosen final (target) time?

The latter option, optimal linear growth, is by far the most commonly investigated. Motivation stems from the observations that the linear operator can be highly non-normal (Farrell 1988; Butler & Farrell 1992; Farrell & Ioannou 1993; Trefethen *et al.* 1993; Reddy & Henningson 1993; Reddy *et al.* 1993). A non-normal operator allows for growth in the total perturbation energy (growth in $\int \hat{\boldsymbol{u}}_{\perp,L} \cdot \hat{\boldsymbol{u}}_{\perp,L}\, \mathrm{d}\Omega$) at subcritical Reynolds numbers, in spite of no nonlinear interactions, and while all eigenvectors $\tilde{v}_{\perp,j}$ linearly decay. This is by virtue of the fact that the eigenvectors of normal operators are orthogonal, while the eigenvectors of highly non-normal operators are highly non-orthogonal. Interest is then specifically in those non-orthogonal eigenvectors which are almost anti-parallel, as if said eigenvectors also have a large difference in decay rate, significant transient growth is produced, as shown schematically in Fig. 3.5. The summation of anti-parallel eigenvectors leads to some cancellation in the initial condition (when summing two vectors, tip to tail, that point in opposite directions, the cancellation is the overlap). As evolution progresses, if the decay of these eigenvectors reduces their cancellation, which is possible for eigenvectors with large differences in

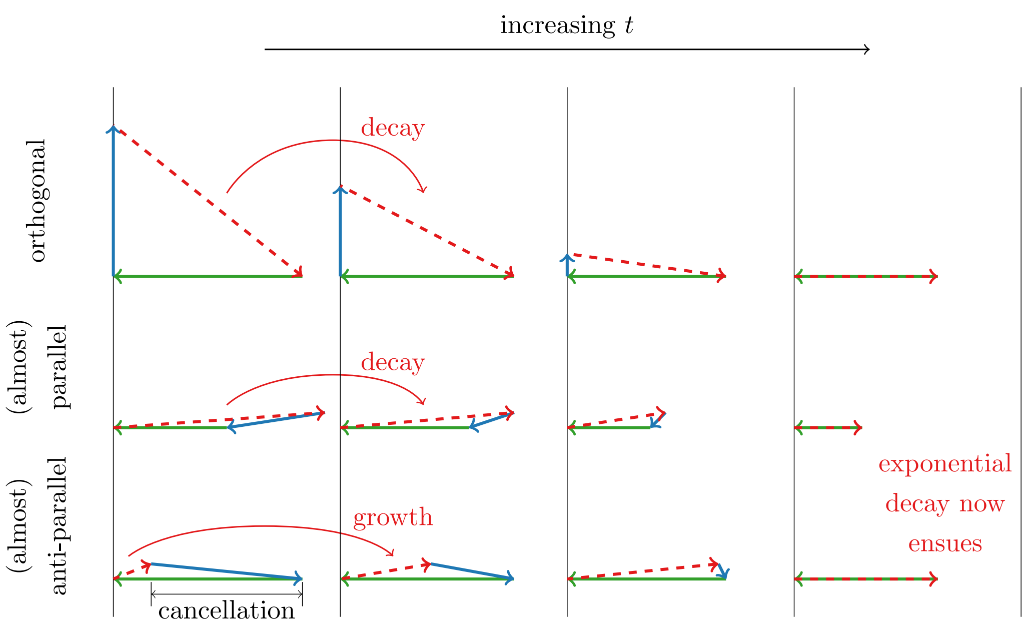

FIGURE 3.5: Examples of transient growth or transient decay of initial conditions composed of two eigenmodes (increasing time from left to right), following Schmid & Henningson (2001). In each case, the green eigenvector decays slowly (still exponentially), while the blue eigenvector decays rapidly. If there is no cancellation in the initial condition, e.g. the eigenvectors are orthogonal (top row), parallel (middle row), or have any acute angle between them, when placed tail to tail, no transient growth occurs (i.e. the magnitude of the sum of the eigenvectors, indicated by the red dashed arrow, reduces). Any non-zero cancellation in the initial condition (i.e. any obtuse angle between the eigenvectors) leads to some initial transient growth, with maximum transient growth achieved by anti-parallel eigenvectors (bottom row). Once the rapidly decaying eigenvector reaches zero magnitude, transient growth ceases, and all cases decay exponentially. Note that growth should be normalized by the initial length of the sum of the eigenvectors (the red dashed arrows). Also note that only approximations of the parallel and antiparallel cases have been drawn, to highlight the contributions of the various eigenmodes to the sum.

decay rate, this then incurs a growth in energy. Note that the predominant contribution of a parallel laminar base flow is downstream advection, hence eigenmodes are predominantly parallel or anti-parallel to the base flow, permitting large cancellation (Grossmann 2000).

This transient growth scenario forms an enticing alternative for reaching nonlinear amplitudes through linear mechanisms. If an initial condition with a linearly small initial energy (not infinitesimal, but still with $\epsilon \ll 1$), underwent sufficient linear growth to drive the perturbation to nonlinear amplitudes, a turbulent transition could be observed at a Reynolds number well below critical. This, in particular, aligns with the aims of this work, in investigating the most efficient route to turbulence, where efficiency is quantified based on both the magnitude of the Reynolds number and initial energy. However, interestingly, it will not prove the most efficient route to turbulence, at the very least in Q2D systems, as discussed in Chapter 7.

The optimal linear growth in perturbation energy over all non-zero initial conditions is given by (Schmid & Henningson 2001)

$$G(t) = \max \frac{\hat{v}_{\perp,L}(t)}{\hat{v}_{\perp,L}(t=0)} = \max \frac{\gamma(t)}{\gamma(t=0)} = ||e^{-\mathrm{i}\boldsymbol{\Lambda}t}||, \tag{3.28}$$

recalling, in particular, Eqs. (3.3) and (3.27). For further details, see Reddy & Henningson (1993), Reddy *et al.* (1993) and Schmid & Henningson (2001), or Farrell (1988) and Butler & Farrell (1992) for a similar, variational approach.

An alternate means to compute linear growth is by direct forward evolution of the linear perturbation evolution equation, Eq. (3.10), rewritten here as

$$\begin{aligned}\frac{\partial \hat{v}_{\perp,L}}{\partial t} &= \left[\mathscr{L}^{-1}\left(\mathrm{i}\alpha\frac{\partial^2 U_\perp}{\partial y^2} - \mathrm{i}\alpha U_\perp \mathscr{L} + \frac{1}{Re}\mathscr{L}^2\right) - \frac{H}{Re}\right]\hat{v}_{\perp,L} \\ &= \boldsymbol{L}\hat{v}_{\perp,L}.\end{aligned} \tag{3.29}$$

Note that the linear operator $\boldsymbol{L}$ still remains identical to that introduced previously, with $\mathscr{L} = \partial^2/\partial y^2 - \alpha^2$ as before; note $\texttt{eig}(\mathrm{i}\boldsymbol{L})$ yields the eigenmodes for perturbations with exponential time dependence assumed, as for a steady base flow. While Eq. (3.29) can compute the linear growth of any initial condition, to specifically determine which initial condition obtains optimal growth requires penalizing all other initial conditions which yield less growth (for a given time interval). To filter out the initial conditions yielding less growth, a Lagrange multiplier, the adjoint velocity perturbation $\hat{\boldsymbol{\xi}}_{\perp,L}$, is introduced (the properties of the adjoint will be discussed shortly). A perturbation, with evolution governed by the direct (forward) linear operator $\boldsymbol{L}$, and always assumed normalized to unit initial energy, has an energy growth at the time $t = \tau$ optimized over all initial conditions given by

$$\begin{aligned}G(\tau) = (\hat{v}_{\perp,L}(\tau), \hat{v}_{\perp,L}(\tau)) = (\boldsymbol{L}\hat{v}_{\perp,L}(0), \boldsymbol{L}\hat{v}_{\perp,L}(0)) = (\hat{v}_{\perp,L}(0), \boldsymbol{L}^{\ddagger}\boldsymbol{L}\hat{v}_{\perp,L}(0)) \\ = (\hat{v}_{\perp,L}(0), \hat{\xi}_{\perp,L}(0))\end{aligned} \tag{3.30}$$

where $(\cdot,\cdot)$ denotes the inner product in the energy norm introduced in Eq. (3.3), $\boldsymbol{L}^{\ddagger}$ is the adjoint evolution operator and $\hat{\boldsymbol{\xi}}_{\perp,L} = (\hat{\eta}_{\perp,L}, \hat{\xi}_{\perp,L})$ the adjoint velocity perturbation. The adjoint evolution operator is derived from the definition of the adjoint, e.g. for the wall-normal perturbation (Schmid & Henningson 2001),

$$\int_{-1}^{1} \hat{\xi}_\perp \boldsymbol{L} \hat{v}_\perp \, \mathrm{d}y = \int_{-1}^{1} \hat{v}_\perp (\boldsymbol{L}^\ddagger \hat{\xi}_\perp)^* \, \mathrm{d}y, \tag{3.31}$$

where $*$ represents complex conjugation. Note that the choice of norm *defines* the adjoint operator; the norm introduced in Eq. (3.3) defines the linear adjoint operator in the energy norm. It is important to note that the chosen norm is always 'built-in' to an adjoint operator, and henceforth, any computations in the adjoint system, based on $\boldsymbol{L}^\ddagger$, are confined to the energy norm. This is beneficial, as the energy norm is physically meaningful, and thus no further conversions are required to compute the adjoint eigenvectors in the energy norm. Note that this also greatly simplifies the computation of the optimal excitation; see below, compared to Farrell (1988), where in the latter, the forward system with an adjustment from L_2 to energy norm is instead employed. After integrating Eq. (3.31) by parts, and defining boundary conditions of $\hat{\xi}_{\perp,L}(y = \pm 1) = \partial \hat{\xi}_{\perp,L}/\partial y|_{y=\pm 1} = 0$, the adjoint evolution operator is determined to be

$$\begin{aligned} \frac{\partial \hat{\xi}_{\perp,L}}{\partial t} &= \left[\mathscr{L}^{-1} \left(2\mathrm{i}\alpha \frac{\partial U_\perp}{\partial y} \frac{\partial}{\partial y} + \mathrm{i}\alpha U_\perp \mathscr{L} + \frac{1}{Re} \mathscr{L}^2 \right) - \frac{H}{Re} \right] \hat{\xi}_{\perp,L} \\ &= \boldsymbol{L}^\ddagger \hat{\xi}_\perp. \end{aligned} \tag{3.32}$$

An auxillary benefit of this approach is that it can compute linear modal or nonmodal growth for base flows with any time variation (e.g. those which are periodic, rather than time steady), as discussed in Chapter 8 (Camobreco *et al.* 2021a) and Barkley *et al.* (2008), as the time dependence of the perturbation evolved is completely arbitrary.

It is worth taking a moment to point out some of the key features of the forward and adjoint systems (see Luchini & Bottaro 2014, particularly its supplemental material, for further details). First, the eigenvalues of both the direct and adjoint systems are identical; i.e. $\lambda_j = \lambda_j^{\ddagger *}$ for all j. Note that as the adjoint system is already in the physically meaningful energy norm, the eigenmodes for the adjoint system are directly obtained by discretizing the adjoint operator, and calling $\texttt{eigs}(-\mathrm{i}\boldsymbol{L}^\ddagger)$ in MATLAB, assuming $\exp(+\mathrm{i}\lambda_j^\ddagger t)$ time dependence. Note also that the conjugate in the eigenvalue equality accounts for a return to a positive time measure, as naturally the growth of the adjoint modes is backwards in time, which is equivalent to the decay of the forward modes forward in time. Second, the forward and adjoint eigenvectors are mutually orthogonal; i.e. $\hat{\boldsymbol{u}}_{\perp,L,i} \cdot \hat{\boldsymbol{\xi}}_{\perp,L,j} = \delta_{ij}$, where δ_{ij} is the Kronecker delta. Thus, the j'th adjoint eigenvector, evolved via the forward operator $\boldsymbol{L}$, in the limit of $t \to \infty$, will yield the j'th forward eigenvector. Even more importantly, the j'th adjoint eigenvector represents the initial condition with the largest projection (of all initial conditions) on the j'th forward eigenvector as $t \to \infty$. As in, $\hat{\boldsymbol{u}}_{\perp,L,i} \cdot \hat{\boldsymbol{\xi}}_{\perp,L,j} = \delta_{ij}$ ensures that the j'th adjoint eigenvector must have zero projection (amplitude) in all but the $i = j$'th forward eigenvector in the limit $t \to \infty$. Thus, the j'th adjoint eigenvector will optimally excite the j'th forward eigenvector, in the sense that it will generate the largest linear transient growth subject to the constraint that in the limit $t \to \infty$, all energy is contained in the j'th forward eigenvector. Equally the amplitudes (weighting coefficients in the forward eigenvector basis) will obey, e.g. $\gamma_1 \to 1$ and $\gamma_{\neg 1} \to 0$ as $t \to \infty$, where $\neg$ represents not equal to, if $i = j = 1$. Furthermore, as $t \to \infty$, these amplitudes will yield the largest ratio of 'final' to initial perturbation energy, of all initial conditions, as eventually they decay slowest/grow fastest. Thus, to optimally excite the leading eigenmode of the forward system, the initial condition should be the leading eigenmode of the adjoint system. No other optimization is required when the desired goal is optimal excitation, when working in the energy norm. See also Farrell (1988) and Farrell & Ioannou (1999).

The same is not true when the goal is optimal linear growth at finite target times, which requires optimizing the initial condition maximizing growth. With (a starting guess for the) initial condition $\hat{v}_{\perp,L}(t = 0)$, forward evolution proceeds via Eq. (3.29) to a target time τ, providing $\hat{v}_{\perp,L}(\tau) = \boldsymbol{L}\hat{v}_{\perp,L}(0)$. Defining an 'initial' condition of $\hat{\xi}_{\perp,L}(\tau) = \boldsymbol{L}\hat{v}_{\perp,L}(0)$, backward evolution via Eq. (3.32) to $t = 0$ gives $\hat{\xi}_{\perp,L}(0) = \boldsymbol{L}^{\ddagger}\boldsymbol{L}\hat{v}_{\perp,L}(0)$. Importantly, note that Eq. (3.32) has been written so that when time integrating (temporal iteration index i) with the 3rd-order Adams–Bashforth scheme

$$\hat{v}_{\perp,L}^{i+3} = \hat{v}_{\perp,L}^{i+2} + \Delta t \left(\frac{23}{12}[\boldsymbol{O}\,\hat{v}_{\perp,L}]^{i+2} - \frac{16}{12}[\boldsymbol{O}\,\hat{v}_{\perp,L}]^{i+1} + \frac{5}{12}[\boldsymbol{O}\,\hat{v}_{\perp,L}]^{i} \right), \tag{3.33}$$

the operator $\boldsymbol{O}$ can represent either $\boldsymbol{L}$ or $\boldsymbol{L}^{\ddagger}$ without having to step backward in time (computationally, both forward and adjoint evolutions proceed from $t = 0$ to $t = \tau$). Each forward-backward evolution is normalized to unit energy at $t = 0$, with a seed of random noise applied to initiate the iterative procedure. Forward-backward iterations continue until a desired tolerance is reached. This tolerance may be the change in $G(\tau)$ between iterations, if the growth is computed directly from integrating the perturbation energy over the computational domain at the start and end of the forward iterations, or from Eq. (3.30). Alternately, to aid convergence, the eigenvalues $\lambda_{\mathrm{G},j}$ representing growth under the combined action of the discretized $\boldsymbol{L}^{\ddagger}\boldsymbol{L}$ operator can be computed with a Krylov subspace scheme. Either the change in the eigenvalue each iteration,

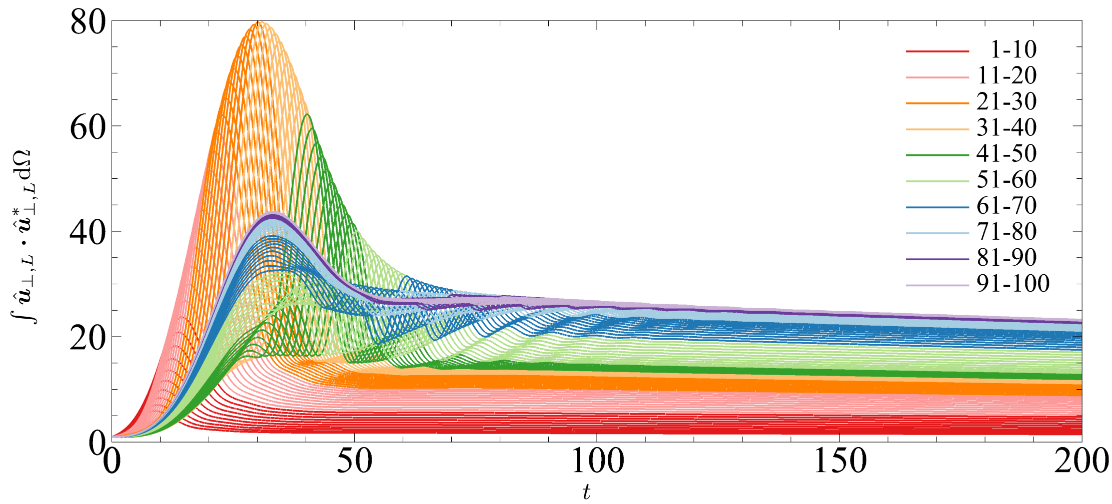

FIGURE 3.6: Energy norm $\int \hat{\boldsymbol{u}}_{\perp,L} \cdot \hat{\boldsymbol{u}}^*_{\perp,L} \mathrm{d}\Omega$ as a function of time, evolving initial conditions optimized for various τ, as annotated in legend (each normalized to unit initial energy). From $\hat{v}_{\perp,L}$, the streamwise velocity perturbation is computed as $\hat{u}_{\perp,L} = \mathrm{i}(\partial \hat{v}_{\perp,L}/\partial y)/\alpha$. From this, the optimal growth over $\tau \in [1, 100]$ at $H = 10$, $r_\mathrm{c} = 0.9$ and $\alpha = 1$ is determined to be $\tau_\mathrm{opt} \approx 31$ (the first light orange curve).

or the size of the imaginary component of the eigenvalue (for linear transient growth computations only, as it should be zero) can then form convergence tolerances. With eigenvalues sorted in ascending order by largest real component, the maximum growth over all initial conditions at a specified τ is $G(\tau) = \lambda_{\mathrm{G},1}$.

For a given Re, H and α, the optimal initial condition yielding the maximum growth (over all initial conditions) for a given target time τ can be computed. However, the growth at $t = \tau$ may not be the largest growth achieved over all times through which that initial condition evolves, nor may it be the largest growth obtained by any other linear initial condition. Thus, τ is varied until the maximal growth over all τ and all initial conditions is determined. This process is depicted in Fig. 3.6. A similar process can be performed for all other α, which then yields the maximum growth achievable at that H and Re, defined as G_max, which occurs at τ_opt, α_opt. Note that if $Re > Re_\mathrm{c}$, then $G_\mathrm{max} \to \infty$ and $\tau_\mathrm{opt} \to \infty$, if at a wave number yielding positive growth rates. Thus, usually $Re < Re_\mathrm{c}$ are simulated, or a local maximum (with τ of order 100) found if $Re > Re_\mathrm{c}$ are worth investigating. Note that a lower bound of $G_\mathrm{max} = 1$ is also of interest, as it defines the energetic Reynolds number Re_E, below which transient growth does not occur. This bound signifies that the sum of dissipation and friction exceed production at all times, rather than just at large times. However, as it is such a small focus of this work, energetic analysis is not discussed further here.

3.3.2 The physical mechanisms by which Q2D nonmodal perturbations grow

In the modal stability section, § 3.2, only the physical mechanism which generated the Tollmien–Schlichting wave instability was of interest. However, an analogous form of the modal TS wave can be observed in nonmodal initial value problems. Important differences exist between the modal and nonmodal TS waves. Discussion as to which is best at triggering subcritical turbulence is contained in Chapter 7. Note that the nonmodal TS wave only truly recovers the modal TS wave as $t \to \infty$ (and with optimal excitation only if the initial condition was the mutually orthogonal adjoint eigenvector). Here, the formation process and evolution of the nonmodal TS wave are discussed; refer to § 3.2 for the modal equivalent.

Nonmodally, in 2D or Q2D parallel shear flows, there is only one mechanism capable of transiently growing perturbation energy. This is the well known Orr mechanism (Orr 1907; Butler & Farrell 1992; Schmid & Henningson 2001), which, with the appropriate initial conditions, generates the nonmodal TS wave. Other common nonmodal growth mechanisms, such as the oblique-wave and lift-up mechanisms, require the out-of-plane dimension. The dynamics behind the Orr mechanism are highlighted in the Reynolds–Orr energy equation. In 2D or Q2D systems, the production term (the only means for perturbation energy growth) has only a single component for streamwise invariant base flows, rewritten here from Eq. (3.8),

$$\int -2\hat{u}_{\perp,L}\hat{v}_{\perp,L}\frac{\partial U_\perp}{\partial y}\,\mathrm{d}\Omega = -2\int \frac{\hat{v}_{\perp,L}}{\hat{u}_{\perp,L}}\hat{u}^2_{\perp,L}\frac{\partial U_\perp}{\partial y}\,\mathrm{d}\Omega = -2\int \left.\frac{\partial y}{\partial x}\right|_\psi \hat{u}^2_{\perp,L}\frac{\partial U_\perp}{\partial y}\,\mathrm{d}\Omega, \quad (3.34)$$

following Butler & Farrell (1992), where the definition of a streamline $\partial y/\partial x|_\psi = \hat{v}_{\perp,L}/\hat{u}_{\perp,L}$, a line everywhere tangent to the velocity vector, is introduced. Note that the production term is linear (valid for any ϵ) and inviscid, and thus so too is the Orr mechanism. Note specifically, as discussed earlier, that the production term is only linear due to the chosen definition for a perturbation. If contributions from the mean flow, or even just the zeroth perturbation harmonic, were included in Eq. (3.34), a nonlinear analogue of the Orr mechanism would instead be observed. In any case, Eq. (3.34) highlights that any region of the fluid domain where perturbation streamlines $\partial y/\partial x|_\psi = \hat{v}_{\perp,L}/\hat{u}_{\perp,L}$ have the opposite sign as the base flow gradient is a source of production (energy is transferred from the base flow, or equivalently, the pressure gradient, or wall motion, driving the flow). Any region where streamlines have the same sign as the base flow gradient are a sink of production (energy is transferred from the perturbation to the base flow). Note that perturbation energy then reduces due to the production, dissipation and friction terms. Structures which are a production source or sink are respectively termed a structure with tilt (lean) opposite to the base flow, or tilt into the base flow. Note that tilting is driven by $U\partial\hat{v}_{\perp,L}/\partial x$, recalling Eq. (3.9).

Although Eq. (3.34) identifies regions where perturbation energy is produced, in proportion with $\hat{u}_{\perp,\mathrm{nm}}^2 = -(\partial\hat{v}_{\perp,\mathrm{nm}}/\partial y)^2/\alpha^2$, it does not explain the energy growth (e.g. how the size of $\hat{\boldsymbol{u}}_{\perp,L}$ increases). To do so, it is worth considering two key aspects of the tilting process. The first aspect is highlighted in Fig. 3.7, and is related to the continuity constraint $\partial\hat{u}_{\perp,L}/\partial x = -\partial\hat{v}_{\perp,L}/\partial y$. Note that, as drawn in Fig. 3.7(a), the approximation $\Delta\hat{v}_{\perp,L}/\Delta y$ over finite distances is considered. Two phase lines intersecting the maximum and minimum perturbation velocity have a small distance Δy between them at $t = 0.7071$. As the initial condition eventually tilts, as observed at the much later $t = 49.50$, Δy has greatly increased, such that $\Delta\hat{v}_{\perp,L}$ must also have increased to satisfy continuity. This is reflected in $\max(|\hat{v}_{\perp,L}|)$ having increased over 40 fold between Figs. 3.7(a) and (b). The greater the tilt opposite the base flow shear in the initial condition, or equivalently the smaller the initial Δy, the greater the transient growth achieved by the perturbation. Further perturbation growth occurs so long as the phase lines remain opposite the mean shear. This is the case until the time of optimal growth in Fig. 3.7(c), with the structure then upright. As time progresses, the perturbation decays as it leans into the mean shear, Fig. 3.7(d). If the viscous and Hartmann dissipation (which act through the entire process) are neglected, cumulative energy decay (transfers from the perturbation to the base flow) for $t > \tau_{\mathrm{opt,S}}$ cancels all cumulative energy growth (transfers from the base flow to the perturbation) for $t < \tau_{\mathrm{opt,S}}$, if $Re < Re_{\mathrm{c}}$. Finally, note that the statement '$\Delta\hat{v}_{\perp,L}$ must also have increased to satisfy continuity' is actually a slight misnomer. As $\hat{u}_{\perp,L} = \mathrm{i}(\partial\hat{v}_{\perp,L}/\partial y)/\alpha$, continuity is always satisfied by default. Given that the initial condition was a source of production, by virtue of Eq. (3.34), it follows that increases in the magnitudes of $\hat{v}_{\perp,L}$ and $\hat{u}_{\perp,L}$ were likely, although equally both could have fallen and continuity still been satisfied (so long as $\Delta\hat{v}_{\perp,L}$ fell further, given that Δx in $\Delta\hat{u}_{\perp,L}/\Delta x$ is fixed from linearity). Thus, the initial evolution process is further considered, to highlight how

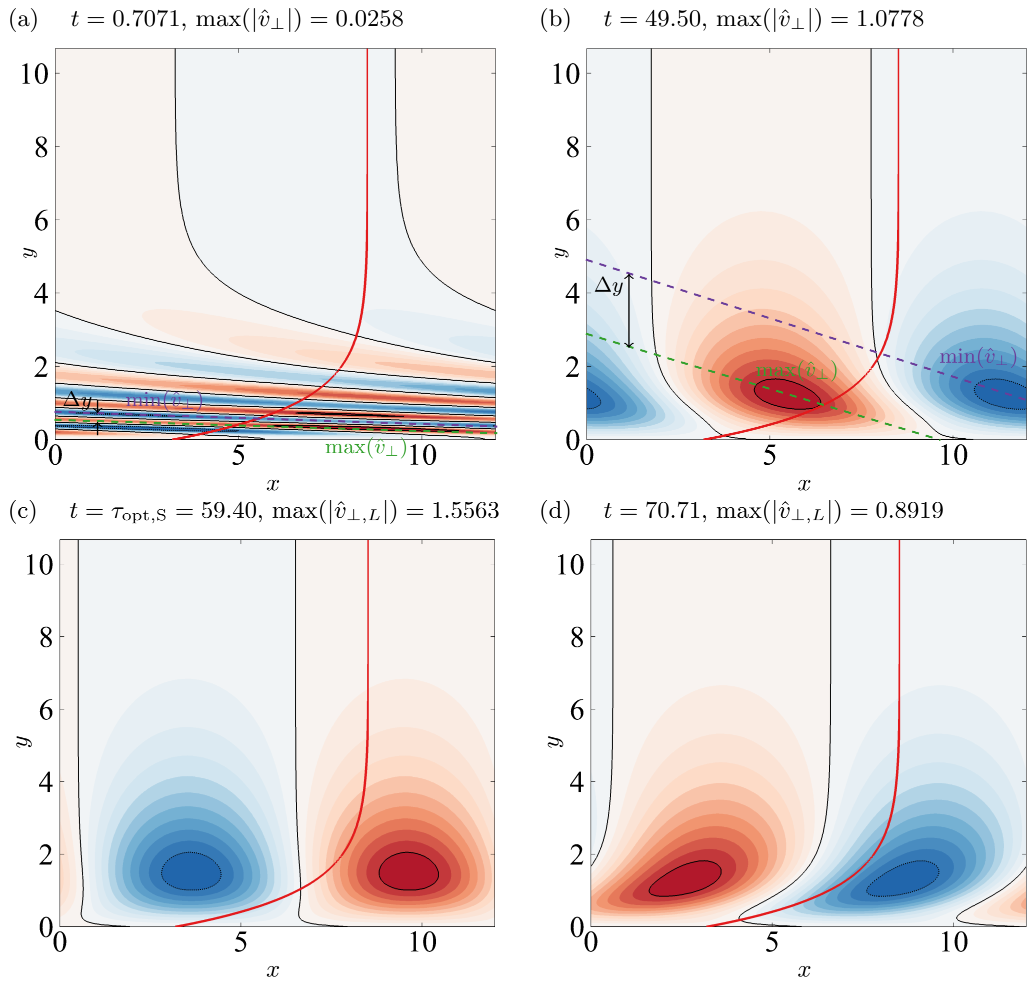

FIGURE 3.7: Snapshots of $\hat{v}_{\perp,L}$ linearly evolving into a nonmodal TS wave at $Re_{\mathrm{S}} = 1.414 \times 10^4$ in an isolated exponential boundary layer, $U_\perp(y) = 1 - \exp(-y)$, with sketched lines following Jiménez (2013). Lengths were non-dimensionalized by δ_{S}, so the Shercliff layer is one wall-normal unit thick. The base flow velocity profile is overlayed with a red solid line in each subfigure. An indication of energy growth at each t is provided by $\max(|\hat{v}_\perp|)$, with growth peaking at $t = \tau_{\mathrm{opt,S}}$. Note the structure has advected through the domain once over this set of subfigures. Solid lines (red flooding) denote positive $\hat{v}_{\perp,L}$, dotted lines (blue flooding) negative; lines are only applied to the zero, maximum and minimum velocity contours. Phase lines intersect the maximum and minimum $\hat{v}_{\perp,L}$, to provide a rough guide of the tilt of the perturbation, and aid in the assessment of $\Delta\hat{v}_{\perp,L}/\Delta y$. Note that phase shifts aside, the wall normal velocity contours are of very similar appearance to the streamlines, such that the latter are not overlayed, although are more relevant to Eq. (3.34).

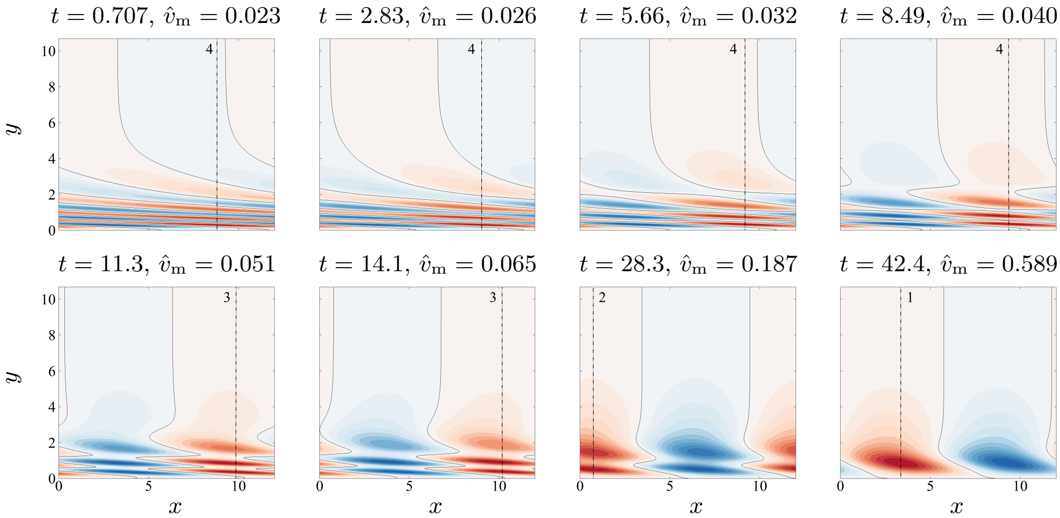

FIGURE 3.8: Snapshots of $\hat{v}_{\perp,L}$ linearly evolving (eventually into a nonmodal TS wave) at $Re_{\rm S} = 1.414 \times 10^4$ in an isolated exponential boundary layer, $U_\perp(y) = 1 - \exp(-y)$. Lengths were non-dimensionalized by $\delta_{\rm S}$, so the Shercliff layer is one wall-normal unit thick. As shorthand, $\hat{v}_{\rm m} = \max(|\hat{v}_{\perp,L}|)$, to provide an indication of energy growth at various t. On each subfigure, the annotation denotes the number of local maxima in $\hat{v}_{\perp,L}$ along the corresponding dashed vertical lines (which each roughly intersect the overall local maximum of the flow field). Note for the streamwise perturbation velocity, recall that $\hat{u}_{\perp,\rm nm} = \mathrm{i}(\partial\hat{v}_{\perp,\rm nm}/\partial y)/\alpha$, so if $\partial\hat{v}_{\perp,\rm nm}/\partial y$ has multiple local maxima along a line in the wall normal direction, then $\hat{u}_{\perp,\rm nm}$ is varying between positive and negative values along that line also. Note also that the structure has (or substructures have) yet to advect once through the domain (this first occurs at $t \approx 70$). Solid lines (red flooding) denote positive $\hat{v}_{\perp,L}$, dotted lines (blue flooding) negative.

growth in $\hat{v}_{\perp,L}$ is initiated, which then helps force growth in $\hat{u}_{\perp,L}$. Note that the perturbation pressure, the physical means by which continuity is enforced, also plays a role in inhibiting the streamwise velocities at small times, which then leads to growth in $\hat{u}_{\perp,L}$ as the inhibition diminishes due to the structures tilting (Jiménez 2013).

The perturbation evolution over early times is depicted in Fig. 3.8. The first interesting thing to note is that tilting is not observed before $t \approx 30$, in the sense of the tilting shown in Figs. 3.7(b-d); i.e. where advection of the nonmodal TS wave advects both the structure as a whole, and causes the upper regions to roll over the lower regions. This highlights the second key aspect of the Orr mechanism, growth due to constructive interference of in-phase waves. Considering Fig. 3.7(a), the initial condition makes an acute angle with the Shercliff wall (measured clockwise from the $-x$ direction). At this $Re_{\rm S}$, the initial condition then covers four full periods of the domain. Note that each subfigure is annotated with the number of local maxima along a vertical line through the duct, which at this t, is still representative of the number of layers in (or windings of) the initial condition. However, travelling along the diagonal windings of the initial condition (e.g. starting at the wall and staying only in red regions of the $t = 0.7071$ subfigure, like travelling along the phase lines drawn in Fig. 3.7(a)), the magnitude of $\hat{v}_{\perp,L}$ varies. As advection (or 'tilting') is driven by $U\partial\hat{v}_{\perp,L}/\partial x = \mathrm{i}\alpha U\hat{v}_{\perp,L}$, then if $\hat{v}_{\perp,L}$ is sufficiently small further from the wall where $U_\perp$ is larger, these upper regions are able to stay in phase with the local maxima of the layers of each of the waves below. Streamwise perturbation velocities also partially cancel between layers, resisting sliding and helping keep the layers in phase, recalling the caption of Fig. 3.8. This allows for constructive interference between the various layers of the initial condition, so long as the positive $\hat{v}_{\perp,L}$ regions in each layer remain in phase (with the same true for the negative $\hat{v}_{\perp,L}$ regions). As time passes, from $t = 2.828$ to $t = 8.485$, the four local maxima clearly remain in phase as all four layers advect along, constructively interfering as they do. They also become more distinct, and by $t = 8.485$, are almost completely separated in the streamwise direction (e.g. the red regions are very narrow between the blue regions, and vice versa). By $t = 11.31$, the underlying form of two separate structures is visible, and from constructive interference, only three local maxima in the wall-normal direction remain (two having combined). However, $\hat{v}_{\perp,L}$ is still small enough that tilting of the entire structure does not yet occur. This allows further interference between the layers, leading to still larger $\hat{v}_{\perp,L}$. By $t = 28.28$ there are only two local maxima in the wall-normal direction. Soon thereafter, a structure with a single local maximum in the wall-normal direction forms, which has large $\hat{v}_{\perp,L}$ far from the wall, such that the rotation observed in Fig. 3.7 proceeds. Therefore, the more acute the angle the initial condition makes with the Shercliff wall, the more layers there will be in the initial condition and the more highly sheared it is. Thus, there will be more local maxima (one for each layer) able to constructively interfere with one another, resulting in a larger overall transient growth.

It is worth mentioning, following Jiménez (2013), that although the Orr mechanism is inherently linear, a more general nonlinear form of the Orr mechanism can be considered. In essence, linearity is not essential to the Orr mechanism. In the previous discussion, linearity ensures that the streamwise spacing of structures does not vary, with implications on the continuity constraint. However, the key to the Orr mechanism is not just amplification via pressure (continuity), as growth is predominantly driven by the interaction between waves at different wall-normal heights (and thereby different levels of base flow shear). So long as the waves remain in phase, aided by the cancelling of streamwise perturbation velocities, then the wall-normal perturbation velocities can constructively interfere. This interference is in no way related to the linear interaction between, or evolution of, the waves, which can equally behave nonlinearly, so long as they remain in phase, as aided by continuity. In either case, the more (layers of) waves that remain in phase, and the longer the waves remain in phase, the greater the transient growth.

Having discussed the relevant linear growth mechanisms, the remainder of this introduction focuses on, and formalizes some of, the various roles of nonlinearity. Again, recall that this in no way implies that linear mechanisms are not important even when nonlinear effects are considered, as the perturbation energy growth required to both transition to and sustain turbulence has a linear origin. However, one way or another, nonlinearity must be considered when dealing with turbulence. The first consideration will be the nonlinear equivalent of linear transient growth, which will be framed both from the conventional viewpoint of an initial value problem (much like this section), as well as from the perspective of the fixed points and attractors of a dynamical system.

3.4 A dynamical systems perspecitive of transitions to turbulence, and some criteria to aid identification of turbulence

Discussion now turns to the dynamical systems viewpoint, and the means by which the edge states of the turbulent attractor can be found. Some additional methods to determine edge states are detailed in Beneitez *et al.* (2020), and references therein. First, some definitions are provided, which are hopefully precise enough to illustrate the general concepts, while bypassing the more exacting mathematical details and terminology (which are not directly relevant to the aims of this thesis):

- A **dynamical system** $\dot{\boldsymbol{x}} = F(\boldsymbol{x})$ governs the time variation of the set of points $\boldsymbol{x}$.

- A **state space** is the set of all configurations of the points $\boldsymbol{x}$; here the set of all solutions of the Navier–Stokes equations. Each solution corresponds to a point $\boldsymbol{x}$, with the state space configured in some manner such that moving between points corresponds to evolution of the Navier–Stokes equations.

- A **metric** is the norm by which different points in the state space are compared, e.g. an L_2 or kinetic energy norm.

- A **trajectory** is a path through the state space as time varies. Trajectories of interest must necessarily connect points in the state space in a manner following evolution of the Navier–Stokes equations and satisfying applied boundary conditions. The initial condition starts the trajectory.

- An **attractor** is a configuration in the state space to which nearby trajectories converge, which could be a fixed point, or a subset of points which themselves form a trajectory.

- A **laminar attractor** is specifically the only linearly stable fixed point in the entire state space (Duguet *et al.* 2013).

- A **laminar basin** is a region of the state space, which if the initial condition is within the laminar basin, will result in the trajectory converging to the laminar fixed point.

- A **turbulent attractor** or **turbulent state** is a region of the state space toward which trajectories not initially on or in the laminar basin converge.

- A **laminar/turbulent basin boundary**, **separatrix**, **edge manifold**, **edge** or Σ is an invariant set delineating those trajectories which converge toward either the laminar fixed point, for initial conditions within the laminar basin, or converge toward the turbulent state (Vavaliaris *et al.* 2020), for initial conditions within the turbulent basin. Initial conditions on the edge manifold will have trajectories that remain on the edge manifold for all time (Duguet *et al.* 2013). Note that no trajectories commencing in the laminar basin can cross the edge manifold and thereby leave the laminar basin. If trajectories commencing in the turbulent basin can cross out of the basin, it is termed a weak edge, if such trajectories cannot, it is termed a strong edge (Beneitez *et al.* 2020).

- A **relative attractor** or **edge state** is (typically) a saddle point embedded on the edge manifold, corresponding to a travelling wave, periodic orbit, torus or chaotic attractor (Beneitez *et al.* 2020). Each saddle point is an intersection point between a stable manifold (the edge) and an unstable manifold.

- An **edge trajectory** travels along (or nearby to) the edge manifold until it reaches an edge state, at which point the trajectory departs toward either the laminar or turbulent attractor (Duguet *et al.* 2009). Thus, edge trajectories transiently visit flow solutions which are exact coherent states.

- A **minimal seed** is an initial condition just across the (stable) edge manifold, on the turbulent basin's side, but with the smallest value of the chosen metric, as measured relative to the laminar fixed point. A trajectory with the minimal seed as initial condition will thereby most efficiently (in the chosen metric) reach turbulence. If the minimal seed has been found, it represents an initial condition (almost) on the edge manifold, and therefore must be attracted to at least one edge state before transitioning to turbulence. Both the minimal seed and corresponding edge state accessed for transition are important, and are discussed in Chapter 7 for Q2D subcritical transitions.

With these definitions in hand, the bypass transition process (Reshotko 2001; Zammert & Eckhardt 2019) can be described at subcritical Reynolds numbers, which ensures the fixed point is linearly stable. To further aid this discussion, a schematic of the state space is provided in Fig. 3.9, valid for a single streamwise wave number α. First, consider perturbations maximizing linear transient growth (denoting IC1 as the mode with leading growth, and IC2 the next best growth, for an optimized target time), which have flow structures independent of amplitude. With zero perturbation energy, the trajectories corresponding to any initial condition start at the laminar fixed point L. However, by incrementally increasing the initial energy of each initial condition (i.e. starting from a point further outward along the dashed lines in the schematic), a number of interesting trajectories can be observed. Those that are of particular interest are the edge trajectories, which have been drawn with colored arrows. With a small change in the initial energy, the initial condition near M has a trajectory either starting just inside, or just outside, the laminar basin. Both initial conditions follow the edge Σ, growing for a while, before decaying toward a saddle point S1 embedded on the edge manifold. At this saddle point, the two trajectories, which had very similar initial energy, diverge. One returns to the laminar fixed point and the other transitions to a turbulent state. Note that a trajectory with initial condition outside the laminar basin need not be turbulent for all time, but must reach the turbulent region of the state space at least once. Still considering IC1, with a much larger initial energy, the edge of the turbulent basin can again be found, in a region between O and another saddle point S2 embedded in the edge. These two locations in the state space, M and O, denote the lower and upper edge states, delineating initial conditions which either transition to turbulence, or return to the laminar fixed point.

In 3D systems, although possibly not in Q2D systems, it can be quite difficult to determine the minimal seed, after having determined the locations M and O with a linearly optimized initial condition (IC1). For example, using a different initial condition, IC2, the locations N and P in the state space can be found, which also yield edge trajectories with vastly different final states (L and T). Having drawn the entire edge Σ in Fig. 3.9, it is immediately apparent that M is the minimal seed, as M is closer to the fixed point than either N, or any other point on the edge. If the entire edge had not been drawn, as in practice only a fraction of the edge can be explored, another location of the edge could well have been closer to L, and yielded a more efficient route to turbulence. And this is where nonlinear transient growth becomes particularly useful.

For linear transient growth to identify the optimal route to turbulence requires (for a given α and Re) that a linear initial condition intersects the edge at M. With a linear scheme, where the only means of varying the structure of the initial condition is through the target time τ, this is by no means guaranteed, as the state space encompasses all solutions of the Navier–Stokes equations, not just those which are infinitesimally small. For canonical flows in three-dimensions, it appears unlikely that linear schemes are capable of finding M (Duguet *et al.* 2009; Pringle & Kerswell 2010; Cherubini *et al.* 2011; Pringle *et al.* 2012; Duguet *et al.* 2013; Kerswell *et al.* 2014; Khapko *et al.* 2014; Cherubini *et al.* 2015; Pringle *et al.* 2015; Marensi *et al.* 2019; Budanur *et al.* 2020; Vavaliaris *et al.* 2020). Thus, nonlinear transient growth, which has access to the entire state space, becomes necessary.

The nonlinear transient growth scheme can employ a small target time τ, to determine equivalent nonlinear optimals in the vicinity of L, in the hope that M is close enough to L for these to be useful. Alternately, the target time can be set large enough for an initial condition to reach the turbulent attractor by $t \leq \tau$. Both methods are useful. The latter method directly determines if a trajectory has an initial condition

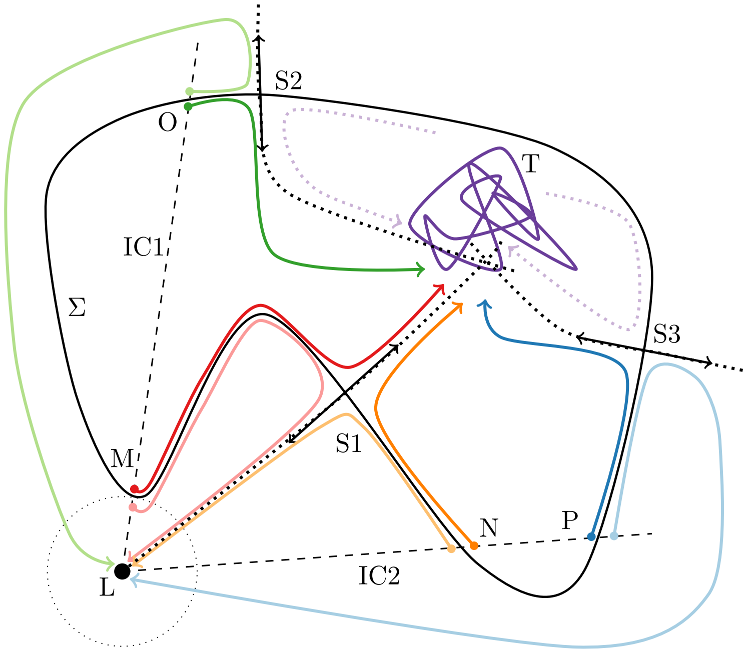

FIGURE 3.9: Pedagogical sketch of the state space, following Duguet *et al.* (2013) and Budanur *et al.* (2020). All points other then L have non-zero perturbation energy. The sketch assumes equal energy growth in $\hat{u}_\perp$ and $\hat{v}_\perp$ corresponds to trajectories travelling at 45° from the horizontal (e.g. roughly from L to T). The black filled circle represents the laminar fixed point (L). The laminar-turbulent basin boundary (stable edge manifold) is denoted by Σ. Any trajectory starting (colored filled circles) on the laminar side of the basin boundary returns to L. All other trajectories reach turbulence (T), although do not necessarily remain turbulent for all time thereafter (purple dotted arrows). Solid double-sided black arrows denote the saddle-point edge states (S). Black dotted lines denote unstable manifolds (a saddle point is an intersection between the stable edge and an unstable manifold). Radial dashed black lines denote initial conditions (IC) with identical appearance along the dashed line and with initial energy proportional to distance from the laminar fixed point (e.g. a rescaled linear transient growth optimal). If the black dashed lines curved through the state space, they might better represent nonlinear transient growth optimals (which have energy dependent structures) with a similar optimization goal. The dotted circle around L denotes a constant value of the energy metric. M denotes the minimal seed, as it is closer to L than N, although both access the same lower edge state (S1). O and P access different upper edge states (S2 and S3) when transitioning to turbulence.

outside the laminar basin. Once such an initial condition is found, the initial energy is incrementally reduced (rerunning the nonlinear scheme), until the edge, and likely M, is found. However, determination of the minimal seed still remains a function of the target time. A nonlinearly evolving initial condition can remain laminar until τ, by appearing to saturate to a finite amplitude state (which is linearly unstable but nonlinearly stable), but may be able transition to turbulence with a much larger τ (Pringle *et al.* 2012). Thus, even nonlinear transient growth can struggle to find M, due to the expense of computations with large τ. Due to the size of τ necessary to reach turbulence in Q2D systems, this method of using nonlinear transient growth appears unfeasible; nonlinear transient growth with smaller τ is primarily used to validate the linear-nonlinear scheme employed in Chapters 5 (Camobreco *et al.* 2020) and 7. Note that this discussion presumes the edge state and minimal seed are being determined for a single α and Re; the effects of varying both α and Re are considered in Chapters 5 (Camobreco *et al.* 2020) and 7, and are found to be as important as τ.

With the transition process discussed, some interpretations of turbulence from the dynamical systems framework are provided. These are quite speculative, given the current level of understanding of turbulence, and are an amalgamation of various conjectures (Grossmann 2000; Biau & Bottaro 2009; Duguet *et al.* 2009, 2013; Khapko *et al.* 2014; Budanur *et al.* 2020). The criteria for a flow to be deemed turbulent applied in this work follows Grossmann (2000), in that subcritical turbulence has:

- A transition with a double threshold, based on both initial energy E_0 and Reynolds number, i.e. if a given E_0-Re combination incite transition, the transtion only has a double threshold if, at fixed Re, reductions in E_0 eventually lead to initial conditions unable to trigger transition *and*, if at fixed E_0, reductions in Re eventually lead to initial conditions unable to trigger transition. Note that supercritical transitions have a single threshold, as at a fixed supercritical Re, there may be no finite E_0 for which transition would not occur.

- A state space dimension (number of degrees of freedom) that becomes very large rapidly after the transition. Note that it is still unproven whether turbulence can be truly represented with a finite number of degrees of freedom, although Hopf (1948) conjectured that the turbulent state should be asymptotically confined to a finite dimensional manifold of the state space, at finite Reynolds number. In practice, turbulence is identified by all resolved Fourier modes (in the order of 100 modes) being appreciably energized, compared to a chaotic flow that may exhibit 10 to 20 energized Fourier modes.

- Turbulent fluctuations which cannot be individually identified, i.e. in the time for a single turbulent region to both form and decay, other turbulent regions of the fluid will have spawned or spread, such that each cannot be individually tracked or identified. Note that fluctuations are always transient by definition. At large enough Re, the turbulent fluctuations (or chaotic dynamics) should continually overlap. These topics will be discussed further in § 3.6.

- A scale independent energy cascade, over an inertial subrange of wave numbers, to be introduced in § 3.7.

In the dynamical systems framework, the turbulent flow is presumed to be composed of strongly chaotic dynamics, organized around a finite (hopefully small) set of exact coherent solutions. Chaotic trajectories in the state space occur as the flow visits one exact coherent solution after another, travelling between them via the stable and unstable manifolds (e.g. travelling in some loop along the black solid and/or dotted lines of Fig. 3.9). If a chaotic repeller is present, the trajectory can be kept within the turbulent basin indefinitely, thereby sustaining turbulence, which may or may not be fully developed (i.e. domain filling). Whether the turbulence is intermittent (i.e. exhibiting relaminarization interspersed between turbulent episodes) may then depend on the clustering of the edge states. Note that, as drawn in Fig. 3.9, the turbulent region of the state space is quite small. An actual state space, at large Re, may exhibit chaotic dynamics over a much larger region of the state space. However, chaotic dynamics do not necessarily meet the definitions of turbulence; conditions solely met within the vicinity of T. It is also unclear whether the edge manifold can exhibit chaotic dynamics, or if only points within the turbulent basin can. Although Budanur *et al.* (2020) observe a chaotic upper edge state in pipe flow, it can be difficult to prove that a simple invariant state would not be approached with longer time evolution, made possible by selecting an initial energy that ensures the trajectory commences from a point closer to the edge manifold (Khapko *et al.* 2014). A chaotic upper edge state may also be observed in Chapter 5 (Camobreco *et al.* 2020).

At lower Re, the turbulent region of the state space may instead be occupied by a chaotic saddle, rather than an attractor (Khapko *et al.* 2014). As a consequence, the stable edge manifold may be entagled with the turbulent dynamics (e.g. the solid black and purple lines in Fig. 3.9 may intermingle). Thus, a flow which becomes turbulent may relaminarize, 'using' turbulence to cross the stable edge manifold out of the turbulent basin (the edge is no longer a strong enough chaotic repeller as for larger Re). This may result in a high probability of relaminarization for almost any turbulent trajectory, which may be observed in this work when α is far from $\alpha_{\max}$, see Chapters 5 (Camobreco *et al.* 2020) and 7.

This concludes the discussion of nonlinear transient growth and the dynamical systems viewpoint of subcritical transitions (based around varying the initial energy of linear or nonlinear optimals, before either is nonlinearly evolved). The next section considers two alternate theories of how subcritical transitions may occur, with the aid of some simplifying approximations.

3.5 Some theoretical routes to turbulence

At subcritical Reynolds numbers, instantaneous perturbation energy growth is governed by linear mechanisms. However, turbulence is distinctly nonlinear, and thus cannot be attained (from a perturbed laminar state) solely via linear transient growth. Although nonlinear transient growth simulates entire routes to turbulence (e.g. linear and nonlinear stages, if both exist), it can can be difficult to discern the importance of specific flow features or setup parameters, or else is computationally prohibitive. These issues warrant consideration of alternate methods of elucidating routes to turbulence. Two alternate methods, minimal defect theory and weakly nonlinear analysis, are discussed here. While both leave some gaps in explaining how a perturbation of the laminar fixed point leads to turbulence, they help clarify which underlying flow features are important, and how they interact.

3.5.1 Minimal defect theory

Minimal defect theory (Bottaro *et al.* 2003; Biau & Bottaro 2004, 2009; Nouar & Bottaro 2010) is attractively simple. A streamwise invariant modulation to a reference base flow U_{ref}, with sufficiently large (although small in practice) energy norm

$$\zeta = \int_{-1}^{1} (U_{\perp} - U_{\mathrm{ref}})^2 \, \mathrm{d}y, \tag{3.35}$$

may permit exponential growth at subcritical Reynolds numbers. Note that subcritical always refers to the reference base flow.

This work only investigates minimal defects modulating the Shercliff reference base flow at $H = 10$, recalling Eq. (3.14), and only in this section of the introduction. Although the idea behind minimal defect theory, of a base flow modulation driving a subcritical reference profile supercritical, may be quite important, as discussed in Chapter 7, minimal defect theory is not investigated in detail as its mathematical foundations are quite tenuous. This is predominantly due to the modulation not being a full solution of the Navier–Stokes equations. As the modulation is streamwise invariant, it is a solution of the Euler equations, but is otherwise subject to time unsteadiness due to diffusion. Thus, accurate linear computations of the growth rate of the modulated profile can be problematic, as discussed below.

In theory, the plan is as follows: determine a modulated base flow profile $U_{\perp}(y) = U_{\mathrm{ref}}(y) + U_{\mathrm{mod}}(y)$ capable of shifting at least one eigenvalue to the positive (unstable) complex half plane, while at a subcritical Reynolds number. The modulation U_{mod} capable of achieving this with the minimum norm ζ is the minimal defect. However, as mentioned, there are complications. In particular, no matter how well U_{mod} is designed, attempting to destabilize a single eigenmode will also disturb the other eigenmodes of the linear system. This can be either beneficial or detrimental to linear transient growth (which is ultimately based on a large number of eigenmodes, and particularly those most sensitive to perturbation), depending on the modulation profile and streamwise wave number. Furthermore, the linearized analysis of § 3.2, for which minimal defect theory pertains, assumes a time steady base flow. Any modulation to the reference base flow is subject to decay, via both viscous diffusion and Hartmann friction. Minimal defect theory presumes these processes occur at timescales much larger than that of linear growth, which cannot be guaranteed. More importantly, the timescale for linear growth tends to infinity as the modulated profile approaches neutral stability. Thus, in the vicinity of neutral stability, base flow timescales must necessarily be smaller than those of the modulation, invalidating a frozen linear stability analysis (which approximates the base flow as time steady). A possible counterpoint, particularly relevant to uncovering routes to turbulence, is that nonlinear processes could forseeably regenerate a base flow modulation, via production from higher harmonics, counteracting friction and diffusion and thereby reducing unsteadiness. However, if such additional harmonics reduced unsteadiness, they may themselves invalidate the linear assumptions of scale separation. Scale separation in the linearized analysis permits inclusion of only terms of magnitude $\epsilon \ll 1$ and $\epsilon \gg \epsilon^2$. If the base flow modulation also had magnitude $\epsilon \ll 1$, and if this magnitude was sufficient to modify the growth rate of the leading instability, then higher-order feedback regenerating the base flow modulation may not invalidate scale separation (although, if true, this would likely be very difficult to prove). The final complication is that once the base flow is modulated, the wave number maximizing the growth rate of the leading modal instability changes. In the linearized analysis, computations of the reference and modulated base flows can easily be performed at different wave numbers. However, in a nonlinear analysis, such wave number adjustments cannot be easily accommodated.

The minimal defect generates the largest improvement in the growth rate of a single targeted i'th eigenmode, for a given Re and ζ. Note that the eigenmode to target, which provides the greatest improvement in growth rate for a given ζ, is not known for the Q2D Shercliff profile. Although the leading eigenvalues have the largest growth rates on the reference base flow (are naturally closest to the upper half plane), their optimally modulated growth rates can be eclipsed by modulations targeting eigenmodes with larger sensitivities; e.g. those modes with eigenvalues near the branch intersection (Reddy & Henningson 1993; Reddy *et al.* 1993; Bottaro *et al.* 2003). At large Re, operator conditioning issues limited accurate computations when targeting eigenmodes near the branch intersection. Of the eigenmodes which could be targeted, only results for the leading mode ($i = 1$) will be discussed, given the importance of the TS wave in Q2D systems. However, targeting $i = 6$ often yielded much larger improvements in growth rates, even at weakly subcritical Re.

An example optimal modulation (for $i = 1$) at a weakly subcritical $r_{\mathrm{c}} = 0.9$ is considered in Fig. 3.10, before the details of the optimization scheme are provided. Note that the aim of the optimization procedure is to shift at least one (target) eigenvalue into the upper half plane with the minimum modulation norm ζ. Figure 3.10(a) depicts eigenvalue spectra for the reference and modulated base flows. From the scale of the plot, it is difficult to observe the shift in the target (leading) eigenmode, whereas there is clear movement of the far more sensitive eigenvalues near the branch intersection. Figure 3.10(b) zooms in on a section of the eigenvalue spectrum, and highlights that the target leading eigenvalue is just unstable (has crossed into the positive half plane),

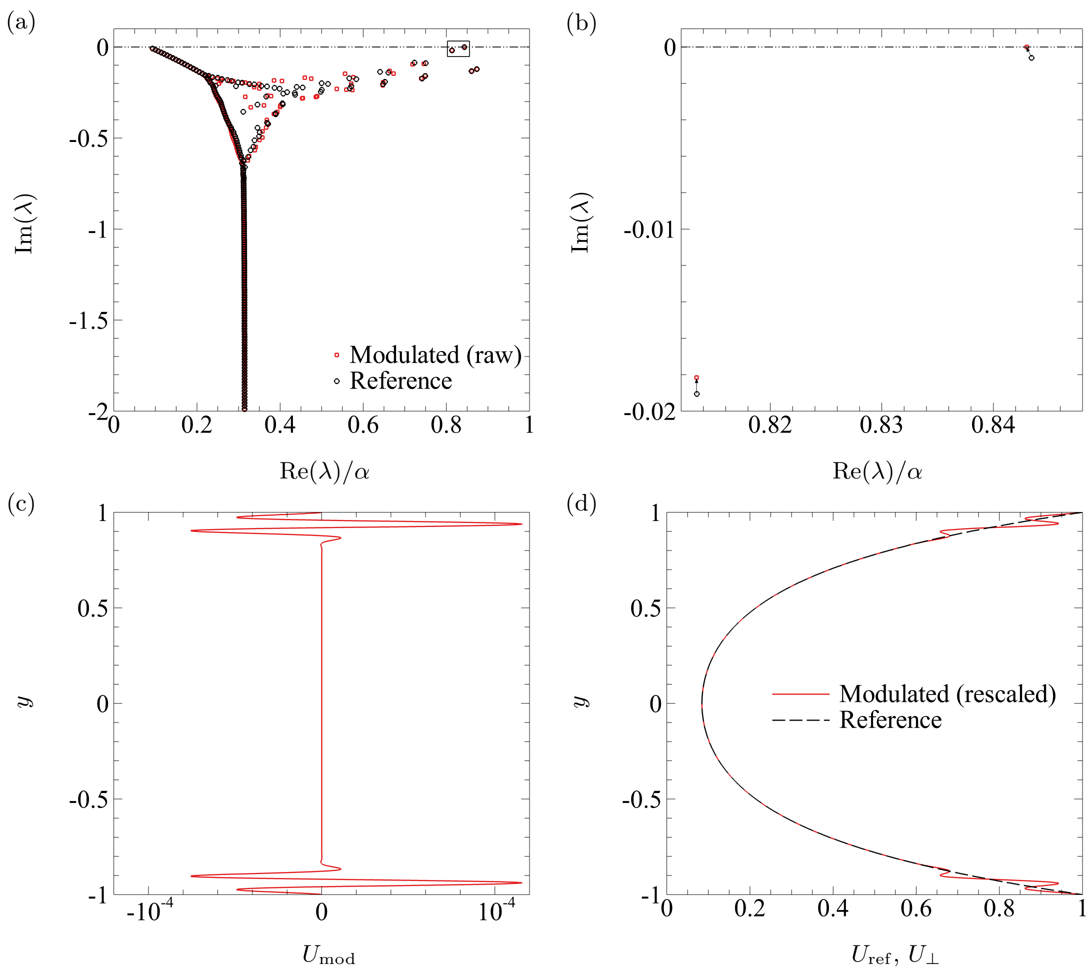

FIGURE 3.10: Optimized base flow modulation at $r_c = 0.9$ for the Shercliff flow profile at $H = 10$, with $\zeta = 8.1225 \times 10^{-10}$, targeting the leading eigenmode. (a) Eigenvalue spectrum for the reference and optimally modulated base flow. (b) Zoomed view of the rectangular region of the eigenvalue spectrum in (a), with arrows indicating the shift of the eigenvalues. Note the leading eigenvalue just crosses into the complex half plane with this ζ. (c) The optimal base flow modulation. (d) The reference base flow U_{ref}, compared to the total base flow $U_\perp = U_{\mathrm{ref}} + 1000U_{\mathrm{mod}}$, where the modulation is arbitrarily rescaled by a factor of 1000 for visibility; see (c) for the raw magnitude of the modulation.

with any modulation norm $\zeta \geq 8.1225 \times 10^{-10}$ for this Re, in Shercliff flow at $H = 10$. Note that the modulated base flow maximizes growth at $\alpha_{\max} = 0.988264$, rather than $\alpha_{\max} = 0.979651$ (the difference in α grows with decreasing Re), with some slight implications for direct numerical simulation. The raw base flow modulation designed to target the leading eigenmode is provided in Fig. 3.10(c), and exhibits near zero magnitude over most of the duct, to minimize the energy norm. Due to its small magnitude, the modulation is arbitrarily rescaled for the sake of visualization, and the total modulated base flow shown in Fig. 3.10(d), relative to the reference profile. Without the rescaling both profiles would be indistinguishable by eye, yet even such a slight change in the base flow is capable of driving an eigenvalue to the positive half plane.

The minimal defect computation is as follows. Variations to the base flow $U_\perp + \delta U_\perp$, eigenvalue $\lambda + \delta\lambda$ and eigenvector $\tilde{v}_\perp + \delta\tilde{v}_\perp$ are introduced into Eq. (3.12). Taking the inner product of Eq. (3.12) with the adjoint eigenvector $\hat{\xi}_\perp$ yields (Bottaro *et al.* 2003),

$$\begin{aligned}\frac{\delta\lambda}{\alpha}\int_{-1}^{1}\hat{\xi}_\perp^* \mathscr{L}\tilde{v}_\perp\,\mathrm{d}y &= \int_{-1}^{1}\delta U_\perp\left[\hat{\xi}_\perp^*\mathscr{L}\tilde{v}_\perp - \frac{\partial^2(\hat{\xi}_\perp^*\tilde{v}_\perp)}{\partial y^2}\right]\mathrm{d}y \\ &= \int_{-1}^{1}\delta U_\perp G_{\mathrm{U}}\,\mathrm{d}y \end{aligned} \tag{3.36}$$

where $\mathscr{L} = \partial^2/\partial y^2 - \alpha^2$ and $*$ represents complex conjugation as before, and where G_{U} is the linear response of an eigenvalue, corresponding to eigenvector $\tilde{v}_\perp$, to a change in the base flow, $\delta\lambda/\alpha = (G_{\mathrm{U}}, \delta U_\perp)$. $\hat{\xi}_\perp$ is normalized to ensure the left most integral of Eq. (3.36) evaluates to unity.

Selecting the i'th eigenmode, and for a given ζ, the largest change in λ_i is attained by rendering the functional (Bottaro *et al.* 2003; Nouar & Bottaro 2010)

$$f := \lambda_i + \chi\left(\int_{-1}^{1}(U_\perp - U_{\mathrm{ref}})^2\,\mathrm{d}y - \zeta\right) \tag{3.37}$$

stationary with respect to $\delta U_\perp$, where χ is a Lagrange multiplier enforcing Eq. (3.35). Setting $\delta f/\delta U_\perp$ to zero, and with $\delta\omega = (G_{\mathrm{U}}, \delta U_\perp)$, gives

$$0 = \mathrm{Im}(G_{\mathrm{U}}) + 2\chi(U_\perp - U_{\mathrm{ref}}). \tag{3.38}$$

Thus, the modulated profile $U_{\mathrm{mod}} = U_\perp - U_{\mathrm{ref}} = -\mathrm{Im}(G_{\mathrm{U}})/2\chi$ is directly related to the imaginary part of the eigenvalue sensitivity G_{U}, where from Eqs. (3.35) and (3.38),

$$\chi = \left(\frac{1}{4\zeta}\int_{-1}^{1}\mathrm{Im}(G_{\mathrm{U}})^2\,\mathrm{d}y\right)^{1/2}. \tag{3.39}$$

The optimal modulation is iteratively computed with an under-relaxed scheme (Nouar & Bottaro 2010), to ensure the same eigenmode is always tracked through the complex half plane.

Minimal defect theory thereby forms a simple means of ensuring growth of even infinitesimal perturbations at subcritical Reynolds numbers. However, the large 'gap' in the theory regards how the base flow becomes modulated in the first place. Originally, minimal defect theory proposed that a base flow modulation could account for finite amplitude uncertainty in an experimental setup, due to imperfect wall boundary conditions or measurement error (Bottaro *et al.* 2003). If the uncertainty were larger than the norm ζ, then the experimental setup may actually be operating at a supercritical Reynolds number (relative to the modulated profile), even when the experimentalist sets a flow rate corresponding to a subcritical Reynolds number (relative to the reference profile). This could then explain the appearance of turbulence at subcritical Reynolds numbers. However, in a purely computational environment, where such factors do not exist, the base flow can only be modulated by nonlinear interactions. Even simplified models of turbulence involve some modulation, feedback, or regeneration of modulations of the base flow (Biau & Bottaro 2009; Lozano-Durán *et al.* 2021). However, there is not necessarily a simple means of computing the higher wave number ($\kappa \geq 1$) modes necessary to nonlinearly generate a minimal defect. Furthermore, an optimal modulation only guarantees the improved growth rate of a single eigenmode, an eigenmode which may have little to do with the base flow regeneration process. Thus, depending how the modulation interacts with other eigenmodes, and how eigenmodes interact with one another, this could hamper the ability to regenerate the optimal modulation. It would indeed be beneficial if the feedback loop were far simpler. If the modulation improved the growth of the (targeted) leading eigenmode, and the leading eigenmode were then almost solely responsible for generating/regenerating the base flow modulation (through nonlinear interaction/production), a simple route to turbulence could be foreseen, as once the modulation is sufficient to ensure the leading eigenmode has a positive growth rate, the system should runaway to turbulence. However, as this process occurs (i.e. while the base flow modulation is being generated by the leading eigenmode, and the feedback process is beginning to improve the growth rate of the leading eigenmode), other mechanisms are required to offset the initial decay of the leading eigenmode. Such processes are at the heart of weakly nonlinear analysis, as follows.

3.5.2 Weakly nonlinear analysis

Weakly nonlinear analysis revolves around the leading eigenmode. Specifically, interest is in the leading eigenmode and a truncated set of its nonlinear interactions (Schmid & Henningson 2001; Moresco & Alboussiére 2003; Drazin & Reid 2004; Hagan & Priede 2013b), one of which will be the base flow modulation we desire. These interactions may often be referred to as modes, but it is worth making the clear distinction that these interactions do not have anything to do with any of the other eigenmodes of the linear operator. The term harmonics will be henceforth used to denote these nonlinear interactions. Note that for weakly nonlinear analysis to remain accurate, the leading eigenmode and its harmonics must have growth rates outstripping those of the other eigenmodes. Thus, for the purpose of identifying bifurcations in this work, weakly nonlinear analysis is performed at Reynolds number, wave number combinations just inside the neutral stability curve, resulting in growth rates of the leading mode which are just slightly positive (order 10^{-7} at most) and ensuring all other eigenmodes decay. Depending on α and Re, one of two bifurcations in the amplitude-Reynolds number space ($|A|$-Re) could be identified. A supercritical bifurcation corresponds to a point in $|A|$-Re space at which, for smaller Re, only one stable amplitude exists (zero), and at larger Re, the amplitude of the stable solutions continuously increases (a finite amplitude is stable). Conversely at Re past a subcritical bifurcation, the amplitude of the stable solution discontinuously increases, while at smaller Re, two stable amplitudes exist in the vicinity of the subcritical bifurcation point (zero and finite amplitude; the stable finite amplitude continuously increasing with reducing Re).

To properly explain the roles of the harmonics in the weakly nonlinear process, it is instructive to begin with the Stuart–Landau equation (Landau 1944; Stuart 1958; Drazin & Reid 2004),

$$\frac{\partial |A|^2}{\partial t} = 2\mu_1(Re - Re_{\mathrm{c}})|A|^2 - \mu_2|A|^4, \tag{3.40}$$

which governs the magnitude of the complex amplitude A of the leading eigenmode, with $|Re - Re_{\mathrm{c}}| \ll 1$. As written, the equation is truncated to include only the linear term, where $\mu_1(Re - Re_{\mathrm{c}})$ is the linear growth rate correction, and the first nonlinear term, where μ_2 is the first Landau coefficient (there may be infinitely many other Landau coefficients, but under certain circumstances they can be neglected). Even with just these two terms, four non-trivial behaviors are observed; trivial results are $\mu_2 = 0$, resulting in linear behavior, and $\mu_1 = \mu_2 = 0$, describing neutral stability. Only two of the four non-trivial behaviors are viable routes to either turbulence, or similarly chaotic dynamics, with the discussion following Drazin & Reid (2004).

- $\mu_1(Re-Re_{\mathrm{c}}) > 0$ and $\mu_2 > 0$ or supercritical stability (not turbulent). As the base flow is linearly unstable, positive μ_1 forces growth from the laminar fixed point.

Initially linear growth leads to an increase in perturbation amplitude, which is attenuated by the leading nonlinear term, recalling the negative sign in front μ_2 in Eq. (3.40). The perturbed flow is thus nonlinearly (or supercritically) stable, and saturates to an equilibrium amplitude. If this equilibrium amplitude A_e is not large (e.g. not order unity), higher order terms may not be required in Eq. (3.40). In this case, the equilibrium amplitude depends only on the relative magnitudes of $\mu_1(Re - Re_\mathrm{c})$ and μ_2, as $|A_\mathrm{e}| = [2\mu_1(Re - Re_\mathrm{c})/\mu_2]^{1/2}$. Such a supercritcally (nonlinearly) stable laminar flow is independent of the initial condition, excepting phase differences for travelling wave states.

- $\mu_1(Re - Re_\mathrm{c}) < 0$ and $\mu_2 > 0$ or subcritical stability (not turbulent). With μ_1 negative, the initial perturbation linearly decays toward the laminar fixed point. This decay is exacerbated by the leading nonlinear term, further hastening decay toward the laminar fixed point. Technically, subcritical stability can be observed at $Re > Re_\mathrm{c}$ if at a wave number outside the neutral curve. Thus, subcritical stability really implies $\mu_1(Re - Re_\mathrm{marg}) < 0$, where Re_marg is the Reynolds number intersecting the neutral stability curve at the α of interest.

- $\mu_1(Re - Re_\mathrm{c}) > 0$ and $\mu_2 < 0$ or supercritical instability (turbulent). Again the base flow is linearly unstable, and positive μ_1 generates exponential growth from the laminar fixed point. This is assisted by the nonlinear term, resulting in super-exponential growth as the amplitude rapidly increases. Once the amplitude is of order unity, higher order terms must be included to prevent breakdown of the solution. One could argue that this forms the simplest route to turbulence, as the large amplitude solution is able to simply excite and energize more and more harmonics, meeting the large state space requirement of turbulence. Note for this case that the transition to turbulence does not have a double E_0-Re threshold (where E_0 is the finite initial perturbation energy), as exponential growth can excite an infinitesimally small initial perturbation. Thus, there is only a single transition threshold parameter, Re.

- $\mu_1(Re - Re_\mathrm{c}) < 0$ and $\mu_2 < 0$ or subcritical instability (turbulent), and the scenario of greatest interest to this work. Interestingly, in fully 3D hydrodynamic transitions, a bypass route to turbulence is often observed, which does not revolve around the leading eigenmode (Zammert & Eckhardt 2019). However, the leading eigenmode is intrinsic to the Q2D transitions in Chapter 7, hence the interest in this subcritical instability scenario. Linearly, a finite amplitude perturbation would decay toward the finite amplitude fixed point. However, as $\mu_2 < 0$, the first nonlinear term is generating growth in amplitude. The question then becomes whether nonlinear growth outweighs linear decay, which is a function only of the initial amplitude. Below a critical initial amplitude $|A_c| = [2\mu_1(Re - Re_c)/\mu_2]^{1/2}$, nonlinear growth reduces the rate of perturbation decay, but is ultimately insufficient in preventing decay back to the laminar fixed point. However, for initial amplitudes greater than $|A_c|$, nonlinear growth outpaces linear decay, eventually leading to solution breakdown at large times, similar to the supercritical instability scenario. Once the amplitude grows to order unity (although the growth is not super-exponential any more), all higher harmonics become energized, thus possibly generating a turbulent flow. However, given the slow growth, higher order terms may become relevant at amplitudes below unity in an observable manner. This may be of relevance as the transition scenarios observed in Chapter 7 often depict the energization of an increasing number of modes toward the time of transition (although the growth is rarely slow). Note that although the expressions for A_e and A_c are identical, they represent the opposite behaviors (A_c delineates initial conditions which exhibit either net decay or growth, while A_e is a saturation amplitude).

The subcritical instability scenario is of greatest interest to this work, although it is interesting to consider a slight complexity. Instead of assuming that the initial condition is the leading eigenmode, one could instead apply a nonmodal instability exciting the leading eigenmode at a later time. It would then be at that later time that the perturbation amplitude should be compared to the critical 'initial' amplitude of the subcritical scenario. At that point in the evolution, if the current amplitude were below the critical amplitude, decay to the laminar fixed point would be expected. However, if the current amplitude exceeded the critical amplitude, instability and a transition to turbulence would follow. Effectively exciting the leading eigenmode (e.g. via the leading adjoint eigenmode) at a later time would then be exceedingly important for efficient subcritical transitions to turbulence. The flow state when the leading eigenmode (and its weakly nonlinear iteractions) reach the critical 'initial' amplitude may then represent an exact coherent structure on an edge manifold. Evolution would continue along the edge manifold, approximately maintaining this critical amplitude with a departure at the edge state (saddle point) toward turbulence if the perturbation has an amplitude just above the critical amplitude (with a return to the laminar fixed point for an amplitude slightly below critical). Such an edge state would then be predominantly composed of only three harmonics (0 through 2), based around the TS wave (harmonic 1).

A second complexity can also be introduced to the subcritical scenario. Although weakly nonlinear analysis involves the excitation of higher harmonics, it also modulates lower harmonics, and thereby modulates the base flow. Conceivably, this could couple back to the leading eigenmode, altering its growth rate, such that μ_1 is then also time and amplitude dependent (usually only μ_2 contains such effects). In particular, a scenario could be envisaged where this coupling, having altered μ_1, further improves feedback to the base flow, which further increases μ_1, before eventually μ_1 becomes positive, and the subcritical growth scenario becomes supercritical (relative to the modulated base flow).

Details of the weakly nonlinear calculations up to the second harmonic follow, as the subcritical transition scenario, and particularly the transitions observed in Chapter 7, are predominantly governed by the zeroth through second harmonics. The full weakly nonlinear calcuations, up to the third harmonic, were performed to determine the bifurcation type (e.g. subcritical or supercritical) along the neutral curve, as detailed in Chapter 6 (Camobreco *et al.* 2021b). However, interest is often in α-Re locations further from the neutral curve, and at these points, the computations along the neutral curve are a guide at best, although they do help rule out supercritical stability as an explanation for the lack of observed transitions at low H in Chapter 6 (Camobreco *et al.* 2021b). Fig. 3.11 depicts an example neutral curve for $H = 10$ Shercliff flow and indicates the sign of μ_1 and μ_2 just inside the neutral curve. From Fig. 3.11(a), $\mu_1(Re - Re_{\mathrm{marg}})$ is everywhere positive, as μ_1 is only negative in regions where $Re - Re_{\mathrm{marg}}$ is also negative, recalling all computations are performed just inside the neutral curve. Thus, the sign of μ_2 alone defines whether the flow is supercritically stable or unstable just inside the neutral curve, being supercritically unstable where μ_2 is positive, and supercritically stable where μ_2 is negative (only a small region along the lower branch). The five most commonly investigated α-Re points are also marked on Fig. 3.11, indicating that these locations are all likely subcritically unstable (4 markers), or supercritically unstable (1

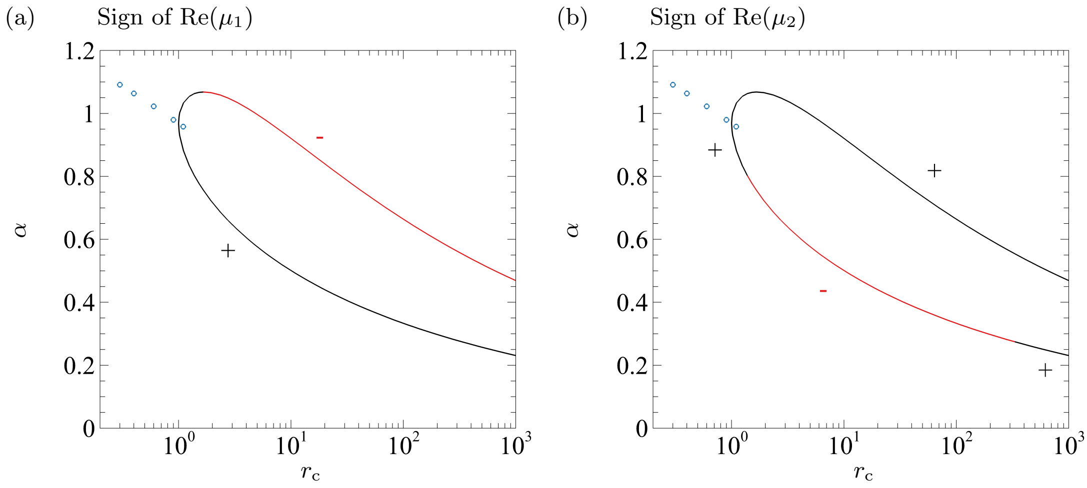

FIGURE 3.11: Bifurcation behavior along the neutral stability curve as a function of Reynolds number, for the Shercliff flow profile at $H = 10$. (a) Indication of the sign (black: positive, red: negative) of the linear growth rate correction coefficient, $\mathrm{Re}(\mu_1)$. (b) Indication of the sign of the Landau coefficient, $\mathrm{Re}(\mu_2)$. Anywhere where both $\mathrm{Re}(\mu_1)$ and $\mathrm{Re}(\mu_2)$ are positive indicates an achievable subcritical bifurcation. The five markers indicate the most commonly investigated parameter combinations in this work, in Chapters 6 (Camobreco *et al.* 2021b) and 7.

marker). For the full details of the weakly nonlinear computations, see Hagan & Priede (2013b) and Chapter 6 (Camobreco *et al.* 2021b).

The weakly nonlinear computations follow. Note that the weakly nonlinear computations are numerically simplified by a different scaling to that used previously. The eigenvalues and eigenvectors in the preceding sections were λ and $\hat{v}_\perp$, in this section, the equivalent eigenvalues and eigenvectors are ω and $\hat{w}_\perp$, respectively. These translate through $\lambda = -\mathrm{Im}(\omega)/(Re\alpha) + \mathrm{i}\mathrm{Re}(\omega)$ and $\hat{v}_\perp = Re\hat{w}_\perp$ (in the latter, normalization renders the change in definition irrelevant, for all except the zeroth harmonic).

To perform weakly nonlinear analysis, the amplitude dependence of the (leading) eigenmode $\hat{w}_{\perp,n}(y) = \hat{w}_\perp(y)e^{\mathrm{i}\alpha n x}$ is expanded as a sum of its harmonics

$$\hat{w}_{\perp,n} = \sum_{m=0}^{\infty} \epsilon^{|n|+2m}\tilde{A}^{|n|}|\tilde{A}|^{2m}\hat{w}_{\perp,n,|n|+2m}, \tag{3.41}$$

where $\hat{w}_{\perp,n,|n|+2m}$ denotes an individual harmonic (specifically, the first subscript is its harmonic number, the second its amplitude), and where $\tilde{A} = A/\epsilon$ is the normalized amplitude. Nonlinear interaction between the leading eigenmode $\hat{w}_{\perp,1,1}$ and itself excites a second harmonic $\hat{w}_{\perp,2,2}$. Nonlinear interaction between the leading eigenmode $\hat{w}_{\perp,1,1}$ and its complex conjugate $\hat{w}_{\perp,-1,1}$ generates a modification to the base flow $\hat{u}_{\perp,0,2}$ (Hagan & Priede 2013b). Details for computation of $\hat{u}_{\perp,0,2}$, $\hat{w}_{\perp,1,1}$ and $\hat{w}_{\perp,2,2}$ are relegated to Chapter 6 (Camobreco *et al.* 2021b). In the subcritical transition scenario, $\hat{w}_{\perp,1,1}$ will be a TS wave, while ω_1 will be complex, with a negative growth rate. If the weakly nonlinear perturbation $\hat{w}_{\perp,2,2}$ exceeds the critical amplitude, the second harmonic may generate sufficient perturbation energy growth to both offset the decay of the leading eigenmode, and drive the flow toward turbulence. However, it is important to note that $\hat{u}_{\perp,0,2}$ can also modify the growth rate of the leading eigenmode, in a manner similar to that proposed by minimal defect theory.

As the effect of $\hat{u}_{\perp,0,2}$ on the growth rate of $\hat{w}_{\perp,1,1}$ is not directly included in the weakly nonlinear analysis, due to the time dependence of the base flow modulation $\hat{u}_{\perp,0,2}$ (i.e. $\hat{w}_{\perp,1,1}$ is based solely on the time steady U_{ref}) it shall be briefly considered here. Thus, the effect of $\hat{u}_{\perp,0,2}$ on $\hat{w}_{\perp,1,1}$ is shown in Fig. 3.12, computed as discussed in Chapter 6 (Camobreco *et al.* 2021b), and recalling Fig. 3.10 for comparison between the optimal and weakly nonlinear modulations. The eigenvalue spectrum with the frozen modulated base flow $U_{\perp} = U_{\mathrm{ref}} + \hat{u}_{\perp,0,2}$, where $\hat{u}_{\perp,0,2}$ is scaled to norm $\zeta = 2.2137 \times 10^{-7}$, indicates the possibility of linear growth of the leading eigenmode, without support from its weakly nonlinear interaction $\hat{w}_{\perp,2,2}$. Given how small ζ is, weakly nonlinear modulations may still be able to provide access to supercritical transition scenarios, if the modulated profile provides exponentially growing eigenmodes, even when at subcritical *Re* (relative to the reference profile). More importantly, the means of generating and regenerating the weakly nonlinear modulation, solely via the leading eigenmode, is clear (and possibly quite efficient, given how self contained the system is), unlike the minimal defect.

This concludes the discussion of the various transition processes investigated in this work, which were: supercritical modal, subcritical nonmodal and finally optimally or weakly nonlinearly modulated. The final sections of the introduction will discuss the current state of the art in predicting the routes and Reynolds number thresholds for both hydrodynamic and MHD turbulent transitions, and then concludes with a brief discussion of some of the key features of established turbulent states.

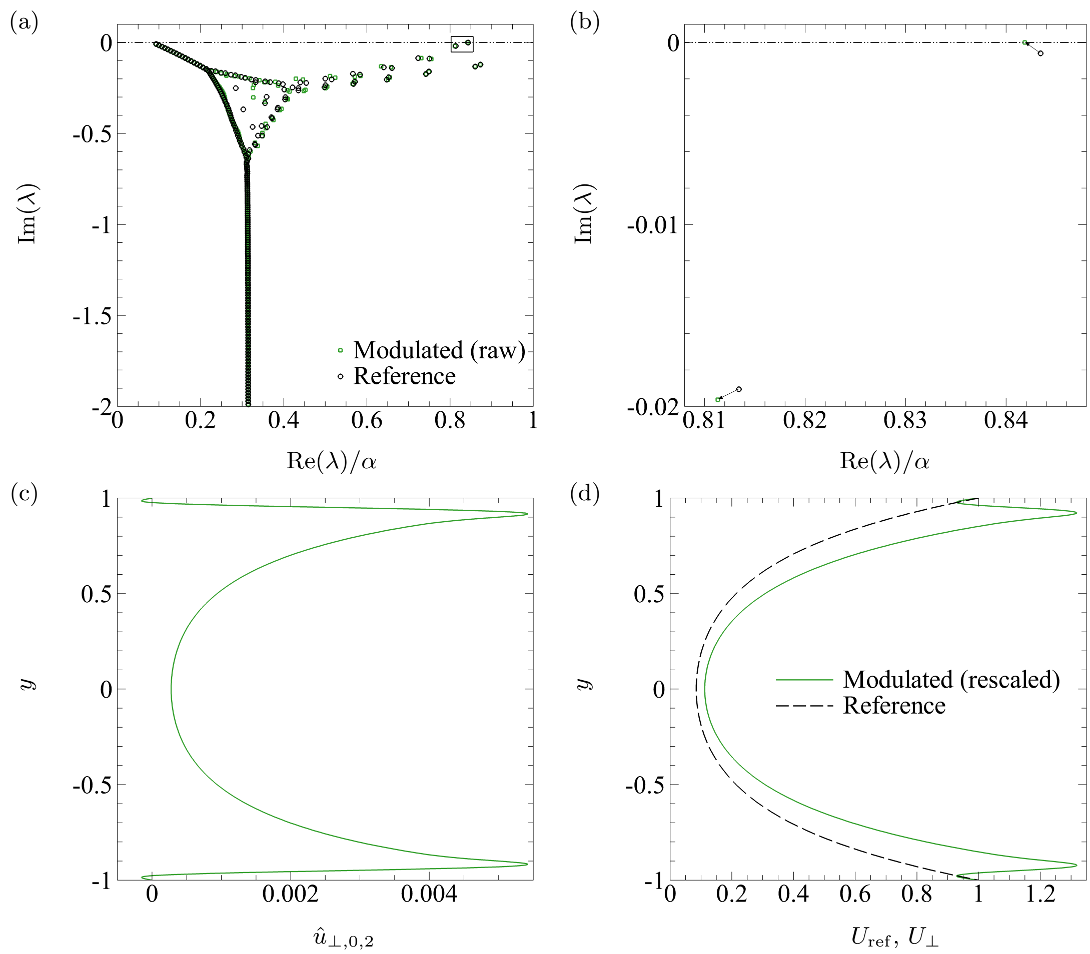

FIGURE 3.12: Weakly nonlinear modulation (wave number optimized) at $r_{\mathrm{c}} = 0.9$ for Shercliff flow at $H = 10$, with $\zeta = 2.2137 \times 10^{-7}$, targeting the leading eigenmode. (a) Eigenvalue spectrum for the reference and weakly nonlinearly modulated base flow. (b) Zoomed view of the rectangular region of the eigenvalue spectrum in (a), with arrows indicating the shift of the eigenvalues. Note the leading eigenvalue just crosses into the complex half plane with this ζ. (c) The weakly nonlinear base flow modulation $\hat{u}_{\perp,0,2}$. (d) The reference base flow U_{ref}, compared to the total base flow $U_{\perp} = U_{\mathrm{ref}} + 100\hat{u}_{\perp,0,2}$, where the modulation is arbitrarily rescaled by a factor of 100 for visibility.

3.6 Predicting and observing turbulent transitions; a literature review

This work has two overarching motivations. The first, of theoretical interest, regards how quasi-two-dimensional duct flows transition to turbulence, particularly at subcritical Reynolds numbers. The previous sections have introduced various tools to analyse how *laminar* perturbations may give rise to turbulence. From a theoretical point of view, it is unlikely that turbulent (or random) perturbations, excluding those at vanishingly small energy, are as useful in truly understanding the process of a laminar-turbulent transition. For how can the route *to* turbulence be found, if a turbulent initial condition is applied? However, the current understanding of subcritical routes to turbulence generated by purely laminar perturbations still leaves much to be desired. Nonlinear transient growth has begun to improve the overall level of understanding, but there is still much to elucidate. Hence, the first theoretical motivation of this work.

There is, of course, a great deal of work on subcritical transition thresholds, where turbulent (or a mix of laminar and turbulent) initial conditions are applied. With turbulent perturbations (i.e. perturbations obtained by decomposing the instantaneous flow at a higher Reynolds number, which produced turbulence, and adding this higher Re turbulent perturbation onto a base flow at a lower Re), or white noise perturbations, these works manage to obtain excellent agreement between DNS and experiments, with two case studies discussed below. Given the second, practical motivation of this work, of efficiently triggering turbulence in operating coolant duct flows, it is important to introduce these works, as they form a practical means of generating sustained turbulence. However, it is still an open question whether the route to Q2D turbulence is purely Q2D, or is via short-lived 3D turbulence, which may also depend on the magnetic field strength and/or aspect ratio. Which route to turbulence is more efficient, in terms of both E_0 and Re, is also unknown.

3.6.1 Case Study 1: Hartmann channel flow

The first case study regards Hartmann channel flow (Hartmann 1937). The Hartmann channel setup differs from the duct setup, as it does not have Shercliff walls. To numerically achieve such a setup, the parallel (y) direction would also have periodic boundary conditions applied, in the same manner as the streamwise direction. Experimentally, behavior similar to a Hartmann channel was achieved by applying high magnetic field strengths (> 4 T was sufficient, with field strengths up to 13 T tested) in an annular configuration (Moresco & Alboussiére 2004). At these high field strengths, secondary flows are not overly relevant. By comparing the experimentally measured wall friction relative to that of a laminar flow solution, Moresco & Alboussiére (2004) were able to obtain a fairly sharp Reynolds number $R_{\mathrm{H}} = Re/Ha \approx 380$ demarcating the transition to turbulence. R_{H} is the Reynolds number based on the Hartmann boundary thickness, and is the relevant non-dimensional parameter when Ha is large. The transition threshold for Re was only weakly dependent on magnetic field strength over the range $130 < Ha < 1690$.

With an experimental transition threshold to validate against, Krasnov *et al.* (2004) numerically tested a hypothesized two-step transition process, put forward for hydrodynamic shear flows, in an attempt to match transition at $R_{\mathrm{H}} \approx 380$. The two-step transition process is as follows (Schmid & Henningson 2001; Krasnov *et al.* 2004):

- A laminar roll, or streamwise invariant linear transient growth optimal, is seeded onto the laminar base flow, with small (but finite) initial energy. Growth of the finite energy linear optimal modulates the laminar base flow. Note that the laminar roll is optimized for maximum linear growth over target times and both wave numbers perpendicular to the magnetic field. The laminar roll is streamwise invariant as the optimal streamwise wave number was zero.

- The base flow, once sufficiently modulated (at $t > 0$) becomes linearly unstable with respect to fully three-dimensional perturbations. Application of small, but again finite, 3D noise triggers a transition to fully fledged turbulence.

As a brief aside, note two key differences between theirs and the present work. First, with a Q2D domain, the second stage of the transition process cannot be replicated. Interestingly, turbulence is still able to be triggered in Q2D flows regardless of this fact, as shown in Chapter 7. Second, Q2D streamwise invariant flow features can only decay (so a streamwise invariant solution is no longer optimal), with linear transient growth greatly reduced without amplification by three-dimensional growth mechanisms.

The results of Krasnov *et al.* (2004), regarding the first stage of the transition process, are as follows. The initial energy of the 2D laminar roll was varied between 10^{-5} and 10^{-1}. The smaller the initial energy the larger the transient growth, with maximum energies approximately 30 and 1.4 times the initial energies of 10^{-5} and 10^{-1} at $R_{\mathrm{H}} = 200$, respectively. However, larger initial energy linear optimals generated larger base flow modulations. Base flow modulation proved so important for the second stage of the transition process that the magnitude of any linear growth in the first stage did not appear to be particularly relevant (although only if local inflection points formed in the base flow profile). The insignificance of transient growth, and the importance of base flow modulation, are clear themes of this work, particularly in Chapter 7.

Three dimensional noise was then applied in Krasnov *et al.* (2004)'s numerical simulations. Interestingly, the effect of the noise was not observable until well after it had been applied, and was always observed after the time of maximum growth of the two-dimensional streamwise invariant linear optimal (even if the 3D noise is applied at $t = 0$ with the linear optimal). Although the magnitude of the 3D noise required to trigger transition varied with Re, it became small quickly. For example, at the admittedly supercritical $R_\mathrm{H} = 1000$ ($r_\mathrm{c} \approx 2.63$), 3D noise of amplitude 1.5×10^{-14} was sufficient to trigger turbulence. However, without this 3D noise, turbulence was not triggered (e.g. numerical truncation 'noise' was insufficient), even at supercritical conditions.

Finally, Krasnov *et al.* (2004) attempted to match the threshold Reynolds number of Moresco & Alboussiére (2004) at $Ha = 10$, testing initial energies of the streamwise invariant optimal up to 10^{-1}, and for the 3D noise up to 10^{-3}. For $R_\mathrm{H} < 350$, turbulence was not triggered at the largest initial energies tested. For $R_\mathrm{H} > 400$, transition could always be achieved, so long as the initial energy of the streamwise invariant optimal was sufficient to generate inflection points in the modulated base flow. For $350 < R_\mathrm{H} < 400$, there was an initial energy for the first stage streamwise optimal below which second stage three-dimensional noise of any tested magnitude could not trigger turbulence, but above this (R_H dependent) initial energy threshold turbulence could be observed. However, the instability and transition could not be correlated to the formation or lack of inflection points in the modulated base flow in this regime. To further improve the match with Moresco & Alboussiére (2004), Zienicke & Krasnov (2005) simulated $Ha >$ 10. With increasing Ha, the first Re for which turbulence could be triggered increased weakly. At $Ha = 10$, 40 and 100, the corresponding R_H required to observe turbulence were $R_\mathrm{H} = 350$, 370 and 390, respectively. The agreement at larger Ha, between the DNS of Zienicke & Krasnov (2005) and experiments of Moresco & Alboussiére (2004) was excellent, with slight differences assumed due to wall roughness. Thus, the two-stage process appeared a promising contender for describing the turbulent transition in this regime. Note that at all these conditions the interaction parameter was small, with $N < 1$. Thus, the transitions in these regimes were far from exhibiting Q2D dynamics, but were transitions of strongly three-dimensional MHD flows in a channel setup.

Analysis of turbulent transitions in a numerical setup closer to the duct setup approximated in this work was performed in Krasnov *et al.* (2008). The magnetic field was aligned with the y direction (spanwise), however, the y direction was periodic, unlike for a duct flow. With this modification, the linear transient growth optimal is no longer streamwise invariant at large Ha (at small Ha, $\alpha \to 0$ is still optimal). Instead with increasing Ha, the optimal spanwise wave number $\beta \to 0$. Thus, a two-dimensional Orr mode, with axis aligned with the magnetic field, became most efficient at generating linear transient growth as $Ha \to \infty$ (although the growth falls off as Ha^{-2}). The dependence of the transition process on the initial condition was also tested. With streamwise rolls ($\alpha = 0$, β), in the same manner as Krasnov *et al.* (2004), the addition of 3D noise to low energy 2D initial perturbations was unable to trigger turbulence, but above a certain initial (2D) energy, the 3D noise could trigger turbulence. With a single oblique wave (α, β), the transition process was more efficient, with turbulence triggered by initial energies as low as 100 times smaller, but ultimately 3D noise was still required to initiate the transition. However, with an initial condition of two oblique waves (α, β) and (α, $-\beta$), the three dimensional noise became unnecessary, with the initial perturbations all that were required to trigger turbulence. As each oblique wave mode could nonlinearly interact with the other, additional Fourier modes were quickly excited, and the flow developed a high degree of three-dimensionality that triggered a turbulent transition. Of particular note was the rapid excitation of the Orr mode (2α, $\beta = 0$) by the two oblique waves, so that a single oblique wave transition (for which 3D noise was required) also attained less growth than a dual oblique wave transition.

Purely Orr mode (α, $\beta = 0$) initial conditions were also tested in Krasnov *et al.* (2008). At sufficiently high Re, growth of the Orr mode was able to modulate the base flow. At $Ha = 100$ and with large initial energies, the Orr mode evolved into a purely 2D nonlineary stable finite amplitude state (simulated at the subcritical $Re = 5000$). A hydrodynamic equivalent to this finite amplitude state has been observed (Jiménez 1990). However, the application of 3D noise destabilized the nonlinearly stable 2D finite amplitude state, either preventing evolution toward the nonlinearly stable state, or inducing decay back to the laminar fixed point. As this behavior was observed for $Ha \geq 30$, Krasnov *et al.* (2008) tentatively concluded that if only Orr modes remain at high Ha, it would be unlikely they could generate turbulence. This thesis focuses on this latter point in particular, given the high Ha of fusion environments, and as the configuration investigated in this thesis is effectively the $Ha \to \infty$ (strictly 2D) limit of Krasnov *et al.* (2008). Much of this thesis is devoted to comparing the ability for Orr modes (which provide optimal Q2D transient growth) and TS wave eigenmodes (which maximize exponential growth) to generate and sustain turbulence. Indeed, with certain setup parameters, either Orr or TS wave modes will prove able to generate turbulence, while at other setup parameters, behaviors similar to Krasnov *et al.* (2008) will be observed (in which turbulence is either not generated, or not sustained).

3.6.2 Case Study 2: Hydrodynamic pipe flow

The second case study, indicating clear agreement between numerical and experimental results, and a distinct transition threshold, does not pertain to MHD flows. Findings presented in this section predominantly pertain to hydrodynamic pipe (Poiseuille) flow driven with a fixed flow rate based on the laminar profile $U_{\mathrm{p}}(r) = 1 - r^2$, and defined by a Reynolds number based on the mean flow velocity and pipe diameter. Experimentally, pipes were thousands of diameters long, permitting observations times of the order of 10^5 time units, while numerically, periodic pipes had lengths of the order of hundreds of diameters (observation times of the order of 10^4 time units). The precision of the Reynolds number threshold, below which sustained turbulence was not observed, was quite remarkable (to within $\approx \pm 0.5\%$ of the threshold value). Note that the Reynolds number threshold does not demarcate a transition per se, as the threshold was not shown to depend on initial energy (recalling the criteria for turbulent transitions in § 3.4 that this works follows). However, unlike the present work, the initial conditions considered in this second case study were turbulent (or chaotic); no laminar perturbations were investigated.

A distinct Reynolds number threshold was established by comparing two stochastic properties of turbulence (Avila *et al.* 2011). Specifically, if the mean lifetime of a turbulent region (e.g. a puff in the pipe flow lexicon) was shorter than its mean splitting time, then in the thermodynamic limit of large times, all turbulent regions should vanish (Avila *et al.* 2011), with the flow remaining laminar for all time thereafter (all Re being subcritical for pipe flow). This condition is equivalent to a greater probability for the decay of, rather than splitting of, a turbulent flow feature. The turbulent fraction (percentage of the domain occupied by turbulent flow features) is then zero, as the entire flow has returned to the laminar fixed point. By definition, all Re below the threshold Reynolds number have zero turbulent fraction (Barkley 2016). However, for all Re above the threshold, for which the probability of splitting is greater than the probability of decay, a non-zero turbulent fraction should, on average, exist. To show this, the Re dependence of the probabilities of decay and splitting events are required (Hof *et al.* 2006; Avila *et al.* 2011). Note that splitting is quite a harsh term, as at larger Re, the turbulent patches spread increasingly smoothly, with newly spawned turbulent regions difficult to identify (Avila *et al.* 2011; Avila & Hof 2013); this fits well with the criteria for turbulence introduced in § 3.4.

The probability for decay events was determined first, experimentally (Hof *et al.* 2006), and later numerically (Avila & Hof 2013). Characteristic lifetimes of turbulent puffs as a function of Reynolds number were determined. The probability P of observing a turbulent flow feature at a time t, when the same turbulent flow feature formed at the previous time t_0, took the form $P_{\mathrm{D}}(t, Re) = \exp[-(t - t_0)/\tau_{\mathrm{D}}(Re)]$, where only the characteristic lifetime τ_{D} is a function of Reynolds number. The exponential dependence indicated a memoryless process, in which the chance of decay does not depend on the lifetime of any individual turbulent region. Note that the time t_0, when a turbulent flow feature is observed to form, is not necessarily the seeding time of the initial turbulent perturbation. However it is important in ensuring the process is memoryless (Avila *et al.* 2011). As a memoryless process, like radioactive decay (half-life), the decay of a turbulent flow feature cannot be deterministically predicted. By ensemble averaging many realizations of the experiment (a pipe with length 7500 times the diameter) the characteristic lifetime was shown to exponentially depend on Reynolds number (Hof *et al.* 2006). This was contrary to previous predictions of an infinite characteristic lifetime for sufficiently large Reynolds numbers (Faisst & Eckhardt 2004; Peixinho & Mullin 2006). Thus, any turbulent flow feature is predicted to decay, eventually, at any finite Reynolds number, for a sufficiently (ludicrously) long pipe observed for a sufficiently long time. Alternately interpreted, the probability of a turbulent region surviving forever (against dissipation) asymptotically approaches unity with increasing Reynolds number. To clarify, when a turbulent flow feature splits, it should be thought of as one 'new' and one 'old' turbulent flow feature, although identifying which is which would not necessarily be possible at increasingly large Re (the generation of the 'new' flow features allows the turbulence as a whole to survive forever, although each individual turbulent region must eventually decay at finite Re).

With the dependence of the key characteristic time scale established, the dependence of key turbulent length scales was numerically assessed in Avila & Hof (2013). A similar approach was taken, with the probability of a turbulent flow feature having length $L > l$

taking the form $P_{\mathrm{T}}(t, Re) = \exp[(l - L_{\mathrm{T},0})/L_{\mathrm{T}}(Re)]$; laminar flow features had the same functional dependence, see Avila & Hof (2013) for the laminar/turbulent classification criteria. These scalings were determined to be independent of the pipe length and initial condition, and were considered to be an intrinsic property of the system in the thermodynamic limit. The Re dependence of the turbulent length scale L_{T} was found to be superexponential. Thus, turbulent flow features rapidly spread with increasing Re, until they dominate the entire domain. However, if the superexponential fit is extrapolated to larger Re it would still predict a continuous increase in L_{T} with Re. Thus, neither the characteristic turbulent length or time scales diverge with increasing Re. Therefore, a fully (100%) turbulent flow is predicted to be unattainable at finite Re, with the chance of even extreme relaminarization events always possible, however unlikely (although random and deterministically unpredictable).

However, this is only half the story, as to obtain a clear threshold Reynolds number, the Re dependence of both decay and splitting probabilities is required. Although each turbulent flow feature (puff) must inevitably decay, if it can split, and spawn multiple descendant turbulent puffs before it decays, the turbulent fraction of the flow can increase. Such predictions of the probability of spreading events, and computations of the turbulent fraction of the flow in the thermodynamic limit, have been performed for pipe (Avila *et al.* 2011), Taylor–Couette (Lemoult *et al.* 2016) and Waleffe (Chantry *et al.* 2017) flows. For pipe flows, Avila *et al.* (2011) show that the splitting probability has the same functional dependence as the decay probability $P_{\mathrm{S}}(t, Re) = 1 - \exp[-(t - t_0)/\tau_{\mathrm{S}}(Re)]$. Again, the splitting process is memoryless, with the splitting probability not depending on the lifetime of the turbulent flow feature, and depending solely on Re. Thus, the Reynolds number at which the characteristic lifetimes τ_{D} and τ_{S} intersect yields a threshold between flows which will be purely laminar in the thermodynamic limit if $\tau_{\mathrm{D}} < \tau_{\mathrm{S}}$ (decay faster than split), or intermittently turbulent if $\tau_{\mathrm{D}} > \tau_{\mathrm{S}}$ (split faster than decay). For pipe flow this threshold was observed at $Re \approx 2040$, based on a mean velocity and pipe diameter (Avila *et al.* 2011), and further supported with additional validation (Mukund & Hof 2018). With increasing Reynolds number, the turbulent fraction in the thermodynamic limit then continuously increases, asymptotically approaching unity (thus, less and less intermittency is observed with increasing Re). Note that the characteristic timescales at the threshold Reynolds number were of the order of 10^7, and with superexponential dependence on Re, meant that less than a one percent shift in Re would result in the splitting rate outweighing the decay rate by a factor of 4 (or vice versa). Thus, the threshold Reynolds number can be considered relatively distinct, and dependent only on the base flow profile of the laminar fixed point. Note also that although the characteristic timescales determined numerically and experimentally agreed well, numerical methods were of limited use near the threshold Reynolds number, given the time horizon required to reach a close approximation of the thermodynamic limit (Avila *et al.* 2011).

3.6.3 Case study summary

Hopefully, these two cases studies have highlighted two distinctly different means of predicting turbulent transitions, or threshold Reynolds numbers, to similar effect. Furthermore, these case studies highlight very different aspects of the dynamics underlying 3D transitions. However, to generate purely Q2D transitions, an alternate route to turbulence will be demonstrated, and specifically one which is distinctly different not only because it is Q2D, but also because the initial conditions are always purely laminar at subcritical Re. The use of laminar perturbations is partly driven by the strong theoretical foundations laid by Stuart and Landau (Landau 1944; Stuart 1958; Drazin & Reid 2004) in weakly nonlinear analysis. However, as mentioned earlier, it also concerns the sensibility of using turbulent initial conditions to analyse the route to turbulence, and allows a more detailed assessment of which features of the initial condition are important in either generating or sustaining turbulence. Furthermore, laminar perturbations can modulate the base flow at much slower timescales than turbulent flow features (Barkley 2016; Lozano-Durán *et al.* 2021), which may provide highly efficient routes to turbulence if the base flow is appropriately modulated.

3.7 Kinetic energy budgets and identifying turbulence via Fourier spectra

A significant portion of this thesis is devoted to analysing transitions to turbulence. For this reason, perturbations were defined relative to the laminar fixed point, $\hat{\boldsymbol{u}}_\perp = \boldsymbol{u}_\perp - \boldsymbol{U}_\perp$. This decomposition will be contrasted with the Reynolds decomposition, which is more common when analysing turbulent flows in engineering applications. However, the Reynolds decomposition is not used to analyse DNS results, for reasons to be discussed shortly. In particular, the perturbation decomposition is applied to compute Fourier spectra, to assess whether flows become turbulent (if they meet the criteria introduced in § 3.4).

This section also discusses some of the larger scale (domain averaged) measures of turbulence sustainment, given the practical motivations of this work, such as production-dissipation balances, and the role of the base flow in regard to this. Such concepts are not the most common when discussing turbulence sustainment. However, the conventional three-stage description of a self-sustaining turbulent process (Waleffe 1997) is not applicable to Q2D turbulence. The conventional sustainment process revolves around streamwise invariant rolls (structures which provide optimal transient growth in 3D, but only decay in Q2D), creating spanwise inflections (streaks) of the streamwise velocity, leading to fully 3D travelling waves. The interaction of the travelling waves and their complex conjugates regenerate the streamwise rolls, allowing the process to repeat indefinitely (as breifly discussed in § 3.5, the interaction of a travelling wave instability and its complex conjugate can generate a streamwise invariant base flow modulation in any generic, Q2D or 3D, flow). However, all stages of this conventional self-sustaining process are three-dimensional, and thus inapplicable to Q2D flows. Thus, as a Q2D sustainment mechanism cannot yet be described, this section is instead devoted to concepts generic to sustaining either Q2D or 3D turbulence, in particular, the turbulent kinetic energy budget, and the roles of dissipation and production.

Finally, before proceeding with said discussion, it is worth making some mention of the computational costs associated with the direct numerical simulations of Q2D transitions and turbulence to be performed. As quasi-two-dimensional flows are simulated on a 2D-meshed domain, it is compuationally most efficient to perform simulations on a single processor (as was the case for all simulations performed). These meshes required approximately 4 gigabytes of memory for the subcritical DNS presented in Chapters 5 (Camobreco *et al.* 2020) and 7, and approximately 8 gigabytes for the supercritical DNS presented in Chapters 6 (Camobreco *et al.* 2021b) and 8 (Camobreco *et al.* 2021a); extended up to 16 gigabytes of memory for the simulations presented in Appendix C. On a single processor, DNS to determine the edge state behaviour took approximately one week, while verification that finite amplitude states were stable, or that subcritical turbulence was sustained, took 6 to 12 months. Attempts to time average turbulent flows were simulated for well over 12 months, but had yet to converge. Although the domains were two dimensional, the large (order 10^5) Reynolds numbers required very small time steps for turbulent evolution, ultimately leading to computationally expensive direct numerical simulations, and to difficulties in extracting time-averaged information. The additional wall-normal resolution, due to the sharper gradients present in the base flows at higher friction parameters, was also a factor adding noticeable computational expense, particularly in terms of the time step size.

3.7.1 Reynolds-averaged Navier–Stokes

The are a few key differences between the laminar-perturbation and mean-fluctuation (Reynolds) decompositions. First, as introduced in § 3.1, the laminar base flow is independent of perturbation amplitude, whereas the mean flow is not, which had ramifications on the linearity of instantaneous energy growth. Second, following Pope (2000), the Reynolds decomposition defines fluctuations

$$\acute{\boldsymbol{u}}_\perp = \boldsymbol{u}_\perp - \langle \boldsymbol{u}_\perp \rangle, \tag{3.42}$$

of the instantaneous velocity field $\boldsymbol{u}_\perp$ about the time mean $\langle \boldsymbol{u}_\perp \rangle$, where $\langle \ldots \rangle$ represent taking the time mean unless stated otherwise. Thus, fluctuations have a time mean of zero, unlike perturbations which must include a time mean component, except in the unlikely event of $U_\perp = \langle \boldsymbol{u}_\perp \rangle$. Like perturbations, both the fluctuation and time mean satisfy $\boldsymbol{\nabla}_\perp \cdot \acute{\boldsymbol{u}}_\perp = 0$ and $\boldsymbol{\nabla}_\perp \cdot \langle \boldsymbol{u}_\perp \rangle = 0$. Substituting Eq. (3.42), into the final form of the SM82 momentum equations, Eq. (2.55), and time averaging the result, yields, in tensor notation, an evolution equation for the mean flow

$$\frac{\partial \langle u_{\perp j} \rangle}{\partial t} = -\langle u_{\perp i} \rangle \frac{\partial \langle u_{\perp j} \rangle}{\partial x_i} - \frac{\partial \langle \acute{u}_{\perp i} \acute{u}_{\perp j} \rangle}{\partial x_i} - \frac{\partial \langle p_\perp \rangle}{\partial x_j} + \frac{1}{Re} \boldsymbol{\nabla}_\perp^2 \langle u_{\perp j} \rangle - \frac{H}{Re} \langle u_{\perp j} \rangle. \tag{3.43}$$

The mean flow would evolve in an identical manner to the instantaneous flow if not for the Reynolds stress term, where the 4 (3 unique) component Reynolds stresses are $\langle \acute{u}_{\perp i} \acute{u}_{\perp j} \rangle$. This relatively innocuous Reynolds stress term is the reason why the Reynolds decomposition is not used in this work, as to determine the fluctuation in Eq. (3.42) at an observation time t_1, requires knowing the mean (time independent) flow $\langle \boldsymbol{u}_\perp \rangle$. The closure problem (Pope 2000) prohibits Eq. (3.43) from being expressed solely as a function of $\langle \boldsymbol{u}_\perp \rangle$. Thus, to compute $\langle \boldsymbol{u}_\perp \rangle$ requires averaging DNS results of the full SM82 equations, Eqs. (2.55) and (2.56), in theory to $t \to \infty$, to then have information about the fluctuation at the previous time t_1. As the Q2D turbulent flows in this work are at large Re, and exhibit intermittent turbulence, the time horizon required to obtain the time average flow to any useful accuracy is beyond practical computational limits. As a useful approximation of the mean flow $\langle \boldsymbol{u}_\perp \rangle$ is not feasibly attained, the laminar-perturbation definition $\hat{\boldsymbol{u}}_\perp = \boldsymbol{u}_\perp - \boldsymbol{U}_\perp$ is applied when the flow is turbulent.

In spite of this, it is still worth introducing the equation governing the time evolution of the fluctuation, and thereby the turbulent kinetic energy (TKE) of the fluctuation (in this work the perturbation kinetic energy will be the analogous quantity). Subtracting Eq. (3.43) from Eq. (2.55), and substituting Eq. (3.42) yields an evolution equation for the fluctuation

$$\frac{\partial \acute{u}_{\perp j}}{\partial t} = -\acute{u}_{\perp i}\frac{\partial \acute{u}_{\perp j}}{\partial x_i} - \acute{u}_{\perp i}\frac{\partial \langle u_{\perp j}\rangle}{\partial x_i} + \frac{\partial \langle \acute{u}_{\perp i}\acute{u}_{\perp j}\rangle}{\partial x_i} - \frac{\partial \acute{p}_\perp}{\partial x_j} + \frac{1}{Re}\boldsymbol{\nabla}_\perp^2 \acute{u}_{\perp j} - \frac{H}{Re}\acute{u}_{\perp j}, \quad (3.44)$$

where the Reynolds stress term now has the opposite sign, where the analagous equation for the perturbation is Eq. (3.6), and where $\acute{p} = p_\perp - \langle p_\perp \rangle$.

Taking the dot product of Eq. (3.44) with $\acute{u}_{\perp j}$, and time averaging, yields an equation for the turbulent kinetic energy

$$\begin{aligned} \frac{\partial \langle \acute{u}_{\perp j}\acute{u}_{\perp j}\rangle/2}{\partial t} + \langle u_{\perp i}\rangle \frac{\partial \langle \acute{u}_{\perp j}\acute{u}_{\perp j}\rangle/2}{\partial x_i} + \boldsymbol{\nabla}_\perp \cdot \Bigg[\frac{1}{2}\langle \acute{u}_{\perp i}\acute{u}_{\perp j}\acute{u}_{\perp j}\rangle + \langle \acute{u}_{\perp i}\acute{p}_\perp\rangle \\ - \frac{1}{Re}\left\langle \acute{u}_{\perp j}\left(\frac{\partial \acute{u}_{\perp i}}{\partial x_j} + \frac{\partial \acute{u}_{\perp j}}{\partial x_i}\right)\right\rangle\Bigg] = -\langle \acute{u}_{\perp i}\acute{u}_{\perp j}\rangle \frac{\partial \langle u_{\perp i}\rangle}{\partial x_j} \\ - \left[\frac{1}{2Re}\left\langle \left(\frac{\partial \acute{u}_{\perp i}}{\partial x_j} + \frac{\partial \acute{u}_{\perp j}}{\partial x_i}\right)\left(\frac{\partial \acute{u}_{\perp i}}{\partial x_j} + \frac{\partial \acute{u}_{\perp j}}{\partial x_i}\right)\right\rangle\right] - \frac{H}{Re}\langle \acute{u}_{\perp j}\acute{u}_{\perp j}\rangle/2, \quad (3.45) \end{aligned}$$

or

$$\frac{\partial k}{\partial t} + \langle u_{\perp i}\rangle \frac{\partial k}{\partial x_i} + \boldsymbol{\nabla}_\perp \cdot \acute{T}_i = \mathcal{P} - \epsilon_{\mathrm{D}} - \frac{H}{Re}k, \quad (3.46)$$

where k is the turbulent kinetic energy, $\acute{T}_i$ the turbulent transport terms (due to triple correlations, pressure and viscosity; first set of large square brackets), $\mathcal{P}$ the turbulent production and ϵ_{D} the turbulent dissipation (second set of large square brackets). Recall the analogous production term for perturbations introduced in Eq. (3.8), $-2\hat{u}_\perp \hat{v}_\perp \partial U_\perp/\partial y$. However, while only a single production term contributed to Q2D *perturbation* energy growth, there are four non-zero components contributing to Q2D turbulent *fluctuation* energy growth.

To sustain turbulence, or equally to maintain a given amount of TKE, requires that the production term $\mathcal{P}$ balances both the friction and dissipation terms $\epsilon_{\mathrm{F}} = \epsilon_{\mathrm{D}} + Hk/Re$, as the transport terms only redistribute TKE. Note that the only time dependence in the production term $-\langle \acute{u}_{\perp i}\acute{u}_{\perp j}\rangle \partial \langle u_{\perp i}\rangle/\partial x_j$ is in the fluctuations, as the true mean flow $\langle u_{\perp i}\rangle$ is time independent. Only the true time mean profile has sampled the turbulence (statistics) at all times, and so may be able to balance the dissipation of any of its instantaneously observed turbulent fluctuations.

In practice, sustaining turbulence is a fine balance. The modulated base flow produces TKE, to counteract dissipation and friction, while the turbulent fluctuations attempt to feedback and drive the modulated base flow toward its (unknown) time mean. This feedback from the turbulent fluctuations is represented by the Reynolds stress term in Eq. (3.43), or equally by noting that the production term $\mathcal{P}$ in Eq. (3.46) is not always positive (recall from § 3.3 that production from even the reference base flow can be both positive and negative, based on tilting into or opposite the base flow shear). Note that TKE is always reduced by dissipation and friction, while TKE can increase or decrease depending whether production is positive (and greater than ϵ_{F}), or negative. However, TKE lost to dissipation and friction is converted to heat (this heat is neglected), whereas TKE 'lost' due to negative production reappears as an increase in the energy of the modulated base flow profile, via the Reynolds stress term. Note also that production is a local quantity, and so regions of negative production can modulate the base flow (hopefully toward the time mean profile), even when overall production may yield an increase in TKE. Base flow modulations also increase wall shear stresses, thereby requiring an increase in the driving pressure gradient, if aiming to maintain a constant flow rate. However, this work simulates flows driven by constant pressure gradients — as shown in Chapter 8 (Camobreco *et al.* 2021a) by converting wall motion to a pressure driven equivalent condition — rather than constant flow rates.

3.7.2 A return to the laminar base flow-perturbation decomposition

Without the time mean flow, the true production term cannot be computed. However, the analogous terms based on a laminar-perturbation decomposition can. The total production to/from the modulated base flow (the modulated base flow includes the laminar base flow and the zeroth perturbation harmonic) from/to the n'th perturbation harmonic ($n > 0$) is (Jin *et al.* 2021)

$$\mathcal{P}^{(n)} = \mathcal{P}^{(Ln)} + \mathcal{P}^{(0n)} = -\left[\int \hat{v}_{\perp}^{(n)} \frac{\partial U_{\perp}}{\partial y} \hat{u}_{\perp}^{(-n)} \,\mathrm{d}\Omega + \int \hat{v}_{\perp}^{(n)} \frac{\partial \hat{u}_{\perp i}^{(0)}}{\partial y} \hat{u}_{\perp i}^{(-n)} \,\mathrm{d}\Omega\right], \qquad (3.47)$$

where harmonics are now denoted by a bracketed exponent, and where $(-n)$ denotes the complex conjugate to harmonic (n). Note that the modulated base flow must be streamwise invariant, but the time mean flow need not be. Note also that the direction of energy transfer is unknown until the integral in Eq. (3.47) is computed.

The total production is then the integral over all harmonics κ, which must balance the corresponding dissipation and friction integrals for the integrated turbulent kinetic energy of the perturbation to remain relatively constant. In this subsection, TKE refers to the turbulent kinetic energy of the perturbation, rather than the TKE of the fluctuation, as in the previous subsection. Having defined the production, and for completeness providing the corresponding expression for nonlinear energy transfers (Jin *et al.* 2021) between harmonics (n) and (m),

$$\mathcal{N}^{(mn)} = -\int \hat{u}_{\perp j}^{(n-m)} \frac{\partial \hat{u}_{\perp i}^{(m)}}{\partial x_j} \hat{u}_{\perp i}^{(n)} + \hat{u}_{\perp j}^{(n+m)} \frac{\partial \hat{u}_{\perp i}^{(-m)}}{\partial x_j} \hat{u}_{\perp i}^{(-n)} \,\mathrm{d}\Omega, \tag{3.48}$$

for $m \neq n$, a simplified picture of turbulence can be painted, see Fig. 3.13. The simplification is in part due to unanswered questions about turbulence, and in part due to the use of the modulated base flow, rather than the time mean flow. Note that for the remainder of this section, the use of the word dissipation will refer to both the viscous dissipation and Hartmann friction terms of Eq. (3.46), e.g. ϵ_{F} rather than ϵ_{D}.

Turbulence is sustained when, on average, production balances dissipation (this discussion assumes everything is on average, unless specified otherwise). A relatively large amount of TKE is produced by the laminar base flow. However, the TKE produced in/by each harmonic rapidly falls off with increasing harmonic (production depends on the velocity magnitudes of each harmonic, and the velocity magnitudes of the higher harmonics are invariably quite small). Thus, to satisfy the definition of turbulence, which requires a large number of energized harmonics, nonlinearity must play a vital role in transferring energy between harmonics. This will be discussed in more detail shortly. Staying with the lower harmonics, some will exhibit negative production, representing a loss of TKE, which acts to generate or regenerate the base flow modulation. Others will exhibit positive production, acting to increase TKE at the expense of the modulated base flow's gradients. Note that when the pressure gradient is held constant (or equivalent boundary conditions imposed), the modulation is not supplied energy by the driving force; only the laminar profile is, assuming the pressure gradient is set based on the laminar profile. Thus, for the modulation to furnish TKE to the fluctuations, it *must* come at the expense of its own velocity gradients. The velocity gradients of the modulation will not naturally replenish, and require feedback from fluctuations if the modulated profile is to be sustained, let alone approach the time mean profile. Note also that shear in the modulated profile is usually much larger near the wall, and relatively

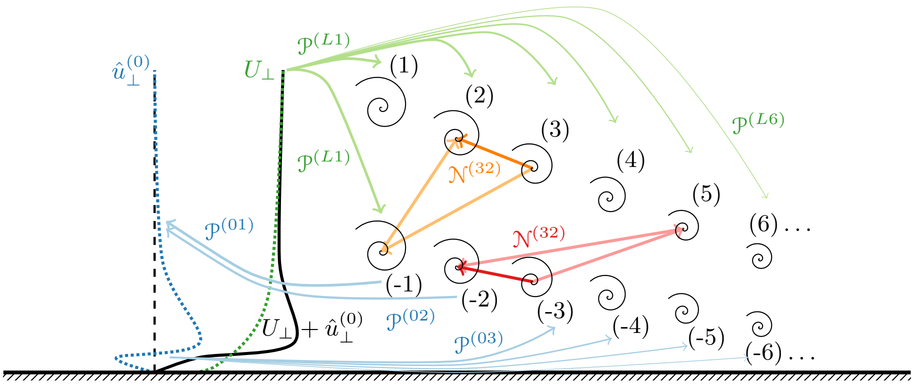

FIGURE 3.13: Schematic representing a few of the key features of turbulence near the wall at an instant in time, partially following Lozano-Durán *et al.* (2021). The key components are the laminar base flow $U_\perp$ (time steady), the streamwise component of the streamwise invariant base flow modulation $\hat{u}_\perp^{(0)}$ (which differs from the time mean flow), and a series of harmonics representing streamwise Fourier modes $\hat{\boldsymbol{u}}_\perp^{(n)} = (\hat{u}_\perp^{(n)}, \hat{v}_\perp^{(n)})$ and their conjugates $\hat{\boldsymbol{u}}_\perp^{(-n)}$; although only the first 6 modes of each are drawn. Focus is placed on production, with the actions of both dissipation and friction *not* represented (two energy-conserving nonlinear transfers are also indicated). The green arrows represent production from the laminar base flow to the Fourier modes. As drawn, all reduce the energy in the laminar profile, which is offset by the driving pressure gradient, to generate an increase in TKE in each mode. More energy is produced in the lower harmonics, represented by thicker arrows. The blue arrows represent production from the base flow modulation, which reduces TKE in the leading two harmonics (1 and 2), and increases TKE in harmonics 3 through 6 (again, having a greater effect on the lower harmonics). Thus, harmonics 1 and 2 are acting to regenerate the base flow modulation (e.g. increasing its gradients, at the expense of their TKE), while harmonics 3-6 are degrading the modulation (e.g. eroding its gradients, to increase their TKE). Note that production requires both the n and $-n$ harmonics, and is only drawn correctly for $\mathcal{P}^{(L1)}$ (the modulated profile doesn't just effect the negative harmonics, and the laminar profile the positive). The locations of the arrows are also arbitrary, and do not necessarily represent local increases or reductions in base flow gradients.

small in the bulk flow (mean velocity profiles in turbulent flows are often flat in the core due to modulation of the laminar profile, see Fig. 3.13 for an idealized example). Thus, most positive production to/from the modulation occurs near the wall, and negative production in the bulk, whereas positive production in the bulk flow is predominantly due to the laminar profile.

Thus, two balances are required for the sustainment of turbulence. First, the production in each harmonic must, on average, balance the dissipation in said harmonic, to maintains its TKE (in the thermodynamic limit of large times). Second, there must be a balance in production to and from the base flow modulation, such that it can eventually become time independent (e.g. become the mean flow). Recall that this is required if the Reynolds stress term is non-zero, the laminar base flow then not being a solution of the evolution equation for the time mean flow, Eq. (3.43).

Depending on the level of dissipation, proportional to Re^{-1}, these balances are not guaranteed. Thus, in the thermodynamic limit, there may be no turbulence whatsoever, intermittent turbulence, or fully developed turbulence (Barkley 2016). The first case, no turbulence whatsoever, simply occurs when dissipation is too great, and any incited turbulence decays. Intermittent turbulence is somewhat more complicated. If turbulence is triggered by the laminar profile, generation of the base flow modulation may begin, at the expense of TKE of the newly incited turbulence. However, the cost of generating the modulation may be too great (observable when the the total modulated profile becomes quite flat in the core), with the turbulent state then collapsing. With the collapse of turbulence, the base flow eventually settles back to the reference profile, which can again trigger turbulence. This process repeats, with unsustainable modulations forming, followed by the collapse of the turbulent states thereafter, and the settling back to the reference base flow. Finally, fully developed turbulence is obtained when the base flow modulation is sustained (and approaches the mean flow), and when TKE is maintained in all harmonics by the modulated base flow. Note that intermittent turbulence is often referred to as localized, when the base flow modulation is not streamwise invariant, as only patches or puffs of turbulence are observed. Once turbulence spreads throughout the duct it is considered fully developed (Barkley 2016), although instantaneously, its behavior is still stochastic (recall that turbulent lifetimes are memoryless, with an exponential chance of decay with increasing time). Thus, there is always the possibly of isolated relaminarization events, where turbulence is not sustained locally, with a laminar island transiently appearing (Avila & Hof 2013). The true limit of fully developed turbulence (e.g. turbulence absolutely everywhere for all time) is only reached asymptotically as $Re \to \infty$ (Avila *et al.* 2011; Avila & Hof 2013).

Before moving on to nonlinear interactions, it is worth noting that dissipation depends on the local fluctuation magnitude, whereas production depends on local fluctuation magnitude weighted by the local base flow gradient, recalling Eq. (3.45). Thus, near the wall, production often outweighs dissipation, as base flow shear near the wall is high, supporting turbulence. However, far from the wall, dissipation often outweighs production. When the base flow is flat far from the wall, either naturally (e.g. due to friction present in the system), or due to modulation from lower harmonics, this impact to bulk production can significantly hamper the ability to sustain turbulence (Budanur *et al.* 2020), leading to intermittency.

Although nonlinear interactions conserve TKE, they play a very important role in both generating and sustaining turbulence. In many of the transition scenarios introduced earlier, nonlinearity provides a downscale transfer of energy from the leading harmonics (0 through 2) to the higher harmonics. Particularly in supercritical bifurcation scenarios, the remaining harmonics rapidly become energized, generating turbulence. Although energized, the fluctuation magnitudes in these intermediate harmonics are small, and thereby so too is dissipation. Thus, in spite of low levels of production, they can still remain energized. However, dissipation (although not friction) also depends on length scale. Thus, once even higher harmonics becomes energized, a regime will eventually be reached, where the gradients of the fluctuations, and thereby dissipation, become too large for production to maintain a constant TKE.

Interestingly, the role of nonlinearity then differs drastically for flows with are 3D, and those which are Q2D/2D. The general arguments for production and dissipation remain the same. Dissipation is largest in the smallest scales, once their local gradients outweigh small fluctuation velocities, while production from the mean flow is largest at the largest scales. However, between the smallest and largest scales, for sufficiently large Re, an inertial subrange can form. Within these intermediate scales, the nonlinear transfer term of Eq. (3.46) is dominant, relative to production and dissipation, and transfers of TKE within the subrange are independent of scale. However, for 3D flows, net transfers within the inertial subrange are commonly downscale, toward higher harmonics. Whereas in Q2D/2D, net transfers of energy are always upscale, toward lower harmonics, as the vortex stretching/strain self-amplification mechanisms which drive net downscale transfers of energy cannot occur (Bos 2021). Note that in Q2D, enstrophy can still cascade downscale, as discussed shortly. Interestingly for 3D MHD flows, a clear cutoff between upscale transfers of energy (lower '2D' harmonics) and downscale transfers of energy (higher '3D' harmonics) can be observed (Baker *et al.* 2018). Note that energy does not build up in Q2D/2D systems due to friction, which damps energy at all scales. If only viscous dissipation were present, insufficient energy would be removed from the system at the smallest scales to permit thermodynamic equilibrium in domains of finite size (with realistic boundary conditions).

The inertial subrange covers all scales very large relative to the highly dissipative scales, and very small relative to the highly productive scales. Regardless of the direction of transfer, for the inertial subrange in Q2D and 3D flows, the turbulent kinetic energy varies as $k(\kappa) \sim \kappa^{-5/3}$ (Pope 2000), assuming no other extrinsic mechanisms are present. Before considering an example of this $-5/3$ spectrum, there are three things worth noting. First, the inertial subrange forms only at large Re, when scale separation is significant. Second, the power law scaling for the inertial subrange is based on an integral measure, thus transfers over the subrange are not all downscale (if 3D), or all upscale (if 2D/Q2D). In particular, recalling Fig. 3.13, all nonlinear transfers require an intermediary (the harmonic responsible for advection of the velocity gradient). Because of the intermediary, a net upscale transfer must necessarily have some downscale component, and vice versa. Third, for Q2D flows, although energy is transferred upscale, dissipative scales can still be identified by a downscale enstrophy cascade, $\mathcal{E}(\kappa) \sim \kappa^{-3}$. The (Q2D) enstrophy $\mathcal{E} = \int |\omega_z|^2 \, \mathrm{d}\Omega$ forms a useful measure of dissipation, by measuring velocity gradients via vorticity magnitude (Kraichnan 1967; Sommeria 1986). Hence, the sole observation of an inverse energy cascade is not sufficient to fully characterize Q2D turbulence.

To assist this discussion, time-averaged Fourier coefficients (where instantaneous snapshots of sustained turbulent DNS velocity fields were time-averaged) are provided in Fig. 3.14. Note that the Fourier coefficients measure the perturbation energy $E = \hat{k} = \int \hat{u}_\perp^2 + \hat{v}_\perp^2 \, \mathrm{d}\Omega$, not the turbulent kinetic energy k, as computing the time mean flow was prohibitively expensive. However, this simplification does not appear to have any significant implications on analysis. Note the three subdivisions of Fig. 3.14. Technically, there should be a large scale separation between the ranges representing dominant production, nonlinear transfer, and dissipation. However, the demarcating lines have been intentionally placed to indicate which harmonics are predominantly responsible for each of the key features of turbulence. Computations (not shown) of the production integral, Eq. (3.47), indicate that the first six harmonics have relatively large contributions to production, and often have negative production relative to the base flow modulation (indicating regeneration of the modulation at the expense of TKE). Hence, the energy-containing range is shown spanning $1 \leq \kappa \leq 6$. Nonlinear transfers dominate in the inertial subrange, and as a $\kappa^{-5/3}$ fit best approximates the Fourier coefficients over $7 \lesssim \kappa \lesssim 70$, this may indicate the formation of an inertial subrange at

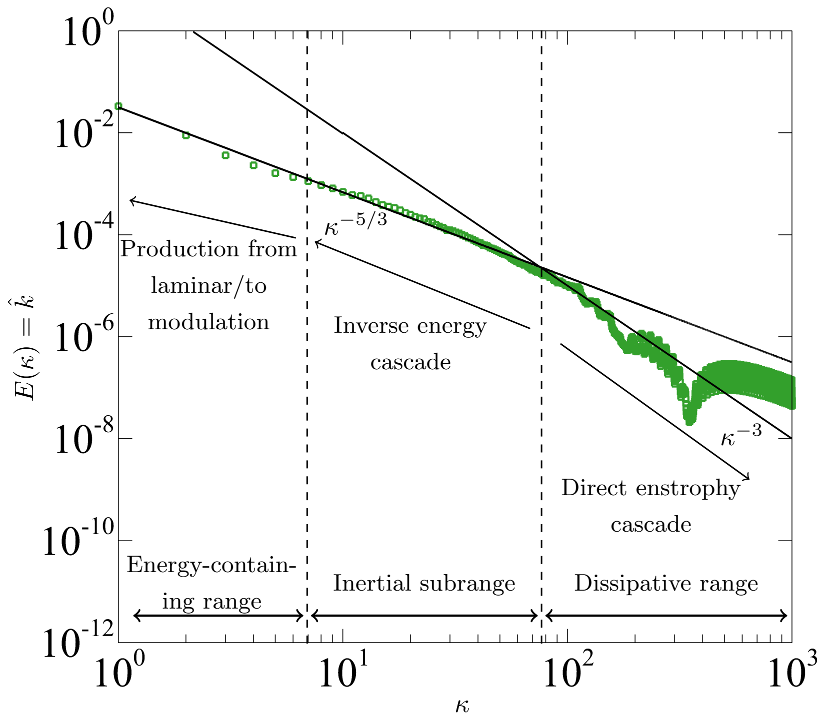

FIGURE 3.14: Time and y-averaged Fourier coefficients for Shercliff flow at $H = 10$, $r_c = 1.1$ ($Re = 8.70355 \times 10^4$), see Chapter 6 (Camobreco *et al.* 2021b) for details. $E = \hat{k}$ is a measure of the perturbation energy (about the laminar profile), whereas k is a measure of the fluctuation energy (about the time mean). The latter was not feasible to compute, given the time required for the mean flow to saturate. The terminology of Pope (2000) is followed, noting that production is dominant in the energy-containing range, dissipation dominant in the dissipative range, nonlinear transfers dominant in the inertial subrange and friction scale independent (although still proportional to fluctuation magnitude). Scale separation between the various ranges is assumed large; representative sharp κ bounds indicated by the dashed lines separate the ranges. In the energy-containing range, production is (on average) from the reference profile and to the modulation profile (the computations indicating this is the case for $\kappa \lesssim 6$ not shown). Numerical resolution was insufficient to identify a clear direct enstrophy cascade, with κ over a few hundred underresolved, although a "direct enstrophy cascade" label has been included on the figure anyway, solely for illustrative purposes. Finally, while it is not possible to infer the existence of an inverse energy cascade, solely by observing the $\kappa^{-5/3}$ trend in the inertial subrange, inverse cascades have been observed previously in Q2D systems (Sommeria 1986). However, if different trends had been present in the Fourier coefficients, they could have ruled out an inverse energy cascade.

this Re. It is also likely that an inverse energy cascade occurs throughout the inertial subrange, although quasi-two-dimensionality only ensures that all nonlinear transfers are net upscale (but not necessarily scale independent). Finally, the dissipative range covers modes $\kappa \gtrsim 70$ (perhaps $\kappa \gtrsim 100$ if properly considering scale separation between the various ranges). However, as the streamwise direction of the DNS domain is discretized, the threshold for well-resolved Fourier modes lies somewhere between $\kappa = 100$ and 200. Thus, the Fourier coefficients deviate from a κ^{-3} direct (forward) enstrophy cascade, which would otherwise be expected at sufficiently large Re.

Finally, the physical mechanisms behind the inverse energy cascade in 2D (and possibly Q2D) flows are briefly discussed, culminating in some filtered examples of Q2D turbulence. In 2D, and absent of external forcing, vorticity is a conserved quantity. Comparatively, in 3D, velocity gradients perpendicular to a vorticity component can stretch (amplify) vorticity. This is an impossibility in Q2D flows, as ω_z is the only non-zero vorticity component, while all velocity gradients in the out-of-plane direction ∂_z are necessarily zero, and so incapable of vortex stretching. With similar reasoning, self-strain amplification, the other dominant means of driving a direct cascade of energy (Carbone & Bragg 2020; Bos 2021), can also be disregarded in Q2D flows.

Thus, a different mechanism drives inverse cascades than forward cascades. It was originally presumed that vortex merger events were responsible for the inverse energy cascade (Rivera 2000), as merger events are commonly observed in decaying turbulence (Jiménez 2020). However, vortex merger events provide no means of transferring energy over a large range of scales (Xiao *et al.* 2009). Currently, numerical and experimental studies indicate that vortex thinning is the key mechanism driving the inverse energy cascade in 2D turbulence (Chen *et al.* 2006; Xiao *et al.* 2009), or more precisely vorticity thinning, as vortices are not a necessity. It is important to note that this explanation of inverse energy cascades pertains to 2D (box) turbulence; it remains an open question whether the same mechanism applies to inverse cascades in Q2D turbulence in duct flows. Vortex thinning relies on the conservation of vorticity in Q2D/2D flows. For example, if an initially circular vortex were sheared in one direction, the resulting elliptic vortex would have an identical area, but reduced velocity magnitudes, given the increased circumference. An identical area, or equally an identical line integral of (reduced) velocity about the (increased) circumference, is ensured by vorticity conservation. The reduced velocity magnitudes, and thereby energy, must be transferred

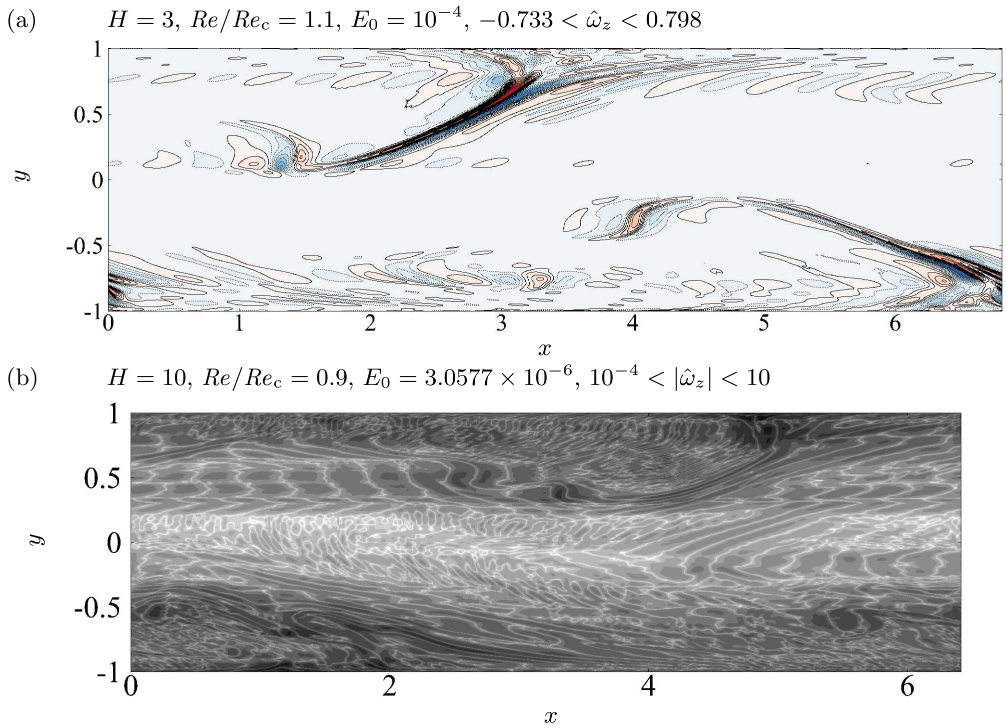

FIGURE 3.15: Streamwise high-pass-filtered snapshots of Shercliff flow shortly after the transition to turbulence. Streamwise Fourier coefficients of modes $|\kappa| \leq 9$ have been removed. (a) In-plane perturbation vorticity; solid lines (red flooding) denote positive vorticity, dotted lines (blue flooding) negative. (b) Absolute value of in-plane perturbation vorticity.

somewhere. Given that the ellipse is now long and thin, the circumferential velocities are now predominantly directed along the major axis. Thus, shear along the major axis increases. Hence, if a small scale circular vortex is subjected to a large scale strain field, deforming it into an elliptic vortex, the deformation will generate a shear stress aligned with, and thereby reinforcing, the large scale strain. Thus, any energy lost by the small scale vortex is transferred to the large scale strain field. Note that ‘energy’ stored in the strain field is equally ‘energy’ stored in velocity gradients, as the strain rate $S = (1/2)[(\boldsymbol{\nabla}_\perp \hat{\boldsymbol{u}}_\perp + (\boldsymbol{\nabla}_\perp \hat{\boldsymbol{u}}_\perp)^{\mathrm{T}}]$. It is worth noting that as stresses at the small scales must be aligned with the large scale strains for an inverse cascade, then the small scale strains (velocity gradients) must necessarily act at 45° angles to the large scale strains (Chen *et al.* 2006).

To finish this discussion of the physical mechanisms behind the inverse energy cascade, some snapshots of Q2D turbulence from DNS are provided. The inclusion of Fig. 3.15 here not only allows for familiarization with what Q2D turbulence looks like, as it is not as widely depicted as its 3D counterpart, but also indicates the prevalence of narrow, highly sheared layers of vorticity; see Chapters 6 (Camobreco *et al.* 2021b) and 7 for further details. Such structures are particularly common, and long-lived, in the Q2D turbulence observed in this thesis. Given the previous discussion of the mechanisms of the inverse cascade, it is interesting to note the inclination (although not 45°) of the weakly unsteady highly thinned vortical structures, relative to the streamwise parallel walls which drive the flow

With this tantalizing snapshot of Q2D turbulence, the introduction is concluded. Having detailed the necessary information, the aims are now discussed, and clarified into specific questions this research seeks to answer. Overall, these aims focus on elucidating transition scenarios, and particularly, in identifying those features desirable in initial conditions to most efficiently trigger turbulence, and to indefinitely sustain turbulence. Obtaining an understanding of the ensuing turbulent flows, such as the energy transfer mechanisms, is a challenge left open for future work.

Chapter 4

Aims

From the theoretical perspective, this research would seek solely to further understanding of subcritical routes to Q2D turbulence. However, practical aspects only necessitate a decrease in the Reynolds number required to sustain turbulence, subcritical or otherwise. This work will thereby investigate both subcritical and supercritical routes to Q2D turbulence. Specific aims for both subcritical and supercritical investigations follow; in each case, directions are provided to locate individual results of interest.

Investigations of subcritical routes to turbulence involve the following:

- **Establishing the regions of the parameter space within which subcritical transitions can be triggered.** See Chapter 6 (Camobreco *et al.* 2021b) for weakly nonlinear bifurcation analysis of the α-Re space toward answering this question, and see Chapters 5 (Camobreco *et al.* 2020) and 7 for the fully nonlinear analysis of the double threshold E_0-Re space, indicating a possible lower and upper delineating energy, or edge state, for a given Re.

- **Elucidating the key stages and physical mechanisms behind subcritical routes to turbulence.** See Chapter 5 (Camobreco *et al.* 2020) for the role of nonlinear growth, and particularly nonlinear modifications to the later stages of the Orr mechanism. See Chapter 7 for a full breakdown of the transition, into the key stages of initial linear transient growth, weakly nonlinear edge trajectory and fully nonlinear departure to turbulence upon reaching the edge state. Also see Chapter 7 for the clearest identification of the lower edge state.

- **Determining the most efficient route to sustained turbulence, to assist predictions of turbulence in practical application.** See Chapter 7 for the importance of optimal energization of the leading eigenmode in efficiently triggering turbulence. Optimal energization by the leading adjoint mode is shown to be far more important than optimal linear or nonlinear growth in both sustaining, and efficiently triggering, turbulence.

- **Considering the transport of a passive scalar after sustained subcritical turbulence has been achieved, for practical application of cooling efficiency**. See Appendix B for the heat transfer enhancement ratios with a passive thermal field in either the sustained turbulent, or saturated finite amplitude, flow conditions of Chapter 7.

Investigations of supercritical routes to turbulence involve the following:

- **Establishing the effect of the friction parameter H on steady base flows**. See Chapter 6 (Camobreco *et al.* 2021b) for a thorough coverage of the linear stability, energetics, transient growth and weakly nonlinear bifurcation behavior of the family of MHD-Couette-Shercliff profiles over a wide range of H. Focus is placed on the interplay between base flow symmetries and the magnitude of H, with symmetric Shercliff (or pressure-driven equivalent) profiles always least stable.

- **Assessing the ability to generate and sustain supercritical turbulence over a wide range of H**. See Chapter 6 (Camobreco *et al.* 2021b) and Appendix C for the Re, H combinations able to sustain turbulence. When weakly supercritical, small H are unable to trigger turbulence (strongly supercritical cases are able to trigger turbulence). High H could trigger turbulence, but are unable to sustain turbulence, likely due to a lack of base flow production. Only intermediate H could both trigger and sustain turbulence when weakly supercritical. Also compare to Chapter 8 (Camobreco *et al.* 2021a), in which supercritical turbulence is not observed at any H tested, due to extreme linear growth resulting in detrimental nonlinear base flow modulation.

- **Considering methods to reduce the critical Reynolds numbers.** See Chapter 8 (Camobreco *et al.* 2021a) for an investigation of symmetric base flows including both a steady an oscillatory component. Optimising the frequency and amplitude of the oscillatory flow component results in large reductions in the critical Reynolds number.

Chapter 5

Subcritical route to turbulence via the Orr mechanism in a quasi-two-dimensional boundary layer

5.1 Perspective

This chapter presents the first paper, published in 2020 in *Physical Review Fluids*, entitled a "*Subcritical route to turbulence via the Orr mechanism in a quasi-two-dimensional boundary layer*". As the current (nonlinear) literature were simulating Reynolds and Hartmann numbers still well below those expected at fusion relevant conditions, recalling Table 2.1, a new approach was taken. Given the small thickness of Shercliff boundary layers, an isolated Q2D boundary layer could be simulated, of thickness $\delta_{\mathrm{S}} = L_y/H^{-1/2}$, at a given $Re_{\mathrm{S}} = U_0\delta_{\mathrm{S}}/\nu$, and the results directly translated to finite H and $Re = U_0 L_y/\nu$ (and thereby any specific fusion reactor configuration). This circumvented the issue of simulating either large Re at small H, or small Re at large H, or the extrapolation of results. The generality of the isolated Q2D boundary layer also permits extension of the results to a variety of geophysical and astrophysical flows.

The current state of the art in transitions to turbulence was also reviewed. This revolved around nonlinear transient growth, or similar edge tracking algorithms, composed of individually linear growth stages. After first establishing that linear and nonlinear transient growth were effectively equivalent in Q2D systems, as only the Orr mechanism was present, initial conditions were constructed based on linear optimization maximizing transient growth. This permitted both a baseline comparison to other works (in different systems) using similar strategies, as well as allowed investigation of the various linear and nonlinear stages of Orr growth toward turbulence. From nonlinear evolution of linear initial conditions, possibly the first simulated transient Q2D turbulence was triggered from a Q2D laminar initial condition at a subcritical Reynolds number (further supported by additional analysis included in Appendix A). Key flow features were also identified and characterized. Both streamwise sheets of negative velocity, and arched jets of vorticity (emanating from the region where the wall-normal velocity changes sign near the wall) were observed, and will be consistently observed in all future works in this thesis. The former flow feature, streamwise velocity sheets, appeared detrimental to sustaining turbulence, whereas the latter jetting phenomenon appeared key to generating turbulence. While turbulence was not sustained in the following paper, jets were observed in sustained subcritical turbulence in Chapter 7, as contrasted in Appendix D.

In either case, it is of particular theoretical interest that turbulence was triggered without the use of 3D noise (and so was purely Q2D) and with an initial condition composed of only a single energized harmonic ($\kappa = 1$), rather than some small scale (high harmonic) forcing. Under these constraints, the region of the parameter space in which purely Q2D subcritical transitions were viable was established, for the practical import of self-sufficient fusion blanket operation. However, only weakly subcritical Re_{S} were capable of inciting transitions to turbulence, and once scaled to finite H, remained at quite large Re (likely practically unrealisable, but not unrealistically large). Analysis at weakly subcritical Re_{S} revealed the presence of both lower and upper delineating energies; the latter only recently reported in 3D hydrodynamic flows (Budanur *et al.* 2020). However, even at initial energies between the lower and upper bounds, turbulence was unable to be sustained, which is of concern for practical application. Although attempts to extend the turbulent episode were successful, by considering larger Re_{S} (supercritical but outside the neutral curve) and longer domains, the results were not of immediate practical application. Theoretically, the form of the state space generating a single turbulent episode was tantalizing, as tests in longer domains indicated no change in the lower delineating energy, but a raising of the upper delineating energy, which may permit turbulent episodes at lower Re_{S}. Note that the form of the state space, and the generation of sustained turbulence (rather than single turbulent episodes) will be revisited in Chapter 7. For now, the first published article is included in the pages to follow.

PHYSICAL REVIEW FLUIDS **5**, 113902 (2020)

Subcritical route to turbulence via the Orr mechanism in a quasi-two-dimensional boundary layer

Christopher J. Camobreco [1,*] Alban Pothérat, [2,†] and Gregory J. Sheard [1,‡]
[1] *Department of Mechanical and Aerospace Engineering, Monash University, VIC 3800, Australia*
[2] *Fluid and Complex Systems Research Centre, Coventry University, Coventry CV15FB, United Kingdom*

(Received 22 July 2020; accepted 28 October 2020; published 23 November 2020)

A subcritical route to turbulence via purely quasi-two-dimensional mechanisms, for a quasi-two-dimensional system composed of an isolated exponential boundary layer, is numerically investigated. Exponential boundary layers are highly stable and are expected to form on the walls of liquid metal coolant ducts within magnetic confinement fusion reactors. Subcritical transitions were detected only at weakly subcritical Reynolds numbers (at most ≈70% below critical). Furthermore, the likelihood of transition was very sensitive to both the perturbation structure and initial energy. Only the quasi-two-dimensional Tollmien–Schlichting wave disturbance, attained by either linear or nonlinear optimization, was able to initiate the transition process, by means of the Orr mechanism. The lower initial energy bound sufficient to trigger transition was found to be independent of the domain length. However, longer domains were able to increase the upper energy bound, via the merging of repetitions of the Tollmien–Schlichting wave. This broadens the range of initial energies able to exhibit transitional behavior. Although the eventual relaminarization of all turbulent states was observed, this was also greatly delayed in longer domains. The maximum nonlinear gains achieved were orders of magnitude larger than the maximum linear gains (with the same initial perturbations), regardless if the initial energy was above or below the lower energy bound. Nonlinearity provided a second stage of energy growth by an arching of the conventional Tollmien–Schlichting wave structure. A streamwise independent structure, able to efficiently store perturbation energy, also formed.

DOI: 10.1103/PhysRevFluids.5.113902

I. INTRODUCTION

There is significant interest in understanding transitions to quasi-two-dimensional (Q2D) turbulence, given the wide range of natural and industrial flows which exhibit quasi-two-dimensionality. These include magnetohydodynamic (MHD), shallow channel, and atmospheric flows [1,2]. The conditions under which 3D MHD turbulence becomes quasi-two dimensional, and the appearance of three-dimensionality in Q2D MHD turbulence have been clarified [3–6]. However, a clear subcritical path to Q2D turbulence from a Q2D laminar state has not been identified. The aim of the present work is thus to establish a purely Q2D subcritical route to turbulence. This is motivated by the design of coolant ducts in magnetic confinement fusion reactors, where pervading field strengths range between 4 and 10 T [7,8]. Understanding transition in coolant ducts is important for ensuring sufficient heat transfer at the plasma-facing (Shercliff) wall [9–13] and to establish the feasibility of self-cooled reactor designs [7]. Limits on maximum pressure gradient [9,14,15] and

*christopher.camobreco@monash.edu
†alban.potherat@coventry.ac.uk
‡greg.sheard@monash.edu

pumping efficiency [11,16–18] motivate seeking the most efficient route to turbulence. However, quasi-two-dimensional turbulence is unlikely to arise in blankets via strongly three-dimensional turbulence [7]. Thus, this work limits itself only to the use of an initial two-dimensional perturbation; secondary excitations with three-dimensional random noise are not applied.

Transitions in MHD flows have previously been initiated by a perturbation comprising either two three-dimensional oblique-waves or a two-dimensional initial field with three-dimensional random noise [19,20], which are routes prohibited in Q2D systems. Using these techniques, for Hartmann channel flow, Ref. [19] found excellent agreement with the critical Reynolds numbers at which transition was observed experimentally [21], observing a strongly three-dimensional subcritical transition. Although less energetic perturbations generated more growth, they did not sufficiently modulate the base flow. The perturbations which attained the highest maximum energy, regardless of initial energy, were most likely to incite transition. Complicating matters at high field strengths, three-dimensional noise relaminarized the flow, instead of triggering transition.

To assess subcritical transitions in Q2D MHD flows, the SM82 model [3] is applied, as realistic magnetic confinement field strengths (4–10 T) are currently beyond the capability of three-dimensional numerics. The SM82 model governs the evolution of a velocity field averaged along uniform magnetic field lines. In the limit of quasistatic Q2D MHD, the magnetic field is imposed and the Lorentz force dominates all other forces. The bulk flow is two-dimensional, with thin Hartmann layers formed along walls perpendicular to field lines. In the SM82 model, the presence of Hartmann layers is modeled with linear friction on the average flow. The validity of the SM82 approximation is well supported in the quasi-two-dimensional limit [22–25]. Departure from the two-dimensional average has been observed in regions of strong viscosity or inertia. Reference [23] demonstrates errors less than 10% between quasi-two-dimensional and laminar three-dimensional Shercliff layers, which do not vanish, even in the asymptotic limit when the Lorentz force dominates. There is also excellent agreement at high magnetic field strengths [26] between the linear transient growth of full three-dimensional simulations, and Q2D simulations based on the SM82 model.

The linear stability and linear transient growth of duct flows under strong magnetic fields are determined solely by boundary layer dynamics [27,28]. Direct numerical simulations depict instabilities isolated to the Shercliff layers, on walls parallel to the magnetic field [26,29]. As such, an exponential boundary layer in isolation is considered. The isolated quasi-two-dimensional boundary layer profile is identical to an asymptotic suction boundary layer [30], where friction replaces wall suction. The analogy has been highlighted in [31], by performing a change of variables, such that the wall suction boundary condition becomes impermeable. This introduces an additional term in the governing equations for the transformed velocity, of the form $-(\partial \boldsymbol{u}/\partial y)/\mathrm{Re}$. Comparatively, the friction term in the SM82 model is $-\boldsymbol{u}/\mathrm{Re}$. However, as the underlying exponential boundary layer remains the same, both flows are very stable [30,32].

Nonlinear optimization and edge tracking algorithms have been widely used to assess subcritical turbulent transitions in hydrodynamic pipe [33,34], plane Couette [35,36], and plane Poiseuille flows [37,38], as well as in Blasius [39–42] and asymptotic suction [43,44] boundary layers. A fundamental part of this process involves searching the state space for seperatrices, which divide the basins of attraction of the laminar fixed point and turbulent state [43]. The minimal seed is then the nonlinearly optimized perturbation with the smallest initial energy that is able to cross the separatrix [33]. Separatrix 1 is henceforth defined as a segment of the laminar-turbulent basin boundary where the minimal seed crosses. Hydrodynamic studies of three-dimensional turbulent transitions have determined that the laminar-turbulent basin boundary is the "edge" of a stable manifold. At a saddle node (the edge state) an unstable solution crosses [43,45]. However, such an unstable solution is not necessarily the minimal seed [36] as the seperatrix can be closer to the fixed laminar point elsewhere in the state space. This discussion is aided by Fig. 1, which depicts two initial conditions with slightly different initial energies. One perturbation has an initial energy $E_0 < E_{\mathrm{D}}$ and returns back to the laminar state without crossing separatrix 1, such that E_{D} is the minimum initial energy sufficient to cross separatrix 1. The case with $E_0 > E_{\mathrm{D}}$ continues on to

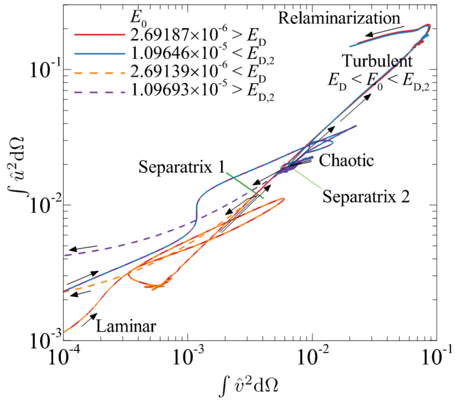

FIG. 1. A state space representation of the problem. Four cases are considered, two with initial energies E_0 just below and above the minimum initial energy sufficient to cross separatrix 1 (E_D) and two with E_0 just above and below the maximum initial energy sufficient to cross separatrix 2 ($E_{\mathrm{D},2}$). An initial energy $E_\mathrm{D} < E_0 < E_{\mathrm{D},2}$ either crosses separatrix 1 (red curve crosses solid dark green line) or avoids crossing separatrix 2 (blue curve eventually avoids solid light green line) to transition to turbulence. Eventually the turbulent state relaminarizes.

the turbulent attractor. An upper bound on the edge state was also identified by [45]. It stemmed from additional dissipation generated by distortion of overly energized initial seeds. This segment of the laminar-turbulent boundary is henceforth defined as separatrix 2. The perturbation with initial energy $E_0 > E_{\mathrm{D},2}$ crosses seperatrix 2, missing the trajectory toward the turbulent attractor, such that $E_{\mathrm{D},2}$ is the maximum initial energy sufficient to avoid separatrix 2. The perturbation with $E_0 < E_{\mathrm{D},2}$ reaches the turbulent attractor, following an almost identical trajectory to the turbulent state as the perturbation with $E_0 > E_D$. After remaining in the basin of the turbulent attractor for some time, relaminarization occurs.

Nonlinear optimization has also been used to demonstrate that nonlinear transient growth occurs solely via the collaboration of multiple linear transient growth mechanisms [34]. This cannot occur in two-dimensional systems, as only the Orr mechanism is present. Thus, nonlinear optimization effectively degenerates to linear optimization. The two-dimensional inviscid Orr mechanism is characterized by an initial perturbation that is tilted opposite to the mean shear [46]. Energy from the mean shear transiently grows the perturbation energy, as the base flow advects the structure into an upright position. Perturbation energy decays as the structure is further tilted into the mean shear, returning energy to the base flow [47]. Initially, this work compares linearly and nonlinearly optimized perturbations, which may form the minimal seeds for inciting subcritical turbulent transitions.

Therefore, this paper considers:

(1) What roles linear transient growth (in particular, the Orr mechanism) and nonlinearity play in Q2D transition scenarios.
(2) Whether distinct initial energies representing separatrix 1 and 2 on the laminar-turbulent boundary can be defined, as for 3D systems.
(3) How sensitive transition is to the structure and wavelength of the initial field.

This paper proceeds as follows: the problem setup, Sec. II, establishes the Shercliff boundary layer domain and base flow. Section III details the determination, validation and results of the linear transient growth analysis, as linear optimals form the initial seeds for nonlinear simulations. Section IV discusses and validates the approach for determining nonlinear optimals and compares the linear optimals to their nonlinear counterparts for small target times. Section V validates the

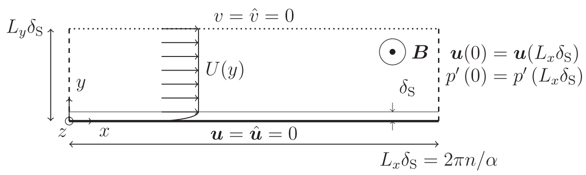

FIG. 2. Schematic diagram of the sidewall domain with a characteristic length of the Shercliff boundary layer height δ_S. The thick horizontal line represents an impermeable no-slip boundary. The dotted line represents a stress-free parallel flow condition. The vertical dashed lines represent a periodicity constraint on velocity and fluctuating pressure. A uniform magnetic field is directed into the page. The out-of-plane Hartmann walls (the sources of linear friction) are not drawn.

nonlinear evolutions of linear optimals, for prescribed initial energies, and then considers the energies delineating transitional states, perturbation structures through growth and decay stages, and the effect of domain length. Conclusions are drawn in Sec. VI.

II. PROBLEM SETUP AND SOLUTION PROCESS

A. Problem setup

An incompressible Newtonian fluid with density ρ, kinematic viscosity ν and electric conductivity σ flows through a duct with rectangular cross-section of width a (z direction) and height $2L$ (y direction). A uniform magnetic field $B\boldsymbol{e}_z$ is imposed. Quasi-two-dimensionality, based on the SM82 model [3,23] is assumed. The revelant length scale is the Q2D Shercliff boundary layer thickness $\delta_S = L/H^{1/2}$, where the Hartmann friction parameter $H = L^2(2B/a)(\sigma/\rho\nu)^{1/2}$ [27]. Normalizing lengths by δ_S, velocities by maximum undisturbed duct velocity U_0, time t by δ_S/U_0 and pressure p by ρU_0^2, the governing momentum and mass conservation equations become

$$\frac{\partial \boldsymbol{u}}{\partial t} = -(\boldsymbol{u}\cdot\nabla_\perp)\boldsymbol{u} - \nabla_\perp p + \frac{1}{\mathrm{Re_S}}\nabla_\perp^2\boldsymbol{u} - \frac{1}{\mathrm{Re_S}}\boldsymbol{u}, \tag{1}$$

$$\nabla_\perp\cdot\boldsymbol{u} = 0, \tag{2}$$

where $\boldsymbol{u} = (u, v)$ is the quasi-two-dimensional velocity vector, representing the z-averaged field, and $\nabla_\perp = (\partial_x, \partial_y)$ and $\nabla_\perp^2 = \partial_x^2 + \partial_y^2$ are the quasi-two-dimensional gradient and vector Laplacian operators, respectively. The flow is governed by one dimensionless parameter, a Reynolds number based on the boundary layer thickness, $\mathrm{Re_S} = U_0\delta_S/\nu$. Hereafter, quantities are expressed in dimensionless form unless specified otherwise. The rightmost term in Eq. (1) is a linear friction term describing Hartmann braking from the two out-of-plane duct walls [3]. At $H \gg 100$, $\delta_S \ll L$ [26,27], such that the sidewall boundary layer that dictates transition behavior is isolated. A domain extending from the sidewall a distance L_y into the flow is considered, with streamwise-periodic length L_x, as depicted in Fig. 2. The streamwise length $L_x = nl_x$ spans n integer repetitions of a flow structure having streamwise length $l_x = 2\pi/\alpha$ and streamwise wave number α.

Instantaneous variables $(\boldsymbol{u}, p)$ are decomposed into base $(\boldsymbol{U}, P)$ and perturbation $(\hat{\boldsymbol{u}}, \hat{p})$ components via small parameter ϵ, as $\boldsymbol{u} = \boldsymbol{U} + \epsilon\hat{\boldsymbol{u}}$; $p = P + \epsilon\hat{p}$, for use in linear transient growth analysis. The fully developed, time steady, parallel flow $\boldsymbol{U} = U(y)\boldsymbol{e_x}$, with boundary conditions $U(y = 0) = 0$, $U(y \to \infty) = 1$, and a constant driving pressure gradient scaled to achieve a unit maximum velocity, is $\boldsymbol{U} = [1 - \exp(-y), 0]$.

B. Solver

An in-house nodal spectral element solver temporally integrates Eqs. (1) and (2) using a third-order backward differencing scheme with operator splitting. The two-dimensional Cartesian domain is discretized with quadrilateral spectral elements over which Gauss–Legendre–Lobatto nodes are placed. The Navier–Stokes solver, with the inclusion of the friction term, has been previously introduced and validated [11,26,48,49]. No-slip velocity boundary conditions are applied at the impermeable wall, $\boldsymbol{u} = \hat{\boldsymbol{u}} = 0$, supplemented by high-order Neumann pressure boundary conditions [50]. Pressure is decomposed into a constant pressure gradient, and a fluctuating component p', and periodicity is imposed between the upstream and downstream boundaries on the velocity and fluctuating pressure. At the stress-free boundary a parallel flow condition ($v = \hat{v} = 0$) is strongly enforced. A constant flow rate condition is also enforced in nonlinear simulations, by appropriate adjustment of the flow rate after each time step.

III. LINEAR TRANSIENT GROWTH

A. Formulation and validation

At subcritical Reynolds numbers, all eigenmodes of the linear evolution operator decay. Thus, to begin establishing a subcrtical route to turbulent transitions, the linear initial value problem is considered. Linear growth is generated by the superposition of decaying nonorthogonal Orr–Sommerfeld modes [51,52]. To interrogate the transient growth of a perturbation, total kinetic energy $E = (1/2)\int \hat{\boldsymbol{u}} \cdot \hat{\boldsymbol{u}}\, d\Omega = (1/2)\|\hat{\boldsymbol{u}}\|$ is chosen to quantify growth, following [53,54], where Ω represents the computational domain. The maximum possible linear transient growth is found by determining the initial condition for perturbation $\hat{\boldsymbol{u}}_\tau(t = 0)$ maximizing $G = \|\hat{\boldsymbol{u}}(\tau)\|/\|\hat{\boldsymbol{u}}(0)\|$ via evolution to time τ. For a given $\mathrm{Re_S}$, $G_{\max} = \max[G(\tau,\alpha)]$ is sought, along with the optimal time horizon τ_{opt} and streamwise wave number α_{opt}. Thereby $l_{x,\mathrm{opt}} = 2\pi/\alpha_{\mathrm{opt}}$. The analysis proceeds with integration of the linearized forward evolution equations,

$$\frac{\partial \hat{\boldsymbol{u}}}{\partial t} = -(\hat{\boldsymbol{u}} \cdot \nabla_\perp)\boldsymbol{U} - (\boldsymbol{U} \cdot \nabla_\perp)\hat{\boldsymbol{u}} - \nabla_\perp \hat{p} + \frac{1}{\mathrm{Re_S}}\nabla_\perp^2 \hat{\boldsymbol{u}} - \frac{1}{\mathrm{Re_S}}\hat{\boldsymbol{u}}, \tag{3}$$

$$\nabla_\perp \cdot \hat{\boldsymbol{u}} = 0, \tag{4}$$

from time $t = 0$ to $t = \tau$. This is followed by backward time integration of the adjoint equations,

$$\frac{\partial \hat{\boldsymbol{u}}^\ddagger}{\partial t} = (\nabla_\perp \boldsymbol{U})^{\mathrm{T}} \cdot \hat{\boldsymbol{u}}^\ddagger - (\boldsymbol{U} \cdot \nabla_\perp)\hat{\boldsymbol{u}}^\ddagger - \nabla_\perp \hat{p}^\ddagger - \frac{1}{\mathrm{Re_S}}\nabla_\perp^2 \hat{\boldsymbol{u}}^\ddagger - \frac{1}{\mathrm{Re_S}}\hat{\boldsymbol{u}}^\ddagger, \tag{5}$$

$$\nabla_\perp \cdot \hat{\boldsymbol{u}}^\ddagger = 0, \tag{6}$$

for the Lagrange multiplier of the velocity perturbation $\hat{\boldsymbol{u}}^\ddagger$, from $t = \tau$ to $t = 0$. Boundary conditions $\hat{\boldsymbol{u}} = \hat{\boldsymbol{u}}^\ddagger = 0$ are applied at the wall and $\hat{v} = \hat{v}^\ddagger = 0$ at the stress-free boundary. “Initial” conditions for forward and backward evolution are $\hat{\boldsymbol{u}}(0) = \hat{\boldsymbol{u}}^\ddagger(0)$ and $\hat{\boldsymbol{u}}^\ddagger(\tau) = \hat{\boldsymbol{u}}(\tau)$, respectively. G is then the largest real eigenvalue of the operator representing the sequential action of forward then adjoint evolution [53,54], obtained by a Krylov subspace scheme. The scheme iterates until a specified eigenvalue tolerance is reached. The corresponding eigenvector contains the optimal initial field (optimal for short).

The mesh for computation of linear optimals has a region of high resolution near the wall, with sparse resolution further away. Element spacing is also sparse in the streamwise direction, as the variation must be sinusoidal (from linearity). Three key factors are considered when assessing accuracy, the number of elements in the wall normal direction, the temporal resolution and the domain height where the stress-free condition is applied, as shown in Tables I and II. Based on the magnitude and behavior of the errors, the highest near wall resolution ($N_{\mathrm{el}} = 154$ mesh from Table I) was selected, with $\Delta t = 1.25 \times 10^{-3}$. Based on Table II, $L_y = 14.14$ is sufficient for determining the linear τ_{opt} and α_{opt}. However, it was deemed pertinent to increase L_y to 28.28 and to recompute time and wave number optimized fields to initiate the nonlinear evolutions reported in Sec. V. This ensures that the parallel flow assumption remains valid if structures increase in height due to vortex merging.

TABLE I. The real component of the leading eigenvalue, at $\mathrm{Re_S} = 7.071 \times 10^3$, $\alpha = 0.7071$, and $\tau = 42.43$ (close to optimal), with domain height $L_y = 14.14$ and polynomial order $N_p = 15$ for various numbers of elements. Meshes with 1, 2, and 4 elements per unit height ($N_{el} = 70$, 98, and 154, respectively) within the first five units from the wall are compared. Absolute percentage errors are quoted for each mesh separately, relative to the smallest time step case, except the last row, which compares to the $N_{el} = 154$ mesh. The eigenvalue convergence tolerance is 10^{-7}.

Δt	$N_{el} = 70$	|% Error|	$N_{el} = 98$	|% Error|	$N_{el} = 154$	|% Error|
2.5×10^{-3}	33.25571762	2.45×10^{-1}	33.36191967	2.59×10^{-3}	33.36189331	2.60×10^{-3}
1.25×10^{-3}	33.23149556	1.72×10^{-1}	33.36145641	1.20×10^{-3}	33.36142823	1.20×10^{-3}
6.25×10^{-4}	33.20232632	8.45×10^{-2}	33.36122729	5.15×10^{-4}	33.36119843	5.15×10^{-4}
3.125×10^{-4}	33.17957603	1.59×10^{-2}	33.36111304	1.73×10^{-4}	33.36108413	1.72×10^{-4}
1.5625×10^{-4}	33.17428683	0	33.36105549	0	33.36102678	0
		5.60×10^{-1}		8.61×10^{-5}		

B. Results

At least one infinitisemal disturbance can achieve exponential growth at Reynolds numbers above the critical Reynolds number $\mathrm{Re_{S,crit}}$. $\mathrm{Re_{S,crit}}$ thereby forms a bound above which transition to turbulence is possible, so long as the domain length has a corresponding wave number within the neutral curve. For this problem, $\mathrm{Re_{S,crit}}$ can be determined by rescaling the results of Ref. [27]; changing length scale from L to δ_S. Thus $\mathrm{Re_{S,crit}} = 4.835 \times 10^4$ and $\alpha_{S,crit} = 0.1615$. The ratio $r_c = \mathrm{Re_S}/\mathrm{Re_{S,crit}}$ is then defined.

Linear transient growth results are presented in Fig. 3. Duct results from Ref. [27] at finite H are also included in Fig. 3(a), supporting the argument that the boundary layer at each duct wall is sufficiently isolated at large H, and can be modeled separately. At $r_c = 0.00135$, $G_{max} = 1$, while by $r_c = 1$, $G_{max} \approx 100$. This modest rise in gain with increasing r_c may be attributed to two factors. The first is that the base flow is naturally highly stable [32]. The second is that two-dimensional systems only permit growth via the Orr mechanism [47]. This greatly reduces optimal growth, and produces the modest scaling of $G_{max} \sim \mathrm{Re_S^{2/3}}$ for large $\mathrm{Re_S}$. Representative initial and optimal fields are provided in Fig. 4, which exhibit the classic initial condition of a strongly sheared wave which transiently grows as it is advected upright, until τ_{opt}. The modes otherwise resemble those of Ref. [27], excepting wall confinement effects at low H in the aforementioned work.

IV. NONLINEAR TRANSIENT GROWTH

A. Formulation and validation

In this work, nonlinear transient growth is employed solely to assess the similarities between the linear and nonlinear optimals for small target times ($\tau \sim \tau_{opt}$). Admittedly, nonlinear transient

TABLE II. The real component of the leading eigenvalue, varying the domain height, for various $\mathrm{Re_S}$. Initially, $\mathrm{Re_S} = 7.071 \times 10^3$ at $\alpha = 0.7071$ and $\tau = 42.43$ was tested as part of a formal validation, $N_{el} = 154$ for $L_y = 14.14$, $\Delta t = 2.5 \times 10^{-3}$, $N_p = 15$. The optimals at $\mathrm{Re_S} = 7.071 \times 10^2$ and 7.071×10^4 were tested post validation, $N_{el} = 250$ for $L_y = 14.14$, $\Delta t = 1.25 \times 10^{-3}$, $N_p = 13$.

L_y	7.071×10^2	|% Error|	7.071×10^3	|% Error|	7.071×10^4	|% Error|
14.14	6.11779740087	3.14×10^{-6}	33.3619198126	2.66×10^{-6}	166.410928536	1.04×10^{-3}
28.28	6.11779759275	7.63×10^{-10}	33.3619206992	7.05×10^{-10}	166.409189845	2.76×10^{-9}
56.57	6.11779759280	0	33.3619206994	0	166.409189849	0

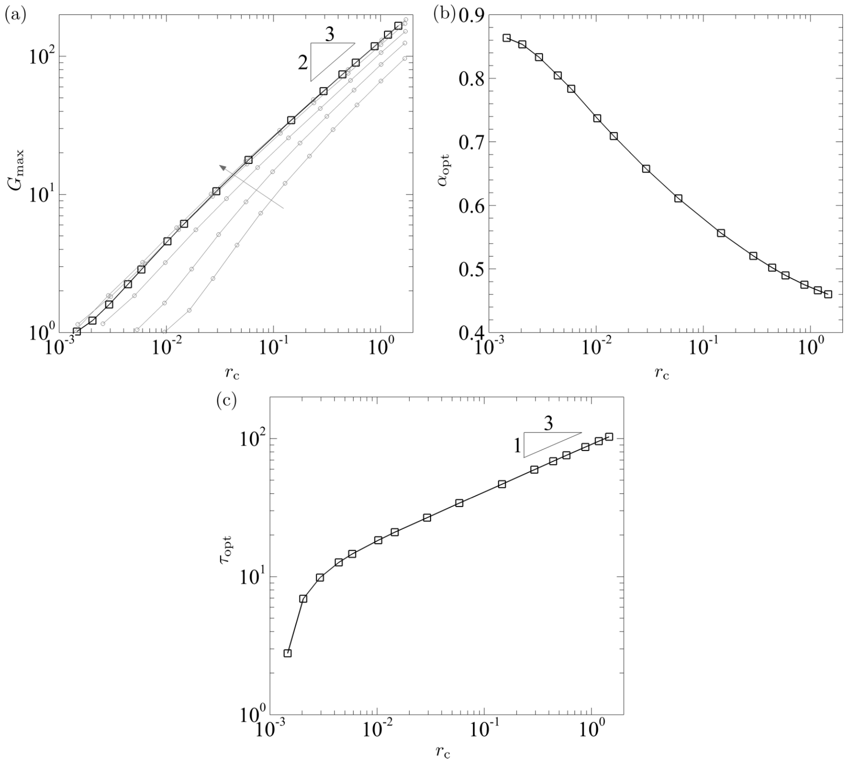

FIG. 3. Linear transient growth of an exponential boundary layer as a function of $r_{\mathrm{c}} = \mathrm{Re}_{\mathrm{S}}/\mathrm{Re}_{\mathrm{S,crit}}$. (a) Growth optimized over initial field, wave number and time interval. Present data (squares) are compared against Q2D duct results from [27] (circles). The arrow indicates increasing H through 1, 3, 10, 100, and 1000. With increasing H, the duct results [27] approach the isolated exponential boundary layer results (this work). (b) Optimal wave number. (c) Optimal time interval.

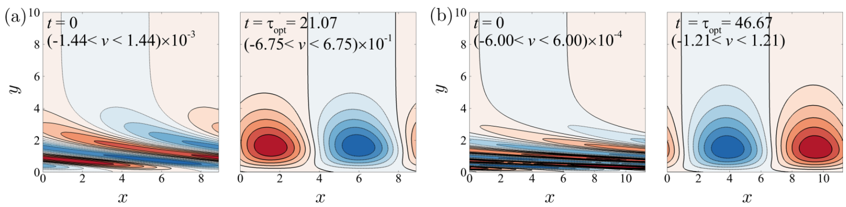

FIG. 4. Optimized $\hat{v}$-velocity fields. (a) $r_{\mathrm{c}} = 0.0146$, $\alpha_{\mathrm{opt}} = 0.7071$. (b) $r_{\mathrm{c}} = 0.146$, $\alpha_{\mathrm{opt}} = 0.5586$. Simulations computed with $L_y = 28.28$ and images clipped at $y = 10$. Solid lines (red flooding) positive; dotted lines (blue flooding) negative.

growth routines can identify the initial energy representing separatrix 1, if the target time specified is long enough to allow the minimal seed to reach the turbulent attractor [33,34]. This target time is not known a priori. It is shown in Sec. V that the turbulent attractor is reached between $t = 1.4 \times 10^3$ and $t = 2 \times 10^3$ at $r_c = 0.585$. As $\tau_{opt} = 75.94$ at $r_c = 0.585$ (Fig. 3) the additional computation cost is proportional to $t/\tau_{opt} = 18.44$–26.34. In contrast, the hydrodynamic pipe flow work in [33] had $\tau_{opt} \lesssim 30$, while the minimal seed reached the turbulent attractor by $t = 75$, so $t/\tau_{opt} \lesssim 2.5$. Thus, for this problem, it was not amenable to determine separatrix 1 directly from the nonlinear transition growth algorithm.

The scheme to determine the nonlinear growth $G_N = \|\hat{\boldsymbol{u}}(\tau)\|/\|\hat{\boldsymbol{u}}(0)\|$, for a specified target time τ, optimized over all initial perturbations, requires maximizing the functional [33,55],

$$\begin{aligned}\mathscr{L} := &\left\langle \frac{1}{2}\hat{\boldsymbol{u}}(\tau)^2 \right\rangle - \lambda_0 \left[\left\langle \frac{1}{2}\hat{\boldsymbol{u}}(0)^2 \right\rangle - E_P \right] - \int_0^\tau \langle \Pi \boldsymbol{\nabla}_\perp \cdot \hat{\boldsymbol{u}} \rangle dt - \int_0^\tau \Gamma(t) \langle \hat{\boldsymbol{u}} \cdot \boldsymbol{e_z} \rangle dt \\ &- \int_0^\tau \left\langle \hat{\boldsymbol{u}}^\ddagger \cdot \left[\frac{\partial \hat{\boldsymbol{u}}}{\partial t} + (\boldsymbol{U} \cdot \boldsymbol{\nabla}_\perp)\hat{\boldsymbol{u}} + (\hat{\boldsymbol{u}} \cdot \boldsymbol{\nabla}_\perp)\boldsymbol{U} + (\hat{\boldsymbol{u}} \cdot \boldsymbol{\nabla}_\perp)\hat{\boldsymbol{u}} + \frac{1}{\rho}[\Lambda(t)\boldsymbol{e_z} + \boldsymbol{\nabla}_\perp p'] \right.\right. \\ &\left.\left. - \frac{1}{\mathrm{Re_S}}\nabla_\perp^2 \hat{\boldsymbol{u}} + \frac{1}{\mathrm{Re_S}}\hat{\boldsymbol{u}} \right] \right\rangle dt, \end{aligned} \tag{7}$$

where the Lagrange multipliers λ_0, Π and $\Gamma(t)$ are constraints on the specified initial energy of the perturbation $E_P = (1/2)\int \hat{\boldsymbol{u}}(0)^2 d\Omega$, mass conservation and flow rate, respectively. Pressure is decomposed into a time-varying pressure gradient $\Lambda(t)$, to maintain the flow rate, and fluctuating component p'. $\langle \ldots \rangle$ represent integrals over the computational domain. The Lagrange multiplier $\hat{\boldsymbol{u}}^\ddagger$ ensures that the full nonlinear Navier–Stokes equations are enforced over all times $0 < t < \tau$ [56]. Each iteration j of the optimization procedure begins with the forward evolution, from $t = 0$ to $t = \tau$, of the nonlinear perturbation equation [within the square brackets of the last term of Eq. (7)]. If G_N for iteration j is larger than for iteration $j-1$, then the adjoint "initial" field is $\hat{\boldsymbol{u}}^\ddagger(\tau) = \hat{\boldsymbol{u}}(\tau)$ and the iteration continues with backward evolution via the adjoint equations,

$$\begin{aligned}\frac{\partial \hat{\boldsymbol{u}}^\ddagger}{\partial t} &= (\boldsymbol{\nabla}_\perp \boldsymbol{U})^{\mathrm{T}} \cdot \hat{\boldsymbol{u}}^\ddagger - (\boldsymbol{U} \cdot \boldsymbol{\nabla}_\perp)\hat{\boldsymbol{u}}^\ddagger + (\boldsymbol{\nabla}_\perp \hat{\boldsymbol{u}})^{\mathrm{T}} \cdot \hat{\boldsymbol{u}}^\ddagger - (\hat{\boldsymbol{u}} \cdot \boldsymbol{\nabla}_\perp)\hat{\boldsymbol{u}}^\ddagger \\ &\quad + \Gamma(t)\boldsymbol{e_z} - \boldsymbol{\nabla}_\perp \Pi - \frac{1}{\mathrm{Re_S}}\nabla_\perp^2 \hat{\boldsymbol{u}}^\ddagger - \frac{1}{\mathrm{Re_S}}\hat{\boldsymbol{u}}^\ddagger, \end{aligned} \tag{8}$$

$$\boldsymbol{\nabla}_\perp \cdot \hat{\boldsymbol{u}}^\ddagger = 0, \tag{9}$$

from time $t = \tau$ to $t = 0$. An under-relaxation factor ϵ_N is chosen (say, 0.5) for the first iteration, or adjusted as described in Ref. [33]. The initial field for the $j+1$ iteration is $\hat{\boldsymbol{u}}^{j+1}(0) = \hat{\boldsymbol{u}}^j(0) + \epsilon_N[-\lambda_0 \hat{\boldsymbol{u}}^j(0) + \hat{\boldsymbol{u}}^{\ddagger,j}(0)]/\lambda_0$, where λ_0 is sought such that $\langle \hat{\boldsymbol{u}}^{j+1}(0) \cdot \hat{\boldsymbol{u}}^{j+1}(0) \rangle = 2E_P$. However, if G_N does not increase in iteration j, then adjoint evolution is not performed, as the updated field (iteration j) is further from the optimal than the previous ($j-1$) field. An additional adjustment is then made to the under-relaxation factor, $\epsilon_N \to \epsilon_N/4$. The forward iteration restarts with $\hat{\boldsymbol{u}}^j(0) = \hat{\boldsymbol{u}}^{j-1}(0) + \epsilon_N[-\lambda_0 \hat{\boldsymbol{u}}^{j-1}(0) + \hat{\boldsymbol{u}}^{\ddagger,j-1}(0)]/\lambda_0$. This ensures monotonic growth in successive iterations, and avoids contaminating the initial field after iterations with too large an ϵ_N. Iterations continue until the relative change in λ_0 and residual $[\delta\mathscr{L}/\delta\hat{\boldsymbol{u}}(0)]/\lambda_0^2$ are both below a specified tolerance, following Ref. [33].

Validation of the nonlinear transient growth is provided in Table III at $r_c = 0.293$, considering the polynomial order and time step, for two initial energies. The same mesh for determination of the linear optimals is used, with $L_y = 28.28$. As the nonlinear transient growth scheme does not evolve the perturbations through turbulent states, the resolution requirements are similar to those of the linear computations, Sec. III A, rather than the nonlinear forward evolutions, Sec. V A. For consistency, the same time step of $\Delta t = 1.25 \times 10^{-3}$ was selected, with $N_p = 15$.

TABLE III. Validation of the time step and polynomial order for the nonlinear transient growth, for initial perturbation energies of 10^{-6} and 10^{-4}, at $r_c = 0.293$, $n = 1$. The mesh is based on the $N_{el} = 154$ case from linear optimization, except with $L_y = 28.28$. The tolerance for convergence was 10^{-7}. Nonlinear computations use the linear α_{opt} and τ_{opt}.

Δt	G_N; $E_P = 10^{-6}$	|% Error|	N_p	G_N; $E_P = 10^{-4}$	|% Error|
5×10^{-3}	55.9721743040676	1.88×10^{-5}	11	54.6714139912327	5.24×10^{-4}
2.5×10^{-3}	55.9721692244256	9.69×10^{-6}	13	54.6711233880979	7.81×10^{-6}
1.25×10^{-3}	55.9721654578752	2.96×10^{-6}	15	54.6711274190738	4.31×10^{-7}
6.25×10^{-4}	55.9721633006764	8.91×10^{-7}	17	54.6711283768056	1.32×10^{-6}
3.125×10^{-4}	55.9721637995307	0	19	54.6711276549269	0

B. Results

Nonlinear optimals were computed with $\tau = \tau_{opt}$ and domain lengths based on $n = 1$, $n = 2$ or $n = 3$ repetitions of $l_{x,opt}$, for various initial energies. These results are shown in Fig. 5(a), which compares the difference between the linear transient growth of the linear optimal and the nonlinear transient growth of the nonlinear optimal (red data points), with the former always greater than the latter (all results are positive valued). As nonlinear collaboration between linear transient growth mechanisms cannot occur, the maximum growth obtained at vanishingly small initial energy is greater than with finite initial energy. Figure 5(a) also shows that for an initial energy defined per unit duct length, the results are not dependent on domain length. Thus, it is the initial energy density that is the important parameter.

Additionally, Fig. 5(a) compares the difference in the linear transient growth of the linear optimal and the nonlinear transient growth of the linear optimal scaled to E_0 (square symbols). These results are almost coincident with those for the nonlinear growth of the nonlinear optimal (triangle symbols). Thus, the difference between the nonlinear and linear growth is mostly due to the finite

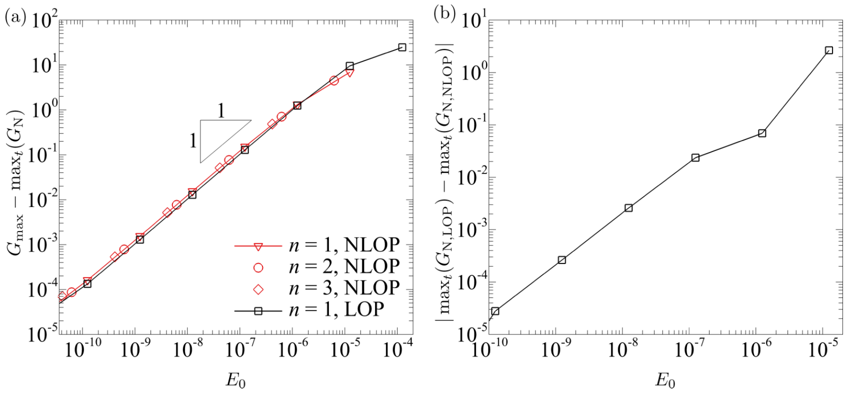

FIG. 5. Comparison between linear and nonlinear optimals for various initial energies $E_0 = \int \hat{u}^2 + \hat{v}^2 \, d\Omega / \int U^2 \, d\Omega$ at $r_c = 0.293$. (a) Difference in the maximum linear growth obtained with the linear optimal (LOP) and maximum nonlinear growth with the nonlinear optimal (NLOP), for three domain lengths, and difference in the linear growth of the LOP and the nonlinear growth of the LOP scaled to E_0 ($n = 1$ only). (b) Comparison between the nonlinear growth of the NLOP and nonlinear growth of the LOP scaled to E_0 ($n = 1$). The linear growth of the LOP is $G_{max} = 55.9876$.

energy of the initial field. The mode structure is only very weakly dependent on initial energy (the linear and nonlinear optimals are virtually indistinguishable; not shown). This supports a remark made by [34], that in two-dimensional systems the nonlinear optimal contains the linear mode trivially. This comparison is further highlighted in Fig. 5(b), which directly compares the nonlinear growth of the nonlinear optimal to the nonlinear growth of the linear optimal. This difference is very small for initial energies up to $E_0 \approx 10^{-6}$, where $E_0 = \int \hat{u}^2 + \hat{v}^2 \, d\Omega / \int U^2 \, d\Omega$ is considered to account for the varying domain length.

For $E_0 \gtrsim 10^{-6}$ the nonlinear growth of the nonlinear optimal then slightly exceeds the nonlinear growth of the rescaled linear optimal. However, the differences are still small at $E_0 = 10^{-5}$, which is an initial energy more than sufficient to generate large amounts of nonlinear second-stage growth, as is discussed in detail in Sec. V. Thus, there is little "error" in estimating the minimal seed energy with the linear optimal, for the initial energies of interest.

V. NONLINEAR EVOLUTION AT SPECIFIED INITIAL ENERGIES

A. Validation

The initial energy of each linear optimal is scaled to E_0 when seeded onto the base flow. Forward evolution of the full nonlinear Eqs. (1) and (2) then commences. The measures $E_{\mathrm{v}} = (1/2) \int \hat{v}^2 \, d\Omega$ and $E = (1/2) \int \hat{u}^2 + \hat{v}^2 \, d\Omega$ are defined. These separate the growth of the perturbation, captured by E_{v}, and the effective modulation of the base flow, via a streamwise-independent structure, captured by E.

The effect of time step variation is depicted in Figs. 6(a) and 6(b). These show negligible differences between $\Delta t = 1.25 \times 10^{-3}$ and significantly smaller time step sizes. $\Delta t = 1.25 \times 10^{-3}$ was therefore deemed satisfactory. The polynomial order has to be more carefully selected, as the spatial accuracy is strongly dependent on Re_{S} and E_0, as shown in Figs. 6(c) and 6(d). Discrepancies within chaotic regions cannot reasonably be avoided, although the trajectories thereafter match well. A polynomial order of $N_{\mathrm{p}} = 19$ is sufficient for smaller initial energies (all r_{c}), and either $N_{\mathrm{p}} = 23$ ($r_{\mathrm{c}} = 0.293$ or 0.585) or $N_{\mathrm{p}} = 29$ ($r_{\mathrm{c}} = 1.463$) for larger initial energies, based on resolution testing approximately 40 different $\mathrm{Re}_{\mathrm{S}} - E_0$ combinations.

B. Delineation energy

The nonlinear evolution of linear optimal perturbations in domains with lengths based on $n = 1$ repetitions of $l_{x,\mathrm{opt}}$ are considered first. The lower delineation energy E_{D}, representing separatrix 1, is shown in Fig. 7(a) as a function of Reynolds number. Figures 7(b) and 7(c) demonstrate how the delineation energy is determined at $r_{\mathrm{c}} = 0.585$ ($E_{\mathrm{D}} = 2.69187 \times 10^{-6}$). E_{D} is determined with a bisection method [35,41,42]. However, the bisection method is modified as when $E_0 = E_{\mathrm{D}}$ the energy-time history does not hover about a mean value [41], as the solution is not on the edge of a stable manifold. Furthermore, all turbulent flows eventually relaminarize. Thus, the flow is deemed returning to a laminar state if its energy reaches a secondary local maximum, and is deemed to be turbulent if its energy exhibits a secondary local inflection point. An initial energy between the largest initial energy that remains laminar, and smallest that incurs transition to turbulence, is then tested, and defined as either the new laminar or new turbulent bound. This process is repeated until E_{D} is determined to 4 significant figures.

For the r_{c} simulated, Fig. 7(a), there is no clear trend in E_{D} with Re_{S} (the dashed guideline has an r_{c}^{-1} trend). A dot-dashed line at $r_{\mathrm{c}} = 0.293$ provides a rough lower estimate for the Re_{S} at which no perturbation is capable of reaching the turbulent attractor, with any initial energy (in an $n = 1$ domain). At $r_{\mathrm{c}} = 0.293$ nonlinear second-stage growth yielded a maximum in E greater than the initial linear maximum, at best. For $r_{\mathrm{c}} \leqslant 0.146$ the linear growth provided the global maximum in E.

A second delineation energy $E_{\mathrm{D},2} = 1.09646 \times 10^{-5}$ could also be defined for $r_{\mathrm{c}} = 0.585$, denoting seperatrix 2. The bisection method is unchanged, except that now it is the larger initial energy

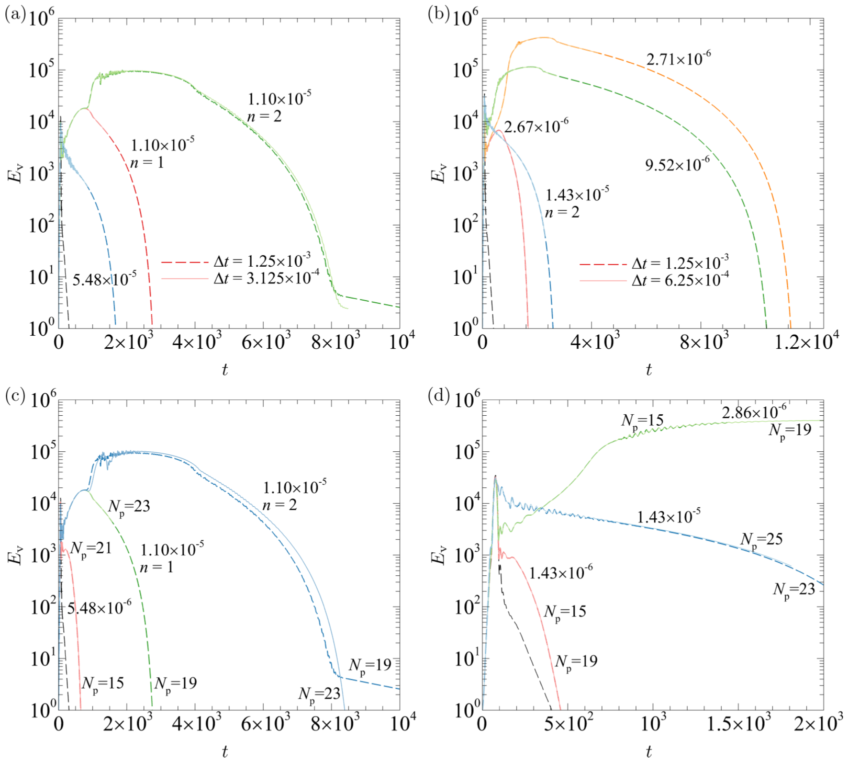

FIG. 6. (a, b) temporal and (c, d) spatial resolution testing of the nonlinear evolution of linear optimals, for various initial energies E_0. (a & c) $r_c = 0.293$. (b & d) $r_c = 0.585$. The smaller polynomial order (value annotated for each curve), or larger time step (see legend), is denoted by a long dashed line for each E_0. $n = 1$ unless otherwise stated. A black long dashed line represents the linear evolution.

that is considered laminar, and the smaller initial energy that transitions to tuburbulence. Thus, there is only a finite band of initial energies $E_D \leqslant E_0 \leqslant E_{D,2}$ able to attain a temporary turbulent state. Only perturbations which resemble conventional, linearly grown TS waves were able take advantage of the nonlinear second-stage growth, which appears to be the only subcritical route to high energy turbulent states. This process is disrupted at larger E_0, which noticeably distort the perturbation, inducing rapid decay after the linear growth, similar to the discussion in Ref. [45]. These arguments are also supported by additional nonlinear simulations, at $r_c = 0.585$ and $r_c = 1.463$. The initial seeds tested for comparison were the eigenvector field which generates the second largest linear growth in τ_{opt}, and random noise, in the same size domains and over a wide range of initial energies. In none of these simulations was a TS wave structure observed akin to that necessary to obtain the nonlinear second-stage growth observed in Fig. 7(b). The eigenvector generating the second largest linear growth managed to achieve only very small amounts of nonlinear second-stage growth. Random noise seeds monotonically decayed. Overall, only the eigenvector which generates the largest linear growth was able to transition to turbulence, by virtue of at least an additional order of

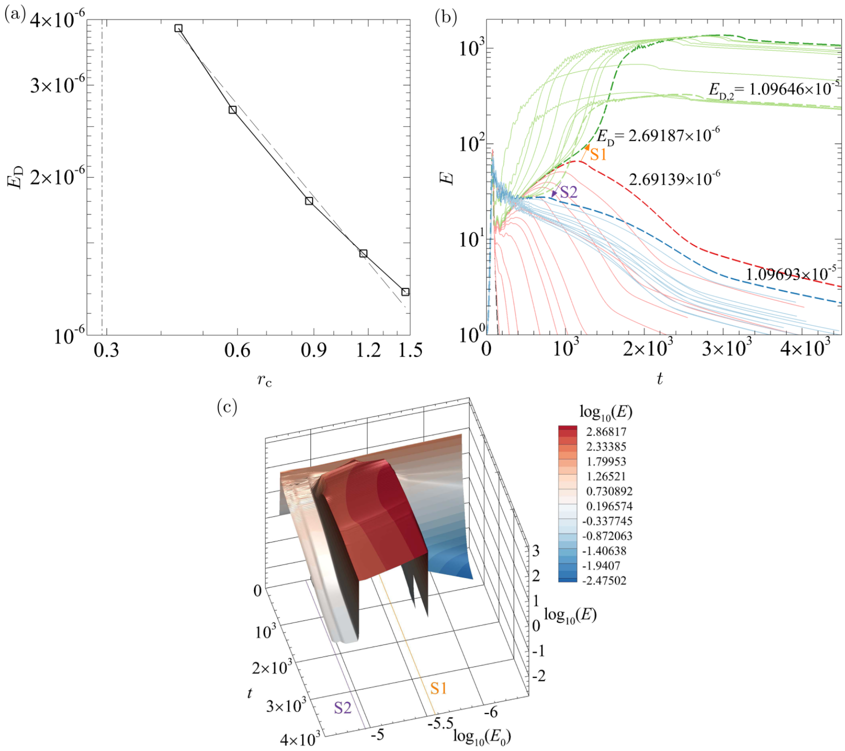

FIG. 7. (a) The lower delineation energy as a function of $r_c = \mathrm{Re_S}/\mathrm{Re_{S,crit}}$ ($n = 1$ domain). The dot-dashed line roughly approximates the maximum r_c for which the delineation energy is undefined. (b) Energy time histories at $r_c = 0.585$, varying E_0. Light red curves with $E_0 < E_D$ have a secondary local maximum at best. The orange arrow indicates the switch from local maximum to inflection point, and the lowest initial energy (dashed dark green curve; E_D) sufficient to cross separatrix 1. All green curves transition to turbulence. The largest initial energy that avoids crossing separatrix 2 ($E_{D,2}$) is also dashed. Light blue curves with $E_0 > E_{D,2}$, which are briefly chaotic, all cross separatrix 2, with the purple arrow indicating the switch back from an inflection point to a local maximum. All curves are rescaled to start at unity to aid visualization, and the linear curve is denoted with a black long dashed line. At $r_c = 0.585$, $G_{max} = 89.9630$, while the maximum gain at $E_0 = E_D$ exceeds 10^3. (c) Same results as (b), except depicted as a 3D surface, to accentuate the discontinuous changes at the separatrices.

magnitude of nonlinear growth. It will be shown later that E_D does not vary with n (for $r_c \geqslant 0.439$) but that $E_{D,2}$ does.

C. Temporal evolution of optimals

The observable effects of nonlinearity are similar so long as nonlinear second-stage growth occurs and regardless whether $E_0 > E_D$, $E_0 < E_D$ or if E_D is even defined ($r_c = 0.293$). As such, a linearized evolution at $r_c = 0.293$ is depicted in Fig. 8 and compared to the corresponding nonlinear evolution at $E_0 = 1.10 \times 10^{-5}$ in Fig. 9. Animations comparing the linear and nonlinear evolutions

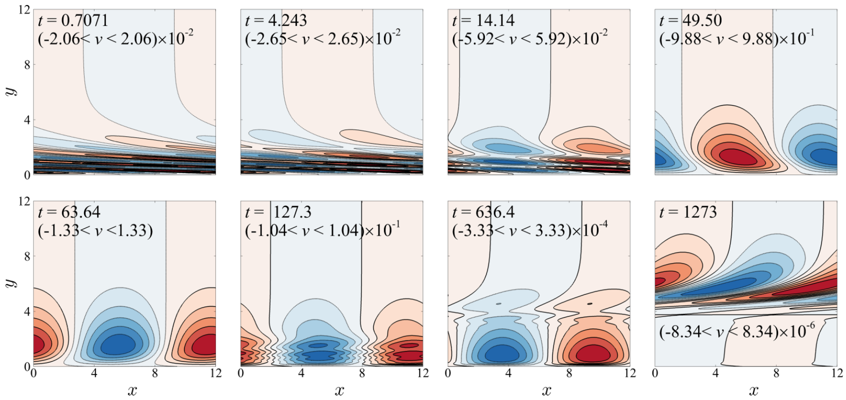

FIG. 8. Linearized evolution at $r_c = 0.293$, $L_y = 28.28$; $\hat{v}$-velocity contours. Solid lines (red flooding) positive; dotted lines (blue flooding) negative.

are also provided as supplementary material [57]. The first relevant differences are discerned at $t = 49.50$. The nonlinear evolution shows a mode which appears pinched at the wall, while the linear structure remains flat-bottomed. Following the nonlinear case, as time progresses, the structure rolls over this more slowly moving pinch point. At $t = 63.64$, additional localized circulation has appeared near the wall, with a very small region of negative velocity immediately upstream of the pinch point (at $x \sim 10.5$). Nonlinear second-stage growth then occurs, as the structure alternates between an arched TS wave ($t = 155.6$) and structures which break apart ($t = 169.7$) and coalesce into an arched TS wave again ($t = 282.8$). After this occurs a few times, the arched TS wave structure retains the form seen at $t = 282.8$ for over a thousand times units [see Fig. 13(b) for the corresponding energy time history], unlike the rapidly decaying linear counterpart. The advecting arched TS wave structure is eventually smoothed out near the wall (online animation only), and

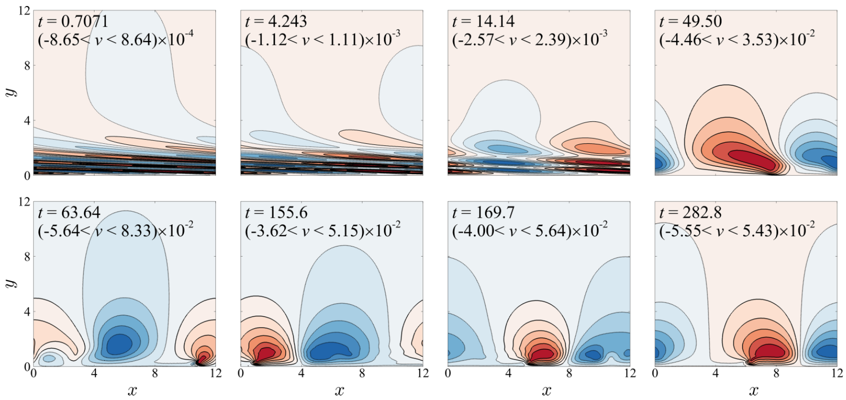

FIG. 9. Nonlinear evolution at $r_c = 0.293$, $L_y = 28.28$, $E_0 = 1.10 \times 10^{-5}$; $\hat{v}$-velocity contours. Solid lines (red flooding) positive; dotted lines (blue flooding) negative.

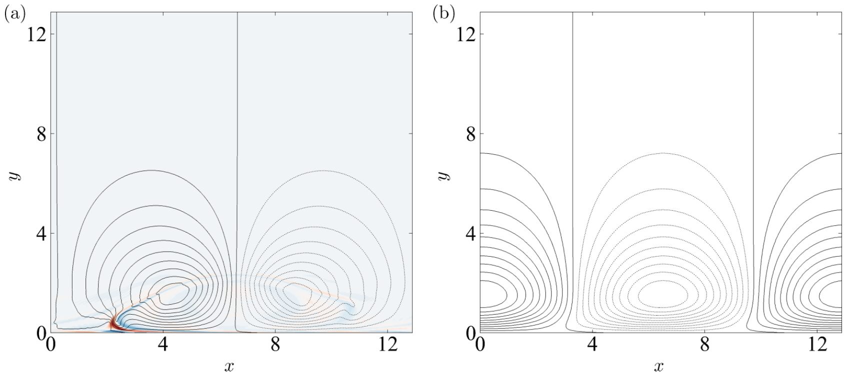

FIG. 10. (a) An example of the arched TS wave depicted by the $\hat{v}$-velocity contour lines (solid positive; dotted negative), at $r_c = 0.585$, $E_0 = 2.69187 \times 10^{-6} > E_D$, $t = 2.121 \times 10^3$. The underlying backbone of the arch is highlighted by overlaying the high-pass-filtered vorticity $\hat{\omega}_z$, where streamwise Fourier coefficients of modes $\kappa \leqslant 3$ have been removed. (b) An example of the conventional TS wave from the linear transient growth analysis, at $r_c = 0.585$, $t = 77.78$.

finally decays in the same manner as the linear counterpart. The linearized evolution monotonically decays as the structure leans into the mean shear ($t = 63.64$). This decay is more rapid for the near wall structure, leaving teardrop-shaped remnants outside the boundary layer as shown at $t = 1273$.

The arching of the TS wave appears paramount to the second-stage growth, as flatter TS waves only decay, if outside the neutral curve. An enlarged arched TS wave is shown in Fig. 10(a). A high-pass-filtered in-plane vorticity $\hat{\omega}_z = \partial\hat{v}/\partial x - \partial\hat{u}/\partial y$ is overlaid (streamwise Fourier coefficients of modes $\kappa \leqslant 3$ have been removed) to help guide the eye along the backbone of the arch, which is a thin, highly sheared layer. The largest vorticity magnitudes are still near the pinch point. To highlight the differences, a conventional TS wave is provided in Fig. 10(b), in its upright position, from the linear simulation. The arch is distinctly nonlinear, as the high-pass-filtered vorticity is zero for the conventional, linear TS wave. With increasing time, the conventional TS wave will tilt into the mean shear, whereas the arched TS wave remains upright, and will continue advecting through the domain relatively unchanged.

D. Roles of streamwise and wall-normal velocity components

The disturbance is now considered in more detail by separating growth solely in E, Fig. 11(a), and E_v, Fig. 11(b), for E_0 just greater than E_D. Growth appears larger in the latter measure as the wall-normal velocity makes up a smaller fraction of the energy in the initial field. Both $\hat{u}^2$ and $\hat{v}^2$ show noticeable second-stage growth. However, the $\hat{v}$-velocity magnitudes rapidly decrease after the second-stage growth, while the $\hat{u}$-velocity magnitudes, and thus E, decrease slowly.

The flow structures throughout this evolution are depicted in Fig. 12(a) for $\hat{u}$ and Fig. 12(b) for $\hat{v}$. While the maximum and minimum $\hat{v}$-velocities have similar magnitude, the $\hat{u}$ structures have a much larger magnitude minimum velocity (compared to the positive maximum). The $\hat{u}$ structures elongate until they eventually become uniform in the streamwise direction. Thus, as $\hat{v}$ decays, rather than reducing the magnitude of $\hat{u}$, continuity [Eq. (2)] is instead satisfied by reducing $\partial\hat{u}/\partial x$. This stores perturbation energy, recalling the slow decay of E in Fig. 11(a). The streamwise-independent structure forms regardless if $E_0 > E_D$ or $E_0 < E_D$. However, there is more perturbation energy to store if the flow transitions to turbulence, when $E_0 > E_D$. Last, it is worth noting that in this configuration, any nonsinusoidal streamwise variation indicates nonlinearity. Thus, the formation

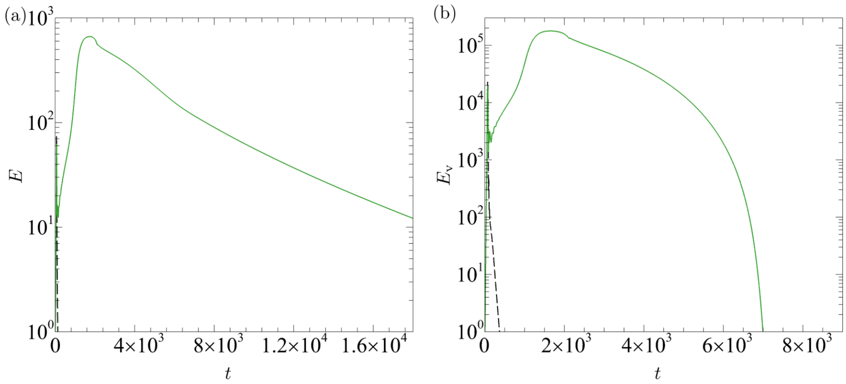

FIG. 11. Energy growth at $r_c = 0.439$, $E_0 = 3.869 \times 10^{-6} > E_D$, $n = 1$. (a) $E = (1/2)\int \hat{u}^2 + \hat{v}^2\, d\Omega$. (b) $E_v = (1/2)\int \hat{v}^2\, d\Omega$. At $r_c = 0.439$, $G_{max} = 73.9706$, and $E_D = 3.853 \times 10^{-6}$. All curves are rescaled to unit initial energy. The linear evolution is shown as a black long dashed line.

of the streamwise-independent structure is distinctly nonlinear. Streamwise-independent structures are also commonly observed in the final form of 3D simulations, e.g., Ref. [19]. By comparison, the $\hat{v}$ structures maintain similar size until they rapidly decay to a structure resembling the long time state of the linear optimal.

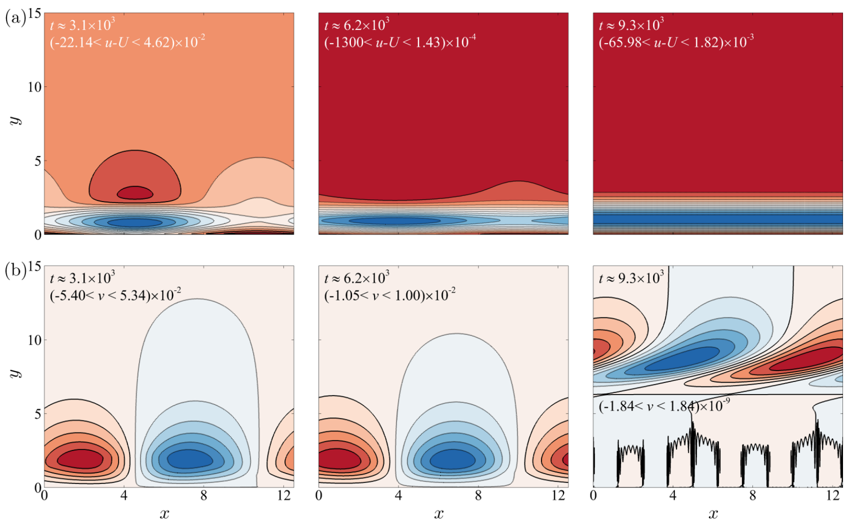

FIG. 12. Temporal evolution at $r_c = 0.439$, $L_y = 28.28$, $n = 1$, with $E_0 = 3.869 \times 10^{-6} > E_D$. (a) Streamwise perturbation $\hat{u} = u - U$. (b). Wall-normal perturbation $\hat{v} = v$. Solid lines (red flooding) positive; dotted lines (blue flooding) negative.

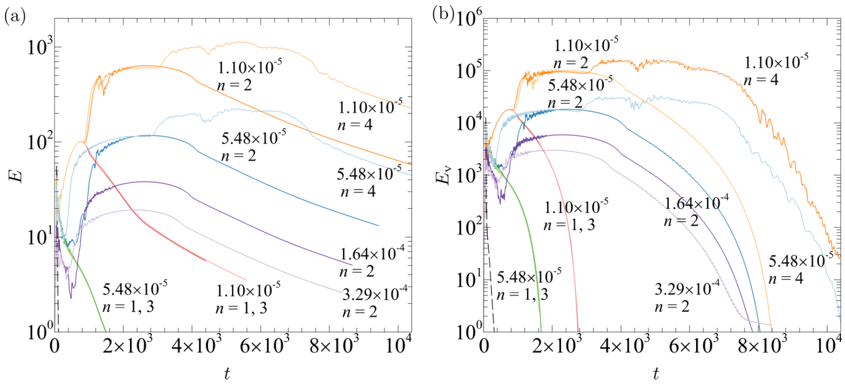

FIG. 13. Energy time histories at $r_c = 0.293$, varying the initial energy and domain length via repetitions n of $l_{x,\mathrm{opt}}$. (a) $E = (1/2)\int \hat{u}^2 + \hat{v}^2\, d\Omega$. (b) $E_v = (1/2)\int \hat{v}^2\, d\Omega$. Additional nonlinear growth is provided for even multiples of n, for all initial energies tested at $r_c = 0.293$, via pairwise coalescence of TS wave repetitions. All curves are rescaled to unit initial energy. The linear curves are presented with black long dashed lines. At $r_c = 0.293$, $G_{\max} = 55.9876$.

E. Influence of domain length

In Sec. V B, E_D and $E_{D,2}$ were considered in $n = 1$ domains. The effect of increasing the domain length on E_D and $E_{D,2}$ is now discussed, for integer repetitions up to $n = 4$ ($L_x = nl_{x,\mathrm{opt}}$). Growth measures E and E_v are shown in Fig. 13 for $r_c = 0.293$, with four distinct influences of domain length discussed. Recall that in the $n = 1$ domain at $r_c = 0.293$ some E_0 can attain growth to a secondary local maximum (e.g., $E_0 = 1.10 \times 10^{-5}$) but no E_0 transition to turbulence (cross separatrix 1). The first influence of domain length is that if two instances of the same perturbation evolve in an $n = 2$ domain, an inflection point appears in the energy-time history, indicating a crossing of separatrix 1. This occurs as the two individual repetitions of the TS wave structure coalesce into a single wave structure, with a rapid jump in energy at the secondary maximum from the $n = 1$ case. Second, at $E_0 = 1.10 \times 10^{-5}$, but with an $n = 3$ domain, this extra jump in energy does not occur ($n = 3$ follows $n = 1$). There would be a mismatch in wavelengths if only one pair of structures coalesced, prohibiting the interaction of all three repetitions. Third, again at $E_0 = 1.10 \times 10^{-5}$, the $n = 4$ case can experience both the $n = 2$ pairwise coalescence ($4 \rightarrow 2$ repetitions), and then another coalescence ($2 \rightarrow 1$ repetition), which allows for an additional, albeit smaller, jump in energy. In the $E_0 = 1.10 \times 10^{-5}$ case, the $n = 4$ curve closely follows the $n = 2$ curve early on, indicating the time it takes for the lower energy case to sense the full domain length. However, fourth, the $E_0 = 5.48 \times 10^{-5}$ case differs between $n = 2$ and $n = 4$, with the structure able to increase in size more rapidly in the latter case when reforming to an arched TS wave structure. This is inhibited in smaller ($n = 1$) domains, in which the structure decays because it is distorted by too large an initial energy. The same is true of even larger initial energies, $E_0 = 1.64 \times 10^{-4}$ and 3.29×10^{-4}, which undergo second-stage growth in the $n = 2$ domain, while the $n = 1$ cases only decay after the linear maximum.

The $\hat{v}$-velocity fields are depicted in Fig. 14 for $E_0 = 5.48 \times 10^{-5}$, $n = 2$ at $r_c = 0.293$. Recall that with $n = 1$, $E_0 = 1.10 \times 10^{-5}$ attains second-stage growth, whereas $E_0 = 5.48 \times 10^{-5}$ is too highly energized and rapidly decays, as the flow field does not resemble an arched TS wave, e.g., Fig. 10(a). The two repetitions of the distorted TS wave shown in Figs. 14(a), 14(b) are not yet interacting. The interaction between the two wavelengths is shown in Fig. 14(c), where one repetition becomes dominant, and will shortly subsume the other, Fig. 14(d). In Fig. 14(e), the wave

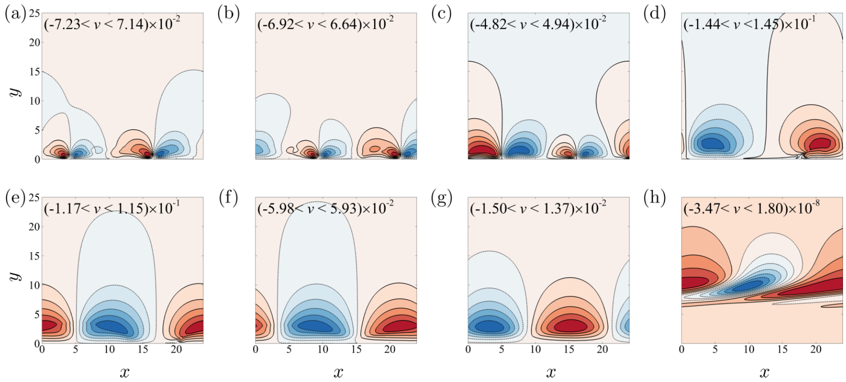

FIG. 14. Temporal evolution at $r_c = 0.293$, $L_y = 28.28$, $n = 2$, $E_0 = 5.48 \times 10^{-5}$; $\hat{v}$-velocity contours. Solid lines (red flooding) positive; dotted lines (blue flooding) negative. This case decays in an $n = 1$ domain, but undergoes second-stage growth in an $n = 2$ domain because it restructures to an arched TS wave after the coalescence of the two individual perturbation repetitions.

has re-formed into a single repetition of the arched TS wave structure. The arched TS wave then undergoes nonlinear second-stage growth, as it slowly relaxes back to a conventional TS wave, Fig. 14(g). It finally decays to a field resembling the long time solution of a linear transient growth computation. However, unlike a linear optimal, this process will still have stored perturbation energy in a sheet of negative $\hat{u}$-velocity, visible when comparing the energy measures shown in Figs. 13(a) and 13(b).

The energy growth at larger Reynolds numbers is depicted in Fig. 15. These illustrate the length of time over which high energy states are maintained when $E_0 > E_D$. At $r_c = 0.585$, $n = 1$, $E_0 =$

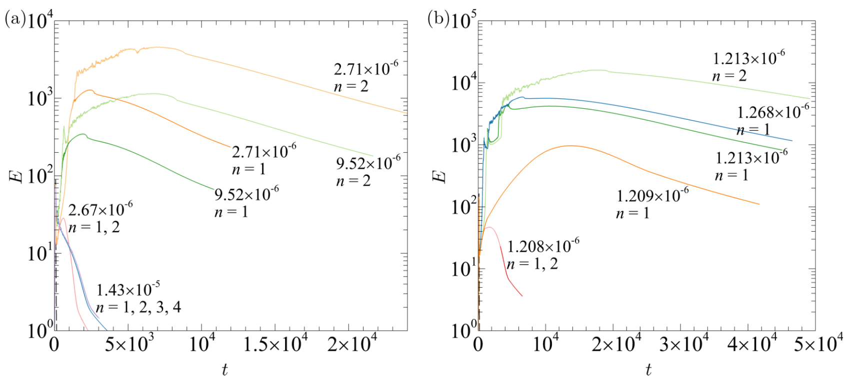

FIG. 15. Energy time histories, varying the initial energy and domain length via repetitions n of $l_{x,\mathrm{opt}}$. (a) $r_c = 0.585$, $G_{\max} = 89.9630$, $E_D = 2.6919 \times 10^{-6}$, maximum nonlinear gain observed for $E_0 > E_D$ is $\approx 4 \times 10^3$ ($n = 2$). (b) $r_c = 1.463$, $G_{\max} = 166.4092$, $E_D = 1.2096 \times 10^{-6}$, maximum nonlinear gain observed for $E_0 > E_D$ is $\approx 2 \times 10^4$ ($n = 2$). All curves are rescaled to unit initial energy. $E_0 < E_D$ are unable to take advantage of the extra domain length, and still rapidly decay.

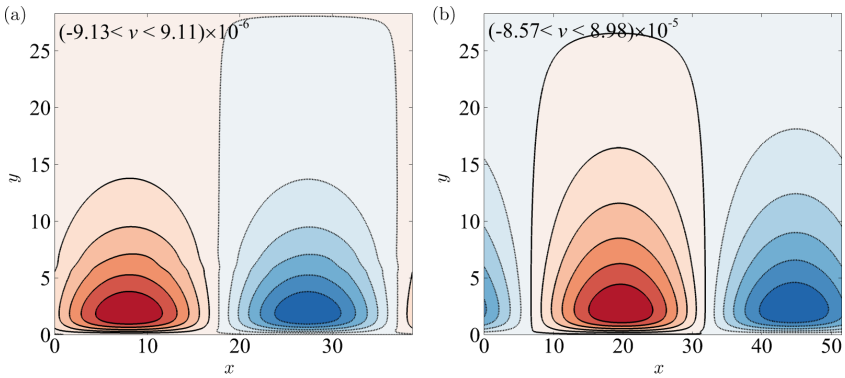

FIG. 16. Contours of $\hat{v}$-velocity at $r_c = 0.585$, $E_0 = 1.43 \times 10^{-5}$, $L_y = 28.28$ at $t \approx 2.8 \times 10^3$. (a) $n = 3$. (b) $n = 4$. Solid lines (red flooding) positive; dotted lines (blue flooding) negative. Although the $n = 3$ and $n = 4$ cases coalesce, without the TS wave having an arched appearance, they decay monotonically.

$2.67 \times 10^{-6} < E_D$ rapidly decays, while $E_0 = 2.71 \times 10^{-6} > E_D$ maintains large energies for the order of 10^4 time units, particularly so when $n = 2$. This is even clearer at $r_c = 1.463$, with very large amounts of growth, and a very slow decay, when $E_0 = 1.213 \times 10^{-6} > E_D$. A case $E_0 = 1.209 \times 10^{-6}$ just slightly below $E_D = 1.2096 \times 10^{-6}$ provides a clearer indication of the additional growth due to reaching the turbulent attractor, compared to the underlying nonlinear second-stage growth (to a local maximum). Of additional interest is that it takes a far greater time to relaminarize turbulent states in larger domains. The oscillations appear to be less energetic, or otherwise damped out more rapidly, in the $n = 1$ domains. Last, all $r_c = 0.585$ and $r_c = 1.463$ cases show that $E_0 < E_D$ cannot take advantage of the extra space afforded in $n = 2$ domains, and decay following the $n = 1$ curves, such that E_D does not depend on domain length. Note that at $r_c = 1.463$ the wave numbers in $n = 1$ and $n = 2$ domains are outside the neutral curve.

One final influence of the domain length is considered. At $r_c = 0.585$, $E_{D,2} = 1.09646 \times 10^{-5}$ when $n = 1$, Fig. 7(b). Over-energized cases, with $E_0 = 1.43 \times 10^{-5} > E_{D,2}$ and in longer domains ($n = 2$ through $n = 4$), are shown in Fig. 15(a). These all appear to decay coincidentally with the $n = 1$ case, seemingly implying that $E_{D,2}$ has not significantly changed with increasingly domain length, at $r_c = 0.585$. Comparatively, at $r_c = 0.293$ with $n = 2$ (Fig. 13) second-stage growth is observed (akin to cases with $E_D \leqslant E_0 \leqslant E_{D,2}$), in multiple over-energized situations, via the restructuring depicted in Fig. 14. This would imply that at $r_c = 0.293$, $E_{D,2}$ has changed noticeably with increasing domain length. At $r_c = 0.585$, with a larger initial energy, the vortex merging process may occur too rapidly, unlike the $r_c = 0.293$, $n = 2$ cases. At $r_c = 0.585$ the $n = 3$ and $n = 4$ cases reformed into the simpler conventional flat bottomed TS wave structure, shown part way through their decay in Fig. 16, rather than arched TS waves capable of nonlinear second-stage growth. This issue may also be exacerbated by the wavelength restrictions imposed by the periodic boundary conditions, recalling the $r_c = 0.293$, $n = 3$ case indicated that a mismatch in wavelength between TS wave instances can also prevent growth. Overall, results in longer domain do not contradict the fact that $E_0 = 1.43 \times 10^{-5}$ does not incite sustained turbulence at $r_c = 0.585$, so that separatrix 2 is still clearly defined. However, they do indicate that $E_{D,2}$ can be very difficult to accurately determine, as consistent behavior was not observed across all Reynolds numbers tested. As a final note, the investigations at $r_c = 0.585$, $n = 3$ and $n = 4$ also highlight that the energy growth is due to the form of the merged structure, and not coalescence, as the cases monotonically decay after the linear peak, during which time they are merging.

VI. CONCLUSIONS

The present work has numerically illustrated a subcritical route to turbulence driven by purely quasi-two-dimensional mechanisms, in a laminar Q2D exponential boundary layer. This system approximates a magnetohydrodynamic duct flow under a strong transverse magnetic field. It was shown that the linear optimals form an excellent approximation of the nonlinear optimals, when tested for small (linear τ_{opt}) target times. The transition process then has two stages. First, linear transient growth, via the Orr mechanism. This was followed by a second stage of substantial nonlinear growth, able to propel the flow across the laminar-turbulent basin boundary. However, only linear optimals with specific initial energies $E_{\mathrm{D}} \leqslant E_0 \leqslant E_{\mathrm{D},2}$ were capable of following this route to a temporary turbulent state, before later relaminarizing. The lower bound, E_{D}, defines the minimal seed energy capable of transition. The upper bound, $E_{\mathrm{D},2}$, represents an initial perturbation too highly energized, which chaotically distorts the TS wave, inducing rapid dissipation, rather than transitioning to turbulence.

The additional nonlinear growth which leads to the existence of the delineation energy E_{D} (separating states which rapidly relaminarize, and those which temporarily maintain turbulence) is linked to the formation of an arched TS wave, which forms when a conventional TS wave becomes pinched close to the wall. The arched TS wave still provides significant nonlinear growth when $E_0 < E_{\mathrm{D}}$, but does not transition because the optimal is too far (measured in an energy norm) from the boundary of the turbulent attractor. While closer to the basin boundary at $E_0 > E_{\mathrm{D},2}$, distortion of the conventional TS wave prevents the arch from forming. If the arch forms, then the relaxing of the arched TS wave into its conventional counterpart eventually results in the decay of the perturbation. However, during this process, perturbation energy is stored in a streamwise sheet of negative velocity, which effectively becomes a modulation to the original base flow. This modulated base flow may prove easier to re-excite if targeted by flow control methods. Overall, this quasi-two-dimensional system was found to be highly sensitive to the energy and structure of the initiating perturbation, with only the optimal initial field capable of transition for tests in shorter domains.

Larger domain lengths were also investigated. First, this showed that successive vortex merging may be capable of increasing the upper delineating energy $E_{\mathrm{D},2}$, by allowing distorting structures which would naturally rapidly decay, to instead coalesce into an arched TS wave structure, capable of sustaining turbulence over longer times. However, for sufficiently large initial energy, even very long domains still indicated the existence of high energy states which only rapidly decay after the initial linear growth. Perturbations with energy below the lower delineating energy E_{D} could not make use of the merging process, and still decayed in longer domains. Perturbations with $E_0 > E_{\mathrm{D}}$, which are sufficient to transition to turbulence, made use of the longer domains by pairwise coalescence of TS wave repetitions, achieving up to an order of magnitude of additional growth (compared to the shorter domains). The largest nonlinear gains are therefore achieved with $E_0 > E_{\mathrm{D}}$ and in longer domains. The comparison between the nonlinear growth of the linear optimal and the linear growth of the linear optimal is striking at larger Reynolds numbers. The nonlinear gains achieved, at Reynolds numbers approximately 40% below and above critical, were $\approx 4 \times 10^3$ and $\approx 2 \times 10^4$, respectively, compared to the optimized linear gains of 89.96 and 166.4, respectively. Furthermore, it appeared to take noticeably longer for turbulent oscillations to become subdued in longer domains.

The prospect of subcritical transitions is promising for the feasibility of self-cooled liquid metal reactor ducts. However, the fact that all Reynolds numbers are scaled on the boundary layer thickness must be kept in mind. Although a sidewall Reynolds number of 10^5 provided both very large growth, and slow relaminarization, at a realistic magnetic field strength, the corresponding Reynolds number based on the half duct height would be around 10^7. This is well beyond what is currently expected for reactor operation, which range from 10^4 to 10^6 [7,58,59]. Furthermore, no assessment of the sensitivity to wall properties on the formation of the arched TS wave has been performed, which given the thermal, electrical and slip issues considered in magnetohydrodynamic coolant duct flows [60–63], provides an important avenue for future work for self-cooled reactor designs.

Last, further investigation is warranted from a theoretical point of view. Although subcritical turbulent transitions were obtained, it is curious that all turbulent flow fields relaminarized. It would be worth exploring whether the turbulent states are in a true basin of attraction. The Q2D turbulent states may be unstable, such that a small deviation from their trajectory drives them out of the basin, causing relaminarization. However, it cannot be excluded that the behavior originates from the numerical method, or choice of periodic boundary conditions.

ACKNOWLEDGMENTS

The authors are grateful for discussions with Ashley Willis regarding the iterative approach applied to the nonlinear transient growth scheme. C.J.C. receives an Australian Government Research Training Program (RTP) Scholarship. A.P. is supported by Wolfson Research Merit Award Scheme Grant No. WM140032 from the Royal Society. This research was supported by the Australian Government via the Australian Research Council (Discovery Grants No. DP150102920 and No. DP180102647), the National Computational Infrastructure (NCI) and Pawsey Supercomputing Centre (PSC), and Monash University via the MonARCH cluster.

[1] E. Lindborg, Can the atmospheric kinetic energy spectrum be explained by two-dimensional turbulence? J. Fluid Mech. **388**, 259 (1999).

[2] A. Pothérat and J. Schweitzer, A shallow water model for magnetohydrodynamic flows with turbulent Hartmann layers, Phys. Fluids **23**, 055108 (2011).

[3] J. Sommeria and R. Moreau, Why, how, and when MHD turbulence becomes two-dimensional, J. Fluid Mech. **118**, 507 (1982).

[4] A. Thess and O. Zikanov, Transition from two-dimensional to three-dimensional magnetohydrodynamic turbulence, J. Fluid Mech. **579**, 383 (2007).

[5] R. Klein and A. Pothérat, Appearance of Three-Dimensionality in Wall Bounded MHD Flows, Phys. Rev. Lett. **104**, 034502 (2010).

[6] A. Pothérat and R. Klein, Why, how and when MHD turbulence at low R_m becomes three-dimensional, J. Fluid Mech. **761**, 168 (2014).

[7] S. Smolentsev, R. Moreau, and M. Abdou, Characterization of key magnetohydrodynamic phenomena in PbLi flows for the US DCLL blanket, Fusion Eng. Des. **83**, 771 (2008).

[8] V. Klüber, L. Bühler, and C. Mistrangelo, Numerical simulations of 3D magnetohydrodynamic flows in dual-coolant lead lithium blankets, Fusion Eng. Des. **146**, 684 (2019).

[9] L. Barleon, U. Burr, K. J. Mack, and R. Stieglitz, Heat transfer in liquid metal cooled fusion blankets, Fusion Eng. Des. **51**, 723 (2000).

[10] U. Burr, L. Barleon, U. Müller, and A. Tsinober, Turbulent transport of momentum and heat in magnetohydrodynamic rectangular duct flow with strong sidewall jets, J. Fluid Mech. **406**, 247 (2000).

[11] O. G. W. Cassels, W. K. Hussam, and G. J. Sheard, Heat transfer enhancement using rectangular vortex promoters in confined quasi-two-dimensional magnetohydrodynamic flows, Int. J. Heat Mass Transf. **93**, 186 (2016).

[12] C. Mistrangelo and L. Bühler, Influence of helium cooling channels on magnetohydrodynamic flows in the HCLL blanket, Fusion Eng. Des. **84**, 1323 (2009).

[13] C. Mistrangelo, L. Bühler, and G. Aiello, Buoyant-MHD flows in HCLL blankets caused by spatially varying thermal loads, IEEE Trans. Plasma Sci. **42**, 1407 (2014).

[14] S. Smolentsev, C. Wong, S. Malang, M. Dagher, and M. Abdou, MHD considerations for the DCLL inboard blanket and access ducts, Fusion Eng. Des. **85**, 1007 (2010).

[15] C. Mistrangelo and L. Bühler, Magnetohydrodynamic pressure drops in geometric elements forming a HCLL blanket mock-up, Fusion Eng. Des. **86**, 2304 (2011).

[16] W. K. Hussam, M. C. Thompson, and G. J. Sheard, Enhancing heat transfer in a high Hartmann number magnetohydrodynamic channel flow via torsional oscillation of a cylindrical obstacle, Phys. Fluids **24**, 113601 (2012).
[17] A. H. A. Hamid, W. K. Hussam, and G. J. Sheard, Combining an obstacle and electrically driven vortices to enhance heat transfer in a quasi-two-dimensional MHD duct flow, J. Fluid Mech. **792**, 364 (2016).
[18] A. H. A. Hamid, W. K. Hussam, and G. J. Sheard, Heat transfer augmentation of a quasi-two-dimensional MHD duct flow via electrically driven vortices, Numer. Heat Tr. A-Appl. **70**, 847 (2016).
[19] D. S. Krasnov, E. Zienicke, O. Zikanov, T. Boeck, and A. Thess, Numerical study of the instability of the Hartmann layer, J. Fluid Mech. **504**, 183 (2004).
[20] D. Krasnov, M. Rossi, O. Zikanov, and T. Boeck, Optimal growth and transition to turbulence in channel flow with spanwise magnetic field, J. Fluid Mech. **596**, 73 (2008).
[21] P. Moresco and T. Alboussiére, Experimental study of the instability of the Hartmann layer, J. Fluid Mech. **504**, 167 (2004).
[22] B. Mück, C. Günther, U. Müller, and L. Bühler, Three-dimensional MHD flows in rectangular ducts with internal obstacles, J. Fluid Mech. **418**, 265 (2000).
[23] A. Pothérat, J. Sommeria, and R. Moreau, An effective two-dimensional model for MHD flows with a transverse magnetic field, J. Fluid Mech. **424**, 75 (2000).
[24] V. Dousset and A. Pothérat, Numerical simulations of a cylinder wake under a strong axial magnetic field, Phys. Fluids **20**, 7104 (2008).
[25] N. Kanaris, X. Albets, D. Grigoriadis, and S. Kassinos, Three-dimensional numerical simulations of magnetohydrodynamic flow around a confined circular cylinder under low, moderate, and strong magnetic fields, Phys. Fluids **25**, 074102 (2013).
[26] O. G. W. Cassels, T. Vo, A. Pothérat, and G. J. Sheard, From three-dimensional to quasi-two-dimensional: Transient growth in magnetohydrodynamic duct flows, J. Fluid Mech. **861**, 382 (2019).
[27] A. Pothérat, Quasi-two-dimensional perturbations in duct flows under transverse magnetic field, Phys. Fluids **19**, 074104 (2007).
[28] T. Vo, A. Pothérat, and G. J. Sheard, Linear stability of horizontal, laminar fully developed, quasi-two-dimensional liquid metal duct flow under a transverse magnetic field heated from below, Phys. Rev. Fluids **2**, 033902 (2017).
[29] D. Krasnov, O. Zikanov, M. Rossi, and T. Boeck, Optimal linear growth in magnetohydrodynamic duct flow, J. Fluid Mech. **653**, 273 (2010).
[30] P. H. Roberts, *An Introduction to Magnetohydrodynamics* (Longmans, Green, New York, 1967).
[31] O. Levin, E. N. Davidsson, and D. S. Henningson, Transition thresholds in the asymptotic suction boundary layer, Phys. Fluids **17**, 114104 (2005).
[32] T. Albrecht, R. Grundmann, G. Mutschke, and G. Gerbeth, On the stability of the boundary layer subject to a wall-parallel Lorentz force, Phys. Fluids **18**, 098103 (2006).
[33] C. C. T. Pringle, A. P. Willis, and R. R. Kerswell, Minimal seeds for shear flow turbulence: Using nonlinear transient growth to touch the edge of chaos, J. Fluid Mech. **702**, 415 (2012).
[34] R. R. Kerswell, C. C. T. Pringle, and A. P. Willis, An optimization approach for analyzing nonlinear stability with transition to turbulence in fluids as an exemplar, Rep. Prog. Phys. **77**, 085901 (2014).
[35] Y. Duguet, P. Schlatter, and D. S. Henningson, Localized edge states in plane Couette flow, Phys. Fluids **21**, 111701 (2009).
[36] Y. Duguet, A. Monokrousos, L. Brandt, and D. S. Henningson, Minimal transition thresholds in plane Couette flow, Phys. Fluids **25**, 084103 (2013).
[37] M. Farano, S. Cherubini, J.-C. Robinet, and P. D. Palma, Subcritical transition scenarios via linear and nonlinear localized optimal perturbations in plane poiseuille flow, Fluid Dyn. Res. **48**, 1409 (2016).
[38] S. Zammert and B. Eckhardt, Transition to turbulence when the Tollmien–Schlichting and bypass routes coexist, J. Fluid Mech. **880**, R2 (2019).
[39] Y. Duguet, P. Schlatter, D. S. Henningson, and B. Eckhardt, Self-Sustained Localized Structures in a Boundary Layer Flow, Phys. Rev. Lett. **108**, 044501 (2012).
[40] S. Cherubini, P. D. Palma, J.-C. Robinet, and A. Bottaro, The minimal seed of turbulent transition in the boundary layer, J. Fluid Mech. **689**, 221 (2011).

[41] M. Beneitez, Y. Duguet, P. Schlatter, and D. S. Henningson, Edge tracking in spatially developing boundary layer flows, J. Fluid Mech. **881**, 164 (2019).

[42] C. Vavaliaris, M. Beneitez, and D. S. Henningson, Optimal perturbations and transitions thresholds in boundary layer shear flows, Phys. Rev. Fluids **5**, 062401(R) (2020).

[43] T. Khapko, Y. Duguet, T. Kreilos, P. Schlatter, B. Eckhardt, and D. S. Henningson, Complexity of localized coherent structures in a boundary-layer flow, Eur. Phys. J. E **37**, 32 (2014).

[44] S. Cherubini, P. D. Palma, and J.-C. Robinet, Nonlinear optimals in the asymptotic suction boundary layer: Transition thresholds and symmetry breaking, Phys. Fluids **27**, 4108 (2015).

[45] N. B. Budanur, E. Marensi, A. P. Willis, and B. Hof, Upper edge of chaos and the energetics of transition in pipe flow, Phys. Rev. Fluids **5**, 023903 (2020).

[46] P. J. Schmid and D. S. Henningson, *Stability and Transition in Shear Flows* (Springer-Verlag, New York, 2001).

[47] K. M. Butler and B. F. Farrell, Three-dimensional optimal perturbations in viscous shear flow, Phys. Fluids A **4**, 1637 (1992).

[48] W. K. Hussam, M. C. Thompson, and G. J. Sheard, Optimal transient disturbances behind a circular cylinder in a quasi-two-dimensional magnetohydodynamic duct flow, Phys. Fluids **24**, 024105 (2012).

[49] G. J. Sheard, M. J. Fitzgerald, and K. Ryan, Cylinders with square cross-section: Wake instabilities with incidence angle variation, J. Fluid Mech. **630**, 43 (2009).

[50] G. E. Karniadakis, M. Israeli, and S. A. Orszag, High-order splitting methods for the incompressible Navier-Stokes equations, J. Comput. Phys. **97**, 414 (1991).

[51] S. C. Reddy, P. J. Schmidt, and D. S. Henningson, Pseudospectra of the Orr–Sommerfeld operator, SIAM J. Appl. Math. **53**, 15 (1993).

[52] L. N. Trefethen, A. E. Trefethen, S. C. Reddy, and T. A. Driscoll, Hydrodynamic stability without eigenvalues, Science **261**, 578 (1993).

[53] D. Barkley, H. M. Blackburn, and S. J. Sherwin, Direct optimal growth analysis for timesteppers, Int. J. Numer. Methods Fluids **57**, 1435 (2008).

[54] H. M. Blackburn, D. Barkley, and S. J. Sherwin, Convective instability and transient growth in flow over a backward-facing step, J. Fluid Mech. **603**, 271 (2008).

[55] C. C. T. Pringle, A. P. Willis, and R. R. Kerswell, Fully localized nonlinear energy growth optimals in pipe flow, Phys. Fluids **27**, 064102 (2015).

[56] C. C. T. Pringle and R. R. Kerswell, Using Nonlinear Transient Growth to Construct the Minimal Seed for Shear Flow Turbulence, Phys. Rev. Lett. **105**, 154502 (2010).

[57] See Supplemental Material at http://link.aps.org/supplemental/10.1103/PhysRevFluids.5.113902 for comparisons of linear and nonlinear evolution; short and long time histories.

[58] E. M. de les Valls, L. Batet, V. de Medina, J. Fradera, and L. A. Sedano, Qualification of MHD effects in dual-coolant DEMO blanket and approaches to their modeling, Fusion Eng. Des. **86**, 2326 (2011).

[59] N. Vetcha, Study of instability and transition in MHD flows as applied to liquid metal blankets, Doctor of Philosophy, University of California, Los Angeles (2012).

[60] L. Bühler, The influence of small cracks in insulating coatings on the flow structure and pressure drop in MHD channel flows, Fusion Eng. Des. **27**, 650 (1995).

[61] L. Bühler, Instabilities in quasi-two-dimensional magnetohydrodynamic flows, J. Fluid Mech. **326**, 125 (1996).

[62] L. Bühler, Laminar buoyant magnetohydrodynamic flow in vertical rectangular ducts, Phys. Fluids **10**, 223 (1998).

[63] S. Smolentsev, MHD duct flows under hydrodynamic “slip” condition, Theor. Comput. Fluid Dyn. **23**, 557 (2009).

Chapter 6

Transition to turbulence in quasi-two-dimensional MHD flow driven by lateral walls

6.1 Perspective

This chapter comprises the paper "*Transition to turbulence in quasi-two-dimensional MHD flow driven by lateral walls*", as published in *Physical Review Fluids* in 2021. The paper was inspired by the idea of 'designer turbulence', which employs active or passive flow controls to adjust key flow features to attain desirable turbulent properties. Rather than looking at flow control, per se, the aim was to ascertain whether variations in key properties of the base flow (symmetry and base flow gradients), would ease inciting and sustaining turbulence within this broadened parameter space. Given the two additional parameters upon which the base flow depends, a supercritical analysis was deemed a suitable place to start, avoiding the introduction of a third parameter, the initial perturbation energy.

Of the two aspects of the base flow that were varied, the degree of symmetry and magnitude of gradients (base flow flatness in the bulk), both proved important in very different ways. Symmetric base flows (Shercliff profiles, or their pressure-driven equivalent) always resulted in the lowest critical Reynolds numbers. The introduction of asymmetry to the base flow reduced constructive interference between instabilities forming in the Shercliff boundary layers, and lead to increased critical Reynolds numbers. With enough asymmetry, and at sufficiently low friction parameters (the friction parameter controlling the level of interference between the boundary layers), the critical Reynolds number would asymptote to infinity, completely cutting off the supercritical route to turbulence. This is of theoretical interest, as the basis of the nonmodal Orr mechanism is the constructive interference between multi-layered instabilities at each wall, recalling Fig. 3.8. Varying the level of symmetry provided examples of both complete destructive interference (infinite Re_{c} at low H with any non-zero amount of asymmetry), or increasing constructive interference between both modal instabilities across the duct with reducing asymmetry (if H was not too large). The latter result proved to be of importance to the study presented in Chapter 7. The former result may also be of some theoretical interest, given the speculation of Falkovich & Vladimirova (2018), that the MHD-Couette base flow may be the only global attractor in Q2D, as aided by destructive interference. However, variations in base flow symmetry appeared to provide little practical gain, given that only the symmetric base flow could be generated in a pressure driven conduit, and that this was already the least stable. Furthermore, the energetics and linear transient growth varied little when varying the degree of base flow symmetry. Both energetics and linear transient growth predominantly depended on base flow flatness, even by intermediate $H \approx 10$. Transient growth was also relatively subdued in Q2D flows. However, weakly nonlinear analysis promisingly indicated that subcritical transitions were feasible over large regions of the α-Re parameter space, with their dependence on H elucidated.

Finally, fully nonlinear simulations indicated the possibility for sustained Q2D turbulence. Lower H were unable to trigger turbulence even at 10% supercritical Reynolds numbers. As weakly nonlinear analysis suggested that subcritical bifurcations should be possible at nearby parameters, this inability to trigger turbulence was presumed due to even supercritical Re being too small to trigger turbulence, an explanation supported in Appendix C. Much larger H triggered a single turbulent episode, much like the subcritical $H \to \infty$ results reported in Chapter 5 (Camobreco *et al.* 2020). Large near wall gradients likely provide sufficient production to trigger turbulence, while bulk flow flatness, over a large portion of the duct, leads to insufficient production to sustain turbulence. However, at the intermediate $H = 10$, the first supercritical Q2D turbulence to be both triggered and sustained was observed. Given this confirmation of the ability to sustain turbulence, subcritical investigations at $H = 10$ were quickly planned, and are reported in the work continued in Chapter 7. For now, the published article is included in the following pages.

PHYSICAL REVIEW FLUIDS **6**, 013901 (2021)

Transition to turbulence in quasi-two-dimensional MHD flow driven by lateral walls

Christopher J. Camobreco[1,*] Alban Pothérat[2,†] and Gregory J. Sheard[1,‡]
[1]*Department of Mechanical and Aerospace Engineering, Monash University, Victoria 3800, Australia*
[2]*Fluid and Complex Systems Research Centre, Coventry University, Coventry CV15FB, United Kingdom*

(Received 30 September 2020; accepted 22 December 2020; published 14 January 2021)

This work investigates the mechanisms that underlie transitions to turbulence in a three-dimensional domain in which the variation of flow quantities in the out-of-plane direction is much weaker than any in-plane variation. This is achieved using a model for the quasi-two-dimensional magnetohydrodynamic flow in a duct with moving lateral walls and an orthogonal magnetic field, where three dimensionality persists only in regions of asymptotically small thickness. In this environment, conventional subcritical routes to turbulence, which are highly three dimensional (with large variations from nonzero out-of-plane wave numbers), are prohibited. To elucidate the remaining mechanisms involved in quasi-two-dimensional turbulent transitions, the magnetic field strength and degree of antisymmetry in the base flow are varied, the latter via the relative motion of the lateral duct walls. Introduction of any amount of antisymmetry to the base flow drives the critical Reynolds number infinite, as the Tollmien-Schlichting instabilities take on opposite signs of rotation and destructively interfere. However, an increasing magnetic field strength isolates the instabilities, which, without interaction, permits finite critical Reynolds numbers. The transient growth obtained by similar Tollmien-Schlichting wave perturbations only mildly depends on the base flow, with negligible differences in growth rate for friction parameters $H \gtrsim 30$. Weakly nonlinear analysis determines the local bifurcation type, which is always subcritical at the critical point, and along the entire neutral curve just before the magnetic field strength becomes too low to maintain finite critical Reynolds numbers. Direct numerical simulations, initiated with random noise, indicate that a subcritical bifurcation is difficult to achieve in practice, with only supercritical behavior observed. For $H \leqslant 1$, supercritical exponential growth leads to saturation but not turbulence. For higher $3 \leqslant H \leqslant 10$, a turbulent transition occurs and is maintained at $H = 10$. For $H \geqslant 30$, the turbulent transition still occurs, but is short lived, as the turbulent state quickly collapses. In addition, for $H \geqslant 3$, an inertial subrange is identified, with the perturbation energy exhibiting a $-5/3$ power law dependence on wave number.

DOI: 10.1103/PhysRevFluids.6.013901

I. INTRODUCTION

This work is concerned with the mechanisms that underpin transitions to turbulence in quasi-two-dimensional (Q2D) shear flows, specifically, flow in a rectangular duct pervaded by a transverse magnetic field. A number of natural and industrial flows exhibit quasi-two-dimensional dynamics, where departures from two dimensionality are either asymptotically small in amplitude or only

*christopher.camobreco@monash.edu
†alban.potherat@coventry.ac.uk
‡greg.sheard@monash.edu

occur in regions of asymptotically small thickness (for example, boundary layers). This invariably raises the challenge of understanding the appearance of turbulence. In the context of magnetohydrodynamics (MHD), motivation arises from the search for an efficient design of liquid metal cooling blankets, which extract heat from the adjacent plasma in proposed nuclear fusion reactors [1]. The strength of the plasma-confining magnetic field, which extends into the adjacent blanket ducts, makes the flow there mostly quasi-two-dimensional. Furthermore, turbulence is rapidly damped via the Lorentz force [2]. Though less pertinent to this problem, a second motivation to study Q2D MHD flows has been their remarkable ability to reproduce at laboratory scale the main features of two-dimensional turbulence observed in shallow channel and atmospheric flows [3–5].

Two- or quasi-two-dimensional MHD turbulence was first encountered as a limit state of three-dimensional MHD turbulence at low magnetic Reynolds number [6–8] in domains where out-of-plane boundaries were respectively periodic and no slip. In this limit, the induced magnetic field can be neglected [9], and predominantly the Lorentz force diffuses momentum along the magnetic field lines [10]. When the Lorentz force dominates both diffusive and inertial forces (in the ratios Ha^{-2} and N^{-1}, respectively, where Ha and N are the Hartmann number and interaction parameter), the flow becomes two- or quasi-two-dimensional depending on the boundary conditions [11–14]. Along walls perpendicular to magnetic field lines, viscous forces oppose momentum diffusion by the Lorentz force, forming Hartmann boundary layers of thickness $\approx \mathrm{Ha}^{-1}$ [10,15]. A cutoff length scale $l_\perp^c \sim N^{2/3}$ separates the larger Q2D scales from the smaller 3D ones [10,16]. However, this cutoff scale cannot drop below that of horizontal viscous friction, so boundary layers parallel to the magnetic field, of thickness $\approx \mathrm{Ha}^{-1/2}$, remain intrinsically three-dimensional [17].

The conditions at which 3D MHD turbulence becomes quasi-two-dimensional and the formation of three dimensionality in Q2D turbulence have been clarified [10,13,18,19]. However, a clear path to Q2D turbulence from a quasi-two-dimensional laminar state is yet to be established. This question is specifically important in the context of duct flows and particularly in fusion blanket design. Indeed, if quasi-two-dimensional turbulence is to arise in blankets, it is unlikely to do so out of three-dimensional turbulence [1].

Research on transition to turbulence in MHD conduits has been mostly experimental [20] or based on fully three-dimensional simulations at moderate values of Ha ($<$100) and N, when the turbulent state can be expected to remain three dimensional [21,22]. However, these regimes stand very far from fusion relevant regimes ($\mathrm{Ha} \simeq 10^4$). The only study to date approaching these regimes indicated that the growth of three-dimensional perturbations in electrically insulating ducts was impeded at Hartmann numbers as low as $\mathrm{Ha} \simeq 300$, where the less efficient, quasi-two-dimensional Orr mechanism remains the only source of transient growth [23]. The corresponding optimal growth stood at least one order of magnitude below its 3D counterpart, raising the question as to whether the sort of subcritical transition normally associated with shear flows may indeed take place in the quasi-two-dimensional limit.

With these limitations in mind, a number of shallow water models can be derived to represent MHD flows in a quasi-two-dimensional state [10,24–26] very much in the spirit of shallow water models in rotating flows [27]. Such models have proved to be accurate, sometimes surprisingly so, for a number of complex flows including simple straight ducts [17,23,28], vortex lattices [29–31], sheared turbulence [24,32], flows around obstacles [33–37], and convective flows [38], linearly and nonlinearly. The clear advantage of these models is their low computational cost, as full three-dimensional numerics are prohibitively expensive for large Re, Ha, and N. As such, they offer a unique chance to identify and obtain insight into laminar to turbulent transitions in duct flows in these regimes.

In these regimes, traditional subcritical routes to turbulence may be obstructed, which would be detrimental to the efficient extraction of heat in the blanket coolant ducts [1]. Hence, beyond the classical Shercliff profile of insulating ducts [39], it is legitimate to consider whether alternative profiles may more efficiently generate turbulence or be less prone to suppressing it. As modifications to the base flow appear to be a more promising direction for turbulence suppression than influencing turbulent fields directly [40], it is instead worth exploring whether it is more efficient to select an

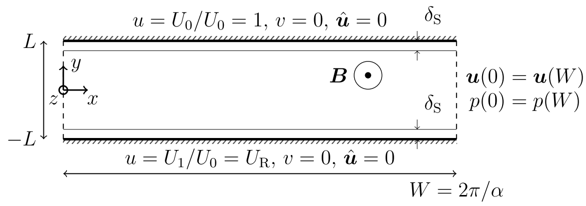

FIG. 1. Schematic diagram of the problem setup, with characteristic length of the duct half height L. The vertical dashed lines denote a periodicity constraint. The thick horizontal lines represent impermeable, no-slip boundaries, where the velocity is fixed (nondimensional boundary conditions provided), with an extent based on the streamwise wavelength or corresponding wave number being considered. Fully developed Shercliff boundary layers form on these walls, of thickness δ_{S}, which is a function of the friction parameter H. A uniform magnetic field is imposed normal to the page. The fixed out-of-plane Hartmann walls are the sources of the linear friction (not drawn).

optimal base flow, rather than an optimal perturbation, to generate and sustain turbulence. Although the flow was not natively quasi-two-dimensional, Refs. [40] and [41] applied forces designed to flatten the base flow away from the walls in an attempt to suppress turbulence. In both cases, the preferred force accelerates flow near the walls and decelerates flow in the bulk. Flatter base flows noticeably reduce turbulence production [42] and if sufficiently flattened can relaminarize the flow. This may take place in plug-like Shercliff flows. Linear transient growth was also found to be a good proxy for turbulent production far from the wall [42]. A different strategy was taken by Ref. [43], where base flow inflexion points were smoothed to eliminate turbulence. Conversely, Ref. [28] applied the inverse strategy of introducing inflexion points for the promotion of turbulence in MHD duct flows. As such, understanding the role of the base flow in the transition process appears to be crucial both in the fusion context and more generally. In particular, the questions we set out to answer are the following:

(1) What are the quasi-two-dimensional linear mechanisms promoting the growth of perturbations in quasi-two-dimensional duct flows?
(2) What is the nature of the bifurcation to any turbulent states that ensue?
(3) Can a subcritical transition take place at fusion-relevant parameters?
(4) Do the answers to these questions change, as the base flow profile is varied?

We address these questions by studying a quasi-two-dimensional wall-driven duct flow using the shallow water (SM82) model proposed in Ref. [10], where electromagnetic forces reduce to a linear friction exerted by the Hartmann layers on the bulk flow. The relative velocity of the walls can be continuously varied to achieve a range of base flows from symmetric to antisymmetric with an inflexion point. These flows are introduced in Sec. II. We then perform linear modal and nonmodal analyses to identify the linear growth mechanisms (Secs. III and V). A lower bound for their activation is obtained via the energy stability method (Sec. IV). The nature of the bifurcation is then sought through weakly nonlinear stability analysis (Sec. VI) before addressing the question of the fully nonlinear transition by means of two-dimensional DNS (Sec. VII) over a limited range of parameters.

II. PROBLEM FORMULATION

A. Problem setup

An incompressible Newtonian fluid, with density ρ, kinematic viscosity ν, and electrical conductivity σ flows through a duct of height $2L$ (y direction) and width a (z direction), see Fig. 1. The flow over a streamwise length W is periodic in the x direction. The duct walls are impermeable, no-slip, and electrically insulating. Fluid motion is generated by the streamwise motion of the walls at $y = \pm L$, at dimensional velocities U_0 (top) and U_1 (bottom). A homogeneous magnetic flux density (hereafter magnetic field for brevity) $B\mathbf{e}_z$ pervades the entire domain. In the limit where the Lorentz force outweighs viscous and inertial forces, the flow is quasi-two-dimensional, with z variation of pressure and velocity exclusively localized in boundary layers on the out-of-plane walls. The bulk velocity outside these layers is $O(\mathrm{Ha})$ close to the local z-averaged velocity along the duct and accurately represented by the SM82 model [10],

$$\nabla_\perp \cdot \boldsymbol{u} = 0, \tag{1}$$

$$\frac{\partial \boldsymbol{u}}{\partial t} + (\boldsymbol{u} \cdot \nabla_\perp)\boldsymbol{u} = -\nabla_\perp p + \frac{1}{\mathrm{Re}}\nabla_\perp^2 \boldsymbol{u} - \frac{H}{\mathrm{Re}}\boldsymbol{u}, \tag{2}$$

where the last term on the right-hand side of Eq. (2) represents the source of friction. Here, the nondimensional variables t, p, and $\boldsymbol{u} = (u, v)$ represent time, pressure, and the 2D z-averaged velocity vector, respectively, while $\nabla_\perp = (\partial_x, \partial_y)$ and $\nabla_\perp^2 = \partial_x^2 + \partial_y^2$ are the 2D gradient and Laplacian operators, respectively. These were scaled by L/U_0, ρU_0^2, U_0, $1/L$, and $1/L^2$, respectively. The relevant nondimensional groupings are the Reynolds number (representing the ratio of inertial to viscous forces at the duct scale)

$$\mathrm{Re} = \frac{U_0 L}{\nu}, \tag{3}$$

and the friction parameter (representing the ratio of friction in the Hartmann layers to viscous forces at the duct scale)

$$H = 2\frac{L^2}{a^2}\mathrm{Ha} = 2\frac{L^2}{a^2}aB\left(\frac{\sigma}{\rho\nu}\right)^{1/2}. \tag{4}$$

The SM82 approximation assumes $\mathrm{Ha} \gg 1$ and $\mathrm{Ha}^2/\mathrm{Re} \gg 1$, which are obtainable for any H with appropriate choice of a, as discussed in Ref. [38]. The last governing nondimensional grouping is the dimensionless bottom wall velocity

$$U_\mathrm{R} = \frac{U_1}{U_0}. \tag{5}$$

U_R varies in the range $[-1, 1]$, where the quasi-two-dimensional counterpart of MHD-Couette flow is represented by $U_\mathrm{R} = -1$ and Shercliff flow by $U_\mathrm{R} = 1$.

B. Base flows

The steady, fully developed solution for the parallel base flow, $\boldsymbol{U} = U(y)\boldsymbol{e_x}$, without a driving pressure gradient, is

$$U(y) = C_1 \exp(-H^{1/2}y) + C_2 \exp(H^{1/2}y), \tag{6}$$

where

$$C_1 = \frac{U_\mathrm{R}\exp(H^{1/2}) - \exp(-H^{1/2})}{\exp(2H^{1/2}) - \exp(-2H^{1/2})}, \quad C_2 = \frac{\exp(H^{1/2}) - U_\mathrm{R}\exp(-H^{1/2})}{\exp(2H^{1/2}) - \exp(-2H^{1/2})}. \tag{7}$$

Example base flows for various values of U_R are provided in Fig. 2. $U_\mathrm{R} = -1$ constitutes the MHD-Couette limit, in which $U(y) = \sinh(H^{1/2}y)/\sinh(H^{1/2})$. This simplifies to pure Couette flow in the hydrodynamic case: As $H \to 0$, $U(y) = y$. $U_\mathrm{R} = 1$ constitutes the Shercliff limit, in which $U(y) = \cosh(H^{1/2}y)/\cosh(H^{1/2})$. This expression differs from the Shercliff profile derived by Ref. [17] for pressure-driven flows, by the finite wall velocity (an unavoidable translation), and by a negative multiplicative factor reflecting different ratios of centerline to bottom wall velocity in pressure-driven and wall-driven flows (the coefficient of Ref. [17] can be matched with appropriate choice of U_R, or by redefining Re). The Shercliff profile, with $U_\mathrm{R} = 1$, does not simplify to the Poiseuille

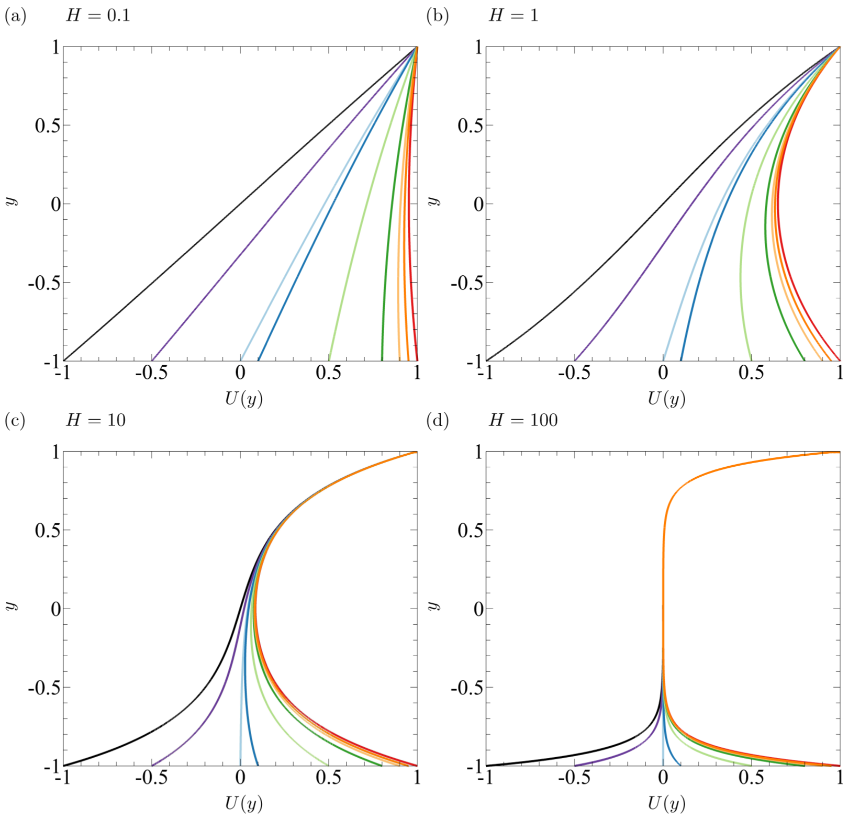

FIG. 2. Base flow profiles $U(y)$, at various H, for $U_R = -1, -0.5, 0, 0.1, 0.5, 0.8, 0.9, 0.95, 1$.

flow solution in the limit $H \to 0$ because of the absence of a pressure gradient, unlike the profile derived in Ref. [17]. In the hydrodynamic wall-driven flow, viscous diffusion is unopposed and the momentum imparted by the walls is fully diffused across the channel, unlike in finite pressure gradient Poiseuille flow. Interestingly, when $H > 0$ Hartmann friction balances diffusion in both wall- or pressure-driven flows, in an identical fashion, which explains the similarity between the profiles in this work and those in Ref. [17].

Varying U_R therefore varies the base flow through the family of MHD-Couette-Shercliff profiles. Unlike in the classical MHD-Couette or Shercliff flows, the nondimensional velocity $1 - U_{\min}$, where $U_{\min} = \min\{U(y)\}$, depends on the friction parameter H (recalling that velocities are nondimensionalized by U_0). Therefore, it is useful to express our results using an alternative definition of the Reynolds number

$$\mathrm{Re}_\Delta = \frac{U_\Delta L}{\nu} = \mathrm{Re}\,(1 - U_{\min}), \tag{8}$$

based on a velocity scale $U_\Delta = U_0\,(1 - U_{\min})$. Similarly, a nondimensional timescale $t_\Delta = t\,U_0/U_\Delta = t/(1 - U_{\min})$ is also defined.

C. Perturbation equations

Much of this work is dedicated to analyzing infinitesimal perturbations ($\hat{\boldsymbol{u}}$, $\hat{p}$) about the base flow,

$$\boldsymbol{u} = U(y)\mathbf{e}_x + \hat{\boldsymbol{u}}\ ,\ p = \hat{p}. \tag{9}$$

The equations governing $\hat{\boldsymbol{u}}$ are obtained by substituting Eq. (9) into Eqs. (1) and (2) and neglecting terms of $\mathcal{O}(|\hat{\boldsymbol{u}}|^2)$, yielding

$$\boldsymbol{\nabla}_\perp \cdot \hat{\boldsymbol{u}} = 0, \tag{10}$$

$$\frac{\partial \hat{\boldsymbol{u}}}{\partial t} + (\hat{\boldsymbol{u}} \cdot \boldsymbol{\nabla}_\perp)\boldsymbol{U} + (\boldsymbol{U} \cdot \boldsymbol{\nabla}_\perp)\hat{\boldsymbol{u}} = -\boldsymbol{\nabla}_\perp \hat{p} + \frac{1}{\mathrm{Re}}\boldsymbol{\nabla}_\perp^2 \hat{\boldsymbol{u}} - \frac{H}{\mathrm{Re}}\hat{\boldsymbol{u}}. \tag{11}$$

On the lateral walls, $\hat{\boldsymbol{u}} = \partial_y \hat{\boldsymbol{u}} = 0$ boundary conditions are applied.

III. LINEAR STABILITY

A. Formulation

A sufficient condition for the base flow to be unstable is determined by seeking the least stable infinitesimal perturbation. Taking twice the curl of Eq. (11), substituting Eq. (10), and projecting along $\boldsymbol{e_y}$ provides an equation for the wall-normal component of the velocity perturbation

$$\frac{\partial}{\partial t}\nabla_\perp^2 \hat{v} = \frac{\partial^2 U}{\partial y^2}\frac{\partial}{\partial x}\hat{v} - U\frac{\partial}{\partial x}\nabla_\perp^2 \hat{v} + \frac{1}{\mathrm{Re}}\nabla_\perp^4 \hat{v} - \frac{H}{\mathrm{Re}}\nabla_\perp^2 \hat{v}. \tag{12}$$

As linearity is assumed, each mode evolves independently, with perturbations decomposed into plane waves (by virtue of the problem's invariance in the streamwise direction)

$$\hat{v}(y) = \mathrm{Re}\{\tilde{v}(y)e^{i\alpha x}e^{-i\lambda t}\}, \tag{13}$$

with eigenvalue λ, eigenvector $\tilde{v}(y)$, streamwise wave number α, exponential growth rate $\mathrm{Im}(\lambda)$, and wave speed $\mathrm{Re}(\lambda)/\alpha$. Substituting Eq. (13) into Eq. (12) provides an SM82 modification to the Orr-Sommerfeld equation [44],

$$[-i\lambda(D^2-\alpha^2)]\tilde{v} = \left[i\alpha U'' - i\alpha U(D^2-\alpha^2) + \frac{1}{\mathrm{Re}}(D^2-\alpha^2)^2 - \frac{H}{\mathrm{Re}}(D^2-\alpha^2)\right]\tilde{v}, \tag{14}$$

where, respectively, primes and D^n represent derivatives and the nth order derivative operator, with respect to y. Boundary conditions are now $\tilde{v} = D\tilde{v} = 0$.

Equation (14) is discretized with N_c Chebyshev collocation points [45]. Differentiation matrices $\boldsymbol{D^n}$ and boundary conditions are implemented following Ref. [46]. The eigenvalue problem is solved in MATLAB in the standard form at default tolerance of 10^{-14}. λ_j is defined as the jth eigenvalue of the discretized operator, sorted by descending growth rate, with corresponding eigenvector $\tilde{v}_j$. The critical Reynolds number is attained when $\mathrm{Im}(\lambda_1)$ is zero for a single wave number α_c. For the linear stability analysis, for all base flows, operators are discretized with $N_\mathrm{c} = 200$, 350, 500, and 800 for $H \leqslant 10^2$, 5×10^2, 10^3, and 10^4, respectively, which ensures at least 30 Chebyshev points reside within a single Shercliff boundary layer. This enables the dominant wave number and growth rate to be determined to respective precisions of seven and nine significant figures (Table I). Spurious eigenvalues [47] are not an issue for the linear analysis, as they are situated sufficiently far below the real axis.

B. Results

The linear stability results for the family of Q2D mixed MHD-Couette-Shercliff flows are shown in Fig. 3. Figure 3(a) depicts the critical Reynolds number $\mathrm{Re}_{\Delta\mathrm{c}}$ as a function of the friction parameter H. The symmetric Shercliff flow [17,38] has finite $\mathrm{Re}_{\Delta\mathrm{c}}$ for all nonzero H. Once the

TABLE I. Resolution testing for eigenvalue problems. Left: energetic stability at $H = 100$, $\mathrm{Re} = 500$, MHD-Couette flow ($U_{\mathrm{R}} = -1$). Right: linear stability at $H = 1000$, $\mathrm{Re} = 10^7$, Shercliff flow ($U_{\mathrm{R}} = 1$). The bold resolutions were chosen, as discussed in Secs. III A and IV A. $\alpha_{\max}$ is the wave number with max $[\mathrm{Im}(\lambda_1)]$ for a given Re.

N_c	$\alpha_{\max}$	10^1 max $[\mathrm{Im}(\lambda_1)]$	N_c	$\alpha_{\max}$	10^2 max $[\mathrm{Im}(\lambda_1)]$
20	6.38246470	−1.53187927830825	200	3.48248937	1.78999418074040
40	6.42263964	−1.53055895392212	300	3.47528224	1.79276681627594
60	6.42263962	−1.53055895418749	400	3.47527862	1.79275949928794
80	6.42263963	−1.53055895418486	**500**	3.47527864	1.79275949851556
100	6.42263954	−1.53055895418970	600	3.47527873	1.79275949846157

symmetry of the base flow is broken, a value of H, $H^{\infty}(U_{\mathrm{R}})$ exists, below which the critical Reynolds number is infinite. Hence, except for the symmetric Shercliff flow, $\mathrm{Re}_{\Delta c}$ can initially be reduced with increasing H. $\mathrm{Re}_{\Delta c}$ decreases to a minimum for $H > H^{\infty}$, so that past this minimum, increasing the friction parameter stabilizes all flows to infinitesimal perturbations ($\mathrm{Re}_{\Delta c}$ increases monotonically with increasing H). A greater degree of antisymmetry (U_{R} closer to -1) requires a larger value of H before the critical Reynolds number becomes finite (H^{∞} monotonically increases with decreasing U_{R}), and provides increasing stability to infinitesimal perturbations. As such, the antisymmetric MHD-Couette flow is the most stable base flow for a given H and has finite $\mathrm{Re}_{\Delta c}$ for $H \gtrsim 15.102$. The asymptotic behavior is also reflected in the critical wave numbers, Fig. 3(b), where $\alpha_c \to 0$ for sufficiently small H. As discussed in Ref. [48], disturbances with finite wavelength are stable in the inviscid limit, $\mathrm{Re}_{\Delta} \to \infty$. Hence, a finite wave number cannot be maintained as $\mathrm{Re}_{\Delta c} \to \infty$.

As observed in Ref. [49] for the even and odd modes of Hartmann flow, the asymptotic behavior ($\mathrm{Re}_{\Delta c} \to \infty$, $\alpha_c \to 0$) is explained by the interaction between the Tollmien-Schlichting (TS) wave

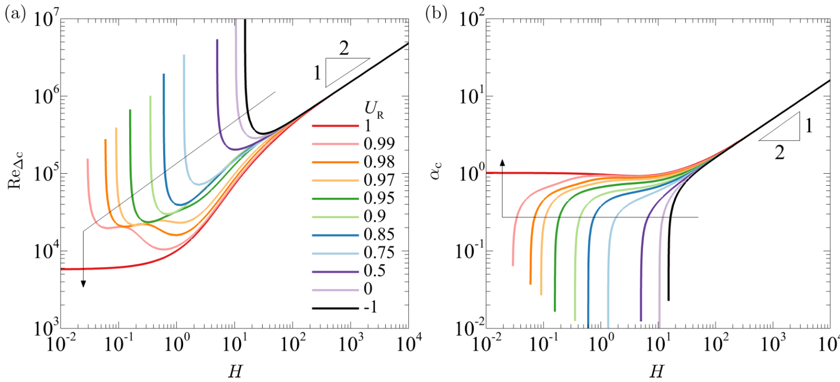

FIG. 3. Linear stability results, with arrows indicating increasing U_{R}. (a) Critical Reynolds number. (b) Critical wave number. $\mathrm{Re}_c \to \infty$ asymptotes are computed to $\mathrm{Re} = 10^7$. As $H \to \infty$, $\mathrm{Re}_{\Delta c} = 4.83468 \times 10^4 H^{1/2}$ and $\alpha_c = 0.161513 H^{1/2}$, which agree well with Ref. [17]. As $H \to 0$, $\mathrm{Re}_{\Delta c} \to 5772.22$ for $U_{\mathrm{R}} = 1$. MHD-Couette ($U_{\mathrm{R}} = -1$) results are modified by a factor of $1/2$. The isolated boundary layer on the top wall sees an effective local minimum velocity of $U_{\min,\mathrm{eff}} = 0$, just at the edge of the boundary layer. However, the velocity profile across the entire duct still has $U_{\min} = -1$, at the bottom wall, resulting in $(1 - U_{\min,\mathrm{eff}})/(1 - U_{\min}) = 1/2$.

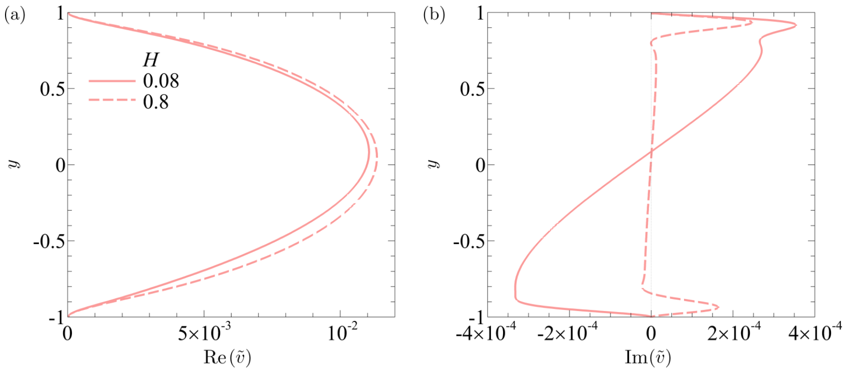

FIG. 4. Eigenvectors $\tilde{v}_1$ from the linear stability analysis, $U_R = 0.99$ ($H^\infty = 0.02898$). Comparison between $H = 0.8$, $\mathrm{Re}_{\Delta c} = 1.07724 \times 10^4$ ($\mathrm{Re}_{\Delta c}$ is smaller, due to constructive interference; indicated by approximate symmetry in imaginary component) and $H = 0.08$, $\mathrm{Re}_{\Delta c} = 1.99932 \times 10^4$ ($\mathrm{Re}_{\Delta c}$ is larger, due to destructive interference; indicated by approximate antisymmetry in imaginary component). (a) Real components. (b) Imaginary components.

structures running along the top and bottom walls. Note that as the base flow is not symmetric (respectively, antisymmetric) unless $U_R = 1$ (respectively, $U_R = -1$), the entire domain $y \in [-1, 1]$ is always simulated. This allows natural, sometimes approximate, symmetries in the dominant eigenmode to be observed. For symmetric modes, which can only be supported by symmetric base flows, the instabilities at the top and bottom walls rotate in the same direction, and constructively interfere along the centerline, causing additional destabilization (compared to an isolated TS wave). For antisymmetric modes, the instabilities rotate in the opposite direction along the top and bottom walls, and hence destructively interfere. The destructive interference is maximum at $U_R = -1$ and $H = 0$, to the point of preventing the growth of any perturbation, such that $\mathrm{Re}_{\Delta c}$ diverges in this limit. Increasing H from 0, for a given value of U_R, reduces the length scale of the TS waves attached to the top and bottom wall, causing them to separate from each other, which reduces interference. For $H > H^\infty$, the destructive interference between TS waves is insufficient to prevent the growth of all perturbations and the flow becomes linearly unstable. Subsequent increases in H further reduce the level of destructive interference, leading to a drop in $\mathrm{Re}_{\Delta c}(H)$. Once all destructive interference has been eradicated, a subsequent increase in H only results in higher friction that impedes modal growth. As such, $\mathrm{Re}_{\Delta c}(H)$ increases. This explains the presence of a minimum in $\mathrm{Re}_{\Delta c}(H)$. Similarly, increasing U_R progressively from -1 introduces increasingly more symmetry in the most unstable mode, which forms an alternate means of decreasing the amount of destructive interference. As such, lower values of H become sufficient to suppress complete destructive interference, and $H^\infty(U_R)$ decreases monotonically with increasing U_R. For U_R sufficiently close to 1, and for H sufficiently above H^∞, the mode can even experience noticeable constructive interference (resulting in a second set of local minima, recalling Fig. 3, which appear slightly above the curve for the purely symmetric $U_R = 1$ case). A comparison of the two local minima is considered in Fig. 4, for $U_R = 0.99$ (almost symmetric base flow). The degree of symmetry in the imaginary component of the eigenvector provides a clear indication of the type of interference. There is a much greater degree of antisymmetry in the imaginary component at $H = 0.08$, near the first local minimum, indicating some destructive interference, than at $H = 0.8$, near the second local minimum, which experiences significant constructive interference (the imaginary component is almost symmetric). However, as the real component has a much larger magnitude than the imaginary component, the overall mode structures look very similar.

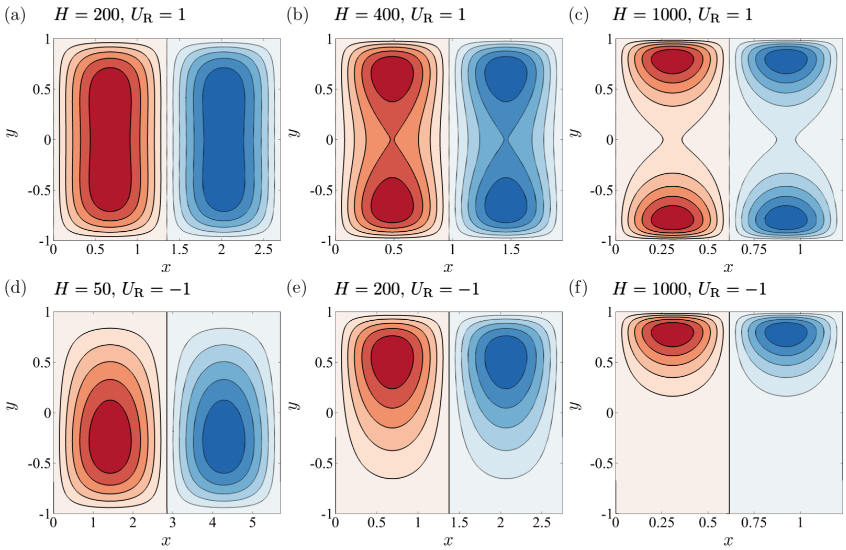

FIG. 5. Dominant eigenvectors of the linear stability analysis, $\hat{v}$-velocity contours; solid lines (red flooding) positive; dotted lines (blue flooding) negative. [(a)–(c)] Shercliff flow. [(d)–(f)] MHD-Couette flow.

The collapse of the critical Reynolds numbers and wave numbers in the limit $H \to \infty$ is due to the isolation of the boundary layers, already noted for Shercliff [17] and Hartmann layers [50,51]. For these large H, the critical Reynolds numbers and wave numbers scale with $H^{1/2}$, consistent with the thickness of a Shercliff boundary layer. The separation mechanism for TS waves at high H is illustrated in Fig. 5, for Shercliff [Figs. 5(a)–5(c)] and MHD-Couette [Figs. 5(d)–5(f)] flows. The TS wave pattern in the Shercliff flow displays the progressive separation of one central wave structure into two distinct TS wave structures as H increases, as found in the Hartmann flow [52]. Conversely, for flows with any degree of antisymmetry (excepting MHD-Couette flow) the velocity gradient at one wall will always be larger than at the other, drawing and confining the central mode toward the more highly sheared wall region as H increases, which isolates the modes to a greater degree when U_R is smaller, for a given H.

IV. ENERGETIC ANALYSIS

A. Formulation

The largest Reynolds number at which any perturbation would decay monotonically, Re_E, is determined from the equation governing the evolution of the perturbation energy. Following Ref. [44], taking the dot product of the perturbation u_i with Eq. (11) and integrating over a volume V, such that all divergence terms vanish, yields

$$\frac{dE}{dt} = -\frac{1}{2}\int_V u_i u_j \left(\frac{\partial U_i}{\partial x_j} + \frac{\partial U_j}{\partial x_i}\right) dV - \frac{1}{\mathrm{Re}}\int_V \frac{\partial u_i}{\partial x_j}\frac{\partial u_i}{\partial x_j} dV - 2E\frac{H}{\mathrm{Re}}. \tag{15}$$

The terms on the right-hand side respectively describe energy transfer from mean shear, viscous dissipation, and Hartmann friction [17]. The perturbation that maximizes $1/\mathrm{Re}$ is found by using variational calculus and introducing a Lagrange multiplier to enforce the constraint of mass

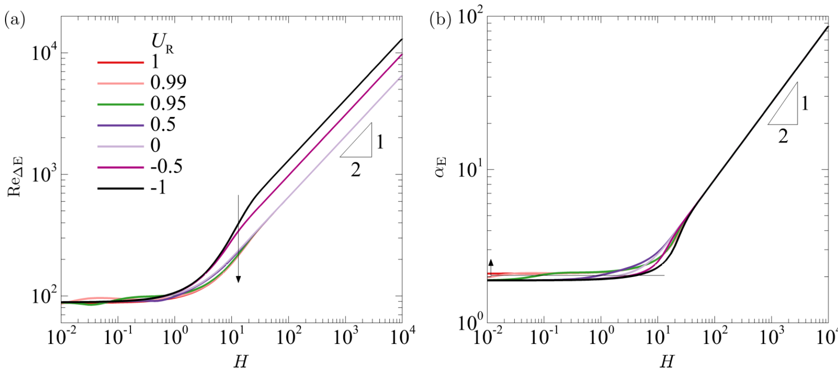

FIG. 6. Energetic analysis results, with arrows indicating increasing U_R. (a) Energy Reynolds number ($U_R = -1$ and -0.5 cases collapse at high H if Re_E is plotted, but appear translated with $Re_{\Delta E}$ plotted, as discussed for $U_R = -1$ in the caption of Fig. 3). (b) Energy wave number. As $H \to \infty$, $Re_{\Delta E} = 65.3288H^{1/2}$ and $\alpha_E = 0.863470H^{1/2}$, which agree well with Ref. [17]. As $H \to 0$, $Re_{\Delta E} \to 87.5933$ for $U_R = 1$.

conservation [44,53,54], which, once eliminated and when we seek plane-wave solutions, leads to the following eigenvalue problem:

$$[-i\lambda_E(D^2 - \alpha^2)]\tilde{v}_E = \left[\frac{1}{2}i\alpha U'' + i\alpha U'D + \frac{1}{Re}(D^2 - \alpha^2)^2 - \frac{H}{Re}(D^2 - \alpha^2)\right]\tilde{v}_E. \qquad (16)$$

Equation (16) is discretized and solved in an identical manner to the linear stability problem in Sec. III A. Re_E is obtained when the largest imaginary component over all eigenvalues $\lambda_{E,j}$ is zero for a single wave number α_E. $N_c = 60$, 80, and 140 for $H \leqslant 10^2$, 10^3, and 10^4 again allow the dominant wave number and growth rate to be determined to respective precisions of seven and nine significant figures (Table I).

B. Results

The energetic Reynolds numbers are shown in Fig. 6(a). Unlike the linear stability analysis, Fig. 3(a), none of the curves asymptote to infinite Reynolds number, for profiles with any degree of antisymmetry, at low H. Overall, the energetic analysis indicates a limited influence of the base flow profile, as using the appropriate velocity scale in the Reynolds number, the results are virtually coincident for all MHD-Couette-Shercliff profiles, for all H. Note that in the high-H region, the curves collapse in Re_E rather than $Re_{\Delta E}$, as only the local difference in the maximum and minimum velocity over an isolated boundary layer is important. The collapse to dynamics dominated by an isolated boundary layer occurs for all base flows simultaneously, and is initiated at much lower H ($H \gtrsim 30$) than the linear analysis (which collapses between $H \gtrsim 300$ for $U_R = -1$ to $H \gtrsim 1000$ for $U_R = 1$). The wave numbers from the energetic analysis, Fig. 6(b), are also notably larger than those from the linear stability analysis, Fig. 3(b).

The eigenvectors from the energetic analysis are provided in Fig. 7. Unlike the linear stability analysis, these modes do not directly represent solutions to the SM82 equations [17]. Similar to the linear stability analysis, at higher H, a wall mode forms, which again is increasingly compacted toward the wall as H increases. Discounting the irrelevant symmetry or antisymmetry, as in focusing on $-1 < y < 0$ in Fig. 7, the modes effectively appear identical. Thus, varying the base flow through

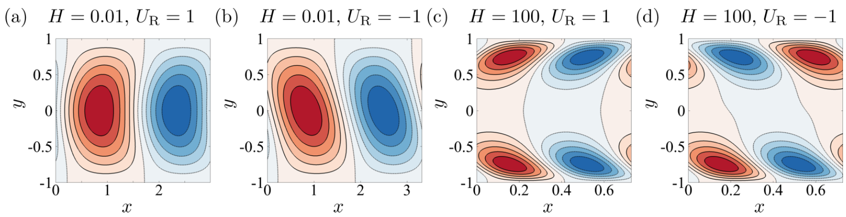

FIG. 7. Dominant eigenvectors of the energetic analysis, comparing Shercliff and MHD-Couette flows, $\hat{v}$-velocity contours: solid lines (red flooding) are positive; dotted lines (blue flooding) are negative.

U_R has little effect on the overall dynamics of the dominant modes of the energetic analysis (when comparing the same H).

V. LINEAR TRANSIENT GROWTH AND PSEUDOSPECTRA

A. Formulation

A lower bound for the Reynolds number at which an instability exponentially grows, and an upper bound on the Reynolds number at which all instabilities monotonically decay, have been derived in the preceding sections. However, nonorthogonality of the linearized evolution operator can lead to the transient growth of a superposition of linearly decaying eigenvectors [44]. To this end, transient growth analysis is performed for $\mathrm{Re}_E < \mathrm{Re} \lesssim \mathrm{Re}_c$. The maximum possible transient growth is found by seeking the initial condition for perturbation $\hat{\mathbf{u}}_\tau(t = 0)$ that maximizes the gain functional $G = ||\hat{\mathbf{u}}(t = \tau)||/||\hat{\mathbf{u}}(t = 0)||$ at prescribed time $t = \tau$ of the pertubation's linearized evolution. G represents the gain in perturbation kinetic energy as per Ref. [55] under the norm $||\hat{\boldsymbol{u}}|| = \int \hat{\boldsymbol{u}} \cdot \hat{\boldsymbol{u}}\, \mathrm{d}\Omega$, where Ω represents the computational domain. The maximum possible gain $G_{\max}$ is found at optimal time τ_{opt} for which the value $G_{\max}(\tau_{\mathrm{opt}})$ of the optimized functional is maximum. In practice, since $\hat{\mathbf{u}}$ is a plane wave, $\hat{v}_\tau(t = 0)$ is obtained as the solution of an optimization problem with the linearized evolution equation

$$\frac{\partial \hat{v}}{\partial t} = (D^2 - \alpha^2)^{-1}\left[-i\alpha U(D^2 - \alpha^2) + i\alpha U'' + \frac{1}{\mathrm{Re}}(D^2 - \alpha^2)^2 - \frac{H}{\mathrm{Re}}(D^2 - \alpha^2)\right]\hat{v} \tag{17}$$

as constraint. The optimal is obtained iteratively from a timestepper, set up in MATLAB, which first evolves Eq. (17) to time τ, then evolves the adjoint equation

$$\frac{\partial \hat{\xi}}{\partial t} = (D^2 - \alpha^2)^{-1}\left[i\alpha U(D^2 - \alpha^2) + 2i\alpha U' D + \frac{1}{\mathrm{Re}}(D^2 - \alpha^2)^2 - \frac{H}{\mathrm{Re}}(D^2 - \alpha^2)\right]\hat{\xi}, \tag{18}$$

for the Lagrange multiplier of the velocity perturbation $\hat{\xi}$, from $t = \tau$ to $t = 0$, until $\hat{\mathbf{u}}_\tau(t = 0)$ has converged to the desired precision. A third-order forward Adams-Bashforth scheme [56] is used to integrate Eqs. (17) and (18) in time, subject to $\hat{v}$ and $\hat{\xi}$ satisfying boundary conditions $\hat{v} = D\hat{v} = \hat{\xi} = D\hat{\xi} = 0$ at all walls, and "initial" condition $\hat{\xi}(\tau) = \hat{v}(\tau)$. The jth eigenvalue $\lambda_{G,j}$ of the operator representing the action of direct then adjoint evolution is determined with a Krylov subspace scheme [55,57]. With eigenvalues sorted in descending order by largest real component, the optimized growth $G = \lambda_{G,1}$. The iterative scheme is initialized with random noise for $\hat{v}(t = 0)$.

Validation against literature is provided in Table II. Validation against the rescaled results of Ref. [58] is also visible in Fig. 8. To maintain six significant figure accuracy in $G_{\max}$ requires a time step of $\Delta t = 2\times10^{-5}$, 20 forward-backward iterations, and $N_c = 60$, 80 and 100 Chebyshev points for $H \leqslant 10$, 30, and 100, respectively (for $\mathrm{Re} \leqslant 10^5$). τ_{opt} and α_{opt} are computed to three significant figures.

TABLE II. Comparisons of the G_{max} calculated in the present work, and those calculated by Ref. [23] for various H, MHD-Poiseuille flow profile, at $\mathrm{Re} = 5\times10^3$ and 1.5×10^4. The results of Ref. [23], kindly provided from their Fig. 2, are wave number optimized in a full three-dimensional domain, but time optimized at the 3D optimal wave number in a two-dimensional domain. The discrepancy at low H reflects the breakdown of the quasi-two-dimensionality assumption, not numerical error.

	$\mathrm{Re} = 5\times10^3$			$\mathrm{Re} = 1.5\times10^4$		
H	Ref. [23]	Present	Error (%)	Ref. [23]	Present	Error (%)
10	14.65	14.8272	1.195	27.4	34.0552	19.542
30		7.62330		17.7	17.7515	0.290
50	6.08	6.13073	0.827	14.2	14.4036	1.414
100	4.61	4.60979	0.004	11.0	11.0476	0.431
150	3.88	3.89381	0.355	9.43	9.44834	0.194
300	2.90	2.90575	0.198	7.11	7.19654	1.203
600	2.16	2.16392	0.181	5.43	5.44425	0.262
800	1.91	1.91680	0.355	4.83	4.83895	0.185

Additionally there was excellent agreement with results obtained with the matrix method (provided in Appendix A of Ref. [44]) at low Reynolds and Hartmann numbers. As such, the matrix method is used to further assess the transient growth capability by considering the non-normality of the operator, via the pseudospectrum and condition number of the energy norm weight matrix. A point z on the complex plane is within the ϵ_p pseudospectrum of the SM82-modified Orr-Sommerfeld operator if $||(zI - \mathcal{L}_{\mathrm{OS}})^{-1}|| \geqslant \epsilon_p^{-1}$ [59]. For a normal operator, a point z on the complex plane will be at most at a distance ϵ_p from any eigenvalue. A greater degree of non-normality is correlated with a greater ratio of the distance between a point z and the nearest eigenvalue, to the bounding value of ϵ_p at the point z. The extent of the pseudospectra into the complex upper half-plane forms a lower bound on transient growth [44,46,59–61]. The pseudospectrum is computed by evaluating $||\boldsymbol{W}\,(1/(z\boldsymbol{I} - \lambda))\boldsymbol{W}^{-1}||_2$, with energy norm weight matrix $\boldsymbol{W}$ [44], identity matrix $\boldsymbol{I}$, and diagonalized eigenvalues λ of the discretized SM82-modified Orr-Sommerfeld operator. Computations were performed with a discretization of $N_c = 400$ and truncated to the 240 modes with largest imaginary component.

B. Results: Transient growth

The optimized growth for various base flows, over a range of H values, is depicted in Fig. 8. Unlike in 3D flows where the lift-up mechanism incites significant growth [44,62], Q2D transient growth is driven by the less efficient Orr mechanism. The maximum transient growth found in the present study is accordingly lower, scaling as $G_{max} \sim \mathrm{Re}^{2/3}$, with magnitudes of only $G_{max} \simeq 10^2$ for Reynolds numbers of 10^4 to 10^5, depending on H and U_{R}. At $H = 30$, the transient growth already closely matches that of an isolated exponential boundary layer (long dashed lines in Fig. 8) for all U_{R}. By $H = 100$, G_{max}, α_{opt}, and τ_{opt} all respectively collapse to that limit. As in the energetic analysis, this collapse occurs at far lower H than the linear stability analysis. This could be due to the much larger wave numbers at which the transient growth and energetic analysis optimals occur. The TS waves thereby penetrate a shorter distance into the bulk (see Fig. 9) and therefore become isolated at a smaller friction parameter. The TS wave optimals otherwise have the same general appearance as the linear stability eigenmodes (Fig. 5), except that both MHD-Couette and Shercliff flows have wave structures at both walls, which thereby require similar friction parameters to isolate. This leads to the overall difference in transient growth across the family of profiles to be negligible even at relatively low $H \geqslant 30$. Constructive interference between modes at the top and bottom walls may be the cause of the slightly larger growth observed for symmetric base flows at smaller

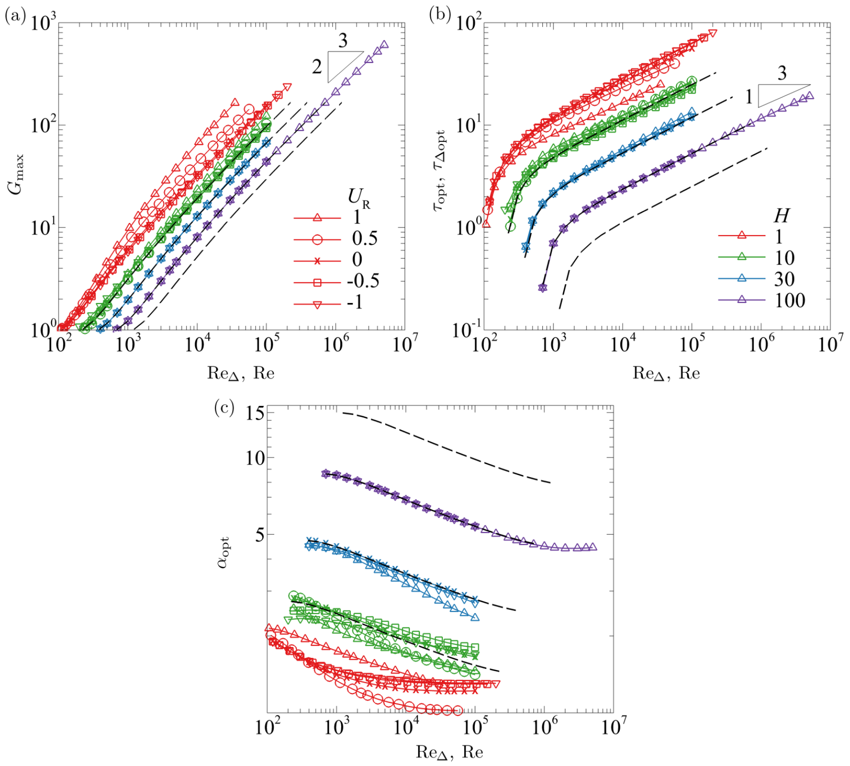

FIG. 8. Transient growth results for various U_R and H. (a) Time and wave number optimized maximum growth. (b) Optimal time interval. (c) Optimal wave number. Re_Δ and $\tau_{\Delta opt} = \tau_{opt}/(1 - U_{min})$ are plotted for $H = 1$, and Re and τ_{opt} for $H = 10$, 30, and 100. The black long dashed lines correspond to an isolated Shercliff boundary layer [58], at $H = 10$, 30, 100, and 300. For these, plotted quantities are $Re = Re_S H^{1/2}$, $\alpha_{opt} = \alpha_{opt,S} H^{1/2}$, and $\tau_{opt} = \tau_{opt,S}/H^{1/2}$. The $Re^{2/3}$ and $Re^{1/3}$ power laws for G_{max} and τ_{opt} are approximate.

H. However, even this is not large, such that the base flow does not make a significant difference in generating Q2D linear transient growth. Furthermore, the degree of symmetry in the base flow is not relevant once H is sufficiently large to flatten the central region, and isolate the boundary layers, after which all growth values collapse to those of an isolated exponential boundary layer.

C. Results: Pseudospectra

The transient growth results are also supported by the pseudospectra. Figure 10 depicts pseudospectra obtained at $Re_\Delta \approx 10^4$ for both the Shercliff and MHD-Couette base flows, at $H = 10$ and $H = 100$. Increasing the Reynolds number directly brings more eigenvalues close to the real axis, allowing smaller perturbations to cross to the positive imaginary half-plane, thereby generating more transient growth [59]. However, as demonstrated in Fig. 10, increasing the Hartmann friction parameter mainly stretches the pseudospectra along the real axis, with the further separation of the eigenvalues appearing to lead to reduced transient growth for a given Reynolds number. This is

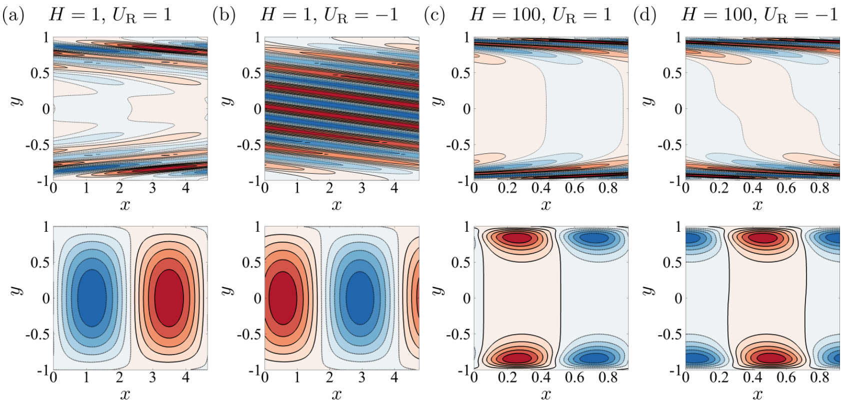

FIG. 9. Optimized perturbations at $\mathrm{Re}_\Delta \approx 10^4$, at $t = 0$ (top row) and linearly evolved to $t = \tau_{\mathrm{opt}}$ (bottom row), comparing Shercliff and MHD-Couette flows. $\hat{v}$-velocity contours: solid lines (red flooding) are positive; dotted lines (blue flooding) are negative.

supported by determining the condition number of the basis, $\kappa = ||\boldsymbol{W}||_2||\boldsymbol{W}^{-1}||_2$ [44,59], recalling that a normal operator has a condition number of unity. At or near hydrodynamic conditions, the condition number of MHD-Couette flow is much higher than for Shercliff flow. This was observed in 3D non-MHD Couette and Poiseuille flows [59] and remains unexplained. For example, at $H = 1$, $\mathrm{Re}_\Delta \approx 10^3$, the condition numbers for Shercliff and MHD-Couette flows are 1.9×10^3 and 1.2×10^8, respectively (at α_{opt}). However, at $H = 100$, $\mathrm{Re}_\Delta \approx 10^3$, the condition numbers are respectively 1.0×10^4 and 1.3×10^6. Hence, an increasing Hartmann friction parameter acts to reorient eigenvectors such that they are more normal for MHD-Couette flow and less normal for Shercliff flow. It also indicates the increasing similarity between these base flow profiles with increasing H.

VI. WEAKLY NONLINEAR STABILITY

A. Formulation

By assuming a small perturbation amplitude $O(\epsilon)$, to allow linearization, linear stability analysis becomes amplitude independent. However, if amplitude dependence is maintained, a weakly nonlinear analysis can be performed. To remain accurate, the weakly nonlinear analysis is concerned only with expansion about a leading perturbation which is close to neutrally stable. This ensures only one mode is unstable [53]. Linearly, a single unstable mode would either slowly grow or decay exponentially. However, if weakly nonlinear self-interaction occurs, the overall growth rate will increase or decrease, depending on whether the leading nonlinear growth term is positive or negative. A positive nonlinear growth can outweigh a negative linear growth rate if the linear growth is sufficiently small (close to the neutral curve), such that growth occurs at $\mathrm{Re} < \mathrm{Re}_c$ until a saturation amplitude, or a turbulent state, is reached (in which case the bifurcation is subcritical). If the nonlinear term is negative, $\mathrm{Re} > \mathrm{Re}_c$ is required for nontransient growth (the bifurcation is supercritical). The amplitude dependence of the plane-wave mode $\hat{w}_n(y) = w(y)e^{i\alpha nx}$ is expanded as

$$\hat{w}_n = \sum_{m=0}^{\infty} \epsilon^{|n|+2m} \tilde{A}^{|n|} |\tilde{A}|^{2m} \hat{w}_{n,|n|+2m}, \tag{19}$$

where $\hat{w}_{n,|n|+2m}$ now denotes a perturbation (the first subscript is the harmonic, the second is the amplitude), in line with Ref. [49], and $\tilde{A} = A/\epsilon$ is the normalized amplitude. The wave frequency

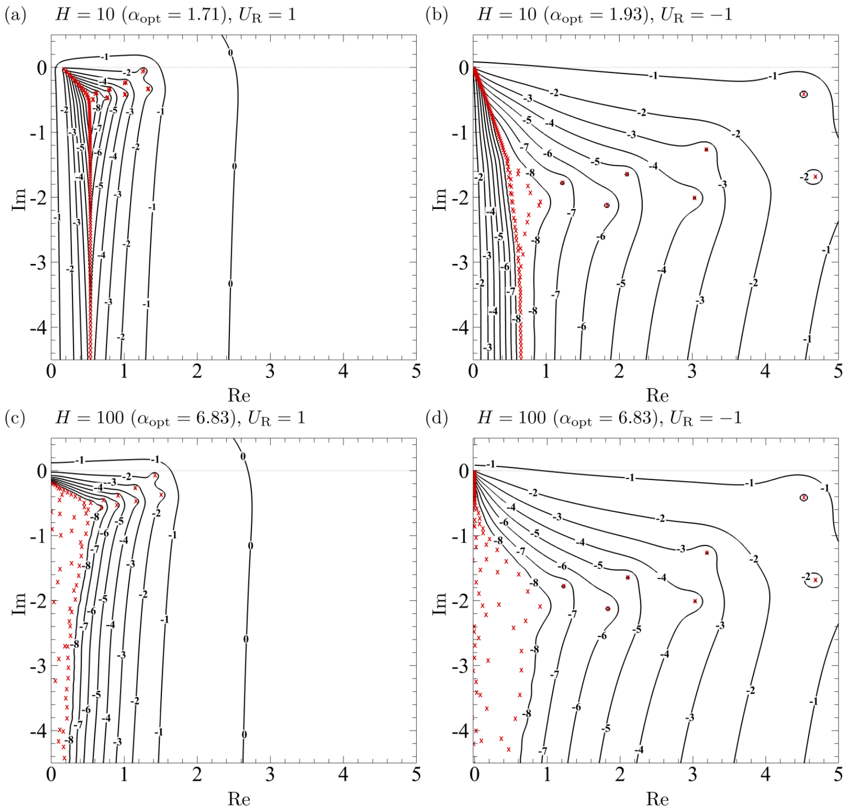

FIG. 10. Pseudospectra (contours from 10^{-8} to 1, labeled by exponent) at $\text{Re}_\Delta \approx 10^4$, comparing Shercliff and MHD-Couette flows (the latter symmetric about the imaginary axis). Red crosses denote eigenvalues from the linear stability analysis λ, computed at the same parameters as the linear transient optima.

ω is also expanded as $\omega = \omega_0 + \epsilon^2\tilde{\omega}_2 + \cdots$, where the normalized amplitude $\tilde{\omega}_2 = \omega_2/\epsilon^2$. The linearly unstable mode $\hat{w}_{1,1}$ (which is $\hat{v}$ under rescaling) of $\mathcal{O}(\epsilon)$ excites via self-interaction through the nonlinear term a second harmonic $\hat{w}_{2,2}$ and a modification to the base flow $\hat{u}_{0,2}$ (zeroth harmonic), which both have amplitude of $\mathcal{O}(\epsilon^2)$ [49]. These harmonics also interact with the original perturbation, resulting in another harmonic $\hat{h}^w_{1,3}$ with amplitude of $\mathcal{O}(\epsilon^3)$ [49]. Higher order terms are neglected, as they have a rapidly increasing radius of convergence [44]. However, such an expansion is sufficient to define the bifurcation type as sub- or supercritical and determine whether the system is sensitive to subcritical perturbations of finite amplitude.

The weakly nonlinear stability is calculated following the method outlined in Ref. [49], where the key equations are provided here. Denoting $U = \hat{u}_0$ in line with Ref. [49], the equations governing higher order harmonics of the base flow and the perturbation are

$$D^2\hat{u}_{0,2m} - H\hat{u}_{0,2m} = \hat{g}_{0,2m}, \tag{20}$$

$$\mathcal{L}_n\hat{w}_n = \left[\left(D_n^2 - i\lambda n\right)D_n^2 - HD_n^2 - i\alpha n\left(\hat{u}_0'' - u_{0,0}D_n^2\right)\right]\hat{w}_n = \hat{h}^w_{n,|n|+2m}, \tag{21}$$

respectively, where $D_n = \partial/\partial y \boldsymbol{e}_y + in\alpha \boldsymbol{e}_x$ and where the right-hand sides, representing the curl of the nonlinear term, are

$$\hat{g}_{0,2m} = i \sum_{m\neq 0}^{\infty} (\alpha m)^{-1} \hat{w}_m^* D^2 \hat{w}_m, \tag{22}$$

$$\hat{h}^w_{n,|n|+2m} = n \sum_{m\neq 0}^{\infty} m^{-1} \big(\hat{w}_{n-m} D_m^2 D\hat{w}_m - D(\hat{w}_m) D_{n-m}^2 \hat{w}_{n-m}\big). \tag{23}$$

Here $*$ denotes complex conjugation. Equations (20) and (21) are identical to those used to determine the base flows in Sec. II B and the linear stability results in Sec. III, respectively, if the right-hand sides are set to zero (taking $m = 0$, $n = 1$). Equations (20) through (23) are discretized into matrix operators and solved as follows, noting that after determining the right-hand sides of Eqs. (20) and (21), the amplitude expansion for $\hat{w}_n$ should be substituted in. First, the SM82-modified Orr-Sommerfeld eigenvalue problem

$$\big[\boldsymbol{A}_1^{-1}\boldsymbol{M}_1(u_{0,0}) - \lambda \boldsymbol{I}\big] w_1 = 0 \tag{24}$$

is solved in the standard form, which provides the leading eigenvalue λ_1, with frequency $\omega_0 = \mathrm{Im}(\lambda_1)$, and the corresponding right and left eigenvectors, $w_{1,1}$ and $w^\dagger_{1,1}$, respectively. Re_c and α_c are determined from the linear stability problem, Eq. (24), with neutral conditions satisfying $\mathrm{Re}(\lambda_1) = 0$ in this formulation. The following are then solved:

$$u_{0,2} = -2\alpha^{-1}(\boldsymbol{D}^2 - H\boldsymbol{I})^{-1}\mathrm{Im}(w^*_{1,1}\boldsymbol{F}_0\boldsymbol{D}^2 w_{1,1}), \tag{25}$$

$$w_{2,2} = (\boldsymbol{M}_2 - 2i\omega_0\boldsymbol{A}_2)^{-1}[2\boldsymbol{F}_2\boldsymbol{D}(\boldsymbol{D}(w_{1,1}\boldsymbol{D}w_{1,1}) - 2(\boldsymbol{D}w_{1,1})^2)], \tag{26}$$

$$h^w_{1,3} = 0.5[w^*_{1,1}\boldsymbol{A}_2\boldsymbol{D}w_{2,2} - \boldsymbol{D}(w_{2,2})\boldsymbol{A}_1 w^*_{1,1}] - [w_{2,2}\boldsymbol{A}_1\boldsymbol{D}w^*_{1,1} - \boldsymbol{D}(w^*_{1,1})\boldsymbol{A}_2 w_{2,2}], \tag{27}$$

where

$$\boldsymbol{A}_n = \boldsymbol{D}^2 - n^2\alpha^2\boldsymbol{I}, \quad \boldsymbol{N}_n(u_{0,0}) = i\alpha(u''_{0,0}\boldsymbol{I} - u_{0,0}\boldsymbol{A}_n), \quad \boldsymbol{M}_n = \boldsymbol{F}_n\big[\boldsymbol{A}_n^2 - H\boldsymbol{A}_n + \mathrm{Re}\boldsymbol{N}_n\big], \tag{28}$$

with boundary condition matrix $\boldsymbol{F}_n$ as given in Refs. [47,49]. $w_{1,1}$ is normalized such that $D^2 w_{1,1}(1) = 1$, and $w^\dagger_{1,1}$ such that $w_{1,1}\cdot w^\dagger_{1,1} = 1$.

The $n = 3$ harmonic of Eq. (21) only has a solution when the right-hand side is not proportional to $w_{1,1}$. Thus, the right-hand side must be orthogonal to the adjoint eigenfunction $w^\dagger_{1,1}$ [49]. The $n = 3$ harmonic is

$$\big(\boldsymbol{A}_1^{-1}\boldsymbol{M}_1 - i\omega_0\boldsymbol{I}\big)w_{1,3} = \boldsymbol{A}_1^{-1}\big(\boldsymbol{F}_1 h^w_{1,3} + |A|^{-2}\{\boldsymbol{F}_1\boldsymbol{N}_1[(\mathrm{Re}-\mathrm{Re}_c)u_0 + |A|^2 u_{0,2}] + i\omega_2\boldsymbol{A}_1\}w_{1,1}\big). \tag{29}$$

The right-hand side will be zero once orthogonal to $w^\dagger_{1,1}$ if the frequency perturbation satisfies

$$i\omega_2 = \mu_1(\mathrm{Re}-\mathrm{Re}_c) + \mu_2|A|^2, \tag{30}$$

where

$$\mu_1 = w^\dagger_{1,1}\cdot\boldsymbol{A}_1^{-1}\boldsymbol{F}_1\boldsymbol{N}_1 w_{1,1}, \tag{31}$$

$$\mu_2 = w^\dagger_{1,1}\cdot\boldsymbol{A}_1^{-1}\boldsymbol{F}_1\big(\boldsymbol{N}_1(u_{0,2})w_{1,1} - h^w_{1,3}\big). \tag{32}$$

The linear growth rate correction is then $\mu_1(\mathrm{Re}-\mathrm{Re}_c)$ and the first Landau coefficient μ_2 [44,53]. Rearranging the real part of Eq. (30) yields $|A|^2 = -(\mathrm{Re}-\mathrm{Re}_c)\mathrm{Re}(\mu_1)/\mathrm{Re}(\mu_2)$. Thus, $\mathrm{Re}(\mu_1) > 0$ is required for the existence of a finite amplitude state, while $\mathrm{Re}(\mu_2) > 0$ (respectively, $\mathrm{Re}(\mu_2) < 0$) defines a subcritical (respectively, supercritical) bifurcation. Note that all coefficients quoted in this paper are rescaled by $\alpha^2\mathrm{Re}$, following Refs. [49] and [63].

Weakly nonlinear analysis is valid only near the neutral curve, such that only one mode is ever unstable. However, MHD-Couette flow yields a conjugate pair of equally unstable modes.

TABLE III. Resolution testing for the weakly nonlinear analysis, MHD-Couette flow ($U_R = -1 + 10^{-10}$) at $H = 1000$, $\mathrm{Re}_c = 1.52886\times10^6$, $\alpha_c = 5.10748$. The bold resolution was chosen, identical to that for the linear stability analysis.

N_c	10^{-6} Re (μ_1)	10^{-8} Im (μ_1)	10^3 Re (μ_2)	10^4 Im (μ_2)
400	1.02741326199010	−1.78689676323013	1.08671495177896	5.88065081880331
500	1.02741326027113	−1.78689676325672	1.08671494954617	5.88065083277250
600	1.02741326031740	−1.78689676325717	1.08671494979183	5.88065083423307
700	1.02741326030699	−1.78689676325563	1.08671494908700	5.88065083086592

This issue has been circumvented by taking $U_R = -1 + 10^{-10}$ to approximate MHD-Couette flow, which breaks antisymmetry above machine precision. This ensures that there is only one unstable eigenvalue, while having a negligible effect on the linear computations.

Extensive literature comparisons [63–65] were performed when Ref. [49] validated their method, for the $H = 0$ Posieuille flow problem. Testing the present formulation against this benchmark recovered the values for μ_1 and μ_2 to all six significant figures provided in Ref. [49]. The resolution required for higher H, Table III, demonstrates that the discretization for the linear stability problem yields acceptable results for the additional weakly nonlinear computations.

B. Results

Figure 11 depicts the weakly nonlinear behavior solely at the critical points (Fig. 3). Locally, the transition is subcritical ($\mu_2 > 0$) and the finite amplitude state can be reached ($\mu_1 > 0$) at all critical points, including along the $\mathrm{Re}_c \to \infty$ asymptotes. However, the magnitude of μ_2 directly quantifies the level of subcriticality of the transition. The variations of $\mathrm{Re}(\mu_2(H))$ are opposite to those of $\mathrm{Re}_c(H)$. As such, for the larger values of H, $\mathrm{Re}(\mu_2)$ scales with the Shercliff layer thickness and decreases as $\mathrm{Re}(\mu_2) \sim H^{-1/2}$. Near asymptotes where Re_c diverges, on the other hand, $\mathrm{Re}(\mu_2)$ increases sharply with H from $-\infty$. This is expected, since in this limit, any growth of finite amplitude takes place at a vanishingly small critical parameter $\mathrm{Re}/\mathrm{Re}_c - 1$. The by-product of this is that the saturation amplitude at which the perturbation is large enough for nonlinear effects to be important increases with H, as $|A|^2 \sim H^{5/2}$ for large H; see Fig. 11(c). However, to compare between H, a constant $\mathrm{Re}/\mathrm{Re}_c$ scaling of $|A|^2 \sim H^2$ is more appropriate, as $\mathrm{Re}_c \sim H^{1/2}$ for large H. Since, at constant Re, linear transient growth decreases at least as $H^{-1/2}$ [23], it is unlikely to provide a mechanism to support the growth of perturbations at large H. Thus, although subcritical bifurcations exist, they are unlikely to be obtained, given the lack of transient growth at subcritical Re.

$\mathrm{Re}(\mu_2)$ is depicted along neutral curves from the linear stability analysis in Fig. 12, for Shercliff, MHD-Couette, and mixed ($U_R = 0.85$) base flows. For Shercliff flow, at $H = 1$ and 10, $\mathrm{Re}(\mu_2)$ changes sign twice along the lower branch, so the bifurcation associated with modes on this branch is supercritical between these two points and subcritical elsewhere. At $H = 100$, the bifurcation becomes supercritical at a much higher Reynolds number (likely because the TS mode does not define the edge of the neutral curve there) and remains supercritical to the computed extent of the lower branch (to $\mathrm{Re} = 10^7$). Comparatively, for MHD-Couette flow, at $H = 15.11$ and 30, there is no supercritical region. At $H = 100$, a supercritical bifurcation appears along the lower branch, as at higher H, there is less sensitivity to the exact base flow profile. The mixed flow displays a clearer transition from subcritical to supercritical bifurcation with increasing H. At H near H^∞ (0.601 and 1), the bifurcation is everywhere subcritical. At $H = 10$, a small region of supercritical bifurcation exists along the lower branch. By $H = 100$, this region of supercritical bifurcation is much larger and does not switch back to subcritical to the computed extent of the neutral curve ($\mathrm{Re} = 10^7$). However, the top branch always remains open to subcritical bifurcation.

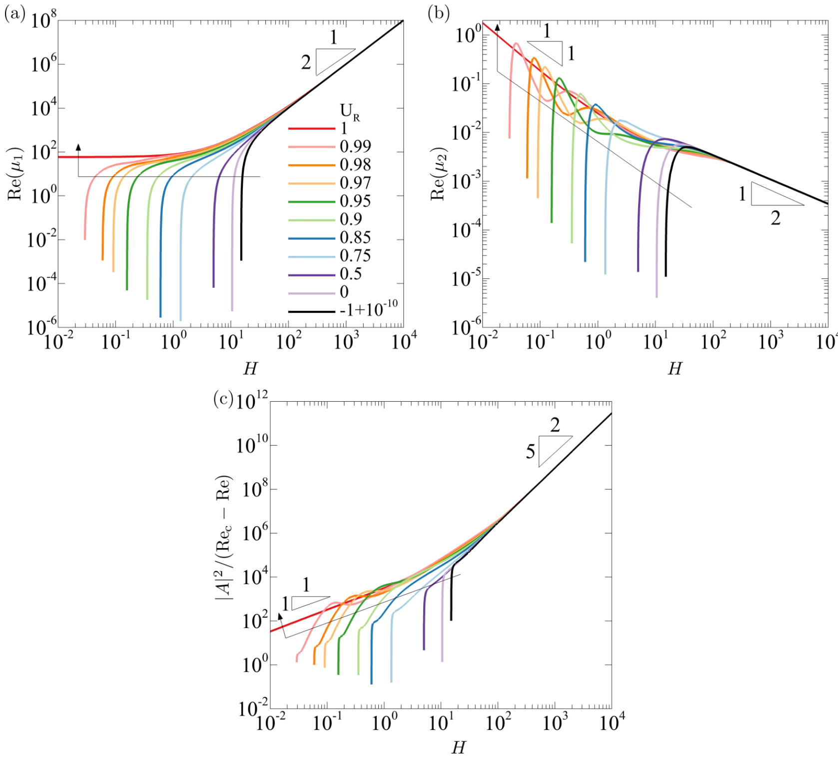

FIG. 11. Weakly nonlinear stability for various U_{R} at the critical points (recall Fig. 3). (a) Real part of linear growth rate correction coefficient. (b) Real part of first Landau coefficient. (c) Normalized amplitude. Arrows indicate increasing U_{R}. As $H \to \infty$, $|A|^2 = 29.8970H^{5/2}(\mathrm{Re_c} - \mathrm{Re})$.

At large Reynolds numbers, the scalings $\alpha \sim \mathrm{Re}^{-1}$, $\mathrm{Re}(\mu_1) \sim \mathrm{Re}^{-1}$, and $\mathrm{Re}(\mu_2) \sim \mathrm{Re}^{-1}$ hold, and the phase speed asymptotes to a constant. Furthermore, as $\mathrm{Re}(\mu_1)(\mathrm{Re_{marg}} - \mathrm{Re})$ always remains positive, the finite amplitude state can always be reached ($\mathrm{Re_{marg}}$ is the Reynolds number on the neutral curve).

VII. DIRECT NUMERICAL SIMULATIONS

A. Formulation

Finally, we shall now assess whether transition to quasi-two-dimensional turbulence may actually take place under the full nonlinear dynamics, by performing direct numerical simulations (DNS) of Eqs. (1) and (2). Natural conditions are reproduced with white noise added in varying fraction $E_0(t=0) = \int_{-1}^{1} \hat{u}^2 + \hat{v}^2 \, d\Omega / \int_{-1}^{1} U^2 \, d\Omega$, where Ω represents the computational domain. Periodic boundary conditions, $\boldsymbol{u}(x=0) = \boldsymbol{u}(x=W)$ and $p(x=0) = p(x=W)$, are applied at the downstream and upstream boundaries of a domain with length $W = 2\pi/\alpha_{\max}$ set to match the wave number that achieved maximal linear growth. The simulations typically exhibited a rapid drop in disturbance energy, followed by a linear phase of exponential growth, which is finally superseded

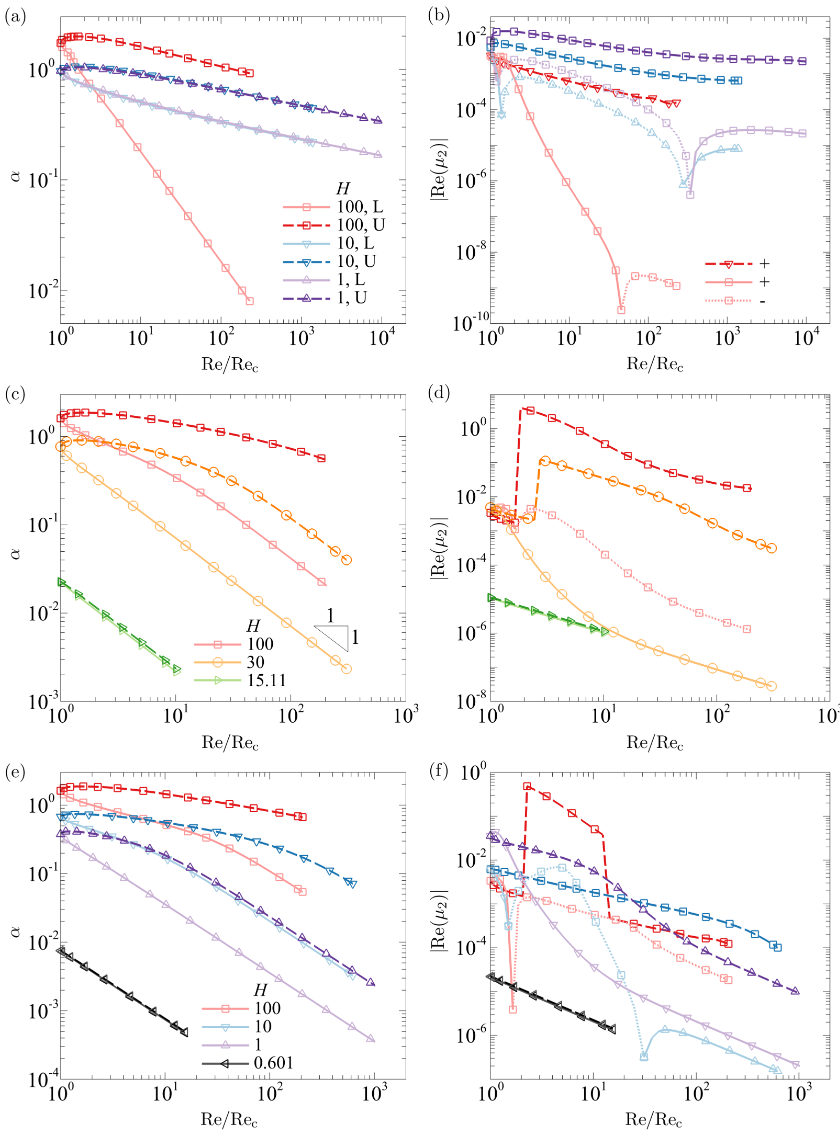

FIG. 12. Weakly nonlinear stability along the neutral curve. [(a), (b)] $U_R = 1$. [(c), (d)] $U_R = -1 + 10^{-10}$. [(e), (f)] $U_R = 0.85$. Neutrally stable wave numbers (left column) and real part of the first Landau coefficient (right column). Dotted lines denote where $\mathrm{Re}(\mu_2)$ was negative, indicating supercritical bifurcation. "L" and "U" denote the lower and upper branches of the neutral curve, respectively.

TABLE IV. DNS mesh resolution testing at $H = 100$ and $\mathrm{Re} = 10^6$, for Shercliff ($\mathrm{Re_c} = 4.40223\times10^5$; $\alpha_{\max} = 1.52813$ at $\mathrm{Re} = 10^6$) and MHD-Couette ($\mathrm{Re_c} = 4.87187\times10^5$; $\alpha_{\max} = 1.39883$ at $\mathrm{Re} = 10^6$) flow. The interpolant for each spectral element is order $N_\mathrm{p} = 19$ and the time step is $\Delta t = 1.25\times10^{-3}$, as validated in Ref. [58]. The final resolution choices are in bold, where E_x and E_y represent the number of elements per unit length in x and y, respectively. The chosen resolution has roughly 650 elements and 6.25×10^5 degrees of freedom for these wave numbers.

E_x	E_y	$\sigma_{\Delta\max}$, $U_\mathrm{R} = 1$	Error (%)	$\sigma_{\Delta\max}$, $U_\mathrm{R} = -1$	Error (%)
3	12	5.13119051×10^{-3}	2.236×10^{-1}	3.92816302×10^{-3}	1.367×10^{-1}
6	12	5.13138001×10^{-3}	2.273×10^{-1}	3.92831007×10^{-3}	1.394×10^{-1}
3	**24**	5.11994480×10^{-3}	3.959×10^{-3}	3.93378788×10^{-3}	6.248×10^{-3}
6	24	5.11998768×10^{-3}	4.797×10^{-3}	3.93158203×10^{-3}	4.983×10^{-2}
LSA	LSA	5.11974211×10^{-3}		3.93354213×10^{-3}	

by nonlinear effects. The exponential growth rate $\sigma_{\max}$ from the linear growth regime is obtained by fitting the natural logarithm of $\int |v|\, d\Omega$ data over a few thousand time units. As $t_\Delta = t/(1 - U_{\min})$, the rescaled growth rate $\sigma_{\Delta\max} = \sigma_{\max}/(1 - U_{\min})$.

The random noise seeds (perturbations) are evolved with an in-house spectral element solver, which employs a third-order backward differencing scheme, with operator splitting, for time integration [66]. High-order Neumann pressure boundary conditions are imposed on impermeable walls to maintain third-order time accuracy [66]. The Cartesian domain is discretized with quadrilateral elements over which Gauss-Legendre-Lobatto nodes are placed ($N_\mathrm{p} = 19$ nodes per element to take advantage of spectral convergence). Elements are uniformly distributed in both streamwise and transverse directions, with greater element compression in the wall-normal direction. At the highest H value simulated, at least 20 nodes reside within the Shercliff boundary layer. The solver, incorporating the SM82 friction term, has been previously introduced and validated [23,35,37,67].

Mesh validation results are provided in Table IV, comparing growth rates measured in the DNS against linear stability analysis (LSA) predictions. The agreement is excellent in the exponential growth (or decay) stages. Some additional comparisons at the chosen resolution (3 elements per unit length in x, 24 elements per unit height in y) can be found in Table V.

Fourier analysis is also performed at select instants in time, exploiting the streamwise periodicity of the domain. The absolute values of the Fourier coefficients $c_\kappa = |(1/N_\mathrm{f})\sum_{n=0}^{n=N_\mathrm{f}-1}[\hat{u}^2(x_n) + \hat{v}^2(x_n)]e^{-2\pi i\kappa n/N_\mathrm{f}}|$ were obtained using the discrete Fourier transform in MATLAB, where x_n represents the nth x location linearly spaced between $x_0 = 0$ and $x_{N_\mathrm{f}} = W$, interpolating in the discretized domain when necessary, and taking $N_\mathrm{f} = 10\,000$. A mean Fourier coefficient $\bar{c}_\kappa$ is obtained by averaging the coefficients obtained at 21 y values. A time-averaged mean Fourier coefficient $\langle\bar{c}_\kappa\rangle_t$ is also determined by averaging over approximately 20 time instants, for stages after the initial linear

TABLE V. Subcritical test cases for Shercliff flow at $H = 1$, with different levels of criticality at $E_0 = 10^{-2}$ (left) and with different values of E_0 at $\mathrm{Re}/\mathrm{Re_c} = 0.9$ (right).

	$10^4\sigma_{\Delta\max}$				$10^4\sigma_{\Delta\max}$		
$\mathrm{Re}/\mathrm{Re_c}$	LSA	DNS	Error (%)	E_0	LSA	DNS	Error (%)
0.5	−76.4704	−76.4726	2.9×10^{-3}	10^{2}	−8.97961	−8.98230	3.0×10^{-2}
0.6	−52.0623	−52.0586	7.1×10^{-3}	10^{-0}	−8.97961	−8.98277	3.5×10^{-2}
0.7	−33.9759	−33.9774	4.4×10^{-3}	10^{-2}	−8.97961	−8.98232	3.0×10^{-2}
0.8	−20.0392	−20.0420	1.4×10^{-2}	10^{-4}	−8.97961	−8.98240	3.1×10^{-2}
0.9	−8.97961	−8.98232	3.0×10^{-2}	10^{-6}	−8.97961	−8.94802	3.5×10^{-1}

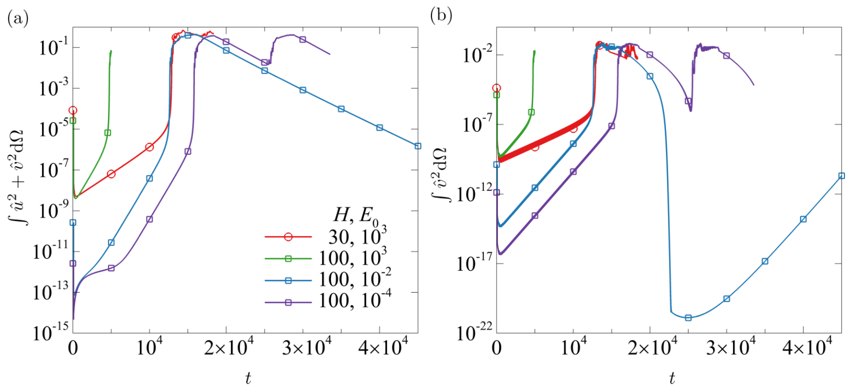

FIG. 13. Temporal evolution of perturbations initiated with random noise for MHD-Couette flow ($U_R = -1$) at $\mathrm{Re}/\mathrm{Re_c} = 1.1$, and various $H > H^\infty$ and E_0. (a) $\int \hat{u}^2 + \hat{v}^2\, d\Omega$. (b) $\int \hat{v}^2\, d\Omega$.

and nonlinear growth. Note that although the number of sample points N_f is high, only κ up to about 100 to 200 are well resolved by the spatial discretization, depending on H.

B. Subcritical regime

The results for DNS at subcritical Reynolds numbers are collated in Table V. All initial seeds decayed exponentially, with excellent agreement to the LSA decay rates and without any observable linear transient growth. It appears that supercritical Reynolds numbers are required to induce nonlinear behavior and transitions to turbulence, if the initial field is random noise, more in line with a supercritical bifurcation. Thus, subcritical transitions may only be attainable for a small range of Reynolds numbers near $\mathrm{Re_c}$. Subcritical tests of MHD-Couette flow for $H < H^\infty$ (for which $\alpha_{\max} \to 0$) were also simulated, with $W = 20\pi$ arbitrarily chosen; only monotonic decay was observed. Note that in all these cases, the transient growth optimals have wavelengths shorter than the domain length required to maximize linear growth, and are hence not excluded.

C. Supercritical regime

The energy growth for supercritical MHD-Couette flow (for $H > 15.102$) is shown in Fig. 13 and for supercritical Shercliff flow in Fig. 14. These are separated into growth in $\int \hat{u}^2 + \hat{v}^2 d\Omega$, to represent the total perturbation kinetic energy and to highlight the formation of streamwise independent structures, and growth in $\int \hat{v}^2 d\Omega$, which better isolates the growth or decay of the perturbation. The linear growth, nonlinear growth, and initial turbulent stages are very similar between the MHD-Couette and Shercliff flows. However, the relaminarization and decay stages are quite different. For MHD-Couette flow (Fig. 13), $\int \hat{v}^2 d\Omega$ displays clear re-excitations. The $H = 30$ and $H = 100, E_0 = 10^{-4}$ cases relaminarize, but are both quickly re-excited (very rapidly in the $H = 30$ case) while at high amplitudes, when nonlinearity still plays a role. The $H = 100, E_0 = 10^{-2}$ case cleanly decays to the floor, after which growth begins again, via the linear mechanism. This was not observed for Shercliff flow, with both (smaller E_0) $H = 30$ and $H = 100$ cases relaminarizing and rapidly monotonically decaying (the larger E_0 cases require exceedingly small time steps and as such their final behaviors remain unknown). The smaller E_0 case at $H = 30$ also relaminarizes and decays more rapidly than at $H = 100$, in spite of less Hartmann friction. Note that the energy in the Shercliff and MHD-Couette base flows at the same H differ, so it is not necessarily appropriate to compare the same E_0 between different base flows.

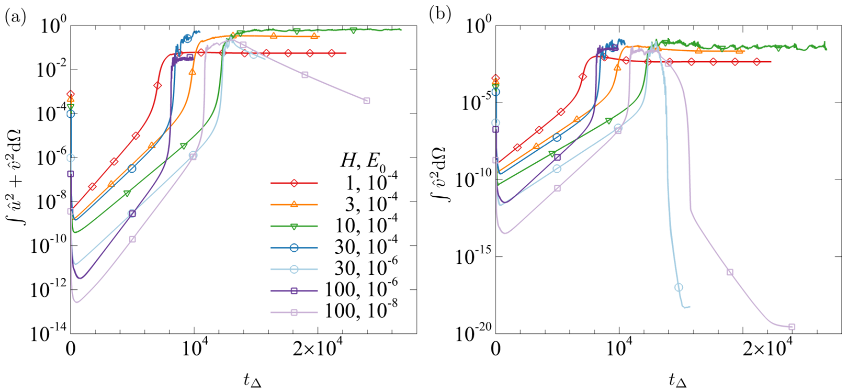

FIG. 14. Temporal evolution (rescaled time) of perturbations initiated with random noise for Shercliff flow ($U_{\mathrm{R}} = 1$) at $\mathrm{Re}/\mathrm{Re_c} = 1.1$, and various H and E_0. (a) $\int \hat{u}^2 + \hat{v}^2\, d\Omega$. (b) $\int \hat{v}^2\, d\Omega$.

Computations of Shercliff flow reveal two interesting changes in behavior with decreasing H. Unlike the relaminarization and monotonic decay for $H \geqslant 30$, the $H = 3$ and $H = 10$ cases (with $E_0 = 10^{-4}$) maintain turbulent states. At $H = 3$ relaminarization again occurs, but the perturbation saturates to a stable finite amplitude state, rather than decaying. However, $H = 10$ maintains the turbulent state for the computed extent of the simulation, excepting two brief attempts at relaminarization, which are not stable, resulting in a return to turbulence. With further decreasing $H \leqslant 1$, no turbulent state is triggered by the linear and nonlinear growth, with only an eventual saturation to a stable finite amplitude state. This behavior echoes that discussed in Ref. [68], which observes that for all $\mathrm{Ha} \geqslant 0$ a purely two-dimensional finite-amplitude state can be reach via evolution of an Orr mode formed of purely spanwise vortices (recall Sec. V B indicating that the transient Orr optimal was almost identical to the linear optimal). However, the addition of three-dimensional noise to the finite-amplitude state triggers (3D) turbulence at low Ha but destabilizes the finite-amplitude state at high Ha such that the solution decays back to the laminar base state, with only short-lived turbulence. It is presumed by Ref. [68] that this is due to nonlinear interactions feeding energy from 2D modes to 3D modes, which are then more rapidly dissipated at high Ha. Since this could not occur in these purely Q2D simulations, a different mechanism may be at play. References [41] and [42] argue that in hydrodynamic pipe flows, the flattening of the mean profile reduces turbulence production in the bulk, such that turbulence cannot be sustained. In the present configuration, production is almost solely due to $\hat{u}\hat{v}\partial U/\partial y$. The vanishing of this term in the core flow for $H \gtrsim 30$ may therefore explain why turbulence collapses in this parameter regime. Turbulence can still be re-excited as $\partial U/\partial y$ remains large near the wall. A possible explanation of the lack of transition at lower H then follows, as with reducing H, $\partial U/\partial y$ near the wall reduces, and so too production.

Figures 15 and 16 depict the y-averaged Fourier coefficients $\bar{c}_\kappa$ to compare the three different behaviors observed when $H \lesssim 1$ (high amplitude nonturbulent), $1 < H < 30$ (possibly long-lived turbulence), or $H \gtrsim 30$ (short-lived turbulence). Very few modes are energized throughout the linear region, with a rapid jump in the number of modes energized in the nonlinear growth phase. This is shown in any one of Figs. 15(a)–15(d), by comparing the fourth and fifth curves, which are closely spaced in time but which exhibit approximately an order of magnitude increase in the number of noticeably (relative to the floor) energized modes. For the $H = 1$ case, there is then no further change in the general form of the $\bar{c}_\kappa$ curves. However, for $H \geqslant 3$ even more modes continue to be energized, until the spectra are contaminated by under-resolution for $\kappa \gtrsim 200$. This is also shown in

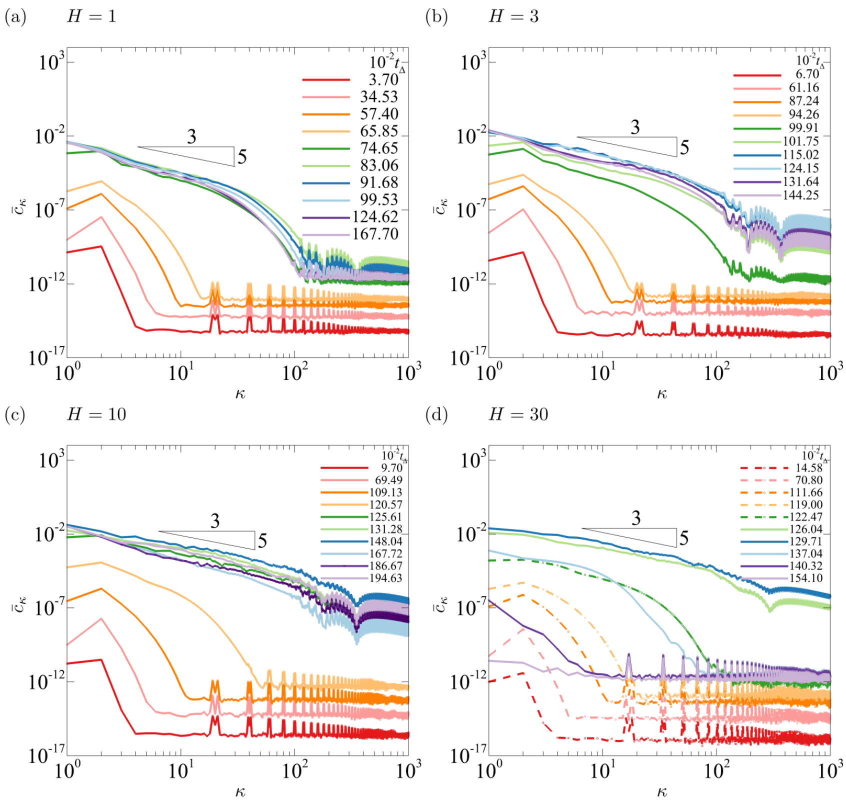

FIG. 15. Instantaneous (rescaled time) values of the y-averaged Fourier coefficients for $1 < \kappa < 10^3$, for Shercliff flow ($U_R = 1$) at $\mathrm{Re}/\mathrm{Re}_c = 1.1$; $E_0 = 10^{-4}$ for $H \leqslant 10$; $E_0 = 10^{-6}$ for $H = 30$.

Fig. 16(a) by comparing the time-averaged $\bar{c}_\kappa$, averaged only after the initial nonlinear growth. Only the cases with $H \geqslant 3$, for either Shercliff or MHD-Couette flow, demonstrate a range of wave numbers with perturbation energy with a $\kappa^{-5/3}$ dependence, which suggests the formation of an inertial subrange. There is also a sudden jump in the spectral floor for cases with $H \geqslant 3$ (also shown in Fig. 15, particularly at $H = 10$, comparing the curves at times $t_\Delta = 1.2057\times10^4$ and $t_\Delta = 1.2561\times10^4$). This is a good indication of a transition to turbulence, as the chaotic state with a limited number of excited modes becomes a turbulent state, where all available modes are excited. Conversely, the $H = 1$ data do not hold to the $\kappa^{-5/3}$ dependence for any distinct inertial subrange of κ, and a floor of low-energy modes is always observed, such that the low-H state never becomes turbulent. The $H = 30$ case in Fig. 15 also shows the resulting decay of the perturbation at larger times, with a rapid reduction in the number of energized modes, until the energy in all modes reaches the floor (the $-5/3$ trend holds briefly before this occurs). Figure 16(b) further supports the temporary turbulent nature of the flow in this $H = 30$ case, with the clear energization of all modes at $t_\Delta \approx 1.25\times10^4$, and the rapid decay of all but the zeroth mode (the streamwise independent structure) shortly thereafter, at $t_\Delta \approx 1.4\times10^4$. It also provides a different means of

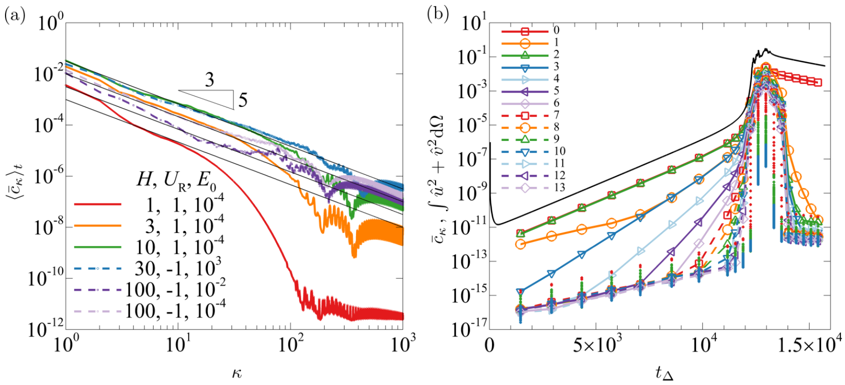

FIG. 16. (a) Time and y-averaged Fourier coefficients for $1 < \kappa < 10^3$, for both Shercliff and MHD-Couette flows at $\mathrm{Re}/\mathrm{Re_c} = 1.1$, for various H and E_0. The thin black lines show $\kappa^{-5/3}$ trends. $H \geqslant 30$ for Shercliff flow are not shown as the turbulence is short lived. (b) y-averaged Fourier coefficients as a function of rescaled time t_Δ for Shercliff flow at $\mathrm{Re}/\mathrm{Re_c} = 1.1$, $H = 30$, and $E_0 = 10^{-6}$. Modes $0 < \kappa < 13$ are as defined in the legend. Thereafter, every fifth mode is plotted, with $15 < \kappa < 100$ in red, $105 < \kappa < 1000$ in green, and $1005 < \kappa < 5000$ in blue. The black solid line is twice the perturbation energy, identical to that from Fig. 14(a).

viewing the energization of an increasing number of modes before noticeable nonlinear growth is achieved.

Representative flow fields are depicted for MHD-Couette flow in Fig. 17, at $H = 100$, $\mathrm{Re}/\mathrm{Re_c} = 1.1$, and $E_0 = 10^{-2}$ (energy growth depicted in Fig. 13). In the linear growth region, $2\times10^2 \lesssim t \lesssim 1.24\times10^4$, a pattern of similar structure to the linear stability eigenvector is observed in Fig. 17(a) (recall Fig. 5), although both the left and right running eigenvectors are observable in the nonlinear computation. Most of the energy in $\hat{u}^2$ is located where gradients in $\hat{v}$ are largest, i.e., very close to the walls. During the initial nonlinear growth period, $1.24\times10^4 \lesssim t \lesssim 1.26\times10^4$, the additional growth originates from the TS wave arching, as visible in the $\hat{v}$ field in Fig. 17(c), and the form of this dominant structure persists through the turbulent stage, $1.26\times10^4 \lesssim t \lesssim 1.78\times10^4$. Some underlying smaller scale features are also visible in Fig. 17(c). This dominant modulated TS wave can periodically break down and reform (as energy is driven to larger scales) throughout the turbulent stages. Linear transient optimals were found to experience a secondary nonlinear growth through the same mechanism in isolated exponential boundary layers [58], with a large-scale arched TS wave structure similarly persistent. The appearance of $\hat{u}$ also starkly changes with the nonlinear growth and transition to turbulence, with two elongated streamwise structures rapidly forming at each wall, which tend to reduce the local shear. These structures store perturbation energy, as shown by the slow decay of the zeroth mode in Fig. 16(b), and by comparing Figs. 13(a) and 13(b). After relaminarization, $1.78\times10^4 \lesssim t \lesssim 2.5\times10^4$, the TS wave flattens out [Fig. 17(e)], is pushed away from the high shear region (by the streamwise independent structure), and cleanly decays. As the Reynolds number is supercritical, the linear mode is re-excited from noise at the numerical floor.

However, the smaller turbulent scales in Fig. 17 are occluded by the dominance of the arched TS wave. Figure 18 depicts two snapshots revealing key flow features present in the smaller scales. In these snapshots, a high-pass filter has been applied to remove streamwise Fourier modes $|\kappa| \leqslant 9$ from the flows. Strongly localized jets emanating from the sidewalls entrain narrow shear layers, observable in the example at $H = 3$, while at $H = 100$ a myriad of smaller scale features are present.

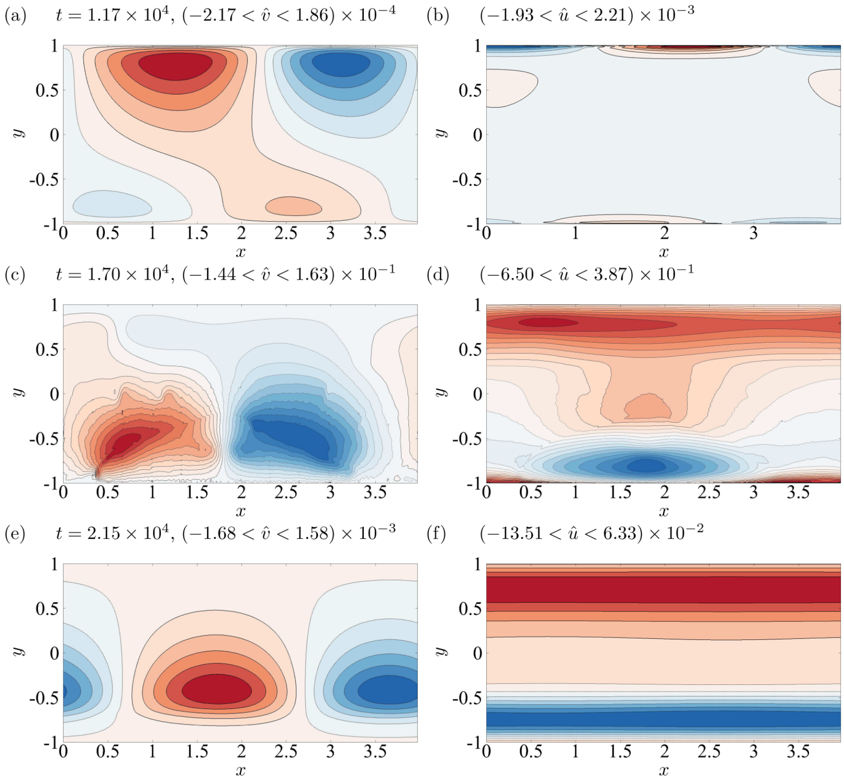

FIG. 17. Temporal snapshots of MHD-Couette flow at $\mathrm{Re}/\mathrm{Re}_c = 1.1$, $H = 100$, $E_0 = 10^{-2}$ (Fig. 13). Wall-normal velocity perturbation $\hat{v}$ (left); streamwise velocity perturbation $\hat{u}$ (right). Solid lines (red flooding) positive; dotted lines (blue flooding) negative. The linear TS wave evolves into an arched TS wave, leading to a turbulent state and the rapid growth of a streamwise independent structure. The TS wave then flattens out and relaminarization occurs.

VIII. CONCLUSIONS

This work examined the influence of the base flow in the scenario of transition to turbulence in a quasi-two-dimensional duct flow with a transverse magnetic field. The base flow is varied through the relative velocity of the two lateral walls. This is of particular importance in the context of recent developments in flow control, where turbulence is suppressed via the introduction of a friction effect to flatten the base flow [40,41,43]. Ideas along the same lines can be conversely applied to the promotion, rather than the suppression, of turbulence. Promoting turbulence to enhance heat transfer is indeed necessary for one of the motivations of this work: to assess the feasibility of dual-purpose liquid metal coolant ducts in magnetic confinement fusion reactors [1]. Fluid structures have a strong tendency to two dimensionalize within these ducts, which exhibit naturally flat base flows, due to the action of the Lorentz force. The linear stability of quasi-two-dimensional MHD-Couette-Shercliff base flows provided two key insights. First, the addition of any amount of antisymmetry to the base flow eventually leads to unconditional stability to infinitesimal perturbations at sufficiently

(a) $H = 3$, $E_0 = 10^{-4}$, $t_\Delta = 1.11 \times 10^4$, $-0.733 < \hat{\omega}_z < 0.798$

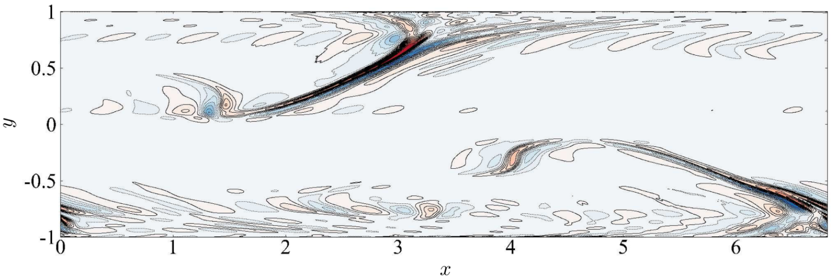

(b) $H = 100$, $E_0 = 10^{-8}$, $t_\Delta = 1.28 \times 10^4$, $-7.788 < \mathrm{sgn}(\hat{v}) \log_{10}(|\hat{v}|) < 7.876$

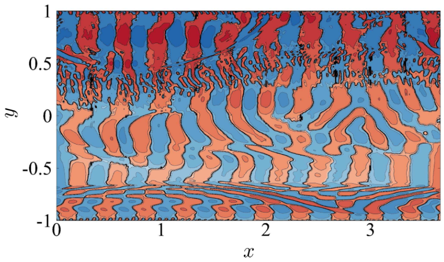

FIG. 18. Streamwise high-pass-filtered snapshots of Shercliff flow shortly after the transition to turbulence at $\mathrm{Re}/\mathrm{Re}_c = 1.1$. Streamwise Fourier coefficients of modes $|\kappa| \leqslant 9$ have been removed. Solid lines (red flooding) positive; dotted lines (blue flooding) negative.

low friction parameters H. The reason is that the antisymmetric part of the base flow drives the TS wave structures to destructively interfere, preventing growth. Conversely, an increasing friction parameter, beyond a critical value H^∞, flattens the central region of the base flow and isolates the wave structures at each wall, limiting their interaction, allowing growth to occur at finite critical Reynolds numbers. H^∞ increases with decreasing velocity of the bottom wall U_R, which controls the level of antisymmetry in the base flow (the top wall is at fixed velocity of unity). Only a symmetric, Shercliff base flow has finite Re_c for all nonzero H. Second, the critical parameters collapse to those of an isolated exponential boundary layer at high H, which occurs with noticeably lower imposed friction for increasingly antisymmetric base flow profiles. Antisymmetric profiles have a larger base flow velocity gradient at one wall than the other, leading the TS wave instability to preferentially form at only the one wall where the mean shear is largest. In such cases, friction need only keep the instability sufficiently far from the other wall to avoid any interference. This requires comparatively less friction than isolating two waves from one another (the greatest constructive interference thereby occurs in the symmetric Shercliff flow).

Conversely, the energetics of all Q2D MHD-Couette-Shercliff flows show little dependence on the degree of antisymmetry in the base flow. As such, the energetic Reynolds numbers are always finite. Furthermore, the transient growth of Q2D MHD-Couette-Shercliff flows is also not strongly dependent on the degree of antisymmetry in the base flow, with variations in growth between base flows only visible at $H \leqslant 10$. Destructive interference could explain the slight reduction in transient growth for more strongly antisymmetric base flows when H is small enough to permit interference. At larger friction parameters, $H \gtrsim 30$, transient growth is almost identical for all base flows. The growth attained is equivalent to that of an isolated exponential boundary layer [58] and is increasingly damped with increasing H. Given that H would be of order 10^4 in a realistic fusion environment, linear transient growth may not be very relevant in their context.

The weakly nonlinear analysis also compounds the difficulties in promoting turbulence in realistic fusion environments, given the scaling of the equilibrium amplitude with $H^{5/2}$ for all base flows. However, the weakly nonlinear analysis still indicates the possibility of subcritical transitions for any H. Supercritical bifurcations are only found along the lower branch of the neutral curve and only for $H \gg H^{\infty}$. At lower friction parameters, for base flows with any degree of antisymmetry, the entire computed neutral curve indicates a subcritical bifurcation.

As the transient growth depicted little base flow dependence and has been previously analyzed in Ref. [58], direct numerical simulations target the exponential growth predicted by the linear stability analysis. There are two key findings. First, the relaminarization of turbulent states in symmetric Shercliff flows always occurred through a monotonic decay, while MHD-Couette flows experienced re-excitation to a turbulent state, in some cases at amplitudes where nonlinearity was relevant. Second, the magnitude of the friction parameter seemed to largely dictate the ability to trigger turbulence. At low $H \leqslant 1$, the linear and nonlinear growth led only to a saturated state, without turbulence. At intermediate $3 \leqslant H \leqslant 10$, a transition to turbulence was observed, and at $H = 10$ the turbulence state was maintained to the computed extent of simulations. Fourier analysis also indicated the presence of an inertial subrange, where the perturbation energy exhibited a wave number dependence of $\kappa^{-5/3}$. At higher $H \geqslant 30$ (the bound above which transient growth is equivalent to that of an isolated exponential boundary layer), although transition was observed, the turbulent state quickly collapsed. In all cases, the nonlinear growth and turbulence were dominated by a persistent large-scale arched TS wave. Streamwise independent structures also formed, which stored perturbation energy and which reduced the gradients in the boundary layers. Overall, the general features of the secondary nonlinear growth mirror that observed for the finite-amplitude linear transient optimals simulated in Ref. [58], where nonlinear growth is due to the arching of the conventional TS wave.

As a final word, the results of this paper indicate that it may be exceedingly difficult to obtain Q2D subcritical transitions with random, and even optimized, initial conditions. Future work may therefore be best focused on directly reducing Re_c, permitting supercritical transitions at lower Reynolds numbers. Inflection points, introduced to the base flow with increasing antisymmetry, were not beneficial in this work due to their location. However, investigating the capabilities of inflection points within the boundary layers remains as a promising avenue for destabilizing Q2D flows (an ongoing work), which can be achieved through the use of time-periodic, rather than steady, wall motion.

ACKNOWLEDGMENTS

The authors are grateful to Jānis Priede for discussions regarding the implementation of the weakly nonlinear stability analysis. C.J.C. receives support from the Australian Government Research Training Program (RTP). A.P. is supported by the Royal Society (Wolfson Research Merit Award Scheme Grant No. WM140032). This research was supported by the Australian Government via the Australian Research Council (Discovery Grants No. DP150102920 and No. DP180102647), the National Computational Infrastructure (NCI), Pawsey Supercomputing Centre (PSC), Monash University via the MonARCH cluster, and the Royal Society under the International Exchange Scheme between the UK and Australia (Grant No. E170034).

[1] S. Smolentsev, R. Moreau, and M. Abdou, Characterization of key magnetohydrodynamic phenomena in PbLi flows for the US DCLL blanket, Fusion Eng. Des. **83**, 771 (2008).

[2] P. A. Davidson, *An Introduction to Magnetohydrodynamics* (Cambridge University Press, Cambridge, UK, 2001).

[3] J. Sommeria, Experimental study of the two–dimensional inverse energy cascade in a square box, J. Fluid Mech. **170**, 139 (1986).
[4] J. Sommeria, Electrically driven vortices in a strong magnetic field, J. Fluid Mech. **189**, 553 (1988).
[5] E. Lindborg, Can the atmospheric kinetic energy spectrum be explained by two-dimensional turbulence? J. Fluid Mech. **388**, 259 (1999).
[6] H. K. Moffatt, On the suppression of turbulence by a uniform magnetic field, J. Fluid Mech. **28**, 571 (1967).
[7] A. Alemany, R. Moreau, P. L. Sulem, and U. Frisch, Influence of an external magnetic field on homogeneous MHD turbulence, J. Méc. **18**, 277 (1979).
[8] Y. B. Kolesnikov and A. B. Tsinober, Experimental investigation of two-dimensional turbulence behind a grid, Fluid Dyn. **9**, 621 (1974).
[9] P. H. Roberts, *An Introduction to Magnetohydrodynamics* (Longmans, Green, New York, 1967).
[10] J. Sommeria and R. Moreau, Why, how, and when MHD turbulence becomes two-dimensional, J. Fluid Mech. **118**, 507 (1982).
[11] U. Schumann, Numerical simulation of the transition from three- to two-dimensional turbulence under a uniform magnetic field, J. Fluid Mech. **74**, 31 (1976).
[12] O. Zikanov and A. Thess, Direct numerical simulation of forced MHD turbulence at low magnetic Reynolds number, J. Fluid Mech. **358**, 299 (1998).
[13] A. Thess and O. Zikanov, Transition from two-dimensional to three-dimensional magnetohydrodynamic turbulence, J. Fluid Mech. **579**, 383 (2007).
[14] A. Pothérat and V. Dymkou, DNS of low-R_m MHD turbulence based on the least dissipative modes, J. Fluid Mech. **655**, 174 (2010).
[15] A. Pothérat and K. Kornet, The decay of wall-bounded MHD turbulence at low R_m, J. Fluid Mech. **783**, 605 (2015).
[16] N. T. Baker, A. Pothérat, L. Davoust, and F. Debray, Inverse and Direct Energy Cascades in Three-Dimensional Magnetohydrodynamic Turbulence at Low Magnetic Reynolds Number, Phys. Rev. Lett. **120**, 224502 (2018).
[17] A. Pothérat, Quasi-two-dimensional perturbations in duct flows under transverse magnetic field, Phys. Fluids **19**, 074104 (2007).
[18] R. Klein and A. Pothérat, Appearance of Three-Dimensionality in Wall Bounded MHD Flows, Phys. Rev. Lett. **104**, 034502 (2010).
[19] A. Pothérat and R. Klein, Why, how and when MHD turbulence at low R_m becomes three-dimensional, J. Fluid Mech. **761**, 168 (2014).
[20] P. Moresco and T. Alboussiére, Experimental study of the instability of the Hartmann layer, J. Fluid Mech. **504**, 167 (2004).
[21] D. Krasnov, O. Zikanov, M. Rossi, and T. Boeck, Optimal linear growth in magnetohydrodynamic duct flow, J. Fluid Mech. **653**, 273 (2010).
[22] D. Krasnov, O. Zikanov, and T. Boeck, Numerical study of magnetohydrodynamic duct flow at high Reynolds and Hartmann numbers, J. Fluid Mech. **704**, 421 (2012).
[23] O. G. W. Cassels, T. Vo, A. Pothérat, and G. J. Sheard, From three-dimensional to quasi-two-dimensional: Transient growth in magnetohydrodynamic duct flows, J. Fluid Mech. **861**, 382 (2019).
[24] L. Bühler, Instabilities in quasi-two-dimensional magnetohydrodynamic flows, J. Fluid Mech. **326**, 125 (1996).
[25] A. Pothérat, J. Sommeria, and R. Moreau, An effective two-dimensional model for MHD flows with a transverse magnetic field, J. Fluid Mech. **424**, 75 (2000).
[26] A. Pothérat and J. Schweitzer, A shallow water model for magnetohydrodynamic flows with turbulent Hartmann layers, Phys. Fluids **23**, 055108 (2011).
[27] J. Pedlosky, *Geophysical Fluid Dynamics* (Springer-Verlag, Berlin, 1987).
[28] J. Young, S. Smolentsev, and M. Abdou, Study of instabilities in a quasi-2D MHD duct flow with an inflectional velocity profile, Fusion Eng. Des. **89**, 1163 (2014).
[29] A. Thess, Instabilities in two–dimensional spatially periodic flows. Part I: Kolmogorov flow, Phys. Fluids A **4**, 1385 (1992).

[30] A. Thess, Instabilities in two-dimensional periodic flows. Part III: Square eddy lattice, Phys. Fluids A **4**, 1396 (1992).

[31] A. Thess, Instabilities in two-dimensional periodic flows. Part III: Inviscid triangular lattice, Phys. Fluids A **5**, 335 (1993).

[32] A. Pothérat, J. Sommeria, and R. Moreau, Numerical simulations of an effective two-dimensional model for flows with a transverse magnetic field, J. Fluid Mech. **534**, 115 (2005).

[33] V. Dousset and A. Pothérat, Numerical simulations of a cylinder wake under a strong axial magnetic field, Phys. Fluids **20**, 017104 (2008).

[34] W. K. Hussam, M. C. Thompson, and G. J. Sheard, Enhancing heat transfer in a high Hartmann number magnetohydrodynamic channel flow via torsional oscillation of a cylindrical obstacle, Phys. Fluids **24**, 113601 (2012).

[35] W. K. Hussam, M. C. Thompson, and G. J. Sheard, Optimal transient disturbances behind a circular cylinder in a quasi-two-dimensional magnetohydodynamic duct flow, Phys. Fluids **24**, 024105 (2012).

[36] A. H. A. Hamid, W. K. Hussam, A. Pothérat, and G. J. Sheard, Spatial evolution of a quasi-two-dimensional Karman vortex street subjected to a strong uniform magnetic field, Phys. Fluids **27**, 053602 (2015).

[37] O. G. W. Cassels, W. K. Hussam, and G. J. Sheard, Heat transfer enhancement using rectangular vortex promoters in confined quasi-two-dimensional magnetohydrodynamic flows, Int. J. Heat Mass Transfer **93**, 186 (2016).

[38] T. Vo, A. Pothérat, and G. J. Sheard, Linear stability of horizontal, laminar fully developed, quasi-two-dimensional liquid metal duct flow under a transverse magnetic field heated from below, Phys. Rev. Fluids **2**, 033902 (2017).

[39] J. C. R. Hunt and J. A. Shercliff, Magnetohydrodynamics at high Hartmann number, Annu. Rev. Fluid Mech. **3**, 37 (1971).

[40] E. Marensi, A. P. Willis, and R. R. Kerswell, Stabilisation and drag reduction of pipe flows by flattening the base profile, J. Fluid Mech. **863**, 850 (2019).

[41] J. Kühnen, B. Song, D. Scarselli, N. B. Budanur, M. Riedl, A. P. Willis, M. Avila, and B. Hof, Destabilizing turbulence in pipe flow, Nat. Phys. **14**, 386 (2018).

[42] N. B. Budanur, E. Marensi, A. P. Willis, and B. Hof, Upper edge of chaos and the energetics of transition in pipe flow, Phys. Rev. Fluids **5**, 023903 (2020).

[43] B. Hof, A. de Lozar, M. Avila, X. Tu, and T. M. Schneider, Eliminating turbulence in spatially intermittent flows, Science **327**, 1491 (2010).

[44] P. J. Schmid and D. S. Henningson, *Stability and Transition in Shear Flows* (Springer-Verlag, New York, 2001).

[45] J. A. C. Weideman and S. C. Reddy, A MATLAB differentiation matrix suite, ACM Trans. Math. Software **26**, 465 (2001).

[46] L. N. Trefethen, *Spectral Methods in MATLAB* (Society for Industrial and Applied Mathematics, Philadelphia, 2000).

[47] J. Hagan and J. Priede, Capacitance matrix technique for avoiding spurious eigenmodes in the solution of hydrodynamic stability problems by Chebyshev collocation method, J. Comput. Phys. **238**, 210 (2013).

[48] T. Kakutani, The hydromagnetic stability of the modified plane Couette flow in the presence of a transverse magnetic field, J. Phys. Soc. Jpn. **19**, 1041 (1964).

[49] J. Hagan and J. Priede, Weakly nonlinear stability analysis of magnetohydrodynamic channel flow using an efficient numerical approach, Phys. Fluids **25**, 124108 (2013).

[50] M. Takashima, The stability of the modified plane Couette flow in the presence of a transverse magnetic field, Fluid Dyn. Res. **22**, 105 (1998).

[51] R. J. Lingwood and T. Alboussière, On the stability of the Hartmann layer, Phys. Fluids **11**, 2058 (1999).

[52] C. Airiau and M. Castets, On the amplification of small disturbances in a channel flow with a normal magnetic field, Phys. Fluids **16**, 2991 (2004).

[53] P. G. Drazin and W. H. Reid, *Hydrodynamic Stability* (Cambridge University Press, Cambridge, UK, 2004).

[54] D. D. Joseph, *Stability of Fluid Motions I* (Springer-Verlag, Berlin, 1976).

[55] D. Barkley, H. M. Blackburn, and S. J. Sherwin, Direct optimal growth analysis for timesteppers, Int. J. Numer. Methods Fluids **57**, 1435 (2008).

[56] E. Hairer, S. P. Nørsett, and G. Wanner, *Solving Ordinary Differential Equations I: Nonstiff Problems* (Springer-Verlag, Berlin, 1993).

[57] H. M. Blackburn, D. Barkley, and S. J. Sherwin, Convective instability and transient growth in flow over a backward-facing step, J. Fluid Mech. **603**, 271 (2008).

[58] C. J. Camobreco, A. Pothérat, and G. J. Sheard, Subcritical route to turbulence via the Orr mechanism in a quasi-two-dimensional boundary layer, Phys. Rev. Fluids **5**, 113902 (2020).

[59] S. C. Reddy, P. J. Schmidt, and D. S. Henningson, Pseudospectra of the Orr-Sommerfeld operator, SIAM J. Appl. Math. **53**, 15 (1993).

[60] S. C. Reddy and D. S. Henningson, Energy growth in viscous channel flows, J. Fluid Mech. **252**, 209 (1993).

[61] L. N. Trefethen, A. E. Trefethen, S. C. Reddy, and T. A. Driscoll, Hydrodynamic stability without eigenvalues, Science **261**, 578 (1993).

[62] K. M. Butler and B. F. Farrell, Three-dimensional optimal perturbations in viscous shear flow, Phys. Fluids A **4**, 1637 (1992).

[63] P. K. Sen and D. Venkateswarlu, On the stability of plane Poiseuille flow to finite-amplitude disturbances, considering the higher-order Landau coefficients, J. Fluid Mech. **133**, 179 (1983).

[64] W. C. Reynolds and M. C. Potter, Finite-amplitude instability of parallel shear flows, J. Fluid Mech. **27**, 465 (1967).

[65] K. Stewartson and J. T. Stuart, A non-linear instability theory for a wave system in plane Poiseuille flow, J. Fluid Mech. **48**, 529 (1971).

[66] G. E. Karniadakis and S. J. Sherwin, *Spectral/HP Element Methods for Computational Fluid Dynamics* (Oxford University Press, Oxford, UK, 2005).

[67] G. J. Sheard, M. J. Fitzgerald, and K. Ryan, Cylinders with square cross-section: Wake instabilities with incidence angle variation, J. Fluid Mech. **630**, 43 (2009).

[68] D. Krasnov, M. Rossi, O. Zikanov, and T. Boeck, Optimal growth and transition to turbulence in channel flow with spanwise magnetic field, J. Fluid Mech. **596**, 73 (2008).

Chapter 7

Subcritical transitions to sustained turbulence in quasi-two-dimensional duct flows

7.1 Perspective

Immediately apparent from the previous work, is that when at friction parameter $H = 10$, a 10% supercritical Re could trigger and sustain Q2D turbulence, while turbulence was not triggered at subcritical Re. Both larger and smaller H required much larger ratios of Re/Re_{c} to incite and possibly sustain turbulence, as shown in Appendix C. Thus, this chapter, presenting work currently being prepared for publication, places sole focus on $H = 10$, at subcritical Re. However, note that Chapter 6 (Camobreco *et al.* 2021b) simulates conditions maximizing the exponential growth rate of a modal instability, while Chapter 5 (Camobreco *et al.* 2020) simulates conditions maximizing the transient growth of a nonmodal instability. Thus, there were two key differences between the studies contained in Chapters 5 (Camobreco *et al.* 2020) and 6 (Camobreco *et al.* 2021b), excluding the different Re for the moment. First, there was a different H. Second, there was a different wave number, representing different perturbations via an altered perturbation aspect ratio $L/(2\pi/\alpha)$; discussed further in Appendix D. To isolate each effect, the work contained herein first compares nonmodal instabilities at different wave numbers, while holding H and Re constant. Note that all initial conditions employed in this chapter are nonmodal perturbations; different target perturbations, selected via α, are attained once the initial condition is evolved to a specified target time. This preliminary investigation leads to quite an interesting result. Targeting the nonmodal instability maximizing linear growth is less efficient at triggering turbulence, and leads to turbulence which is not sustained. By comparison, targeting the modal instability minimizing exponential decay is more efficient at triggering turbulence, in spite of less linear transient growth, and leads to sustained turbulence.

To explain these results, a few factors have to be separated. The first factor regards why targeting the modal instability is more efficient. Simulations holding the wave number constant, while linearly (or nonlinearly) optimizing with larger and larger target times, leads to less linear growth, but more efficient transitions to turbulence (a reduction in the initial energy required). As the target time is increased, the resulting nonmodal perturbation contains an increasingly greater fraction of energy in the leading modal instability at the target time. Growth is effectively maximized at large times by compromising between an initial spurt of linear growth, and transferring a large fraction of energy to the slowest decaying eigenmode. Thus, the initial condition converges toward the perturbation optimally energizing the leading eigenmode, i.e. the leading adjoint mode, which does not generate the maximum possible transient growth, but most efficiently triggers turbulence.

The second factor regards the theories proposed by Stuart and Landau (Landau 1944; Stuart 1958; Drazin & Reid 2004) on subcritical bifurcations. Recalling the discussion of Chapter 3, § 3.5, when performing an amplitude expansion about the leading modal instability, for a given Re, a critical amplitude exists. Above the critical amplitude, the decay of the leading eigenmode is offset by the nonlinear growth of its harmonic, with excess growth to spare. This slow growth (nonlinear minus linear) is predicted to eventually excite additional harmonics, and incite a transition to turbulence. This theory will match most of the following results well. When the nonmodal instability maximizing linear growth is targeted, the leading eigenmode is not well energized, and does not generate the necessary additional harmonic to offset its decay. However, the nonmodal instability minimizing linear decay (optimally energizing the leading eigenmode), can go on, through weakly nonlinear interaction, to generate the harmonic required to offset its decay. If the initial energy (multiplied by some linear growth) exceeds the critical amplitude, the system should transition to turbulence, and more importantly, sustain said turbulence. It is also interesting to note that the dynamical systems viewpoint of the edge state and edge trajectory, recalling Chapter 3, § 3.4, also parallels this discussion. The edge trajectory represents being exactly at the critical amplitude, while energization to slightly above the critical amplitude represents an initial condition with trajectory beginning within the turbulent basin. The edge state, or saddle point, from which the edge trajectory turns toward turbulence, is then the superposition of the linear eigenmode and its weakly nonlinear interactions.

Although it is pleasing that much of the following work will fit with previous theories and interpretations, some complications remain. The first is that growth from the edge state toward turbulence appears to be superexponential, which does not match the slow growth of a subcritical bifurcation. A possible explanation is that the Stuart–Landau theory (Landau 1944; Stuart 1958; Drazin & Reid 2004) may not appropriately account for the weakly nonlinear interaction of the leading eigenmode and its complex conjugate. Admittedly, a simultaneous coupling of the leading eigenmode modulating the base flow, and a corresponding adjustment to the exponential growth rate by the modulation, was mentioned by Stuart (1958), but not explicitly considered as it is in this chapter. Importantly, this base flow modulation can be fed more and more energy by the lower harmonics (negative production from harmonics to the modulation), the longer the trajectory remains near the edge. Eventually, the modulated base flow may become supercritical, which would explain the superexponential growth. Such supercritical modulations have been theorized, in the minimal defect theory discussed in Chapter 3, § 3.5. However, production to the minimal defects is unaccounted for in said theories, and could introduce significant inefficiencies to transitions via the minimal defect. These inefficiencies are not present in the modified Stuart–Landau theory, as the weakly nonlinear modulation (suboptimally) improves the growth rate of the leading eigenmode, but maintains direct feedback from the leading eigenmode, via negative production, to the modulation. Note that if properly accounting for the base flow modulation, the perturbation aspect ratio to target would be the leading eigenmode minimizing decay on the modulated, rather than the unmodulated, base flow (which may yield a lower critical amplitude and more efficient route to turbulence).

The second complication regards the intermittent behavior of the sustained turbulence. Although introduced for hydrodynamic pipe flows in Chapter 3, § 3.6, turbulent intermittency, as measured by a turbulent fraction, exhibited a superexponential dependence on Re. However, considering the simulations in both this chapter, and in Chapter 6 (Camobreco *et al.* 2021b), intermittency is observed over $0.9 < r_{\mathrm{c}} < 1.1$ at the very least. Compared to Avila *et al.* (2011), this is quite a large range of Reynolds numbers over which extreme relaminarization events are observed (although domain length effects cannot be ruled out).

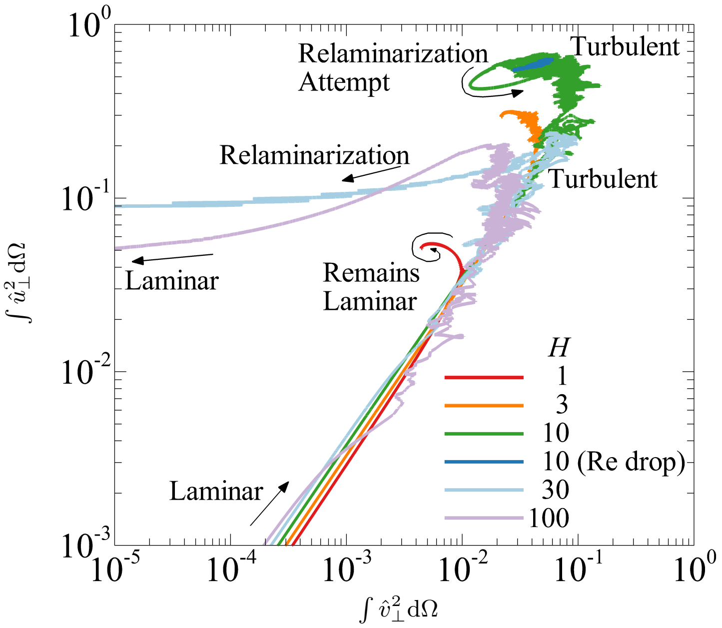

FIGURE 7.1: State space representation of turbulent transitions, based on domain integrated streamwise and wall-normal perturbation velocities. Random noise initial conditions at the maximal wave number for exponential growth of a modal instability at $r_c = 1.1$, for various H (one case at $H = 10$ slowly dropped to $r_c = 0.9$ post transition). At $H = 10$, intermittent turbulence was sustained, subcritically and supercritically.

7.2 State space representation of sustained turbulence

Before proceeding with this chapter, some initial evidence that turbulence can be indefinitely sustained at subcritical Re is provided in Fig. 7.1. Note that the data sets at supercritical Re presented in Fig. 7.1, which target modal instabilities, are the same as those in Chapter 6 (Camobreco *et al.* 2021b), except with some cases having extended time histories, and with the inclusion of a single case at $H = 10$ with the Reynolds number dropped to $r_c = 0.9$. Recall that at $H \geq 30$, weakly supercritical Reynolds numbers transitioned to turbulence, but were unable to sustain turbulence, while at $H \leq 3$, turbulence was either not sustained or not triggered at all (as shown in Appendix C, this was due to the magnitude of Re). However, at $H = 10$, turbulence was both triggered and indefinitely sustained, excluding multiple brief attempts at relaminarization, both at $r_c = 1.1$, and at $r_c = 0.9$, after having incrementally reduced r_c from 1.1 to 0.9. Thus, $H = 10$ forms the focus of this chapter.

This chapter proceeds as follows. After introducing the problem setup, § 7.3, the common 'edge tracking' approach (Pringle *et al.* 2012; Kerswell *et al.* 2014; Duguet *et al.* 2013; Zammert & Eckhardt 2019; Farano *et al.* 2016; Duguet *et al.* 2012; Cherubini *et al.* 2011; Beneitez *et al.* 2019; Duguet *et al.* 2009; Vavaliaris *et al.* 2020; Khapko *et al.* 2014; Cherubini *et al.* 2015; Budanur *et al.* 2020) is employed to identify the edge state, based on nonmodal instabilities targeting domains with lengths based on either the optimal nonmodal growth (case 0) or minimal modal decay (case 1), in § 7.4. For each case, the asymptotic edge state(s) on the laminar-turbulent basin boundary (or edge manifold), and the delineation energy, representing the energy of an initial condition just past the edge manifold, are determined. Only the lower branch (or separatrix) is investigated in this chapter. Although the upper edge can also be identified, its basis is in chaotic distortion of the initial condition (Budanur *et al.* 2020), and is of less interest in efficiently triggering turbulence. The laminar and turbulent Fourier spectra for these cases (cases 0 and 1) are investigated, and the ability to sustain turbulence compared. The composition of the edge state, derived from the minimal modal decay scenario (case 1), is scrutinized, and compared to the weakly nonlinear interactions of the leading eigenmode in § 7.5. Variations in the target time for optimization are considered in § 7.6, with significant ramifications on the delineation energy, and further extended over a broader range of Reynolds numbers. Nonlinear optimals are shown to be effectively identical to their linear counterparts, over this larger range of target times, for the initial energies of interest, in § 7.7. Overall conclusions are provided in § 7.8.

7.3 Problem formulation

A streamwise invariant duct flow with streamwise periodic x-direction (wave number α), wall-normal height $2L$ (y-direction) and out-of-plane width a (z-direction), is investigated. Only the x-y (perpendicular) plane of the duct is shown in Fig. 7.2, as Q2D approximations of the z-averaged 3D solution are of interest. Flow is driven by the synchronous motion of the lateral walls at constant velocity U_0.

With length, velocity, time and pressure non-dimensionalized by L, U_0, L/U_0 and ρU_0^2, respectively, the Q2D equivalent of the Navier–Stokes equations become

$$\boldsymbol{\nabla}_\perp \cdot \boldsymbol{u}_\perp = 0, \tag{7.1}$$

$$\frac{\partial \boldsymbol{u}_\perp}{\partial t} + (\boldsymbol{u}_\perp \cdot \boldsymbol{\nabla}_\perp)\boldsymbol{u}_\perp = -\boldsymbol{\nabla}_\perp p_\perp + \frac{1}{Re}\boldsymbol{\nabla}_\perp^2 \boldsymbol{u}_\perp - \frac{H}{Re}\boldsymbol{u}_\perp, \tag{7.2}$$

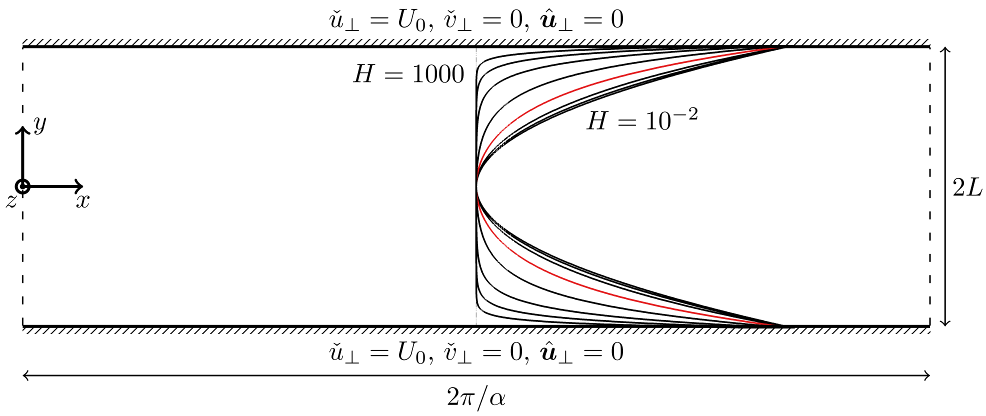

FIGURE 7.2: A schematic representation of the system. Dimensional variables are indicated as, e.g. $\check{u}_\perp$. Solid lines denote lateral walls moving with constant dimensional velocity U_0. Short dashed lines represent the streamwise extent of the periodic domain, with wave number α. Examples of the laminar base flow velocity profile are plotted for H of (left to right) 1000, 300, 100, 30, 10 (red), 3, 1, 10^{-2}. Flow is in the positive x direction.

where $\boldsymbol{u}_\perp = (u_\perp,\ v_\perp)$ and $\boldsymbol{\nabla}_\perp = (\partial_x, \partial_y)$, with non-dimensional boundary conditions of $\boldsymbol{u}_\perp(y = \pm 1) = (1, 0)$. The only difference between the Q2D and 2D Navier–Stokes equations is the linear friction term $-H\boldsymbol{u}_\perp/Re$ that models the effect of shear stresses acting at the out-of-plane duct walls. Although this term breaks the natural Galilean invariance of the 2D Navier–Stokes equations, it also permits exact conversion between wall-driven and pressure-driven flow dynamics for non-zero H, as shown in Chapter 8 (Camobreco *et al.* 2021a). The governing non-dimensional parameters, $H = 2(L^2/a)B_0(\sigma/\rho\nu)^{1/2}$ and $Re = U_0L/\nu$, have been previously introduced.

Perturbations are defined as

$$\hat{\boldsymbol{u}}_\perp = \boldsymbol{u}_\perp - \boldsymbol{U}_\perp,\ \ \hat{p}_\perp = p_\perp, \tag{7.3}$$

to place focus on the deviation between the instantaneous flow $(\boldsymbol{u}_\perp, p_\perp)$ and the laminar fixed point $\boldsymbol{U}_\perp$. In this chapter, the fixed point is the streamwise independent, time steady, parallel base flow $\boldsymbol{U}_\perp(y) = (U_\perp,\ 0)$, where $U_\perp(y) = \cosh(H^{1/2}y)/\cosh(H^{1/2})$. $H = 10$ is of particular interest to this work, with this base flow highlighted in Fig. 7.2.

7.4 Edge tracking

7.4.1 Formulation

The edge tracking process has three components. First, the initial condition maximizing linear transient growth is computed. Second, the initial condition is rescaled to a specified finite energy, and seeded onto the laminar base flow for full DNS. Third, the initial condition is classified as either remaining laminar, or reaching the turbulent attractor, and the second component is iterated towards the initial energy required to just reach the turbulent attractor. Further details for these three components follow.

First, the initial condition maximizing growth in the functional $G = ||\hat{\boldsymbol{u}}_\perp(t = \tau)||/||\hat{\boldsymbol{u}}_\perp(t = 0)||$ is sought, for a prescribed target time τ, and wave number α. G represents the gain in perturbation kinetic energy under the norm $||\hat{\boldsymbol{u}}_\perp|| = \int \hat{\boldsymbol{u}}_\perp \cdot \hat{\boldsymbol{u}}_\perp \,\mathrm{d}\Omega$ (Barkley *et al.* 2008), over computational domain Ω. The initial condition is computed with two independent solvers; the MATLAB solver is detailed here. For the primitive variable solver, see Chapter 5 (Camobreco *et al.* 2020).

The perturbation definitions, Eq. (7.3), are substituted into Eqs. (7.1) and (7.2), and all terms linear in the perturbation are isolated. Taking twice the curl of the result, applying the divergence free constraint on the perturbation, and assuming plane wave solutions with streamwise variation $\exp(\mathrm{i}\alpha x)$, provides the linearized perturbation evolution equation

$$\frac{\partial \hat{v}_\perp}{\partial t} = \mathcal{A}^{-1}\left[-\mathrm{i}\alpha U_\perp \mathcal{A} + \mathrm{i}\alpha U_\perp'' + \frac{1}{Re}\mathcal{A}^2 - \frac{H}{Re}\mathcal{A}\right]\hat{v}_\perp, \tag{7.4}$$

where $\mathcal{A} = D^2 - \alpha^2$, and D represents ∂_y. The adjoint evolution equation

$$\frac{\partial \hat{\xi}_\perp}{\partial t} = \mathcal{A}^{-1}\left[\mathrm{i}\alpha U_\perp \mathcal{A} + 2\mathrm{i}\alpha U_\perp' D + \frac{1}{Re}\mathcal{A}^2 - \frac{H}{Re}\mathcal{A}\right]\hat{\xi}_\perp, \tag{7.5}$$

is derived from Eq. (7.4) based on the definition of the adjoint velocity perturbation $\hat{\xi}_\perp$ introduced in Schmid & Henningson (2001). The domain $y \in [-1, 1]$ is discretized with $N_\mathrm{c} + 1$ Chebyshev nodes (Trefethen 2000; Weideman & Reddy 2001), and D (and higher orders) approximated with derivative matrices incorporating boundary conditions (Trefethen 2000). A third-order forward Adams–Bashforth scheme (Hairer *et al.* 1993) integrates Eq. (7.4) from $t = 0$ to $t = \tau$, and with 'initial' condition $\hat{\xi}_\perp(\tau) = \hat{v}_\perp(\tau)$, integrates Eq. (7.5) from $t = \tau$ back to $t = 0$. After normalizing to $||\hat{v}_\perp(0)|| = 1$ the next iteration proceeds. Boundary conditions are $\hat{v}_\perp = D\hat{v}_\perp = \hat{\xi}_\perp = D\hat{\xi}_\perp = 0$ at all walls. The j'th eigenvalue $\lambda_{\mathrm{G},j}$ of the operator representing the sequential action of direct and adjoint evolution is determined with a Krylov subspace scheme (Barkley *et al.* 2008; Blackburn *et al.* 2008). With eigenvalues sorted in ascending order by largest real component, the optimized growth $G = \lambda_{\mathrm{G},1}$ with corresponding eigenvector $\tilde{v}_{\perp,G}(t=0)$. The iterative scheme is initialized with random noise.

Second, the initial condition is seeded onto the base flow $\boldsymbol{u}_{\perp}(t=0) = U_{\perp} + \hat{\boldsymbol{u}}_{\perp,G}$, where $\hat{\boldsymbol{u}}_{\perp,G} = \chi \mathrm{Re}[(\mathrm{i}\partial_y \tilde{v}_{\perp,G}/\alpha, \tilde{v}_{\perp,G}) \exp(\mathrm{i}\alpha x)]$, and where χ allows the initial perturbation energy, quoted as $E_0(t=0) = \int \hat{\boldsymbol{u}}^2_{\perp,G}(t=0)\mathrm{d}\Omega / \int U^2_{\perp}\mathrm{d}\Omega$, to be varied. Nonlinear evolution of $\hat{\boldsymbol{u}}_{\perp}$ commences, via Eqs. (7.1) and (7.2), using a primitive variable spectral element solver (linear optimals were recomputed in the primitive variable solver, see Table 7.1). The time integration scheme is third order backward differencing, with operator splitting, while high-order Neumann pressure boundary conditions are imposed on the lateral walls to maintain third order time accuracy (Karniadakis *et al.* 1991). The x-y plane is discretized with quadrilateral elements, within which Gauss–Legendre–Lobatto nodes (polynomial order N_{p}) are distributed. The mesh design is based on the resolution testing contained in Chapters 5 (Camobreco *et al.* 2020) and 6 (Camobreco *et al.* 2021b). 12 spectral elements are equispaced in the streamwise direction, and 48 in the wall-normal direction (the latter are geometrically biased toward both lateral walls, with bias ratio 0.7). A polynomial order of $N_{\mathrm{p}} = 13$ was sufficient for recomputing linear optimals, increased to $N_{\mathrm{p}} = 19$ for nonlinear evolution, as these results agreed well with further validation in this setup at $N_{\mathrm{p}} = 23$ (not shown). The timestep of $\Delta t = 1.25 \times 10^{-3}$, as in Chapters 5 (Camobreco *et al.* 2020) and 6 (Camobreco *et al.* 2021b), was also employed (although a greatly reduced Δt is required once turbulence is triggered).

Third, the initial condition is either classified as reaching the turbulent attractor, or remaining laminar. E_0 is adjusted downward or upward as appropriate, and the second and third steps are repeated until an accuracy of 4 significant figures is reached in the lower delineation energy E_{D}. Note that 4 significant accuracy is maintained by simulations with either half the time step size, or double the streamwise resolution. However, additional accuracy in E_{D} cannot be guaranteed unless temporal and streamwise resolutions are increased. In addition, a higher accuracy in E_{D} requires that trajectories remain in the vicinity of the edge for increasingly large times, and thus noticeably increases the computational expense.

Depending on the choice of α and Re, two definitions are considered for this edge

Case	MATLAB	Linear primitive	|% Error|	Nonlinear primitive	|% Error|
0	97.55253053	97.55254271	1.25×10^{-5}	97.55170092	8.50×10^{-4}
1	78.14835970	78.14836801	1.06×10^{-5}	78.14805012	3.96×10^{-4}
2	91.63907657	91.63914267	7.21×10^{-5}	91.63846567	6.67×10^{-4}

TABLE 7.1: Validation of the transient growth $G(\tau)$ achievable for various cases (differing α, τ) at $r_c = 0.9$. The MATLAB solver had $N_c = 80$ Chebyshev points, timestep $\Delta t = 4 \times 10^{-5}$ and 20 forward-backward iterations. The discretization for the linear transient growth solver is detailed in the text, with $\Delta t = 1.25 \times 10^{-3}$, and a convergence tolerance of 10^{-7} between iterations. The nonlinear transient growth computations (details in § 7.7) had identical degrees of freedom, timestep and tolerance. However, the non-zero initial energy ($E_0 = 10^{-8}$) induces a finite 'error' when comparing linear and nonlinear cases. Percent errors are relative to MATLAB results.

tracking process. If the turbulent state is sustained, and if the edge state is able to maintain a near constant energy for an arbitrarily long time (as $E_0 \to E_D$), the classical definition (Duguet *et al.* 2009; Beneitez *et al.* 2019; Vavaliaris *et al.* 2020), as introduced in Chapter 3, § 3.4, suffices. Two energy bounds, one above and one below the edge state energy are specified. If an initial condition crosses the upper bounding energy (from below), it is considered to reach the turbulent attractor, while if it crosses the lower bounding energy (from above) it is considered to remain laminar. However, if the delineating energy does not yield a clear edge state, the alternate definition introduced in Chapter 5 (Camobreco *et al.* 2020) is adopted. In such cases, if the energy time history attains a secondary local maximum after the initial linear transient growth, the initial condition is considered to remain laminar. Instead, if there is a secondary inflection point after the linear transient growth, the initial condition is classed as reaching the turbulent attractor.

To support the classification of initial conditions realizing turbulence, energy spectra are computed at select instants in time, as the discretized streamwise direction is periodic. Fourier coefficients $c_\kappa = |(1/N_f)\sum_{n=0}^{n=N_f-1}[\hat{u}_\perp^2(x_n) + \hat{v}_\perp^2(x_n)]e^{-2\pi i\kappa n/N_f}|$ were computed with the discrete Fourier transform in MATLAB, where x_n represents the n'th x-location linearly spaced between $x_0 = 0$ and $x_{N_f} = 2\pi/\alpha$. A mean Fourier coefficient $\bar{c}_\kappa$ is obtained by averaging the coefficients obtained at 21 y-values. Although $N_f = 10000$ was chosen, only the first 70 to 80 Fourier modes are well resolved by the streamwise discretization.

Three types of initial condition are investigated, to determine the conditions necessary to sustain turbulence. Different initial conditions are obtained by varying the domain length (via α) and the target time to achieve optimal growth. The first type, hereafter case 0, simulates conventional linear transient growth optimals, with both α and τ optimized to yield the largest growth over all initial conditions, wave numbers and target times. The second, case 1, has the wave number set to that achieving minimal decay rate of the leading modal instability (henceforth α_{max}) at the chosen Re, with τ optimized for maximal growth at this fixed wave number. The third, case 2, again sets the wave number to α_{max}, but is time optimized at $\alpha = 2\alpha_{\text{max}}$, so that the optimal initial condition has two repetitions within the full α_{max} based domain. Thus, case 2 initially has an effective wave number closer to α_{opt}, but if a period doubling occurs, will have an effective wave number of α_{max}. All results until § 7.6 are at a critical Reynolds number ratio $r_{\text{c}} = Re/Re_{\text{c}} = 0.9$, where $Re_{\text{c}} = 79123.2$ at $H = 10$, recalling Chapter 6 (Camobreco *et al.* 2021b), as $r_{\text{c}} = 0.9$ has been shown to sustain turbulence that was generated from a supercritically evolved modal instability. For reference, at $r_{\text{c}} = 0.9$, $\alpha_{\text{opt}} = 1.49$ and $\alpha_{\text{max}} = 0.979651$ (all modal instability results are computed with the MATLAB solver). Validation for this setup is provided in Table 7.1; the agreement is excellent.

7.4.2 Results

With the linear optimals computed, edge tracking is performed for the three cases previously discussed; see Table 7.2 for the key results. Of particular interest is the delineation energy E_{D}. Examples of how E_{D} was defined are shown in the left column of Fig. 7.3. Case 2 exhibits the largest E_{D}, and so is furthest from the turbulent attractor, and of least interest. Case 2 represents a compromise between maintaining the largest linear transient growth while still having access to α_{max}, via period doubling. Although period doubling was often observed in an isolated exponential boundary layer, recalling Chapter 5 (Camobreco *et al.* 2020), it was prohibited by the extra constriction from the upper wall in a full duct flow; Fig. 7.3(c), right column, indirectly implies that period doubling did not occur. Case 0 focused solely on maximizing linear transient growth, in the hope that this would yield the lowest E_{D}. Compared to case 2, case 0 generated approximately 6% more linear transient growth, yet reduced E_{D} by a factor of more than one half. However, the maximal linear transient growth still does not yield the lowest E_{D}. This, in itself, may imply that searching for the most explosively growing initial conditions is not optimal when attempting to trigger transitions to turbulence.

Case	α	τ	$G/G_{\max}$	E_{D}
2	0.979651 ($\alpha_{\max}$)	19.4	0.939	2.547×10^{-4}
0	1.49 (α_{opt})	23.4	1	6.347×10^{-5}
1	0.979651 ($\alpha_{\max}$)	31.0	0.801	3.0577×10^{-6}

TABLE 7.2: Key results for the three cases investigated. Case 1 yields the smallest E_{D}, in spite of the smallest linear transient growth, by energizing the leading modal instability.

Since in Q2D flows $G_{\max}$ is typically 100 times lower than in 3D flows, this may indicate that linear transient growth is less relevant to Q2D transitions to turbulence. Case 1 simultaneously generated the least linear transient growth and yielded the lowest E_{D} (for all the α and τ considered thus far at $r_{\mathrm{c}} = 0.9$), with E_{D} over 20 times smaller than for case 0. Case 1 selected the wave number minimizing the decay rate of the leading modal instability. As the modal instability is important in nonmodal analysis (Reddy & Henningson 1993; Reddy *et al.* 1993), after the initial linear transient growth, the optimal adjusts, so as to contain most of its energy to the leading eigenmode. This minimizes its decay rate, and keeps G large for larger τ (Trefethen *et al.* 1993). Hence, targeting the leading eigenmode (by selecting $\alpha_{\max}$) may be more important than solely optimising G. Overall, as τ has increased, E_{D} has decreased, which is investigated further in § 7.6.

Returning to how the delineation energy is computed (the left column of Figure 7.3), as measured in the perturbation energy $E = \int \hat{\boldsymbol{u}}_{\perp,G}^2 \mathrm{d}\Omega$, it is interesting to note that the cases (0 and 2) not relying on the modal instability can only define E_{D} based on the local maximum criteria introduced in Chapter 5 (Camobreco *et al.* 2020). However, case 1, which yields the lowest E_{D}, and directly targets the modal instability, satisfies both the local maximum criterion (although unable to be observed at the scale of the plot), and the more conventional constant energy criterion usually used to define edge states (Duguet *et al.* 2009; Beneitez *et al.* 2019; Vavaliaris *et al.* 2020). It is also interesting to note, by considering the Fourier spectra at select instants in time in the right column of Fig. 7.3, that while cases 0 and 2 are unable to sustain turbulence, case 1 can. Further numerical evidence of this is provided in Appendix A.

Turbulence is identified with two key measures, the number of energized modes (Grossmann 2000), and the formation of an inertial subrange, identified by a (y-averaged) perturbation energy spectrum $\bar{c}_\kappa$ with ($-5/3$) power law dependence (Pope 2000). Considering the Fourier spectra of Fig. 7.3(b), as it focuses on the initial tran-

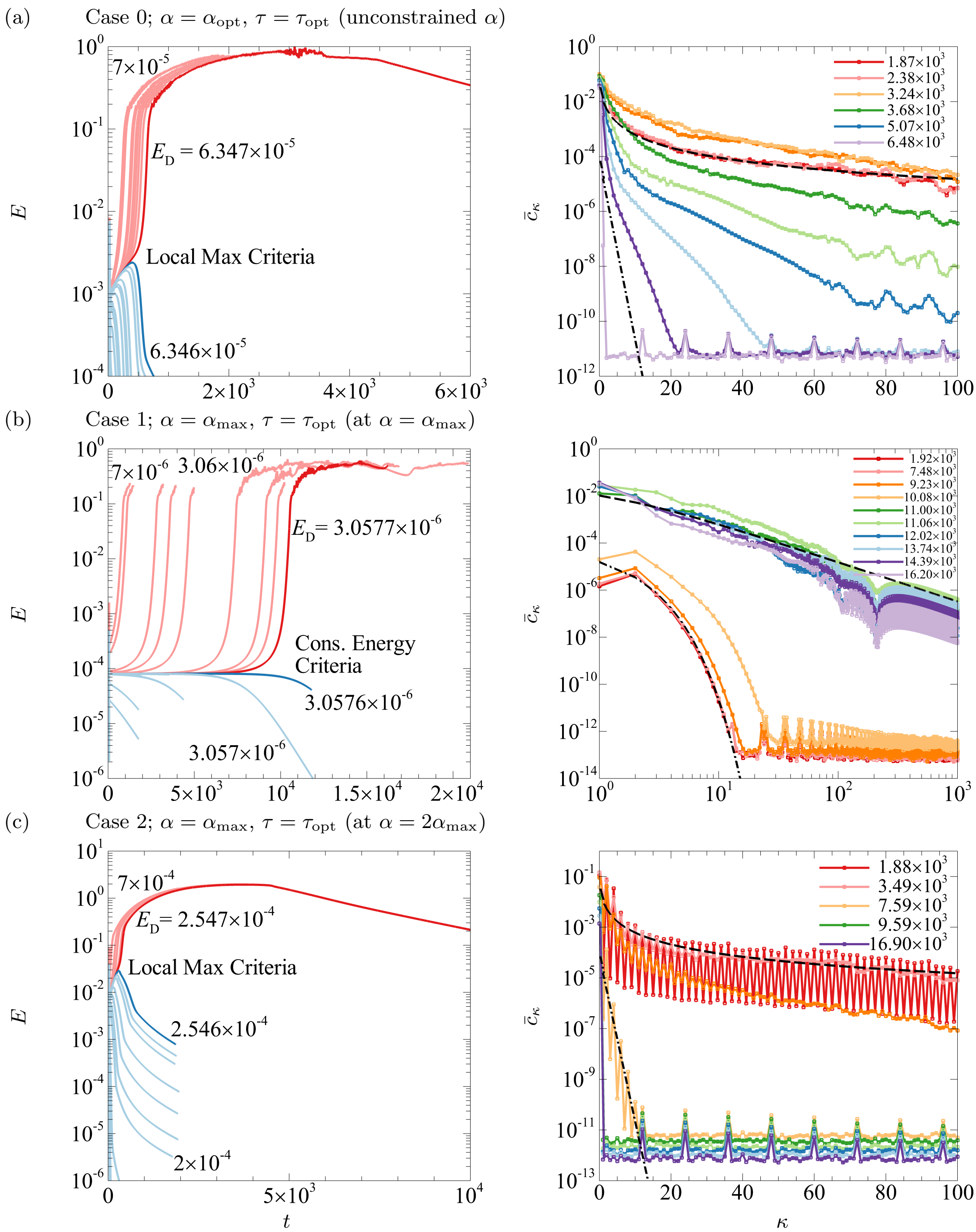

FIGURE 7.3: Nonlinear evolution of linear optimals at $r_{\rm c} = 0.9$, for the three cases (domain/initial condition combinations) of interest. Left column: determination of delineation energy. Right column: Fourier spectra at select instants in time (see legends) to indicate whether a flow (with $E_0 > E_{\rm D}$) sustains turbulence. Dashed black lines denote $\kappa^{-5/3}$ trends; dash-dotted black lines denote $\exp(-3\kappa/2)$ trends.

sition, while on the edge state ($1.92 \times 10^3 < t < 9.23 \times 10^3$), only 10-15 modes have non-floor energy levels. Upon departing the edge state there is a steady increase in the number of energized modes, with 30 or so energized by $t = 1.008 \times 10^4$. Once a turbulent state is achieved around $t = 1.100 \times 10^4$, all resolvable modes are appreciably energized. Furthermore, for $t \geq 1.100 \times 10^4$, even without a time average, results from instantaneous velocity fields for case 1 scale with $\kappa^{-5/3}$ quite well. However, for cases 0 and 2, the $\kappa^{-5/3}$ scaling is not maintained. In the case 0 example, Fig. 7.3(a), recorded times $1.87 \times 10^3 \lesssim t \lesssim 2.38 \times 10^3$ fit such a trend, indicating that turbulence was triggered. However, at later times, the energy in each mode decays. At even larger times, only the base flow modulation ($\kappa = 0$) has appreciable energy, although it too slowly decays. Similarly, case 2 unsustainably triggers turbulence, with relaminarization and rapid decay of all but the zeroth (slowly decaying) mode. Overall, case 1, being both at $\alpha_{\max}$ and targeting an instability that energized the leading eigenmode (large τ), was the only combination able to sustain turbulence. Thus, it is likely that to sustain turbulence, the modal instability must be significantly energized, and sufficient domain length must be afforded. Whether the modal instability has a positive or negative growth rate on the nonlinearly modulated base flow is investigated in § 7.5. However, for a 3D flow, Lozano-Durán *et al.* (2021) have shown that turbulence can be sustained, if, after transition occurs, all modal instabilities decay (by artificially introducing linear friction to ensure all growing modes instead decay). It is also remarkable to note that the turbulence observed in case 1 is temporally intermittent. The flow returns on a relaminarization path multiple times, as was previously observed supercritically at $H = 10$ in Chapter 6 (Camobreco *et al.* 2021b) and highlighted in the state space representation in § 7.2. However, even when relaminarization is achieved, the turbulence consistently reappears. For 3D flows, Hof *et al.* (2006) and Avila & Hof (2013) have shown that turbulence remains intermittent at any finite *Re*, even in domains hundreds to thousands of times the duct (or pipe) height. However, the characteristic turbulent length scale varies superexponentially with *Re*, so extreme relaminarization events, or laminar islands (Avila & Hof 2013), become exceedingly rare even at relatively moderate *Re*. Although domain length effects cannot be ruled out, the ability to observe extreme relaminarization events at large *Re* (also see Appendix F) may plausibly be explained by the stabilizing effects of the friction term.

While either on the edge state and before a turbulent transition, for case 1, or after

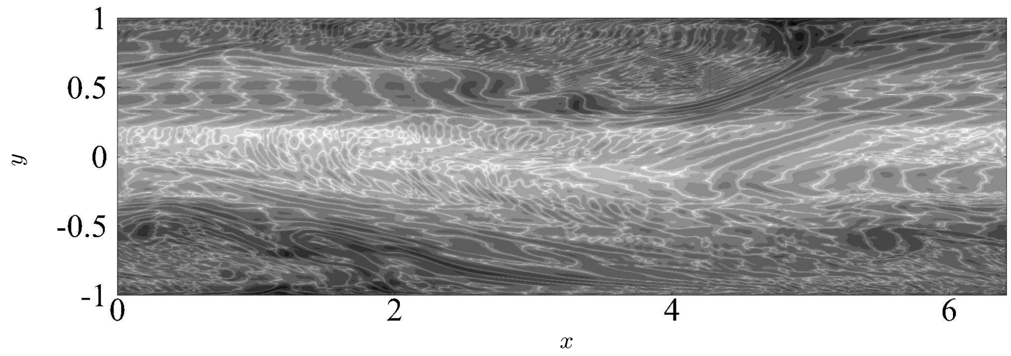

FIGURE 7.4: Streamwise high-pass filtered snapshot of $10^{-4} < |\hat{\omega}_{z,|\kappa|\geq 10}| < 10$ shortly after the transition to turbulence, at $t = 1.1 \times 10^4$, $r_c = 0.9$, case 1.

the turbulent state relaminarizes, for case 0 in particular, the energy contained in each Fourier mode scales exponentially with wave number. This is highlighted in Fig. 7.3(b), where for $1.92 \times 10^3 < t < 7.48 \times 10^3$, the energy contained in each mode varies as $\exp(-3\kappa/2)$ for the case 1 edge state. The κ coefficient (with magnitude less than 3/2 for $t < 6.48 \times 10^3$) is time dependent as the flow relaminarizes for case 0, Fig. 7.3(a), but the energy variation is still approximately exponential. Note that exponential trends implicitly define a key length scale, while power law trends are scale-independent.

To conclude this section, and to give some idea of the appearance of Q2D turbulence, a snapshot of the turbulent state is provided in Fig. 7.4. This is only made possible by applying a high-pass filter, to exclude the most energetic (low wave number) streamwise Fourier modes.

7.5 Edge state

7.5.1 Formulation

Henceforth, only case 1 is investigated, as it yielded the lowest E_D, and transitions from the edge state developed into sustained turbulence. In this section the edge state, a travelling wave, is scrutinized. Analysis of the initial conditions that generate the edge state can be found in §§ 7.6 and 7.7. To verify the importance of the leading modal instability in generating the edge state, DNS results along the edge are decomposed into Fourier modes, by isolating each wave number. The $\kappa = 1$ mode extracted from DNS is directly compared to the linearly computed modal instability. Further comparisons are made by assuming that if the edge state is evolved for large times, but still well before transition, the leading eigenmode has sufficient time to self-interact (supported by the energy being predominantly contained in the leading few modes). The weakly nonlinear interaction of the leading eigenmode with itself is compared to the $\kappa = 2$ mode extracted from DNS, and the weakly nonlinear interaction of the leading eigenmode with its complex conjugate to the $\kappa = 0$ mode extracted from DNS. Recall from Fig. 7.3(b) that the energy of the edge state is about four orders of magnitude below the magnitudes at which turbulence is observed, supporting the validity of weakly nonlinear analysis.

To perform weakly nonlinear analysis, the amplitude dependence of the plane-wave mode $\hat{v}_{\perp,n}(y) = \hat{v}_{\perp}(y)e^{\mathrm{i}\alpha n x}$ is expanded as

$$\hat{v}_{\perp,n} = \sum_{m=0}^{\infty} \epsilon^{|n|+2m} \tilde{A}^{|n|} |\tilde{A}|^{2m} \hat{v}_{\perp,n,|n|+2m}, \tag{7.6}$$

where $\hat{v}_{\perp,n,|n|+2m}$ denotes a perturbation (n is the harmonic, $|n|+2m$ the amplitude), in line with Hagan & Priede (2013b), and $\tilde{A} = A/\epsilon$ is the normalized amplitude. Nonlinear interaction between the linear mode $\hat{v}_{\perp,1,1}$ and itself excites a second harmonic $\hat{v}_{\perp,2,2}$. Nonlinear interaction between the linear mode $\hat{v}_{\perp,1,1}$ and its complex conjugate $\hat{v}_{\perp,-1,1}$ generates a modification to the base flow $\hat{u}_{\perp,0,2}$ (Hagan & Priede 2013b). The equations necessary to compute $\hat{u}_{\perp,0,2}$, $\hat{v}_{\perp,1,1}$ and $\hat{v}_{\perp,2,2}$, are detailed in Chapter 6 (Camobreco *et al.* 2021b), which also provides the details to compute higher harmonics.

The linear ($\hat{v}_{\perp,1,1}$) and weakly nonlinear ($\hat{u}_{\perp,0,2}$, $\hat{v}_{\perp,2,2}$) results are compared to Fourier components from DNS of the edge state. Fourier components were obtained by projecting the $N_{\mathrm{p}} = 19$ DNS results to $N_{\mathrm{p}} = 50$, and computing the Fourier coefficients, $c_\kappa = |(1/N_{\mathrm{f}}) \sum_{n=0}^{n=N_{\mathrm{f}}-1} \hat{f}(x_n) e^{-2\pi \mathrm{i}\kappa n/N_{\mathrm{f}}}|$, along 4000 y-slices, each with $N_{\mathrm{f}} = 1000$, where $\hat{f}$ is the variable of interest, e.g. $\hat{v}_{\perp}$. All except the j'th (and $N_{\mathrm{f}} - j$'th) Fourier coefficients were set to zero $c_{\kappa,\neg j} = 0$, and the inverse discrete Fourier transform $\hat{f}_{|\kappa|=j} = \sum_{\kappa=0}^{\kappa=N_{\mathrm{f}}-1} c_{\kappa,j} e^{2\pi \mathrm{i}\kappa n/N_{\mathrm{f}}}$ computed, isolating the j'th mode in the physical domain.

7.5.2 Results

The edge state generated by a nonlinearly evolved linear transient growth optimal with $E_0 = 3.5077 \times 10^{-6} > E_{\mathrm{D}}$ is analysed for case 1 here. First, snapshots from the fully nonlinear DNS are provided in Fig. 7.5 at $t = 7.38 \times 10^3$. The edge state is a travelling wave taking the form of a nonlinearly modulated Tollmien–Schlichting (TS) wave. A slight negative slant appears in the negative velocity half-wave, and a slight positive

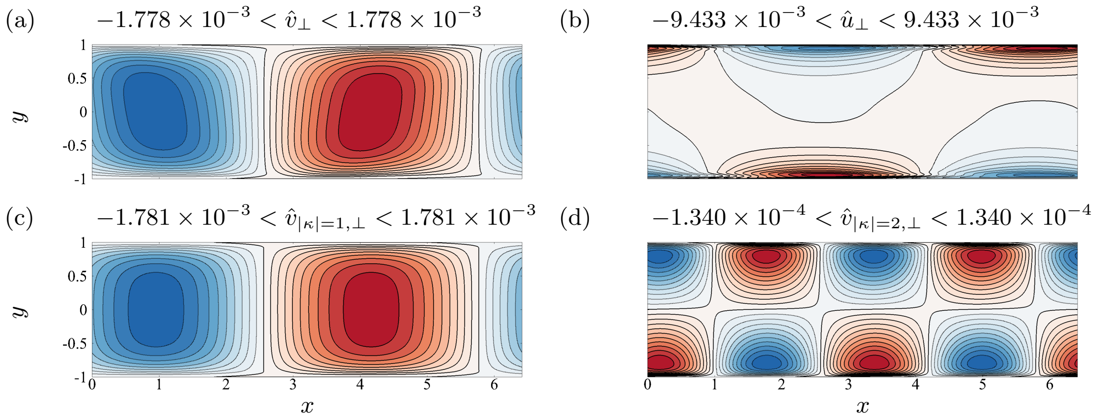

FIGURE 7.5: Snapshots of the DNS velocity field, a travelling wave, representing the edge state (at $t = 7.48 \times 10^3$). (a-b) All Fourier modes. (c) Only the $\kappa = 1$ mode, the TS wave modal instability. (d) Only the $\kappa = 2$ mode, which leads to the slanting of the TS wave observed in (a). Solid lines (red flooding) denote positive velocities, dotted lines (blue flooding) negative.

slant to the positive velocity half-wave in Fig. 7.5(a). Otherwise the resemblance to the TS wave is remarkable. To highlight the similarity, Fig. 7.5(c) depicts the $\kappa = 1$ Fourier component of the DNS, which is observed to be an unmodulated TS wave. The $\kappa = 2$ mode, Fig. 7.5(d), is predominantly responsible for the modulation of the full TS wave, as the positive and negative velocity regions reinforce the $\kappa = 1$ mode in the appropriate locations for the negative-positive slant indicated. Note that at $t = 7.38 \times 10^3$, the cumulated energy up to modes of $\kappa = 0$, 1 and 2 contribute 43.0%, 56.3% and 93.7% of the total energy of the full DNS result, respectively; and $> 99.9\%$ once six modes are included (or thirteen if counting conjugates separately). Note that the $\kappa = 1$ mode contributes relatively little to the energy sum (13.3%) as its streamwise velocity contribution is small. This is not shown, although the magnitude of $\hat{u}_{\perp}$ can be inferred from wall-normal gradients in $\hat{v}_{\perp}$. The $\kappa = 0$ and $\kappa = 2$ modes have much larger streamwise velocity contributions, particularly for $\kappa = 0$, and thus contain much greater energy overall. The percentage contributions vary little at all times for which the edge state is maintained, and thus, only the first three modes are considered. The energy in the leading three modes ($\kappa = 0$ through 2) drops to around 60% of the total once turbulence is triggered.

To assess the role of the leading modal instability, and further scrutinize the edge state, $x = cons.$ slices of the $\kappa = 0$, 1 and 2 DNS Fourier components are compared to

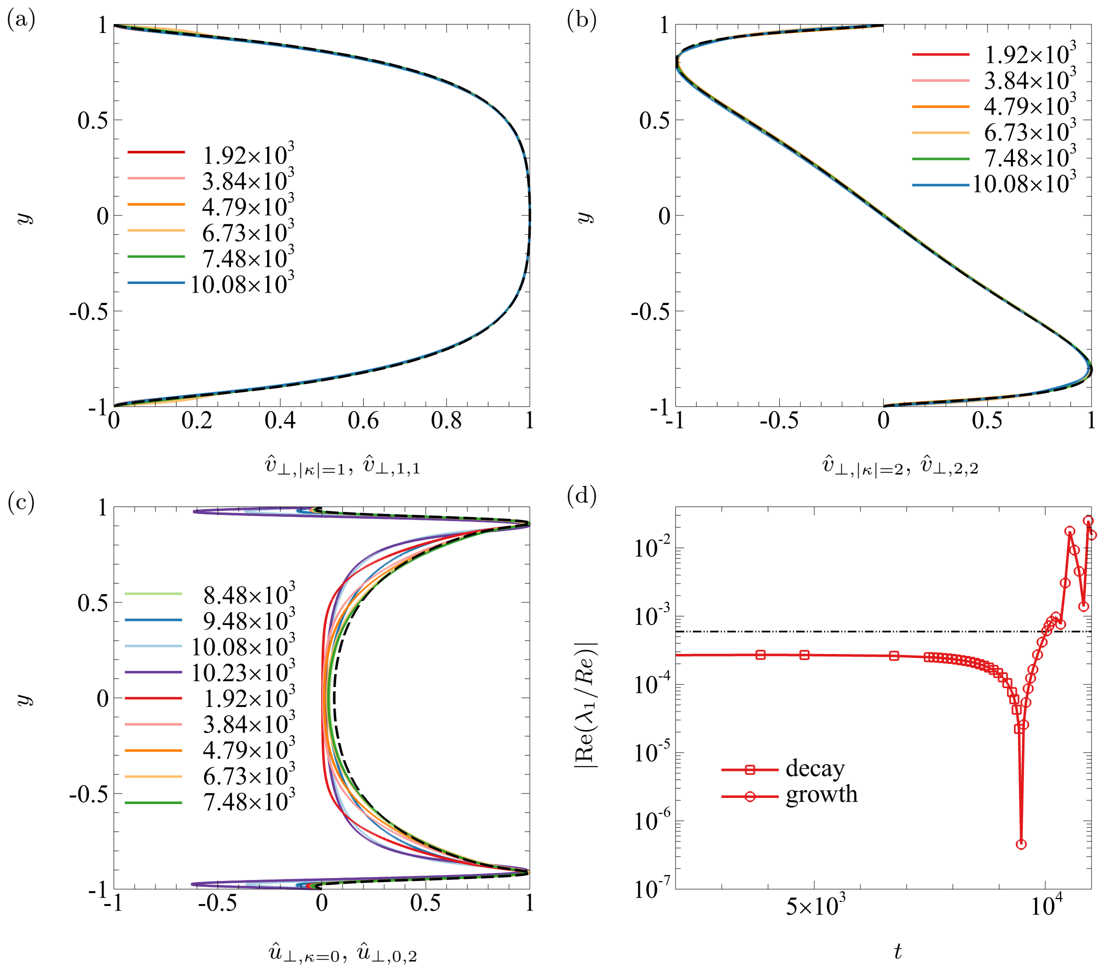

FIGURE 7.6: Linear ($\hat{v}_{\perp,1,1}$) and weakly nonlinear ($\hat{v}_{\perp,2,2}$ and $\hat{u}_{\perp,0,2}$) perturbations (dashed black lines) compared to the corresponding Fourier components from DNS at different times (solid colored lines; see legends). The trajectory remains in the neighborhood of the edge for $1.92 \times 10^3 \lesssim t \lesssim 7.48 \times 10^3$, while $t = 10.08 \times 10^3$ is just after departing the edge state. (a) $\kappa = 1$, wall-normal velocity. (b) $\kappa = 2$, wall-normal velocity. (c) $\kappa = 0$, streamwise velocity. (d) Absolute value of the growth rate of the leading modal instability on the modulated streamwise invariant base flow, once the edge state is attained (the dot-dashed line represents the corresponding absolute decay rate for the reference base flow).

the linear and weakly nonlinear results in Fig. 7.6(a-c). Note that all comparisons are normalized to unit maximum to avoid any phase differences (after isolating individual Fourier components, the DNS results are at $x = 0$). The absolute values of the complex perturbations $\hat{v}_{\perp,1,1}$ and $\hat{v}_{\perp,2,2}$ are also normalized to unity, with the sign adjusted where appropriate. Figure 7.6(a) further supports the agreement between the $\kappa = 1$ DNS component and the leading modal instability at all times on the edge state (as shown for extractions from $t = 1.92 \times 10^3$ to $t = 7.48 \times 10^3$). The importance of the modal instability is also highlighted in Fig. 7.6(b), as the $\kappa = 2$ DNS component again almost exactly matches the weakly nonlinear interaction of the linear eigenmode with itself, at all times on the edge state. The only slight differences between weakly nonlinear and full DNS results are observed in Fig. 7.6(c), which depicts the streamwise invariant base flow modulations on the edge state (compared to the interaction of the linear eigenmode and its complex conjugate). Although the differences are quite large at early times on the edge state ($t = 1.92 \times 10^3$), the longer the edge state is maintained, the closer the extractions come to the weakly nonlinear result, with little difference by $t = 7.48 \times 10^3$. Thereafter, the edge state is departed toward the turbulent attractor. If E_{D} were computed to higher accuracy (6+ significant figures), the edge state could be maintained for longer times, and the collapse of the full DNS result to the profile predicted by the weakly nonlinear analysis improved. Between $t = 7.48 \times 10^3$ and $t = 8.48 \times 10^3$, there is almost no visible change in the modulation (they appear coincident as plotted). Extractions at $t \geq 9.48 \times 10^3$ show the modulation clearly departing the weakly nonlinear result, particularly with large jets of negative velocity forming near the walls. However, the $\kappa = 1$ and $\kappa = 2$ profiles are slower to adjust, and are yet to show meaningful changes by $t = 10.08 \times 10^3$. Overall, as the first three modes contain 93.8% of the total energy, the modal instability, and its weakly nonlinear interactions, provide a comprehensive picture of the edge state and its behavior. Although the edge bears some clear resemblances to the modal TS wave, there is still a significant adjustment that either linear or nonlinear mechanisms must provide for an initial condition to be able to evolve to the edge state (if it would otherwise evolve into a modal TS wave).

As the streamwise base flow modulation is most sensitive to the initial departure from the edge state (toward the turbulent attractor), its linear stability is further investigated, as shown in Fig. 7.6(d). The reference base flow is modulated by the $\kappa = 0$ Fourier component from the full DNS, as $U_{\perp,\mathrm{mod}} = U_{\perp} + \hat{u}_{\perp,\kappa=0}$, and the linear eigenvalue problem, solved in exactly the same manner as when the base flow was unmodulated (replacing $U_{\perp}$ by $U_{\perp,\mathrm{mod}}$). Note that the linear growth predictions treat $\hat{u}_{\perp,\kappa=0}$ as time steady for each extraction. Although this is not the case, variations are minor while on the edge state, and particularly around $t = 7.48 \times 10^3$. The absolute value of the growth rates are plotted in Fig. 7.6(d), with the growth rate rescaled as $\mathrm{Re}(\lambda_1/Re)$ to the more conventional form (Schmid & Henningson 2001).

While on the edge state, the decay rate of the leading eigenmode is roughly constant, around $\mathrm{Re}(\lambda_1/Re) = -2.5 \times 10^{-4}$, compared to $\mathrm{Re}(\lambda_1/Re) = -5.94084 \times 10^{-4}$ for the unmodulated base flow. The magnitude of the decay rate rapidly decreases for $7.48 \times 10^3 \lesssim t \lesssim 9.43 \times 10^3$, before growth of the leading instability is first attained at $t = 9.48 \times 10^3$. Up until $t = 1.023 \times 10^4$ the growth rate of the leading instability monotonically increases, before a turbulent state is achieved.

7.6 Reynolds number and target time variation

7.6.1 Formulation

The methodologies used in this section are identical to those introduced in § 7.4.1. All setups are case 1, with results at subcritical Reynolds number ratios $r_\mathrm{c} = 0.3$, 0.4 and 0.6 compared to those at $r_\mathrm{c} = 0.9$. Additional supporting computations at $r_\mathrm{c} = 0.7$ and 0.8 are included in Appendix G. The nonlinear behavior of the linear optimals maximizing growth at larger target times is also investigated. Ratios of the target time to the optimal target time $T = \tau/\tau_\mathrm{opt}$ up to 8 are simulated, where τ_opt corresponds to the time for optimal growth constrained by $\alpha = \alpha_\mathrm{max}$ (α_max varying with r_c).

The initial condition most efficiently energizing the leading eigenmode of the forward linear evolution operator is also of interest. The leading adjoint mode is the initial condition with the largest projection onto the (slowest decaying) leading forward mode as $T \to \infty$, as discussed in Chapter 3, § 3.3. Although the leading forward mode decays equally as slowly as the leading adjoint mode as $t \to \infty$, the leading adjoint mode also generates some linear transient growth (which the leading forward mode is incapable of), thus yielding the largest energization in the limit of large times.

The leading adjoint mode, in the energy norm, can be computed directly from (a large, but truncated set of) the eigenvectors of the forward linear evolution operator, as shown in Farrell (1988). However, it is more accurate to determine the leading adjoint mode $\tilde{\xi}_{\perp,1}$ directly from Eq. (7.5), which was derived in the energy norm, either directly by timestepping, or by calling $\texttt{eigs}(-\mathrm{i}\boldsymbol{L}^\ddagger)$ in MATLAB, where $\boldsymbol{L}^\ddagger$ is the linear adjoint evolution operator. This assumes $\exp(+\mathrm{i}\lambda_j^\ddagger t)$ time dependence, with the adjoint eigenvalues $\lambda_j^\ddagger$ to be sorted in ascending order. As the leading adjoint mode most efficiently energizes the leading forward mode (as $t \to \infty$), it is a prime candidate for efficiently generating turbulence through weakly nonlinear routes.

For clarity, the initial condition nonlinearly evolved from in DNS is always the

	$r_c = 0.3$		$r_c = 0.4$		$r_c = 0.6$		$r_c = 0.9$	
T	E_G/G	$10^3 E_D$	E_G/G	$10^4 E_D$	E_G/G	$10^5 E_D$	E_G/G	$10^6 E_D$
1	1	2.630	1	3.142	1	4.328	1	3.058
2	0.3700	1.535	0.3653	2.970	0.3940	3.382	0.4127	1.954
3	0.5463	0.7984	0.5532	1.792	0.5518	2.351	0.5461	1.495
4	0.5799	0.7453	0.5726	1.727	0.5618	2.304	0.5520	1.475
6	0.5857	0.7379	0.5759	1.718	0.5635	2.298	0.5530	1.473
8	–	–	0.5761	1.717	0.5636	2.297	0.5530	1.473

TABLE 7.3: Convergence to a minimum overall E_D with increasing T for each r_c. This is in spite of the reduced linear transient growth, where $E_G = \max[E(t \le T\tau_{opt})]/E(t = 0)$ represents the maximum growth at any $t \le T\tau_{opt}$, relative to $G(1\tau_{opt})$. Note that $r_c = 0.3$ has $G(8\tau_{opt}) < 1$, and so does not provide an equivalent converging optimal in the primitive variable solver. E_D is computed to 4 significant figures.

nonmodal perturbation optimising linear transient growth at the target time τ, and is never the initial condition $\tilde{\xi}_{\perp,1}$ optimally energizing the leading eigenmode; the use of $\tilde{\xi}_{\perp,1}$ directly is left for future work.

7.6.2 Results

The growth ratios and delineation energies for r_c from 0.3 to 0.9 and $T = \tau/\tau_{opt}$ from 1 to 8 are provided in Table 7.3. The delineation energy increases by about an order of magnitude for each of the r_c reductions shown in Table 7.3, which is problematic for efficiently triggering turbulence subcritically. However, for each r_c, E_D appears to be converging with increasing T. Thus, increasing T yields a more efficient initial condition to trigger a turbulent transition, with the initial field possibly converging on some global optimum. The global optimum appears to be the leading adjoint mode, which optimally energizes the leading forward mode, and which most efficiently triggers turbulence in this Q2D setup. Additional computations, as a precursor to future work, indicate that use of the leading adjoint mode $\tilde{\xi}_{\perp,1}$ directly yields E_D identical to four significant figures to the $T = 8$ nonmodal perturbations for $0.4 \le r_c \le 0.9$.

The linear optimals for various T at $r_c = 0.9$ are depicted in Fig. 7.7. From Fig. 7.7(a) it is clearly visible that by selecting a larger T, the perturbation at the time τ comes closer to matching the profile of the leading eigenmode, with the two profiles coincident by eye for $T \ge 4$. Thus, increasing T has allowed for a more effective energization of the leading mode $\hat{v}_{\perp,1,1}$, which can go on, through weakly nonlinear interaction, to generate $\hat{u}_{\perp,0,2}$ and $\hat{v}_{\perp,2,2}$, and thereby maintain a edge state, consistent with the findings of § 7.5. The initial condition most efficiently energizing the leading

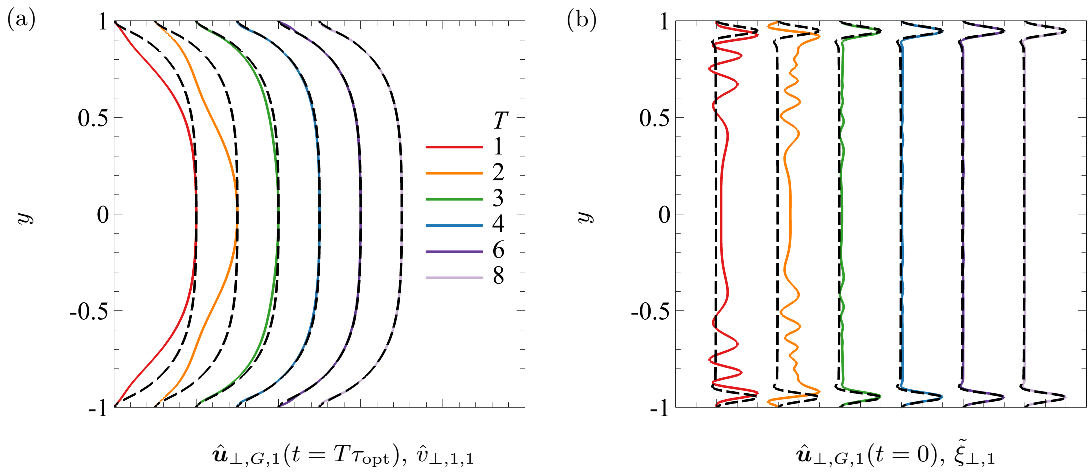

FIGURE 7.7: (a) Comparison between the linear transient optimal evolved to $t = T\tau_{\mathrm{opt}}$ and the leading direct eigenmode (dashed black lines), for various T, on a shared abscissa. (b) Comparison between the linear transient optimal at $t = 0$ and the leading adjoint eigenmode (dashed black lines).

eigenmode is also compared to the initial conditions attained for various T. There are marked differences at small times, with the additional undulations in the initial conditions providing the larger transient growth attained at smaller T (recalling $T = 1$ yields optimal growth). However, the agreement is excellent by $T = 8$. Thus, a larger T leads to improved energization of the leading mode, thereby reducing E_{D}. More importantly, this implies that seeking the initial condition that yields the largest transient growth is not likely to be the most efficient at reaching the edge state, and thereby not the most efficient at triggering a transition. Instead, the initial condition most efficiently energizing the leading eigenmode is of greatest interest.

The energy-time histories for $r_{\mathrm{c}} = 0.9$ through $r_{\mathrm{c}} = 0.3$ are displayed in Fig. 7.8, for all T tested. It is immediately apparent, for a given r_{c}, that regardless of T, the edge state attained is the same, although cases with larger T reach the edge state from a smaller E_0. This allows for identification of the edge state energy E_{E} for each r_{c} (although only very roughly for $r_{\mathrm{c}} = 0.3$), see Table 7.4. The edge state energy also allows for an alternate means of determining the efficiency of an initial condition. The $T = 1$ case generates a great deal of inconsequential linear transient growth, before falling back to the edge state. The overshoot for $T = 2$ through 8 are much smaller, although still hint at some inconsequential growth.

Departures from the edge state, for cases with $E_0 > E_{\mathrm{D}}$, differ vastly with r_{c}.

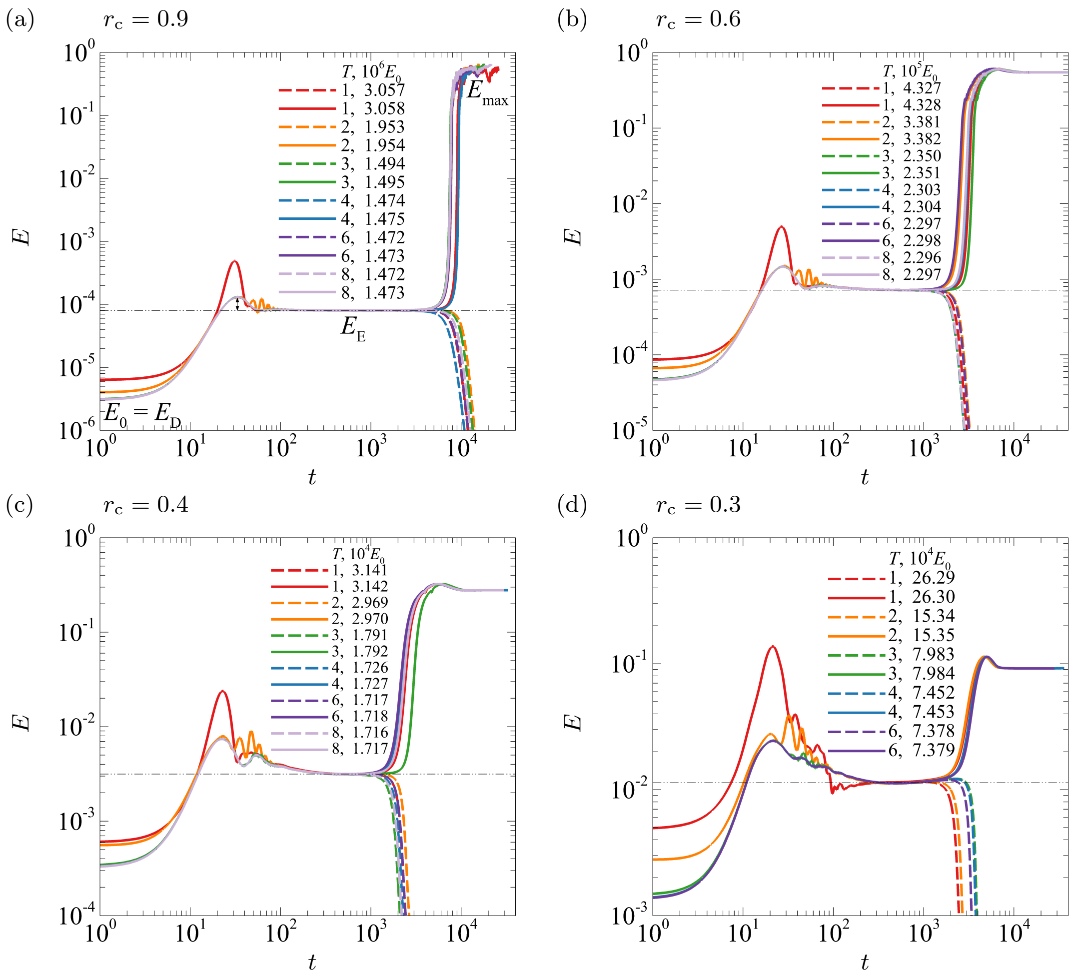

FIGURE 7.8: DNS of linear transient optimals with T of 1 through 8 for r_c of 0.9 through 0.3. E_0 are selected to be just above and just below E_D (E_D varying with T). Regardless of T, the edge state energy E_E (dot-dashed line) is the same for each r_c. However, larger T have smaller E_0, and overshoot E_E less.

r_c	0.3	0.4	0.6	0.9
E_D	7.379×10^{-4}	1.717×10^{-4}	2.297×10^{-5}	1.473×10^{-6}
E_E	1.25×10^{-2}	3.15×10^{-3}	7.18×10^{-4}	8.03×10^{-5}
E_E/E_D	16.9	18.3	31.3	54.5
E_{max}	1.136×10^{-1}	3.243×10^{-1}	6.060×10^{-1}	6.582×10^{-1}
E_{max}/E_E	9.09	1.03×10^2	8.44×10^2	8.20×10^3

TABLE 7.4: For various r_c (largest T cases), the energy of the edge state, E_E, the amplitude yielding a balance in decay of the linear and growth of the weakly nonlinear mode(s), is compared to the delineation energy E_D, and maximum energy over all t, E_{max}. Note that E_E roughly varies as $r_c^{-4.5}$ and E_D as $r_c^{-5.6}$

Nonlinear growth from the edge state, quantified by the ratio of E_{max} to E_{E}, are also included in Table 7.4, as are the ultimate values of E_{max}. The additional propensity for growth at $r_{\mathrm{c}} = 0.6$ and $r_{\mathrm{c}} = 0.9$, as well as the larger E_{max}, allow both these r_{c} to transition to turbulence. While intermittent turbulence is sustained at $r_{\mathrm{c}} = 0.9$, the flow quickly relaminarizes at $r_{\mathrm{c}} = 0.6$. Additional simulations performed at $r_{\mathrm{c}} = 0.7$ and $r_{\mathrm{c}} = 0.8$ are also included in Appendix G (just $T = 1$ and $T = 8$), to obtain an improved estimate of the threshold r_{c} required to indefinitely sustain Q2D turbulence at $H = 10$ (in the thermodynamic limit of large times). However, to improve the estimate of this threshold r_{c} requires increasingly long time evolutions, with an estimate of $r_{\mathrm{c}} \gtrsim 0.8$ as the requirement for sustained turbulence the best that was attained. At $r_{\mathrm{c}} = 0.4$, the secondary nonlinear growth still well exceeds the linear growth, although turbulence is not triggered. For simplicity, an E_{D} is still 'defined' for this r_{c} (and $r_{\mathrm{c}} = 0.3$), as a clear edge state behavior, reminiscent of the pull of a turbulent attractor, is observed. Interestingly, the nonlinear growth allows flows at $r_{\mathrm{c}} \leq 0.4$ to develop into a stable finite amplitude state, in case 1 setups, but not case 0. Even at $r_{\mathrm{c}} = 0.9$, recalling Figs. 7.3(a & c), cases 0 and 2 decay to a slowly diffusing, streamwise-invariant modulation, with modes $\kappa \geq 1$ devoid of energy.

The neutral stability of the finite amplitude state at $r_{\mathrm{c}} = 0.3$, post nonlinear growth, and at $r_{\mathrm{c}} = 0.6$, post relaminarization, is further assessed via the Fourier spectra depicted in Fig. 7.9. $r_{\mathrm{c}} = 0.3$ displays an exponential variation with κ for all t, Fig. 7.9(a). In particular, the finite amplitude state settles to an $\exp(-0.156\kappa)$ dependence. Unlike the exponential wave number dependence observed on the edge state, recalling Fig. 7.3(b), here a large number of modes exhibit non-zero energy once the stable finite amplitude state forms. However, the first three modes still cumulatively contain a very similar fraction (94.3%) of the total energy. At $r_{\mathrm{c}} = 0.4$, the story is similar, although the trend is $\exp(-0.098\kappa)$. At $r_{\mathrm{c}} = 0.6$, the flow is briefly turbulent, before relaminarizing, and settling to an $\exp(-0.055\kappa)$ dependence (the first three modes cumulatively containing 93.2% of the total energy). Otherwise, none of the $r_{\mathrm{c}} \leq 0.6$ tested show signs of decaying back to the original laminar fixed point, or to the edge state. Example flow fields of the stable finite amplitude states are provided in Fig. 7.10, for each r_{c}. There are clear similarities between the flow structures at all three r_{c} (0.3, 0.4 and 0.6), regardless of whether the finite amplitude state forms after a brief turbulent episode, or whether the flow remains laminar through the entire nonlinear

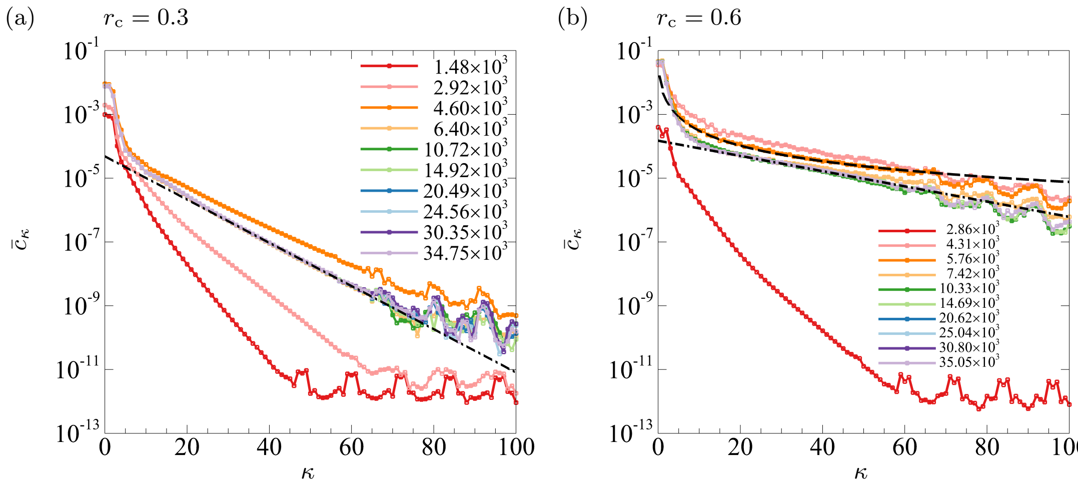

FIGURE 7.9: Fourier spectra at select instants in time (see legends). At large times, the Fourier spectra settle as a stable finite amplitude state forms. (a) $r_c = 0.3$. The dash-dotted black line denotes an $\exp(-0.156\kappa)$ trend. (b) $r_c = 0.6$. The dashed black line denotes a $\kappa^{-5/3}$ trend, and dash-dotted black line an $\exp(-0.055\kappa)$ trend.

growth stage. In addition, the finite amplitude states have similar appearance to their 2D hydrodynamic equivalent (Jiménez 1990). Last, note that frozen linear stability analysis of the modulated streamwise invariant base flows for these finite amplitude states (at all three r_c) yielded decaying leading eigenmodes. Thus, it is again likely that higher wave numbers $\kappa \geq 2$ are transferring energy to the leading eigenmode, which remains as the basis of the finite amplitude state, offsetting its decay.

7.7 Nonlinear transient growth

7.7.1 Formulation

In an isolated Q2D boundary layer, the linear and nonlinear transient growth was remarkably similar for the initial energies of interest, $E_0 \lesssim E_D$, as shown in Chapter 5 (Camobreco *et al.* 2020), hence the use of only linear optimals thus far. However, it is still worth ensuring that the same holds for the present setup, and worth considering some target time variation. As Q2D nonlinear transient growth pales in comparison to 3D nonlinear transient growth (Pringle & Kerswell 2010; Cherubini *et al.* 2011), the time to reach the turbulent attractor can be very large. Thus, nonlinear transient growth is not directly used to identify E_D. For example, consider a 3D hydrodynamic pipe flow, with large nonlinear transient growth, and a turbulent transition by $t/\tau_{opt} \gtrsim 2.5$

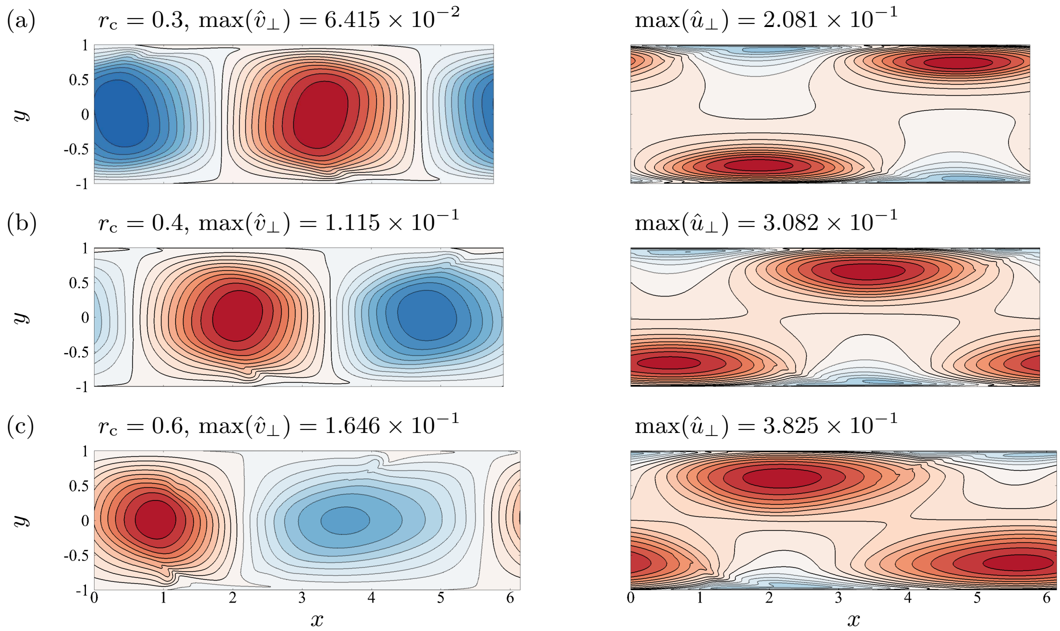

FIGURE 7.10: Snapshots of the DNS velocity fields representing the stable finite amplitude state. (a) $r_c = 0.3$ at $t = 1.492 \times 10^4$. (b) $r_c = 0.4$ at $t = 1.099 \times 10^4$. (c) $r_c = 0.6$ at $t = 1.762 \times 10^4$ (post relaminarization). Solid lines (red flooding) denote positive velocities, dotted lines (blue flooding) negative.

(Pringle *et al.* 2012). The Q2D results for an isolated boundary layer were already restrictively expensive with transitions occurring between $t/\tau_{\mathrm{opt}} = 18.44$ to 26.34 (at $r_c = 0.585$), as discussed in Chapter 5 (Camobreco *et al.* 2020). At the most commonly investigated $r_c = 0.9$, case 1 setup in this work, the turbulent attractor is reached at the prohibitively expensive $t/\tau_{\mathrm{opt}} = 248$ to 297 (depending on the T chosen for linear optimization of the initial condition). However, the edge state is reached much earlier than this, and instead forms a viable target for nonlinear verification.

The nonlinear growth $G_{\mathrm{N}} = \|\hat{\boldsymbol{u}}_\perp(\tau)\| \,/\, \|\hat{\boldsymbol{u}}_\perp(0)\|$, for a specified target time τ, optimized over all initial perturbations, is determined by maximizing the functional (Pringle *et al.* 2012, 2015)

$$\begin{aligned}\mathscr{L}(\hat{\boldsymbol{u}}_\perp(t=0)) = \left\langle \frac{1}{2}\hat{\boldsymbol{u}}_\perp(\tau)^2 \right\rangle - \lambda_0 \left[\left\langle \frac{1}{2}\hat{\boldsymbol{u}}_\perp(0)^2 \right\rangle - E_{\mathrm{P}}\right] - \int_0^\tau \langle \Pi \boldsymbol{\nabla}_\perp \cdot \hat{\boldsymbol{u}}_\perp \rangle \mathrm{d}t \\ - \int_0^\tau \Gamma(t)\langle \hat{\boldsymbol{u}}_\perp \cdot \boldsymbol{e_z}\rangle \mathrm{d}t - \int_0^\tau \left\langle \hat{\boldsymbol{u}}_\perp^\ddagger \cdot \left[\frac{\partial \hat{\boldsymbol{u}}_\perp}{\partial t} + (\boldsymbol{U}_\perp \cdot \boldsymbol{\nabla}_\perp)\hat{\boldsymbol{u}}_\perp + (\hat{\boldsymbol{u}}_\perp \cdot \boldsymbol{\nabla}_\perp)\boldsymbol{U}_\perp \right.\right. \\ \left.\left. + (\hat{\boldsymbol{u}}_\perp \cdot \boldsymbol{\nabla}_\perp)\hat{\boldsymbol{u}}_\perp + \frac{1}{\rho}[\Lambda(t)\boldsymbol{e_z} + \boldsymbol{\nabla}_\perp p'_\perp] - \frac{1}{Re}\boldsymbol{\nabla}_\perp^2 \hat{\boldsymbol{u}}_\perp + \frac{H}{Re}\hat{\boldsymbol{u}}_\perp\right]\right\rangle \mathrm{d}t, \quad (7.7)\end{aligned}$$

where λ_0, Π and $\Gamma(t)$ are Lagrange multipliers for the conditions constraining initial perturbation energy $E_\mathrm{P} = (1/2)\int \hat{\boldsymbol{u}}_\perp(0)^2 \mathrm{d}\Omega$, mass conservation and the flow rate, respectively. Pressure is decomposed into a time-varying pressure gradient $\Lambda(t)$, to maintain a constant flow rate, and a fluctuating component $p'_\perp$. $\langle \dots \rangle$ represent integrals over the computational domain. Each iteration j begins with forward evolution of the nonlinear perturbation equation (within the large square brackets of the last term of Eq. (7.7)) from $t = 0$ to $t = \tau$. The adjoint 'initial' field is $\hat{\boldsymbol{u}}^\ddagger_\perp(\tau) = \hat{\boldsymbol{u}}_\perp(\tau)$, with backward evolution from time $t = \tau$ to $t = 0$ proceeding via

$$\frac{\partial \hat{\boldsymbol{u}}^\ddagger_\perp}{\partial t} = (\boldsymbol{\nabla}_\perp \boldsymbol{U}_\perp)^\mathrm{T} \cdot \hat{\boldsymbol{u}}^\ddagger_\perp - (\boldsymbol{U}_\perp \cdot \boldsymbol{\nabla}_\perp)\hat{\boldsymbol{u}}^\ddagger_\perp + (\boldsymbol{\nabla}_\perp \hat{\boldsymbol{u}}_\perp)^\mathrm{T} \cdot \hat{\boldsymbol{u}}^\ddagger_\perp + \Gamma(t)\boldsymbol{e}_\mathbf{z} - \boldsymbol{\nabla}_\perp \Pi - \frac{1}{Re}\boldsymbol{\nabla}^2_\perp \hat{\boldsymbol{u}}^\ddagger_\perp - \frac{H}{Re}\hat{\boldsymbol{u}}^\ddagger_\perp, \quad (7.8)$$

$$\boldsymbol{\nabla}_\perp \cdot \hat{\boldsymbol{u}}^\ddagger_\perp = 0. \quad (7.9)$$

The initial field for the $(j+1)$'th iteration is $\hat{\boldsymbol{u}}^{j+1}_\perp(0) = \hat{\boldsymbol{u}}^{j}_\perp(0) + \epsilon_\mathrm{N}(-\lambda_0 \hat{\boldsymbol{u}}^{j}_\perp(0) + \hat{\boldsymbol{u}}^{\ddagger,j}_\perp(0))/\lambda_0$, with λ_0 ensuring $\langle \hat{\boldsymbol{u}}^{j+1}_\perp(0) \cdot \hat{\boldsymbol{u}}^{j+1}_\perp(0)\rangle = 2E_\mathrm{P}$ and under-relaxation factor ϵ_N. Iterations continue until the relative changes in λ_0 and residual $(\delta\mathscr{L}/\delta\hat{\boldsymbol{u}}_\perp(0))/\lambda_0^2$ drop below a specified tolerance, following Pringle *et al.* (2012). For further details of the iterative procedure, see Chapter 5 (Camobreco *et al.* 2020).

7.7.2 Results

The similarity between the linear and nonlinear optimals is highlighted in Table 7.5, for T of 1 through 8. The percentage difference in the ratio of the nonlinear energy growth at the target time, between linear and nonlinear initial conditions, is $< 7\%$ for all T investigated at $r_\mathrm{c} = 0.9$. Furthermore, the rate of increase of the percentage error reduces with T. The linear growth of the linear optimal is also included for each T, to give an idea of how small the magnitude of the growth differences would be (e.g. 6.5% of $G \approx 22$ relative to the almost 4 orders of magnitude of nonlinear growth during the final stage of the transition process).

The capability for the nonlinear scheme to directly simulate the edge state is now assessed. The nonlinear optimals, and corresponding initial conditions, are depicted in Fig. 7.11. For $T = 1$ or $T = 2$ both the initial conditions remain quite complicated and the optimal field does not resemble the edge state (of a slanted TS wave). With $T = 3$ the initial condition is predominantly a single layer of a highly sheared wave near the wall (compared to the three or so layers at each wall with $T = 1$), with the perturbation at the target time having the underlying form of the edge state. With increasing T from

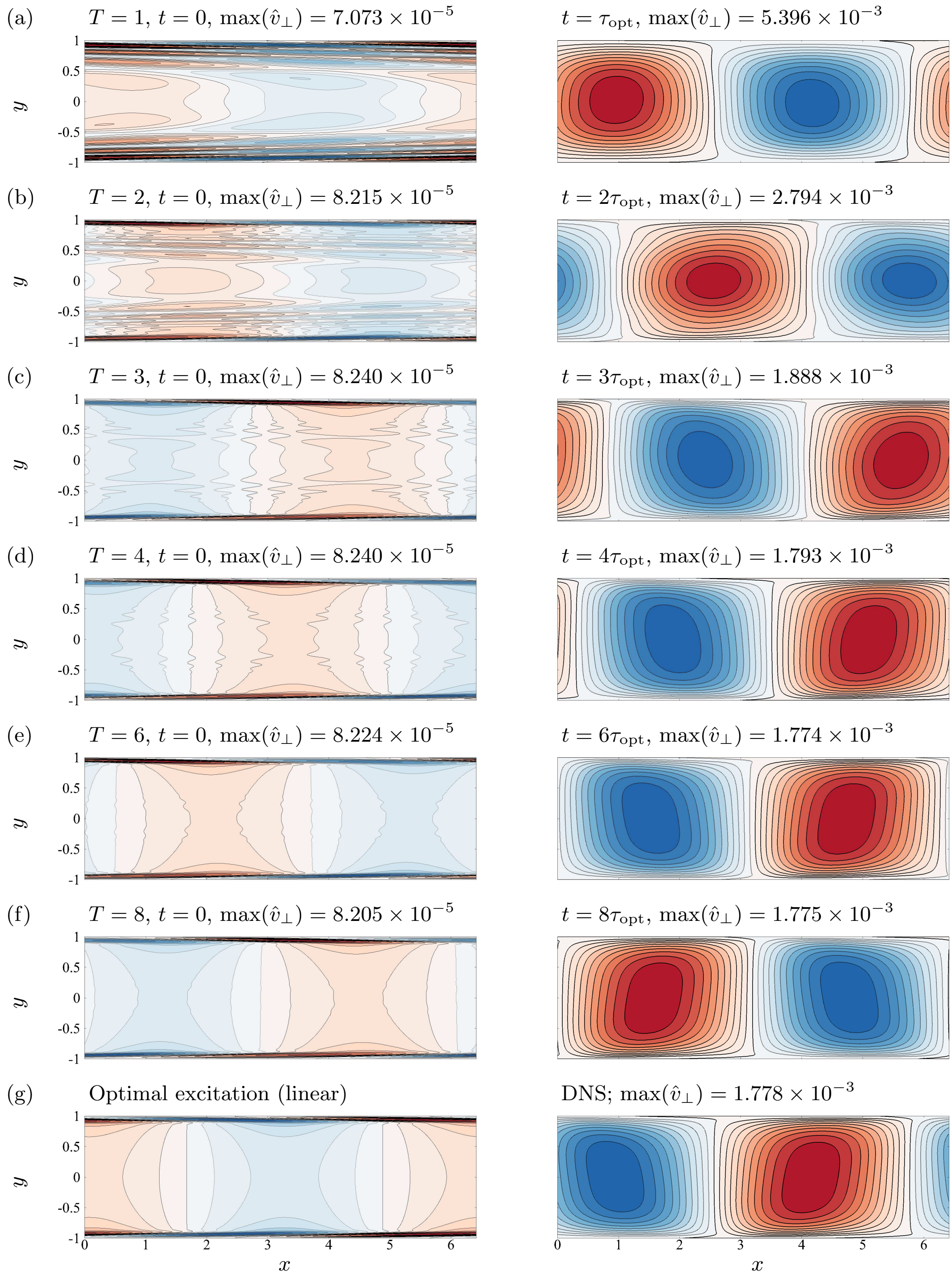

FIGURE 7.11: (a-f) Nonlinear transient growth optimals at $r_c = 0.9$ for various T, at $t = 0$ (left column) and at $t = T\tau_{\rm opt}$ (right column). (g) The optimal excitation of the leading eigenmode (left column) and DNS of the edge state at $t = 7.48 \times 10^3$ (right column). Solid lines (red flooding) denote positive velocities, dotted lines (blue flooding) negative.

Optimal: Evolution:	Linear Linear	Linear Nonlinear	Nonlinear Nonlinear	Comparison Nonlinear
T	G	$(E(t = T\tau_{\text{opt}})/E_{\text{D}})/G$	G_{N}/G	$\lvert\%$ Error$\rvert$
1	78.14835970	0.99699972	0.99881097	0.18
2	30.94185832	0.99127623	1.01459824	2.30
3	26.85825421	1.01943101	1.05902352	3.73
4	25.62489920	1.05079656	1.10210351	4.66
6	23.76862631	1.12126805	1.18981807	5.76
8	22.07877539	1.20110373	1.28485597	6.52

TABLE 7.5: Similarity between the nonlinear growth of linear and nonlinear optimals at $r_{\text{c}} = 0.9$. Nonlinear computations have $E_0 > E_{\text{D}}$. Linear growth results provide a baseline.

4 through 8, the initial condition simplifies through the duct centre, until there only remains a highly sheared wave at each wall (constructive interference between the waves at each wall occurs across the entire duct, yielding perturbation energy growth). At these larger T, the final perturbation clearly resembles the edge state captured by the DNS, with similar maximum velocity magnitude as the DNS result. The convergence of the nonlinearly optimized initial conditions toward the optimal energization the leading eigenmode, from § 7.6, is also clear.

7.8 Conclusions

A quasi-two-dimensional streamwise periodic duct flow was numerically simulated. Importantly, the first subcritical route to sustained, if intermittent, Q2D turbulence was discovered. Thereafter, the aims were three-fold. First, identify the most efficient quasi-two-dimensional routes to turbulence by locating the lower edge state. Second, analyse the lower edge state, and understand the underlying dynamics of the transition process. Third, determine the conditions able to sustain turbulence.

The most efficient route to turbulence was based around the optimal energization of the leading eigenmode, arising from global linear stability analysis. This was shown at a weakly subcritical Reynolds number ratio of $r_{\text{c}} = 0.9$ in two ways. First, by adjusting the wave number of the domain, from α_{opt} (maximizing linear transient growth) to α_{max} (minimizing the decay rate of the leading modal instability); the latter time optimized nonmodal perturbation was found to trigger turbulence with an initial energy ≈ 20 times smaller than the former. This was despite the latter case also generating less linear transient growth. In addition, the latter case generated turbulence which was sustained, if intermittent, while all tested routes to turbulence that did not aim to energize the leading eigenmode quickly decayed back to the laminar fixed point. Second, once having selected α_{max}, the target time τ for optimization of the nonmodal perturbation was increased. The larger the target time, the smaller the linear transient growth obtained, but also the smaller the initial energy required to reach turbulence. As linear transient growth is an initial value problem, it can only generate large growth at small τ. Once τ becomes large, the avenue to maximize growth at τ devolves to a redistribution of energy into the slowest decaying (leading) eigenmode. Thus, the larger τ is, the more energy ends up in the leading eigenmode. As discussed in Farrell (1988), because of the initial transient growth, for a given target time τ it is always more efficient to distribute energy across multiple eigenmodes of the linear operator at $t = 0$, undergo some nonmodal growth for small $t \lesssim \tau_{\text{opt}}$, and then have nonmodal processes redistribute all energy back into the leading eigenmode at large t, than it is solely to put all the initial energy in the leading eigenmode, and have it decay for all t. This work shows that target times of $6\tau_{\text{opt}}$ to $8\tau_{\text{opt}}$ are sufficient for the nonmodal perturbation to be an excellent proxy for the true optimal energization of the leading eigenmode ($\tau \to \infty$, i.e. the leading adjoint mode), and that these initial conditions require the smallest initial energies to reach turbulence. These nonmodal perturbations also all manage to sustain turbulence, although the turbulence was intermittent. Furthermore, performing nonlinear transient growth with increasingly large target times also showed convergence toward the optimal energization. Ultimately, in Q2D systems, maximizing linear transient growth was never the most efficient route to triggering turbulence; optimal energization of the leading eigenmode was always best.

The underlying dynamics of the transition process were then analyzed. As discussed, after the initial linear transient growth, the leading eigenmode (the Q2D equivalent of the Tollmien–Schlichting wave) becomes energized, although is decaying. Fully nonlinear DNS shows that the total perturbation energy remains relatively constant between $t \approx 100$ and $t \approx 8000$ (at $r_{\text{c}} = 0.9$). Thus, it is conjectured that the initial condition has reached the neighborhood of an edge manifold, and that the trajectory travels along the edge until reaching the lower edge state. Furthermore, Fourier analysis indicated that three modes contained 93.7% of the total energy while on the edge, or 43.0%, 13.3% and 37.4% for the zeroth, first and second harmonics, respectively. As only three modes were predominantly involved, the behavior appeared to match that of a subcritical bifurcation, where if at the critical amplitude, the decay rate of the leading eigenmode would be exactly offset by the growth of its (the second) harmonic. Thus, the leading three Fourier components from DNS were compared to their weakly nonlinear equivalents. While on the edge, there was excellent agreement between the first and second Fourier components from DNS, and the linear eigenmode and its weakly nonlinear self-interaction, respectively. Some slight differences between the zeroth Fourier mode from the DNS, and the weakly nonlinear interaction of the leading eigenmode and its complex conjugate, were observed. However, the longer the trajectory remained on the edge, the smaller the difference became, and with a more accurate computation of the delineation energy E_{D}, the agreement would likely further improve. Note that due to difficulties arising from abstruse scalings and definitions, the amplitude of the edge state could not be directly compared to the critical amplitude obtained from solution of the Stuart–Landau equation (Drazin & Reid 2004).

As the lower edge state was shown to be well represented by the weakly nonlinear (Stuart–Landau) analysis, the route to turbulence from the edge state was considered. Once the perturbation has an amplitude slightly above the critical amplitude, nonlinear growth of the second harmonic will outweigh linear decay. Eventually, order unity amplitudes would be reached, necessitating the inclusion of higher harmonics in the analysis. However, this is a relatively slow route to turbulence. A superexponential route to turbulence, considering only three modes, is also possible, if both the leading eigenmode and its harmonic have positive growth rates; a supercritical bifurcation recalling Chapter 3, § 3.5. Although the former, slower route to turbulence is plausible, given the results presented, the latter route to turbulence was further investigated. This is primarily as frozen linear stability analysis of the (weakly nonlinearly) modulated base flow showed that the growth rate of the leading eigenmode became positive, while on and just departing the edge state. Thus, the route to turbulence may be through supercritical instability, even though the flow is subcritical relative to the reference base flow. However, the frozen stability assumption, and particularly the behavior of higher order terms, may be worth future consideration. Overall, the most efficient route from the initial condition to the lower edge state, through optimal energization of the leading eigenmode, is clear, while questions remain about the route from the edge to turbulence.

A supercritical instability, relative to a modulated base flow, has been elsewhere conjectured (Bottaro *et al.* 2003; Nouar & Bottaro 2010). These previous works focused on optimal base flow modulations, in the sense of obtaining the largest increase in the exponential growth rate of a target (assumed leading) eigenmode, for a given base flow modulation energy. As shown in Chapter 3, § 3.5, the optimal base flow modulation (minimal defect) has little resemblance to the weakly nonlinear modulation. Some theories regarding why the optimal modulation may not be relevant in this system are briefly discussed. First, the structure of a nonmodal instability able to generate the optimal modulation, once seeded on the reference base flow, remains unknown, and thus may rapidly decay if it shares little resemblance to the leading eigenmode. Second, any base flow modulation is subject to diffusion and friction. As the base flow diffuses toward the steady reference profile, the growth rate of any linear instabilities reduces (in computations frozen at each time). However, in the case of the weakly nonlinear self interaction, not only is the modulation sustained for around 8 000 time units at $r_{\mathrm{c}} = 0.9$, but the modulation continues to approach the weakly nonlinear result, not decay away from it. Thus, nonlinear transfers (production from higher harmonics to the base flow modulation) act to regenerate the profile against diffusion and friction. This occurs even when only the first and second harmonic are present. More importantly, the overall process appears quite efficient. As the leading eigenmode regenerates the base flow modulation, the base flow modulation improves the growth rate of the leading eigenmode, and the positive reinforcement process repeats, in something of a bootstrap route to turbulence. By comparison, any optimal modulation would improve the growth rate of the leading eigenmode (and admittedly would provide a greater improvement to the growth rate of the leading eigenmode for a given modulation energy norm), but would not necessarily be regenerated by that eigenmode, as the leading eigenmode regenerates the weakly nonlinear modulation. Thus, the optimal modulation would require a non-normal (linear or nonlinear) process, to redistribute energy away from the leading eigenmode, to then feed back and regenerate the optimal modulation. Although speculative, the weakly nonlinear modulation may still represent the most efficient route to turbulence, rather than alternate optimized base flow modulations.

To provide further insight into the route to turbulence, and to further establish which subcritical conditions can sustain turbulence, additional r_{c} were investigated. Although a more substantial investigation of the parameter space remains as future work, a wide variety of dynamics were observed. While $r_{\mathrm{c}} = 0.6$ managed to trigger turbulence, like $r_{\mathrm{c}} = 0.9$, the former did not sustain turbulence, manifesting only a single turbulent episode. However, having still energized the leading eigenmode ($\alpha = \alpha_{\max}$ and large τ), relaminarization was not toward the fixed point (like cases at $\alpha_{\rm opt}$), with saturation toward a stable finite amplitude state. This finite amplitude state was also observed at $r_{\rm c} = 0.3$ and $r_{\rm c} = 0.4$, although neither of these lower Re cases triggered turbulence between the nonlinear growth from the edge, and saturation to the stable finite amplitude state. The finite amplitude states showed no signs of decaying, remaining nonlinearly stable for over 20 000 time units (their computed extent). These states were far more complex than the edge, with around 60 Fourier modes clearly excited, and with a perturbation energy following an exponential dependence of $\exp(-C\kappa)$, where C was a constant inversely proportional to Re. With increased streamwise resolution, higher Fourier modes may also have followed these trends. Given the large number of excited Fourier components, and the relatively large amplitude of the finite amplitude state, it is unlikely that these states represent supercritical stability (Drazin & Reid 2004). Frozen linear stability analysis of the base flow modulations of these finite amplitude states also indicates a decaying leading eigenmode, likely offset by growth in higher harmonics. The nonlinear growth from the edge state was also shown to be strongly dependent on $r_{\rm c}$, and may have been a strong contributor to the ability to generate turbulence.

Finally, some further avenues for future work are proposed, besides the widespread use of the leading adjoint mode as an initial condition. Although the effect of domain length in subcritical Q2D transitions was shown to have no effect on the lower delineation energy in Chapter 5 (Camobreco *et al.* 2020), these investigations were of transient growth maxima ($\alpha = \alpha_{\rm opt}$), with turbulent episodes which were not sustained. Thus, the effect of domain length on both the lower and upper delineating energies should be reconsidered (the latter not investigated in this chapter). Furthermore, the effect of domain length on intermittency could be elucidated. Alternately, once the base flow becomes modulated, the wave number maximizing exponential growth shifts. Preliminary investigations indicate that selecting $\alpha_{\max}$ relative to the modulation yields further reductions in $E_{\rm D}$, which may be worth further investigation. Finally, whether optimal energization is most efficient in full 3D DNS is also of interest. Varying the degree of three dimensionality, via the magnetic field, may indicate when optimally energizing the leading eigenmode is more efficient that maximizing nonlinear transient growth (linear and nonlinear transient growth differing greatly hydrodynamically).

Chapter 8

Stability of pulsatile quasi-two-dimensional duct flows under a transverse magnetic field

8.1 Perspective

The previous chapter highlighted that purely Q2D routes to sustained turbulence can be attained at subcritical *Re*. Although an exhaustive search of the parameter space is yet to be performed, the purely Q2D constraint may limit sustained turbulence to only weakly subcritical *Re*. At $H = 10$, turbulence was sustained at critical Reynolds number ratios $r_\mathrm{c} \gtrsim 0.8$, while at lower $r_\mathrm{c} \lesssim 0.7$, nonlinear growth lead to saturation to a finite amplitude state. Thus, to account for practical considerations, two further, separate investigations were performed.

The first involves assessing whether significant improvements in heat transfer can be attained either by the sustained turbulence at $r_\mathrm{c} \approx 0.9$, or by the stable (laminar) finite amplitude states at $r_\mathrm{c} \lesssim 0.6$, as detailed in Appendix B. Overall, from the results of Appendix B, the improvements to heat transfer may not be sufficient to warrant such large *Re*, although Appendix B does only consider heat transfer based on a passive scalar. Furthermore, as the finite amplitude states were only observed at intermediate to low $H \leq 10$, to match this friction parameter at high magnetic field strength, very small aspect ratios (order 0.01) would be required, but may not be feasible in practice.

The second investigation involves redesigning the base flow. This is the focus of this chapter, which contains the paper entitled "*Stability of pulsatile quasi-two-dimensional duct flows under a transverse magnetic field*" published in *Physical Review Fluids* in 2021. These redesigns require both large reductions in the Reynolds number at which turbulence can be sustained, and the ability to observe turbulence at higher H.

The base flow is redesigned via the addition of an oscillating component to the underlying steady base flow. In a practical sense, this would require a time varying driving pressure gradient, which, if slowly varying, is not unfeasible. To ensure net transfer of both tritium and thermal energy through the cooling conduits, only steady flow components which are never smaller than the oscillating components are investigated. Furthermore, this will allow for simple comparisons between the pulsatile (steady + oscillating) and purely steady base flows. In a similar manner to the analysis of steady base flows in Chapters 6 (Camobreco *et al.* 2021b) and 7, supercritical transitions are investigated first (with subcritical transitions to be assessed in future work), which reduces the number of parameters to cover (the base flow now depends on three non-dimensional parameters, and the linear stability behavior on four).

As an initial foray in the investigation, a large amplitude ratio (ratio of the maximum velocities of the steady and oscillating components) of $\Gamma = 100$ was considered. This provided the clearest picture of the role played by the oscillating base flow component's frequency. At low frequencies, those best for practical operation, a small degree of destabilization was observed, while higher frequencies stabilized the flow. The degree of destabilization at low frequencies consistently improved with decreasing amplitude ratio (the inclusion of a greater oscillatory fraction). Furthermore, the percentage reduction in Re_c relative to the steady result was also found to consistently improve with increasing H. This was an especially important result, and one due to the additional degrees of freedom introduced by the extra parameters involved in redesigning the base flow. At high H, the steady Re_c is large, yet the steady, streamwise invariant base flow remains independent of Re. When an Re dependent oscillatory component is added, the critical Reynolds number can be reduced until H and $Sr Re$ (Strouhal by Reynolds number) become of similar magnitude, leading to large percentage reductions in Re_c.

Although the linear stability results were promising, nonlinear modulation of the base flow proved quite detrimental for the smallest tested amplitude ratio, $\Gamma = 1$. Nonlinear modulation of the base flow prevented even supercritical Re (relative to the pulsatile base flow) from transitioning to turbulence. Given the large reductions in Re_c, the magnitude of Re could have hampered transition (weakly supercritical pulsatile Re being order 10^3 rather than order 10^4 as for a steady base flow at $H = 10$). A lack of linear growth was not the issue, with around 18 orders of magnitude of intracyclic growth and decay observed. Worse still, even increasing the amplitude ratio, as shown in Appendix E, was rarely effective at inciting transition, at $H = 10$ or $H = 100$. Even with less linear growth (8 to 9 orders of magnitude at $H = 10$), detrimental nonlinear modulation still inhibited the transition to turbulence. Of further concern, intermediate amplitude ratios are far less effective at reducing Re_{c}. At $H = 10$, and taking 10% supercriticality into account, an equivalent $r_{\mathrm{c}} = 0.737$ was unable to trigger turbulence with a pulsatile base flow (while a steady base flow can sustain turbulence at $r_{\mathrm{c}} \gtrsim 0.8$). Thus, unless the amplitude ratio is quite small, or $H > 10$ simulated, pulsatility may provide little benefit. However, simulations were hampered at higher H, due to operator sensitivity issues. These results are presented in the published article, included on the pages to follow.

PHYSICAL REVIEW FLUIDS **6**, 053903 (2021)

Stability of pulsatile quasi-two-dimensional duct flows under a transverse magnetic field

Christopher J. Camobreco[1,*] Alban Pothérat[2,†] and Gregory J. Sheard[1,‡]
[1]*Department of Mechanical and Aerospace Engineering, Monash University, Victoria 3800, Australia*
[2]*Fluid and Complex Systems Research Centre, Coventry University, Coventry CV15FB, United Kingdom*

(Received 2 February 2021; accepted 7 May 2021; published 25 May 2021)

The stability of a pulsatile quasi-two-dimensional duct flow was numerically investigated. Flow was driven, in concert, by a constant pressure gradient and by the synchronous oscillation of the lateral walls. This prototypical setup serves to aid understanding of unsteady magnetohydrodynamic flows in liquid metal coolant ducts subjected to transverse magnetic fields, motivated by the conditions expected in magnetic confinement fusion reactors. A wide range of wall oscillation frequencies and amplitudes, relative to the constant pressure gradient, were simulated. Focus was placed on the driving pulsation optimized for the greatest reduction in the critical Reynolds number for a range of friction parameters H (proportional to magnetic field strength). An almost 70% reduction in the critical Reynolds number, relative to that for the steady base flow, was obtained toward the hydrodynamic limit ($H = 10^{-7}$), while just over a 90% reduction was obtained by $H = 10$. For all oscillation amplitudes, increasing H consistently led to an increasing percentage reduction in the critical Reynolds number. This is a promising result, given fusion relevant conditions of $H \geqslant 10^4$. These reductions were obtained by selecting a frequency that both ensures prominent inflection points are maintained in the base flow and a growth in perturbation energy in phase with the deceleration of the base flow. Nonlinear simulations of perturbations driven at the optimized frequency and amplitude still satisfied the no net growth condition at the greatly reduced critical Reynolds numbers. However, two complications were introduced by nonlinearity. First, although the linear mode undergoes a symmetry-breaking process, turbulence was not triggered. Second, a streamwise invariant sheet of negative velocity formed, able to arrest the linear decay of the perturbation. Although the nonlinearly modulated base flow maintained a higher time-averaged energy, it also stabilized the flow, with exponential growth not observed at supercritical Reynolds numbers.

DOI: 10.1103/PhysRevFluids.6.053903

I. INTRODUCTION

The aim of this paper is to assess the generation and promotion of turbulence in oscillatory magnetohydrodynamic (MHD) duct flows. Motivation stems from proposed designs of dual purpose tritium breeder/coolant ducts in magnetic confinement fusion reactors [1]. These coolant ducts are plasma facing, hence subjected to both high temperatures and a strong pervading transverse magnetic field [2]. At the same time, obtaining turbulent heat transfer rates is crucial to the long-term operation of self-cooled duct designs [3]. This can be achieved by keeping the flow turbulent.

*christopher.camobreco@monash.edu
†alban.potherat@coventry.ac.uk
‡greg.sheard@monash.edu

Various strategies to promote turbulence in MHD flows include the placement of physical obstacles of various cross sections [4–6], inhomogeneity in electrical boundary conditions [7], electrode stimulation [8,9], and localized magnetic obstacles [10]. The approach to promote turbulence taken in this paper is to superimpose a time periodic flow, of specified frequency and amplitude, onto an underlying steady flow. The benchmark used, particularly in the linear analysis, is the critical Reynolds number for the steady flow. The goal is to obtain the greatest reduction in the critical Reynolds number (considered as the degree of destabilization) with the addition of a time-periodic flow component of optimized frequency and amplitude. Ultimately, this approach seeks an estimate of the lowest Reynolds number at which turbulence may be incited and sustained by the addition of a pulsatile component to the base flow.

In MHD flows, the predominant action of the Lorentz force on the electrically conducting fluid is to diffuse momentum along magnetic field lines [11,12]. When the Lorentz force dominates both diffusive and inertial forces, the flow becomes quasi-two-dimensional (Q2D) [13–15]. In the limit of quasistatic Q2D MHDs, the magnetic field is imposed and the Lorentz force dominates all other forces far from walls normal to the field. Three dimensionality only remains when asymptotically small in amplitude or in regions of asymptotically small thickness. The boundary layers remain intrinsically three-dimensional. Hartmann boundary layers form on walls perpendicular to magnetic field lines, with a thickness scaling as Ha^{-1} [12,16], while the thickness of parallel wall Shercliff boundary layers scales as $\mathrm{Ha}^{-1/2}$ [17]. The Hartmann number $\mathrm{Ha} = aB(\sigma/\rho\nu)^{1/2}$ represents the square root of the ratio of electromagnetic to viscous forces, where a is the distance between Hartmann walls, B the imposed magnetic field strength, and σ, ρ, and ν the incompressible Newtonian fluid's electrical conductivity, density, and kinematic viscosity, respectively. Nevertheless, although not asymptotically small, three-dimensionality in Shercliff layers remains small enough for Q2D models to represent them with high accuracy [18]. The remaining core flow is uniform and well two-dimensionalized in fusion relevant regimes [2]. A Q2D model proposed by Ref. [12] (hereafter the SM82 model) is applied, which governs flow quantities averaged along the magnetic field direction. In the Q2D setup, the Hartmann walls are accounted for with the addition of linear friction acting on the bulk flow, valid for laminar Hartmann layers [12]. Shercliff layers still remain in the averaged velocity field, even in the quasistatic limit of a dominant Lorentz force, of thickness scaling as $H^{-1/2}$ [17], where $H = 2(L/a)^2\mathrm{Ha}$ is the friction parameter and L the characteristic wall-normal length. The accuracy of the SM82 model is well established for the duct problem [19–21], with less than 10% error between the Q2D and the three-dimensional laminar boundary layer profiles [18].

The linear stability of steady Q2D duct flow was analyzed by Ref. [17]. As the magnetic field is strongly stabilizing, the critical Reynolds number for a steady base flow, beyond which modal instabilities grow, scales as $\mathrm{Re}_{\mathrm{crit,s}} = 4.835 \times 10^4 H^{1/2}$ for $H \gtrsim 1000$ [17,22,23]. The Reynolds number $\mathrm{Re} = U_0L/\nu$ represents the ratio of inertial to viscous forces. In this paper, both transient and steady inertial forces will be encapsulated in U_0, a characteristic velocity based on both the steady and oscillating flow components. Instability occurs via Tollmien–Schlichting (TS) waves originating in the Shercliff layers. The instabilities become isolated at the duct walls with increasing magnetic field strength [17,22], eventually behaving as per an instability in an isolated exponential boundary layer [17,22,24]. To the authors' knowledge, oscillatory or pulsatile Q2D flows have yet to be analyzed under a transverse magnetic field. Weak in-plane fields have been analyzed for oscillatory flows, although pulsatility was not considered [25,26].

The destabilization of hydrodynamic plane channel flows with the imposition of an oscillating flow component was assessed by Ref. [27]. Using series expansions to evaluate Floquet exponents, the range of frequencies that induce destabilization was determined. Womersly numbers $1 \leqslant \mathrm{Wo} \lesssim 13$ were destabilizing and $\mathrm{Wo} \geqslant 14$ stabilizing, for low Reynolds numbers and pulsation amplitudes, where the Womersly number $\mathrm{Wo} = \omega L^2/\nu$ characterizes the square root of transient inertial to viscous forces, and where ω is the pulsation frequency. The problem was revisited with advanced computational power and techniques [28,29]. However, even large-scale Floquet matrix problems struggled to adequately resolve larger-amplitude pulsations [28,29], as the required number of Fourier modes rapidly increases with increasing pulsation amplitude. Instead, direct forward evolution of the linearized Navier–Stokes equations is required. Improved bounds for destabilizing frequencies of $5 \leqslant \mathrm{Wo} < 13$ were determined [29], with the optimum frequency for destabilization at $\mathrm{Wo} = 7$. The optimized amplitude ratio for the pulsation was also found to be near unity (steady and oscillatory velocity maximums of equal amplitude) at lower frequencies [28]. In addition, a small destabilization was observed at very high frequencies, for small pulsation amplitudes. Although Ref. [28] did not focus on obtaining the maximum destabilization, an approximately 33% reduction in the critical Reynolds number (relative to the steady result) was observed at the lowest frequency tested, near an amplitude ratio of unity. Further improvement, with an approximately 57% reduction in the critical Reynolds number [30], was attained by the imposition of an oscillation with two modes of different frequencies. Given the size of the parameter space, there remains significant potential to further destabilize both hydrodynamic and MHD flows, with single-frequency optimized pulsations.

At lower frequencies, the perturbation energy varies over several orders of magnitude within a single period of evolution [29,31]. This intracylcic growth and decay predominantly occurs during the deceleration and acceleration phases of the base flow, respectively. The intracylcic growth increases exponentially with increasing pulsation amplitude [29]. At smaller pulsation amplitudes, a cruising regime [29] has been identified, where the perturbation energy remains of similar nonlinear magnitude throughout the entire cycle. At larger pulsation amplitudes and at smaller frequencies, a ballistic regime [29] was identified, where the perturbation energy varies by many orders of magnitude over the cycle, and is propelled from a linear to nonlinear regime through this growth. However, in full nonlinear simulations of Stokes boundary layers, an incomplete decay of the perturbation over one cycle is observed [32]. This has little effect on growth in the next cycle, thereby leading to either an intermittent or sustained turbulent state [32]. Thus, ballistic regimes form an enticing means to sustain turbulence under fusion relevant conditions. To assess the effectiveness of this strategy, we must understand the conditions of transition to turbulence in a duct flow pervaded by a strong enough magnetic field to assume quasi-two-dimensionality. Specifically, this paper seeks to answer the following questions:

(1) Will superimposing an oscillatory flow onto an underlying steady base flow still be effective at reducing the critical Reynolds number in high H, fusion-relevant regimes?

(2) What pulsation frequencies and amplitudes are most effective at destabilizing the flow, both hydrodynamically and toward fusion-relevant regimes?

(3) Are the parameters at which reductions in $\mathrm{Re}_{\mathrm{crit}}$ are observed viable for both SM82 modeling and fusion relevant applications?

(4) Are reductions in $\mathrm{Re}_{\mathrm{crit}}$ sufficient to observe turbulence at correspondingly lower Re?

This paper proceeds as follows: In Sec. II, the problem is nondimensionalized and the base flow for the duct problem derived in the SM82 framework. Particular focus is placed on the dependence of the base flow on all four nondimensional parameters. Pressure- and wall-driven flows are compared before determining the bounds for validity of the SM82 approximation for pulsatile flows. In Sec. III A, the linear problem is formulated and both the Floquet and timestepper methods are introduced. The long-term stability behavior is considered in Sec. III B, with particular focus on the optimal conditions for destabilization. Intracyclic growth and the linear mode structure are analyzed in more detail in Sec. III C. Section IV focuses on targeted direct numerical simulations (DNSs) of the optimized pulsations. Emphasis is placed on comparing linear and nonlinear evolutions and symmetry breaking induced by nonlinearity.

II. PROBLEM SETUP

A. Geometry and base flows

This study considers a duct with rectangular cross section of wall-normal height $2L$ (y direction) and transverse width a (z direction), subjected to a uniform magnetic field $B\boldsymbol{e}_z$, see Fig. 1. The duct is uniform and of infinite streamwise extent (x direction). A steady base flow component is driven by a constant pressure gradient, producing a maximum undisturbed dimensional velocity

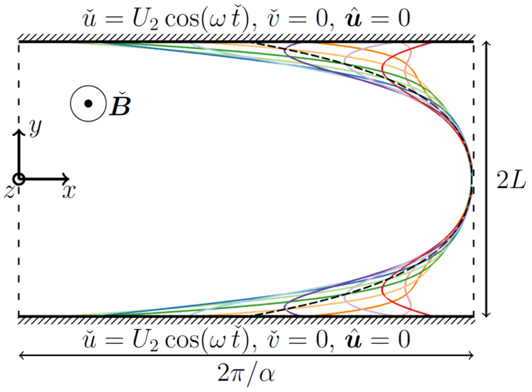

FIG. 1. A schematic representation of the system under investigation. Solid lines denote the oscillating, impermeable, no-slip walls. Short dashed lines indicate the streamwise extent of the periodic domain defined by streamwise wave number α. Examples of the steady base flow component [$U_{1,\mathrm{B}}(y)$; dashed line] and the normalized total pulsatile base flow [$(1 + 1/\Gamma)U(y, t)$; 11 colored lines over the full period, 2π] are overlaid at $H = 10$, $\Gamma = 10$, $\mathrm{Sr} = 5 \times 10^{-3}$, and $\mathrm{Re} = 1.5 \times 10^4$.

U_1. An oscillatory base flow component is driven by synchronous oscillation of both lateral walls at velocity $U_2 \cos(\omega\check{t})$, with maximum dimensional velocity U_2. The pulsatile flow, the sum of the steady and oscillatory components, has a maximum velocity over the cycle of U_0. In the limits $\mathrm{Ha} = aB(\sigma/\rho\nu)^{1/2} \gg 1$ and $N = aB^2\sigma/\rho U_0 \gg 1$, the flow is Q2D and can be approximated with the SM82 model [12,18]. A more detailed assessment of the the validity of the SM82 model follows in Sec. II B. Normalizing lengths by L, velocity by U_0, time by $1/\omega$, and pressure by ρU_0^2, the governing momentum and mass conservation equations become

$$\mathrm{Sr}\frac{\partial \boldsymbol{u}}{\partial t} = -(\boldsymbol{u} \cdot \boldsymbol{\nabla}_\perp)\boldsymbol{u} - \boldsymbol{\nabla}_\perp p + \frac{1}{\mathrm{Re}}\nabla_\perp^2 \boldsymbol{u} - \frac{H}{\mathrm{Re}}\boldsymbol{u}, \tag{1}$$

$$\boldsymbol{\nabla}_\perp \cdot \boldsymbol{u} = 0, \tag{2}$$

where $\boldsymbol{u} = (u, v)$ is the Q2D velocity vector, representing the z-averaged field, and $\boldsymbol{\nabla}_\perp = (\partial_x, \partial_y)$ is the two-dimensional gradient operator. Four nondimensional parameters govern this problem: the Reynolds number $\mathrm{Re} = U_0L/\nu$, the Strouhal number $\mathrm{Sr} = \omega L/U_0$, the Hartmann friction parameter $H = 2B(L^2/a)(\sigma/\rho\nu)^{1/2}$ and the amplitude ratio $\Gamma = U_1/U_2$. $\Gamma = 0$ represents a flow purely driven by oscillating walls (no pressure gradient) and $\Gamma \to \infty$ a pressure driven flow (no wall motion). The Womersly number $\mathrm{Wo}^2 = \mathrm{SrRe}$ is sometimes used instead of Sr as a dimensionless frequency.

The nondimensional pulsatile base flow is $U(y, t) = \gamma_1 U_{1,\mathrm{B}}(y) + \gamma_2 U_{2,\mathrm{B}}(y, t)$, where $\gamma_1 = \Gamma/(\Gamma + 1)$ and $\gamma_2 = 1/(\Gamma + 1)$, following Ref. [28], with steady component $U_{1,\mathrm{B}}(y)$ and oscillating component $U_{2,\mathrm{B}}(y, t)$. This work considers $1 \leqslant \Gamma < \infty$. Thus, the magnitude of the steady component of the base flow is never smaller than that of the oscillating component, ensuring net transfer of tritium/heat is dominant. The nondimensional wall oscillation is $\cos(t)/\Gamma$, and the maximum velocity over the cycle $U_0 = \max_{\{y,t\}}(U) = 1/(1 + 1/\Gamma)$ for $\Gamma \geqslant 1$ (henceforth, $\Gamma \geqslant 1$). The normalized time $t_\mathrm{P} = t/2\pi$ is also defined. To assess the degree of destabilization, the Reynolds number ratio $r_\mathrm{s} = [\mathrm{Re}/(1 + 1/\Gamma)]/\mathrm{Re}_{\mathrm{crit,s}}$ is defined, comparing the Reynolds number in this problem to the critical Reynolds number for a purely steady base flow [17,22,23]. The wave number is similarly rescaled, as $\alpha_\mathrm{s} = \alpha/\alpha_{\mathrm{crit,s}}$.

Instantaneous variables $(\boldsymbol{u}, p)$ are decomposed into base $(\boldsymbol{U}, P)$ and perturbation $(\hat{\boldsymbol{u}}, \hat{p})$ components via small parameter ϵ, as $\boldsymbol{u} = \boldsymbol{U} + \epsilon\hat{\boldsymbol{u}}$; $p = P + \epsilon\hat{p}$. The fully developed, steady parallel flow $\boldsymbol{U}_{1,\mathrm{B}} = U_{1,\mathrm{B}}(y)\boldsymbol{e}_x$, with boundary conditions $U_{1,\mathrm{B}}(y \pm 1) = 0$ and a constant driving pressure gradient scaled to achieve a unit maximum velocity is [17]

$$U_{1,\mathrm{B}} = \frac{\cosh(H^{1/2})}{\cosh(H^{1/2}) - 1}\left(1 - \frac{\cosh(H^{1/2}y)}{\cosh(H^{1/2})}\right). \tag{3}$$

The fully developed, time periodic, parallel flow $\boldsymbol{U}_{2,\mathrm{B}} = U_{2,\mathrm{B}}(t, y)\boldsymbol{e}_x = U_{2,\mathrm{B}}(t + 2\pi, y)\boldsymbol{e}_x$, with boundary conditions $U_{2,\mathrm{B}}(y \pm 1) = \cos(t)$, $\partial U_{2,\mathrm{B}}/\partial t|_{y\pm1} = -\sin(t)$ expresses as

$$U_{2,\mathrm{B}} = \mathrm{Re}\left(\frac{\cosh[(r + si)y]}{\cosh(r + si)}e^{it}\right) = b(y)e^{it} + b^*(y)e^{-it}, \tag{4}$$

where the inverse boundary layer thickness and the wave number of the wall-normal oscillations are represented by

$$\begin{aligned} r &= [(\mathrm{SrRe})^2 + H^2]^{1/4}\cos([\tan^{-1}(\mathrm{SrRe}/H)]/2),\\ s &= [(\mathrm{SrRe})^2 + H^2]^{1/4}\sin([\tan^{-1}(\mathrm{SrRe}/H)]/2), \end{aligned} \tag{5}$$

respectively, $i = (-1)^{1/2}$ and $*$ represents the complex conjugate. In the hydrodynamic limit of $H \to 0$, $r = s = (\mathrm{SrRe}/2)^{1/2}$. In the limit of $H \to \infty$, at constant Re and Sr, $r \sim H^{1/2}$ and $s \to 0$. If Re is also varied, it must vary at a rate H^p, with $p \geqslant 1$, for the limiting cases to differ. Note that the oscillating component of the base flow depends only on two parameters ($\mathrm{SrRe} = \mathrm{Wo}^2$ and H). Although these choices mean the base flow is Re dependent, they allow $\mathrm{Re}_{\mathrm{crit}}$ to be found at a constant frequency (constant Sr), as a constant Wo instead represents a constant oscillating boundary layer thickness. Examples of the base flow at $\Gamma = 1.2$ are illustrated in Fig. 2, with the total pulsatile profile plotted as $(1 + 1/\Gamma)\,U(y, t)$ to show oscillation about the steady component $U_{1,\mathrm{B}}$.

Both dominant transient inertial forces (large Sr) or dominant frictional forces (large H) are capable of flattening the central region of the oscillating flow component. In Fig. 2(a), the oscillating component is flattened by large transient inertial forces, while the steady flow still exhibits a curved Poiseuille-like profile as H is small. Whereas, in Fig. 2(c), it is the large H value that is flattening both the steady and oscillating flow components. However, inflection points, which are important for intracyclic growth, are no longer present in Fig. 2(c), as H is large, but can be observed in the boundary layers of Figs. 2(a) and 2(b), as Sr is large.

It is instructive to consider the velocity profile for the simpler problem of the SM82 equivalent of an isolated Stokes layer, $U(y, t) = e^{-ry}\cos(sy - t)$, where r and s remain as defined in Eq. (5), except scaled by $H^{-1/2}$ to account for the isolated boundary layer nondimensionalization. This highlights the effects of r and s on the boundary layer, as the base flow becomes akin to a damped harmonic oscillator. Increasing either H or SrRe increases r, in turn, and reduces the boundary layer thickness. However, increasing H reduces s. Thus, inflection points are eliminated with increasing H, and the boundary layer just appears as shifted exponential profiles, as is observed in Fig. 2(c). Decreasing SrRe reduces s, and also eliminates inflection points, whereas increasing SrRe increases s, promoting inflection points, but containing them within a thinner oscillating boundary layer.

It is also worth considering the pulsatile base flow in a broader context, as past literature is divided on the method of oscillation. Among many others, Refs. [29,33] impose an oscillatory pressure gradient, while Refs. [28,34] impose oscillating walls. For the unbounded, oscillatory Stokes flow, the eigenvalues of the linear operator, with either imposed oscillation, have been proven identical [35]. Furthermore, it has also been shown that (transient) energy growth is also identical between the two methods of oscillation [36]. However, the full linear and nonlinear problems can be shown to be identical. Defining a motionless frame G and a frame $\bar{G}$ in motion with arbitrary, time varying velocity $\boldsymbol{V}(t)$, the two frames are related through

$$\bar{\boldsymbol{x}} = \boldsymbol{x} - \int \boldsymbol{V}\,\mathrm{d}t, \quad \bar{t} = t, \quad \bar{\boldsymbol{u}} = \boldsymbol{u} - \boldsymbol{V}. \tag{6}$$

Under extended Galilean invariance, $\partial\bar{\boldsymbol{u}}/\partial\bar{\boldsymbol{x}} = \partial\boldsymbol{u}/\partial\boldsymbol{x}$ and $\mathrm{Sr}\partial\bar{\boldsymbol{u}}/\partial\bar{t} + (\bar{\boldsymbol{u}}\cdot\bar{\nabla}_\perp)\bar{\boldsymbol{u}} = \mathrm{Sr}(\partial\boldsymbol{u}/\partial t - \partial\boldsymbol{V}/\partial t) + (\boldsymbol{u}\cdot\nabla_\perp)\boldsymbol{u}$ [37]. In frame G, a constant driving pressure gradient, and oscillatory wall

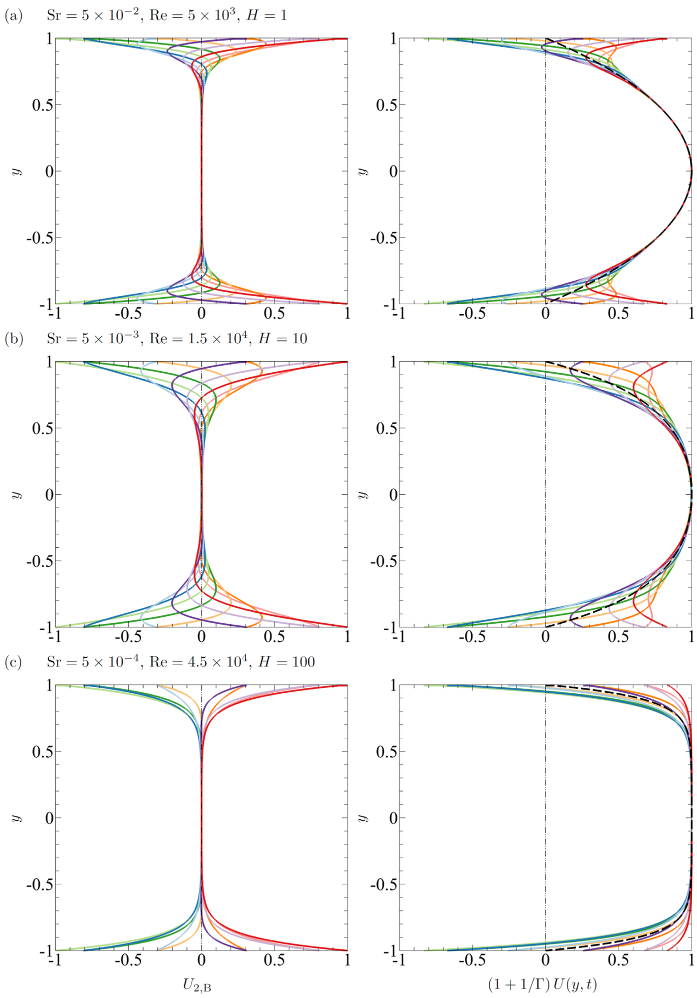

FIG. 2. Base flow profiles at $\Gamma = 1.2$. Equispaced over one period: oscillating component (left), $(1 + 1/\Gamma)$ rescaled pulsatile base flow (right). A black dashed line denotes the steady component, $U_{1,\mathrm{B}}$.

motion $U(y \pm 1, t) = U_{2,\mathrm{B}}(y \pm 1, t)/\Gamma$ are imposed. $\boldsymbol{V}(t) = (U_{2,\mathrm{B}}(y \pm 1, t)/\Gamma, 0)$ is selected so the walls appear stationary, $\bar{U}(y \pm 1, t) = 0$, in the moving frame $\bar{G}$. Substituting the relations in Eq. (6) into Eqs. (1) and (2), the governing equations in the moving frame become

$$\mathrm{Sr}\left(\frac{\partial \bar{\boldsymbol{u}}}{\partial \bar{t}} + \frac{\partial \boldsymbol{V}}{\partial t}\right) = -(\bar{\boldsymbol{u}} \cdot \bar{\boldsymbol{\nabla}}_\perp)\bar{\boldsymbol{u}} - \bar{\boldsymbol{\nabla}}_\perp p + \frac{1}{\mathrm{Re}}\bar{\nabla}_\perp^2 \bar{\boldsymbol{u}} - \frac{H}{\mathrm{Re}}(\bar{\boldsymbol{u}} + \boldsymbol{V}), \tag{7}$$

$$\bar{\boldsymbol{\nabla}}_\perp \cdot \bar{\boldsymbol{u}} = 0. \tag{8}$$

As the pressure does not have a conversion relation, the driving pressure in the moving frame can be freely chosen as

$$\bar{p}(t) = p + \frac{x}{\Gamma}\left(\mathrm{Sr}\frac{\partial U_{2,\mathrm{B}}(y \pm 1, t)}{\partial t} + \frac{H}{\mathrm{Re}} U_{2,\mathrm{B}}(y \pm 1, t)\right). \tag{9}$$

Substituting Eq. (9) into Eq. (7) and canceling yields

$$\mathrm{Sr}\frac{\partial \bar{\boldsymbol{u}}}{\partial \bar{t}} = -(\bar{\boldsymbol{u}} \cdot \bar{\nabla}_\perp)\bar{\boldsymbol{u}} - \bar{\nabla}_\perp \bar{p} + \frac{1}{\mathrm{Re}}\bar{\nabla}_\perp^2 \bar{\boldsymbol{u}} - \frac{H}{\mathrm{Re}}\bar{\boldsymbol{u}}, \tag{10}$$

$$\bar{\nabla}_\perp \cdot \bar{\boldsymbol{u}} = 0. \tag{11}$$

Thus, in frame $\bar{G}$, the governing equations, Eqs. (10) and (11), are identical to the governing equations in G, Eqs. (1) and (2). However, in $\bar{G}$ the walls are stationary, and the pressure forcing $\bar{p}$ is the sum of a steady and oscillatory component. Thus, the linear and nonlinear dynamics when the flow is driven by oscillatory wall motion (G), or an oscillatory pressure gradient ($\bar{G}$), are identical in all respects, as they are both the same problem viewed in different frames of reference. These arguments do not hold if $H = 0$ in the steady limit ($\Gamma \to \infty$, $U_{2,\mathrm{B}} = 0$) or if the oscillation of both walls is not synchronous. Note that the constant pressure gradient in the fixed frame could also be considered as a constant wall motion for nonzero H. If so, the oscillations would be about a finite wall velocity rather than about zero.

B. Validity of SM82 for pulsatile flows

With the pulsatile base flow established, the realm of validity of the SM82 model is assessed. The dimensional equation governing the induced magnetic field $\check{\boldsymbol{b}}$ is [38]

$$\frac{\partial \check{\boldsymbol{b}}}{\partial \check{t}} = B_0(\boldsymbol{e}_z \cdot \check{\nabla})\check{\boldsymbol{u}} + (\check{\boldsymbol{b}} \cdot \check{\nabla})\check{\boldsymbol{u}} - (\check{\boldsymbol{u}} \cdot \check{\nabla})\check{\boldsymbol{b}} + \frac{1}{\mu_0\sigma}\check{\nabla}^2\check{\boldsymbol{b}}, \tag{12}$$

where a background uniform steady field $B_0\boldsymbol{e}_z$ is imposed. The aim is to show that the induced magnetic field diffuses R_m times faster than it locally varies, where the magnetic Reynolds number $R_\mathrm{m} = \mu_0\sigma U_1 L$ and where μ_0 is the permeability of free space. The low-R_m approximation assumes that one of the bilinear terms is much smaller than the diffusive term, $|(\check{\boldsymbol{u}} \cdot \check{\nabla})\check{\boldsymbol{b}}| \ll |(\mu_0\sigma)^{-1}\check{\nabla}^2\check{\boldsymbol{b}}|$. Once nondimensionalized by U_1 and L, this imposes an $R_\mathrm{m} \ll 1$ constraint. This is well satisfied for liquid metal duct flows, with R_m of the order of 10^{-2} [39,40]. Note that $|B_0(\boldsymbol{e}_z \cdot \check{\nabla})\check{\boldsymbol{u}}|$ remains of the same order as $|(\mu_0\sigma)^{-1}\check{\nabla}^2\check{\boldsymbol{b}}|$ when the background magnetic field is imposed.

The quasistatic approximation assumes $|\partial\check{\boldsymbol{b}}/\partial t| \ll |(\mu_0\sigma)^{-1}\check{\nabla}^2\check{\boldsymbol{b}}|$. Note that a low R_m does not necessarily imply that $|\partial\check{\boldsymbol{b}}/\partial\check{t}|$ is small. Based on a typical out-of-plane steady velocity scale of a/U_1, $|\partial\check{\boldsymbol{b}}/\partial\check{t}|$ may be reasonably assumed to scale as $|(\check{\boldsymbol{u}} \cdot \check{\nabla})\check{\boldsymbol{b}}|$, and thereby be small if R_m were small. However, a pulsatile flow introduces an additional velocity timescale, based on the forcing frequency, to also compare against. Hence, nondimensionalizing $|\partial\check{\boldsymbol{b}}/\partial\check{t}| \ll |(\mu_0\sigma)^{-1}\check{\nabla}^2\check{\boldsymbol{b}}|$ based on a timescale of $1/\omega$ yields a constraint on the shielding parameter $R_\omega = \mu_0\sigma\omega L^2 \ll 1$ [39]. This translates to $R_\mathrm{m}\mathrm{Sr} \ll 1$, or $\mathrm{Sr} \ll R_\mathrm{m}^{-1}$, to ensure that diffusion of the induced field is not contained to small boundary regions of the domain. Given R_m of 10^{-2} is typical of liquid metal duct flows at moderate Reynolds numbers [39,40], since $R_\mathrm{m} = \mathrm{RePr}_m$ and the magnetic Prandtl number $\mathrm{Pr}_m = \nu\mu_0\sigma$ is of the order of 10^{-6} for liquid metals [16], the shielding condition of $\mathrm{Sr} \ll R_\mathrm{m}^{-1}$ requires $\mathrm{Sr} \ll 100$.

Furthermore, for the induced magnetic field to be treated as steady, the induced magnetic field must vary rapidly relative to a slowly varying velocity field. This requires the Alfvén timescale (time taken for the Alfvén velocity to cross the duct width) be much smaller than the pulsation (transient inertial) timescale. The Alfvén velocity $v_\mathrm{A} = B/(\mu_0\rho)^{1/2} = (N_L/R_\mathrm{m})^{1/2}(U_1 L/a)$ is expressed in terms of the interaction parameter $N_L = a^2B^2\sigma/\rho U_1 L$. Thus the Alfvén timescale is $\tau_A = a/v_A = (R_m/N_L)^{1/2}(a^2/U_1 L)$, while the steady inertial timescale $\tau_{I,L} = L/U_1$ and the pulsation timescale $\tau_P = 1/\omega$. Thus, $\tau_A/\tau_{I,L} = (R_m/N_L)^{1/2}(a^2/L^2)$ and $\tau_A/\tau_P = (R_m/N_L)^{1/2}Sr(U_0/U_1)(a^2/L^2)$. If $\mathrm{Sr}(U_0/U_1) < 1$, or equally $\mathrm{Sr}(1 + 1/\Gamma) < 1$, no SM82 assumptions are in question. This requires $\mathrm{Sr} < 1/2$ at $\Gamma = 1$ (and $\mathrm{Sr} < 1$ for $\Gamma \to \infty$) at equivalent $N \gg 1$ and $R_m \ll 1$ conditions as for a steady case. Recall that $\mathrm{Sr} \ll 100$ was required from the shielding constraint.

Finally, the quasistatic approximation is only valid if Alfvén waves dissipate much faster than they propagate. This is ensured if $|\partial\check{\boldsymbol{b}}/\partial t| \ll |(\mu_0\sigma)^{-1}\check{\nabla}^2\check{\boldsymbol{b}}|$ is satisfied when considering the last remaining characteristic timescale, the Alfvén timescale $\tau_A = a/v_A$. This places a condition on the Lundquist number $S = (N_L R_m)^{1/2} = \mathrm{Ha}\mathrm{Pr}_m^{1/2} \ll 1$. Given Pr_m of the order of 10^{-6} [16], and with R_m of 10^{-2} [39,40], this translates to conditions on the interaction parameter and Hartmann number of $N_L \lesssim 100$ and $\mathrm{Ha} \lesssim 1000$, respectively.

An additional component of the SM82 model is the Q2D approximation, which requires the timescale for two-dimensionalization to occur via diffusion of momentum along magnetic field lines, $\tau_{2D} = (\rho/\sigma B^2)(a^2/L^2) = (1/N_L)(a^4/U_1 L^3)$ [17], be much smaller than the inertial and pulsation timescales. These ratios are $\tau_{2D}/\tau_{I,L} = (1/N_L)(a^4/L^4)$ and $\tau_{2D}/\tau_P = (\mathrm{Sr}/N_L)(U_0/U_1)(a^4/L^4)$. Thus, if $\mathrm{Sr} < 1/2$ for otherwise equivalent conditions as for a steady case, momentum is diffused across the duct more rapidly by the magnetic field than by steady or transient inertial forces. The SM82 approximation also assumes $1 \ll \mathrm{Ha} \lesssim 1000$ and $N \gg 1$, $N_L \lesssim 100$. These constraints can be met with any H if a and L are chosen appropriately, as discussed in Ref. [23].

The SM82 model is more generally applicable to flows which exhibit a linear friction and a strong tendency to two-dimensionalize. Axisymmetric quasigeostrophic flows, with frictional forces imparted by Ekman layers, and Hele-Shaw (shallow water) flows, with Rayleigh friction, both tend to two-dimensionality if the aspect ratio L/a is small. In these flows, a formally equivalent Q2D model can be derived [7,41] (with the addition of a term representing the Coriolis force in the quasigeostrophic case), although the physical meaning of the friction term differs, as do the bounds of validity [23].

III. LINEAR STABILITY ANALYSIS

A. Formulation and validation

Linear stability is assessed via the exponential growth rate of disturbances, with unstable perturbations exhibiting net growth each period. The linearized evolution equations,

$$\mathrm{Sr}\frac{\partial\hat{\boldsymbol{u}}}{\partial t} = -(\hat{\boldsymbol{u}}\cdot\nabla_\perp)\boldsymbol{U} - (\boldsymbol{U}\cdot\nabla_\perp)\hat{\boldsymbol{u}} - \nabla_\perp\hat{p} + \frac{1}{\mathrm{Re}}\nabla_\perp^2\hat{\boldsymbol{u}} - \frac{H}{\mathrm{Re}}\hat{\boldsymbol{u}}, \tag{13}$$

$$\nabla_\perp\cdot\hat{\boldsymbol{u}} = 0, \tag{14}$$

are obtained by neglecting terms of $O(\epsilon^2)$ in the decomposed Navier–Stokes equations. A single fourth-order equation governing the linearized evolution of the perturbation is obtained by taking twice the curl of Eq. (13) and substituting Eq. (14). By additionally decomposing perturbations into plane-wave solutions of the form $\hat{v}(y,t) = e^{i\alpha x}\tilde{v}(y,t)$, by virtue of the streamwise invariant base flow $U(y,t)$, yields

$$\frac{\partial\tilde{v}}{\partial t} = \mathscr{L}^{-1}\left[\frac{i\alpha}{\mathrm{Sr}}\frac{\partial^2 U}{\partial y^2} - \frac{U i\alpha}{\mathrm{Sr}}\mathscr{L} + \frac{1}{\mathrm{SrRe}}\mathscr{L}^2 - \frac{H}{\mathrm{SrRe}}\mathscr{L}\right]\tilde{v}, \tag{15}$$

where $\mathscr{L} = (\partial^2/\partial y^2 - \alpha^2)$ and where the perturbation eigenvector $\tilde{v}(y,t)$ still contains both exponential and intracyclic time dependence. Integrating Eq. (15) forward in time, with a third-order forward Adams–Bashforth scheme [42] and with the renormalization $\|\tilde{v}\|_2 = 1$ at the start of each period, forms the timestepper method. After sufficient forward evolution, all but the fastest growing mode is washed away, providing the net growth of the leading eigenmode over one period. A Krylov subspace scheme [43] is also implemented to aid convergence and provide the leading few

TABLE I. $\Gamma = 0$, $H = 0$ cases validating and testing the resolution of the Floquet matrix method, considering the real part of even and odd modes separately. From Ref. [34], parameters convert as $\mathrm{Sr} = h_{\mathrm{BB06}}/\mathrm{Re}_{\mathrm{BB06}}$ and $\mathrm{Re} = 2h_{\mathrm{BB06}}\mathrm{Re}_{\mathrm{BB06}}$, where $h_{\mathrm{BB06}} = 16$ and $\mathrm{Re}_{\mathrm{BB06}} = 847.5$. N_c accounts for the entire domain.

N_c ($T = 300$)	$\mathrm{Re}(\lambda_1)$	|% Error|	T ($N_c = 150$)	$\mathrm{Re}(\lambda_1)$	|% Error|
50	0.4719273115651	3.02×10^{1}	200	0.9493815978240	4.04×10^{1}
100	0.6762032203289	6.39×10^{-3}	250	0.6761968753200	5.45×10^{-3}
150	0.6761968755932	5.45×10^{-3}	300	0.6761968755932	5.45×10^{-3}
Ref. [34], even	0.67616	0		0.67616	0
50	0.4689789806609	3.06×10^{1}	200	0.8329627125585	2.33×10^{1}
100	0.6756830883343	6.38×10^{-3}	250	0.6756767389579	5.44×10^{-3}
150	0.6756767389579	5.44×10^{-3}	300	0.6756767389579	5.44×10^{-3}
Ref. [34], odd	0.67564	0		0.67564	0

eigenvalues λ_j with the largest growth rate (real component). The domain $y \in [-1, 1]$ is discretized with $N_c + 1$ Chebyshev nodes. The derivative operators, incorporating boundary conditions, are approximated with spectral derivative matrices [44]. The spatial resolution requirements are halved by incorporating a symmetry (respectively, antisymmetry) condition along the duct centreline, and resolving even (respectively, odd) perturbations separately. Even perturbations were consistently found to be less stable than odd perturbations.

The eigenvalues of the discretized forward evolution operator are also determined with a Floquet matrix approach [28,34]. The exponential and time-periodic growth components of the eigenvector are separated by defining

$$\tilde{v}(y,t) = e^{\mu_{\mathrm{F}} t} \sum_{n=-\infty}^{n=\infty} \tilde{v}_n(y) e^{int}, \tag{16}$$

with Floquet multiplier μ_{F} and harmonic n. This sum is numerically truncated to $n \in [-T, T]$, to obtain a finite set of coupled equations

$$\begin{aligned}\mu \tilde{v}_n = & -\frac{i\alpha}{\mathrm{Sr}}(M\tilde{v}_{n+1} + M^*\tilde{v}_{n-1}) \\ & + \left\{\frac{1}{\mathrm{SrRe}}\mathscr{L}^{-1}\mathscr{L}^2 - \frac{H}{\mathrm{SrRe}} - in - \frac{i\alpha\gamma_1}{\mathrm{Sr}}\left[\mathscr{L}^{-1}\left(U_{1,\mathrm{B}}\mathscr{L} - \frac{\partial^2 U_{1,\mathrm{B}}}{\partial y^2}\right)\right]\right\}\tilde{v}_n,\end{aligned} \tag{17}$$

after substituting Eq. (16) into Eq. (15), where $M = \gamma_2[\mathscr{L}^{-1}(b\mathscr{L} - \partial^2 b/\partial y^2)]$. This system of Chebyshev-discretized equations is set up as a block tridiagonal system, with the coefficients of $\tilde{v}_{n+1}$, $\tilde{v}_n$ and $\tilde{v}_{n-1}$ placed on super, central and subdiagonals, respectively. Spectral derivative matrices are built as before. The MATLAB function `eigs` is used to find a subset of eigenvalues of the block tridiagonal system located near zero real component (neutral stability), with convergence tolerance 10^{-14}. Re and α are varied until only a single wave number, α_{crit}, attains zero growth rate, at $\mathrm{Re}_{\mathrm{crit}}$ (for specified Sr, Γ, and H).

The numerical requirements for the Floquet and timestepper approaches are highly parameter dependent. Validation against the hydrodynamic oscillatory problem [34] is provided in Table I. Further assurance of the validity of the numerical method is provided in the excellent agreement between pulsatile and steady $\mathrm{Re}_{\mathrm{crit}}$ values (e.g., $r_s \to 1$) at very small and large Sr in Sec. III B and the agreement between the timestepper and Floquet growth rates shown in Sec. III B. Sporadic resolution testing, post determination of $\mathrm{Re}_{\mathrm{crit}}$, was also performed, with an example shown in Table II.

As a rough guide, for the Floquet method, N_c varies between 100 and 400 and T between 100 and 600, with an eigenvalue subset size of around 200. For the timestepper, N_c varies between 40 to 240, with 10^5 to 4×10^7 time steps per period, and 6 to 4000 iterations. As discussed in

TABLE II. Resolution test at $H = 10$, $\Gamma = 10$ (at large Re, and small $\mathrm{Sr} = 1.12 \times 10^{-2}$). The Floquet method was used to determine $\mathrm{Re}_{\mathrm{crit}} = 8.1243 \times 10^5$ and $\alpha_{\mathrm{crit}} = 0.91137$, at $N_c = 200$ and $T = 400$. This $\mathrm{Re}_{\mathrm{crit}}$ and α_{crit} were input into the timestepper to validate the timestepper and the Floquet $\mathrm{Re}_{\mathrm{crit}}$ value (note the neutrally stable growth rate $\mathrm{Re}(\lambda_1) \approx 0$). N_c accounts for the entire domain with an even mode enforced.

N_c	Time steps (per period)	Iterations	$\|\tilde{v}\|_2$ (final iteration)	$\mathrm{Re}(\lambda_1)$	$\mathrm{Im}(\lambda_1)$
100	4×10^5	40	0.991293824970121	−0.001391699032636	0.962888347220989
140	4×10^5	20	1.000006449491397	0.000001028054446	0.955814791449918
180	4×10^5	20	0.999993672187703	−0.000001007773833	0.955795855565797
220	7×10^5	20	0.999993546425103	−0.000001027780526	0.955795848436100
240	10^6	10	0.999993662207549	−0.000001011050606	0.955795855979765

Refs. [28,29], with increasing pulsation amplitude (decreasing Γ), decreasing Sr and increasing Re, the intracylcic growth can become stupendously large. The matrix method becomes problematic when the intracylcic growth exceeds four to six orders of magnitude, while the timestepper withstands approximately 10 to 15 orders of magnitude of intracylcic growth (the perturbation norm $\|\tilde{v}\|_2$ does not cleanly converge thereafter). Very roughly, for $\mathrm{Sr} \lesssim 10^{-3}$ and/or $\Gamma \lesssim 2$ and/or $\mathrm{Re} \gtrsim 10^5$ when $H \geqslant 10$ the intracyclic growth was greater than even the timestepper could handle. However, given the specific aims of this paper, this does not obstruct too large a fraction of the parameter space we wish to explore.

B. Long-term behavior

A neutrally stable perturbation exhibits no net growth or decay over each cycle. Neutral stability is first achieved at $\mathrm{Re}_{\mathrm{crit}}$ and α_{crit} as Re is increased. However, such a definition conceals the intracylic dynamics, which strongly influence $\mathrm{Re}_{\mathrm{crit}}$, as is further discussed in Sec. III C. Two key results are shown in Fig. 3, considering the effect of varying H on $\mathrm{Re}_{\mathrm{crit}}$. First, at large H, $\mathrm{Re}_{\mathrm{crit}}$ for a purely steady base flow scales as $H^{1/2}$, while all pulsatile cases scale as H^p, with $1/2 \leqslant p < 1$. For large H, r is dominated by $[(\mathrm{SrRe})^2 + H^2]^{1/4}$, which is always greater than $H^{1/2}$. As the isolated boundary layer thickness is defined by e^{-ry} (Sec. II), increasing H stabilizes pulsatile base flows more rapidly than steady base flows. Thus, the thinner pulsatile boundary layers are always more stable than their thicker counterpart exhibited by steady base flows. Note that in the high H regime, when the boundary layers are isolated for any frequency pulsation, the stability results are defined solely by the dynamics of an isolated boundary layer, as observed in steady MHD or Q2D studies [17,22,23,45], and for high frequency oscillatory hydrodynamic flows [34]. Second, variations in the pulsation frequency and amplitude roughly act to translate the stability curves, without significantly changing the overall trends (a slight change, the local minimums in Fig. 3(c), are explained when considering Sr variations at fixed H shortly). At $\Gamma = 100$, differences between pulsatile and steady results are not easily observed, confirming the accuracy of the Floquet solver. The $\Gamma = 10$ curves overlay the steady trend at respective high and low frequencies of $\mathrm{Sr} = 1$ and $\mathrm{Sr} = 10^{-3}$. At $\mathrm{Sr} = 10^{-2}$, the flow is more unstable as $H \to 0$, with $r_s \to 0.8651$. However, for $H \gtrsim 2400$ the additional stability conferred by thinner pulsatile boundary layers pushes r_s above unity. The pulsatile flow is then more stable than the steady counterpart. Note that so long as $\mathrm{Re}_{\mathrm{crit}}$ varies as H^p with $p < 1$ (as observed for all H simulated), then Re does not increase quickly enough to offset the eventual $s \to 0$ and $r \sim H^{1/2}$ trends as $H \to \infty$. Eventually, the exponent p should settle to $1/2$, after which $\mathrm{Re}_{\mathrm{crit}}$ should vary as $H^{1/2}$ for very large $H > 10^4$. At $\mathrm{Sr} = 10^{-1}$, the flow is hydrodynamically more stable ($r_s \to 2.4258$ as $H \to 0$) and is even more strongly stabilized at higher H. The $\mathrm{Sr} = 10^{-1}$ curve in Fig. 3(c) is not smooth as different least stable modes become dominant, as shown in the jumps in critical wave number, clearest in Fig. 3(d). In steady Q2D flows [17,22,23], α_{crit} also scales with $H^{1/2}$ for high H, like $\mathrm{Re}_{\mathrm{crit}}$. However, perplexingly for the pulsatile cases, the α_{crit} trends are as H^q, with a lower exponent than the steady case, $q \leqslant 1/2$.

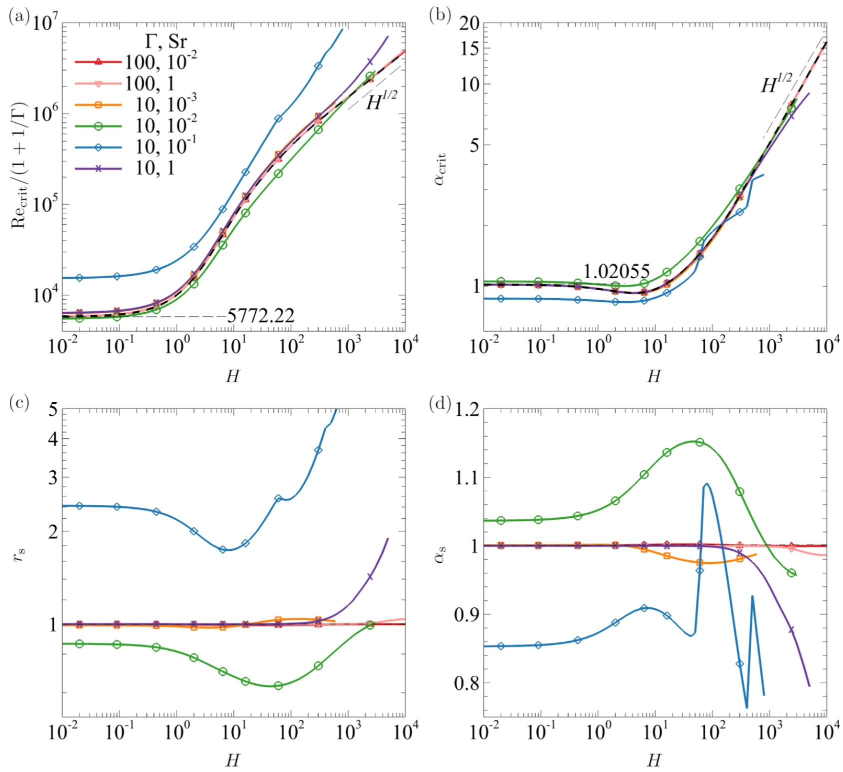

FIG. 3. Rescaled $\mathrm{Re}_{\mathrm{crit}}$ and α_{crit} as a function of H for $10^{-3} \leqslant \mathrm{Sr} \leqslant 1$ and $\Gamma \geqslant 10$. The steady ($\Gamma \to \infty$) results from Ref. [22] have been included for direct comparison in the top row (black dashed lines) and are divided out to compute r_s and α_s in the bottom row.

Variations in r_s as a function of Sr are depicted for various H under a weak pulsatility of $\Gamma = 100$ in Fig. 4(a) and at $\Gamma = 10$ in Fig. 5(a). The deviations from the steady $\mathrm{Re}_{\mathrm{crit}}$ are modest at $\Gamma = 100$ (between -1% and $+4\%$). However, it helps provide a clearer picture of the underlying dynamics. Considering the hydrodynamic case (approximated by $H = 10^{-7}$) as an example, the steady $\mathrm{Re}_{\mathrm{crit}}$ is approached ($r_s \to 1$) as $\mathrm{Sr} \to 0$. In this limit, transient inertial forces act so slowly that viscosity can smooth out all wall-normal oscillations in the velocity profile over the entire duct within a single oscillation period (2π). Although large intracyclic growth occurs during the deceleration phase of the base flow (effectively due to an adverse pressure gradient), this is not augmented by additional growth as inflection points are absent. Therefore, the growth is entirely canceled out by decay (due to an equivalent-magnitude favorable pressure gradient) in the acceleration phase. With increasing Sr, inflection points are present over a greater fraction of the deceleration phase, in spite of the action of viscosity, and become more prominent, providing a reduction in r_s. However, increasing Sr reduces the effective duration of the deceleration phase of the base flow, leaving less time for intracyclic growth. Thus, the local minimum in r_s occurs when the benefits of promoting and maintaining inflection points for a larger time (increasing Sr) is counteracted by reducing the duration of the growth phase (decreasing Sr). However, although increasing Sr promotes inflection points, these

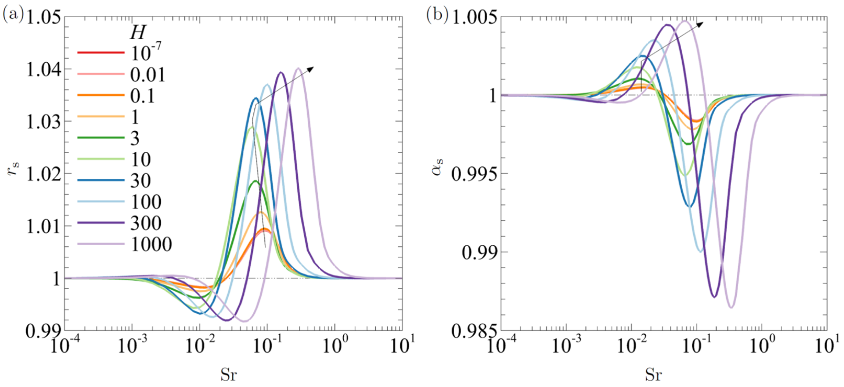

FIG. 4. Variation in r_s and α_s as a function of Sr at $\Gamma = 100$, curves of constant H (arrows indicate increasing H). As $\mathrm{Sr} \to 0$ and $\mathrm{Sr} \to \infty$, the agreement with the steady result is further validation.

points also become increasingly isolated as the oscillating boundary layers become thinner. The thinner boundary layers reduce constructive interference between modes at each wall, stabilizing the flow [22]. Eventually, the oscillating boundary layers become so thin that they are immaterial and r_s drops to recover the steady value ($\mathrm{Sr} \to \infty$).

The other friction parameters are now considered. For larger H, as H is increased, the curves in figure Fig. 4(a) shift to larger Sr. Increasing H smooths inflection points within the pulsatile boundary layer. Recall that a pulsatile isolated SM82 boundary layer has the form $e^{-ry}\cos(sy - t)$, and increasing H decreases s, thereby increasing the wavelength of wall-normal oscillations in the base flow. Larger Sr values are then required to offset the larger H values, ensuring that inflection points remain within the boundary layer, and provide enough intracylic growth to reduce r_s. Thus, the local minimum of r_s does not strongly depend on H, although the corresponding Sr value varies greatly. Importantly, for fusion relevant regimes, the percentage reduction in $\mathrm{Re}_{\mathrm{crit}}$ appears

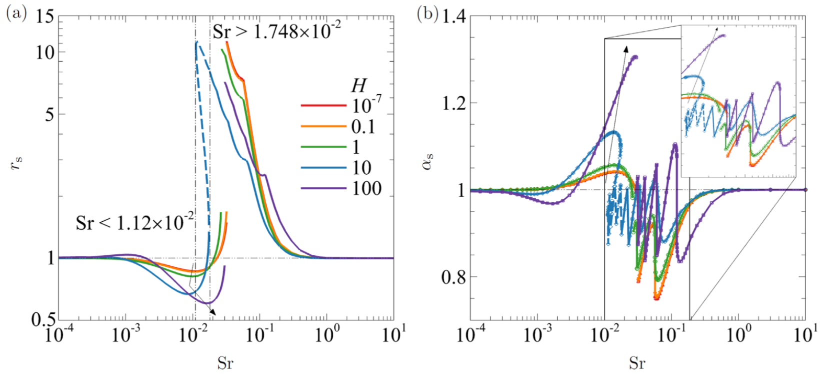

FIG. 5. Variation in r_s and α_s as a function of Sr at $\Gamma = 10$, curves of constant H (arrows indicate increasing H). Dashed curve indicates restabilization and a second destabilization with increasing $\mathrm{Re} > \mathrm{Re}_{\mathrm{crit}}$ at $H = 10$. The stable region is below the continuous solid-dashed-solid curve.

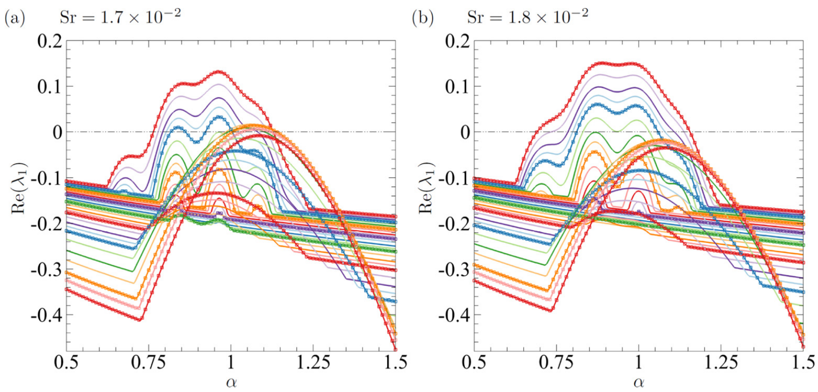

FIG. 6. Exponential growth rate as a function of α with increasing Re (8×10^4 through 8×10^5) at $H = 10$, $\Gamma = 10$, comparing Sr. At $\mathrm{Sr} = 1.8 \times 10^{-2}$ the TS-like mode does not become unstable, thus $\mathrm{Re}_{\mathrm{crit}} = 6.40840 \times 10^5$ is much larger than $\mathrm{Re}_{\mathrm{crit}} = 8.50617 \times 10^4$ at $\mathrm{Sr} = 1.7 \times 10^{-2}$. As additional validation, symbols (timestepper) show excellent agreement with curves (Floquet).

to steadily improve with increasing H, although the shift to higher Sr may eventually invalidate the SM82 assumption requiring $\mathrm{Sr} < 1/2$ for $\Gamma \geqslant 1$. The pulsatile boundary layers also become increasingly isolated with increasing H, as r increases with H, resulting in the steady increase in the maximum of r_s. At $\Gamma = 100$, the variations in $\mathrm{Re}_{\mathrm{crit}}$ are small, with the Reynolds number dependence of the base flow having little effect, relative to the Sr and H variations (this is not the case at $\Gamma = 10$). As a last note, for $\Gamma = 100$, the smooth α_s curves in Fig. 4(b) also show that the variations in r_s represent the same instability mode for all Sr (henceforth the TS-like mode).

At the lower $\Gamma = 10$, Fig. 5, the oscillating component plays a much greater role. The underlying behaviors discussed for $\Gamma = 100$ still hold for smaller Sr, including the region of minimum r_s, and for much larger Sr. Furthermore, the local minimum in r_s still becomes more pronounced with increasing H, with an approximately 33.0% reduction in $\mathrm{Re}_{\mathrm{crit}}$, compared to the steady value at $H = 10$. $H = 1000$ could not be computed over a wide range of Sr at $\Gamma = 10$ but the partial data collected (not shown) demonstrated a further reduction in r_s of up to 42.4%.

The degree of stabilization at $\Gamma = 10$ is far more striking. The sudden jumps in α_s, shown in the inset of Fig. 5(b), indicate different instability modes. These modes are increasingly stable, with much larger accompanying r_s values (the $H = 10$ case peaks with an approximately 804% increase over the steady $\mathrm{Re}_{\mathrm{crit}}$). Because the Reynolds numbers are significantly far from the steady $\mathrm{Re}_{\mathrm{crit}}$ values, the change in Reynolds number has had a noticeable effect on the base flow profiles. At larger Reynolds numbers, the oscillating boundary layers become much thinner, so inflection points are not positioned where they could underpin sizable intracyclic growth.

This explains the discontinuous change in r_s with a slight shift in Sr. At fixed Sr, at Reynolds numbers near the steady $\mathrm{Re}_{\mathrm{crit}}$ value, a TS-like mode is excited, but not necessarily unstable. The TS-like mode is based on the instability of the steady flow, i.e., the TS wave. For $\mathrm{Re} > \mathrm{Re}_{\mathrm{crit}}$, its exponential growth rate increases with increasing Reynolds number. However, the same increase in Re increasingly isolates and thins the boundary layers, thus reducing the exponential growth rate. The isolation of the boundary layers (the effect of Re on the base flow) eventually overcomes any increases in exponential growth rate (the effect of Re on the perturbation). At higher Sr, when the oscillating boundary layers are naturally further apart, the increased isolation prevents the instability of the TS-like mode. This is shown at $\mathrm{Sr} = 1.8 \times 10^{-2}$ in Fig. 6(b), or to the right of the discontinuity in r_s on Fig. 5(a). The sudden increase in r_s in Fig. 5(a) reflects the stabilization

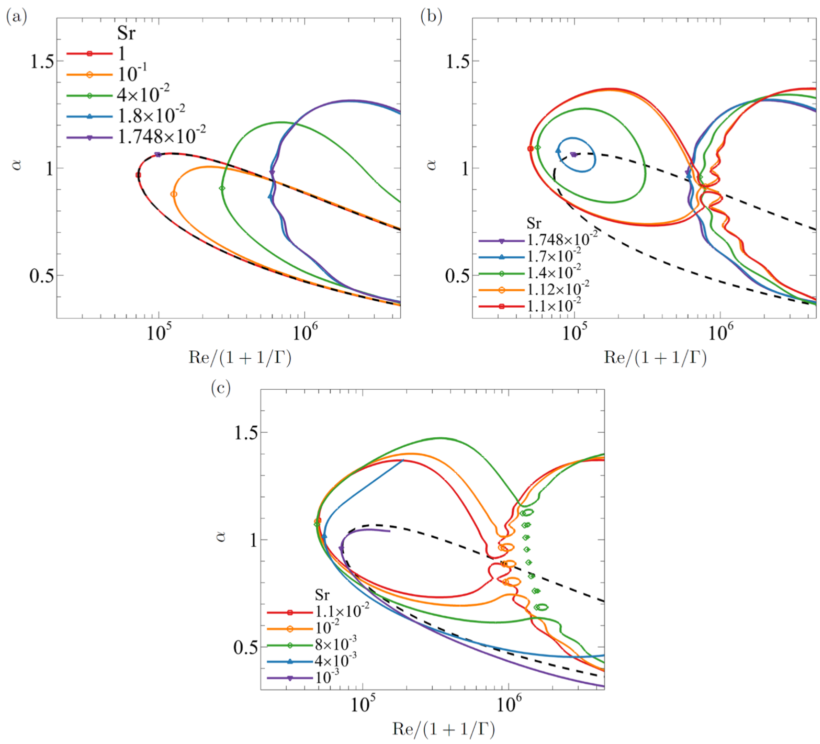

FIG. 7. Neutral curves for various Sr, at $\Gamma = 10$, $H = 10$, with instability to the right of open curves. (a) Sr from the steady result, to the first destabilization of the TS-like mode (unstable pocket) at $\mathrm{Sr} \leqslant 1.748 \times 10^{-2}$. (b) Dominance of the TS-like mode, and eventual vanishing of the restabilization region for $\mathrm{Sr} \leqslant 1.1 \times 10^{-2}$. (c) Instability for all $\mathrm{Re} > \mathrm{Re}_{\mathrm{crit}}$, including the local $\mathrm{Re}_{\mathrm{crit}}$ minimum (near $\mathrm{Sr} = 9 \times 10^{-3}$). However, stable pockets form at higher Re. The black dashed curves correspond to the steady base flow at $H = 10$ [22].

of the TS-like mode (another mode is destabilized at a much higher Re). At smaller Sr, the effect of Re on increasing the growth rate allows the TS-like mode to become unstable, if only briefly at $\mathrm{Sr} = 1.7 \times 10^{-2}$ in Fig. 6(a). With further increasing Re, the isolation and thinning of the boundary layers leads to the TS-like mode becoming stable again; the stable region is bounded by the dashed curve in Fig. 5(a). At $\mathrm{Sr} = 1.7 \times 10^{-2}$, a different mode becomes unstable at much higher Re, as also shown in Fig. 6(a). This mode is a very similar to that at $\mathrm{Sr} = 1.8 \times 10^{-2}$, so the dashed curve in Fig. 5(a) follows the trend of increasing r_s from the right of the discontinuity. Eventually, for all $\mathrm{Sr} < 1.12 \times 10^{-2}$ ($H = 10$, $\Gamma = 10$), with oscillating boundary layers that start out closer together, at least one mode is unstable for all Re.

Further considering $\Gamma = 10$ and $H = 10$, neutral (zero net growth) curves at several Sr are presented in Fig. 7. The $\mathrm{Sr} = 1$ neutral curve is indistinguishable from that of the steady base flow [22]. With decreasing Sr, the critical Reynolds number rapidly increases and the neutral curve broadens, see Fig. 7(a). At $\mathrm{Sr} = 1.8 \times 10^{-2}$, just to the right of the discontinuity, waviness in the neutral curve reflects the excitation of multiple modes, as shown in Fig. 6(b). At $\mathrm{Sr} = 1.748 \times 10^{-2}$, just to the left of the discontinuity, the TS-like mode is first destabilized. The increasing isolation of the oscillating

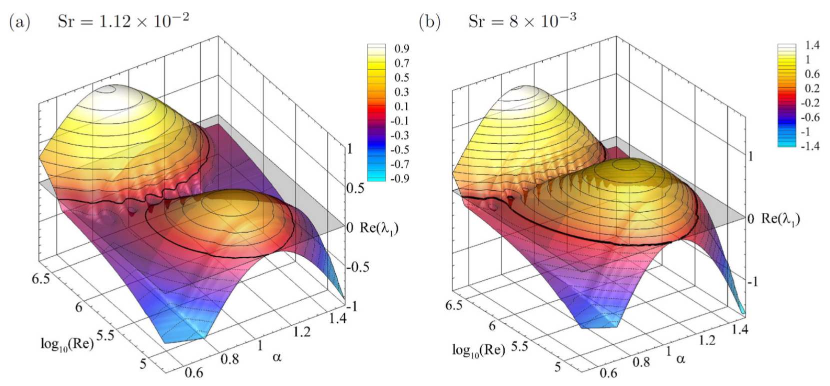

FIG. 8. Exponential growth rate as a function of α and Re ($\mathrm{Re}_{\mathrm{crit}}$ through 5×10^6). At low Re, only the TS-like mode is unstable. After this mode restabilizes, multiple modes are excited, separated by sharp valleys. These modes have negative growth for some Re at $\mathrm{Sr} = 1.12 \times 10^{-2}$, but have positive growth at $\mathrm{Sr} = 8 \times 10^{-3}$. Solid lines denote positive growth; dotted lines negative. Zero growth is emphasized with a thick black line on a gray intersecting plane.

boundary layers quickly restabilizes the flow, resulting in a very small instability pocket. Moving to Fig. 7(b), with slight decreases in Sr, the (TS-like mode's) instability pocket rapidly occupies more of the wave number space, and the pocket terminates before it reaches the broader, pulsatile part of the neutral curve at $\mathrm{Sr} = 1.12 \times 10^{-2}$ (the leftmost point of the dashed curve in Fig. 5). With a slight drop to $\mathrm{Sr} = 1.1 \times 10^{-2}$, the two curves meet, with a small throat allowing a path through wave number space with increasing Re that always attains positive growth. At $\mathrm{Sr} = 1.12 \times 10^{-2}$, also shown in Fig. 8(a), the TS-like mode (the first local maximum) initially peaks and then falls away with increasing Re. A small band of Reynolds numbers fail to produce net growth (along the line of six depressions in the wave-number space). Increasing Re, multiple pulsatile modes become excited from the baseline spectrum and become unstable. At $\mathrm{Sr} = 1.1 \times 10^{-2}$, the rising pulsatile modes outpace the falling TS-like mode, so at least one mode always maintains positive growth, see Fig. 8(b).

At $\mathrm{Sr} = 10^{-2}$, three stable pockets are observed, see Fig. 7(c). At lower Sr, the growth rates of the TS-like mode decrease more rapidly, leaving only pulsatile modes in control of the neutral stability behavior. Because these modes are excited in narrow resonant peaks in wave-number space, stable regions can be present between the peaks. Thus, at lower Sr, multiple stable pockets surrounded by unstable conditions form. Further reduction in Sr produces more resonant peaks, and more interleaved stable pockets, as shown at $\mathrm{Sr} = 8 \times 10^{-3}$ in Fig. 8(b). Further reducing Sr, for large H and Re, reaches the limit of the capability of the timestepper to cleanly resolve the entire neutral curves. By $\mathrm{Sr} = 10^{-3}$, the part of the neutral curve able to be computed is approaching that of the steady base flow [22].

The influence of Γ is now considered. Over $1 \leqslant \Gamma \leqslant 100$, different effects on r_s are observed at $\mathrm{Sr} = 1$, Fig. 9(a), and at $\mathrm{Sr} = 10^{-2}$, Fig. 9(b). As $\mathrm{Sr} = 1$, close to the steady limit, r_s remains near unity. At small H, only stabilization is observed for all $\Gamma \geqslant 1$. With increasing H, a slight destabilization can be observed with increasing H, up to $H \approx 10$. Further increasing H induces restabilization. This echoes the Sr variation, where the local minimum shifts to smaller Sr for $H \lesssim 10$, and shifts back to larger Sr for $H \gtrsim 10$. At higher H, H offsets Sr, so the results for the steady base flow are only recovered at increasingly large Sr. On the other hand, at $\mathrm{Sr} = 10^{-2}$ in Fig. 9(b), r_s is far from unity, and the effect of varying the Reynolds number on the base flow must again be considered. At smaller Re, the oscillating boundary layers are much thicker, with prominent

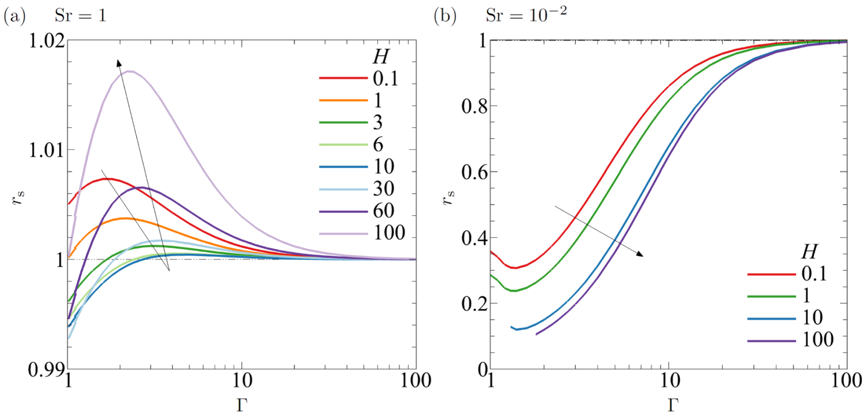

FIG. 9. Variation in r_s as a function of $\Gamma \geqslant 1$ at Sr = 1 and Sr = 10^{-2}, curves of constant H (arrows indicate increasing H). Small Sr and Γ present significant potential for destabilization.

inflection points well placed to promote intracyclic growth. This part of the base flow becomes increasingly dominant with decreasing Γ, favoring the destabilization of the TS-like mode. Given that $(\mathrm{SrRe})^2 \gg H^2$, $\mathrm{Re}_{\mathrm{crit}}$ depends far more on the pulsatile process and only weakly on H, until SrRe becomes small. However, the $\mathrm{Re}_{\mathrm{crit}}$ for the steady base flow strongly depends on H, so r_s reduces with increasing H. r_s continues to decrease up to $\Gamma \gtrsim 1$ for $H \leqslant 10$, matching well with the conclusion of Ref. [28] that the maximum reduction in $\mathrm{Re}_{\mathrm{crit}}$ occurs near unity amplitude ratio. At higher H, the magnitude of intracylic growth eventually limited computations (to $\Gamma > 1$). At $H = 100$, Sr $= 10^{-2}$ no local minimum is observed for $\Gamma \geqslant 1$. However, these results still indicate that for $H \leqslant 100$ and $\Gamma \geqslant 1$, a 70 to 90% reduction in the critical Reynolds number is possible with the addition of pulsatility. They further support that the percentage reduction in $\mathrm{Re}_{\mathrm{crit}}$ improves with increasing H. The mode defining this local minimum, even at small Γ, still appears to be directly related to the TS-like mode (as there were no sharp changes in the dominant α through the entire Sr − Γ − Re space).

Given the results of Fig. 9(b), it is worth considering the maximum reduction in r_s that can be obtained via optimization of the pulsation over $10^{-4} < \mathrm{Sr} < 1$ and $1 < \Gamma < \infty$. These have been tabulated for increasing H in Table III. These optimized pulsations truly highlight how effective pulsatility can be in destabilizing a Q2D channel flow, both at hydrodynamic conditions, with a 69.3% reduction at $H = 10^{-7}$, all the way up to a 90.3% reduction at $H = 10$. Still larger percentage reductions are predicted at higher H, as r_s consistently decreases with increasing H.

C. Intracylcic behavior

This section is focused on processes taking place within each cycle that are obscured in the net growth quantifications. All results in this section are at $\mathrm{Re}_{\mathrm{crit}}$.

The TS-like mode at $\Gamma = 100$ and $H = 100$ is considered first, in Fig. 10, over a range of Sr. The perturbation norm $\|\tilde{v}\|_2$ is compared to $E_{\mathrm{U}}(t) = \int U^2\,\mathrm{d}y - \langle \int U^2\,\mathrm{d}y \rangle_t$ (taking the value of the current base flow energy about the time mean solely to aid figure legibility). There are only simple, sinusoidal energy variations at these conditions and perturbation energies remain order unity over the entire cycle (akin to the cruising regime). The key result is that the phase difference between the perturbation and base flow energy curves changes as Sr is varied. Measuring the phase difference ψ_{d} of the local minimums of the perturbation and base flow energies appears most meaningful and

TABLE III. Optimization of the pulsation (optimizing Γ, Sr, and α) for the greatest reduction in the rescaled critical Reynolds number relative to the steady result. This is achieved at Γ just above unity and pulsation frequencies similar to those of the local minimum for the TS-like mode, Figs. 4(a) and 5(a). Importantly, the percentage reduction improves with increasing H, with over an order of magnitude reduction in critical Reynolds number for $H \geqslant 10$.

H	$\mathrm{Re}_{\mathrm{crit,s}}$	$\alpha_{\mathrm{crit,s}}$	Γ	Sr	$\mathrm{Re}_{\mathrm{crit}}/(1+1/\Gamma)$	α	r_s	α_s	% Reduction
10^{-7}	5772.22	1.02055	1.29	7.8×10^{-3}	1773.29	1.3812	0.3072	1.3534	**69.28**
0.01	5808.04	1.01991	1.29	7.8×10^{-3}	1777.58	1.3804	0.3061	1.3535	**69.39**
0.1	6136.85	1.01435	1.29	7.8×10^{-3}	1816.18	1.3823	0.2959	1.3628	**70.41**
0.3	6908.55	1.00291	1.27	7.6×10^{-3}	1902.79	1.3857	0.2754	1.3816	**72.46**
1	10033.2	0.97163	1.24	7.2×10^{-3}	2215.87	1.3980	0.2209	1.4388	**77.91**
3	21792.6	0.93194	1.19	6.3×10^{-3}	3185.90	1.4343	0.1462	1.5391	**85.38**
10	72436.8	0.96833	1.19	5.6×10^{-3}	7050	1.59	0.0973	1.6420	**90.27**

these values are annotated on Fig. 10. The perturbation energy variation exhibits a lag to the base flow energy variation at $\mathrm{Sr} = 10^{-3}$, with $\psi_d = -0.2446$, and is closer to in phase by $\mathrm{Sr} = 10^{-2}$, $\psi_d = -0.1466$ (the optimal Sr is 1.5×10^{-2} for minimising r_s at $\Gamma = 100$). By $\mathrm{Sr} = 10^{-1}$, the perturbation energy leads the base flow energy (positive ψ_d), and intracyclic growth in noticeably smaller. $\mathrm{Sr} = 1$ is close enough to the $\mathrm{Sr} \to \infty$ limit to produce negligible intracyclic growth. The minimum in r_s tends to occur when the perturbation and base flow energy growths are close to being in phase. Thus, selecting the optimal Sr to minimize r_s at a given Γ (and H) amounts to tuning the frequency of the oscillating flow component to ensure growth in the base flow and perturbation energies coincide.

The energy norms at $\Gamma = 10$, $H = 10$ are displayed in Fig. 11. At $\mathrm{Sr} = 10^{-3}$, Fig. 11(a), toward the steady base flow limit, the variation of the perturbation is again a simple sinusoid, slightly lagging behind the base flow energy variation, as for $\Gamma = 100$, Fig. 10(a). However, at $\Gamma = 10$, the increase in intracylcic growth with reducing Γ can be clearly observed, eclipsing six orders of magnitude. Thus, at lower Γ and Sr, a behavior akin to the ballistic regime is reached. At $\mathrm{Sr} = 10^{-2}$, intracyclic growth remains large (the local minimum in r_s occurs at $\mathrm{Sr} = 9 \times 10^{-3}$). An additional complexity in the form of a brief growth in perturbation energy (at $t_P \approx 0.25$) occurs during the acceleration phase of the base flow and is not detected at $\mathrm{Sr} < 9 \times 10^{-3}$. The additional growth incurred by the presence of inflection points is somewhat obscured by the lower $\mathrm{Re}_{\mathrm{crit}}$ at $\mathrm{Sr} = 10^{-2}$. Increasing Sr to 10^{-1}, the TS-like mode is no longer the least stable. At this Sr, the intracyclic growth is relatively small, likely falling in the cruising regime, while by $\mathrm{Sr} = 1$ the intracylcic growth again becomes trivial.

The linearized evolutions of the leading eigenvector are depicted over the period of the base flow in Fig. 12. At $\Gamma = 100$, the dominant mode is the TS-like mode for all Sr, with a structure that does not observably change with time, as shown in the accompanying animation [46]. The amplitude variations are also small; many repetitions of the wave are visible at lower Sr as the advection timescale is much smaller than the transient inertial timescale. Although the mode has a very similar appearance to that of a steady TS wave, the additional isolation of the boundary layers means that the $H = 100$ pulsatile mode resembles a $H = 400$ steady mode [22]. Once H is reduced, separate TS waves are no longer observed at each wall, but appear as a single conjoined structure. While at larger Sr, the $H = 10$, $\Gamma = 10$ mode structure still displays minimal time variation. Only at $\mathrm{Sr} = 10^{-2}$ is significant unsteadiness observed, slightly towards the walls, and prominently during the disruption of the decay phase (at $t_P \approx 0.25$). However, the general appearance of the structure as a conjoined TS wave persists (this case is also animated [46]).

Finally, at $H = 1$, the optimized conditions ($\Gamma = 1.24$, $\mathrm{Sr} = 7.2 \times 10^{-3}$) and nearby Sr are considered, with the energy norms displayed in Fig. 13. A smaller Γ features staggering intracyclic

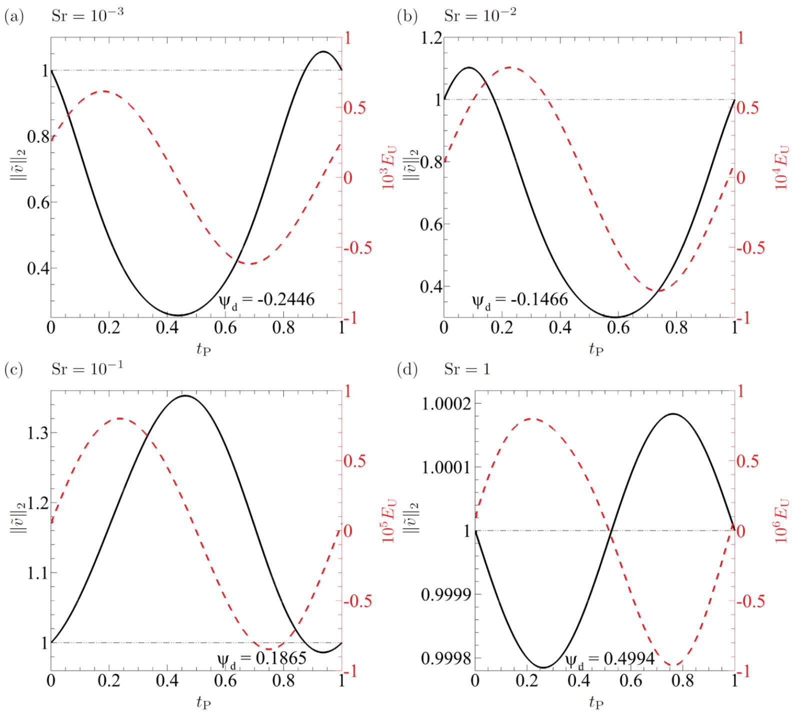

FIG. 10. The perturbation norm (solid; black) and the base flow energy relative to the time mean (dashed; red) over one period at critical conditions at $H = 100$, $\Gamma = 100$, for various Sr. The phase differences ψ_d between the local minimums of each pair of curves are also annotated.

growth, with almost 24 orders of magnitude of growth at Sr $= 10^{-3}$. Similar to previous cases, at lower Sr the local minimum in perturbation energy significantly lags behind the minimum in the base flow energy, $\psi_d = -0.2380$. However, an additional feature at smaller Sr and Γ is that the perturbation decay is more rapid, and almost plateaus at low energies (with neither a smooth transitioning from growth to decay nor sharp bounce back up). At the slightly larger Sr $= 4 \times 10^{-3}$, the decay is not so rapid (decaying over $0.112 < t_P < 0.653$ compared to $0.008 < t_P < 0.491$),with a sharp bounce back to growth and a smaller lag in the locations of the local minima, $\psi_d = -0.0996$. At the optimized Sr $= 7.2 \times 10^{-3}$, the decay rate of the perturbation is matched to the period of the base flow, the local minima in energy are close to coinciding ($\psi_d = -0.0282$), and so inflection points are maintained throughout the deceleration phase (r_s is then minimized). At larger Sr, the perturbation energy leads the base flow energy ($\psi_d = 0.0195$), and the deceleration phase is not used to its full extent.

The evolution of the optimized perturbation at $H = 1$ is shown in Fig. 14, and in a supplementary animation [46]. From $t_P = 0$, the perturbation is slowly growing, aided by the single large inflection points present in each half of the domain. As these become less pronounced, the wings of the perturbation are pulled in ($t_P = 0.2$). By this point, inflection points in the base flow have vanished, as the wall oscillation follows through to negative velocities, although a small amount of residual growth is maintained. The pull of the walls on the central structure sweeps the wings forward ($t_P =$

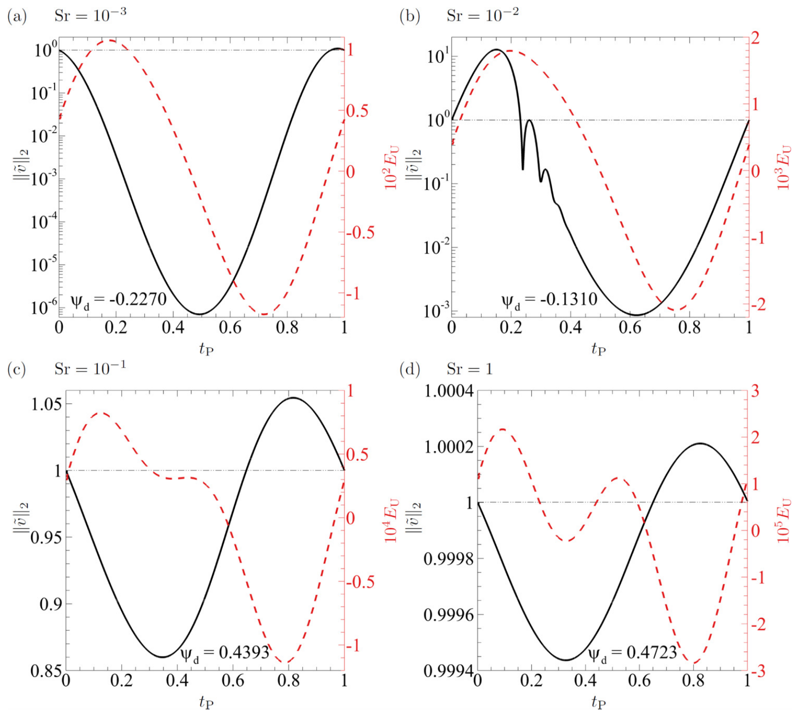

FIG. 11. The perturbation norm (solid, black) and the base flow energy relative to the time mean (dashed, red) over one period at critical conditions at $H = 10$, $\Gamma = 10$, for various Sr. The phase differences ψ_d between the local minimums of each pair of curves are also annotated.

0.3) as the base flow velocity in the central region is smaller than the velocities near the walls. The downstream pull of the walls acts to increasingly shear the structure, with perturbation decay until $t_P = 0.738$. The structure rapidly reorients to the wider forward winged structure just as inflection points reappear in the base flow, near $t_P = 0.75$. As these inflection points become more pronounced, rapid growth occurs, while the wings are swept further forward.

IV. NONLINEAR ANALYSIS

A. Formulation and validation

We now seek to investigate the nonlinear behavior of the optimized pulsations at various H. As a first step in investigating transitions to turbulence, the modal instabilities predicted in the preceding sections are targeted by the DNS. Although linear or nonlinear transiently growing disturbances may initiate bypass transition scenarios [47–51], the modal instability seemed the natural starting point. Furthermore, if the modal instability has a large decay rate, linear transient growth mechanisms can be strongly compromised [52], as observed for cylinder wakes in particular [53]. Finally, previous work on steady Q2D transistions observed that only turbulence generated by a modal instability [22,24] was sustainable in wall-driven channel flows.

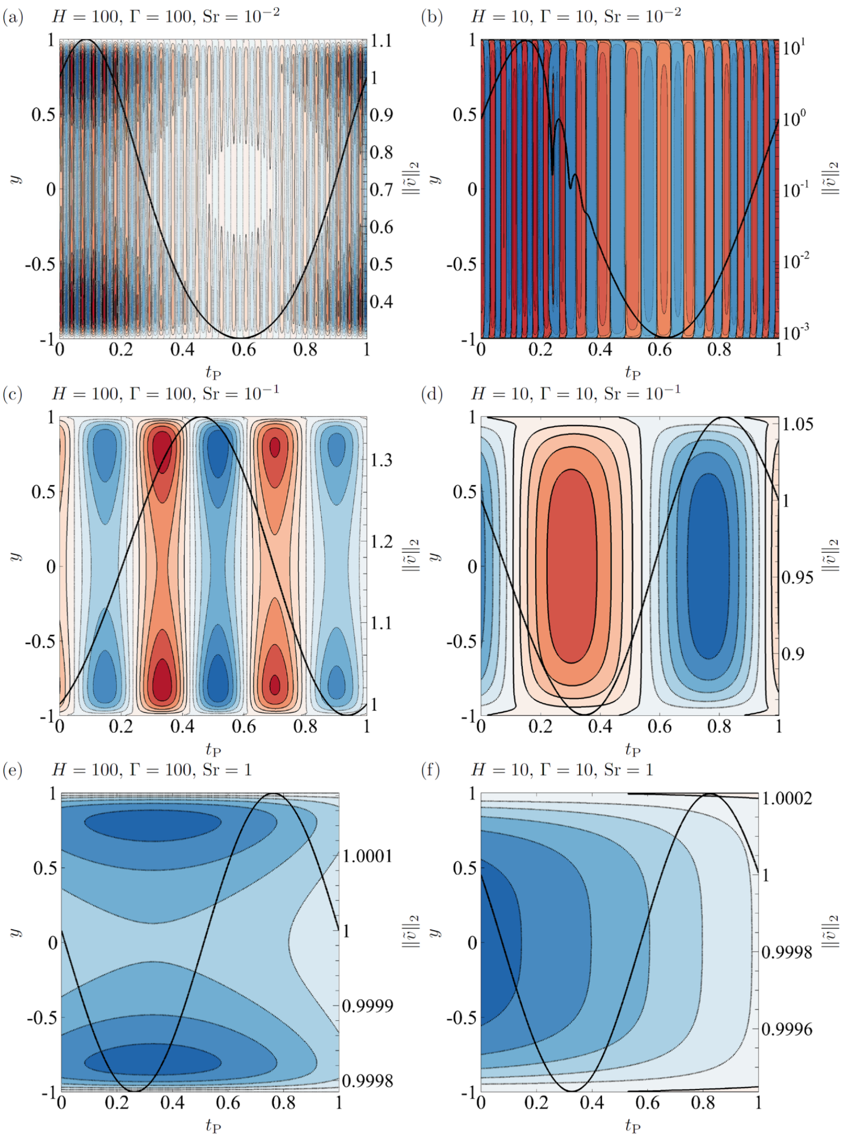

FIG. 12. The linear evolution of the leading eigenvector $\tilde{v}(y, t)$ over one period. Linearly spaced contours between $\pm \max |\tilde{v}|$ are plotted, solid lines (red flooding) denote positive values, dotted lines (blue flooding) negative values, except for $H = 10$, $\mathrm{Sr} = 10^{-2}$, with logarithmically spaced contours between -15 and 15. Perturbation norms $\|\tilde{v}\|_2$ from Figs. 10 and 11 are overlaid.

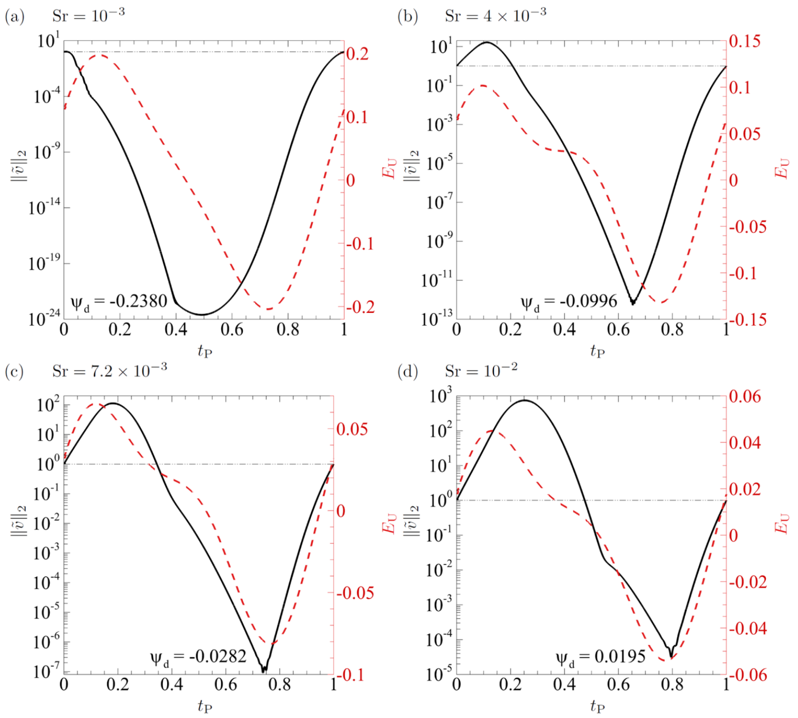

FIG. 13. The perturbation norm (solid, black) and the base flow energy relative to the time mean (dashed, red) over one period at critical conditions at $H = 10$, $\Gamma = 1.24$, for various Sr. The $\mathrm{Sr} = 7.2 \times 10^{-3}$ case represents the optimized pulsation for this H, recalling Table III. The phase differences ψ_d between the local minimums of each pair of curves are also annotated.

The DNS of Eqs. (1) and (2) is performed as follows. The initial field is solely the analytic solution from Sec. II, $\boldsymbol{u} = U(y, t = 0)$. The initial phase did not prove relevant with either an initial seed of white noise, or no initial perturbation. The flow is driven by a constant pressure gradient, $\partial P/\partial x = \gamma_1(\cosh(H^{1/2})/(\cosh(H^{1/2}) - 1))H/\mathrm{Re}$, with the pressure decomposed into a linearly varying and fluctuating periodic component, as $p = P + p'$, respectively. Periodic boundary conditions, $\boldsymbol{u}(x = 0) = \boldsymbol{u}(x = W)$ and $p'(x = 0) = p'(x = W)$, are applied at the downstream and upstream boundaries. The domain length $W = 2\pi/\alpha_{\max}$ is set to match the wave number that achieved maximal linear growth $\alpha_{\max}$. Synchronous lateral wall movement generates the oscillating flow component, with boundary conditions $U(y \pm 1, t) = \gamma_2 \cos(t)$.

Simulations are performed with an in-house spectral element solver, employing a third-order backward differencing scheme, with operator splitting, for time integration. High-order Neumann pressure boundary conditions are imposed on the oscillating walls to maintain third order time accuracy [54]. The Cartesian domain is discretized with quadrilateral elements over which Gauss–Legendre–Lobatto nodes are placed. The mesh design is identical to that of Ref. [22]. The wall-normal resolution was unchanged, although the streamwise resolution was doubled. Elements are otherwise uniformly distributed in both streamwise and transverse directions, ensuring perturbations

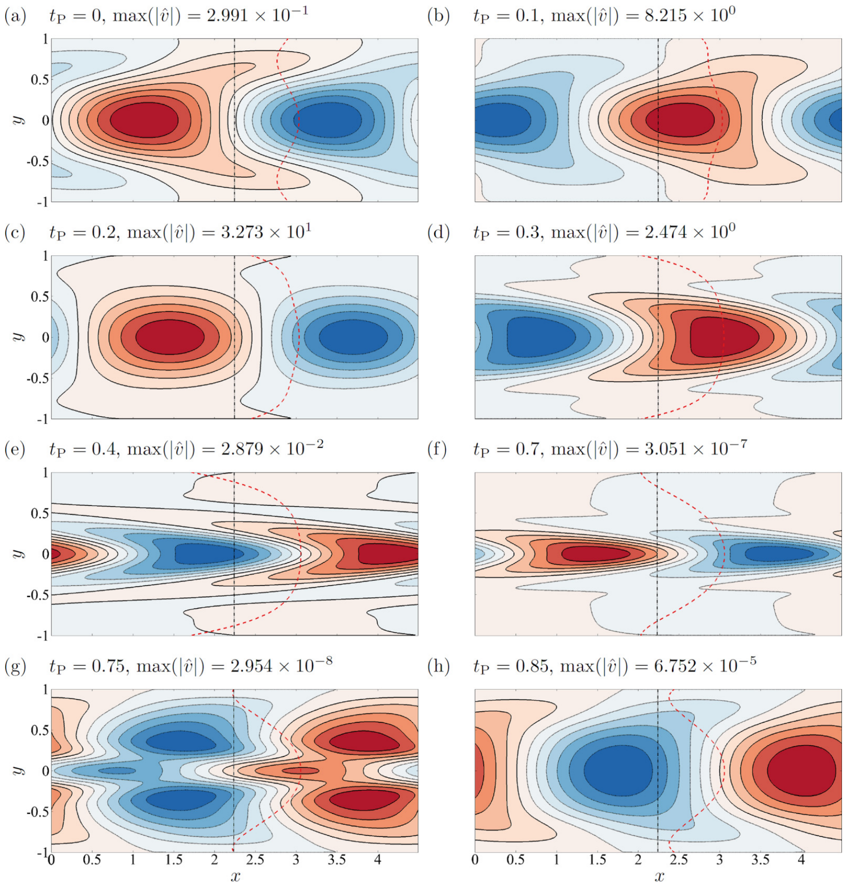

FIG. 14. Snapshots of the eigenvector expanded in the streamwise direction $\hat{v} = \tilde{v}(y, t)\exp(i\alpha x)$ through one cycle $t_P \in [0, 1]$ at $H = 1$, $\Gamma = 1.24$, $\mathrm{Sr} = 7.2 \times 10^{-3}$. The base flow is overlaid (the black dashed line indicates zero base flow velocity). Red flooding positive, blue flooding negative.

remain well resolved during all phases of their growth. The solver, incorporating the SM82 friction term, has been previously introduced and validated [4,19,55,56].

Further validation, depicted in Fig. 15(a), is a comparison between the nonlinear time evolution in primitive variables (the in-house solver, referred to as DNS in the future) and the linearized evolution with the timestepper, introduced earlier. These are both computed using the $\mathrm{Re}_{\mathrm{crit}}$ and α_{crit} from the Floquet method, at $H = 10$, $\Gamma = 10$ and $H = 100$, $\Gamma = 100$, both at $\mathrm{Sr} = 10^{-2}$ (cases discussed in Sec. III C). Initial seeds of white noise have specified initial energy $E_0(t = 0) = \int \hat{u}^2 + \hat{v}^2 \, d\Omega / \int U^2(t = 0) \, d\Omega$, where Ω represents the computational domain. Linearity is ensured with $E_0 = 10^{-6}$. The DNS settles after a short period of decay, and then attains excellent agreement with the intracyclic growth curves from the linearized timestepper, both in magnitude and dynamics over the cycle. The only difference is that for the $\Gamma = 10$ case, at small perturbation amplitudes (near

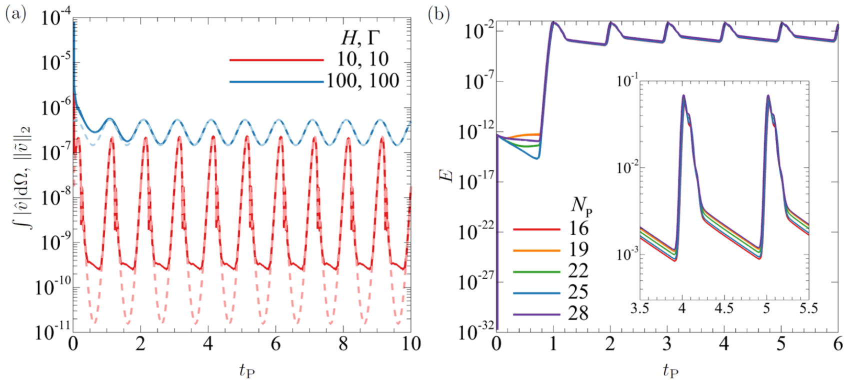

FIG. 15. Resolution testing at critical conditions. (a) Comparison of nonlinear DNS (in-house solver, solid lines) and linearized timestepper (dashed lines) at $\mathrm{Sr} = 10^{-2}$. An initial perturbation of white noise with $E_0 = 10^{-6}$ was applied to the DNS. (b) Nonlinear DNS with no initial perturbation of the $H = 1$ optimized pulsation ($\Gamma = 1.24$, $\mathrm{Sr} = 7.2 \times 10^{-3}$), varying polynomial order.

10^{-10}) the nonlinear evolution cuts out and remains at roughly constant energy until the deceleration phase of the base flow to begin growth again, while the linearized evolution continues on a smooth decay-growth trajectory.

The resolution requirements are assessed by varying the polynomial order N_p of the spectral elements. Figure 15(b) depicts simulations, with no initiating perturbation, driven by the optimized pulsation at $H = 1$, at critical conditions. Excluding the initial growth, which is always resolution dependent, the agreement in the intracylic growth stages is excellent (see box out). The slight differences predominantly originate from the initial growth stage, translating the curves with respect to one another. $N_p = 19$ was deemed sufficient for the pulsatile problem, as for the steady base flow problem [22].

Fourier analysis is also performed in the nonlinear simulations, exploiting the streamwise periodicity of the domain. The absolute values of the Fourier coefficients $c_\kappa = |(1/N_f)\sum_{n=0}^{n=N_f-1}\hat{f}(x_n)e^{-2\pi i\kappa n/N_f}|$ were obtained using the discrete Fourier transform in MATLAB, where x_n represents the nth x location linearly spaced between $x_0 = 0$ and $x_{N_f} = W$. $\hat{f}$ may be $\hat{u}$, $\hat{v}$, $\hat{\omega}_z = \partial\hat{v}/\partial x - \partial\hat{u}/\partial y$ or $\hat{u}^2 + \hat{v}^2$, depending on the property of interest. In the y direction, either a mean Fourier coefficient $\bar{c}_\kappa$ is obtained by averaging the coefficients obtained at 21 y values, and taking $N_f = 10000$. Alternately, considering 912 y values, and taking $N_f = 380$, all except the jth (and $N_f - j$th) Fourier coefficients were set to zero, $c_{\kappa,\neg j} = 0$, and the inverse discrete Fourier transform $\hat{f}_j = \sum_{\kappa=0}^{\kappa=N_f-1} c_{\kappa,j}e^{2\pi i\kappa n/N_f}$ computed. After isolating the jth mode in the physical domain $\hat{f}_j$, an assessment of the degree of symmetry within that mode was determined by computing $\hat{f}_{s,j} = (\sum_{m=0}^{m=N_y}[\hat{f}_j(y_m) - \hat{f}_j(-y_m)]^2)^{1/2}$, where y_m represents the mth y location linearly spaced between $y_0 = -1$ and $y_{N_y} = 0 - 1/(N_y - 1)$ and taking $N_y = 912/2$. Thus, a purely symmetric mode has $\hat{f}_{s,j} = 0$ as $\hat{f}_j(y_m)=\hat{f}_j(-y_m)$ for all y_m.

B. Critical conditions

This section focuses solely on the minimum r_s conditions of Table III, at $\mathrm{Re}_{\mathrm{crit}}$. The first factor is the role of the initial perturbation. Comparing a simulation without an initiating perturbation (e.g., numerical noise), and simulations initiated with white noise of specified magnitude, Fig. 16, yields two key results. The first is that all the initial energy trajectories collapse to the numerical

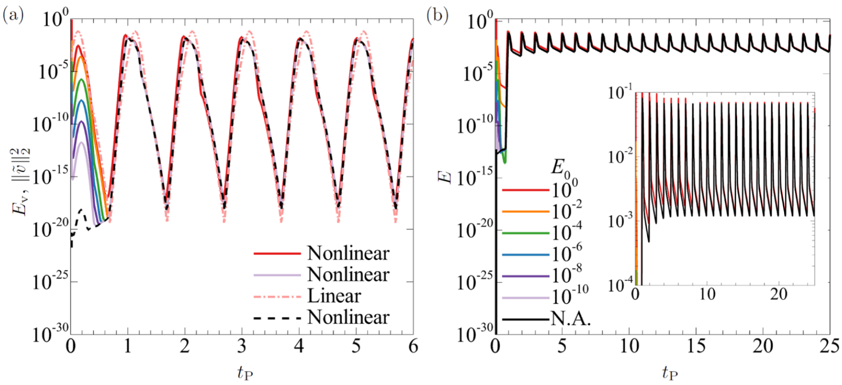

FIG. 16. Effect of varying E_0, between 10^0 and 10^{-10}, on nonlinear evolution, compared to a case without an initial perturbation [black dashed line in (a) and solid line in (b)] and a case linearly evolved (pink dot-dashed line), for the optimized pulsation at $H = 1$, $\Gamma = 1.24$, $\mathrm{Sr} = 7.2 \times 10^{-3}$. (a) $E_v = \int \hat{v}^2 d\Omega$. (b) $E = \int \hat{u}^2 + \hat{v}^2 d\Omega$.

noise result within the first period of evolution, except $E_0 = 1$ (slightly offset). For $E_0 < 1$, the perturbation energy decays no further than for the case initiated from numerical noise and plateaus until the next deceleration phase of the base flow. Once this occurs, all energies grow in unison. As the Γ, Sr optima are within the ballistic regime; they decay to linearly small energies every period [29]. Hence, unless a transition to turbulence occurs in the first period of the base flow, the initial energy has no influence on subsequent cycles. The second key result is that the linear and nonlinear evolutions compared via $E_v = \int \hat{v}^2 d\Omega$ are similar, see Fig. 16(a), while they are not via $E = \int \hat{u}^2 + \hat{v}^2 d\Omega$, Fig. 16(b). In the second period of the base flow, the nonlinear intracyclic decay is largely truncated. After another period, the nonlinear case saturates to relatively constant energy maxima and minima [Fig. 16(b) inset]. Previous works [22,24] have shown that growth in $\hat{v}$ is stored in streamwise independent structures, $\hat{u}$, in nonlinear modal and nonmodal growth scenarios of steady Q2D base flows. A similar process occurs here, as further discussed shortly.

The lack of nonlinear net growth at the critical conditions for the remaining cases in Table III is depicted in Fig. 17, again without specifying an initial perturbation. At higher H, nonlinear intracyclic growth was smaller than expected (linearly, intracyclic growth increased with increasing H at $\mathrm{Re} = \mathrm{Re}_{\mathrm{crit}}$). However, the final result of no net growth is still maintained, as expected at $\mathrm{Re}_{\mathrm{crit}}$. The only slight difference is that at higher H, and thereby larger Re, the maximum and minimum energies reached are becoming inconsistent (see box-out). In the linear solver, such inconsistencies would eventually limit the accurate computation of $\mathrm{Re}_{\mathrm{crit}}$.

C. Supercritical conditions

Supercritical Reynolds numbers are briefly considered, again without specifying an initial perturbation. As the base flow is Reynolds number dependent, only a 10% and a 20% increase (not shown) in the Reynolds number were attempted, for the values of Γ and Sr that minimize r_s for $H \leqslant 10$. The overall behaviors at $\mathrm{Re}/\mathrm{Re}_{\mathrm{crit}} = 1$ (Fig. 17) and $\mathrm{Re}/\mathrm{Re}_{\mathrm{crit}} = 1.1$ (Fig. 18) are virtually identical, even though exponential growth is predicted linearly at $\mathrm{Re}/\mathrm{Re}_{\mathrm{crit}} = 1.1$. Nonlinearly, the intracyclic growth in the first period is large enough to reach nonlinear amplitudes, which quickly modulates the base flow, resulting in the no net growth behavior. However, turbulence is not observed at these supercritical conditions, with only some chaotic behavior following the symmetry breaking of the linear mode. The severity of the decay in the acceleration phase may be the main factor preventing

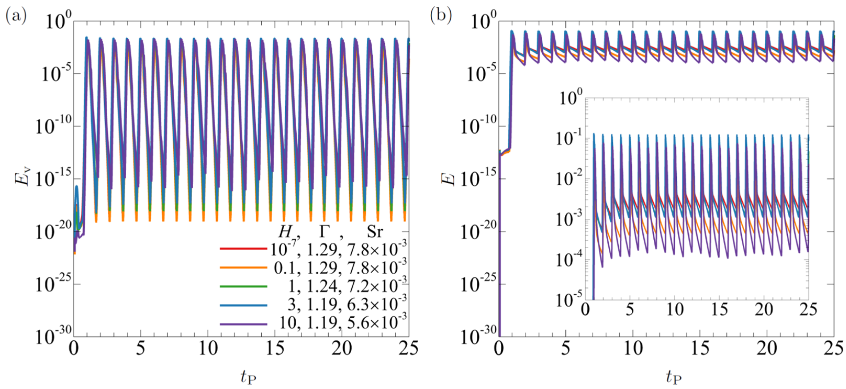

FIG. 17. Nonlinear evolutions of the optimized pulsations, at various H, from Table III. (a) $E_v = \int \hat{v}^2 d\Omega$. (b) $E = \int \hat{u}^2 + \hat{v}^2 d\Omega$. The ultimate result of the nonlinear evolutions is no net growth at $\mathrm{Re}_{\mathrm{crit}}$.

the transition to turbulence. However, the magnitude of H and Re could be a factor, since $H < 3$ are unable to trigger turbulence for the case of a steady base flow at the equivalent $\mathrm{Re}/\mathrm{Re}_{\mathrm{crit}}$ ratio [22]. Although higher H were able to trigger turbulence in the classical duct flow, the magnitude of the Reynolds numbers were larger for the steady base flow, as optimising for minimum r_s results in an order of magnitude reduction in $\mathrm{Re}_{\mathrm{crit}}$.

D. Role of streamwise and wall-normal velocity components

Two aspects of the nonlinear evolution are considered in more detail. The first is the slight difference between the linear and nonlinear growth in $\hat{v}$, observed in Fig. 16(a). Snapshots of the $\hat{v}$ velocity from the DNS are depicted in Fig. 19 over $t_P \in [1.5, 2.5]$; the linear case at the same conditions was shown in Fig. 14, over $t_P \in [0, 1]$. An animation comparing these cases is

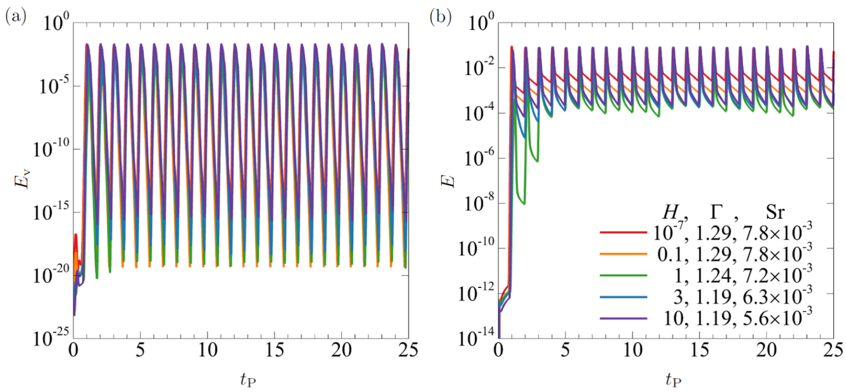

FIG. 18. Nonlinear evolutions of the optimized Sr and Γ for minimum r_s, for various H, at $\mathrm{Re}/\mathrm{Re}_{\mathrm{crit}} = 1.1$. (a) $E_v = \int \hat{v}^2 d\Omega$. (b) $E = \int \hat{u}^2 + \hat{v}^2 d\Omega$. These results are very similar to those at $\mathrm{Re}/\mathrm{Re}_{\mathrm{crit}} = 1$ (Fig. 17) in spite of the fact that linearly, exponential growth is predicted.

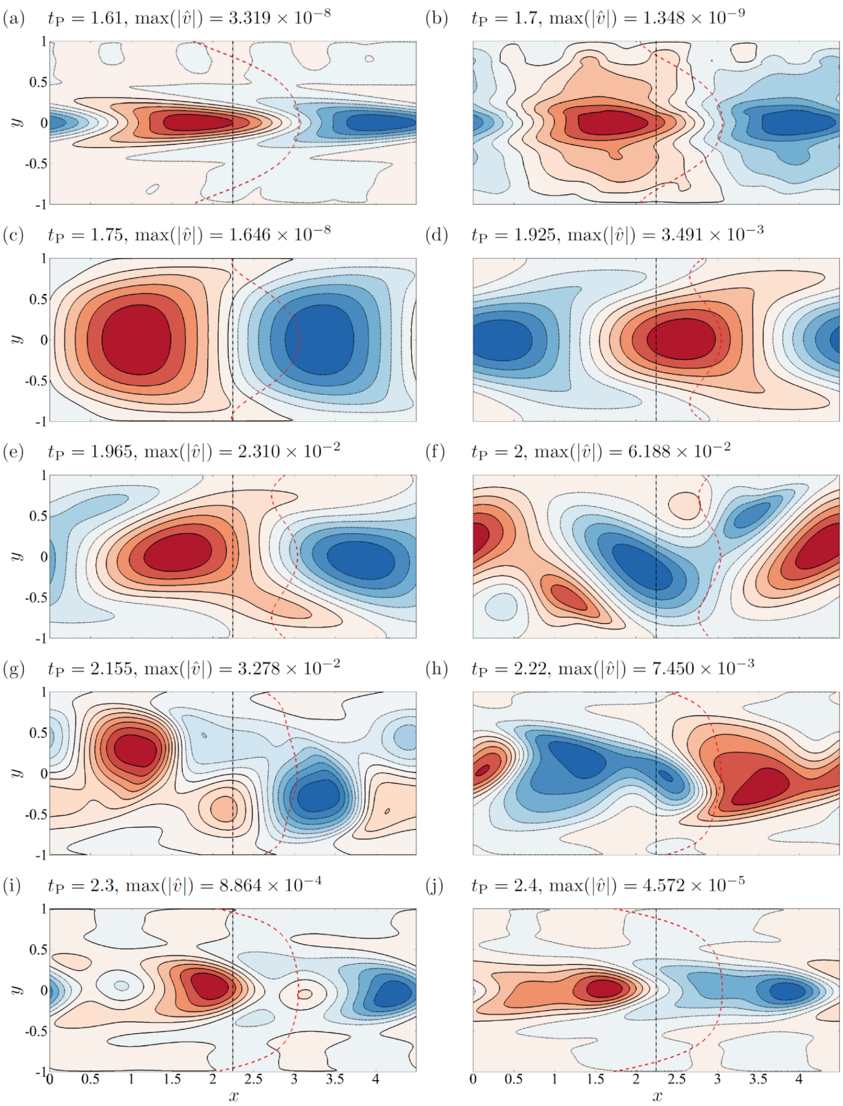

FIG. 19. Nonlinear evolution of $\hat{v}$-velocity perturbation contours at $H = 1$, $\Gamma = 1.24$, $\mathrm{Sr} = 7.2 \times 10^{-3}$ through one cycle $t_P \in [1.5, 2.5]$. The base flow is overlaid (the black dashed line indicates zero base flow velocity). Red flooding positive; blue flooding negative.

also provided [46]. When at small energies at $t_P = 1.61$, the highly sheared structure along the centreline of the nonlinear case has a very similar appearance to its linear counterpart (around $t_P = 1.7$). However, some higher wave number effects are still visible near the walls in the nonlinear case even at these small energies. The reformation of the nonlinear structure, as it spreads over the duct ($t_P = 1.7$–1.75) and as the wings pull forward ($t_P = 1.925$), when inflection points form in the base flow, are also very similar to the linear case. However, past $t_P \approx 1.925$, the linear growth rate slightly diminishes, while the nonlinear growth rate remains higher, again recalling Fig. 16(a). This is related to nonlinearity inducing a symmetry breaking of the linear mode, from around $t_P = 1.965$, with the region of positive $\hat{v}$-velocity structure tilting downward and the region of negative velocity tilting upward. Eventually, secondary structures separate from each core before the structures eventually break apart around $t_P = 2.155$. From $t_P = 2.22$ through to $t_P = 2.5$, the decay induced by the downstream pull of the walls creates a single highly sheared structure along the centreline, as for the linear case.

The second aspect of the nonlinear evolution is the limited decay of $E = \int \hat{u}^2 + \hat{v}^2 d\Omega$, of only three orders of magnitude, compared to the 18 or so orders of magnitude of decay in $E_v = \int \hat{v}^2 d\Omega$ (Fig. 16 or 17). Snapshots of the $\hat{u}$ velocity from the DNS are shown in Fig. 20 over the first two periods. An animation comparing the linear and nonlinear $\hat{u}$ velocity is also provided as Supplemental Material [46]. The $\hat{u}$ perturbation is initially close to symmetric (see animation) with a central positive streamwise sheet of velocity, bounded by two negative sheets at each wall. The negative sheet of velocity near the bottom wall intensifies and expands to fill the lower half of the duct, while pushing the positive sheet of velocity into the upper half of the duct, at $t_P = 0.22$ (the sheet of negative velocity near the top wall almost vanishing). By $t_P = 0.6$, the $\hat{u}$ perturbation is close to purely antisymmetric. However, opposite-signed velocity near the walls begins encroaching on the streamwise sheets around the time when inflection points form in the base flow. This generates the linear mode observable at $t_P = 0.925$. At $t_P = 0.965$, the symmetry breaking observed in $\hat{v}$ is also observed in $\hat{u}$, disrupting the linear mode. This disruption eventually eliminates the positive velocity structures, leaving a wavy sheet of negative velocity, at $t_P = 1.3$. Throughout the acceleration phase of the base flow the sheet smooths out until it is streamwise invariant. This now symmetric sheet of negative velocity stores a large amount of perturbation energy, that produces a relatively large minimum $\hat{u}$-velocity. This sheet acts as a modulation to the base flow, and is highly persistent. Similar behaviors are observed in steady duct flows [22]. Throughout the linear growth stage, the linear perturbation is able to form over the negative sheet, between $t_P = 1.9$ to $t_P = 1.965$, before nonlinearity again breaks symmetry in the linear mode past $t_P = 1.965$.

E. Symmetry breaking

The symmetry-breaking process was further analyzed by measuring the degree of symmetry separately for each mode j, via $\hat{f}_{s,j} = (\sum_{m=0}^{m=N_y} [\hat{f}_j(y_m) - \hat{f}_j(-y_m)]^2)^{1/2}$. This is depicted for $\hat{v}$, $\hat{u}$ and $\hat{\omega}_z$ in Figs. 21(a) through 21(c), while a measure of the y-averaged energy in each mode is provided in Fig. 21(d). The key result is that when the nonlinear DNS had a similar appearance and growth rate to the linear simulation (e.g., from $t_P \approx 0.75 + q$ to $t_P \approx 0.95 + q$, for $q = 0, 1, 2$), every resolved $\hat{v}$ mode ($\kappa = 0$ through 100) is close to purely symmetric, Fig. 21(a). Once symmetry breaking occurs, at $t_P \approx 0.965$, every odd $\hat{v}$ mode (first, third, etc.) becomes antisymmetric. See also see the vorticity measure, Fig. 21(c), for the first 50 or 60 modes. Thus, the symmetry breaking does not appear to be connected to any asymmetry introduced by numerical noise in the initial perturbation, as every mode becomes symmetric through the preceding linear phase. The measure of symmetry in $\hat{u}$ is effectively the photo negative of $\hat{v}$ (if $\hat{v}$ is almost symmetric, $\hat{u}$ is almost antisymmetric). The exception is the zeroth mode, which remains symmetric after the first period. The zeroth mode stores a large amount of perturbation energy, Fig. 21(d), and decays very slowly compared to the higher modes. Hence, the DNS measure of the perturbation energy E closely resembles the energy in the zeroth mode. As a final note, although a large number of modes become appreciably energized, the floor of the energy in the highest modes (after the base flow modulation occurs) is not clearly raised, and no distinct inertial subrange forms (not shown). Hence, as turbulence is not observed, it cannot initiate the symmetry breaking. However, exactly how nonlinearity induces the symmetry breaking remains unknown.

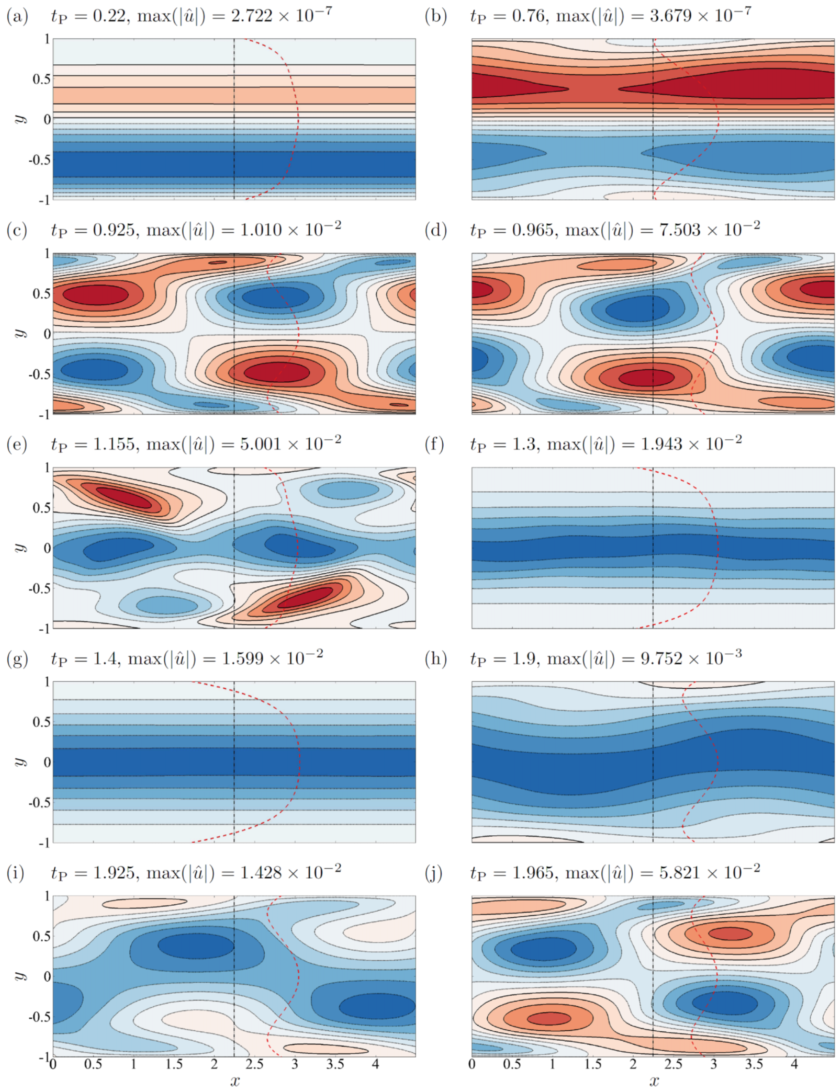

FIG. 20. Nonlinear evolution of $\hat{u}$-velocity perturbation contours at $H = 1$, $\Gamma = 1.24$, $\mathrm{Sr} = 7.2 \times 10^{-3}$ through two cycles $t_P \in [0, 2]$. The base flow is overlaid (the black dashed line indicates zero base flow velocity). Red flooding positive; blue flooding negative.

V. CONCLUSIONS

This work numerically investigates the stability of pulsatile Q2D duct flows, motivated by their relevance to the cooling conduits of magnetic confinement fusion reactors. The linear stability over

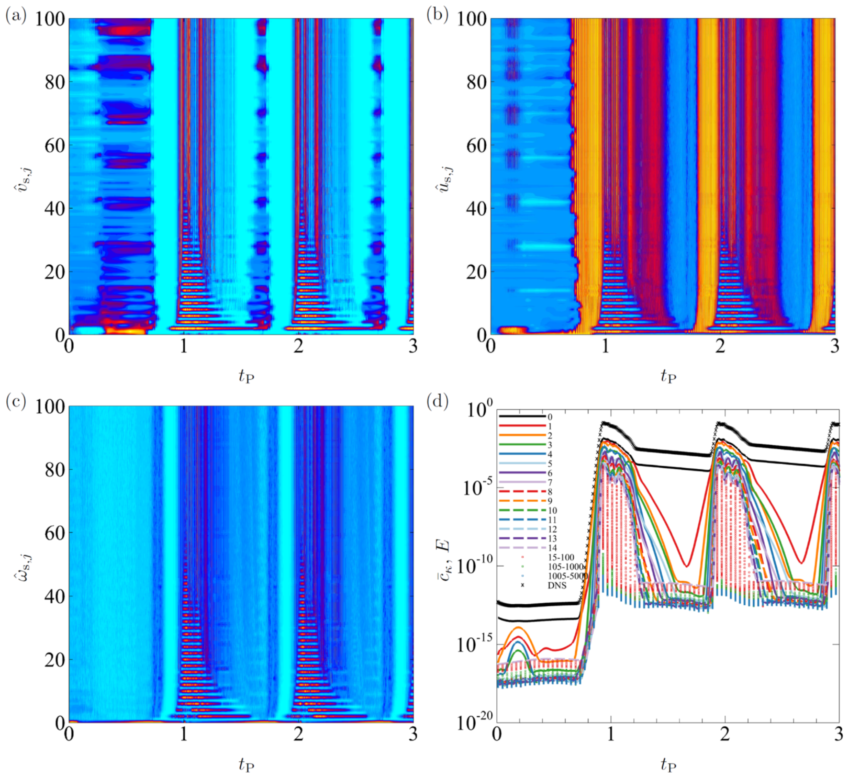

FIG. 21. A measure of the symmetry in the zeroth through one-hundredth isolated streamwise Fourier modes. (a) Wall-normal velocity perturbation. (b) Streamwise velocity perturbation. (c) In-plane vorticity perturbation. Small values of the symmetry measure indicate the mode is almost symmetric (light blue), while large vales indicate the mode is almost antisymmetric (orange/yellow). (d) The y-averaged Fourier coefficient for each mode, based on $\hat{f} = \hat{u}^2 + \hat{v}^2$, compared to the DNS measure $E = \int \hat{u}^2 + \hat{v}^2 \mathrm{d}\Omega$. Note that for modes $100 < \kappa \leqslant 5000$, only every fifth κ is plotted.

a large Re, H, Sr, Γ parameter space was analyzed to both determine the pulsation optimized for the greatest reduction in $\mathrm{Re}_{\mathrm{crit}}$ and more generally to understand the role of transient inertial forces in unsteady MHD duct flows. At large amplitude ratios ($\Gamma = 100$, near the conditions of a steady base flow), the effect of varying Sr was clearest. Increasing Sr lead to both more prominent inflection points, acting to reduce $\mathrm{Re}_{\mathrm{crit}}$, and thinner oscillating boundary layers, acting to increase $\mathrm{Re}_{\mathrm{crit}}$. Although more prominent inflection points generated additional growth during the deceleration of the base flow, the effective length of the deceleration phase increases with decreasing Sr. Thus, by tuning Sr (for a given H, Γ), the minimum $\mathrm{Re}_{\mathrm{crit}}$ is reached as the perturbation and base flow energy variations fall in phase, so long as inflection points remain prominent. Furthermore, the percentage reduction in $\mathrm{Re}_{\mathrm{crit}}$ always improved with increasing H, when free to adjust Sr. This observation, that pulsatility was still effective at destabilizing the flow in (or toward) fusion relevant regimes, satisfies the first question the paper put forward.

At intermediate amplitude ratios ($\Gamma = 10$), the addition of the oscillating flow component lead to large changes in $\mathrm{Re}_{\mathrm{crit}}$ compared to the steady base flow. At these amplitude ratios the effect of Re on the base flow becomes important. Increasing Re reduces the oscillating boundary layer thickness and restabilizes the flow for a small range of frequencies. Although the base flow became more stable with increasing Re, a large enough Re was eventually reached to destabilize other instability modes (different from the TS-like mode).

At smaller, near-unity amplitude ratios (equal steady and oscillating base flow maxima), the largest advancements in $\mathrm{Re}_{\mathrm{crit}}$ over the steady value were observed. At $H = 10^{-7}$, an almost 70% reduction in $\mathrm{Re}_{\mathrm{crit}}$ was attained, while by $H = 10$, there was over an order of magnitude reduction (90.3%). These improvements were attained at Sr of order 10^{-3}, a region of the parameter space more than amenable to both SM82 modeling, and fusion relevant applications. Particularly in the latter case, a low-frequency driving force would be far simpler to engineer than a high-frequency oscillation. These results answer the second and third questions put forth in the paper.

At these conditions, the onset of turbulence was not observed in nonlinear DNS. Within the first oscillation period, the intracyclic growth was able to propel an initial perturbation of numerical noise to nonlinear amplitudes. This modulated the base flow by generating a sheet of negative velocity along the duct centreline. Although this modulated base flow had no effect on the growth of the wall-normal velocity perturbation, it was able to saturate the exponential growth at supercritical Reynolds numbers. Although turbulence was not triggered, the nonlinear growth was still a promising result. However, without a wider nonlinear investigtion of the parameter space, the capability for $\mathrm{Re}_{\mathrm{crit}}$ reductions to translate to reductions in the Re at which turbulence is observed (the fourth question put forward), remains partially unresolved. At nonlinear amplitudes, a symmetry breaking process was observed within each cycle. The ensuing chaotic flow may naturally improve mixing, improving cooling conduit performance, without the severe increase in frictional losses accompanying a turbulent flow [57]. This is an avenue for future work.

Finally, the capability for the optimized pulsations to nonlinearly modulate the base flow within one cycle favors linear transient growth as a strong contender for enabling bypass transitions to turbulence. This is a key area of future research, as if the flow is transiently driven over a partial oscillation cycle (and steadily driven thereafter), turbulence may be rapidly triggered. A caveat to such a method is that it is the continually driven time periodic base flow which yields eigenvalues with positive growth rates at greatly reduced Reynolds numbers. Without such an underlying base flow, the leading eigenvalues may be strongly negative and severely limit any transient growth, as for cylinder wake flows [53]. This may be particularly problematic if large amounts of regenerative transient growth are the key to sustaining turbulent states [52,58], a point that also requires further investigation.

Overall, the large reductions in $\mathrm{Re}_{\mathrm{crit}}$, occurring in a viable region of the parameter space, form too promising a direction to cease investigating. The first steps to this are to assess the heat transfer characteristics of the pulsatile base flow, which may naturally be more efficient than the steady equivalent, and investigating linear transient optimals. Other than linear transient growth, the use of pulsatility in concert with one of the various Q2D vortex promoters [4–10] could aid in sustaining turbulence. Past the Q2D setup, the full 3D duct flow could be tackled. In particular, the interaction between the Stokes and Hartmann layers could result in new avenues to reach turbulence. The reduced constriction of the full 3D domain may also aid in sustaining turbulence. Note that for fusion applications, oscillatory wall motion is not viable. Therefore, in the context of a 3D domain, oscillatory pressure gradients are more relevant (note that the fully nonlinear wall- and pressure-driven flows are only equivalent in the 2D averaged equations). Lastly, with a broader scope, even electrically conducting walls could be investigated. Although less prevalent in self-cooled designs [2], the larger shear present in boundary layers forming on conducting walls provides conditions more susceptible to transitions to turbulence and larger turbulent fluctuations [59]. The interactions between flow pulsatility and electrically conducting walls could yield many new insights.

ACKNOWLEDGMENTS

C.J.C. receives support from the Australian Government Research Training Program (RTP). This research was supported by the Australian Government via the Australian Research Council (Discovery Grant No. DP180102647), the National Computational Infrastructure (NCI) and Pawsey Supercomputing Centre (PSC), by Monash University via the MonARCH HPC cluster, and by the Royal Society under the International Exchange Scheme between the UK and Australia (Grant No. E170034).

[1] M. Abdou, N. B. Morley, S. Smolentsev, A. Ying, S. Malang, A. Rowcliffe, and M. Ulrickson, Blanket/first wall challenges and required R&D on the pathway to DEMO, Fusion Eng. Des. **100**, 2 (2015).

[2] S. Smolentsev, R. Moreau, and M. Abdou, Characterization of key magnetohydrodynamic phenomena in PbLi flows for the US DCLL blanket, Fusion Eng. Des. **83**, 771 (2008).

[3] R. Moreau, S. Smolentsev, and S. Cuevas, MHD flow in an insulating rectangular duct under a non-uniform magnetic field, PMC Phys. B **3**, 3 (2010).

[4] O. G. W. Cassels, W. K. Hussam, and G. J. Sheard, Heat transfer enhancement using rectangular vortex promoters in confined quasi-two-dimensional magnetohydrodynamic flows, Int. J. Heat Mass Transf. **93**, 186 (2016).

[5] W. K. Hussam, M. C. Thompson, and G. J. Sheard, Dynamics and heat transfer in a quasi-two-dimensional MHD flow past a circular cylinder in a duct at high Hartmann number, Int. J. Heat Mass Transf. **54**, 1091 (2011).

[6] W. K. Hussam, M. C. Thompson, and G. J. Sheard, Enhancing heat transfer in a high Hartmann number magnetohydrodynamic channel flow via torsional oscillation of a cylindrical obstacle, Phys. Fluids **24**, 113601 (2012).

[7] L. Bühler, Instabilities in quasi-two-dimensional magnetohydrodynamic flows, J. Fluid Mech. **326**, 125 (1996).

[8] A. H. A. Hamid, W. K. Hussam, and G. J. Sheard, Combining an obstacle and electrically driven vortices to enhance heat transfer in a quasi-two-dimensional MHD duct flow, J. Fluid Mech. **792**, 364 (2016).

[9] A. H. A. Hamid, W. K. Hussam, and G. J. Sheard, Heat transfer augmentation of a quasi-two-dimensional MHD duct flow via electrically driven vortices, Numer. Heat Tr. A-Appl. **70**, 847 (2016).

[10] S. Cuevas, S. Smolentsev, and M. A. Abdou, On the flow past a magnetic obstacle, J. Fluid Mech. **553**, 227 (2006).

[11] P. A. Davidson, *An Introduction to Magnetohydrodynamics* (Cambridge University Press, Cambridge, 2001).

[12] J. Sommeria and R. Moreau, Why, how, and when, MHD turbulence becomes two-dimensional, J. Fluid Mech. **118**, 507 (1982).

[13] A. Pothérat and V. Dymkou, Direct numerical simulations of low-*Rm* MHD turbulence based on the least dissipative modes, J. Fluid Mech. **655**, 174 (2010).

[14] A. Thess and O. Zikanov, Transition from two-dimensional to three-dimensional magnetohydrodynamic turbulence, J. Fluid Mech. **579**, 383 (2007).

[15] O. Zikanov and A. Thess, Direct numerical simulation of forced MHD turbulence at low magnetic Reynolds number, J. Fluid Mech. **358**, 299 (1998).

[16] A. Pothérat and K. Kornet, The decay of wall-bounded MHD turbulence at low *Rm*, J. Fluid Mech. **783**, 605 (2015).

[17] A. Pothérat, Quasi-two-dimensional perturbations in duct flows under transverse magnetic field, Phys. Fluids **19**, 074104 (2007).

[18] A. Pothérat, J. Sommeria, and R. Moreau, An effective two-dimensional model for MHD flows with a transverse magnetic field, J. Fluid Mech. **424**, 75 (2000).

[19] O. G. W. Cassels, T. Vo, A. Pothérat, and G. J. Sheard, From three-dimensional to quasi-two-dimensional: Transient growth in magnetohydrodynamic duct flows, J. Fluid Mech. **861**, 382 (2019).

[20] N. Kanaris, X. Albets, D. Grigoriadis, and S. Kassinos, Three-dimensional numerical simulations of magnetohydrodynamic flow around a confined circular cylinder under low, moderate, and strong magnetic fields, Phys. Fluids **25**, 074102 (2013).

[21] B. Mück, C. Günther, U. Müller, and L. Bühler, Three-dimensional MHD flows in rectangular ducts with internal obstacles, J. Fluid Mech. **418**, 265 (2000).

[22] C. J. Camobreco, A. Pothérat, and G. J. Sheard, Transition to turbulence in quasi-two-dimensional MHD flow driven by lateral walls, Phys. Rev. Fluids **6**, 013901 (2021).

[23] T. Vo, A. Pothérat, and G. J. Sheard, Linear stability of horizontal, laminar fully developed, quasi-two-dimensional liquid metal duct flow under a transverse magnetic field heated from below, Phys. Rev. Fluids **2**, 033902 (2017).

[24] C. J. Camobreco, A. Pothérat, and G. J. Sheard, Subcritical route to turbulence via the Orr mechanism in a quasi-two-dimensional boundary layer, Phys. Rev. Fluids **5**, 113902 (2020).

[25] C. Thomas, A. P. Bassom, and C. Davies, The linear stability of a Stokes layer with an imposed axial magnetic field, J. Fluid Mech. **662**, 320 (2010).

[26] C. Thomas and C. Davies, Global stability of the rotating-disc boundary layer with an axial magnetic field, J. Fluid Mech. **724**, 510 (2013).

[27] C. H. von Kerczek, The instability of oscillatory plane Poiseuille flow, J. Fluid Mech. **116**, 91 (1982).

[28] C. Thomas, A. P. Bassom, P. J. Blennerhassett, and C. Davies, The linear stability of oscillatory Poiseuille flow in channels and pipes, Proc. R. Soc. A **467**, 2643 (2011).

[29] B. Pier and P. J. Schmid, Linear and nonlinear dynamics of pulsatile channel flow, J. Fluid Mech. **815**, 435 (2000).

[30] C. Thomas, P. J. Blennerhassett, A. P. Bassom, and C. Davies, The linear stability of a Stokes layer subjected to high-frequency perturbations, J. Fluid Mech. **764**, 193 (2015).

[31] B. A. Singer, J. H. Ferziger, and H. L. Reed, Numerical simulations of transition in oscillatory plane channel flow, J. Fluid Mech. **208**, 45 (1989).

[32] C. E. Ozdemir, T. Hsu, and S. Balachandar, Direct numerical simulations of transition and turbulence in smooth-walled Stokes boundary layer, Phys. Fluids **26**, 045108 (2014).

[33] A. G. Straatman, R. E. Khayat, E. Haj-Qasem, and D. A. Steinman, On the hydrodynamic stability of pulsatile flow in a plane channel, Phys. Fluids **14**, 1938 (2002).

[34] P. J. Blennerhassett and A. P. Bassom, The linear stability of high-frequency oscillatory flow in a channel, J. Fluid Mech. **556**, 1 (2006).

[35] P. J. Blennerhassett and A. P. Bassom, The linear stability of flat stokes layers, J. Fluid Mech. **464**, 393 (2002).

[36] D. Biau, Transient growth of perturbations in Stokes oscillatory flows, J. Fluid Mech. **794**, R4 (2016).

[37] S. B. Pope, *Turbulent Flows* (Cambridge University Press, Cambridge, 2000).

[38] U. Müller and L. Bühler, *Magnetofluiddynamics in Channels and Containers* (Springer-Verlag, Berlin, Heidelberg, 2001).

[39] R. Moreau, *Magnetohydrodynamics* (Springer-Verlag Dordrecht, Netherlands, 1990).

[40] B. Knaepen, S. Kassinos, and D. Carati, Magnetohydrodynamic turbulence at moderate magnetic Reynolds number, J. Fluid Mech. **513**, 199 (2004).

[41] T. Vo, L. Montabone, and G. J. Sheard, Effect of enclosure height on the structure and stability of shear layers induced by differential rotation, J. Fluid Mech. **765**, 45 (2015).

[42] E. Hairer, S. P. Nørsett, and G. Wanner, *Solving Ordinary Differential Equations I: Nonstiff Problems* (Springer-Verlag, Berlin, Heidelberg, 1993).

[43] D. Barkley, H. M. Blackburn, and S. J. Sherwin, Direct optimal growth analysis for timesteppers, Int. J. Numer. Methods Fluids **57**, 1435 (2008).

[44] L. N. Trefethen, *Spectral Methods in MATLAB* (Society for Industrial and Applied Mathematics, Philadelphia, 2000).

[45] M. Takashima, The stability of the modified plane Couette flow in the presence of a transverse magnetic field, Fluid Dyn. Res. **22**, 105 (1998).

[46] See Supplemental Material at https://link.aps.org/supplemental/10.1103/PhysRevFluids.6.053903 for animations of the linear stability modes and their nonlinear counterparts.

[47] R. R. Kerswell, C. C. T. Pringle, and A. P. Willis, An optimization approach for analysing nonlinear stability with transition to turbulence in fluids as an exemplar, Rep. Prog. Phys. **77**, 085901 (2014).
[48] E. Reshotko, Transient growth: A factor in bypass transition, Phys. Fluids **13**, 1067 (2001).
[49] P. J. Schmid and D. S. Henningson, *Stability and Transition in Shear Flows* (Springer-Verlag, New York, 2001).
[50] L. N. Trefethen, A. E. Trefethen, S. C. Reddy, and T. A. Driscoll, Hydrodynamic stability without eigenvalues, Science **261**, 578 (1993).
[51] F. Waleffe, Transition in shear flows. Nonlinear normality versus non–normal linearity, Phys. Fluids **7**, 3060 (1995).
[52] A. Lozano-Durán, N. C. Constantinou, M.-A. Nikolaidis, and M. Karp, Cause-and-effect of linear mechanisms sustaining wall turbulence, J. Fluid Mech. **914**, A8 (2021).
[53] N. Abdessemed, A. S. Sharma, S. J. Sherwin, and V. Theofilis, Transient growth analysis of the flow past a circular cylinder, Phys. Fluids **21**, 044103 (2009).
[54] G. E. Karniadakis, M. Israeli, and S. A. Orszag, High-order splitting methods for the incompressible Navier–Stokes equations, J. Comput. Phys. **97**, 414 (1991).
[55] W. K. Hussam, M. C. Thompson, and G. J. Sheard, Optimal transient disturbances behind a circular cylinder in a quasi-two-dimensional magnetohydodynamic duct flow, Phys. Fluids **24**, 024105 (2012).
[56] G. J. Sheard, M. J. Fitzgerald, and K. Ryan, Cylinders with square cross-section: Wake instabilities with incidence angle variation, J. Fluid Mech. **630**, 43 (2009).
[57] J. Kühnen, B. Song, D. Scarselli, N. B. Budanur, M. Riedl, A. P. Willis, M. Avila, and B. Hof, Destabilizing turbulence in pipe flow, Nat. Phys. **14**, 386 (2018).
[58] N. B. Budanur, E. Marensi, A. P. Willis, and B. Hof, Upper edge of chaos and the energetics of transition in pipe flow, Phys. Rev. Fluids **5**, 023903 (2020).
[59] U. Burr, L. Barleon, U. Müller, and A. Tsinober, Turbulent transport of momentum and heat in magneto-hydrodynamic rectangular duct flow with strong sidewall jets, J. Fluid Mech. **406**, 247 (2000).

Chapter 9

Conclusions

The most important result to take from this thesis is that using a Q2D, purely laminar initial condition, purely Q2D routes to sustained turbulence were numerically observed. This result relies on four key findings. First, that Q2D linear and nonlinear transient growth are virtually identical, for the initial energies, domain sizes and evolution times of interest. Second, that it is better to optimally energize the leading eigenmode, rather than attempt to maximize Q2D linear transient growth. This is important not only for most efficiently reaching turbulence, but also in ensuring turbulence is sustained. Third, that the lower edge state is almost entirely composed of the leading eigenmode (first harmonic), which is the Q2D equivalent of the Tollmien–Schlichting wave, and its weakly nonlinear self-interactions (zeroth and second harmonics). Thus, the edge state is able to be reached by nonmodal perturbations that reasonably well approximate the initial condition optimally energizing the leading eigenmode, i.e. that reasonably approximate (or are) the leading adjoint mode. Fourth, although subcritical bifurcations are (weakly nonlinearly) predicted over a wide range of friction parameters H, attaining sufficient nonlinear growth to trigger turbulence is not necessarily guaranteed at subcritical Re for those H. When possible, transitions were only observed at weakly subcritical Re. In addition, the ability to sustain turbulence, which strongly depends on base flow production, is compromised by flat base flow profiles at high H. Thus, only a small range of H were viable candidates for observing purely Q2D subcritical routes to turbulence (as shown at $H = 10$).

Regarding the practical application of the research, reducing the Reynolds number required to sustain turbulence in magnetohydrodynamic flows under strong magnetic fields (ultimately to improve turbulent heat transfer rates), these results were quite restrictive. Only observing sustained Q2D turbulence in the vicinity of $H = 10$ constrains the aspect ratio necessary to match the friction parameter to the applied field strength. Even then, only weakly subcritical Re sustain turbulence at $H = 10$. Thus, the linear stability of pulsating base flows, composed of a steady and oscillatory flow component, were analyzed, to inform nonlinear simulations attempting to sustain turbulence at lower Re and higher H. Linear analysis of optimized (amplitude and frequency) base flows indicated large reductions in the critical Reynolds number. Percentage reductions of over an order of magnitude were observed for $H \geq 10$. These optimized parameters corresponded to a low frequency driving force, equally generated by a pressure gradient or wall oscillation, making such a base flow modification feasible to generate in practice. However, turbulence was not triggered in the equivalent nonlinear simulations targeting modal instabilities.

This leads to the considerations for future work. First, as the pulsatile base flow modulations were optimal (attaining maximum growth/minimum decay of the leading eigenmode) in a feasible region of the parameter space, nonmodal perturbations over a wider range of Reynolds numbers are worth investigating. This is of particular importance given the key theoretical finding of this research: the nonmodal perturbation optimally energizing the leading eigenmode not only provides the most efficient route to turbulence, but also generate a base flow modulation capable of sustaining turbulence. Second, of both theoretical and practical interest (in ensuring a feasible aspect ratio), testing whether the optimal energization remains the most efficient initial condition to trigger turbulence in full 3D domains is a priority. It may be that at large Hartmann numbers Ha, linear and nonlinear growth remain similar, with the optimal energization remaining as the most efficient route to turbulence. Eventually, as Ha is reduced, and nonlinear growth via 3D mechanisms becomes significant, maximizing initial nonlinear growth may be a more efficient means of triggering turbulence than optimally energizing the leading eigenmode (assuming a maximized growth strategy also results in sustained turbulence). Alternately, the optimal energization may remain the most efficient route to turbulence at all Ha, even in the $Ha \to 0$ hydrodynamic limit when nonlinear growth far exceeds its linear counterpart. To the author's knowledge, nonlinear hydrodynamic simulations with the leading adjoint mode as the initial condition have not been performed. If the optimal energization is still more efficient in the hydrodynamic limit, it would then be interesting to compare numerically attained Reynolds number transition thresholds to the numerous experimentally obtained ones. Recall that the energization of the leading eigenmode is only 'optimal' as it includes initial linear growth (e.g. via the highly efficient lift-up mechanism), but merely constrains the initial condition to eventually transfer all energy to the leading eigenmode (admittedly some compromise to the growth rate of the leading eigenmode would be required to optimize the initial growth via the lift-up effect). Finally, it is worth investigating whether the numerically predicted purely Q2D routes to turbulence can be observed experimentally. In particular, it is important to verify that the proposed growth mechanisms observed in simulations of the SM82 model can occur in reality. Amplification of the Tollmien–Schlichting wave is intrinsically related to the action of viscosity at the critical layer, a critical layer which is approximately a factor of 6 smaller than the Shercliff boundary layer height, recalling Chapter 3, § 3.2. While the SM82 model does not guarantee accuracy at length scales below the Shercliff boundary layer height, there are examples of SM82 accuracy in shear layers thinner than this limit (Pothérat *et al.* 2000). Experiments are thus crucial to validate the proposed route to turbulence. However, experiments face significant difficulties, not the least of which being how to immerse a sufficiently long duct in a high strength homogeneous magnetic field. Possibly, approximation with an annular flow could be a viable alternative, although it may be difficult to also maintain an acceptable aspect ratio to test friction parameters $H \sim 10$. If such experiments are plausible, and if appropriate analogues of the leading adjoint initial conditions can be designed, it would be interesting to observe whether an intermediate stage of 3D turbulence forms between the Q2D laminar and Q2D turbulent states, or whether the entire route to turbulence remains purely Q2D.

To conclude this thesis, it is worth briefly considering the plausibility of said experiments, or the viability of 3D simulations, in light of the Q2D findings of this study. Ultimately, it is only in 3D domains that the observations of sustained turbulence (for certain parameter values), or a lack thereof (at others), can be either deemed to be accurate representations of reality, or merely artefacts of the Q2D model. Recalling that sustained Q2D turbulence was only convincingly observed in the vicinity of $H = 10$, and at a minimum $Re \approx 7 \times 10^4$, some constraints on 3D setups can be estimated. Recalling the summary of constraints in Table 2.1, for a 3D setup to exhibit Q2D dynamics, and with laminar Hartmann layers to match the Q2D model assumptions, requires $Re/2Ha \lesssim 380$ and $N = Ha^2/Re \gg 1$ (as limits on the required interaction parameter can vary wildly, $N \gtrsim 4$ shall be presumed here). For $Re \approx 7 \times 10^4$, these translate to

$Ha \gtrsim 92$ and $Ha \gtrsim 530$, respectively. While these Hartmann numbers were shown to be reasonably attained under fusion blanket operation, these constraints are somewhat problematic, but not entirely unreasonable, for simulations and experiment. However, bear in mind that $Re \approx 7 \times 10^4$ is also required, which would induce significant difficulty for both well-resolved simulations and experiments. Even then, these difficulties are further compounded by the duct dimensions, as to match a friction parameter of $H = 10$ would require a duct aspect ratio of $A = L_y/L_z \gtrsim 10.3$. Furthermore, anything other than an annular experimental setup would provide unfeasibly short observation times, while a numerical setup would require a significant increase in domain length to safely rule out any influence of periodic boundary conditions (although a formal constraint cannot easily be estimated). Thus, it is unlikely that the parameter values at which Q2D turbulence is sustained, as observed in this thesis, can be translated to more physically realistic simulations or experiments in the immediate future, or if so, with only a vary sparing number of simulations, or exceedingly carefully designed experiments. Furthermore, this makes it nigh impossible to provide an *a posteriori* assessment of the Q2D model validity, or equally to guarantee that the sustained turbulent episodes are physically meaningful.

Appendix A

Support for claims that Q2D turbulence is observed

Throughout this thesis, various flow conditions are defined as having triggered turbulence, sustained turbulence, relaminarized, saturated to a finite amplitude state, etc. Although some support for these claims are provided in the preceding works, particularly in the form of instantaneous snapshots of the streamwise Fourier coefficients (following $\kappa^{-5/3}$ trends), further support is provided here. Large data sets of the time histories for various key cases in Chapters 5 (Camobreco *et al.* 2020), 6 (Camobreco *et al.* 2021b) and 7 are provided in Figs. A.1, A.2 and A.3, covering variations in initial energy, Hartmann friction parameter, and Reynolds number, respectively. Note that due to the size of some of the data sets, the y-averaged Fourier coefficients, $\bar{c}_\kappa$, were averaged over only 7 slices, rather than 21 as for Chapters 6 (Camobreco *et al.* 2021b) and 7. As before, the Fourier coefficients $c_\kappa = |(1/N_\mathrm{f})\sum_{n=0}^{n=N_\mathrm{f}-1}[\hat{u}_\perp^2(x_n)+\hat{v}_\perp^2(x_n)]e^{-2\pi\mathrm{i}\kappa n/N_\mathrm{f}}|$ were computed with the discrete Fourier transform in MATLAB, where x_n represents the n'th x-location linearly spaced between $x_0 = 0$ and $x_{N_\mathrm{f}} = 2\pi/\alpha$.

Figure A.1 bolsters the claims of Chapter 5 (Camobreco *et al.* 2020), that E_D and $E_{\mathrm{D},2}$ are the lower and upper delineating energies bounding those initial conditions which transition to turbulence, or relaminarize. As the transition to turbulence occurs rapidly (if it occurs at all), Fourier coefficients are computed from the time of the initial seeding of the nonmodal perturbation. The initial condition with $E_0 < E_\mathrm{D}$, Fig. A.1(a), does not transition to turbulence. Linear growth occurs within the first ≈ 60 time units, and then nonlinear growth for ≈ 850 time units. Decay is slow at first, then rapid around $t \approx 2000$ time units, after which only the zeroth mode is appreciably energized. Note that energy decayed in the intermediate modes ($30 \lesssim \kappa \lesssim 100$) much

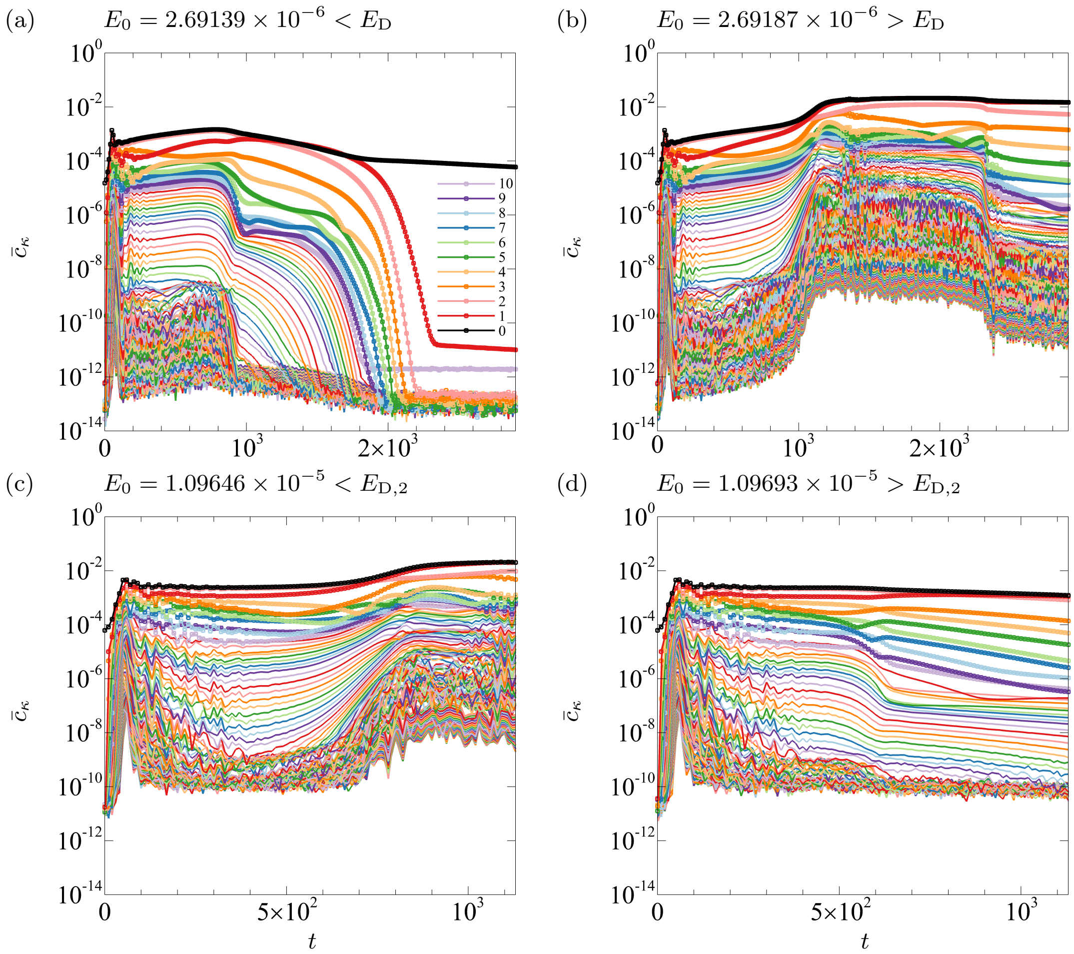

FIGURE A.1: Time histories of y-averaged streamwise Fourier coefficients; nonmodal perturbations maximizing linear transient growth for an isolated exponential boundary layer ($H \to \infty$) at $r_\mathrm{c} = 0.585$. With $E_0 < E_\mathrm{D}$ there is nonlinear growth, but no transition. With $E_\mathrm{D} < E_0 < E_{\mathrm{D},2}$, there is a clear raising of the floor of the Fourier coefficients (all become excited), indicative of a turbulent transition, although with later relaminarization. With $E_0 > E_{\mathrm{D},2}$ transition does not occur. Symbols at each recorded time instant are included on streamwise modes 0 through 10, see legend. Thereafter, only lines are plotted, and only for every 2nd mode, up to the 200th, and then every 100th, up to the 4800th.

earlier, at $t \approx 950$. Comparatively, the initial condition with $E_0 > E_\mathrm{D}$, Fig. A.1(b), undergoes a transition to turbulence, with a clear raising of the floor of energized modes at $t \approx 1100$ time units. However, as discussed in Chapter 7, the leading eigenmode was not well energized by the initial condition maximizing linear transient growth. Due also to the intermediate $r_\mathrm{c} = 0.585$, relaminarization occurs even with $E_0 > E_\mathrm{D}$, appearing quite abruptly around $t \approx 2400$, although overall decay is slow.

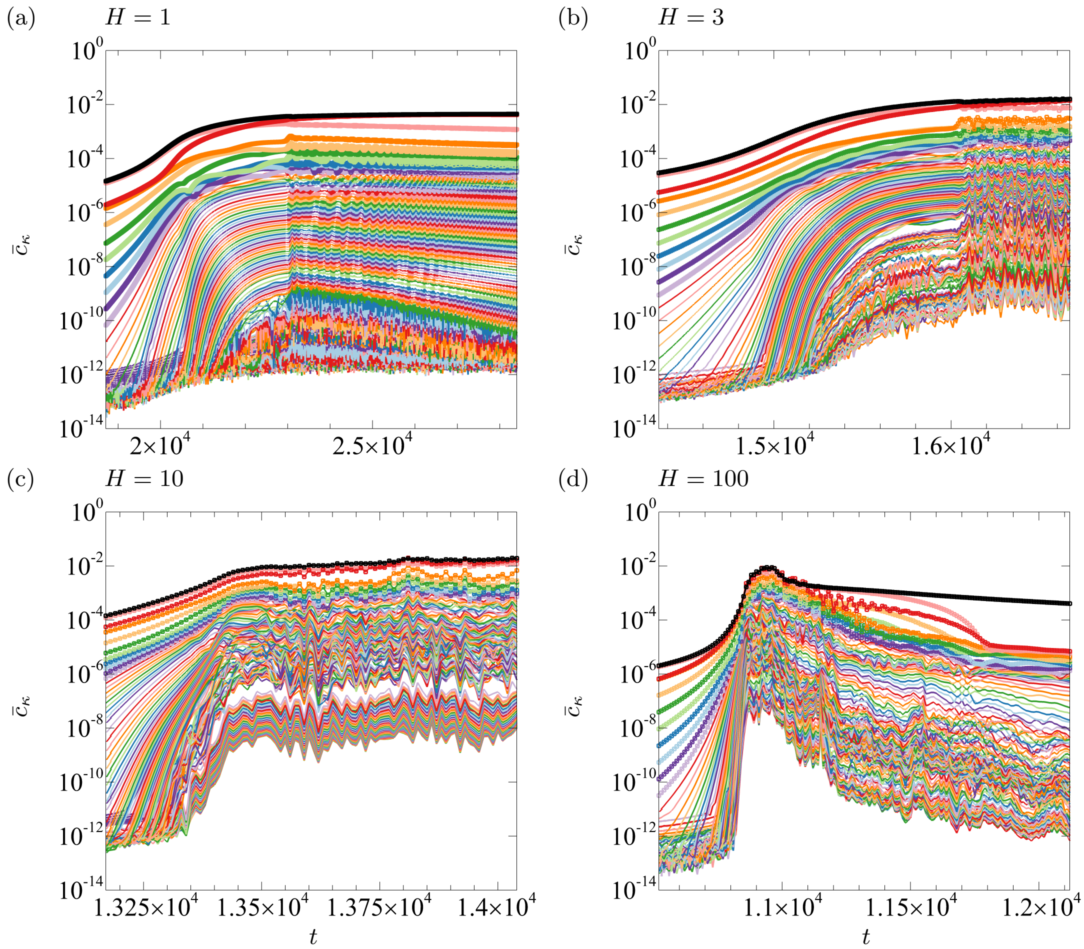

FIGURE A.2: Time histories of y-averaged streamwise Fourier coefficients; random noise initial conditions supercritically evolved for Shercliff flow (various H) at $r_c = 1.1$. At $H = 1$, $r_c = 1.1$ is insufficient to trigger turbulence. It is likely that turbulence is triggered at $H = 3$ ($H = 3$ saturates to a finite amplitude state, like $H = 1$), see Chapter 6 (Camobreco *et al.* 2021b) for more. At $H = 10$ turbulence is clearly triggered, and indefinitely sustained. At $H \geq 30$ (shown at $H = 100$) turbulence is triggered, but rapidly relaminarizes. Symbols are included on streamwise modes 0 through 10, see legend on Fig. A.1(a). Thereafter, lines are plotted for every 2nd mode, up to the 200th, and then every 50th, up to the 2500th.

As for the cases below and above E_D, the cases above and below $E_{D,2}$ are also differentiated by the lack and presence of turbulence, respectively. For $E_0 < E_{D,2}$, Fig. A.1(c), turbulence is triggered, although due to the larger E_0, and a more chaotic initial condition, the shift in the energy floor appears smaller. However, by comparison to $E_0 > E_{D,2}$, Fig. A.1(d), the effect of the slight change in initial energy is still clear. With larger E_0, turbulence is not triggered, with decay setting in around $t \approx 650$.

Having considered the results in the limit of $H \to \infty$, the Fourier coefficients for

Shercliff flow profiles at finite H are now analysed. Note that the initial conditions applied to the finite H cases take significantly longer to trigger turbulence. Thus, data was collected from arbitrarily selected times pre-transition (but well after $t = 0$), and gathered until a reasonable picture of the resulting dynamics could be ascertained.

At $r_c = 1.1$, after a lengthy period of exponential growth, simulations at $H = 1$ and $H = 3$ saturated to a stable finite amplitude state. Note that at $H = 1$, Fig. A.2(a), turbulence was not triggered after either the exponential or nonlinear (superexponential) growth stages. However, at $t \approx 2.3 \times 10^4$, after the nonlinear growth, but before saturation, a broadband oscillation of the energy in all of the Fourier coefficients is observed (this does not change the energy floor, however). The reason for this sudden change is unknown, although is also observed at other H, at Re insufficient to trigger turbulence (see Fig. A.3(b) at $r_c = 0.4$, $H = 10$). At $H = 3$, Fig. A.2(b), it is likely that turbulence is triggered after the exponential and nonlinear growth, although the flow is only briefly turbulent, with saturation to the finite amplitude state thereafter (not shown here).

By comparison, a clear transition (raising of the floor) is observed at $H = 10$, Fig. A.2(c). Turbulence is sustained at $H = 10$, and this was the first setup in which sustained Q2D turbulence was observed in this work. However, at $r_c = 1.1$, turbulence was not sustained for $H \geq 30$. At $H = 100$, Fig. A.2(d), the decay of energy in each Fourier mode appears to begin almost immediately after transition. This high H relaminarization differs from the relaminarization depicted at $H \to \infty$ in Fig. A.1(b), as the latter was due to both insufficient Re, and poor energization of the leading eigenmode (the former only suffers from low Re).

Finally, subcritical r_c variations are considered for the Shercliff profile at $H = 10$. All nonmodal initial conditions were large $T = \tau/\tau_{\mathrm{opt}}$ ($T = 6$ or $T = 8$) approximations of the initial condition optimally energizing the leading eigenmode. Linear growth propels the initial condition to the edge, where the weakly nonlinear edge trajectory is followed (indicated by near constant E), until the edge state is reached. Data gathering begins roughly when the edge is departed. At $r_c = 0.3$, Fig. A.3(a), a small amount of nonlinear growth occurs after departing the edge state. However, this is insufficient to trigger turbulence, or even to slightly excite modes with $\kappa \gtrsim 60$. At $r_c = 0.4$, Fig. A.3(b), nonlinear growth is still insufficient to trigger turbulence. However, there is some energization of all resolved modes. Thus, for this case, the lack of the formation

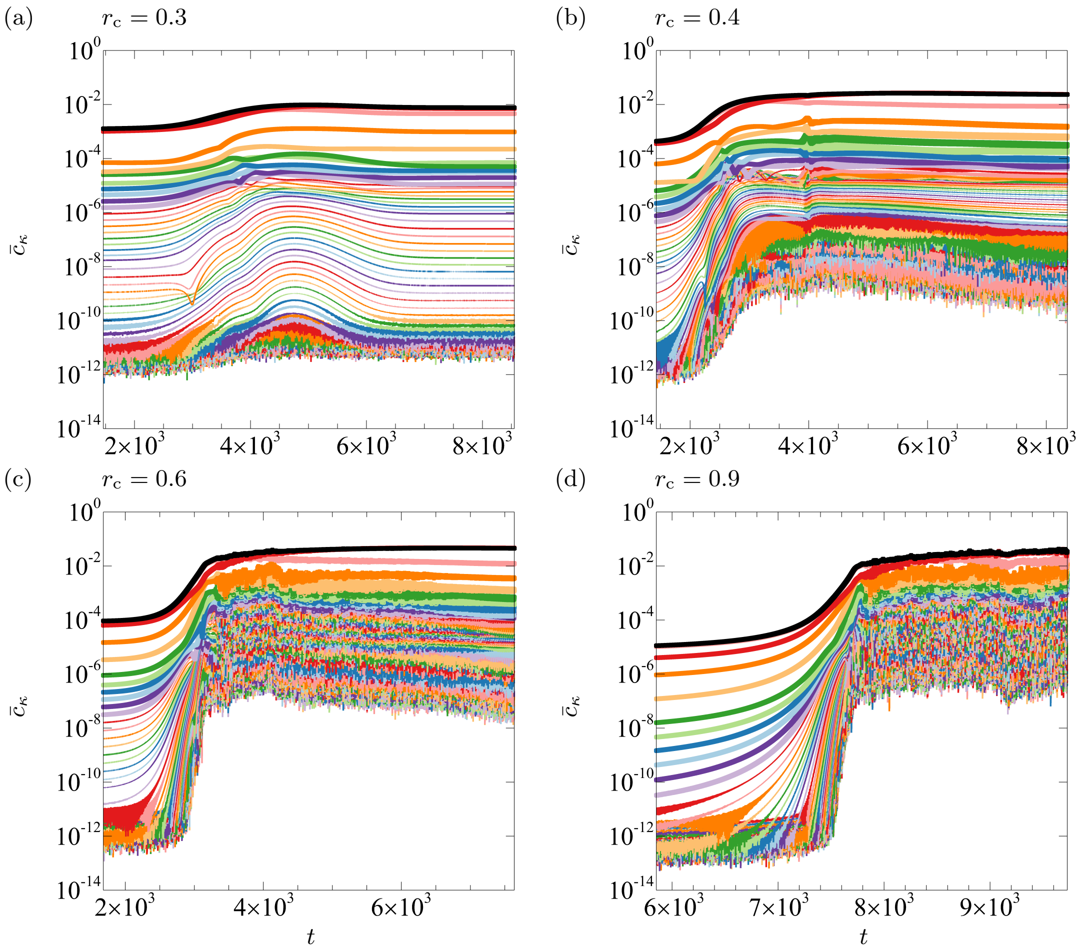

FIGURE A.3: Time histories of y-averaged streamwise Fourier coefficients; nonmodal perturbations almost optimally energizing the leading eigenmode for Shercliff flow at $H = 10$, $r_c < 1$. At $r_c = 0.3$ turbulence is not triggered. At $r_c = 0.4$ it is unclear whether turbulence is triggered, see Chapter 7 for more. At $r_c = 0.6$ turbulence forms, but slowly relaminarizes. At $r_c = 0.9$, turbulence is triggered and indefinitely sustained. Symbols are included on streamwise modes 0 through 10, see legend on Fig. A.1(a). Thereafter, lines are plotted for every 2nd mode, up to the 200th, and then every 6th, up to the 476th.

of an inertial subrange (indicated by an exponential rather than power law dependence on wave number) was used to rule out turbulence at $r_c = 0.4$ (not shown). Although insufficient for turbulence, $r_c = 0.4$ was sufficient for the almost spontaneous introduction of a broadband oscillation of the energy in all Fourier modes, around $t \approx 4 \times 10^3$. This broadband oscillation was also observed at $H = 1$, $r_c = 1.1$, also at Re insufficient to trigger turbulence (even though supercritical). As will be shown in Appendix C, at $H = 1$, $r_c = 2$ is sufficient to trigger turbulence. Thus, the broadband oscillation may indicate that $r_c = 0.4$ is just slightly too small to trigger turbulence.

Returning to the $H = 10$ case in Fig. A.3(c), $r_c = 0.6$ triggers a single turbulent episode. However, relaminarization is to a stable finite amplitude state (one very similar to the stable finite amplitude states observed at $r_c = 0.3$ and $r_c = 0.4$). Note that fluctuations in the lower, smaller κ modes appear to die out earlier, with progressively higher κ modes, which contain less energy, relaminarizing (smoothing out) at increasingly larger times. Finally, at $r_c = 0.9$, Fig. A.3(d), turbulence is triggered and indefinitely sustained. Note that the length of time required to simulate the turbulent phases of the flow (at reduced Δt) limit the ability to gather a continuous data set covering the initial transition, a turbulent phase, a brief relaminarization event, and then a return to turbulence.

Appendix B

Heat transfer enhancement computations with a passive scalar

Ultimately, the practical motivation of this research is to enhance heat transfer, possibly via turbulence. As this work is motivated by self-cooled duct designs, and recalling Chapter 2, Table 2.1, focus is placed on small Richardson numbers, where Ri quantifies the ratio of natural to forced convection, or equivalently, buoyant to inertial forces. Thus, the impact of buoyant forces on the velocity field is assumed minimal. By taking $Ri = 0$, the momentum and energy equations can be decoupled; the former influencing the latter, but the latter not reflecting back on the former. This is equivalent to the evolution of a passive scalar. Thus, in this regime, predictions of turbulence can be made without simulating a scalar field, as has otherwise been performed throughout this thesis, except in this Appendix. To the author's knowledge, no Nusselt number calculations have been performed for high Re electrically insulated (Q2D or 3D) planar MHD duct flows. Thus, the results contained in Appendix B provide a benchmark for high Re electrically insulated duct flows in the limit of purely forced convection.

As evolution is of a passive scalar, the SM82 continuity and momentum equations, Eqs. (2.55) and (2.56), remain unchanged. The SM82 equivalent for the dimensional energy equation is

$$\frac{\partial \check{\theta}_\perp}{\partial \check{t}} + (\check{\boldsymbol{u}}_\perp \cdot \check{\boldsymbol{\nabla}}_\perp)\check{\theta}_\perp = \kappa_{\mathrm{th}} \check{\boldsymbol{\nabla}}_\perp^2 \check{\theta}_\perp, \tag{B.1}$$

where $\check{\theta}_\perp$ is the z-averaged temperature and κ_{th} the fluid's thermal diffusivity. Assuming a constant background streamwise thermal gradient $\partial\check{\Theta}_\perp/\partial x$, the temperature field can be decomposed as

$$\check{\theta}_\perp = \frac{\partial \check{\Theta}_\perp}{\partial \check{x}} \check{x} + \check{\theta}'_\perp, \tag{B.2}$$

where $\breve{\theta}'_\perp$ is a streamwise periodic temperature fluctuation. Substituting Eq. (B.2) into Eq. (B.1) and taking characteristic scales for length, velocity and time as L_y, U_0 and L_y/U_0, as before, yields,

$$\frac{\partial \theta'_\perp}{\partial t} + (\boldsymbol{u}_\perp \cdot \boldsymbol{\nabla}_\perp)\theta'_\perp + \frac{1}{Pr Re Q} u_\perp = \frac{1}{Pr Re} \nabla^2_\perp \theta'_\perp, \tag{B.3}$$

where $Pr = \nu/\kappa_{\text{th}}$ is the Prandtl number of the fluid, and where $Q = \int_{-1}^{1} U_\perp \mathrm{d}y$ is the dimensionless flow rate of the streamwise invariant base flow. Note that the temperature has been non-dimensionalized based on a characteristic temperature difference across the duct of $L_y[\partial\breve{\theta}_\perp/\partial\breve{y}|_{\breve{y}=L_y} - \partial\breve{\theta}_\perp/\partial\breve{y}|_{\breve{y}=-L_y}]$, as from conservation of energy $\partial\breve{\Theta}_\perp/\partial\breve{x} = \kappa_{\text{th}}[\partial\breve{\theta}_\perp/\partial\breve{y}|_{\breve{y}=L_y} - \partial\breve{\theta}_\perp/\partial\breve{y}|_{\breve{y}=-L_y}]/Q$; net heat flux only exits the domain once carried out of by the flow (rate), at the downstream boundary. In the following, to avoid a variable coefficient in Eq. (B.3), Neumann boundary conditions $\partial\theta'_\perp/\partial y|_{y=-1} = -1$ and $\partial\theta'_\perp/\partial y|_{y=1} = 0$ are applied (unity heat flux entering the domain at the bottom wall, and no heat flux exiting the domain at the top wall). Dirichlet boundary conditions would fix the temperature, but would permit variable heat fluxes at each wall. Note that the original simulations of Chapter 7 were driven by constant wall motion, with a fixed flow rate condition not enforced. However, only the flow rate contribution from the base flow is included in Eq. (B.3), which ensures a time steady coefficient.

For baseline comparison, the Nusselt number corresponding to passive scalar transport by the Re independent streamwise invariant base flow is determined. The time steady, streamwise invariant, analytic base flow temperature fluctuation, with boundary conditions $\partial\Theta'_\perp/\partial y|_{y=-1} = -1$ and $\partial\Theta'_\perp/\partial y|_{y=1} = 0$, is

$$\Theta'_\perp = \frac{U_\perp}{QH} - \frac{1}{2}\left(y + \frac{1}{H}\right), \tag{B.4}$$

where $U_\perp = \cosh(H^{1/2}y)/\cosh(H^{1/2})$. Note that $\Theta'_\perp$ is time steady as the non-dimensionalization accounts for the fact that all net heat flux is carried out of the domain by the flow. However, as the analytic solution is defined only up to an arbitrary constant, the additional constraint $\int_{-1}^{1} \Theta'_\perp \mathrm{d}y = 0$ has been imposed. This condition is imposed in the in-house solver, and by translating the temperature profile by this constant, the analytic Nusselt number will be identical regardless if Neumann or Dirichlet boundary conditions had been applied (the translation offsetting the different wall heat fluxes).

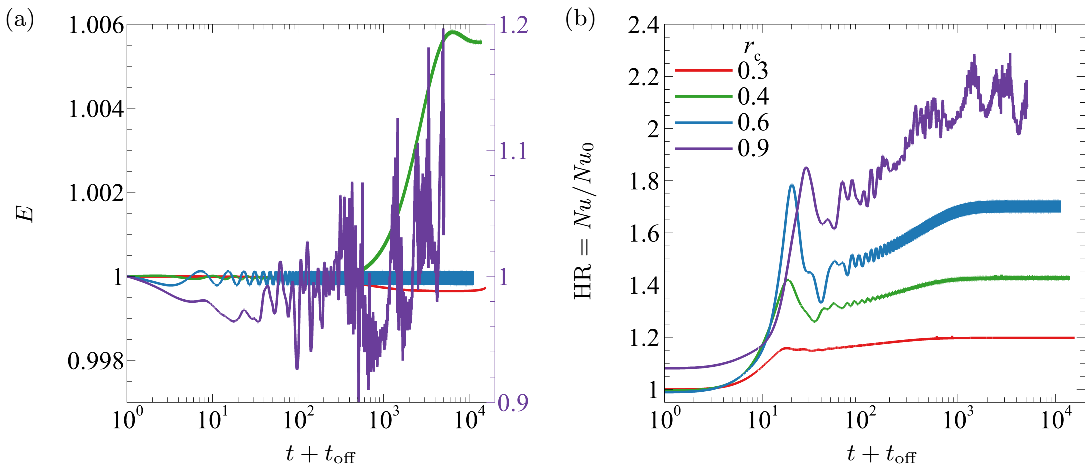

FIGURE B.1: (a) Temporal evolution of perturbation energy $E = \int \hat{u}_\perp^2 + \hat{v}_\perp^2 \mathrm{d}\Omega$ for various r_c ($r_\mathrm{c} \leq 0.6$ on left axis, $r_\mathrm{c} = 0.9$ on right axis). Note the temporal axis has been offset, so that all cases start at $t + t_\mathrm{off} = 1$. The perturbation energy has also been rescaled to unity at $t + t_\mathrm{off} = 1$. (b) Corresponding heat transfer enhancement ratio. Note that some small spikes in the Nusselt number results, particularly noticeable in the lower r_c cases, are due to an issue with the scheme used to numerical integrate Nu (it has limited effect on time averages).

The Nusselt number per unit streamwise length is defined as

$$Nu = \frac{1}{2\pi n/\alpha} \int_0^{2\pi n/\alpha} \frac{1}{\theta'_{\perp,b} - \theta'_\perp(y=-1)} \left.\frac{\partial \theta'_\perp}{\partial y}\right|_{y=-1} \mathrm{d}x, \tag{B.5}$$

where $\theta'_{\perp,b} = \int_{-1}^{1} \theta'_\perp u_\perp \mathrm{d}y / \int_{-1}^{1} u_\perp \mathrm{d}y$. The analytic Nusselt number based on passive transport of $\Theta'_\perp$ by $U_\perp$ is $Nu_0 = 1.731474152252995$ at $H = 10$, independent of Pr and Re. The heat transfer enhancement ratio is defined as $\mathrm{HR} = Nu/Nu_0$, where $Nu(Pr, Re)$ is numerically integrated from the DNS velocity and temperature fields via Eq. (B.5), at $r_\mathrm{c} = 0.3$, 0.4, 0.6 and 0.9. A Prandtl number of $Pr = 0.022$ is selected consistent with previous literature (Cassels *et al.* 2016; Murali *et al.* 2021) and is similar to the Prandtl number of lead lithium at operating temperatures; for lead lithium, Pr varies between 0.0194 and 0.00804 between 600 K and 800 K, respectively (Martelli *et al.* 2019).

Nusselt numbers were computed after the offset time t_off, once the optimally energized simulations of Chapter 7 either began saturating to a finite amplitude state ($r_\mathrm{c} \leq 0.6$), or reached a turbulent state ($r_\mathrm{c} = 0.9$), as indicated by the perturbation energies in Fig. B.1(a). For reference, the offset times are $t_\mathrm{off} = 1.114 \times 10^4$, 1.180×10^4, 2.156×10^4 and 1.080×10^4, for $r_\mathrm{c} = 0.3$, 0.4, 0.6 and 0.9, respectively. However, there is still some slight development of the finite amplitude state at $r_\mathrm{c} = 0.3$ and $r_\mathrm{c} = 0.4$

(although minimal noting the axis scale), whereas $r_c = 0.6$ had saturated well, while the turbulent state at $r_c = 0.9$ was also still in its initial phase.

The corresponding heat transfer enhancement ratios HR $= Nu/Nu_0$ are provided in Fig. B.1(b). Heat flux is introduced at t_{off}, with an initial temperature field of zero. Once thermal diffusion balances advection of the passive scalar (after at least 10^3 time units) some idea of the capability for various r_c to enhance heat transfer is ascertained. Although the temperature field for the turbulent case ($r_c = 0.9$) is yet to settle, it clearly attains the greatest enhancement in heat transfer. However, the turbulent heat transfer rates do not appear to be significantly better than those provided by the finite amplitude states (if one imagined a finite amplitude state, scaled up to $r_c = 0.9$, the heat transfer enhancement ratio may well be relatively similar to the turbulent flow's). For $r_c \leq 0.6$, the lowest three harmonics ($0 \leq \kappa \leq 2$) contain 93% to 94% of the total perturbation energy. Thus, as the finite amplitude states are large scale, overturning (counter-rotating) structures, they may well be quite effective at enhancing heat transfer. At $r_c = 0.9$, the turbulent flow has anywhere from 54% to 86% of the total perturbation energy in the lowest three harmonics, and must instead rely on the smaller scales. However, even though there is still a significant fraction of energy contained in the lowest harmonics when $r_c \leq 0.6$, the actual amount of energy in the harmonics, and thereby the velocity magnitudes, still strongly depend on r_c. This is encapsulated in Table B.1, where by $r_c = 0.3$ (still a relatively large $Re = 2.37370 \times 10^4$) the improvement in the time averaged rate of heat transfer is only 19.7%. At even lower Re, the effectiveness of the finite amplitude states should further worsen.

Four additional ratios have been included in Table B.1. These pressure penalty ratios PR serve to measure the additional pumping costs of turbulent flows, relative to the laminar base line. Note that in the wall driven setup, where the pressure drop is fixed regardless of the flow conditions, the conventional PR is undefined, or unity, depending on frame of reference; the extended Galilean transform is discussed in Chapter 8 (Camobreco *et al.* 2021a). Of the proxy PR which can be constructed, the most useful are based around the ratio of the time averaged measured flow rate to the analytic flow rate. By comparing the heat transfer enhancement ratio to the proxy PR, an overall efficiency for the heat transfer enhancement can be computed (as a measured increase in flow rate, relative to the analytic result, would permit a greater amount of heat to be advected out of the domain, than in the analytic case). The overall efficiency further

r_{c}	0.3	0.4	0.6	0.9
$\mathrm{HR} = \dfrac{Nu}{Nu_0}$	1.1973	1.4274	1.7019	2.1109
$\mathrm{PR_Q} = \dfrac{Q_{\mathrm{m}}}{Q}$	1.1495	1.3143	1.4880	1.4967
$\dfrac{\mathrm{HR}}{\mathrm{PR_Q}}$	1.0416	1.0861	1.1437	1.4104
$\mathrm{PR_f} = \dfrac{f_{\mathrm{m},\nu}}{f_\nu}$	0.9656	1.1614	1.4230	1.7338
$\dfrac{\mathrm{HR}}{\mathrm{PR_f}}$	1.2404	1.2290	1.1960	1.2175
$\dfrac{\mathrm{HR}}{\mathrm{PR_Q}}\dfrac{\mathrm{HR}}{\mathrm{PR_f}}$	1.2921	1.3348	1.3679	1.7171

TABLE B.1: Heat transfer enhancement ratio as a function of r_{c} at $Pr = 0.022$ and $H = 10$ ($Nu_0 = 1.731474152252995$). In addition, the efficiency of the heat transfer enhancement is considered via some proxy pressure penalty ratios (in this setup the actual pressure penalty ratio is unity), where Q_{m} is the measured flow rate, Q the analytic flow rate (Re invariant), $f_{\mathrm{m},\nu}$ the viscous forces integrated over the top and bottom walls per unit length, and f_ν the analytic (Re dependent) integrated viscous force. Note that all measured quantities (Nu, Q_{m} and $f_{\mathrm{m},\nu}$) are time averaged over 4×10^4 data points (a few thousand time units).

highlights the relatively poor performance of the lower r_{c} finite amplitude states, with efficiencies between 4% and 14% (third row of results in Table B.1). The turbulent state then exhibits a clear jump in efficiency, to around 41%.

A proxy PR based on the non-dimensional viscous wall shear stresses was also considered. The wall shear stress $f_{\mathrm{m},\nu} = -(1/Re)(1/(2\pi n/\alpha)) \int_0^{2\pi n/\alpha} [\partial u_\perp/\partial y|_{y=-1} + \partial u_\perp/\partial y|_{y=1}] \mathrm{d}x$, per unit length, was compared to the analytic equivalent f_ν. In this measure, the heat transfer efficiency degrades with increasing Re, for $r_{\mathrm{c}} < 0.6$. However, such a measure would not account for the increased flow rate at larger r_{c}, as the force based measure may only be appropriate when enforcing a fixed flow rate. Both efficiency measures can be considered simultaneously, as shown in the last row of Table B.1.

Appendix C

The effect of higher Reynolds number on sustaining turbulence

As mentioned in Chapter 6 (Camobreco *et al.* 2021b), the supercritical $r_\mathrm{c} = Re/Re_\mathrm{c} = 1.1$ simulations at $H = 1$ and $H = 3$ did not sustain turbulence, as supported by Appendix A. At $H = 1$ turbulence was not triggered, and at $H = 3$ an exceedingly brief turbulent episode was triggered. In both cases, the flow saturated to a stable finite amplitude state, having a very similar appearance to the finite amplitude states observed at subcritical $r_\mathrm{c} \leq 0.6$ at $H = 10$ in Chapter 7. This Appendix contains results at $r_\mathrm{c} = 2$ and $r_\mathrm{c} = 5$, to indicate that the magnitude of the Reynolds number was the key factor hampering transitions to turbulence, at low H in particular.

Note that at $H = 1$, $r_\mathrm{c} = 1.1$ still corresponds to quite a large Reynolds number, $Re_\Delta = 1.10365 \times 10^4$ in the notation of Chapter 6 (Camobreco *et al.* 2021b), yet was unable to trigger turbulence. However, at $H = 1$ and $H = 3$, $r_\mathrm{c} = 2$ and $r_\mathrm{c} = 5$ are both sufficient to trigger turbulence, as shown in Fig. C.1. The turbulence at these $H \leq 3$ is still unable to be sustained at $r_\mathrm{c} = 2$, with eventual relaminarization to a stable finite amplitude state, as shown in the inset of Fig. C.1(a). At $r_\mathrm{c} = 5$, the fate of the simulations remains unknown, due to the expense of simulations with smaller time steps. Note to account for the increased Re, 48 spectral elements were employed in both the streamwise and wall-normal directions, which is approximately 3 times the number of elements in the streamwise direction as employed in the $r_\mathrm{c} = 1.1$ simulations of Chapter 6 (Camobreco *et al.* 2021b). Excepting the use of a smaller initial energy $E_0 = 10^{-8}$, and increased resolution, there are no other differences between these simulations, and those in Chapter 6 (Camobreco *et al.* 2021b). Thus it may be concluded that Re was the key factor hampering the transition to turbulence at low

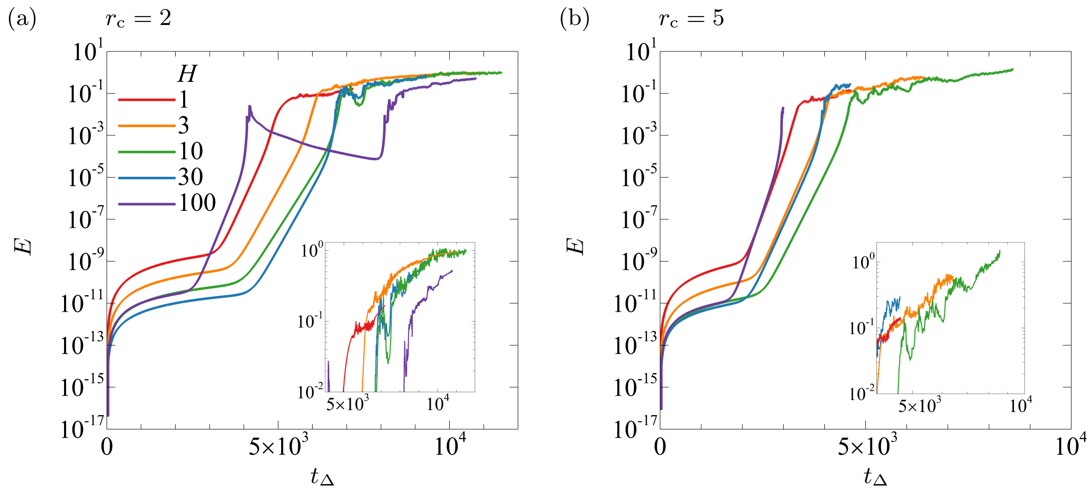

FIGURE C.1: Time histories (rescaled time) of perturbation energy $E = \int \hat{u}_\perp^2 + \hat{v}_\perp^2 \mathrm{d}\Omega$ for various H (see legend); Shercliff flow ($U_\mathrm{R} = 1$) simulations initiated with random noise of initial energy $E_0 = 10^{-8}$. (a) $r_\mathrm{c} = 2$. (b) $r_\mathrm{c} = 5$. Some simulations (larger H) were discontinued as the timestep required to evolve the turbulent flows became unfeasible. The rest just progress slowly due to the increased spatial resolution.

H. However, $r_\mathrm{c} > 2$ appear to be required to sustain turbulence at $H \leq 3$. In contrast, turbulence at $H = 30$ and $H = 100$ appears likely to be sustained at $r_\mathrm{c} = 2$ (although their ultimate fates are unknown, both at $r_\mathrm{c} = 2$ and $r_\mathrm{c} = 5$), whereas turbulence relaminarized at these H at $r_\mathrm{c} = 1.1$ in Chapter 6 (Camobreco *et al.* 2021b). This further supports that different mechanisms lead to relaminarization at high H, than low H, with the former relaminarizing due to a lack base flow production, and the latter due to the magnitude of Re for a given level of criticality.

Appendix D

Flow field comparisons; initial conditions and edge states

This Appendix serves two purposes. First, it highlights some of the key differences between the various initial conditions targeted in or employed by Chapters 5 (Camobreco *et al.* 2020), 6 (Camobreco *et al.* 2021b) and 7. Second, it aims to compare some of the nonlinear flow fields from Chapters 5 (Camobreco *et al.* 2020) and 7, and in particular, indicate how the more complicated structures at lower H, which permit constructive interference between walls, have underlying features which can be observed in the $H \to \infty$ instabilities.

Chapter 5 (Camobreco *et al.* 2020) simulated subcritical transitions in the traditional manner, in selecting the optimal time and wave number to maximize linear transient growth. Having linearly evolved the nonmodal perturbation to this optimal time, the corresponding $H \to \infty$ and $H = 10$ optimals are depicted in Figs. D.1(b) and D.2(b), respectively. These represent what all simulations target in Chapter 5 (Camobreco *et al.* 2020), and what case 0 simulations target in Chapter 7. By comparison, the supercritical simulations of Chapter 6 (Camobreco *et al.* 2021b) target the leading eigenmode, as shown in Figs. D.1(a) and D.2(a), for $H \to \infty$ and $H = 10$, respectively. In particular, note the different aspect ratio. Taking advantage of this difference, the work in Chapter 7 then applies nonmodal linear transient growth techniques to obtain nonmodal equivalents of Figs. D.1(a) and D.2(a). As shown in Chapter 7, for sufficiently large target times, the nonmodal equivalents of the leading eigenmode will be indiscernible from Figs. D.1(a) and D.2(a), with one exception. As discussed in Chapter 3, § 3.3, the nonmodal perturbation is tilted into the base flow shear at early times (extracting energy from the base flow), and is tilted against the base flow shear at large

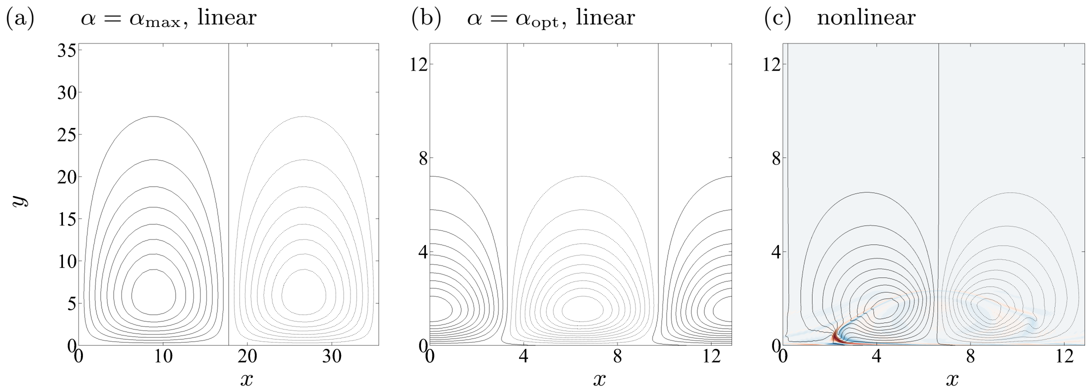

FIGURE D.1: Example flow fields at $r_{\mathrm{c}} = 0.585$, $H \to \infty$. (a) Leading eigenmode. (b) Nonmodal perturbation optimized over all wave numbers and target times (at the optimal time). (c) Nonlinearly evolved linear optimal. Perturbation structures are indicated by $\hat{v}_{\perp}$ velocity contour lines. The nonlinear case also includes the high-pass filtered vorticity $\hat{\omega}_{z,|\kappa|\geq 4}$, where streamwise Fourier coefficients of modes $\kappa < 4$ have been removed. Positive (negative) velocities denoted by solid (dashed) lines; positive (negative) vorticity denoted by red (blue) flooding; plotted between $-\max(|\hat{v}_{\perp}|) < \hat{v}_{\perp} < \max(|\hat{v}_{\perp}|)$, or $-\max(|\hat{\omega}_{z,|\kappa|\geq 4}|) < \hat{\omega}_{z,|\kappa|\geq 4} < \max(|\hat{\omega}_{z,|\kappa|\geq 4}|)$. The vorticity highlights the key arched feature of the TS wave.

times (being upright only near the time of maximum growth). By comparison, the leading eigenmode advects in the upright position for its entire (linear) lifetime, without any tilt. Thus, with any finite target time for nonmodal optimization, there will remain some differences between the nonlinear optimal targeting the leading eigenmode and the leading eigenmode itself. Note that as the wave number maximizing linear growth differs significantly from the wave number minimizing linear decay, the linear optimals employed in Chapter 5 (Camobreco *et al.* 2020) may never appreciably excite the leading eigenmode. Specifically, recall how thin the wave number bands which excite the linear instability are at large H, as shown in Chapter 3, § 3.2. This may have serious implications on the ability to sustain turbulence.

Chapter 5 (Camobreco *et al.* 2020) also introduced a nonlinear equivalent to the Tollmien–Schlichting wave, termed the arched TS wave therein. Figure D.1(c) highlights the two key features of the arched TS wave. The first is the arch itself, a thin jet, or shear layer, of positive and negative vorticity. The vorticity magnitudes in the arch have never been observed to be symmetric (in this case, the upstream half of the arch has larger magnitudes, although sometimes the downstream half may instead). This results in the second key feature, a pinching of the TS wave along the line of the arch,

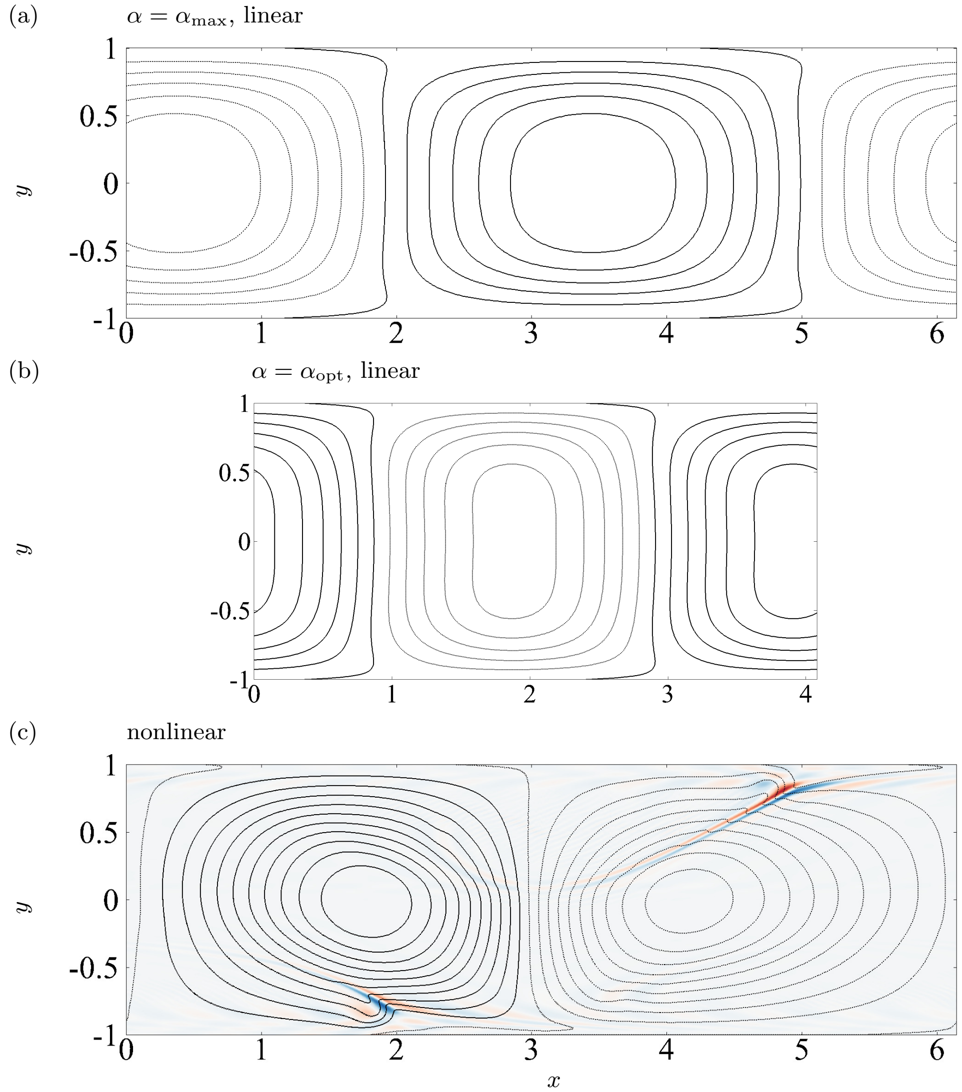

FIGURE D.2: Example flow fields at $r_{\mathrm{c}} = 0.6$, $H = 10$. (a) Leading eigenmode. (b) Nonmodal perturbation optimized over all wave numbers and target times (at the optimal time). (c) Nonlinearly evolved linear optimal. Note that at $H = 10$ the TS waves are conjoined, rather than isolated at each wall, as in Chapter 6 (Camobreco *et al.* 2021b). Perturbation structures are indicated by $\hat{v}_{\perp}$ velocity contour lines. The nonlinear case also includes the high-pass filtered vorticity $\hat{\omega}_{z,|\kappa|\geq 10}$, where streamwise Fourier coefficients of modes $\kappa < 10$ have been removed. Positive (negative) velocities denoted by solid (dashed) lines; positive (negative) vorticity denoted by red (blue) flooding; plotted between $-\max(|\hat{v}_{\perp}|) < \hat{v}_{\perp} < \max(|\hat{v}_{\perp}|)$, or $-\max(|\hat{\omega}_{z,|\kappa|\geq 10}|) < \hat{\omega}_{z,|\kappa|\geq 10} < \max(|\hat{\omega}_{z,|\kappa|\geq 10}|)$. The vorticity still highlights the arched features of the finite amplitude state, which is observed to be stable for over 2×10^4 times units, as shown in Chapter 7.

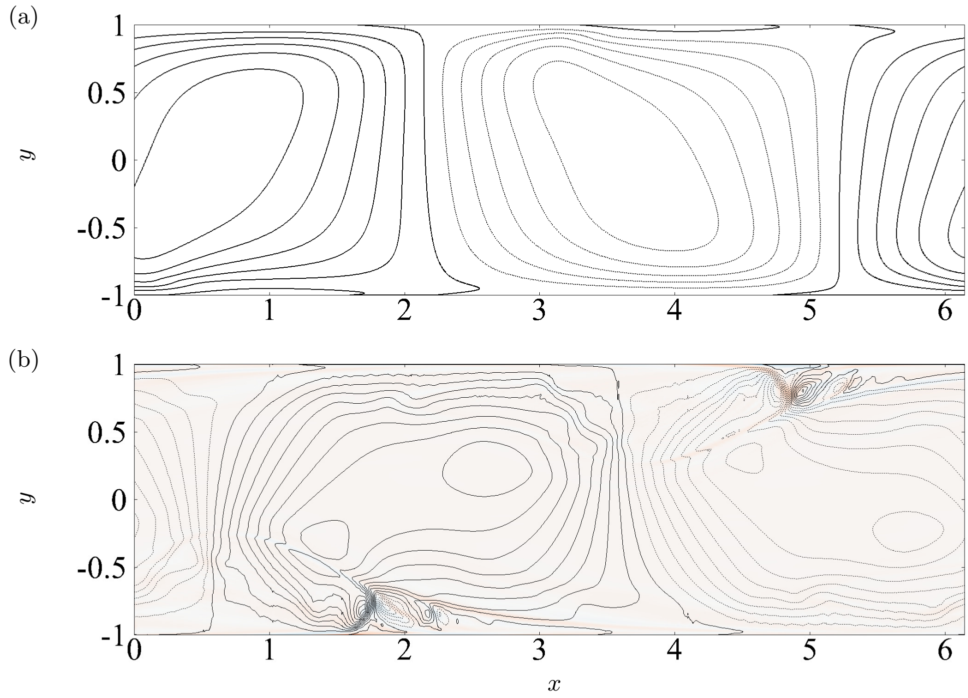

FIGURE D.3: Example flow fields at $r_c = 0.6$, $H = 10$. (a) The slanted TS wave, representative of a slight departure from the weakly nonlinear edge state near the critical amplitude; see Chapter 7 for a breakdown of the edge state. (b) The generation of the arch feature, by virtue of pinch points (velocity dipoles) near the duct walls, which act as a precursor for turbulence. Perturbation structures are indicated by $\hat{v}_{\perp}$ velocity contour lines. Both cases are nonlinear, although only (b) includes the high-pass filtered vorticity $\hat{\omega}_{z,|\kappa|\geq 4}$, where streamwise Fourier coefficients of modes $\kappa < 4$ have been removed. The slanted TS wave is predominantly composed of only three harmonics, which is insufficient to clearly highlight the arch (it is only barely visible in (b) as it is). Positive (negative) velocities denoted by solid (dashed) lines; positive (negative) vorticity denoted by red (blue) flooding; plotted between $-\max(|\hat{v}_{\perp}|) < \hat{v}_{\perp} < \max(|\hat{v}_{\perp}|)$, or $-\max(|\hat{\omega}_{z,|\kappa|\geq 4}|) < \hat{\omega}_{z,|\kappa|\geq 4} < \max(|\hat{\omega}_{z,|\kappa|\geq 4}|)$. Dipoles of $\hat{v}_{\perp}$ velocity (adjacent positive and negative wall-normal velocity) are located near the base of each arch, near $x = 1.7$ along the bottom wall and $x = 4.9$ along the top wall.

originating at a pinch point close to the wall. Although not observable in Fig. D.1(c), the pinch point originates from a localized velocity dipole. The equivalent situation at $H = 10$ is shown in Fig. D.3(b); for $H \to \infty$, the interested reader is referred to the supplementary material accompanying Camobreco *et al.* (2020). Although the arch in Fig. D.3(b) is yet to distinctly form, the underlying lines of the arch can be observed between the velocity dipoles (i.e. near $x = 1.7$ for the bottom wall arch, and $x = 4.9$ for the top wall arch).

Note that the velocity dipoles/pinch points appear to foreshadow turbulent episodes, although whether the turbulence is transient or sustained is a different matter entirely. By comparison, the arches (or jets), which appear related to the dipoles, seem to be an integral component of both sustained supercritical or subcritical turbulence, as observed in high-pass filtered snapshots in Chapters 6 (Camobreco *et al.* 2021b) and 7, respectively. Furthermore, the arches are the dominant feature of the stable (and thereby indefinitely sustained) finite amplitude states observed at $r_c \leq 0.6$ in Chapter 7. Thus, Figs. D.1(c) and D.2(c) compare the respectively unstable and stable finite amplitude states observed in Chapters 5 (Camobreco *et al.* 2020) and 7 at $H \to \infty$ and $H = 10$. Note that the stable finite amplitude state at $H = 10$ has two arches, one at each wall, although the jets emanating from near the top wall are more pronounced. Also note the deformation of the TS wave which the arches induce, which evidently assists its finite amplitude stability. Although the entire conjoined arched TS wave advects through the domain, the snapshots of Fig. D.2(c) and D.3(b) were intentionally selected so there phase was almost identical, to help cement the idea of the arches emanating from the pinch points/velocity dipoles. Exactly why the $H \to \infty$ arched TS wave is not stable at finite amplitudes remains unknown. However, recall that the results of Chapter 5 (Camobreco *et al.* 2020) considered $\alpha = \alpha_{\mathrm{opt}}$, whereas the stable finite amplitude states were observed at $\alpha = \alpha_{\mathrm{max}}$, which may make all the difference. Finally, one additional TS wave image has been included in Fig. D.3(a). This depicts the slight deformation of the slanted TS wave, as in Chapter 7, which eventually leads to the formation of pinch points, and then on to turbulence.

Appendix E

The effect of amplitude ratio on Q2D transitions in pulsatile flows

As discussed in Chapter 8 (Camobreco *et al.* 2021a), transitions to turbulence were not observed for pulsatile flows at $r_{\mathrm{c}} = 1.1$ at $H \leq 10$, $\Gamma = 1$. Although up to 18 orders of magnitude of growth was attained, nonlinear modulation stabilized the base flow, with saturation to a periodic, but evidently laminar, finite amplitude state. Thus, Fig. E.1 depicts the results of simulations both at larger H, as in Chapter 6 (Camobreco *et al.* 2021b) these were better able to transition to turbulence, and at larger Γ (supposing, for the moment, that less linear growth will lead to a less severe nonlinear modulation, and possibly permit turbulence).

Considering $H = 100$ first, a transition to turbulence was observed in the $\Gamma \to \infty$ steady equivalent; see Chapter 6 (Camobreco *et al.* 2021b), Fig. 14 therein. However, relaminarization occurred shortly thereafter. From Fig. E.1(a), at $\Gamma = 100$, no clear transition is observed, although there may be a fleeting turbulent episode. However, neither is there saturation to a stable finite amplitude state. Thus, at large Γ, the base flow has not been nonlinearly stabilized, with relaminarization toward the laminar fixed point. At $\Gamma = 10$ the intracyclic growth is much larger. A first excursion toward the turbulent basin occurs, although its fate is unclear, as for $\Gamma = 100$. Relaminarization appears to be toward the laminar fixed point. However, being at a supercritical Reynolds number, the leading eigenmode is re-excited, with the return of both exponential and intracyclic growth. On the second excursion toward the turbulent basin, clear nonlinear modulation of the base flow is observed, as identified by the intracyclic decay being severely truncated, recalling Chapter 8 (Camobreco *et al.* 2021a). Although turbulence is not clearly observed after this second excursion at $\Gamma = 10$, neither does

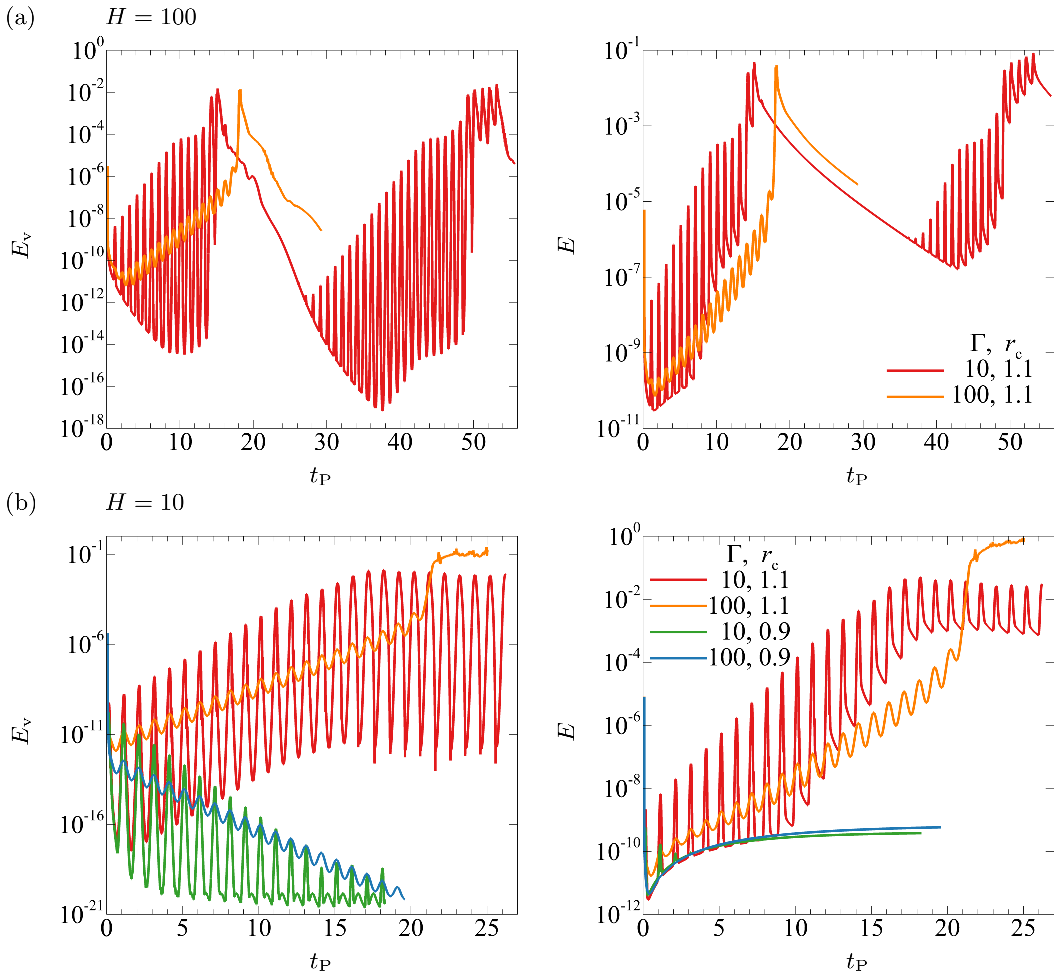

FIGURE E.1: Temporal evolution (rescaled time $t_P = t/2\pi$) of the perturbation energy measured as $E_v = \int \hat{v}_\perp^2 \, d\Omega$ (left column) and $E = \int \hat{u}_\perp^2 + \hat{v}_\perp^2 \, d\Omega$ (right column). (a) $H = 10$. (b) $H = 100$. Simulations initiated with random noise ($E_0 = 10^{-6}$), and at Sr minimizing r_s (the ratio of the critical Reynolds number for the pulsatile base flow to that for the steady base flow). At $r_c = 1$, the optimal Sr is $\approx 9 \times 10^{-3}$ for both $H = 100$ cases, $\approx 1.6 \times 10^{-2}$ for $\Gamma = 10$, $H = 10$ and $\approx 1.5 \times 10^{-2}$ for $\Gamma = 100$, $H = 10$ (the optimal Sr varies weakly for these Γ). $r_c = Re/Re_c$ as before, where Re_c is defined by the pulsatile base flow.

indefinite nonlinear stabilization of the base flow occur, with decay again toward the laminar fixed point.

At $H = 10$, $\Gamma = 10$, intracyclic growth is still quite large, and after the initial stage of both exponential and intracyclic growth, nonlinear stabilization of the base flow ensues. Saturation to the finite amplitude state appears indefinite. However, at $H = 10$, $\Gamma = 100$, being much closer to the steady limit, there is far less intracyclic growth, and thereby reduced nonlinear stabilization of the base flow. In this case, after the exponential growth, a transition to turbulence occurs. While observing transition at

$H = 10$, $\Gamma = 100$ matches theoretical expectations, this result raises practical concerns, as the critical Reynolds number was only reduced by approximately 0.573% relative to the steady equivalent (compared to 33.0% at $H = 10$, $\Gamma = 10$). However, triggering turbulence at $\Gamma = 10$ appears unlikely, at least when targeting the leading eigenmode in this manner.

Note that two subcritical Reynolds numbers were also simulated at $H = 10$ as control cases. They sensibly decay, as expected, and provide a base line for comparison for any nonlinear modulation (which appears in E, but not E_{v}), which is small, but observable.

Appendix F

Support for claims that intermittent turbulence is sustained

Further numerical evidence that intermittent turbulent states are sustained is provided here. The effect of varying the initial condition (through τ, but while at $\alpha = \alpha_{\max}$) at $r_c = 0.9$ is shown in Fig. F.1(a). As shown, turbulence is sustained for all initial conditions tested. Furthermore, the likelihood of brief relaminarization events (intermittency) appears stochastic, with no clear trend when varying $T = \tau/\tau_{\mathrm{opt}}$ (although with such a small sample, it is hard to be conclusive). The effect of r_c, and particularly the criticality, is depicted in Fig. F.1(b). As discussed in Chapter 7, § 7.6, $r_c = 0.6$ is sufficient to trigger, but not sustain, turbulence. Comparatively, $r_c = 0.9$ sustains turbulence, but with stochastic relaminarization events. Thus, $r_c = 1.1$ was also tested, to determine if supercriticality might ensure fully developed turbulence. Both a nonmodal perturbation (the choice of initial energy not greatly relevant) and white noise initial seed were separately evolved at $r_c = 1.1$. Both also appear to sustain turbulence, but again intermittently, even though the Reynolds number is supercritical. Note that the $r_c = 1.1$ white noise case is also depicted in the state space discussed in Chapter 7, § 7.2; the clear relaminarization event shown in the state space corresponding to $t \approx 3.3 \times 10^4$. For direct comparison, a state space representation of the subcritical, nonmodal perturbations yielding the smallest E_D found in Chapter 7, § 7.6 is also provided in Fig. F.2. It bears many resemblances to the state space discussed in Chapter 7, § 7.2, as although the latter was at fixed $r_c = 1.1$, as H varies, so too does the magnitude of the Reynolds number. Thus, criticality does not appear greatly relevant to either ensuring turbulence is sustained, or is fully developed. At very low Re, the flow always remains

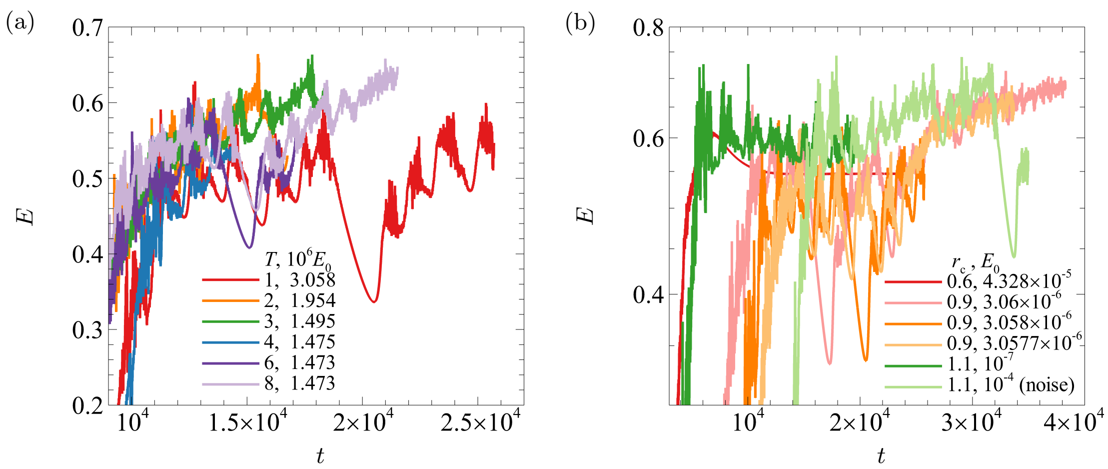

FIGURE F.1: (a) DNS of linear transient optimals with $T = \tau/\tau_{\text{opt}}$ of 1 through 8 at $r_{\text{c}} = 0.9$; data identical to Fig. 7.8(a) except zoomed in. (b) DNS of linear transient optimals with $T = 1$ varying r_{c}; data identical to Figs. 7.3(b) and 7.8(b) except zoomed in, excepting the white noise case, from Chapter 6 (Camobreco *et al.* 2021b).

laminar, at intermediate Re, there is a single turbulent episode, and at large Re (at $r_{\text{c}} > 1$, for $H \leq 3$ and $H \geq 30$, and $r_{\text{c}} < 1$ at $H = 10$), turbulence is sustained, but intermittent.

Finally, the effect of increasing the domain length on intermittency is briefly considered at $r_{\text{c}} = 0.9$. Sadly, due to the additional numerical cost induced by doubling the domain length (the initial condition is composed of two repetitions so that $\alpha = \alpha_{\text{max}}$) these results are not yet convincing, but are presented regardless in Fig. F.3. Promisingly, doubling the domain length has had no effect on E_{D}, which remains identical (to 4 significant figures) to the original domain length cases. However, whether the turbulence which is triggered is intermittent or indefinitely sustained (but not necessarily fully developed, with sporadic relaminarizations present) remains unclear.

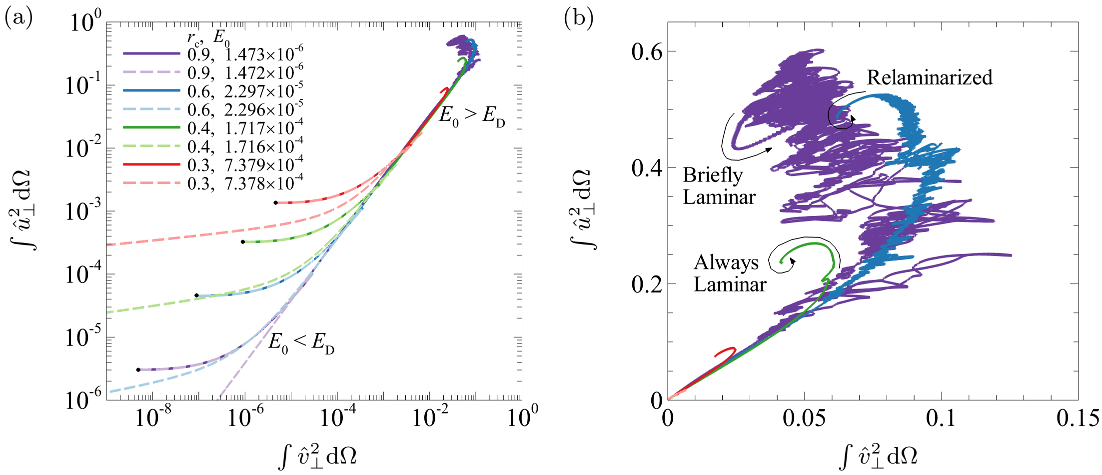

FIGURE F.2: (a) State space representation of the largest T, smallest E_{D} cases for each r_{c} (see legend), with E_0 just above, and just below, E_{D}. The initial conditions are marked with filled black circles. (b) Zoom in on the fate of cases with $E_0 > E_{\mathrm{D}}$.

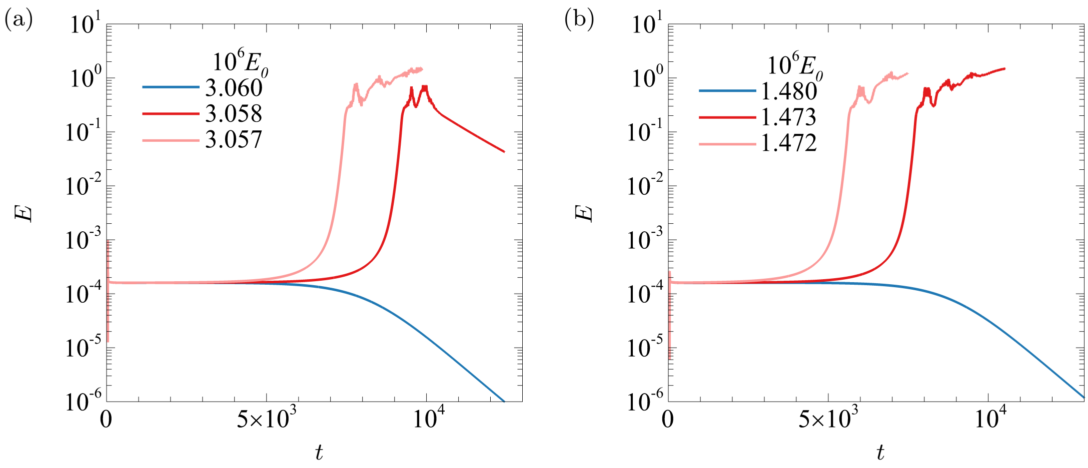

FIGURE F.3: DNS of linear transient optimals at $r_{\mathrm{c}} = 0.9$, varying E_0, with a setup identical to case 1 except with the domain length doubled (and with two repetitions of the initial condition). (a) $T = 1$ ($E_0 = 3.058 \times 10^{-6} > E_{\mathrm{D}}$ unchanged relative to the original domain length simulations). (b) $T = 8$ ($E_0 = 1.473 \times 10^{-6} > E_{\mathrm{D}}$ also unchanged).

Appendix G

An improved estimate for the threshold Reynolds number above which turbulence is sustained

Recalling Chapter 7, $r_\mathrm{c} = 0.6$ was unable to sustain turbulence in the thermodynamic limit of large times, while $r_\mathrm{c} = 0.9$ was able to. Note that Avila *et al.* (2011) indicate that Re is the sole parameter governing the ability to sustain turbulence, at least for hydrodynamic pipe flows in sufficiently long pipes. Thus, this Appendix presents additional computations at $r_\mathrm{c} = 0.7$ and $r_\mathrm{c} = 0.8$ to slightly improve the estimate of the threshold Reynolds number above which turbulence can be indefinitely sustained (at $H = 10$ for case 1). As shown in Fig. G.1, for cases with $E_0 > E_\mathrm{D}$ ($T = 1$ and $T = 8$ initial conditions), $r_\mathrm{c} = 0.7$ eventually relaminarizes. Note that, comparing the times taken to relaminarize ($T = 8$ initial conditions), $r_\mathrm{c} = 0.6$ relaminarizes at $t \approx 7 \times 10^3$, whereas $r_\mathrm{c} = 0.7$ takes approximately twice as long, relaminarizing at $t \approx 1.4 \times 10^4$. If the dependence of relaminarization time on r_c is superexponential, it could take until $t \approx 3 \times 10^4$ to ascertain the fate of turbulence at $r_\mathrm{c} = 0.8$. For now, $r_\mathrm{c} = 0.8$ is tentatively assessed as indefinitely sustaining turbulence, although with additional simulation time this claim could be strengthened.

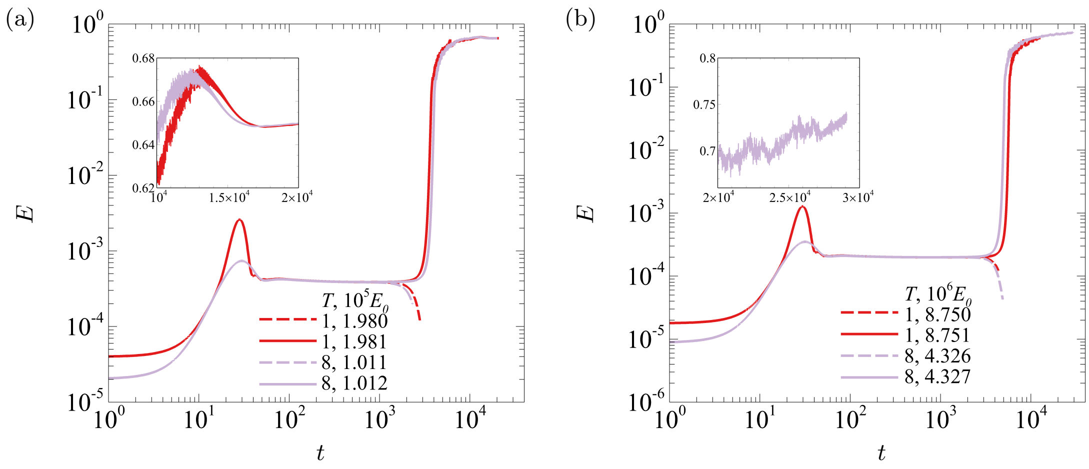

FIGURE G.1: DNS of linear transient optimals at $r_\mathrm{c} = 0.7$ and $r_\mathrm{c} = 0.8$, varying E_0 (after having first determined E_D) for $T = 1$ and $T = 8$ initial conditions. (a) $r_\mathrm{c} = 0.7$; eventual relaminarization, as highlighted in inset. (b) $r_\mathrm{c} = 0.8$; possible indefinite turbulent sustainment, although as highlighted in inset, the turbulence may be yet to saturate.

Bibliography

Abdessemed, N., Sharma, A. S., Sherwin, S. J. & Theofilis, V. 2009 Transient growth analysis of the flow past a circular cylinder. *Phys. Fluids* **21** (4), 044103.

Abdou, M., Morley, N. B., Smolentsev, S., Ying, A., Malang, S., Rowcliffe, A. & Ulrickson, M. 2015 Blanket/first wall challenges and required R&D on the pathway to DEMO. *Fusion Eng. Des.* **100**, 2–43.

Airiau, C. & Castets, M. 2004 On the amplification of small disturbances in a channel flow with a normal magnetic field. *Phys. Fluids* **16** (8), 2991–3005.

Albrecht, T., Grundmann, R., Mutschke, G. & Gerbeth, G. 2006 On the stability of the boundary layer subject to a wall-parallel Lorentz force. *Phys. Fluids* **18**, 098103.

Alemany, A., Moreau, R., Sulem, P. L. & Frisch, U. 1979 Influence of an external magentic field on homogeneous MHD turbulence. *Journal de Méchanique* **18** (2), 277–312.

Alfvén, H. 1942 Existence of electromagnetic-hydrodynamic waves. *Nature* **3805**, 405–406.

Anderson, E., Bai, Z., Bischof, C., Blackford, S., Demmel, J., Dongarra, J., Croz, J. D., Greenbaum, A., Hammarling, S., McKenney, A. & Sorenson, D. 1999 *LAPACK Users' Guide*. Society for Industrial and Applied Mathematics, Philadelphia.

Authié, G., Tagawa, T. & Moreau, R. 2003 Buoyant flow in long vertical enclosures in the presence of a strong horizontal magnetic field. Part 2. Finite enclosures. *Eur. J. Mech. B-Fluids* **22** (3), 203–220.

Avila, K., Moxey, D., de Lozar, A., Avila, M., Barkley, D. & Hof, B. 2011 The onset of turbulence in pipe flow. *Science* **333** (6039), 192–196.

Avila, M. & Hof, B. 2013 Nature of laminar-turbulence intermittency in shear flows. *Phys. Rev. E* **87** (6), 063012.

BAINES, P. G., MAJUMDAR, S. J. & MITSUDERA, H. 1996 The mechanics of the Tollmien–Schlichting wave. *J. Fluid Mech.* **312**, 107–124.

BAINES, P. G. & MITSUDERA, H. 1994 On the mechanism of shear flow instabilities. *J. Fluid Mech.* **276**, 327–342.

BAKER, N. T., POTHÉRAT, A., DAVOUST, L. & DEBRAY, F. 2018 Inverse and direct energy cascades in three-dimensional magnetohydrodynamic turbulence at low magnetic Reynolds number. *Phys. Rev. Lett.* **120**, 224502.

BARKLEY, D. 2016 Theoretical perspective on the route to turbulence in a pipe. *J. Fluid Mech.* **803**, P1.

BARKLEY, D., BLACKBURN, H. M. & SHERWIN, S. J. 2008 Direct optimal growth analysis for timesteppers. *Int. J. Numer. Methods Fluids* **57**, 1435–1458.

BARLEON, L., BURR, U., MACK, K. J. & STIEGLITZ, R. 2000a Heat transfer in liquid metal cooled fusion blankets. *Fusion Eng. Des.* **51-52**, 723–733.

BARLEON, L., BURR, U., MACK, K. J. & STIEGLITZ, R. 2000b Magnetohydrodynamic heat transfer research related to the design of fusion blankets. *Fusion Technol.* **39** (2), 127–156.

BELYAEV, I., FRICK, P., RAZUVANOV, N., SVIRIDOV, E. & SVIRIDOV, V. 2018 Temperature fluctuations in a nonisothermal mercury pipe flow affected by a strong transverse magnetic field. *Int. J. Heat Mass Transf.* **127**, 566–572.

BENEITEZ, M., DUGUET, Y., SCHLATTER, P. & HENNINGSON, D. S. 2019 Edge tracking in spatially developing boundary layer flows. *J. Fluid Mech.* **881**, 164–181.

BENEITEZ, M., DUGUET, Y., SCHLATTER, P. & HENNINGSON, D. S. 2020 Edge manifold as a Lagrangian coherent structure in a high-dimensional state space. *Phys. Rev. Research* **2** (3), 033258.

BIAU, D. 2016 Transient growth of perturbations in Stokes oscillatory flows. *J. Fluid Mech.* **794**, R4.

BIAU, D. & BOTTARO, A. 2004 Transient growth and minimal defects: Two possible initial paths of transition to turbulence in plane shear flows. *Phys. Fluids* **16** (10), 3515.

BIAU, D. & BOTTARO, A. 2009 An optimal path to transition in a duct. *Phil. Trans. R. Soc. A* **367**, 529–544.

BLACKBURN, H. M., BARKLEY, D. & SHERWIN, S. J. 2008 Convective instability and transient growth in flow over a backward-facing step. *J. Fluid Mech.* **603**, 271–304.

Blennerhassett, P. J. & Bassom, A. P. 2002 The linear stability of flat stokes layers. *J. Fluid Mech.* **464**, 393–410.

Blennerhassett, P. J. & Bassom, A. P. 2006 The linear stability of high-frequency oscillatory flow in a channel. *J. Fluid Mech.* **556**, 1–25.

Bos, W. J. 2021 Three-dimensional turbulence without vortex stretching. *J. Fluid Mech.* **915**, A121.

Bottaro, A., Corbett, P. & Luchini, P. 2003 The effect of base flow variation on flow stability. *J. Fluid Mech.* **476**, 293–302.

Bucenieks, I., Krishbergs, R., Platacis, E., Lipsbergs, G., Shishko, A., Zik, A. & Muktepavela, F. 2006 Investigation of corrosion phenomena in EUROFER steel in Pb-Li stationary flow exposed to a magnetic field. *Magnetohydrodynamics* **42** (2/3), 237–251.

Budanur, N. B., Marensi, E., Willis, A. P. & Hof, B. 2020 Upper edge of chaos and the energetics of transition in pipe flow. *Phys. Rev. Fluids* **5**, 023903.

Bühler, L. 1995 The influence of small cracks in insulating coatings on the flow structure and pressure drop in MHD channel flows. *Fusion Eng. Des.* **27**, 650–658.

Bühler, L. 1996 Instabilities in quasi-two-dimensional magnetohydrodynamic flows. *J. Fluid Mech.* **326**, 125–150.

Bühler, L. 1998 Laminar buoyant magnetohydrodynamic flow in vertical rectangular ducts. *Phys. Fluids* **10** (1), 223–236.

Bühler, L. & Mistrangelo, C. 2013 Magnetohydrodyamic flows in breeder units of a HCLL blanket with spatially varying magnetic fields. *Fusion Eng. Des.* **88**, 2314–2318.

Burr, U., Barleon, L., Müller, U. & Tsinober, A. 2000 Turbulent transport of momentum and heat in magnetohydrodynamic rectangular duct flow with strong sidewall jets. *J. Fluid Mech.* **406**, 247–279.

Burr, U. & Müller, U. 2002 Rayleigh–Bénard convection in liquid metal layers under the influence of a horizontal magnetic field. *J. Fluid Mech.* **453**, 345–369.

Butler, K. M. & Farrell, B. F. 1992 Three-dimensional optimal perturbations in viscous shear flow. *Phys. Fluids A* **4** (8), 1637–1650.

Camobreco, C. J., Pothérat, A. & Sheard, G. J. 2020 Subcritical route to turbulence via the Orr mechanism in a quasi-two-dimensional boundary layer. *Phys. Rev. Fluids* **5** (11), 113902.

Camobreco, C. J., Pothérat, A. & Sheard, G. J. 2021a Stability of pulsatile quasi-two-dimensional duct flows under a transverse magnetic field. *Phys. Rev. Fluids* **6** (5), 053903.

Camobreco, C. J., Pothérat, A. & Sheard, G. J. 2021b Transition to turbulence in quasi-two-dimensional MHD flow driven by lateral walls. *Phys. Rev. Fluids* **6** (1), 013901.

Carbone, M. & Bragg, A. D. 2020 Is vortex stretching the main cause of the turbulent energy cascade? *J. Fluid Mech.* **883**, R2.

Cassels, O. G. W., Hussam, W. K. & Sheard, G. J. 2016 Heat transfer enhancement using rectangular vortex promoters in confined quasi-two-dimensional magnetohydrodynamic flows. *Int. J. Heat Mass Transf.* **93**, 186–199.

Cassels, O. G. W., Vo, T., Pothérat, A. & Sheard, G. J. 2019 From three-dimensional to quasi-two-dimensional: transient growth in magnetohydrodynamic duct flows. *J. Fluid Mech.* **861**, 382–406.

Chantry, M., Tuckerman, L. S. & Barkley, D. 2017 Universal continuous transition to turbulence in a planar shear flow. *J. Fluid Mech.* **824**, R1.

Chen, S., Ecke, R. E., Eyink, G. L., Rivera, M., Wan, M. & Xiao, Z. 2006 Physical mechanism of the two-dimensional inverse energy cascade. *Phys. Rev. Lett.* **96** (8), 084502.

Cherubini, S., Palma, P. D. & Robinet, J.-C. 2015 Nonlinear optimals in the asymptotic suction boundary layer: Transition thresholds and symmetry breaking. *Phys. Fluids* **27** (3), 4108.

Cherubini, S., Palma, P. D., Robinet, J.-C. & Bottaro, A. 2011 The minimal seed of turbulent transition in the boundary layer. *J. Fluid Mech.* **689**, 221–253.

Choi, H., Lee, D., Lim, J. & Kim, J. 1997 Control of near-wall streamwise vortices using an electromagnetic force in a conducting fluid. *AIAA Paper 97-2059* .

Cuevas, S., Smolentsev, S. & Abdou, M. A. 2006 On the flow past a magnetic obstacle. *J. Fluid Mech.* **553**, 227–252.

Davidson, P. A. 1995 Magnetic damping of jets and vortices. *J. Fluid Mech.* **299**, 153–186.

Davidson, P. A. 2001 *An Introduction to Magnetohydrodynamics*. Cambridge University Press, Cambridge.

Davidson, P. A. 2013 *Turbulence in rotating, stratified and electrically conducting fluids*. Cambridge University Press, Cambridge.

D'Errico, J. 2019 (Block) tri-diagonal matrices. MATLAB Central File Exchange, (https://www.mathworks.com/matlabcentral/fileexchange/10603-block-tri-diagonal-matrices). Retrieved 2019.

Dousset, V. & Pothérat, A. 2008 Numerical simulations of a cylinder wake under a strong axial magnetic field. *Phys. Fluids* **20** (1), 017104.

Dragoş, L. 1975 *Magnetofluid Dynamics*. Abacus Press.

Drazin, P. G. & Reid, W. H. 2004 *Hydrodynamic Stability*. Cambridge University Press, Cambridge.

Duguet, Y., Monokrousos, A., Brandt, L. & Henningson, D. S. 2013 Minimal transition thresholds in plane Couette flow. *Phys. Fluids* **25** (8), 4103.

Duguet, Y., Schlatter, P. & Henningson, D. S. 2009 Localized edge states in plane Couette flow. *Phys. Fluids* **21** (11), 1701.

Duguet, Y., Schlatter, P., Henningson, D. S. & Eckhardt, B. 2012 Self-sustained localized structures in a boundary layer flow. *Phys. Rev. Lett.* **108** (4), 4501.

Faisst, H. & Eckhardt, B. 2004 Sensitive dependence on initial conditions in transition to turbulence in pipe flow. *J. Fluid Mech.* **504**, 343–352.

Falkovich, G. & Vladimirova, N. 2018 Turbulence appearance and nonappearance in thin fluid layers. *Phys. Rev. Lett.* **121** (16), 164501.

Farano, M., Cherubini, S., Robinet, J.-C. & Palma, P. D. 2016 Subcritical transition scenarios via linear and nonlinear localized optimal perturbations in plane Poiseuille flow. *Fluid Dyn. Res.* **48** (6), 1409.

Farrell, B. F. 1988 Optimal excitations of perturbations in viscous shear flow. *Phys. Fluids* **31** (8), 2093–2102.

Farrell, B. F. & Ioannou, P. J. 1993 Optimal excitation of three-dimensional perturbations in viscous constant shear flow. *Phys. Fluids A* **5** (6), 1390–1400.

Farrell, B. F. & Ioannou, P. J. 1999 Optimal excitation of magnetic fields. *Astrophys. J.* **522** (2), 1079–1087.

Grossmann, S. 2000 The onset of shear flow turbulence. *Rev. Mod. Phys.* **72** (2), 603–618.

Gustavsson, L. H. 1979 Initial-value problem for boundary layer flows. *Phys. Fluids* **22** (9), 1602–1605.

Hagan, J. & Priede, J. 2013a Capacitance matrix technique for avoiding spurious eigenmodes in the solution of hydrodynamic stability problems by Chebyshev collocation method. *J. Comput. Phys.* **238**, 210–216.

Hagan, J. & Priede, J. 2013b Weakly nonlinear stability analysis of magnetohydrodynamic channel flow using an efficient numerical approach. *Phys. Fluids* **25**, 124108.

Hairer, E., Nørsett, S. P. & Wanner, G. 1993 *Solving Ordinary Differential Equations I: Nonstiff Problems*. Springer-Verlag Berlin Heidelberg.

Hamid, A. H. A., Hussam, W. K. & Sheard, A. P. G. J. 2015 Spatial evolution of a quasi-two-dimensional Kármán vortex street subjected to a strong uniform magnetic field. *Phys. Fluids* **27** (5), 053602.

Hamid, A. H. A., Hussam, W. K. & Sheard, G. J. 2016a Combining an obstacle and electrically driven vortices to enhance heat transfer in a quasi-two-dimensional MHD duct flow. *J. Fluid Mech.* **792**, 364–396.

Hamid, A. H. A., Hussam, W. K. & Sheard, G. J. 2016b Heat transfer augmentation of a quasi-two-dimensional MHD duct flow via electrically driven vortices. *Numer. Heat Tr. A-Appl.* **70** (8), 847–869.

Hartmann, J. 1937 Theory of the laminar flow of an electrically conductive liquid in a homogeneous magnetic field. *Mat. Fys. Medd. K. Dan. Vidensk. Selsk.* **15** (6), 1–28.

Henningson, D. 1996 Comment on "Transition in shear flows. Nonlinear normality versus non-normal linearity" [Phys. Fluids 7, 3060 (1995)]. *Phys. Fluids* **8** (8), 2257.

Hof, B., de Lozar, A., Avila, M., Tu, X. & Schneider, T. M. 2010 Eliminating turbulence in spatially intermittent flows. *Science* **327** (5972), 1491–1494.

Hof, B., Westerweel, J., Schneider, T. M. & Eckhardt, B. 2006 Finite lifetime of turbulence in shear flows. *Nature* **443** (7), 59–62.

Hopf, E. 1948 A mathematical example displaying features of turbulence. *Commun. Pure Appl. Math* **1** (4), 303–322.

Hossain, M. A. 1992 Viscous and Joule heating effects on MHD-free convection flow with variable plate temperature. *Int. J. Heat Mass Transf.* **35** (12), 3485–3487.

Hunt, J. C. R. & Shercliff, J. A. 1971 Magnetohydrodynamics at High Hartmann Number. *Annu. Rev. Fluid Mech.* **3** (1), 37–62.

Hussam, W. K., Hamid, A. H., Ng, Z. Y. & Sheard, G. J. 2018 Effect of vortex promoter shape on heat transfer in MHD duct flow with axial magnetic field. *Int. J. Therm. Sci.* **134**, 453–464.

Hussam, W. K. & Sheard, G. J. 2013 Heat transfer in a high Hartmann number MHD duct flow with a circular cylinder placed near the heated side-wall. *Int. J. Heat Mass Transf.* **67**, 944–954.

Hussam, W. K., Thompson, M. C. & Sheard, G. J. 2011 Dynamics and heat transfer in a quasi-two-dimensional MHD flow past a circular cylinder in a duct at high Hartmann number. *Int. J. Heat Mass Transf.* **54**, 1091–1100.

Hussam, W. K., Thompson, M. C. & Sheard, G. J. 2012a Enhancing heat transfer in a high Hartmann number magnetohydrodynamic channel flow via torsional oscillation of a cylindrical obstacle. *Phys. Fluids* **24**, 113601.

Hussam, W. K., Thompson, M. C. & Sheard, G. J. 2012b Optimal transient disturbances behind a circular cylinder in a quasi-two-dimensional magnetohydodynamic duct flow. *Phys. Fluids* **24**, 024105.

Jiménez, J. 1990 Transition to turbulence in two-dimensional Poiseuille flow. *J. Fluid Mech.* **218**, 265–297.

Jiménez, J. 2013 How linear is wall-bounded turbulence? *Phys. Fluids* **25** (11), 110814.

Jiménez, J. 2020 Monte Carlo science. *J. Turb.* **21** ((9-10)), 544–566.

Jin, B., Symon, S. & Illingworth, S. J. 2021 Energy transfer mechanisms and resolvent analysis in the cylinder wake. *Phys. Rev. Fluids* **6** (2), 024702.

Joseph, D. D. 1976 *Stability of Fluid Motions I*. Springer-Verlag Berlin Heidelberg.

Kakutani, T. 1964 The hydromagnetic stability of the modified plane Couette flow in the presence of a transverse magnetic field. *J. Phys. Soc. Jpn.* **19** (6), 1041–1057.

Kanaris, N., Albets, X., Grigoriadis, D. & Kassinos, S. 2013 Three-dimensional numerical simulations of magnetohydrodynamic flow around a confined circular cylinder under low, moderate, and strong magnetic fields. *Phys. Fluids* **25** (7), 074102.

Karniadakis, G. E., Israeli, M. & Orszag, S. A. 1991 High-order splitting methods for the incompressible Navier–Stokes equations. *J. Comput. Phys.* **97** (2), 414–443.

Karniadakis, G. E. & Sherwin, S. J. 2005 *Spectral/hp element methods for computational fluid dynamics*. Oxford University Press.

von Kerczek, C. H. 1982 The instability of oscillatory plane Poiseuille flow. *J. Fluid Mech.* **116**, 91–114.

Kerswell, R. R., Pringle, C. C. T. & Willis, A. P. 2014 An optimization approach for analysing nonlinear stability with transition to turbulence in fluids as an exemplar. *Rep. Prog. Phys.* **77**, 085901.

Khapko, T., Duguet, Y., Kreilos, T., Schlatter, P., Eckhardt, B. & Henningson, D. S. 2014 Complexity of localised coherent structures in a boundary-layer flow. *Eur. Phys. J. E* **37** (4), 1–12.

Klein, R. & Pothérat, A. 2010 Appearance of three dimensionality in wall-bounded MHD flows. *Phys. Rev. Lett.* **104** (3), 034502.

Klüber, V., Bühler, L. & Mistrangelo, C. 2019 Numerical simulations of 3D magnetohydrodynamic flows in dual-coolant lead lithium blankets. *Fusion Eng. Des.* **146**, 684–687.

Knaepen, B., Kassinos, S. & Carati, D. 2004 Magnetohydrodynamic turbulence at moderate magnetic Reynolds number. *J. Fluid Mech.* **513**, 199–220.

Kolesnikov, Y. B. & Andreev, O. V. 1997 Heat-transfer intensification promoted by vortical structures in closed channel under magnetic field. *Exp. Therm. Fluid Sci.* **15** (2), 82–90.

Kolesnikov, Y. B. & Tsinober, A. B. 1974 Experimental investigation of two-dimensional turbulence behind a grid. *Fluid Dyn.* **9** (4), 621–624.

Kraichnan, R. H. 1967 Inertial ranges in two-dimensional turbulence. *Phys. Fluids* **10** (7), 1417–1423.

Krasnov, D., Rossi, M., Zikanov, O. & Boeck, T. 2008 Optimal growth and transition to turbulence in channel flow with spanwise magnetic field. *J. Fluid Mech.* **596**, 73–101.

Krasnov, D., Zikanov, O. & Boeck, T. 2012 Numerical study of magnetohydrodynamic duct flow at high Reynolds and Hartmann numbers. *J. Fluid Mech.* **704**, 421–446.

Krasnov, D., Zikanov, O., Rossi, M. & Boeck, T. 2010 Optimal linear growth in magnetohydrodynamic duct flow. *J. Fluid Mech.* **653**, 273–299.

Krasnov, D. S., Zienicke, E., Zikanov, O., Boeck, T. & Thess, A. 2004 Numerical study of the instability of the Hartmann layer. *J. Fluid Mech.* **504**, 183–211.

Kühnen, J., Song, B., Scarselli, D., Budanur, N. B., Riedl, M., Willis, A. P., Avila, M. & Hof, B. 2018 Destabilizing turbulence in pipe flow. *Nat. Phys.* **14** (4), 386–390.

LANDAU, L. D. 1944 On the problem of turbulence. *Dokl. Akad. Nauk SSSR* **44** (8), 339–349.

LEE, D. & CHOI, H. 2001 Magnetohydrodynamic flow in a channel at low magnetic Reynolds number. *J. Fluid Mech.* **439**, 367–394.

LEHOUCQ, R. B., SORENSEN, D. C. & YANG, C. 1998 *ARPACK Users' Guide: Solution of Large-Scale Eigenvalue Problems with Implicitly Restarted Arnoldi Methods*. Society for Industrial and Applied Mathematics, Philadelphia.

LEMOULT, G., SHI, L., AVILA, K., JALIKOP, S., AVILA, M. & HOF, B. 2016 Directed percolation phase transition to sustained turbulence in Couette flow. *Nat. Phys.* **12**, 254–258.

LEVIN, O., DAVIDSSON, E. N. & HENNINGSON, D. S. 2005 Transition thresholds in the asymptotic suction boundary layer. *Phys. Fluids* **17** (11), 4104.

LINDBORG, E. 1999 Can the atmospheric kinetic energy spectrum be explained by two-dimensional turbulence? *J. Fluid Mech.* **388**, 259–288.

LINGWOOD, R. J. & ALBOUSSIÉRE, T. 1999 On the stability of the Hartmann layer. *Phys. Fluids* **11** (8), 2058–2068.

LOZANO-DURÁN, A., CONSTANTINOU, N. C., NIKOLAIDIS, M.-A. & KARP, M. 2021 Cause-and-effect of linear mechanisms sustaining wall turbulence. *J. Fluid Mech.* **914**, A8.

MARENSI, E., WILLIS, A. P. & KERSWELL, R. R. 2019 Stabilisation and drag reduction of pipe flows by flattening the base profile. *J. Fluid Mech.* **863**, 850–875.

MARTELLI, D., VENTURINI, A. & UTILI, M. 2019 Literature review of lead-lithium thermophysical properties. *Fusion Eng. Des.* **138**, 183–195.

MISTRANGELO, C. & BÜHLER, L. 2009 Influence of helium cooling channels on magnetohydrodynamic flows in the HCLL blanket. *Fusion Eng. Des.* **84** (7), 1323–1328.

MISTRANGELO, C. & BÜHLER, L. 2011 Magnetohydrodynamic pressure drops in geometric elements forming a HCLL blanket mock-up. *Fusion Eng. Des.* **86** (9), 2304–2307.

MISTRANGELO, C., BÜHLER, L. & AIELLO, G. 2014 Buoyant-MHD flows in HCLL blankets caused by spatially varying thermal loads. *IEEE Trans. Plasma Sci.* **42** (5), 1407–1412.

MOFFAT, H. K. 1967 On the suppression of turbulence by a uniform magnetic field. *J. Fluid Mech.* **28** (3), 571–592.

MOREAU, R. 1990 *Magnetohydrodynamics*. Springer-Verlag Dordrecht, Netherlands.

MOREAU, R., SMOLENTSEV, S. & CUEVAS, S. 2010 MHD flow in an insulating rectangular duct under a non-uniform magnetic field. *PMC Phys. B* **3** (1), 3–45.

MORESCO, P. & ALBOUSSIÉRE, T. 2003 Weakly nonlinear stability of Hartmann boundary layers. *Eur. J. Mech. B-Fluids* **22** (4), 345–353.

MORESCO, P. & ALBOUSSIÉRE, T. 2004 Experimental study of the instability of the Hartmann layer. *J. Fluid Mech.* **504**, 167–181.

MÜCK, B., GÜNTHER, C., MÜLLER, U. & BÜHLER, L. 2000 Three-dimensional MHD flows in rectangular ducts with internal obstacles. *J. Fluid Mech.* **418**, 265–295.

MUKUND, V. & HOF, B. 2018 The critical point of the transition to turbulence in pipe flow. *J. Fluid Mech.* **839**, 76–94.

MÜLLER, U. & BÜHLER, L. 2001 *Magnetofluiddynamics in Channels and Containers*. Springer-Verlag Berlin Heidelberg.

MURALI, S., HUSSAM, W. K. & SHEARD, G. J. 2021 Heat transfer enhancement in quasi-two-dimensional magnetohydrodynamic duct flows using repeated flow-facing wedge-shaped protrusions. *Int. J. Heat Mass Transf.* **171**, 121066.

NOUAR, C. & BOTTARO, A. 2010 Stability of the flow of a Bingham fluid in a channel: eigenvalue sensitivity, minimal defects and scaling laws of transition. *J. Fluid Mech.* **642**, 349–372.

ORR, W. 1907 The stability or instability of the steady motions of a perfect liquid and of a viscous liquid. Part II: a viscous liquid. *Proc. R. Irish Acad. A-Math. Phys. Sci.* **27**, 69–138.

OZDEMIR, C. E., HSU, T. & BALACHANDAR, S. 2014 Direct numerical simulations of transition and turbulence in smooth-walled Stokes boundary layer. *Phys. Fluids* **26** (4), 045108.

PEDLOSKY, J. 1987 *Geophysical Fluid Dynamics*. Springer Verlag, New York.

PEIXINHO, J. & MULLIN, T. 2006 Decay of turbulence in pipe flow. *Phys. Rev. Lett.* **96** (9), 094501.

PIER, B. & SCHMID, P. J. 2000 Linear and nonlinear dynamics of pulsatile channel flow. *J. Fluid Mech.* **815**, 435–480.

POPE, S. B. 2000 *Turbulent Flows*. Cambridge University Press, Cambridge.

POTHÉRAT, A. 2007 Quasi-two-dimensional perturbations in duct flows under transverse magnetic field. *Phys. Fluids* **19** (7), 074104.

Pothérat, A. & Dymkou, V. 2010 Direct numerical simulations of low-Rm MHD turbulence based on the least dissipative modes. *J. Fluid Mech.* **655**, 174–197.

Pothérat, A. & Klein, R. 2014 Why, how and when MHD turbulence at low Rm becomes three-dimensional. *J. Fluid Mech.* **761**, 168–205.

Pothérat, A. & Kornet, K. 2015 The decay of wall-bounded MHD turbulence at low Rm. *J. Fluid Mech.* **783**, 605–636.

Pothérat, A. & Schweitzer, J. 2011 A shallow water model for magnetohydrodynamic flows with turbulent Hartmann layers. *Phys. Fluids* **23** (5), 055108.

Pothérat, A., Sommeria, J. & Moreau, R. 2000 An effective two-dimensional model for MHD flows with a transverse magnetic field. *J. Fluid Mech.* **424**, 75–100.

Pothérat, A., Sommeria, J. & Moreau, R. 2005 Numerical simulations of an effective two-dimensional model for flows with a transverse magnetic field. *J. Fluid Mech.* **534**, 115–143.

Pringle, C. C. T. & Kerswell, R. R. 2010 Using nonlinear transient growth to construct the minimal seed for shear flow turbulence. *Phys. Rev. Lett.* **105** (15), 154502.

Pringle, C. C. T., Willis, A. P. & Kerswell, R. R. 2012 Minimal seeds for shear flow turbulence: using nonlinear transient growth to touch the edge of chaos. *J. Fluid Mech.* **702**, 415–443.

Pringle, C. C. T., Willis, A. P. & Kerswell, R. R. 2015 Fully localised nonlinear energy growth optimals in pipe flow. *Phys. Fluids* **27** (6), 064102.

Reddy, S. C. & Henningson, D. S. 1993 Energy growth in viscous channel flows. *J. Fluid Mech.* **252**, 209–238.

Reddy, S. C., Schmidt, P. J. & Henningson, D. S. 1993 Pseudospectra of the Orr–Sommerfeld operator. *SIAM J. Appl. Math.* **53** (1), 15–47.

Reshotko, E. 2001 Transient growth: a factor in bypass transition. *Phys. Fluids* **13** (5), 1067–1075.

Reynolds, O. 1883 An experimental investigation of the circumstances which determine whether the motion of water shall be direct or sinuous, and of the law of resistance in parallel channels. *Phil. Trans. R. Soc. London* **174**, 935–982.

Reynolds, W. C. & Potter, M. C. 1967 Finite-amplitude instability of parallel shear flows. *J. Fluid Mech.* **27** (3), 465–492.

RIVERA, M. K. 2000 The inverse energy cascade of two-dimensional turbulence. Doctor of Philosophy, University of Pittsburgh, Pennsylvania.

ROBERTS, P. H. 1967 *An Introduction to Magnetohydrodynamics*. Longmans, Green, New York.

SAPARDI, A. M., HUSSAM, W. K., POTHÉRAT, A. & SHEARD, G. J. 2017 Linear stability of confined flow around a 180-degree sharp bend. *J. Fluid Mech.* **822**, 813–847.

SCHMID, P. J. & HENNINGSON, D. S. 2001 *Stability and Transition in Shear Flows*. Springer-Verlag New York.

SCHUMANN, U. 1976 Numerical simulation of the transition from three- to two-dimensional turbulence under a uniform magnetic field. *J. Fluid Mech.* **74** (1), 31–58.

SEN, P. K. & VENKATESWARLU, D. 1983 On the stability of plane Poiseuille flow to finite-amplitude disturbances, considering the higher-order Landau coefficients. *J. Fluid Mech.* **133**, 179–206.

SHEARD, G. J., FITZGERALD, M. J. & RYAN, K. 2009 Cylinders with square cross-section: wake instabilities with incidence angle variation. *J. Fluid Mech.* **630**, 43–69.

SINGER, B. A., FERZIGER, J. H. & REED, H. L. 1989 Numerical simulations of transition in oscillatory plane channel flow. *J. Fluid Mech.* **208**, 45–66.

SMOLENTSEV, S. 2009 MHD duct flows under hydrodynamic "slip" condition. *Theor. Comput. Fluid Dyn.* **23** (6), 557–570.

SMOLENTSEV, S., MOREAU, R. & ABDOU, M. 2008 Characterization of key magnetohydrodynamic phenomena in PbLi flows for the US DCLL blanket. *Fusion Eng. Des.* **83** (5), 771–783.

SMOLENTSEV, S., MOREAU, R., BÜHLER, L. & MISTRANGELO, C. 2010a MHD thermofluid issues of liquid-metal blankets: Phenomena and advances. *Fusion Eng. Des.* **85**, 1196–1205.

SMOLENTSEV, S., SAEIDI, S., MALANG, S. & ABDOU, M. 2013 Numerical study of corrosion of ferritic/martensitic steels in the flowing PbLi with and without a magnetic field. *J. Nucl. Mater.* **432**, 294–304.

SMOLENTSEV, S., WONG, C., MALANG, S., DAGHER, M. & ABDOU, M. 2010b MHD considerations for the DCLL inboard blanket and access ducts. *Fusion Eng. Des.* **85**, 1007–1011.

SOMMERIA, J. 1986 Experimental study of the two-dimensional inverse energy cascade in a square box. *J. Fluid Mech.* **170**, 139–168.

Sommeria, J. 1988 Electrically driven vortices in a strong magnetic field. *J. Fluid Mech.* **189**, 553–569.

Sommeria, J. & Moreau, R. 1982 Why, how, and when, MHD turbulence becomes two-dimensional. *J. Fluid Mech.* **118**, 507–518.

Stewartson, K. & Stuart, J. T. 1971 A non-linear instability theory for a wave system in plane Poiseuille flow. *J. Fluid Mech.* **48** (3), 529–545.

Straatman, A. G., Khayat, R. E., Haj-Qasem, E. & Steinman, D. A. 2002 On the hydrodynamic stability of pulsatile flow in a plane channel. *Phys. Fluids* **14** (6), 1938–1944.

Stuart, J. T. 1958 On the non-linear mechanics of hydrodynamic stability. *J. Fluid Mech.* **4** (1), 1–21.

Takashima, M. 1996 The stability of the modified plane Poiseuille flow in the presence of a transverse magnetic field. *Fluid Dyn. Res.* **17** (6), 293–310.

Takashima, M. 1998 The stability of the modified plane Couette flow in the presence of a transverse magnetic field. *Fluid Dyn. Res.* **22** (2), 105–121.

Thess, A. 1992a Instabilities in two-dimensional spatially periodic flows. Part I: Kolmogorov flow. *Phys. Fluids A* **4** (7), 1385–1395.

Thess, A. 1992b Instabilities in two-dimensional spatially periodic flows. Part II: Square eddy lattice. *Phys. Fluids A* **4** (7), 1396–1407.

Thess, A. 1993 Instabilities in two-dimensional spatially periodic flows. Part III: Inviscid triangular lattice. *Phys. Fluids A* **5** (2), 335–343.

Thess, A. & Zikanov, O. 2007 Transition from two-dimensional to three-dimensional magnetohydrodynamic turbulence. *J. Fluid Mech.* **579**, 383–412.

Thomas, B. G., Singh, R., Vanka, S. P., Timmel, K., Eckert, S. & Gerbeth, G. 2015a Effect of single-ruler electromagnetic braking (EMBr) location on transient flow in continuous casting. *J. Manuf. Sci. Prod.* **15** (1), 93.

Thomas, C., Bassom, A. P., Blennerhassett, P. J. & Davies, C. 2011 The linear stability of oscillatory Poiseuille flow in channels and pipes. *Proc. R. Soc. A* **467**, 2643–2662.

Thomas, C., Bassom, A. P. & Davies, C. 2010 The linear stability of a Stokes layer with an imposed axial magnetic field. *J. Fluid Mech.* **662**, 320–328.

THOMAS, C., BLENNERHASSETT, P. J., BASSOM, A. P. & DAVIES, C. 2015b The linear stability of a Stokes layer subjected to high-frequency perturbations. *J. Fluid Mech.* **764**, 193–218.

THOMAS, C. & DAVIES, C. 2013 Global stability of the rotating-disc boundary layer with an axial magnetic field. *J. Fluid Mech.* **724**, 510–526.

TREFETHEN, L. N. 2000 *Spectral Methods in MATLAB*. Society for Industrial and Applied Mathematics, Philadelphia.

TREFETHEN, L. N., TREFETHEN, A. E., REDDY, S. C. & DRISCOLL, T. A. 1993 Hydrodynamic stability without eigenvalues. *Science* **261** (5121), 578–584.

DE LES VALLS, E. M., BATET, L., DE MEDINA, V., FRADERA, J. & SEDANO, L. A. 2011 Qualification of MHD effects in dual-coolant DEMO blanket and approaches to their modelling. *Fusion Eng. Des.* **86** (9), 2326–2329.

VAVALIARIS, C., BENEITEZ, M. & HENNINGSON, D. S. 2020 Optimal perturbations and transitions thresholds in boundary layer shear flows. *Phys. Rev. Fluids* **5** (6), 062401.

VETCHA, N. 2012 Study of instability and transition in MHD flows as applied to liquid metal blankets. Doctor of Philosophy, University of California, Los Angeles.

VO, T., MONTABONE, L. & SHEARD, G. J. 2015 Effect of enclosure height on the structure and stability of shear layers induced by differential rotation. *J. Fluid Mech.* **765**, 45–81.

VO, T., POTHÉRAT, A. & SHEARD, G. J. 2017 Linear stability of horizontal, laminar fully developed, quasi-two-dimensional liquid metal duct flow under a transverse magnetic field heated from below. *Phys. Rev. Fluids* **2**, 033902.

WALEFFE, F. 1995 Transition in shear flows. Nonlinear normality versus non-normal linearity. *Phys. Fluids* **7** (12), 3060–3066.

WALEFFE, F. 1997 On a self-sustaining process in shear flows. *Phys. Fluids* **9** (4), 883–900.

WEIDEMAN, J. A. C. & REDDY, S. C. 2001 A MATLAB differentiation matrix suite. *ACM Trans. Math. Softw.* **26** (4), 465–519.

XIAO, Z., WAN, M., CHEN, S. & EYINK, G. L. 2009 Physical mechanism of the inverse energy cascade of two-dimensional turbulence: a numerical investigation. *J. Fluid Mech.* **619**, 1–44.

YOUNG, J., SMOLENTSEV, S. & ABDOU, M. 2014 Study of instabilities in a quasi-2D MHD duct flow with an inflectional velocity profile. *Fusion Eng. Des.* **89**, 1163–1167.

ZAMMERT, S. & ECKHARDT, B. 2019 Transition to turbulence when the Tollmien–Schlichting and bypass routes coexist. *J. Fluid Mech.* **880**, R2.

ZIENICKE, E. A. & KRASNOV, D. 2005 Parametric study of streak breakdown mechanism in Hartmann flow. *Phys. Fluids* **17**, 114101.

ZIKANOV, O., LISTRATOV, Y. I. & SVIRIDOV, V. G. 2013 Natural convection in horizontal pipe flow with a strong transverse magnetic field. *J. Fluid Mech.* **720**, 486–516.

ZIKANOV, O. & THESS, A. 1998 Direct numerical simulation of forced MHD turbulence at low magnetic Reynolds number. *J. Fluid Mech.* **358**, 299–333.